UNIVERSITY
OF TASMANIA

Kimberlites: Understanding their Petrogenesis and Uncovering the Identity of their Source Composition

Adam Abersteiner

Bsc. University of Melbourne
Bsc. (Hons) University of Tasmania

School of Natural Sciences (Earth Sciences)

Submitted in fulfilment of the requirements for the degree of
Doctor of Philosophy
University of Tasmania

October 2019

Table of Contents

Chapter 12 - Synthesis

List of Figures and Tables

List of Appendices

Abstract

Kimberlites are one of the rarest and most volumetrically insignificant igneous rocks, which are derived from deep-seated (>150 km) magmas that originate in the subcontinental lithospheric mantle (SCLM) or asthenosphere. This deep origin, in conjunction with their intermittent relationship with deep crustal and mantle xenoliths and xenocrysts, including diamonds, renders kimberlites an invaluable tool for studying the composition and nature of intracontinental magmatism and the mantle. Despite more than half a century of research, the identity of parental/primary kimberlite melts in the mantle remains hotly debated. This is largely attributed to numerous processes which inescapably modify kimberlite magmas during magmatic ascent and upon emplacement in the crust. These processes include the entrainment and assimilation of mantle and crustal rocks, volatile (H_2O, CO_2) degassing, magma differentiation and syn- and/or post-magmatic alteration (i.e. serpentinisation). Constraining and quantifying these effects is therefore an essential task for constructing a complete understanding of kimberlite magmatism and petrogenesis. This thesis presents petrographic, geochemical and melt/fluid inclusion data of kimberlitic rocks and minerals from localities worldwide (Russia, South Africa, Finland, Canada) in order to: i) provide new constraints on the composition and evolution of kimberlite melts during and/or prior to magmatic ascent, solidification and post-magmatic alteration, ii) reconstruct the sequence of crystallisation of kimberlite minerals by examining textural relationships, zoning patterns and hosted inclusions, and iii) understand the processes that modify kimberlite magmas and rocks after their emplacement.

An important technique used for examining the composition and evolution of kimberlite magmas prior to post-magmatic processes is the study of different generations (i.e. primary, pseudosecondary and secondary) which can provide snapshots of the melt at a particular stage of magma evolution. Melt/fluid inclusions were examined in xenocrystic olivine and megacrysts, as well as various magmatic groundmass minerals such as olivine, spinel, perovskite, monticellite, apatite and carbonates. Although these inclusions in kimberlitic minerals are extremely heterogeneous in composition and contain a diversity of daughter phase assemblages, they are all consistently shown contain abundant Ca-Mg- and Na-K-Ba-Sr- carbonates, Na-K-chlorides, F-bearing halides, phosphates, sulphates/sulphides and oxides. In contrast, (hydrous-)silicate minerals are either rare or absent. The daughter mineral assemblages in primary melt inclusions hosted by magmatic minerals show a systematic trend, where early crystallising phases (e.g., olivine, chromite) exhibit more silicate-

carbonate compositions, whereas late-stage minerals (e.g., apatite, carbonate) contain more evolved, carbonate-rich compositions that are enriched in phosphates, alkalis/alkali-earths and halogens. These compositional differences likely occurred in response to fractional crystallisation of constituent minerals (e.g., silicates, oxides). Examination of the Benfontein Sill Complex (South Africa) demonstrated that under quiescent intrusive settings, kimberlite magmas may undergo even more extreme degrees of fractionation towards essentially carbonatitic compositions, which are enriched in light rare earth elements (LREEs), high field strength elements (HFSEs), alkalis/alkali-earths and halogens. The abundance of alkalis/alkali-earths and halogens in melt inclusions hosted by kimberlitic minerals is at odds with their very low concentrations in kimberlite whole-rock. Melt inclusion evidence suggests that parental kimberlite melts were potentially much more enriched in alkalis/alkali-earths and halogens. However, these components were likely exsolved from the magma system during magmatic ascent/emplacement, or leached from the groundmass during syn- and/or post-magmatic alteration (i.e. serpentinisation).

A revealing feature of melt inclusions, in particular in groundmass monticellite and monticellite rims replacing kimberlitic olivine, is that they may provide evidence of melt-crystal reactions that occurred during groundmass crystallisation. Combined textural and petrographic data of monticellite partially replacing olivine combined with the presence of abundant periclase inclusions demonstrates that that monticellite in some kimberlites formed as result a decarbonation reaction between the carbonate component of the kimberlite melt and olivine in order to produce monticellite, periclase and CO_2. It is inferred that CO_2 was ultimately lost due to degassing and periclase also existed in the groundmass, but was subsequently altered to brucite during post-magmatic alteration. Furthermore, CO_2 removal is a likely driver of this decarbonation reaction, where additional degassing of CO_2 causes this reaction to proceed further in order to maintain equilibrium. This process may in turn be a commonly overlooked process in the exsolution of CO_2 in kimberlite eruptions.

One of the most intriguing cases that challenge previous kimberlite melt models is the petrologically unique Udachnaya-East (Russia) kimberlite. This locality is characterised by unserpentinised units, which contain fresh olivine and groundmass that is composed of the same alkali- and halogen-rich minerals (e.g., carbonates, chlorides, sulphides/sulphates) that are ubiquitously found in melt inclusions hosted in kimberlitic minerals in this kimberlite, as well as from localities worldwide. Combined petrographic, geochemical and melt inclusion evidence presents new evidence countering the ‘crustal contamination model’, which

previously asserted that Udachnaya-East was either intruded evaporites or were permeated by platform brines. Comparisons between the unserpentinised and serpentinised varieties of the Udachnaya-East kimberlite show that they share numerous mineralogical and geochemical similarities, but are distinguished by: i) the presence of fresh olivine and abundant groundmass Na-K-Cl-S-rich minerals and absence of H_2O-rich phases (i.e. serpentine, iowaite ($Mg_4Fe^{3+}(OH)_8OCl•3(H_2O)$)) in unserpentinised units, and ii) the absence of alkali-Cl-rich groundmass phases and incipient-to-ubiquitous olivine alteration in serpentinised varieties. Examination of melt inclusions in olivine and groundmass minerals in both serpentinised and unserpentinised kimberlite varieties show that they virtually identical and both enriched in alkalis-Cl-S, therefore indicating that these components were an intrinsic part of the kimberlite melt, originating in the mantle. Although the unserpentinised units of the Udachnaya-East kimberlite may represent an example of 'pristinely preserved' kimberlite, it is unique, and thus producing a universal primary kimberlite melt model using this locality is tenuous.

Additional evidence of alkali and halogen enrichment in the parental/primary kimberlite melts in the mantle was obtained from the study of metasomatised mantle minerals. The presence of djerfisherite ($K_6(Fe,Ni,Cu)_{25}S_{26}Cl$) rims surrounding Fe-Ni-Cu sulphides in mantle xenoliths and as inclusions in rock-forming minerals are interpreted to be the result of modal metasomatism by infiltrating K-Cl-bearing kimberlitic melts/fluids reacting with precursory sulphides, which likely occurred close to the timing of, or during kimberlite magma ascent. In addition, large polymineralic inclusions and micro melt inclusions hosted in kimberlite-hosted megacrysts (e.g., clinopyroxene, olivine) are texturally and geochemically interpreted to have formed due to kimberlite melt infiltrating along crystal defects. Significant disequilibria between the megacrysts and the permeating kimberlite melt resulted in the formation of hybrid daughter mineral assemblages within these inclusions. Micro melt inclusions became completely isolated during fracture healing and are shown to contain entrapped remnants of variably differentiated kimberlite melt that was more enriched in alkalis-Cl-S-CO_2 than polymineralic inclusions and the kimberlite whole-rock, which were modified during post-magmatic alteration.

The combined study of melt/fluid inclusions in xenocrystic and magmatic kimberlitic minerals from localities worldwide have all demonstrated a consistent trend, which shows that they interacted and/or entrapped a variably differentiated aluminosilicate- and H_2O-poor, Ca-Mg-, halogen- (F, Cl) and alkali- (Na, K) bearing melt, that contained varying amounts of

alkali-earths (Ba, Sr), phosphorus and sulphur. This composition may be a more likely candidate for primary/parental kimberlite melt compositions, as opposed to the classical 'ultramafic, H_2O- and silicate-bearing' model. In summary, this thesis demonstrates the strong potential of melt/fluid inclusion studies in circumventing processes that intermittently contaminate kimberlite rocks and gain insight into the composition and evolution of kimberlite melts during ascent and emplacement.

Statements and Declarations

Declaration of originality

This thesis contains no material which has been accepted for a degree or diploma by the University or any other institution, except by way of background information and duly acknowledged in the thesis, and to the best of my knowledge and belief no material previously published or written by another person except where due acknowledgement is made in the text of the thesis, nor does the thesis contain any material that infringes copyright

Signed: Dated: 30/10/2019

Authority of access

This thesis may be made available for loan and limited copying and communication in accordance with the Copyright Act 1968.

Signed: Dated: 30/10/2019

Statement regarding published work contained in this thesis

The publishers of the papers comprising Chapters 2 – 11 hold the copyright for that content and access to the material should be sought from the corresponding journals. The remaining non-published content of the thesis may be made available for loan and limited copying and communication in accordance with the Copyright Act 1968.

Signed: Dated: 30/10/2019

Statement of authorship – List of authors

The following people contributed to the preparation, publication and submission of the work undertaken in this thesis:

Candidate, Author 1: Adam Abersteiner, School of Natural Sciences, University of Tasmania.

Author 2: Vadim S. Kamenetsky, Primary Supervisor, School of Natural Sciences, University of Tasmania.

Author 3: Karsten Goemann, Co-Supervisor, Central Science Laboratory, University of Tasmania.

Author 4: Maya Kamenetsky, Co-Supervisor, School of Natural Sciences, University of Tasmania.

Author 5: Andrea Giuliani, KiDs (Kimberlites and Diamonds), School of Earth Sciences, The University of Melbourne, and ARC Centre of Excellence for Core to Crust Fluid Systems (CCFS) and GEMOC, Department of Earth and Planetary Sciences, Macquarie University, Institute of Geochemistry and Petrology, Department of Earth Sciences, ETH Zurich, Zurich, Switzerland.

Author 6: Kathy Ehrig, BHP Olympic Dam.

Author 7: D. Graham Pearson, Department of Earth and Atmospheric Sciences, University of Alberta.

Author 8: Thomas Rodemann, Central Science Laboratory, University of Tasmania.

Author 9: Alexander V. Golovin, Sobolev Institute of Geology and Mineralogy, Siberian Branch Russian Academy of Sciences.

Author 10: Igor S. Sharygin, Sobolev Institute of Geology and Mineralogy, Siberian Branch Russian Academy of Sciences.

Author 11: Zdislav V. Spetsius, Geo-Scientific Investigation Enterprise, ALROSA PJSC.

Author 12: Geoffrey H. Howarth, Department of Geological Sciences, University of Cape Town, and Department of Geology, University of Georgia.

Author 13: Bruce Kjarsgaard, Geological Survey of Canada.

Author 14: Jay Thompson, School of Natural Sciences, University of Tasmania.

Author 15: Alexander Cherry, School of Natural Sciences, University of Tasmania.

Author 16: David Phillips, KiDs (Kimberlites and Diamonds), School of Earth Sciences, The University of Melbourne.

Author 17: Montgarri Castillo-Oliver, ARC Centre of Excellence for Core to Crust Fluid Systems (CCFS) and GEMOC, Department of Earth and Planetary Sciences, Macquarie University.

Author 18: Marina A. Gornova, A.P. Vinogradov Institute of Geochemistry, Siberian Branch of RAS.

Proportion of work undertaken towards papers

Paper 1 - Petrographic and melt-inclusion constraints on the petrogenesis of a magmaclast from the Venetia kimberlite cluster, South Africa

(Chapter 2 – Published in Chemical Geology)

Candidate was the primary author and with authors 2, 5 and 16 contributed to the structure and design of the research, as well as data collection and interpretation. The majority of revisions were provided by authors 2 and 5.

Candidate contributed approximately 85% to the planning, execution, and preparation of this paper.

Paper 2 - Monticellite in group-I kimberlites: Implications for evolution of parental melts and post-emplacement CO_2 degassing

(Chapter 3 – Published in Chemical Geology)

Candidate was the primary author and with authors 2, 3 and 7 contributed to the structure and design of the research. Authors 3, 4, 6 and 8 assisted in data collection and interpretation. The majority of revisions were provided by authors 2 and 7.

Candidate contributed approximately 90% to the planning, execution, and preparation of this paper.

Paper 3 - Significance of halogens (F, Cl) in kimberlite melts: Insights from mineralogy and melt inclusions in the Roger pipe (Ekati, Canada)

(Chapter 4 – Published in Chemical Geology)

Candidate was the primary author and with authors 2 and 3 contributed to the structure and design of the research. Authors 3, 4, 6 and 8 assisted in data collection and interpretation. The majority of revisions were provided by author 2.

Candidate contributed approximately 95% to the planning, execution, and preparation of this paper.

Paper 4 - Was crustal contamination involved in the formation of the serpentine-free Udachnaya-East kimberlite? New insights into parental melts, liquidus assemblage and effects of alteration

(Chapter 5 – Published in Journal of Petrology)

Candidate was the primary author and with authors 2, 3 and 9 contributed to the structure and design of the research. Authors 3 and 4 assisted in data collection and interpretation. The majority of revisions were provided by authors 2 and 9.

Candidate contributed approximately 90% to the planning, execution, and preparation of this paper.

Paper 5 - Djerfisherite in kimberlites and their xenoliths: implications for kimberlite melt evolution

(Chapter 6 – Published in Contributions to Mineralogy and Petrology)

Candidate was the primary author and with authors 2, 3, 5, 9 and 10 contributed to the structure and design of the research. Authors 3, 4, 8, 9, 10 and 11 assisted in data collection and interpretation. The majority of revisions were provided by authors 2, 3, 5, 9 and 10.

Candidate contributed approximately 85% to the planning, execution, and preparation of this paper.

Paper 6 - Composition and emplacement of the Benfontein kimberlite sill complex (Kimberley, South Africa): Textural, petrographic and melt inclusion constraints

(Chapter 7 – Published in Lithos)

Candidate was the primary author and with authors 2, 5, 12 and 17 contributed to the structure and design of the research. Authors 3, 4, 14 and 15 assisted in data collection and interpretation. The majority of revisions were provided by authors 2, 5, 12 and 17.

Candidate contributed approximately 95% to the planning, execution, and preparation of this paper.

Paper 7 - Polymineralic inclusions in kimberlite-hosted megacrysts: Implications for kimberlite melt evolution

(Chapter 8 – Published in Lithos)

Candidate was the primary author and with authors 2, 7, 9 and 10 contributed to the structure and design of the research. Authors 3, 4, 9, 10 and 18 assisted in data collection and interpretation. The majority of revisions were provided by authors 2, 7, 9 and 10.

Candidate contributed approximately 95% to the planning, execution, and preparation of this paper.

Paper 8 - A genetic story of olivine crystallisation in the Mark kimberlite (Canada) revealed by zoning and melt inclusions

(Chapter 9 – Published in Lithos)

Candidate was the primary author and with authors 2 and 13 contributed to the structure and design of the research. Authors 3, 4 and 8 assisted in data collection and interpretation. The majority of revisions were provided by authors 2 and 13.

Candidate contributed approximately 95% to the planning, execution, and preparation of this paper.

Paper 9 - Evolution of kimberlite magmas in the crust: A case study of groundmass and mineral-hosted inclusions in the Mark kimberlite (Lac de Gras, Canada)

(Chapter 10 – Submitted to Lithos)

Candidate was the primary author and with authors 2 and 13 contributed to the structure and design of the research. Authors 3, 4 and 6 assisted in data collection and interpretation. The majority of revisions were provided by authors 2 and 13.

Candidate contributed approximately 95% to the planning, execution, and preparation of this paper.

Paper 10 - A Reply to the Comment by Kostrovitsky, S. and Yakovlev, D. on 'Was crustal contamination involved in the formation of the serpentine-free Udachnaya-East kimberlite? New insights into parental melts, liquidus assemblage and effects of alteration' by Abersteiner et al. [J. Petrol. 59 (2018) 1467-1492]

(Chapter 11 – Published in Journal of Petrology)

Candidate was the primary author and with authors 2 and 9 contributed to the structure and design of the research. The majority of revisions were provided by authors 2 and 9.

Candidate contributed approximately 90% to the planning, execution, and preparation of this paper.

We the undersigned agree with the above stated "proportion of work undertaken" for each of the above published or submitted peer-reviewed papers contributing to the thesis:

Signed:	_____	_____
	Vadim Kamenetsky	Sebastien Meffre
	Supervisor	Head of Discipline (Earth Sciences)
	School of Natural Sciences	School of Natural Sciences
	University of Tasmania	University of Tasmania
Date:	30.10.2019	30.10.2019

Publications during the course of the thesis

Journal articles

Abersteiner, A., Giuliani, A., Kamenetsky V. S., Phillips, D., 2016. Petrographic and melt-inclusion constraints on the petrogenesis of a magmaclast from the Venetia kimberlite cluster, South Africa. *Chemical Geology* **455**, 331-341.

Abersteiner, A., Kamenetsky V. S., Kamenetsky M., Goemann, K., Ehrig, K. 2017a. Monticellite in Group-I kimberlites: Implications for the evolution of parental melts and CO_2 degassing after emplacement. *Chemical Geology* **478**, 76-88.

Abersteiner, A., Kamenetsky V. S., Kamenetsky M., Goemann, K., Ehrig, K., Rodemann, T., 2017b. Significance of halogens (F, Cl) in kimberlite melts: Insights from mineralogy and melt inclusions in the Roger pipe (Ekati, Canada). *Chemical Geology* **478**, 148-163.

Abersteiner, A., Kamenetsky, V. S., Golovin, A. V., Goemann, K., Kamenetsky, M., 2019. Was crustal contamination involved in the formation of the serpentine-free Udachnaya-East kimberlite? New insights into parental melts, liquidus assemblage and effects of alteration. *Journal of Petrology* **59**, 1467-1492.

Abersteiner, A., Kamenetsky, V. S., Goemann, K., Golovin, A. V., Sharygin, I. S., Rodemann, T., Giuliani, A., Spetsius, Z. V., Kamenetsky, M., 2019. Djerfisherite in kimberlites and their xenoliths: Implications for kimberlite melt evolution. *Contributions to Mineralogy and Petrology*, 174:8.

Abersteiner, A., Kamenetsky, V. S., Goemann, K., Giuliani, A., Howarth, G.H., Castillo-Oliver, M., Thompson, J., Kamenetsky, M., Cherry, A., 2019. Composition and emplacement of the Benfontein Kimberlite Sill Complex: Textural, petrographic and melt inclusion constraints (Kimberley, South Africa). *Lithos* **324-325**, 297-314.

Abersteiner, A., Kamenetsky, V.S., Golovin, A.V., Sharygin, I.S., Kamenetsky, M., Goemann., K. 2019. Polymineralic Inclusions in kimberlite-hosted megacrysts: Implications for kimberlite melt evolution. *Lithos* **336-337**, 310-325.

Abersteiner, A., Kamenetsky V. S., Kamenetsky M., Goemann, K., Kjarsgaard, B., Ehrig, K., Rodemann, T. A genetic story of olivine crystallisation in the Mark kimberlite (Canada) revealed by zoning and melt inclusions. *Lithos* **358-359**, 105405.

Abersteiner, A., Kamenetsky V. S., Kamenetsky M., Goemann, K., Kjarsgaard, B., Ehrig, K., Rodemann, T. Evolution of kimberlite magmas in the crust: A case study of groundmass and mineral-hosted inclusions in the Mark kimberlite (Lac de Gras, Canada). *Lithos* (Submitted Manuscript).

Abersteiner, A., Kamenetsky, V. S., Golovin, A. V., 2020. A reply to the comment by Kostrovitsky, S. and Yakovlev, D. on 'Was crustal contamination involved in the formation of the serpentine-free Udachnaya-East kimberlite? New insights into parental melts, liquidus assemblage and effects of alteration' by Abersteiner et al. [J. Petrol. 59 (2018) 1467-1492]. *Journal of Petrology*, 1-7.

Conference publications

Abersteiner, A., Kamenetsky V. S., Kamenetsky M., Goemann, K., Ehrig, K. 2017a. Monticellite in Group-I kimberlites: Implications for the evolution of parental melts and CO_2 degassing after emplacement, in 11th International Kimberlite Conference – September 2017, Gaborone, Botswana

Abersteiner, A., Kamenetsky V. S., Kamenetsky M., Goemann, K., Ehrig, K., Rodemann, T., 2017b. Significance of halogens (F, Cl) in kimberlite melts: Insights from mineralogy and melt inclusions in the Roger pipe (Ekati, Canada), in 11th International Kimberlite Conference – September 2017, Gaborone, Botswana.

Abersteiner, A., Kamenetsky V. S., Kamenetsky M., Goemann, K., 2019. Melt and fluid inclusion perspective on kimberlite melts: Insights into carbon in the subcontinental lithospheric mantle, in Carbon Down Under – July, 2019, Sydney, Australia.

Abersteiner, A., Kamenetsky V. S., Kamenetsky M., Goemann, K., 2019. Reconstructing primary kimberlite melt compositions: Insights from melt inclusions, in (a) Baikal Youth Science Conference in Geology and Geophysics, Ulan-Ude, Russia (August, 2019), (b) The 7th international conference Large Igneous Provinces Through Earth History , Tomsk, Russia, (September, 2019), (c) All Russian Scientific Conference, Yekaterinburg, Russia (September, 2019).

Acknowledgements

Скучно на этом свете, господа!

(It's dull in this world, gentlemen!)

Nikolai Gogol

Kimberlites are perhaps one of the most fascinating and enigmatic frontiers in geoscience as they are surrounded by the allure of diamonds and present a rare and unique opportunity to look into the Earth's mantle. As exciting as this concept may seem, kimberlites are shrouded by an aura of mystique, as the information that they contain is often masked by processes that must first be deciphered. Thus, the pursuit of understanding the origin of kimberlites is no trivial task. My journey into the realm of kimberlite petrology begun in mid-2014 when I met Dima Kamenetsky at UTas after a serendipitous discovery of melt inclusions in kimberlitic chromites during the course of my undergraduate study at the University of Melbourne. It was at that point that Dima introduced me to the exciting world of kimberlite research and the many challenges it faced. So first and foremost, I would like to thank Dima, my primary supervisor, who gave immeasurable guidance, support and most of all wisdom throughout my candidature. Dima has generously shared his wealth of knowledge and vision in order to assist me throughout my PhD. For that, I am extremely grateful. In addition, I would like to thank my co-supervisors, Maya Kamenetsky and Karsten Goemann for their enormous support and expertise in analytical work and data interpretation.

From the UTas, I would like to thank Thomas Rodemann for his assistance in Raman analyses and Jay Thompson for helping with geochronology interpretation. I would also like to thank Kathy Ehrig from BHP for her assistance in whole-rock analyses. Furthermore, my numerous co-authors spread across Australia, Canada, South Africa and Russia have all provided useful ideas, samples and data, which has been essential to making each aspect of my PhD thesis possible. Finally, I would like to thank the two anonymous reviewers of this thesis for provided constructive criticism that further improved this thesis.

My sanity and dedication to my PhD could not have been maintained without support and friendships from my fellow UTas staff, PhD and Honours comrades. My experience would not be complete without the fond discussions, expeditions and memories shared with

these people. In particular, the sapphire laden Frome River (NE, Tasmania) and Tasmanian wilderness provided me with the much needed getaway to refresh my mind! Finally, I would like to thank my family in Melbourne for their unyielding support and encouragement. On one last final note, I would like to say that a thesis is never truly finished. At one point or another you must lay down the pen (or close the document) and submit the thesis, but the pursuit of knowledge will always continue!

Chapter 1 – Introduction

1.0 Definition and classification of kimberlites

Kimberlites are extremely rare and volumetrically insignificant igneous rocks that originate from deeply derived (>150 km) magmas that formed in the subcontinental lithospheric mantle (SCLM) or upper asthenosphere. The study of kimberlites is important as they commonly contain abundant mantle and crustal xenoliths and xenocrysts, including diamond, thereby providing unique insights into the nature and processes of the deep crust and SCLM. This has led kimberlites to attract an almost disproportionate amount of attention from the geoscience and exploration communities, which seek to understand their intermittent relationship with diamonds, petrogenesis and ultimate origin. However, despite more than sixty years of research and eleven international conferences dedicated to this rare rock, many aspects regarding the composition and evolution of primary/parental kimberlite melts, style of emplacement and origin still remain enigmatic. The specific theme of this thesis is to elucidate the original composition of primary/parental kimberlite melts in the mantle and how they evolve during magmatic ascent, upon their emplacement in the upper crust and post-solidification.

Kimberlite geochemistry and mineralogy

The textural, mineralogical and geochemical complexity of kimberlite rocks has resulted in numerous classification models that have been continuously revised. Kimberlites *sensu stricto* (also referred to as Group-I or archetypal kimberlites; Becker and le Roex, 2006; Mitchell, 1995; Smith, 1983) are classified as group of silica-undersaturated, ultramafic, volatile-rich ($CO_2 \pm H_2O$) and potassic (i.e. low Na_2O/K_2O ratios) igneous rocks (Becker and le Roex, 2006; Mitchell, 1986; Scott-smith et al., 2018). In comparison to other ultramafic rocks, kimberlites are distinctly enriched in light rare earth elements (LREEs) and depleted in heavy rare earth elements (HREEs) (Dawson, 1980; le Roex et al., 2003; Mitchell, 1986). Kimberlites are characterised by distinct inequigranular textures due to the presence of macrocrystic and occasionally megacrystic minerals, which are set in a fine groundmass. The macro/megacryst assemblage is comprised of rounded-to-anhedral shaped forsteritic olivine, enstatite, Cr-poor clinopyroxene, phlogopite, Cr-poor titanian pyrope, ilmenite, Ti-poor chromite and zircon as common phases (Gurney et al., 1979; Harte and Gurney, 1981; Mitchell, 1986). Olivine is invariably the most abundant (~25 – 60 vol.%)

mineral in kimberlites, where it may have both macrocrystic and magmatic origins (Arndt et al., 2010; Brett et al., 2009; Kamenetsky et al., 2008; Moore, 1988; Pilbeam et al., 2013). The groundmass typically consists of olivine microphenocrysts, along with varying proportions of phlogopite-kinoshitalite, Cr-Mg-Fe-Ti-Al spinel (titaniferous magnesian aluminous chromite titanian chromite and magnesian ulvöspinel-ulvöspinel-magnetite series), monticellite, diopside, perovskite, apatite, carbonate (e.g., dolomite/calcite) and serpentine. In addition, kimberlites commonly contain fragments of rocks and minerals that are of crustal (e.g., country rock) and mantle (e.g., peridotite, eclogite) origin.

Distribution of kimberlites through time and space

Kimberlites are the products of intra-plate magmatism and have been documented on all continents (Eckstrand et al., 1995; Jelsma et al., 2009; Yaxley et al., 2013). Kimberlites are typically emplaced as clusters or provinces that are restricted to thick Archean cratons and the Palaeoproterozoic mobile belts that surround them. Notable kimberlite provinces include those in Canada, southern Africa, Brazil, Australia, United States, India, Greenland, Tanzania and Siberia (Fig. 1.1). Kimberlite emplacement ages range from between ~2 Ga (Donnelly et al., 2012; Graham et al., 2004; Gurney et al., 2010; Haggerty, 1994; Tappe et al., 2014) through to the Miocene (22 Ma) and present day (9 – 12 ka; Brown et al., 2012). Kimberlite

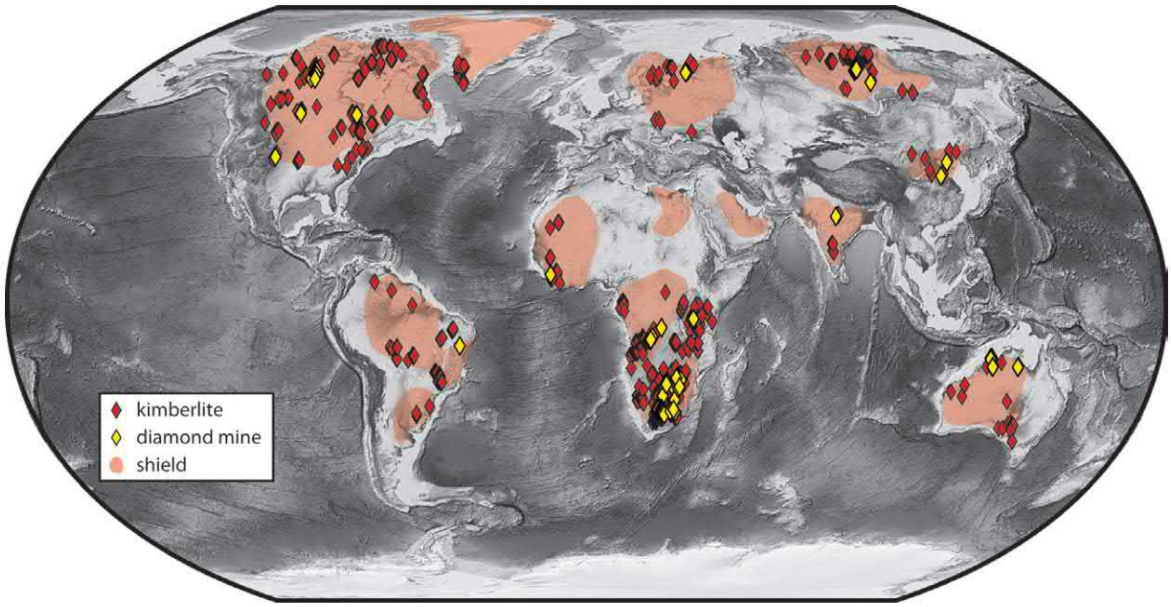

Figure 1.1. Global distribution of kimberlites and economic kimberlite diamond mines (Giuliani et al., 2019).

magmatism appears to be episodic through geological time. Periods of short duration (~10 my) produced prolific kimberlite activity in North America and Yakutia between 48 – 60, 95 – 105 and 150 – 160 Ma, whereas in southern Africa, more continuous kimberlite activity was identified between 70 – 95 and 105 – 120 Ma (Heaman et al., 2003). In addition, numerous other short periods of intensified kimberlite activity has been recorded in the pre-Mesozoic, as well as periods of quiescent kimberlite activity between 250 – 360 Ma. Some kimberlite magmatism events have been spatially and temporally linked to mantle plume-generated large igneous provinces (Ernst and Jowitt, 2013) or the rifting and breakup of supercontinents (Heaman et al., 2003), mantle plume tails (or hotspot tracks; Heaman and Kjarsgaard, 2000), the result of vigorous returning mantle flow into areas near convergent plate margins (Tappe et al., 2013), or with even no obvious link to any of the above processes.

Models of kimberlite magmatism

Kimberlitic magmas ascend very rapidly (several m/s – 20 m/s Canil and Fedortchouk 1999, Sparks et al., 2006) from their mantle source and may be emplaced intrusively within the crust, or upon reaching the surface can erupt explosively (Sparks, 2013). Kimberlites typically form small volume bodies, which are comprised of sub-vertical composite volcanic pipes (i.e. crater and diatreme facies) and intrusive sheets (or root zone, i.e. dykes and sills; Fig. 1.2; Dawson, 1971; Hawthorne, 1975; Mitchell, 1986, Sparks, 2013; Scott-Smith et al., 2018). The upper crater facies is typically composed of pyroclastic, resedimented volcaniclastic and epiclastic volcanic rocks. The diatreme zone is typically infilled by syn-eruptive and/or post-eruptive material (e.g., volcaniclastic, pyroclastic) and the root zone is the deepest part (i.e. hypabyssal) of the kimberlite body and is infilled by coherent material (i.e. unexploded or brecciated).

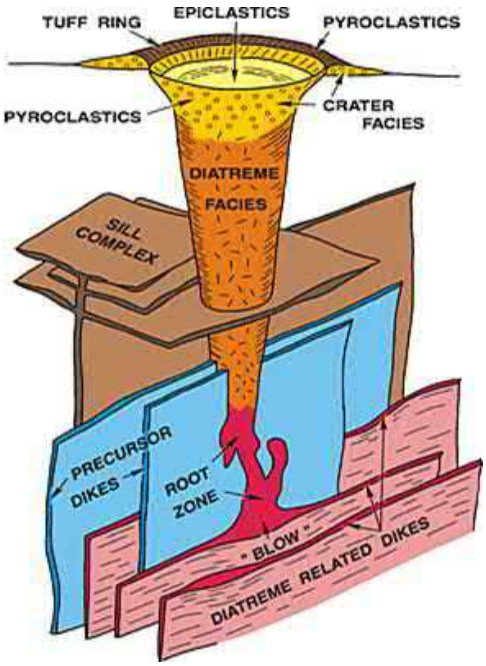

Figure 1.2. A simplified model of the magmatic system of a kimberlite pipe (after Mitchell, 1986), showing the relationships of the zones: crater, diatreme and root zone, which includes dykes and sills.

Generation of kimberlites

Although the exact source composition, volatile-content, as well as pressure and temperature parameters of kimberlite melt generation are not fully understood, there are some general constraints. The low silica-content and enrichment in carbonate and incompatible trace elements in kimberlite melts is considered to be the result of very low degrees of partial melting of either carbonated peridotite (Brey et al., 2008; Dalton and Presnall, 1998) or carbonated eclogite (Nowell et al., 2004; Paton et al., 2009) that may be coupled with metasomatism by asthenospheric melts (e.g., Gaffney et al., 2007). Experimental studies of phase relationships of kimberlite systems suggest melt generation occurs at pressures greater than 60 kbar, or within the diamond stability field (>150 – 200 km; Haggerty, 1994; Pearson et al., 2014; Ringwood et al., 1992; Tainton and McKenzie, 1994; Torsvik et al., 2010). This is supported by the entrainment of deep mantle xenoliths, such as sheared peridotites, which originate from depths >230km (Kennedy et al., 2002) and ultra-deep diamonds (Pearson et al., 2014). Radiogenic isotopic systematics (i.e. Sr-Nd-Hf-Pb) of kimberlites demonstrate overlap with ocean island basalts (OIB; Nowell et al., 2004; Smith, 1983; Tappe et al., 2013), thereby indicating an aesthenospheric or deep lithospheric source of kimberlites. Furthermore, there is growing evidence to show that subducted oceanic crust interacted with mantle rocks within the kimberlite source region (Förster et al., 2019; Gaffney et al., 2007; Nowell et al., 2004).

Diamonds and kimberlites

Diamonds are a rare mineral in kimberlites where they reach only parts-per-billion levels, even within the most diamondiferous kimberlites. However, in rare cases diamonds have been recorded up to 10 – 15 vol.% in eclogitic xenoliths (Shirey et al., 2013). The stability of diamonds has rendered them an ideal mineral for examining the deep carbon cycle. In addition, melt/fluid inclusions that are entrapped in diamond during growth provide important insights into the evolution of physical and chemical conditions of the substrate from which diamonds formed. Until the advent of radiometric dating, diamonds in kimberlites were considered to be an intrinsic part of kimberlite magma crystallisation. However, dating of inclusions in diamonds (i.e. peridotitic or eclogitic mineral associations; Kramers, 1979; Richardson et al., 1984) showed that diamonds are significantly older (billions of years) than the host kimberlite, thereby demonstrating that diamond formation is unrelated to kimberlite magmatism. It is now well-established that diamonds are mantle-

derived xenocrysts entrained by ascending kimberlite magmas, where they originally formed in the SCLM (or the diamonds stability field: >150km), or at even greater depths in the lithospheric mantle and/or mantle transition zone (up to 700km or greater; Boyd and Gurney, 1986; Kaminsky et al., 2001; Moore and Gurney, 1985; Pearson et al., 2014; Stachel et al., 2015). Diamonds are generally thought to be the products of metasomatic processes (e.g., Haggerty 1999; Stachel and Harris, 1997; Taylor et al., 1998) that are related to migrating supercritical C-O-H fluids/melts percolating through mantle rocks (e.g., peridotite, eclogite) in which carbon is reduced via redox reactions. Entrapped fluid inclusions in diamonds reveal a variety of compositions that range from saline (K/Na), siliceous, through to low- and/or high-Mg carbonatitic (Izraeli et al., 2001; Klein-BenDavid et al., 2007, 2009; Navon et al., 1988; Weiss et al., 2015). These entrapped fluids likely represent the growth medium that was in equilibrium with diamonds, however, the source of these fluids in the lithospheric mantle is enigmatic (e.g., Jablon and Navon, 2016). Recent studies have suggested that these alkalis and chlorides may be introduced into the diamond growth region by means of subducted seawater in altered oceanic crust (Förster et al., 2019; Weiss et al., 2015).

1.1 Significance and aims: origin of kimberlite melts

Accurate identification of parental kimberlite melt compositions is essential to understanding its source region, including the depth and temperature of melt generation, as well as triggers for magmatism and the physical properties of the melt. Uncertainty regarding the compositional identity of kimberlite melts in the mantle has subsequently resulted in divergent views. In the absence of quenched magmatic glasses, the traditional approach towards estimating kimberlite melt compositions was through the examination of whole-rock analyses of hypabyssal and/or aphanitic varieties, which broadly describe kimberlite melts to be silica-poor (~25 – 35 wt.%), ultramafic (~25 – 35 wt.%) and CaO-rich (~12 – 20 wt.%) with variable volatile (H_2O, CO_2) concentrations (e.g., Becker and le Roex, 2006; Kjarsgaard et al., 2009; Kopylova et al., 2007; le Roex et al., 2003; Price et al., 2000). However, experimental studies of these reconstructed kimberlite compositions have shown them to contain excessive MgO to have been in equilibrium with their mantle source rocks (Kopylova et al., 2007). Furthermore, experimental studies employing these putative compositions were unsuccessful in reproducing pure melts or dissolving the measured volatile contents at the pressure and temperature conditions of kimberlite emplacement (Brooker et al., 2011; Moussallam et al., 2016; Sparks et al., 2009).

The failure to reconstruct kimberlite melt compositions using whole-rock compositions is partly due to the uniqueness of individual kimberlite occurrences, including its geological settings, emplacement age and host rocks, as well as the type of sample chosen for analysis. Furthermore, kimberlite rocks can no longer be considered representative of their parental melts that formed in the mantle because: i) kimberlites common entrain abundant mantle and crustal xenoliths and xenocrysts, and have been shown to react (e.g., assimilation) with its xenogenic cargo (Buse et al., 2010; Hunter and Taylor, 1982; Kamenetsky and Yaxley, 2015; Soltys et al., 2016; Stripp et al., 2006), as well as the cratonic lithosphere (Tappe et al., 2017) and wall-rocks (Smith et al., 2004), ii) kimberlites never retain their original volatile content due to exsolution and degassing during ascent and upon emplacement (Nowicki et al., 2008; Sparks et al., 2006), iii) the composition of individual kimberlite samples may be influenced by fractional crystallization and flow differentiation, which can change the ratios of major components (Dawson and Hawthorne, 1973; Nielsen and Sand, 2008; Tappe et al., 2014), and iv) following emplacement in the crust, kimberlites are almost ubiquitously modified by deuteric (i.e. late-stage magmatic; Mitchell, 2008, 2013) and/or infiltrating hydrothermal and meteoric fluids (Giuliani et al., 2014, 2017; Sparks et al., 2006, 2009; Stripp et al., 2006). Primary mineral assemblages (e.g., olivine, monticellite, carbonate) are commonly overprinted by serpentine, brucite, chlorite, talc and carbonates (Clement, 1982; Mitchell, 1986; Skinner, 1989; Stripp et al., 2006). In addition, kimberlites may crystallise water-soluble minerals, such as alkali-carbonates or chlorides, which are readily be removed by interactions with hydrous fluids (Kamenetsky et al. 2009, 2012).

An alternative approach towards reconstructing the parental kimberlite melt composition is based on studies discriminating xenocrystic from magmatic components in kimberlite rocks (e.g., Nielsen and Sand, 2008) and experimental works, which suggest that kimberlite melts are more representative of 'transitional silicate-carbonatites', which should be poorer in SiO_2, H_2O and MgO and more enriched in CO_2 and CaO (e.g., Brooker et al., 2011; Moussallam et al., 2016; Sparks et al., 2009) than whole-rock estimates. This notion was supported in an improved whole-rock reconstruction model presented by Soltys et al. (2018), who endeavoured to discriminate and quantify the aforementioned effects of kimberlite melt contamination. These authors applied this to the Bultfontein kimberlite (South Africa) and calculated the melt to contain even less SiO_2 (~17 – 19 wt.%), MgO (~20 – 23 wt.%) and H_2O (~2 wt%), and be more CaO (21 – 22 wt.%) and CO_2 rich (~23 – 25 wt.%). In some kimberlite examples, high-degrees of magma fractionation show

compositions that are transitional to carbonatites, such as the Benfontein sills (South Africa; Dawson and Hawthorne, 1973), Tikiusaaq kimberlite dykes (West Greenland; Tappe et al., 2014) and Igwisi Hills kimberlite (Tanzania; Willcox et al., 2015).

Another view on parental kimberlite melt compositions is largely based on the study of melt inclusions in kimberlitic olivine and groundmass minerals, as well as experimental modelling. This model stipulates that kimberlites originated from melts with essentially carbonatitic compositions, which acquired a 'kimberlite flavour' through the dissolution of mantle silicates *en route* to the surface (Brett et al., 2015; Kamenetsky et al., 2008, 2014, 2015; Russell et al., 2012). This line of research began with a long series of publications on the exceptionally 'fresh' (i.e. unserpentinised) units of the Udachnaya-East kimberlite (Siberia; Golovin et al., 2003, 2007, 2017, 2018; Kamenetsky et al., 2004, 2007a, 2007b, 2008, 2009c, 2014; Mernagh et al., 2011). It was shown that both the groundmass components of the 'fresh' Udachnaya-East kimberlite along with olivine and xenolith minerals contain melt inclusions that are silica-poor, but highly enriched in alkali-carbonates and chlorides. Petrographic relationships and melt inclusion compositions indicate that carbonates were a dominant component of the melt parental to Udachnaya-East, and alkalis and halogens are of magmatic origin. Although these views have been challenged (see contrasting views in Kamenetsky et al., 2014; Kostrovitsky et al., 2013; Kopylova et al., 2013, 2016) due to the petrologically unique nature of the Udachnaya-East kimberlite, numerous complementary studies on melt inclusions hosted in kimberlitic minerals from other localities worldwide (Kamenetsky et al., 2012, 2013; Mernagh et al., 2011) have consistently produced similar results, which suggest that the parental kimberlite melt was more carbonatite-like with higher concentrations of alkalis and halogens. The presence of alkali-halogen-bearing carbonate melts/fluids in the mantle is exemplified by the presence of diamond-hosted microinclusions enriched in these components (Izraeli et al. 2001; Klein-BenDavid et al. 2007; Smith et al. 2012; Weiss et al. 2009; Zedgenizov et al., 2018).

This thesis contributes to our understanding of kimberlite petrogenesis by endeavouring to reconstruct the composition and evolution of primary/parental kimberlite melts. The specific aims of this study are to:

1. Provide comprehensive data and detailed descriptions on kimberlite petrography, textural relationships, mineral and whole-rock compositions, as well as

crystal/melt/fluid inclusions in both xenocrystic and magmatic minerals from kimberlite localities worldwide.

2. Determine how kimberlite melts may evolve during ascent and crystallisation through detailed studies of mineral chemistry and inclusions. Furthermore, how kimberlites may be modification post-emplacement.
3. Compare new results and interpretations with existing models and ultimately produce new and/or additional constraints on kimberlite petrogenesis and parental/primary melt compositions.

Although a truly quantitative and universal model for kimberlite petrogenesis is beyond the scope of this manuscript, identifying potential candidate composition(s) for kimberlite melts and how these systems evolve is an essential step towards elucidating this seemingly enigmatic rock type.

1.2 Methods and approach

The aims of this study are achieved through the combined application of petrography, geochemistry and inclusion analyses on minerals and rocks. These combined methods assist in reconstructing the compositional evolution of magmatic minerals and their sequence of crystallisation from the magma, determining the degree of alteration of rocks and minerals, identify physical and geochemical processes that affected parental magmas, and produce constraints on the parental kimberlite melt composition.

The majority of samples (i.e. surface rocks, mine dump material, drill core) used in this study were generously donated by the many colleagues from different institutes around the world, including The University of Melbourne, University of Cape Town, V.S. Sobolev Institute of Geology and Mineralogy, Geological Survey of Canada, Geological Survey of Finland, Vinogradov Institute of Geochemistry and University of Alberta. Petrography and imaging was conducted on rock-chip mounts, thin sections and mineral separates using optical microscopy and scanning electron microscope (SEM) equipped with energy dispersive X-ray spectroscopy (EDS). Geochemistry of minerals was conducted using EDS, electron microprobe (EMP) and laser ablation-inductively coupled mass spectrometry (LA-ICPMS). Rock geochemistry was performed by doing whole-rock analyses. The study of inclusions was done using a combination of optical microscopy, SEM-EDS, Raman spectroscopy and LA-ICPMS. The majority of analytical work was performed at the

University of Tasmania (including the Central Science Laboratory). Details of each analytical method are provided in each subsequent chapter.

1.3 Thesis Structure

Following this introductory chapter, the results of this thesis are presented as ten submitted and/or published research papers. The chapters are sequential and bear a specific aim and methodology, which endeavours to elucidate a different aspect of kimberlite petrogenesis. Papers published in peer-reviewed scientific journals are presented in their original journal format. Each research paper has only been modified in order to be consistent with page numbering order of the thesis. The research chapters are briefly summarised and listed below:

Chapter 2, published in *Chemical Geology*, presents a detailed petrographic study of a magmaclast recovered from the Venetia kimberlite (South Africa). This applies melt inclusions studies to various magmatic groundmass minerals (spinel, perovskite, apatite and calcite) in order to constrain the compositional evolution of the parental kimberlite melt and formation of magmaclasts.

Chapter 3, published in *Chemical Geology*, examines two monticellite-rich kimberlites (Leslie – Canada, Pipe 1 – Finland) and documents the partial-to-complete replacement of olivine by monticellite pseudomorphs. This study demonstrates that *in-situ* decarbonation reactions may occur between olivine and the carbonate melt component, where it can produce significant quantities of monticellite, periclase and CO_2. This study presents new implications for estimating potential degassing processes in kimberlite magmas and types of solid-melt interactions.

Chapter 4, published in *Chemical Geology*, presents new constraints on the concentration and behaviour of halogens (F, Cl) in kimberlite magmas and rocks. This study examines the unusually F-rich Roger kimberlite (Canada), which exhibits unusual replacement of olivine and mesostasis minerals by fluorite, bultfonteinite and amakinite. Petrographic, geochemical and melt inclusion evidence suggests that fluorine and chlorine could exist in potentially higher abundances in kimberlite melts, but their paucity in kimberlite rocks is attributed to remobilisation during syn- and/or post-magmatic alteration.

Chapter 5, published in *Journal of Petrology*, presents a detailed petrographic, geochemical and melt inclusion data comparing the unserpentinised alkali-chloride and –carbonate rich and serpentinised altered units of the Udachnaya-East kimberlite (Russia).

This study demonstrates that the unserpentinised units are 'pristine' magmatic, and were not contaminated by evaporites or crustal brines. Furthermore, arguments supporting the crustal contamination model are addressed and disproven.

Chapter 6, published in *Contributions to Mineralogy and Petrology*, presents a detailed study on the compositions, occurrences and provenance of the accessory sulphide mineral djerfisherite. This study shows that djerfisherite may have multiple mechanisms of formation in kimberlite and kimberlite-hosted rocks (e.g., crustal and mantle xenoliths) and minerals (e.g., olivine, diamond), ranging from direct crystallisation from melt to metasomatism of pre-existing sulphides by a K-Cl-bearing melts/fluids. Djerfisherite is considered to be an important tracer of K and Cl in kimberlite magmas and petrogenesis.

Chapter 7, published in *Lithos*, presents a detailed petrographic, geochemical and melt inclusion study of the Benfontein sill complex (South Africa). This study demonstrates how kimberlite magmas may differentiate during lateral spreading and evolve to carbonate-rich compositions. In addition, variations in the degree of preservation of groundmass oxides demonstrates that atoll-shaped spinels, a common feature in kimberlite rocks, resulted from the resorption of an intermediate zone of pleonaste surrounding a magnesian ulvöspinel – magnetite or chromite core.

Chapter 8, published in *Lithos*, presents a detailed geochemical and inclusion study of clinopyroxene and olivine megacrysts from various Canadian and Siberian kimberlites. Textural and geochemical evidence suggests that large 'polymineralic inclusions' and their associated 'micro melt inclusions' in megacrysts are the products of kimberlite melt infiltration and disequilibria reactions. These inclusions were shown to preserve remnants of the original kimberlite melt entrapped at depth.

Chapter 9, published in Lithos, documents zoning patterns and types of inclusions hosted in fresh olivine from the Mark kimberlite (Canada). For the first time, primary melt inclusions in olivine were documented and shown to be entrapped within forsterite-rich rinds. In addition, a new stage of olivine zoning was identified. Primary and pseudosecondary melt/fluid inclusions in olivine demonstrate that a variably differentiated silica-poor, halogen-bearing, alkali-dolomitic melt crystallised and transported olivine in the Mark kimberlite.

Chapter 10, submitted to *Lithos*, is a detailed petrographic, geochemical and melt inclusion study of the Mark kimberlite (Canada) and is a follow-up study to Chapter 9.

Textural relationships, zoning patterns and different generations of inclusions from kimberlite groundmass minerals were used to constrain a sequence of crystallisation, as well as the major compositional features of the parental melt.

Chapter 11, published in *Journal of Petrology*, is a Reply to a comment addressing the Journal of Petrology publication presented in Chapter 5. This study reasserts previous arguments and reinforces it with new data and clarifications in order to defend the notion that the unserpentinised alkali-carbonate and –chloride rich units in the Udachnaya-East kimberlite are magmatic in origin and were not contaminated by crustal brines or evaporites.

1.4 References

Arndt, N.T., Guitreau, M., Boullier, A.M., le Roex, A., Tommasi, A., Cordier, P., Sobolev, A., 2010. Olivine, and the origin of kimberlite. Journal of Petrology 51, 573–602.

Becker, M., Le Roex, A.P., 2006. Geochemistry of South African On- and Off-craton, Group I and Group II Kimberlites: Petrogenesis and Source Region Evolution. Journal of Petrology 47, 673-703.

Boyd, F., Gurney, J., 1986. Diamonds and the African Lithosphere. Science (New York, N.Y.) 232, 472-7.

Brett, R.C., Russell, J.K., Moss, S., 2009. Origin of olivine in kimberlite: Phenocryst or impostor? Lithos 112S, 201-212.

Brett, R.C., Russell, J.K., Andrews, G.D.M., Jones, T.J., 2015. The ascent of kimberlite: insights from olivine. Earth and Planetary Science Letters 424, 119–131.

Brey, G.P., Bulatov, V.K., Girnis, A.V., Lahaye, Y., 2008. Experimental melting of carbonated peridotite at 6–10 GPa. Journal of Petrology 49, 797–821.

Brooker, R., Sparks, R., Kavanagh, J., Field, M., 2011. The volatile content of hypabyssal kimberlite magmas: some constraints from experiments on natural rock compositions. Bulletin of Volcanology 73, 959-981.

Brown, R.J., Manya, S., Buisman, I., Fontana, G., Field, M., Niocaill, C.M., Sparks, R.S.J., Stuart, F.M., 2012. Eruption of kimberlite magmas: physical volcanology, geomorphology and age of the youngest kimberlitic volcanoes known on earth (the Upper Pleistocene/Holocene Igwisi Hills volcanoes, Tanzania). Bulletin of Volcanology 74, 1621-1643.

Buse, B., Schumacher, J., Sparks, R., Field, M., 2010. Growth of bultfonteinite and hydrogarnet in metasomatized basalt xenoliths in the B/K9 kimberlite, Damtshaa, Botswana: insights into hydrothermal metamorphism in kimberlite pipes. Contributions to Mineralogy and Petrology 160, 533-550.

Dalton, J.A., Presnall, D.C., 1998. The continuum of primary carbonatitic–kimberlitic melt compositions in equilibrium with lherzolite: data from the system $CaO–MgO–Al_2O_3–SiO_2–CO_2$ at 6 GPa. Journal of Petrology 39, 1953–1964.

Dawson, J.B., 1971. Advances in kimberlite geology. Earth Science Reviews 7, 187-214.

Dawson, J.B., 1980. Kimberlites and their xenoliths. Springer-Verlag, New York, 252 pp.

Dawson, J.B., Hawthorne, J.B., 1973. Magmatic sedimentation and carbonatitic differentiation in kimberlite sills at Benfontein, South Africa. Journal of the Geological Society 129, 61-85.

Donnelly, C.L., Griffin, W.L., Yang, J.-H., O'Reilly, S.Y., Li, Q.-L., Pearson, N.J., Li, X.-H., 2012. In situ U-Pb Dating and Sr-Nd Isotopic Analysis of Perovskite: Constraints on the Age and Petrogenesis of the Kuruman Kimberlite Province, Kaapvaal Craton, South Africa. Journal of Petrology 53, 2497-2522.

Ernst, R.E., Jowitt, S.M., 2013. Large Igneous Provinces (LIPs) and metallogeny. In:Colpron, M., Bissig, T., Rusk, B.G., Thompson, J.F.H. (Eds.), Tectonics, Metallogeny, and Discovery: The North American Cordillera and Similar Accretionary Settings. In: Society Economic Geologists Special Publication, vol. 17, pp. 17–51.

Förster, M.W., Foley, S.F., Marschall, H.R., Alard, O., Buhre, S., 2019. Melting of sediments in the deep mantle produces saline fluid inclusions in diamonds. Science Advances 5, eaau2620.

Gaffney, A.M., Blichert-Toft, J., Nelson, B.K., Bizzarro, M., Rosing, M., Albarede, F., 2007. Constraints on source-forming processes of West Greenland kimberlites inferred from Hf–Nd isotope systematics. Geochimica et Cosmochimica Acta 71, 2820–2836.

Giuliani, A., 2018. Insights into kimberlite petrogenesis and mantle metasomatism from a review of the compositional zoning of olivine in kimberlites worldwide. Lithos 312-313, 322-342.

Giuliani, A., Phillips, D., Kamenetsky, V.S., Fiorentini, M.L., Farquhar, J., Kendrick, M.A., 2014. Stable isotope (C, O, S) compositions of volatile-rich minerals in kimberlites: A review. Chemical Geology 374-375, 61-83.

Giuliani, A., Soltys, A., Phillips, D., Kamenetsky, V.S., Maas, R., Goemann, K., Woodhead, J.D., Drysdale, R., Griffin, W.L., 2017. The final stages of kimberlite petrogenesis: Petrography, mineral chemistry, melt inclusions and Sr-C-O isotope geochemistry of the Bultfontein kimberlite (Kimberley, South Africa). Chemical Geology 455, 342-356.

Giuliani, A., Pearson, D.G., 2019. Kimberlites: From Deep Earth to Diamond Mines. Elements 15, 377-380.

Golovin, A.V., Sharygin, I.S., Kamenetsky, V.S., Korsakov, A.V., Yaxley, G.M., 2018. Alkali-carbonate melts from the base of cratonic lithospheric mantle: Links to kimberlites. Chemical Geology 483, 261-274.

Golovin, A.V., Sharygin, I.S., Korsakov, A.V., 2017. Origin of alkaline carbonates in kimberlites of the Siberian craton: Evidence from melt inclusions in mantle olivine of the Udachnaya-East kimberlite. Chemical Geology 455, 357-375.

Golovin, A.V., Sharygin, V.V., Pokhilenko, N.P., 2007. Melt inclusions in olivine phenocrysts in unaltered kimberlites from the Udachnaya-East pipe, Yakutia: Some aspects of kimberlite magma evolution during late crystallization stages. Petrology 15, 168-183.

Golovin, A.V., Sharygin, V.V., Pokhilenko, N.P., Mal kovets, V.G., Kolesov, B.A., Sobolev, N.V., 2003. Secondary Melt Inclusions in Olivine from Unaltered Kimberlites of the Udachnaya-East Pipe, Yakutia. Doklady Earth Sciences 388, 93-96.

Graham, S., Lambert, D., Shee, S., 2004. The petrogenesis of carbonatite, melnoite and kimberlite from the Eastern Goldfields Province, Yilgarn Craton. Lithos 76, 519-533.

Gurney, J.J., Helmstaedt, H.H., Richardson, S.H., Shirey, S.B., 2010. Diamonds through time. Economic Geology 105, 689-712.

Gurney, J.J., Jakob, W.R.O., Dawson, J.B., 1979. Megacrysts from the Monastery kimberlite pipe, South Africa. In: Boyd, F.R., Meyer, H.O.A. (Eds.), The Mantle Sample: Inclusions in Kimberlites and Other Volcanics. American Geophysical Union, Washington, D. C., 227-243.

Haggerty, S.E., 1994. Superkimberlites: A geodynamic diamond window to the Earth's core. Earth and Planetary Science Letters 122, 57-69.

Harte, B., Gurney, J.J., 1981. The mode of formation of the Cr poor megacrystic suites from kimberlites. Journal of Geology 89, 749-753.

Hawthorne, J.B., 1975. Model of a kimberlite pipe. Physics and Chemistry of the Earth 9, 1-15.

Izraeli, E.S., Harris, J.W., Navon, O., 2001. Brine inclusions in diamonds: a new upper mantle fluid. Earth and Planetary Science Letters 187, 323-332.

Jablon, B.M., Navon, O., 2016. Most diamonds were created equal. Earth and Planetary Science Letters 443, 41-47.

Jelsma, H., Barnett, W., Richards, S., Lister, G., 2009. Tectonic setting of kimberlites. Lithos 112S, 155-165.

Kamenetsky, M.B., Sobolev, A.V., Kamenetsky, V.S., Maas, R., Danyushevsky, L.V., Thomas, R., Pokhilenko, N.P., Sobolev, N.V., 2004. Kimberlite melts rich in alkali chlorides and carbonates: A potent metasomatic agent in the mantle. Geology 32, 845-848.

Kamenetsky, V.S., Golovin, A.V., Maas, R., Giuliani, A., Kamenetsky, M.B., Weiss, Y., 2014. Towards a new model for kimberlite petrogenesis: Evidence from unaltered kimberlites and mantle minerals. Earth-Science Reviews 139, 145-167.

Kamenetsky, V.S., Grutter, H., Kamenetsky, M.B., Goemann, K., 2013. Parental carbonatitic melt of the Koala kimberlite (Canada): Constraints from melt inclusions in olivine and Cr-spinel, and groundmass carbonate. Chemical Geology 353, 96-111.

Kamenetsky, V.S., Kamenetsky, M.B., Golovin, A.V., Sharygin, V.V., Maas, R., 2012. Ultrafresh salty kimberlite of the Udachnaya-East pipe (Yakutia, Russia): A petrological oddity or fortuitous discovery? Lithos 152, 173-186.

Kamenetsky, V.S., Kamenetsky, M.B., Sharygin, V.V., Faure, K., Golovin, A.V., 2007a. Chloride and carbonate immiscible liquids at the closure of the kimberlite magma evolution (Udachnaya-East kimberlite, Siberia). Chemical Geology 237, 384-400.

Kamenetsky, V.S., Kamenetsky, M.B., Sharygin, V.V., Golovin, A.V., 2007b. Carbonate-chloride enrichment in fresh kimberlites of the Udachnaya-East pipe, Siberia: A clue to physical properties of kimberlite magmas? Geophysical Research Letters 34, L09316.

Kamenetsky, V.S., Kamenetsky, M.B., Sobolev, A.V., Golovin, A.V., Demouchy, S., Faure, K., Sharygin, V.V., Kuzmin, D.V., 2008. Olivine in the Udachnaya-East Kimberlite (Yakutia, Russia): Types, Compositions and Origins. Journal of Petrology 49, 823-839.

Kamenetsky, V.S., Kamenetsky, M.B., Weiss, Y., Navon, O., Nielsen, T.F.D., Mernagh, T.P., 2009a. How unique is the Udachnaya-East kimberlite? Comparison with kimberlites from the Slave Craton (Canada) and SW Greenland. Lithos 112S, 334-346.

Kamenetsky, V.S., Maas, R., Kamenetsky, M.B., Paton, C., Phillips, D., Golovin, A.V., Gornova, M.A., 2009b. Chlorine from the mantle: Magmatic halides in the Udachnaya-East kimberlite, Siberia. Earth and Planetary Science Letters 285, 96-104.

Kamenetsky, V.S., Yaxley, G.M., 2015. Carbonate–silicate liquid immiscibility in the mantle propels kimberlite magma ascent. Geochimica et Cosmochimica Acta 158, 48-56.

Kaminsky, F., Zakharchenko, O., Davies, R., Griffin, W., Khachatryan-Blinova, G., Shiryaev, A., 2001. Superdeep diamonds from the Juina area, Mato Grosso State, Brazil. Contributions to Mineralogy and Petrology 140, 734-753.

Kennedy, L.A., Russell, J.K., Kopylova, M.G., 2002. Mantle shear zones revisited: the connection between the cratons and mantle dynamics. Geology 30 (5), 419-422.

Kjarsgaard, B.A., Pearson, D.G., Tappe, S., Nowell, G.M., Dowall, D.P., 2009. Geochemistry of hypabyssal kimberlites from Lac de Gras, Canada: Comparisons to a global database and applications to the parent magma problem. Lithos 112S, 236-248.

Klein-BenDavid, O., Izraeli, E.S., Hauri, E., Navon, O., 2007. Fluid inclusions in diamonds from the Diavik mine, Canada and the evolution of diamond-forming fluids. Geochimica et Cosmochimica Acta 71, 723-744.

Klein-BenDavid, O., Logvinova, A.M., Schrauder, M., Spetius, Z.V., Weiss, Y., Hauri, E.H., Kaminsky, F.V., Sobolev, N.V., Navon, O., 2009. High-Mg carbonatitic microinclusions in some Yakutian diamonds—a new type of diamond-forming fluid. Lithos 112, 648-659.

Kopylova, M.G., Gaudet, M., Kostrovitsky, S.I., Polozov, A.G., Yakovlev, D.A., 2016. Origin of salts and alkali carbonates in the Udachnaya East kimberlite: Insights from petrography of kimberlite phases and their carbonate and evaporite xenoliths. Journal of Volcanology and Geothermal Research 327, 116-134.

Kopylova, M.G., Kostrovitsky, S.I., Egorov, K.N., 2013. Salts in southern Yakutian kimberlites and the problem of primary alkali kimberlite melts. Earth-Science Reviews 119, 1-16.

Kopylova, M.G., Matveev, S., Raudsepp, M., 2007. Searching for parental kimberlite melt. Geochimica et Cosmochimica Acta 71, 3616-3629.

Kostrovitsky, S.I., Kopylova, M.G., Egorov, K.N., Yakovlev, D.A., 2013. The Exceptionally Fresh Udachnaya-East Kimberlite: Evidence for Brine and Evaporite Contamination. In: Pearson, D.G., et al. (Eds.), Proceedings of the 10th International Kimberlite Conference, 75-91.

Kramers, J.D., 1979. Lead, uranium, strontium, potassium and rubidium in inclusion-bearing diamonds and mantle-derived xenoliths from Southern Africa. Earth and Planetary Science Letters 42, 58-70.

le Roex, A.P., Bell, D.R., Davis, P., 2003. Petrogenesis of Group I Kimberlites from Kimberley, South Africa: Evidence from Bulk-rock Geochemistry. Journal of Petrology 44, 2261-2286.

Mernagh, T.P., Kamenetsky, V.S., Kamenetsky, M.B., 2011. A Raman microprobe study of melt inclusions in kimberlites from Siberia, Canada, SW Greenland and South Africa. Spectrochimica Acta Part A: Molecular and Biomolecular Spectroscopy 80, 82-87.

Mitchell, R.H., 1986. Kimberlites: Mineralogy, Geochemistry and Petrology. Plenum Publishing Company, New York, 442 pp.

Mitchell, R.H., 1995. Kimberlites, Orangeites and Related Rocks. Plenum Press, New York, 410 pp.

Mitchell, R.H., 2008. Petrology of hypabyssal kimberlites: Relevance to primary magma compositions. Journal of Volcanology and Geothermal Research 174, 1-8.

Mitchell, R.H., 2013. Oxygen isotope studies of serpentine in kimberlite, Proceedings of the 10th International Kimberlite Conference. Geological Society of India, Bangalore, pp. 1-12.

Moore, A.E., 1988, Olivine: a monitor of magma evolutionary paths in kimberlites and olivine melilitites: Contributions to Mineralogy and Petrology 99, 238 – 248.

Moore, R.O., Gurney, J.J., 1985. Pyroxene solid solution in garnets included in diamond. Nature 318, 553-555.

Moussallam, Y., Morizet, Y., Gaillard, F., 2016. H_2O–CO_2 solubility in low SiO_2-melts and the unique mode of kimberlite degassing and emplacement. Earth and Planetary Science Letters 447, 151-160.

Navon, O., Hutcheon, I.D., Rossman, G.R., Wasserburg, G.J., 1988. Mantle-derived fluids in diamond micro-inclusions. Nature 335 (6193), 784–789.

Nielsen, T.F.D., Sand, K.K., 2008. The Majuagaa kimberlite dike, Maniitsoq region, western Greenland: Constraints on an Mg-rich silicocarbonatitic melt composition from groundmass mineralogy and bulk compositions. The Canadian Mineralogist 46, 1043-1061.

Nowell, G.M., Pearson, D.G., Bell, D.R., Carlson, R.W., Smith, C.B., Kempton, P.D., Noble, S.R., 2004. Hf Isotope systematics of kimberlites and their megacrysts: new constraints on their source regions. Journal of Petrology 45, 1583–1612

Nowicki, T., Porritt, L., Crawford, B., Kjarsgaard, B., 2008. Geochemical trends in kimberlites of the Ekati property, Northwest Territories, Canada: Insights on volcanic and resedimentation processes. Journal of Volcanology and Geothermal Research 174, 117-127.

Paton, C., Hergt, J.M., Woodhead, J.D., Phillips, D., Shee, S.R., 2009. Identifying the asthenospheric component of kimberlite magmas from the Dharwar Craton, India. Lithos 112S, 296–310.

Pearson, D.G., Brenker, F.E., Nestola, F., McNeill, J., Nasdala, L., Hutchison, M.T., Matveev, S., Mather, K., Silversmit, G., Schmitz, S., Vekemans, B., Vincze, L., 2014. Hydrous mantle transition zone indicated by ringwoodite included within diamond. Nature 507, 221 –224.

Pilbeam, L.H., Nielsen, T.F.D., Waight, T.E., 2013. Digestion fractional crystallization (DFC): an important process in the genesis of kimberlites. Evidence from olivine in the Majuagaa kimberlite, southern West Greenland. Journal of Petrology 54, 1399–1425.

Price, S.E., Russell, J.K., Kopylova, M.G., 2000. Primitive Magma From the Jericho Pipe, N.W.T., Canada: Constraints on Primary Kimberlite Melt Chemistry. Journal of Petrology 41, 789-808.

Richardson, S.H., Gurney, J.J., Erlank, A.J., Harris, J.W., 1984. Origin of diamonds in old enriched mantle. Nature 310, 198-202.

Ringwood, A.E., Kesson, S.E., Hibberson, W., Ware, N., 1992. Origin of kimberlites and related magmas. Earth and Planetary Science Letters 113, 521-538.

Russell, J.K., Porritt, L.A., Lavallée, Y., Dingwell, D.B., 2012. Kimberlite ascent by assimilation-fuelled buoyancy. Nature 481 (7381), 352 –356.

Scott-Smith, B.S., Nowicki, T.E., Russell, J.K., Webb, K., Mitchell, R.H., Hetman, C., Robey, J.A., 2018. A Glossary of Kimberlite and Related Terms. Scott-Smith Petrology Incorporated.

Shirey, S.B., Cartigny, P., Frost, D.J., Keshav, S., Nestola, F., Nimis, P., Pearson, D.G., Sobolev, N.V., Walter, M.J., 2013. Diamonds and the Geology of Mantle Carbon. Reviews in Mineralogy and Geochemistry 75, 355-421.

Smith, C.B., 1983. Pb, Sr, and Nd isotopic evidence for sources of African kimberlite. Nature 304, 51 –54.

Smith, E.M., Kopylova, M.G., Nowell, G.M., Pearson, D.G., Ryder, J., 2012. Archean mantle fluids preserved in fibrous diamonds from Wawa, Superior craton. Geology 40, 1071-1074.

Soltys, A., Giuliani, A., Phillips, D., 2018. A new approach to reconstructing the composition and evolution of kimberlite melts: A case study of the archetypal Bultfontein kimberlite (Kimberley, South Africa). Lithos 304-307, 1-15.

Soltys, A., Giuliani, A., Phillips, D., Kamenetsky, V.S., Maas, R., Woodhead, J., Rodemann, T., 2016. In-situ assimilation of mantle minerals by kimberlitic magmas — Direct evidence from a garnet wehrlite xenolith entrained in the Bultfontein kimberlite (Kimberley, South Africa). Lithos 256-257, 182-196.

Sparks, R.S.J., 2013. Kimberlite Volcanism. Annual Review of Earth and Planetary Sciences 41, 497-528.

Sparks, R.S.J., Baker, L., Brown, R.J., Field, M., Schumacher, J., Stripp, G., Walters, A., 2006. Dynamical constraints on kimberlite volcanism. Journal of Volcanology and Geothermal Research 155, 18-48.

Sparks, R.S.J., Brooker, R.A., Field, M., Kavanagh, J., Schumacher, J.C., Walter, M.J., White, J., 2009. The nature of erupting kimberlite melts. Lithos 112S, 429-438.

Stachel, T., Harris, J.W., 1997. Diamond precipitation and mantle metasomatism – evidence from the trace element chemistry of silicate inclusions in diamonds from Akwatia, Ghana. Contributions to Mineralogy and Petrology 129, 143-154.

Stachel, T., Luth, R.W., 2015. Diamond formation — Where, when and how? Lithos 220-223, 200-220.

Stripp, G.R., Field, M., Schumacher, J.C., Sparks, R.S.J., Cressey, G., 2006. Post-emplacement serpentinization and related hydrothermal metamorphism in a kimberlite from Venetia, South Africa. Journal of Metamorphic Geology 24, 515-534.

Tainton, K.M., McKenzie, D.A.N., 1994. The Generation of Kimberlites, Lamproites, and their Source Rocks. Journal of Petrology 35, 787-817.

Tappe, S., Pearson, D.G., Kjarsgaard, B.A., Nowell, G., & Dowall, D. (2013). Mantle transition zone input to kimberlite magmatism near a subduction zone: origin of anomalous Nd–Hf isotope systematics at Lac de Gras, Canada. Earth and Planetary Science Letters 371–372, 235–251.

Tappe, S., Kjarsgaard, B.A., Kurszlaukis, S., Nowell, G.M., Phillips, D., 2014. Petrology and Nd–Hf Isotope Geochemistry of the Neoproterozoic Amon Kimberlite Sills, Baffin Island (Canada): Evidence for Deep Mantle Magmatic Activity Linked to Supercontinent Cycles. Journal of Petrology 55, 2003-2042.

Tappe, S., Brand, N.B., Stracke, A., van Acken, D., Liu, C.-Z., Strauss, H., Wu, F.-Y., Luguet, A., Mitchell, R.H., 2017. Plates or plumes in the origin of kimberlites: U/Pb perovskite and Sr-Nd-Hf-Os-C-O isotope constraints from the Superior craton (Canada). Chemical Geology 455, 57-83.

Taylor, L.A., Milledge, H.J., Bulanova, G.P., Snyder, G.A., Keller, R.A., 1998. Metasomatic Eclogitic Diamond Growth: Evidence from Multiple Diamond Inclusions. International Geology Review 40, 663-676.

Torsvik, T.H., Burke, K., Steinberger, B., Webb, S.J., Ashwal, L.D., 2010. Diamonds sampled by plumes from the core-mantle boundary. Nature 466, 352-355.

Weiss, Y., Kessel, R., Griffin, W.L., Kiflawi, I., Klein-BenDavid, O., Bell, D.R., Harris, J.W., Navon, O., 2009. A new model for the evolution of diamond-forming fluids: Evidence from microinclusion-bearing diamonds from Kankan, Guinea. Lithos 112, 660-674.

Weiss, Y., McNeill, J., Pearson, D.G., Nowell, G.M., Ottley, C.J., 2015. Highly saline fluids from a subducting slab as the source for fluid-rich diamonds. Nature 524, 339-42.

Willcox, A., Buisman, I., Sparks, R.S.J., Brown, R.J., Manya, S., Schumacher, J.C., Tuffen, H., 2015. Petrology, geochemistry and low-temperature alteration of lavas and pyroclastic rocks of the kimberlitic Igwisi Hills volcanoes, Tanzania. Chemical Geology 405, 82-101.

Yaxley, G.M., Kamenetsky, V.S., Nichols, G.T., Maas, R., Belousova, E., Rosenthal, A., Norman, M., 2013. The discovery of kimberlites in Antarctica extends the vast Gondwanan Cretaceous province. Nature Commununications 4, 2921.

Zedgenizov, D.A., Ragozin, A.L., Shatsky, V.S., Griffin, W.L., 2018. Diamond formation during metasomatism of mantle eclogite by chloride-carbonate melt. Contributions to Mineralogy and Petrology 173, 84.

Chemical Geology 455 (2017) 331–341

Contents lists available at ScienceDirect

Chemical Geology

journal homepage: www.elsevier.com/locate/chemgeo

Petrographic and melt-inclusion constraints on the petrogenesis of a magmaclast from the Venetia kimberlite cluster, South Africa

Adam Abersteiner [a,c,*], Andrea Giuliani [b,c], Vadim S. Kamenetsky [a], David Phillips [c]

[a] School of Physical Sciences, University of Tasmania, Hobart, TAS 7001, Australia
[b] ARC Centre of Excellence for Core to Crust Fluid Systems and GEMOC, Department of Earth and Planetary Sciences, Macquarie University, North Ryde 2019, NSW, Australia
[c] KiDs (Kimberlites and Diamonds), School of Earth Sciences, The University of Melbourne, Parkville 3010, VIC, Australia

ARTICLE INFO

Article history:
Received 16 March 2016
Received in revised form 8 August 2016
Accepted 22 August 2016
Available online 24 August 2016

Keywords:
Kimberlite
Magmaclast
Melt inclusions
Alkali-carbonates
Venetia

ABSTRACT

Kimberlitic magmaclasts are discrete ovoid magmatic fragments that formed prior to emplacement from disrupted kimberlite magma. To provide new constraints on the origin and evolution of the kimberlite melts, we document the mineralogy and petrography of a magmaclast recovered from one of the ca. 520 Ma Venetia kimberlites, South Africa. The sample (BI9883) has a sub-spherical shape and consists of a ~ 10 mm diameter central olivine macrocryst, surrounded by porphyritic kimberlite. The kimberlitic material consists of concentrically aligned, altered olivine phenocrysts, set in a crystalline groundmass of calcite, chromite, perovskite, phlogopite, apatite, ilmenite, titanite, sulphides, rutile and magnetite along with abundant alteration phases (i.e. serpentine, talc and secondary calcite). These features are typical of archetypal hypabyssal kimberlites.

We examined primary fluid/melt inclusions in chromite, perovskite and apatite containing a diversity of daughter phases. Chromite and perovskite host polycrystalline inclusions containing abundant alkali-carbonates (i.e. enriched in K, Na, Ba, Sr), phosphates, Na-K chlorides, sulphides and equal to lesser quantities of olivine, phlogopite and pleonaste. In contrast, apatite hosts polycrystalline assemblages with abundant alkali-carbonates and Na-K chlorides and lesser amounts of olivine, monticellite and phlogopite. Numerous solid inclusions of shortite ($Na_2Ca_2(CO_3)_3$), Na-Sr-carbonates and apatite occur in groundmass calcite along with fluid inclusions containing daughter crystals of Na-carbonates and Na-chlorides. The primary inclusions in chromite, perovskite and apatite are considered to represent remnants of fluid(s)/melt(s) trapped during crystallisation of the host minerals, whereas the fluid inclusions in calcite are probably secondary in origin. The component proportions of these primary fluid/melt inclusions were estimated in an effort to constrain the composition of the evolving kimberlite melt. These estimates suggest melt evolution from a silicate-carbonate kimberlite melt that became increasingly enriched in carbonates, phosphates, alkalis and chlorides, in response to the fractional crystallisation of constituent minerals (i.e. olivine to apatite).

The concentric alignment of crystals around the olivine kernel and ovoid shape of the magmaclast can be ascribed to the low viscosity of the kimberlite melt and rapid rotation whilst in a liquid or partial crystalline state, or to progressive layer-by-layer growth of the magmaclast. Although the mineralogy of our sample is similar to hypabyssal kimberlites worldwide, it differs from hypabyssal kimberlite units in the main Venetia pipes, which contain monticellite-phlogopite rich assemblages and segregationary matrix textures. Therefore magmaclast BI9883 probably originated from a batch of magma distinct from those that produced known hypabyssal units within the Venetia kimberlite cluster.

1. Introduction

Kimberlites are relatively rare, silica-poor, volatile-rich igneous rocks that originate from considerable mantle depths (>150–200 km; Dawson, 1980; Clement et al., 1984; Mitchell, 1986; Pearson et al., 2014). Kimberlites occur as sub-vertical pipes, sills and dykes and can be further divided into crater, diatreme and root zones (e.g., Dawson, 1971; Hawthorne, 1975; Mitchell, 1986; Sparks, 2013).

Some kimberlites contain unusual discrete spheroidal-to-ovoid fragments of kimberlite material, termed magmaclasts (Field and Scott Smith, 1998, 1999). Magmaclasts typically range in size from <1 mm up to 100 mm and are thought to have formed prior to emplacement from fragmentation/segregation of kimberlite magmas (Scott-Smith et al., 2013). However, the composition of the kimberlite magma responsible for the formation of magmaclasts and their relationship to the entraining kimberlite magma remains uncertain.

* Corresponding author at: School of Physical Sciences, University of Tasmania, Hobart, TAS 7001, Australia.
E-mail address: adam.abersteiner@utas.edu.au (A. Abersteiner).

http://dx.doi.org/10.1016/j.chemgeo.2016.08.029
0009-2541/

Quantifying the composition of magmaclasts and host kimberlite rocks is hampered by several factors, including: i) kimberlites are inherently hybrid rocks that include xenolithic and magmatic components (e.g., Dawson, 1980; Brett et al., 2009; Arndt et al., 2010; Giuliani et al., 2017-in this issue); ii) kimberlite melts commonly entrain and assimilate mantle and crustal xenoliths and xenocrysts (e.g., Hunter and Taylor, 1982; Kamenetsky and Yaxley, 2015; Soltys et al., 2016), iii) the magmas degas volatiles (CO_2 and H_2O) *en route* to the surface and upon emplacement; iv) kimberlite rocks are often extensively altered by post-emplacement meteoric or hydrothermal fluids (e.g., Sparks et al., 2006, 2009; Giuliani et al., 2014b, this issue). To circumvent these problems, analyses of melt/fluid inclusions trapped within magmatic minerals can provide alternative insights into the kimberlite melt composition prior to post-magmatic alteration (e.g., Kamenetsky et al., 2014).

To provide constraints on the origin and composition of the kimberlite melts that produce kimberlite magmaclasts, we present a detailed study of the petrography and mineralogy of a single magmaclast (BI9883) recovered from a mine dump in the Venetia cluster of kimberlites in north-eastern South Africa. Our petrographic results show that this magmaclast hosts a mineral assemblage typical of Group-I (or archetypal) hypabyssal kimberlites (Smith, 1983; Mitchell, 1986, 2008; Skinner, 1989). Additionally, our analyses of melt/fluid and solid inclusions hosted in a variety of groundmass minerals (chromite, perovskite, apatite and calcite) reveal a systematic change in inclusion compositions, which is broadly related to the relative timing of host mineral crystallisation from the kimberlite melt.

2. Geological setting

The Venetia kimberlite cluster comprises 14 kimberlite pipes and dykes emplaced within an area of 4 km^2 in the north-eastern Limpopo Province of South Africa (Seggie et al., 1999; Kurszlaukis and Barnett, 2003). These kimberlites have intruded Precambrian metamorphic rocks (3.3–2.0 Ga) of the Limpopo Mobile Belt (Barton et al., 2003), which probably developed from the collision between the Kaapvaal and Zimbabwe cratons (Barton et al., 1983; Van Reenen et al., 1987). The Venetia country-rocks include amphibolite gneisses, biotite schists, metaquartzites and marbles (Van Reenen et al., 1987; Allsopp et al., 1995; Fontana et al., 2011). These kimberlites have been classified as Group-I (or archetypal) kimberlites, based on their monticellite-phlogopite mineralogy and major trace element and isotope geochemistry (Seggie et al., 1999). Rb-Sr dating of phlogopite from pipe K1 produced an isochron age of 510 ± 16 Ma (2σ; Allsopp et al., 1995), and ^{40}Ar-^{39}Ar dating of groundmass phlogopite provided an age of 519.2 ± 1.2 Ma (2σ; Phillips et al., 1999). The Venetia kimberlites form pipes of irregular shape, sometimes associated with thin kimberlite dykes occurring around the pipe margins (Brown et al., 2008). The main pipes (i.e. K1, K2) contain a variety of mantle and crustal xenoliths (up to 20–30% vol.%; Walters et al., 2006) and are currently mined for diamonds with an average grade of 122 cpht (Field et al., 2008).

3. Sample description

Sample BI9883 was derived from the Venetia mine dumps and is therefore likely derived from either the K1 or K2 kimberlite pipes. The studied sample represents a coherent kimberlite magmaclast that is sub-spherical in shape and approximately 60 mm in maximum diameter. The sample has a porphyritic texture defined by concentrically aligned olivine phenocrysts (1–5 mm in length) around a central core formed by a single olivine macrocryst (~10 mm; Fig. 1a). The edges of the magmaclast are defined by distorted groundmass textures and extensive mineral alteration (i.e. olivine and phlogopite) to admixtures of serpentine and talc, along with deformation of larger (>100 μm) phlogopite grains. In this sample, olivine is extensively serpentinised, in common with olivine in other samples from the Venetia kimberlites (Allsopp et al., 1995; Stripp et al., 2006; Kurszlaukis and Barnett, 2003). Altered olivine phenocrysts are set in a groundmass of (in order of decreasing abundance) calcite, chromite, perovskite, phlogopite, apatite, ilmenite, titanite, sulphides, rutile and magnetite along with abundant alteration phases (i.e. serpentine, talc and secondary calcite).

Different varieties of magmaclasts have been reported from the Venetia kimberlites, including accretionary (armoured) lapilli (Kurszlaukis and Barnett, 2003), pyroclasts (Medlin, 2005) and pelletal lapilli (Stripp et al., 2006; Gernon et al., 2012). Sample BI9883 bears broad petrographic and mineralogical similarities to descriptions of pelletal lapilli from a pyroclastic intrusion in the Venetia pipe K1, which contains abundant pelletal lapilli and bomb-sized clasts (up to 90 vol.%; Tait and Brown, 2008; Gernon et al., 2012). The pelletal lapilli described by Gernon et al. (2012) commonly contain a sub-angular lithic clast or olivine macrocryst nucleus that is coated by olivine, phlogopite and spinel-bearing kimberlite material, commonly with concentrically aligned crystals around the core. Although mineralogically similar, our sample is considerably larger (~60 mm) than the pelletal lapilli reported by Gernon et al. (2012), which show an average diameter of 9.4 mm, and size range of 0.03–32 mm. Kimberlite samples with similar features have also been described as nucleated autoliths (Ferguson et al., 1973; Danchin et al., 1975); however Clement (1982) and Mitchell (1986, 1995) subsequently described these magmaclasts as varieties of larger pelletal lapilli. Given the ambiguity of these definitions, we prefer the term magmaclast for our current sample.

4. Analytical methods

Polished thin sections of sample BI9883 were prepared using kerosene as a lubricant rather than water to avoid dissolution of any soluble minerals present. Initial mineralogical and textural investigations were undertaken using a petrographic microscope and a Philips (FEI) XL30 ESEM TMP, equipped with an OXFORD INCA energy-dispersive X-ray spectrometer (EDS) at the University of Melbourne.

More detailed examinations of the inclusions in mineral phases were carried out using a Hitachi SU-70 field emission SEM equipped with an Oxford INCA Energy XMax 80 detector at the Central Science Laboratory, University of Tasmania. A beam accelerating voltage of 15 kV was employed to produce high-resolution backscattered electron (BSE) images of minerals and energy-dispersive X-ray spectroscopy (EDS) semi-quantitative analyses and elemental maps of minerals and inclusions. In addition, the inclusions in calcite were characterised using a Renishaw inVia Raman microscope equipped with a 532 nm laser, operated at 225 μW, with 1 s exposure and 10 accumulations, a 1800 l/mm grating and a 50× objective microscope.

The major oxide compositions of chromite and ilmenite were measured at the Central Science Laboratory, University of Tasmania, using a Cameca SX100 electron microprobe with a beam accelerating voltage of 20 kV, beam current of 15 nA and beam size of 2 μm. Detection limits (99% confidence) were 0.01 wt.% for Si, Ti, Al and Ca, 0.02 wt.% for Nb, V, Ni and Mg, and 0.03 wt.% for Zn, Cr, Fe and Mn. Analytical precision (1σ) was 0.01 wt.% for Nb, Si, Zn, V, Ni and Ca, 0.03 wt.% for Ti and Al, 0.04 wt.% for Mn and Mg, and 0.06 wt.% for Cr and Fe.

5. Petrography

Magmaclast sample BI9883 contains a central olivine macrocryst core as well as phenocrysts, micro-phenocrysts and/or xenocrysts of olivine and rare phlogopite microcrysts, set in a fine-grained groundmass. The groundmass (Fig. 1b and c) consists primarily of fine-grained interstitial serpentine and calcite, including aggregates of coarser calcite, with subordinate amounts of (in order of decreasing abundance) chromite, perovskite, phlogopite, apatite, ilmenite, titanite, sulphides, rutile and magnetite. This assemblage is typical of archetypal hypabyssal kimberlites (e.g., Mitchell, 1995, 2008).

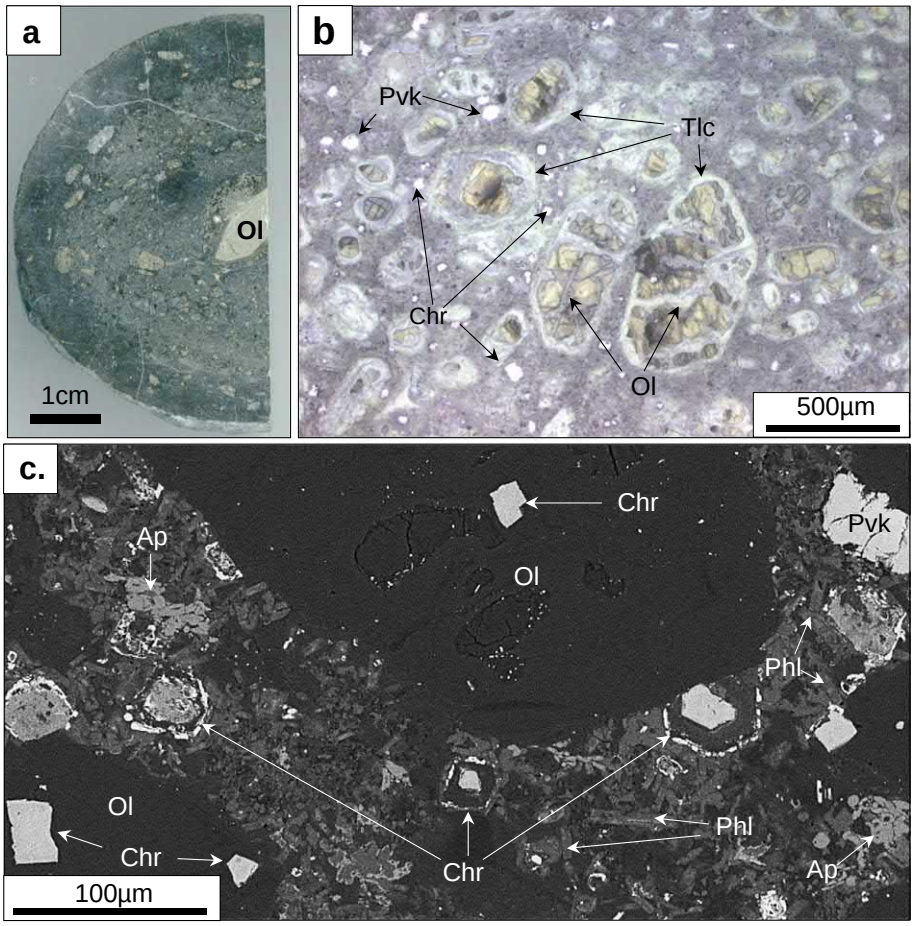

Fig. 1. (a) Off-cut of sample BI9883 showing an olivine macrocyst (Ol) in the core and concentric layering due to preferential orientation of olivine phenocrysts; (b) Reflected-light micrograph and; (c) back-scattered electron (BSE) SEM image of the showing the texture of the second half of kimberlite sample BI9883. Consequently, panel (b) and (c) cannot be assigned locations in panel (a). Olivine is replaced by aggregates of talc (Tlc) and serpentine (Srp). Cr-Spl: Cr-spinel, Pvk: Pervoskite, Phl: Phlogopite, Ap: Apatite.

Forsteritic olivine is the most common constituent in sample BI9883 comprising ~50 vol.% and occurs as subhedral-to-euhedral phenocrysts (0.5–5 mm), microphenocrysts (0.1–0.5 mm) and rarer <5 mm anhedral xenocrysts. Olivine is replaced by serpentine, talc and secondary calcite (Fig. 1b and c). Talc commonly develops thick rims around altered olivine phenocrysts and xenocrysts (Fig. 1b). This feature was also observed by Stripp et al. (2006) and Walters et al. (2006) in volcaniclastic kimberlite rocks from Venetia.

Chromite is relatively abundant in the groundmass (~5 vol.%), ranging in size between 30 and 150 µm. Chromite also occurs as inclusions within olivine phenocrysts (or their alteration products). The groundmass chromite grains are characterised by atoll structures (e.g., Mitchell, 1986; Roeder and Schulze, 2008), where chromite cores are rimmed by a 'lagoon' composed of serpentine, calcite and titanite, and enclosed by a narrow rim(s) (≤5 µm) of Ti-magnetite (Fig. 2a, b and Supplementary Fig. S1). These Ti-magnetite rims are composed of multiple discontinuous layers, which parallel the edges of the spinel core. The spinel core shows multiple zones distinguished by BSE imaging (Fig. 2a and b; see Section 6.1 for details). Chromite grains included in the rims of olivine phenocrysts are typically finer grained (≤ 25 µm) and unzoned. Coarser (>100 µm) grains of Ti-free, chromite are also included in the cores of altered olivine xenocrysts and are probably of mantle origin (see Roeder and Schulze, 2008).

Perovskite forms anhedral, elongated or amoeboid grains with diffuse zonation, and ranges in size from 50 to 100 µm. Many perovskite grains are partially- or completely-mantled by titanite reaction rims of variable thickness (<1–10 µm; Fig. 2c). Aggregates of perovskite grains develop coronae, or 'necklaces' around altered olivine grains (Fig. 2d). Intergrowths of perovskite with chromite (Fig. 2b) and ilmenite (Supplementary Fig. S2a) are also common.

Ilmenite occurs as two textually distinct types: i) small elongated subhedral crystals (≤ 25 µm to 50 µm), which are intergrown with perovskite and/or apatite (Supplementary Fig. S2a), and ii) larger (up to 300 µm) anhedral microcrysts (i.e. 0.1–0.5 mm-large grains of undetermined origin; Fig. 2e and f). Ilmenite microcrysts (Fig. 2e and f) have resorbed margins and host abundant intergrown inclusions of rutile, titanite and calcite. Similar rutile-titanite intergrowths in ilmenite were observed in amphibolite country rocks at Venetia and in lithic clasts from pipes K1 and K2 (Fontana et al., 2011).

Calcite is a common matrix phase interstitial to other groundmass minerals (Fig. 2g and Supplementary Fig. S2). Secondary (i.e. post-magmatic) calcite is a common replacement mineral of olivine and also forms thin (<0.5 mm) veins cross-cutting other groundmass phases.

Phlogopite occurs in the groundmass as elongated grains up to 25 µm in length (Fig. 2g) that are interstitial to most other groundmass minerals. Phlogopite commonly forms discontinuous clusters of crystals aligned parallel to the rims of chromite atolls (Supplementary Fig. S1).

Apatite is a minor groundmass component, occurring as isolated crystals, clusters of small (≤30 µm) grains (Supplementary Fig. S2b) and larger (up to ~100 µm) interstitial segregations around olivine (Fig. 2h).

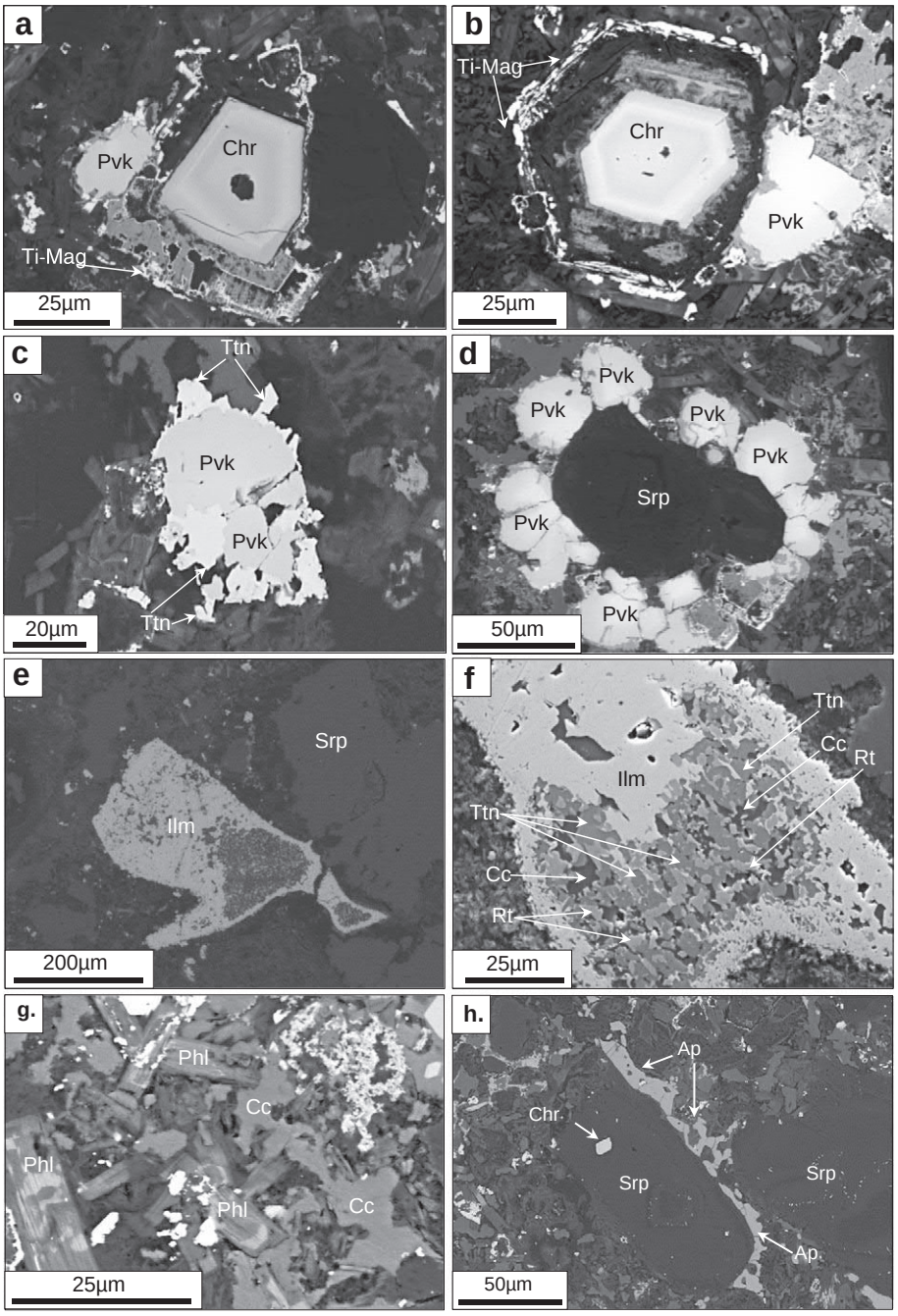

Fig. 2. Back-scattered electron (BSE) SEM images of minerals in kimberlite sample BI9883. (a, b) Atoll-shaped grains of chromite (Chr) grains showing pronounced compositional zoning in the core surrounded by a thin rim of Ti-magnetite (Ti-Mag). (c) Perovskite (Pvk) grain in the groundmass surrounded by discontinuous clusters of titanite (Ttn). (d) Necklace of perovskite crystals around an olivine phenocryst that has been completely replaced by serpentine (Srp). (e, f) Ilmenite (Ilm) microcrysts with abundant inclusions of titanite (Ttn), calcite (Cc) and rutile (Rt). (g) Phlogopite (Phl) grains in the kimberlite groundmass showing complex zoning from Ba-rich (lighter) to Ba-poor (darker) compositions; also note the interstitial habit of calcite (Cc) with respect to other groundmass phases. (h) Apatite (Ap) segregation interstitial to serpentinised olivine (Srp) and other groundmass phases.

6. Mineral compositions: chromite and ilmenite

Detailed microprobe analyses were conducted in order to determine core to rim compositional changes across zoned grains of chromite and to characterise the composition of ilmenite microcrysts (Tables 1 and 2).

6.1. Chromite

The spinel cores are zoned, with Cr_2O_3 concentrations decreasing from 45 to 50 wt.% in the centre to ≤30 wt.% along the rims. In contrast, Al_2O_3, FeO and TiO_2 contents increase from core to rim (Fig. 3a and b; Table 1). The cores are classified as titanian magnesian aluminous chromite (TIMAC; Mitchell, 1986), with compositions trending towards magnesian ulvöspinel-magnetite (MUM; Mitchell, 1986) and pleonaste (Fig. 3c). This trend is common in archetypal kimberlites and is attributed to magma differentiation (Mitchell, 1986; Roeder and Schulze, 2008). Analyses of atoll rims surrounding chromites in sample BI9883 were not attempted, as they are too thin (≤5 µm) for accurate EMP analyses; as noted above, SEM-EDS analyses indicate Ti-magnetite compositions for these rims.

6.2. Ilmenite

The compositions of the ilmenite microcrysts in sample BI9883 are intermediate between ilmenite ($FeTiO_3$) and pyrophanite ($MnTiO_3$)

Table 1
Representative Cr-spinel grains in the groundmass of kimberlite sample BI9883 (Venetia, South Africa).

Grain sample	1	1-Rim	2	2	2	3	3	4	5	5	5	5	5-Rim	6	6	6
SiO_2	0.14	0.07	0.41	0.08	0.07	0.13	0.12	0.17	0.16	0.15	0.08	0.06	0.46	0.12	0.07	0.08
TiO_2	3.83	5.96	1.30	4.12	6.32	3.38	3.33	3.45	4.06	3.93	3.48	4.40	7.69	3.75	3.21	3.81
Al_2O_3	14.38	15.84	15.95	10.47	12.66	16.04	16.52	14.36	11.21	12.25	13.64	9.47	13.65	12.77	14.85	9.18
Cr_2O_3	47.00	33.88	49.13	49.56	40.82	45.47	45.00	45.08	49.53	48.67	47.74	48.24	30.63	48.44	46.48	48.72
FeO_{tot}	18.26	24.42	15.40	19.85	23.26	18.02	18.00	18.94	19.09	18.57	18.41	20.87	26.76	18.75	18.11	21.01
MnO	0.31	0.34	0.21	0.28	0.31	0.31	0.25	0.29	0.23	0.27	0.27	0.29	0.35	0.22	0.22	0.32
MgO	14.80	15.41	14.19	14.12	15.47	15.22	15.37	14.89	14.34	14.31	14.28	13.26	14.27	14.55	14.42	12.93
NiO	0.23	0.13	0.09	0.12	0.09	0.17	0.12	0.12	0.25	0.23	0.15	0.10	0.15	0.23	0.17	0.10
ZnO	0.03	0.05	0.11	0.07	0.01	0.07	0.06	0.06	0.07	0.06	0.07	0.07	0.02	0.06	0.05	0.06
V_2O_3	0.26	0.17	0.22	0.23	0.17	0.27	0.26	0.20	0.26	0.25	0.24	0.20	0.14	0.28	0.24	0.20
Total	99.76	97.45	98.26	99.51	100.15	99.63	99.63	98.45	99.73	99.19	98.91	97.72	95.41	99.67	98.34	97.14
Fe_2O_3	4.08	10.57	2.37	5.15	8.48	4.73	4.82	5.79	4.50	4.04	4.16	5.43	10.10	4.55	4.28	5.86
FeO	14.58	14.91	13.26	15.21	15.63	13.76	13.66	13.73	15.04	14.93	14.66	15.98	17.67	14.65	14.26	15.74
Mg#	0.64	0.65	0.66	0.62	0.64	0.66	0.67	0.66	0.63	0.63	0.63	0.60	0.59	0.64	0.64	0.59
Cr#	0.69	0.59	0.67	0.76	0.68	0.66	0.65	0.68	0.75	0.73	0.70	0.77	0.60	0.72	0.68	0.78
Si	0.005	0.002	0.013	0.003	0.002	0.004	0.004	0.005	0.005	0.005	0.002	0.002	0.016	0.004	0.002	0.003
Ti	0.092	0.148	0.031	0.102	0.154	0.081	0.079	0.084	0.099	0.096	0.085	0.112	0.197	0.091	0.078	0.098
Al	0.540	0.615	0.603	0.404	0.483	0.599	0.615	0.549	0.429	0.469	0.520	0.376	0.548	0.485	0.566	0.368
V	0.007	0.004	0.006	0.006	0.004	0.007	0.007	0.005	0.007	0.007	0.006	0.005	0.004	0.007	0.006	0.006
Cr	1.185	0.883	1.246	1.284	1.045	1.139	1.124	1.156	1.272	1.249	1.222	1.285	0.825	1.235	1.188	1.311
Fe^{2+}	0.487	0.673	0.413	0.544	0.630	0.478	0.476	0.514	0.519	0.504	0.498	0.588	0.762	0.506	0.490	0.598
Fe^{3+}	0.000	0.000	0.000	0.000	0.000	0.000	0.000	0.000	0.000	0.000	0.000	0.000	0.000	0.000	0.000	0.000
Mn	0.008	0.009	0.006	0.008	0.009	0.008	0.007	0.008	0.006	0.007	0.007	0.008	0.010	0.006	0.006	0.009
Mg	0.704	0.757	0.679	0.690	0.746	0.719	0.724	0.720	0.694	0.692	0.689	0.666	0.725	0.699	0.695	0.656
Ni	0.006	0.003	0.002	0.003	0.002	0.004	0.003	0.003	0.007	0.006	0.004	0.003	0.004	0.006	0.004	0.003
Zn	0.001	0.001	0.003	0.002	0.000	0.002	0.001	0.001	0.002	0.001	0.002	0.002	0.000	0.002	0.001	0.002

end-members (Table 2). The average major oxide composition of 12 representative grains is 23.9 ± 2.3 wt.% FeO, 21.2 ± 2.4 wt.% MnO and on average 0.08 wt.% MgO. Microprobe and EDS analyses show minor variations in MnO and FeO contents throughout the ilmenite grains, regardless of no apparent zoning in BSE images.

7. Carbonate-rich inclusions in groundmass minerals

Inclusions are common in chromite, perovskite, apatite and calcite in the groundmass (Table 3). Inclusions in olivine were not characterised as the majority of olivine grains are completely serpentinised. Chromite, perovskite and apatite host randomly distributed polycrystalline inclusions which appear unrelated to any fracture system. Therefore, these inclusions are interpreted to be primary.

Twenty-seven primary polycrystalline inclusions in chromite were examined. These inclusions range in size from 2 to 8 μm (Figs. 4a and 5; Supplementary Fig. S3) and have irregular shapes. The inclusions are dominated by carbonates, primarily calcite and dolomite with minor amounts of alkali (Na, K, Ba, Sr) carbonates (e.g., shortite ($Na_2Ca_2(CO_3)_3$) and fairchildite $K_2Ca(CO_3)_2$)), phlogopite, phosphates (F-rich apatite and bradleyite $Na_3Mg(PO_4)(CO_3)$), olivine, halite/sylvite, and Fe-Cu-Ni (arseno-)sulphides. It is noteworthy that phlogopite and olivine are abundant in some inclusions (Fig. 5), but rare in others (Supplementary Fig. S3).

Six primary polycrystalline inclusions <5 μm in size were examined in perovskite, which hosts fewer inclusions than chromite. Cross-cutting fractures have exposed some inclusions to post-entrapment alteration, which has resulted in the formation of serpentine and/or calcite. In unaltered inclusions, minerals identified include dolomite, alkali (Na-K-Ca) carbonates, F-rich apatite, halite and rare forsteritic olivine (Fig. 4b). Pleonaste spinel is present as monocrystalline inclusions in perovskite, and lacks association with the carbonate-rich inclusions.

Fourteen primary polycrystalline inclusions in apatite were examined. Inclusions in apatite are uncommon and small (≤5 μm in size; Figs. 4c and 6). The inclusions are dominated by alkali (Na-K-Ca-Sr) carbonates (some bearing F) with rare olivine, monticellite and sulphides (Fig. 6). Similar to perovskite, fracturing in some grains has exposed some inclusions to post-entrapment alteration.

Groundmass calcite contains numerous scattered clusters of very small (<1 μm) polycrystalline inclusions. EDS analyses show that these inclusions contain minor Na and Cl (Na ≥ Cl), which indicates the presence of Na-chlorides and Na-carbonate phases (Fig. 7e). Additionally, monocrystalline inclusions of 5–25 μm-sized Na-carbonate (Fig. 7a–c), rare small (<~3 μm) Na-Sr carbonate grains and disseminated apatite also occur in calcite. The Na-carbonate was identified as shortite ($Na_2Ca_2(CO_3)_3$) (Fig. 7d) by micro-Raman and EDS analyses.

Table 2
Representative ilmenite microcrysts in kimberlite sample BI9883 compared to other high manganese ilmenites from worldwide kimberlites.

Sample	1	2	3	4	5	6	7	8	9	10	11	12	Average
TiO_2	51.41	51.35	51.07	51.61	51.16	50.82	50.26	51.47	50.96	48.54	49.22	50.30	50.68
Al_2O_3	0.03	BDL	BDL	0.02	0.03	0.02	0.03	BDL	0.05	0.06	0.01	0.09	0.03
ZnO	BDL	BDL	BDL	BDL	BDL	BDL	BDL	BDL	BDL	0.02	0.01	BDL	BDL
Cr_2O_3	0.02	0.02	0.03	0.02	0.03	0.04	0.02	0.02	0.02	0.04	0.20	0.19	0.06
FeO	22.32	24.66	24.25	24.33	24.94	25.98	24.78	24.24	24.23	27.37	20.43	18.97	23.88
MnO	23.59	20.82	21.41	21.72	19.70	20.27	19.32	22.13	20.92	16.10	25.75	22.43	21.18
MgO	0.03	0.02	0.05	0.03	0.03	0.02	0.36	0.05	0.03	0.28	0.01	0.02	0.08
V_2O_3	0.07	BDL	0.07	0.03	0.07	0.07	0.06	0.08	0.09	0.09	0.04	0.04	0.06
Nb_2O_5	0.39	0.12	0.32	0.22	0.15	0.20	0.13	0.17	0.15	0.15	1.36	1.11	0.37
NiO	0.03	BDL	0.01	BDL	0.01	BDL	BDL	0.01	0.01	BDL	BDL	0.01	BDL
TOTAL	97.89	96.99	97.21	97.98	96.12	97.42	94.96	98.17	96.46	92.65	97.03	93.16	–

n.d = not determined, BDL = below detection limit (detection limit <0.01).

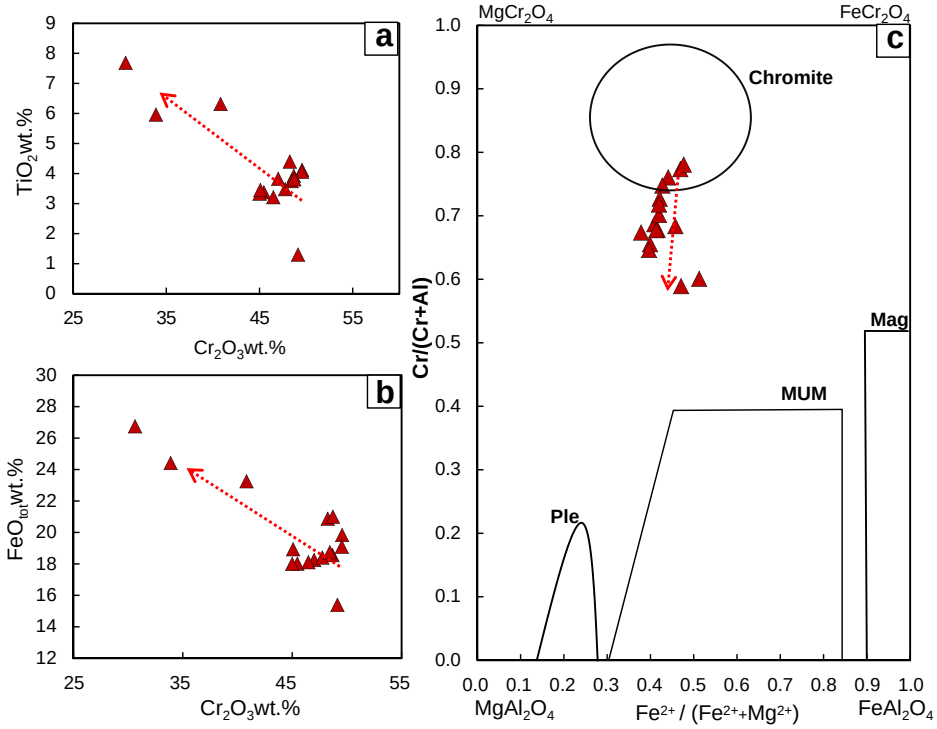

Fig. 3. a) TiO_2 and b) FeO (total) vs Cr_2O_3 concentrations for spinel grains in the groundmass of the Venetia sample BI9883. c) Cr/(Cr + Al) vs. $Fe^{2+}/(Fe^{2+}+Mg^{2+})$ of spinel grains in sample BI9883.

8. Discussion

8.1. Crystallisation history of sample BI9883

Reconstruction of the precise crystallisation history of the magmaclast is complicated by pervasive alteration of original mineral phases (e.g., olivine replacement by serpentine, talc and secondary calcite). Previous studies have shown that olivine is the earliest phase to crystallise in kimberlites along with chromite (e.g., Fedortchouk and Canil, 2004; Mitchell, 1986, 2008). This is confirmed in our sample by the occurrence of chromite inclusions within olivine phenocrysts. Based on textual observations, Mitchell (1972, 1986) inferred that perovskite crystallises after olivine and spinel, but before carbonates in kimberlite magmas. This is reflected in our sample by clusters/coronae of perovskite around olivine and chromite grains (Fig. 2d). Groundmass phlogopite forms euhedral grains that commonly surround chromite (Supplementary Fig. S1) and perovskite grains, whereas calcite fills interstitial voids between other groundmass minerals (Fig. 2g; Supplementary Fig. S2). This suggests that phlogopite crystallised after spinel and perovskite, but before carbonates. Apatite is commonly considered to crystallise late in kimberlite magmas, after olivine, spinel and perovskite (Mitchell, 2008). Interstitial segregations of apatite around oxide minerals and altered olivine grains (Fig. 2h) in our sample confirm its lower temperature crystallisation. The late-stage crystallisation of carbonates is a typical feature of kimberlite magmas (e.g., Armstrong et al., 2004; Mitchell, 2008). Olivine alteration has been attributed to late-stage deuteric fluids (Mitchell, 2008, 2013) and/or external meteoric/hydrothermal fluids (Ukhanov et al., 1986; Sparks et al.,

Table 3
Summary of the daughter mineral phases included in groundmass minerals of the Venetia kimberlite sample BI9883, listed in order of decreasing abundance.

Chromite	Distribution (%)	Perovskite	Distribution (%)	Apatite	Distribution (%)	Calcite	Distribution (%)
Calcite $CaCO_3$	35	Dolomite $CaMg(CO_3)_2$	40	Alkali-carbonates (Na, K, Ca, Sr) + F	85	Halite NaCl	55
Dolomite $CaMg(CO_3)_2$	25	Alkali-carbonates (Na, K, Ca)	35	Halite/Sylvite NaCl/KCl	9	Alkali-carbonates (Na, Sr)	45
Bradleyite $Na_3Mg(PO_4)(CO_3)$	9	Apatite $Ca_5(PO_4)_3(F,Cl,OH)$	10	Olivine/Monticellite $Mg_2SiO_4/CaMgSiO_4$	4		
Fairchildite/Shortite $K_2Ca(CO_3)_2/Na_2Ca_2(CO_3)_3$	9	Halite/Sylvite NaCl/KCl	8	Sulphides Fe, Ni	2		
Phlogopite $KMg_3AlSi_3O_{10}(F,OH)_2$	9	Olivine Mg_2SiO_4	7				
Olivine Mg_2SiO_4	5						
Apatite $Ca_5(PO_4)_3(F,Cl,OH)$	4						
Halite/Sylvite NaCl/KCl	2						
Sulphides Fe, Cu, Ni, As	2						

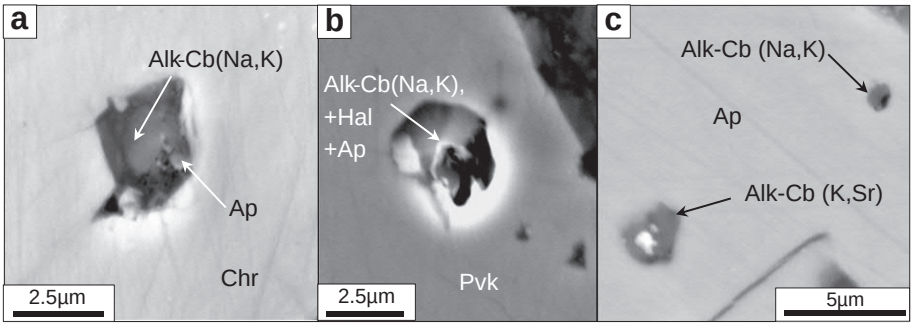

Fig. 4. Back-scattered electron SEM images of primary inclusions in: a) chromite (Chr), b) perovskite (Pvk) and c) apatite (Ap) in sample BI9883. The polycrystalline inclusions in chromite, perovskite and apatite host daughter crystals of a) alkali-carbonates (Na, K) plus apatite, b) alkali-carbonates (Na, K), apatite plus halite, and c) alkali-carbonates (Na, K, Sr) respectively.

2006, 2009; Stripp et al., 2006; Giuliani et al., 2014b). In summary, the order of crystallisation is considered to be olivine formation followed by chromite, perovskite, phlogopite, apatite and carbonate.

8.2. Significance of the carbonate-rich inclusions

Chromite, perovskite and apatite in sample BI9883 all host polycrystalline mineral inclusions with heterogeneous compositions. These inclusions are randomly distributed in the host minerals, appear unrelated to any fractures and are therefore interpreted to be primary. The inclusions probably represent remnants of fluid(s)/melt(s), which were trapped during the crystallisation of these kimberlitic minerals and, therefore, provide insights into the compositional evolution of associated fluids/melts. Chromite, perovskite and apatite contain different polycrystalline assemblages (Table 3) and therefore record variable melt/fluid compositions. Chromite and perovskite, which formed early in the crystallisation sequence, contain inclusions with abundant Ca-Mg carbonates, common *Si*-Al-rich minerals (i.e. olivine and phlogopite in chromite, and olivine and pleonaste spinel in perovskite), alkali-rich (Na, K, Ba, Sr) carbonates and lesser amounts of Na-K-chlorides, phosphates, sulphides and Fe-Ti oxides. Based on relative phase abundances within inclusions in chromite and perovskite (Table 3), the overall proportion of silicate and alumina minerals compared to carbonate minerals is significantly less. Melt inclusions in apatite, a later crystallising phase in sample BI9883, are more enriched in alkali-carbonates, phosphates, chlorides and sulphides and contain only very minor silicate minerals, typically forsteritic olivine and monticellite.

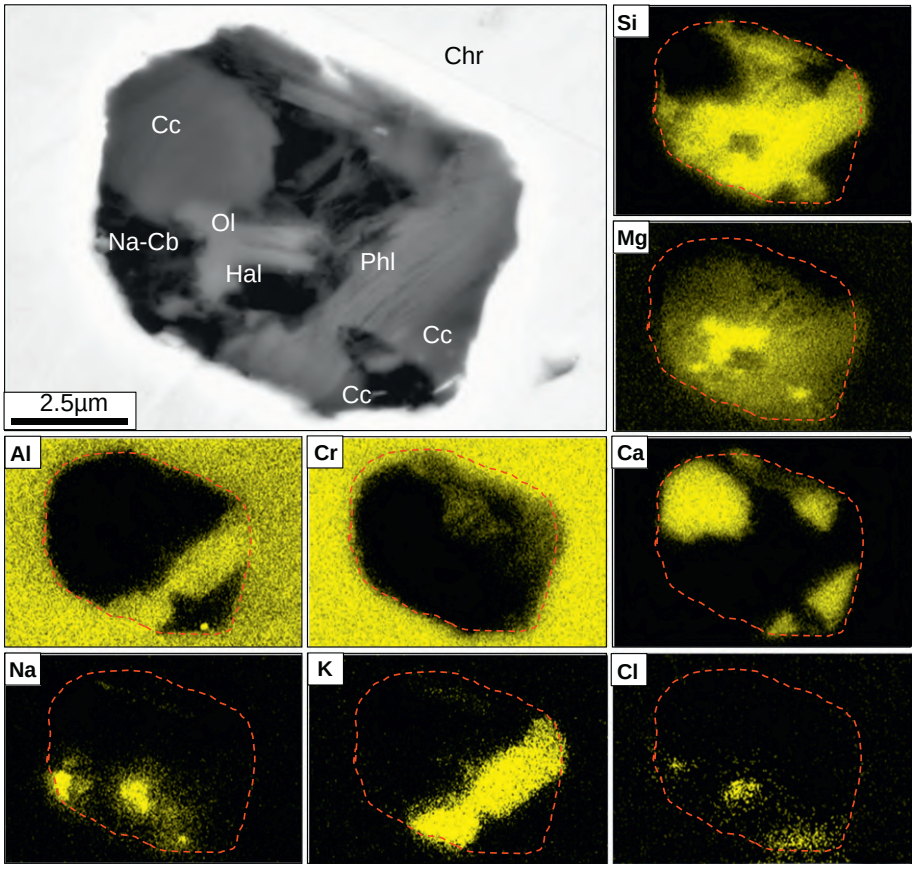

Fig. 5. Back-scattered electron SEM image and X-ray elemental map of a representative inclusion in chromite (Chr). Detected minerals include dolomite (Dol), phlogopite (Phl), halite (Hal), Na-carbonate (Na-Cb), olivine (Ol) and calcite (Cc). The red line indicates the boundary of the inclusion.

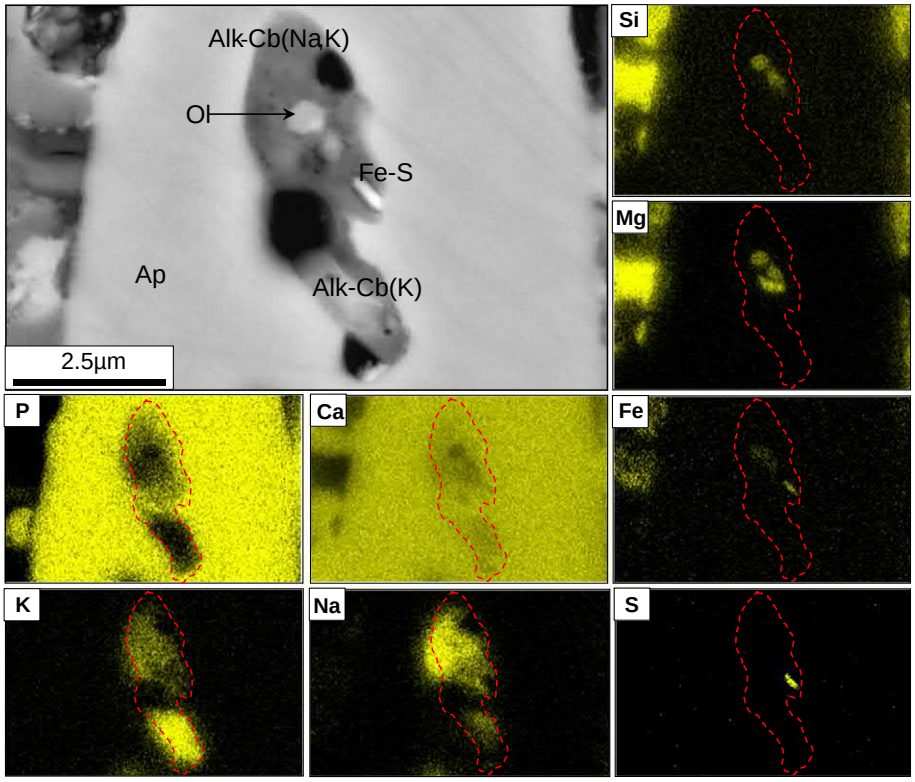

Fig. 6. Back-scattered electron SEM image and x-ray elemental map of a representative inclusion in apatite (Ap). Detected minerals include: alkali-carbonates (Alk-Cb), olivine (Ol) and Fe-rich sulphide (Fe-S). The red line indicates the boundary of the inclusion.

In summary, there is a systematic change in the composition of melt/fluid inclusions across the crystallisation sequence of sample BI9883. Daughter silicate minerals are more abundant in melt inclusions hosted in the earlier crystallised minerals chromite and perovskite, and are rare or absent in inclusions hosted in later crystallised apatite. This progressive change in fluid/melt inclusion compositions indicates that CO_2, alkalis, phosphorus and chlorine become increasingly enriched, whereas Si and Al are depleted in the residual kimberlite melt in response to the crystallisation of olivine, spinel and phlogopite.

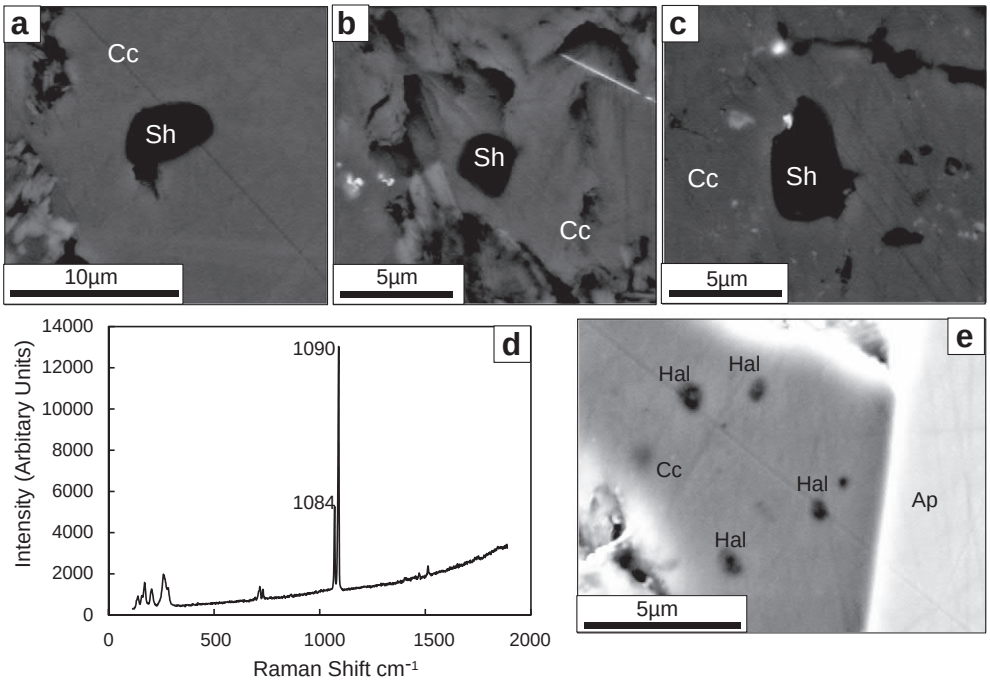

Fig. 7. a–c) Back-scattered electron SEM images and d) Raman spectrum of shortite (Sh; ($Na_2Ca_2(CO_3)_3$)) inclusion in groundmass calcite (Cc). e) Halite-rich secondary inclusions in groundmass calcite (Cc). Ap: apatite.

Groundmass calcite also contains abundant multiphase inclusions (<1 μm) that consist of mixtures of Na-carbonates and Na-chlorides (i.e., halite; Fig. 7e). Groundmass carbonates are generally considered to be of primary magmatic origin (Dawson, 1980; Mitchell, 1986; Armstrong et al., 2004; Wilson et al., 2007; Giuliani et al., 2014b), but have also been attributed to externally derived post-magmatic fluids (Exley and Jones, 1983; Podvysotskiy, 1985; Armstrong et al., 2004; Giuliani et al., 2014b, this issue). Furthermore, the propensity of calcite to dissolve or re-precipitate in kimberlites (Mitchell, 1986) indicates that the Na-Cl enriched inclusions in calcite are likely to be of secondary origin, representing a Ca-Na-Cl enriched late-stage fluid. This alkali-Cl-rich carbonate fluid could represent the culmination of the differentiation process of the initially *Si*-bearing kimberlite melt and/or infiltration from external fluids (i.e. hydrothermal).

The presence of abundant inclusions of shortite (Fig. 7) in calcite and daughter Na-bearing carbonates in fluid/melt inclusions hosted by spinel (Figs. 4a, 5 and Supplementary Fig. S3), perovskite (Fig. 4b) and apatite (Figs. 4c and 6) contrasts with the very low concentrations of sodium commonly recorded in bulk-rock analyses of kimberlites, including aphanitic varieties (e.g., Price et al., 2000; le Roex et al., 2003; Becker and le Roex, 2006; Kopylova et al., 2007; Nielsen and Sand, 2008; Kjarsgaard et al., 2009; Kopylova et al., 2013). Although a volumetrically insignificant feature in our sample, the abundance of Na in inclusions suggests that Na could exist in potentially higher (yet undetermined) concentrations in the parental kimberlite melt or hosted within groundmass phases, but was subsequently removed from kimberlite rocks during alteration. Kamenetsky et al. (2013, 2014) described that the low concentrations of Na in kimberlite rocks and absence of Na-bearing minerals from the kimberlite groundmass is likely due to: 1) Na in kimberlites resides in water-soluble minerals, such as carbonates, chlorides, sulfates, phosphates etc., which are removed during the low-T evolution and associated serpentinisation of kimberlite rocks; 2) exsolution of Na-rich fluids upon kimberlite emplacement, which then 'fenitise' country rocks (Smith et al., 2004).

The carbonate-rich inclusions in sample BI9883 bear broad similarities to primary melt inclusions in spinel grains from the Koala kimberlite (Canada; Kamenetsky et al., 2013), which are dominated by alkali-carbonates and chlorides with rare phlogopite. Furthermore, olivine and ilmenite in mantle polymict breccia xenoliths, which are thought to be failed kimberlite intrusions that stalled at mantle depths (e.g., Lawless et al., 1979; Pokhilenko, 2009), contain primary melt inclusions with similar *Si*-bearing, alkali-rich Ca-Mg carbonate compositions (Giuliani et al., 2012, 2013, 2014a).

The main Venetia kimberlite pipes (K1 and K2) contain abundant mantle and crustal xenoliths (up to 20–30 vol.%; Walters et al., 2006). High levels of crust/mantle entrainment are also evident in sample BI9883, as shown by the presence mantle olivine xenocrysts and crustal Mn-ilmenite grains. Contamination of the kimberlite magma represented by sample BI9883 with crustal material could explain the occurrence of Al-rich pleonaste inclusions in perovskite and higher silicate abundance in melt/fluid inclusions in chromite and perovskite, compared to primary melt inclusions in chromite from the Koala kimberlite (Kamenetsky et al., 2013). Alternatively, the starting composition of the kimberlite melt that formed sample BI9883 was slightly different to that of the Koala kimberlite, or that pleonaste was originally a common groundmass constituent in magmaclast BI9883, but was subsequently altered.

Unlike the previous studies of secondary melt inclusions in kimberlitic olivine (e.g., Golovin et al., 2007; Kamenetsky et al., 2004; Kamenetsky et al., 2007a, 2007b, Kamenetsky et al., 2009a, 2009b; Kamenetsky et al., 2012, Kamenetsky et al., 2013; Mernagh et al., 2011), the current investigation of primary inclusions in multiple magmatic minerals may provide a potentially more holistic approach towards constraining fluid/melt evolution during kimberlite crystallisation. Our analyses of melt/fluid inclusions suggest that kimberlite-related melts/fluids at different stages of differentiation can be trapped within magmatic minerals that crystallised at distinct times from the same magma batch. Previous studies of melt inclusions that were limited to secondary inclusions only in olivine may provide an incomplete representation of the composition of kimberlite melts.

8.3. Origin of Venetia magmaclast BI9883

The ovoid shape of the magmaclast, the concentric alignment of crystals around the olivine macrocryst core (Fig. 1a), and deformation of minerals adjacent to the magmaclast margins could be explained by rapid rotation of this sample whilst in a liquid or partially crystalline state. Under this scenario, surface tension of a low-viscosity kimberlite melt (Dawson, 1980; Mitchell, 1986, 1995; Sparks et al., 2006) is the likely factors controlling the texture of this magmaclast. Alternatively, the internal layering of the magmaclast could be due to progressive accretion of kimberlitic material around the olivine kernel. However, based on its hypabyssal mineralogy, sample BI9883 is not an example of an accretionary lapillus (Fisher and Schmincke, 1984). It is suggested that magmaclast BI9883 represents a fragment of magmatic kimberlite melt that aggregated around an olivine macrocryst core and began to crystallise in the upper crust, before being entrained by a subsequent pulse of kimberlite magma, such as the various volcaniclastic units present in the Venetia kimberlites.

Few studies have examined the composition of kimberlitic magmaclasts, their mineral constituents and contained inclusions (e.g., Field and Scott Smith, 1998; Skinner and Marsh, 2004; Mitchell et al., 2009; Howarth and Skinner, 2012). Although sample BI9883 exhibits broad mineralogical similarities to hypabyssal kimberlites (Mitchell, 2008), the matrix mineralogy differs from that of hypabyssal kimberlites emplaced in the Venetia K1 and K2 pipes; these units host abundant monticellite (and phlogopite), and include abundant segregationary matrix textures (Allsopp et al., 1995; Seggie et al., 1999), which are notably absent in magmaclast sample BI9883. The differences between the magmaclast and Venetia hypabyssal rocks suggest that the former was probably derived from an earlier batch of compositionally distinct kimberlitic magma. Alternatively, the distinct mineralogical differences between the main Venetia hypabyssal units and the studied magmaclast may be due to a combination of: a) pervasive groundmass alteration, where magmaclast minerals such as monticellite were completely serpentinised; b) the magmaclast crystallised under potentially higher P-T conditions. Experimental studies have estimated that monticellite crystallises from kimberlite magmas at relatively low pressures (< 0.5–1 GPa; Franz and Wyllie, 1967; Fedortchouk and Canil, 2004; Piouffle and Canil, 2012). The apparent absence of monticellite from the groundmass of sample BI9883 suggests that this magmaclast might have been entrained at greater depths.

9. Conclusions

Venetia sample BI9883 an unusually large (~60 mm), sub-spherical magmaclast comprised of a central olivine macrocryst, surrounded by concentrically aligned porphyritic kimberlite that exhibits a matrix mineralogy that is typical of archetypal hypabyssal kimberlites worldwide.

Studies of primary melt/fluid inclusions in chromite, perovskite and apatite, and secondary fluid inclusions in groundmass calcite provide new insights into the compositional evolution of kimberlite melts/fluids during crystallisation. The earlier crystallised minerals, chromite and perovskite, contain inclusions hosting abundant daughter crystals of Ca—Mg and alkali (Na, K, Ba, Sr)-rich carbonates, low to moderate amounts of *Si*-Al-bearing minerals (olivine, phlogopite, pleonaste) and lesser chlorides, phosphates, sulphides and Fe—Ti oxides. In contrast, melt/fluid inclusions in later crystallised apatite contain higher abundances of carbonates, chlorides, phosphates and sulphides, and rare silicate minerals. Groundmass calcite hosts secondary inclusions of Na-carbonate and Na-chlorides. The variation in melt/fluid inclusion components reflects progressive differentiation of the kimberlite melt

from alkali-rich, silicate-carbonate (inclusions in chromite and perovskite) to Si-poor alkali-carbonate (inclusions in apatite) and, finally, to a Na-Cl-rich carbonate fluid (inclusions in calcite). More comprehensive studies of melt/fluid inclusions in magmatic minerals in kimberlites worldwide are necessary to provide a more complete view of the evolution of kimberlite magmas.

The sub-spherical to ovoid shape of this sample and concentric alignment of olivine crystals within the magmaclast is attributed to rapid rotation of a partially crystalline, low viscosity kimberlite melt or to progressive accretion of kimberlitic material around the olivine kernel. It is suggested that the magmaclast represents kimberlitic material that was entrained by a later magma pulse, such as one of those responsible for the volcaniclastic intrusions in the Venetia K1 pipe.

Acknowledgements

We thank Simon Shee for providing this sample (BI9883), Thomas Rodemann and Karsten Goemann at the Central Science Laboratory (University of Tasmania) for their assistance with Raman and electron microprobe analyses, and Graham Hutchinson for support with SEM analyses at the University of Melbourne. This manuscript has benefitted of comments by two anonymous reviewers and the efficient editorial handling of Sebastian Tappe. The study was supported by the Australian Research Council (ARC). Financial support was provided by the Australian Research Council (Discovery grant DP130100257, 2013-2015) and University of Tasmania (New Star Professorship, 2010-2014) to V. Kamenetsky. This is contribution 836 from the ARC Centre of Excellence for Core to Crust Fluid Systems (http://www.ccfs.mq.edu.au) and 1100 in the GEMOC Key Centre (http://www.gemoc.mq.edu.au).

Appendix A. Supplementary data

Supplementary data to this article can be found online at http://dx.doi.org/10.1016/j.chemgeo.2016.08.029.

References

Allsopp, H.L., Smith, C.B., Seggie, A.G., Skinner, E.M.W., Colgan, E.A., 1995. The emplacement age and geochemical character of the Venetia kimberlite bodies, Limpopo Belt, northern Transvaal. S. Afr. J. Geol. 98, 239–244.
Armstrong, J.P., Wilson, M., Barnett, R.L., Nowicki, T., Kjarsgaard, B.A., 2004. Mineralogy of primary carbonate-bearing hypabyssal kimberlite, Lac de Gras, Slave Province, northwest territories, Canada. Lithos 76, 415–433.
Arndt, N.T., Guitreau, M., Boullier, A.M., Le Roex, A., Tommasi, A., Cordier, P., Sobolev, A., 2010. Olivine, and the Origin of Kimberlite. J. Petrol. 51, 573–602.
Barton Jr., J.M., Ryan, B., Fripp, R.E.P., 1983. Rb-Sr and U-Th-Pb isotopic studies of the Sand River gneisses, central zone, Limpopo Mobile Belt. In: Van Biljon, W.J., Legg, J.H. (Eds.), The Limpopo Belt 8. Geological Society of South Africa Special Publication, pp. 9–18.
Barton, J.M., Barnett, W.P., Barton, E.S., Barnett, M., Doorgapershad, A., Twiggs, A., Klemd, R., Martin, R., Mellonig, L., Zenglein, R., 2003. The geology of the area surrounding the Venetia kimberlite pipes, Limpopo Belt, South Africa: a complex assembly of terranes and granitoid magmatism. S. Afr. J. Geol. 106, 109–128.
Becker, M., Le Roex, A.P., 2006. Geochemistry of south African on- and off-craton, group I and group II kimberlites: Petrogenesis and source region evolution. J. Petrol. 47, 673–703.
Brett, R.C., Russell, J.K., Moss, S., 2009. Origin of olivine in kimberlite: Phenocryst or impostor? Lithos 112S, 201–212.
Brown, R.J., Buse, B., Sparks, R.S.J., Field, M., 2008. On the welding of pyroclasts from very low-viscosity magmas: examples from kimberlite volcanoes. J. Geol. 116, 354–374.
Clement, C.R., 1982. A comparative geological study of some major kimberlite pipes in the Northern Cape and Orange Free State. Ph.D. Thesis. University of Cape Town, South Africa unpublished. 406pp.
Clement, C.R., Skinner, E.M.W., Smith, B.H., Scott, 1984. Kimberlite Redefined. Vol. 223. University of Chicago Press.
Danchin, R.V., Ferguson, J., McIver, J.R., Nixon, P.H., 1975. The composition of late stage kimberlite liquids as revealed by nucleated autoliths. Phys. Chem. Earth 9, 235–245.
Dawson, J.B., 1971. Advances in kimberlite geology. Earth-Sci. Rev. 7, 187–214.
Dawson, J.B., 1980. Kimberlites and Their Xenoliths. Springer-Verlag, New York.
Exley, R.A., Jones, A.P., 1983. $^{87}Sr/^{86}Sr$ in kimberlitic carbonates by ion microprobe: hydrothermal alteration, crustal contamination and relation to carbonatite. Contrib. Mineral. Petrol. 83, 288–292.
Fedortchouk, Y., Canil, D., 2004. Intensive variables in kimberlite magmas, Lac de Gras, Canada and implications for diamond survival. J. Petrol. 45, 1725–1745.
Ferguson, J., Danchin, R.V., Nixon, P.H., 1973. Petrochemistry of kimberlite autoliths. In: Nixon, P.H. (Ed.), Lesoth Kimberlites. Lesotho National Development Corporation, Maseru, pp. 285–293.
Field, M., Scott Smith, B.H., 1998. Textural and genetic classification schemes of kimberlites: new perspective. Extended Abstracts of the Seventh International Kimberlite Conference, pp. 214–216 Cape Town, South Africa.
Field, M., Scott Smith, B.H., 1999. Contrasting geology and near-surface emplacement of kimberlite pipes in southern Africa and Canada. Proceedings of the 7th International Kimberlite Conference. Vol. 1, pp. 214–237.
Field, M., Stiefenhofer, J., Robey, J., Kurszlaukis, S., 2008. Kimberlite-hosted diamond deposits of southern Africa: a review. Ore Geol. Rev. 34, 33–75.
Fisher, R.V., Schmincke, H.U., 1984. Pyroclastic Rocks. Springer, New York.
Fontana, G., Mac Niocaill, C., Brown, R., Sparks, R., Field, M., 2011. Emplacement temperatures of pyroclastic and volcaniclastic deposits in kimberlite pipes in southern Africa. Bull. Volcanol. 73, 1063–1083.
Franz, G.W., Wyllie, P.J., 1967. Experimental studies in the system CaO-MgO-SiO2-CO2-H2O. In: Wyllie, P.J. (Ed.), Ultramafic and Related Rocks. John Wiley & Sons, New York, pp. 323–326.
Gernon, T.M., Brown, R.J., Tait, M.A., Hincks, T.K., 2012. The origin of pelletal lapilli in explosive kimberlite eruptions. Nat. Commun. 3, 832.
Giuliani, A., Kamenetsky, V.S., Phillips, D., Kendrick, M.A., Wyatt, B.A., Goemann, K., 2012. Nature of alkali-carbonate fluids in the sub-continental lithospheric mantle. Geology 40, 967–970.
Giuliani, A., Kamenetsky, V.S., Kendrick, M.A., Phillips, D., Wyatt, B.A., Maas, R., 2013. Oxide, sulphide and carbonate minerals in a mantle polymict breccia: metasomatism by proto-kimberlite magmas, and relationship to the kimberlite megacrystic suite. Chem. Geol. 353, 4–18.
Giuliani, A., Phillips, D., Kamenetsky, V.S., Kendrick, M.A., Wyatt, B.A., Goemann, K., Hutchinson, G., 2014a. Petrogenesis of mantle polymict breccias: insights into mantle processes coeval with kimberlite magmatism. J. Petrol. 55, 831–858.
Giuliani, A., Phillips, D., Kamenetsky, V.S., Fiorentini, M.L., Farquhar, J., Kendrick, M.A., 2014b. Stable isotope (C, O, S) compositions of volatile-rich minerals in kimberlites: a review. Chem. Geol. 374-375, 61–83.
Giuliani, A., Phillips, D., Kamenetsky, V.S., Goemann, K., 2016. Constraints on kimberlite ascent mechanisms revealed by phlogopite compositions in kimberlites and mantle xenoliths. Lithos 240-243, 189–201.
Giuliani, A., Soltys, A., Phillips, D., Kamenetsky, V.S., Maas, R., Woodhead, J.D., Drysdale, R., Goemann, K., Griffin, W.L., 2017. The final stages of kimberlite petrogenesis: petrography, mineral chemistry, melt inclusions and Sr-Nd-C-O isotope geochemistry of the Bultfontein kimberlite (Kimberley, South Africa). Chem. Geol. 455, 337–351 (in this issue) (under review).
Golovin, A.V., Sharygin, V.V., Pokhilenko, N.P., 2007. Melt inclusions in olivine phenocrysts in unaltered kimberlites from the Udachnaya-East pipe, Yakutia: some aspects of kimberlite magma evolution during late crystallization stages. Petrology 15, 168–183.
Hawthorne, J.B., 1975. Model of a kimberlite pipe. Phys. Chem. Earth 9, 1–15.
Howarth, G.H., Skinner, E.M.W., 2012. The geology and emplacement of the volcaniclastic infill at the Voorspoed group II kimberlite (orangeite) pipe, Kroonstad cluster, South Africa. J. Volcanol. Geotherm. Res. 231-232, 24–38.
Hunter, R.H., Taylor, L.A., 1982. Instability of garnet from the mantle: glass as evidence of metasomatic melting. Geology 10, 617–620.
Kamenetsky, V.S., Yaxley, G.M., 2015. Carbonate–silicate liquid immiscibility in the mantle propels kimberlite magma ascent. Geochim. Cosmochim. Acta 158, 48–56.
Kamenetsky, M.B., Sobolev, A.V., Kamenetsky, V.S., Maas, R., Danyushevsky, L.V., Thomas, R., Pokhilenko, N.P., Sobolev, N.V., 2004. Kimberlite melts rich in alkali chlorides and carbonates: A potent metasomatic agent in the mantle. Geology 32, 845–848.
Kamenetsky, V.S., Kamenetsky, M.B., Sharygin, V.V., Faure, K., Golovin, A.V., 2007a. Chloride and carbonate immiscible liquids at the closure of the kimberlite magma evolution (Udachnaya-East kimberlite, Siberia). Chem. Geol. 237, 384–400.
Kamenetsky, V.S., Kamenetsky, M.B., Sharygin, V.V., Golovin, A.V., 2007b. Carbonate-chloride enrichment in fresh kimberlites of the Udachnaya-East pipe, Siberia: a clue to physical properties of kimberlite magmas? Geophys. Res. Lett. 34.
Kamenetsky, V.S., Kamenetsky, M.B., Weiss, Y., Navon, O.M., Nielsen, T.F.D., Mernagh, T.P., 2009a. How unique is the Udachnaya-East kimberlite? Comparison with kimberlites from the slave craton (Canada) and SW Greenland. Lithos 112, 334–346.
Kamenetsky, V.S., Maas, R., Kamenetsky, M.B., Paton, C., Phillips, D., Golovin, A.V., Gornova, M.A., 2009b. Chlorine from the mantle: magmatic halides in the Udachnaya-East kimberlite, Siberia. Earth Planet. Sci. Lett. 285, 96–104.
Kamenetsky, V.S., Kamenetsky, M.B., Golovin, A.V., Sharygin, V.V., Maas, R., 2012. Ultrafresh salty kimberlite of the Udachnaya-East pipe (Yakutia, Russia): a petrological oddity or fortuitous discovery? Lithos 152, 173–186.
Kamenetsky, V.S., Grutter, H., Kamenetsky, M.B., Goemann, K., 2013. Parental carbonatitic melt of the koala kimberlite (Canada): constraints from melt inclusions in olivine and Cr-spinel, and groundmass carbonate. Chem. Geol. 353, 96–111.
Kamenetsky, V.S., Golovin, A.V., Maas, R., Giuliani, A., Kamenetsky, M.B., Weiss, Y., 2014. Towards a new model for kimberlite petrogenesis: evidence from unaltered kimberlites and mantle minerals. Earth Sci. Rev. 139, 145–167.
Kjarsgaard, B.A., Pearson, D.G., Tappe, S., Nowell, G.M., Dowall, D.P., 2009. Geochemistry of hypabyssal kimberlites from lac de Gras, Canada: comparisons to a global database and applications to the parent magma problem. Lithos 112, 236–248.
Kopylova, M.G., Matveev, S., Raudsepp, M., 2007. Searching for parental kimberlite melt. Geochim. Cosmochim. Acta 71, 3616–3629.
Kopylova, M.G., Kostrovitsky, S.I., Egorov, K.N., 2013. Salts in southern Yakutian kimberlites and the problem of primary alkali kimberlite melts. Earth Sci. Rev. 119, 1–16.
Kurszlaukis, S., Barnett, R.L., 2003. Volcanological and structural aspects of the Venetia kimberlite cluster – a case study of South African kimberlite maar-diatreme volcanoes. S. Afr. J. Geol. 106, 165–192.

Lawless, P.J., Gurney, J.J., Dawson, J.B., 1979. Polymict peridotites from the Bultfontein and de Beers mines, Kimberly, South Africa. In: Boyd, F.R., Meyer, H.O.A. (Eds.), The Mantle Sample. 2nd International Kimberlite Conference. American Geophysical Union, pp. 145–155.
le Roex, A.P., Bell, D.R., Davis, P., 2003. Petrogenesis of group I kimberlites from Kimberley, South Africa: evidence from Bulk-rock geochemistry. J. Petrol. 44, 2261–2286.
Medlin, C.C., 2005. Spherical, multi-shelled, juvenile magmaclasts in kimberlite, Venetia Mine. Unpublished B.Sc. Hons. Thesis. University of Pretoria, Pretoria.
Mernagh, T.P., Kamenetsky, V.S., Kamenetsky, M.B., 2011. A Raman microprobe study of melt inclusions in kimberlites from Siberia, Canada, SW Greenland and South Africa. Spectrochim. Acta A Mol. Biomol. Spectrosc. 80, 82–87.
Mitchell, R.H., 1972. Composition of perovskite in kimberlite. Am. Mineral. 57, 1748–1753.
Mitchell, R.H., 1986. Kimberlites: Mineralogy, Geochemistry and Petrology. Plenum Publishing Company, New York.
Mitchell, R.H., 1995. Kimberlites, Orangeites and Related Rocks. Plenum Press, New York.
Mitchell, R.H., 2008. Petrology of hypabyssal kimberlites: relevance to primary magma compositions. J. Volcanol. Geotherm. Res. 174, 1–8.
Mitchell, R.H., 2013. Oxygen isotope studies of serpentine in kimberlite. Proceedings of the 10th International Kimberlite Conference. Vol. 1, pp. 1–12.
Mitchell, R.H., Skinner, E.M.W., Scott Smith, B.H., 2009. Tuffisitic kimberlites from the Wesselton mine, South Africa: Mineralogical characteristics relevant to their formation. Lithos 112, 452–464.
Nielsen, T.F.D., Sand, K.K., 2008. The Majuagaa kimberlite dike, Maniitsoq region, western Greenland: constraints on an Mg-rich silicocarbonatitic melt composition from groundmass mineralogy and bulk compositions. Can. Mineral. 46, 1043–1061.
Pearson, D.G., Brenker, F.E., Nestola, F., McNeill, J., Nasdala, L., Hutchison, M.T., Matveev, S., Mather, K., Silversmit, G., Schmitz, S., Vekemans, B., Vincze, L., 2014. Hydrous mantle transition zone indicated by ringwoodite included within diamond. Nature 507, 221–224.
Phillips, D., Kiviets, G.B., Barton, E.S., Smith, C.B., Viljoen, F., Fourie, L.F., 1999. 40Ar/39Ar dating of kimberlites and related rocks: problems and solutions. 7th International Kimberlite Conference. Vol. 2, pp. 677–688.
Pioufle, A., Canil, D., 2012. Iron in monticellite as an oxygen barometer for kimberlite magmas. Contrib. Mineral. Petrol. 163, 1033–1046.
Podvysotskiy, V.T., 1985. Serpentine-carbonate mineralization in kimberlites. Int. Geol. Rev. 27, 810–823.
Pokhilenko, N.P., 2009. Polymict breccia xenoliths: Evidence for the complex character of kimberlite formation. Lithos 112, 934–941.
Price, S.E., Russell, J.K., Kopylova, M.G., 2000. Primitive magma from the Jericho pipe, N.W.T., Canada: constraints on primary kimberlite melt chemistry. J. Petrol. 41, 789–808.
Roeder, P.L., Schulze, D.J., 2008. Crystallization of groundmass spinel in kimberlite. J. Petrol. 49, 1473–1495.
Scott Smith, B.H., Nowicki, T.E., Russell, J.K., Webb, K.J., Mitchell, R.H., Hetman, C.M., Harder, M., Skinner, E.M.W., Robey, Jv.A., 2013. Kimberlite Terminology and Classification. Proceedings of 10th International Kimberlite Conference. Vol. 2, 1–17.
Seggie, A.G., Hannweg, G.W., Colgan, E.A., Smith, C.B., 1999. The geology and geochemistry of the Venetia kimberlite cluster, Northern Province, South Africa. Proceedings of the VIIth International Kimberlite Conference. 2, pp. 750–756.
Skinner, E.M.W., 1989. Contrasting Group 1 and Group 2 kimberlite petrology: towards a genetic model for kimberlites. Proceedings of the Fourth International Kimberlite Conference. Geological Society of Australia Special Publication 14, Perth, Australia, pp. 528–544.
Skinner, E.M.W., Marsh, J.S., 2004. Distinct kimberlite pipe classes with contrasting eruption processes. Lithos 76, 183–200.
Smith, C.B., 1983. Pb, Sr and Nd isotopic evidence for sources of southern African cretaceous kimberlites. Nature 304, 51–54.
Smith, C.B., Sims, K., Chimuka, L., Duffin, A., Beard, A.D., Townend, R., 2004. Kimberlite metasomatism at Murowa and Sese pipes, Zimbabwe. Lithos 76, 219–232.
Soltys, A., Giuliani, A., Phillips, D., Kamenetsky, V.S., Maas, R., Woodhead, J., Rodemann, T., 2016. In-situ assimilation of mantle minerals by kimberlitic magmas — Direct evidence from a garnet wehrlite xenolith entrained in the Bultfontein kimberlite (Kimberley, South Africa). Lithos 256-257, 182–196.
Sparks, R.S.J., 2013. Kimberlite volcanism. Annu. Rev. Earth Planet. Sci. 41, 497–528.
Sparks, R.S.J., Baker, L., Brown, R.J., Field, M., Schumacher, J., Stripp, G., Walters, A., 2006. Dynamical constraints on kimberlite volcanism. J. Volcanol. Geotherm. Res. 155, 18–48.
Sparks, R.S.J., Brooker, R.A., Field, M., Kavanagh, J., Schumacher, J.C., Walter, M.J., White, J., 2009. The nature of erupting kimberlite melts. Lithos 112S, 429–438.
Stripp, G.R., Field, M., Schumacher, J.C., Sparks, R.S.J., Cressey, G., 2006. Post-emplacement serpentinization and related hydrothermal metamorphism in a kimberlite from Venetia, South Africa. J. Metamorph. Geol. 24, 515–534.
Tait, M.A., Brown, R.J., 2008. Explosive fissure eruption of a large kimberlite pipe: Venetia K01 kimberlite pipe, Limpopo, RSA. Proceedings of the 9th International Kimberlite Conference, Frankfurt am Main, Germany, pp. 1–3.
Ukhanov, A.V., Ustinov, V.I., Devirts, A.L., 1986. Low Temperatures of Serpentinization of Kimberlite in Yakutia: Evidence From Oxygen Isotopic Study. 288. Doklady Academy Science USSR, pp. 466–469 in Russian.
Van Reenen, D.D., Barton Jr., J.M., Roering, C., Smith, C.A., Van Schalkwyk, J.F., 1987. Deep crystal response to continental collision: the Limpopo belt of southern Africa. Geol. Soc. Am. 15, 11–14.
Walters, A.L., Phillips, J.C., Brown, R.J., 2006. The role of fluidisation in the formation of volcanic kimberlite: grainsize observations and experimental investigations. J. Volcanol. Geotherm. Res. 155, 119–137.
Wilson, M.R., Kjarsgaard, B.A., Taylor, B., 2007. Stable isotope composition of magmatic and deuteric carbonate phases in hypabyssal kimberlite, Lac de Gras field, northwest territories, Canada. Chem. Geol. 242, 435–454.

Appendix 2.1 – Supplementary Figures

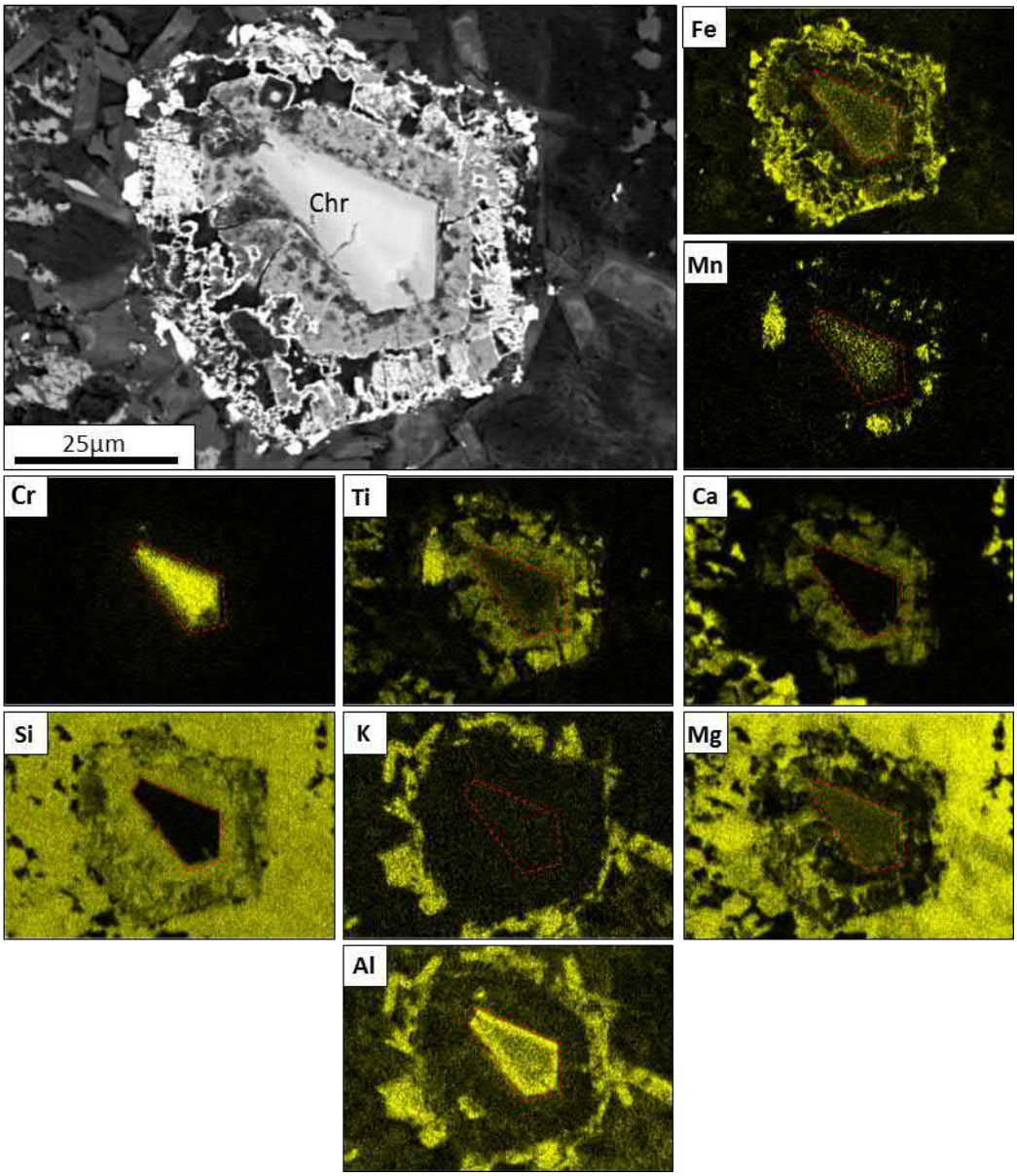

Supplementary Figure S1. Back-scattered electron SEM image and x-ray elemental map of a chromite (Chr) grain. Zonation in the core is reflected through decreasing Cr and increasing Al content. The of Al and K enrichment around chromite is due to a cluster of phlogopite grains. The red line indicates the boundary of the chromite core.

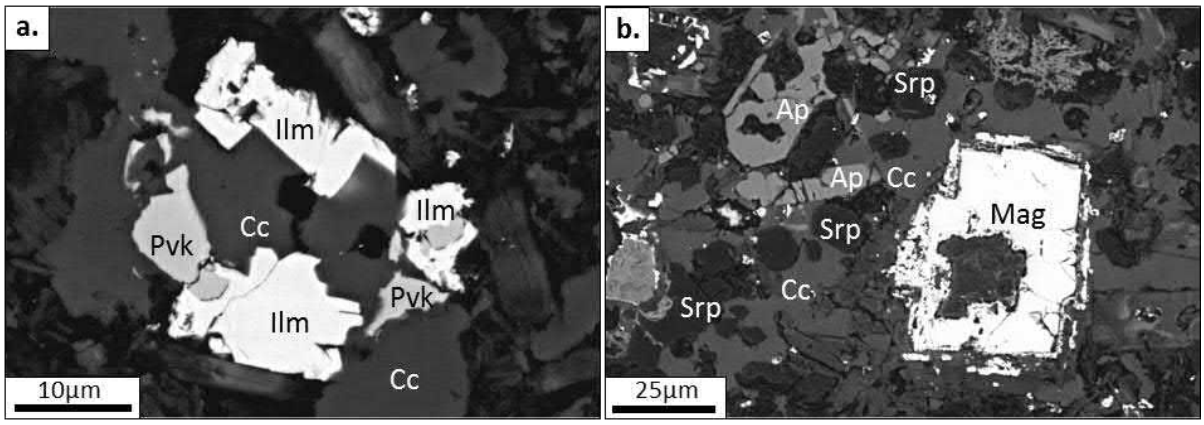

Supplementary Figure S2. Back-scattered electron (BSE) SEM images of interstitial groundmass calcite (Cc) growth in kimberlite sample BI9883. Intergrowth of calcite with: (a) perovskite (Pvk) and ilmenite (Ilm), (b) apatite (Ap), serpentine (Srp) and magnetite (Mag).

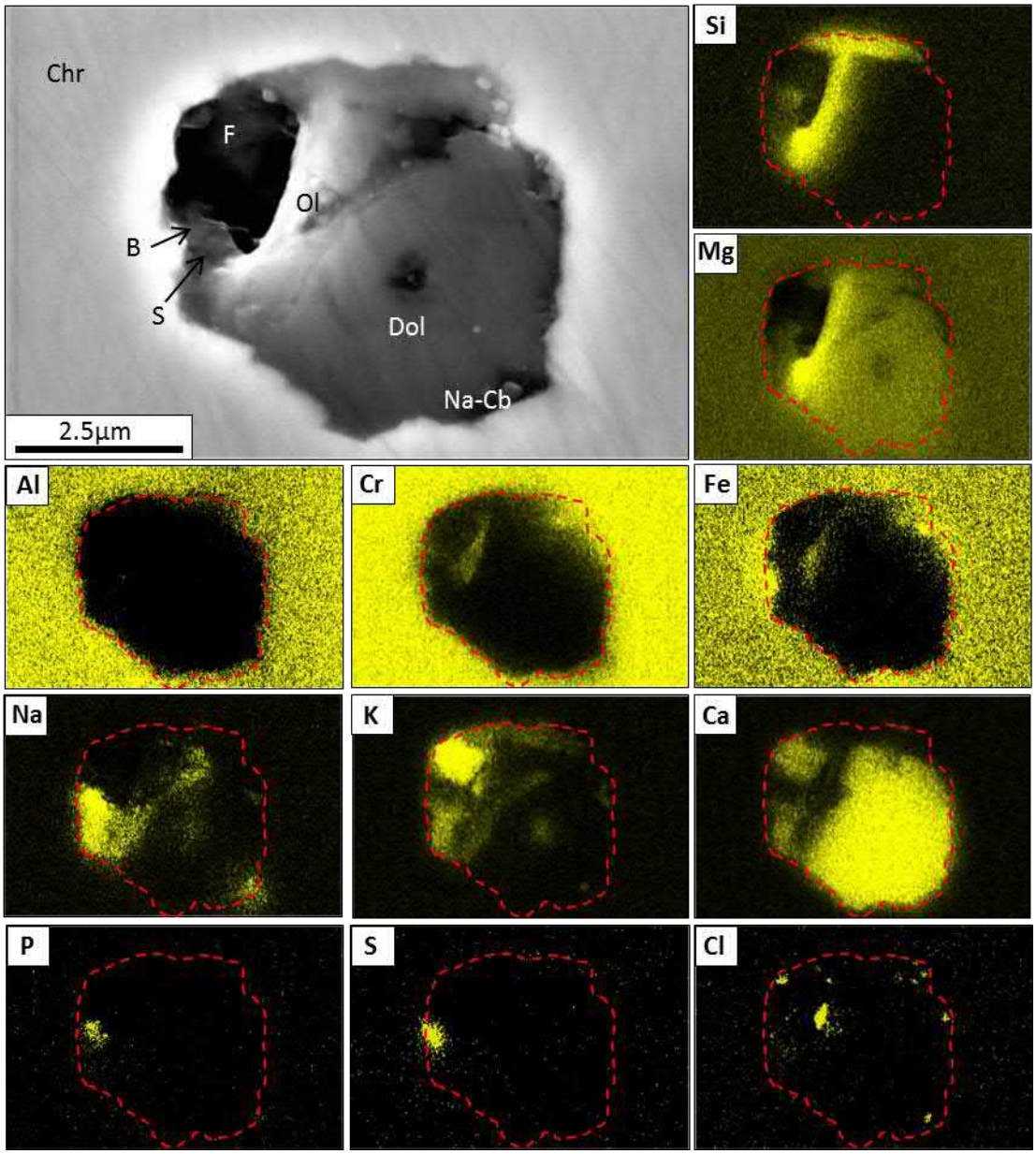

Supplementary Figure S3. Back-scattered electron SEM image and X-ray spectra of a representative inclusion in chromite (Chr). Detected minerals include dolomite (Dol), fairchildite (F), bradleyite (B), sulphide (S), olivine (Ol), phlogopite (Phlg) and Na-carbonate (Na-Cb).

Chemical Geology 478 (2018) 76–88

Contents lists available at ScienceDirect

Chemical Geology

journal homepage: www.elsevier.com/locate/chemgeo

Monticellite in group-I kimberlites: Implications for evolution of parental melts and post-emplacement CO_2 degassing

Adam Abersteiner[a,*], Vadim S. Kamenetsky[a], D. Graham Pearson[b], Maya Kamenetsky[a], Karsten Goemann[c], Kathy Ehrig[d], Thomas Rodemann[c]

[a] School of Physical Sciences, University of Tasmania, Hobart, Tasmania 7001, Australia
[b] Department of Earth and Atmospheric Sciences, University of Alberta, 1-26 Earth Sciences Building, Edmonton, Alberta T6G 2E3, Canada
[c] Central Science Laboratory, University of Tasmania, Hobart, Tasmania 7001, Australia
[d] BHP Billiton Olympic Dam, Adelaide, SA 5000, Australia

ARTICLE INFO

Keywords:
Kimberlite
Monticellite
Periclase
Melt inclusions
Alkali-carbonate
CO_2 degassing

ABSTRACT

Monticellite is a magmatic and/or deuteric mineral that is often present, but widely varying in concentrations in Group-I (or archetypal) kimberlites. To provide new constraints on the petrogenesis of monticellite and its potential significance to kimberlite melt evolution, we examine the petrography and geochemistry of the minimally altered hypabyssal monticellite-rich Leslie (Canada) and Pipe 1 (Finland) kimberlites. In these kimberlites, monticellite (Mtc) is abundant (25–45 vol%) and can be classified into two distinct morphological types: discrete and intergrown groundmass grains (Mtc-I), and replacement of olivine (Mtc-II).

Primary multiphase melt inclusions in monticellite, perovskite and Mg-magnetite contain assemblages dominated by alkali (Na, K, Ba, Sr)-enriched Ca-Mg-carbonates, chlorides, phosphates, spinel, silicates (e.g. olivine, phlogopite) and sulphides. These melt inclusions probably represent snapshots of a variably differentiated kimberlite melt that evolved in-situ towards carbonatitic and silica-poor compositions. Although unconstrained in their concentration, the presence of alkali-carbonates and chlorides in melt inclusions suggests they are a more significant component of the kimberlite melt than commonly recorded by whole-rock analyses.

We present petrographic and textural evidence showing that pseudomorphic Mtc-II resulted from an in-situ reaction between olivine and the carbonate component of the kimberlite melt in the decarbonation reaction: Forsterite + Carbonate (melt) ⇌ Monticellite + Periclase + CO_2.

This reaction is supported by the preservation of abundant primary inclusions of periclase and to a lesser extent Fe-Mg-oxides in monticellite, perovskite and Mg-magnetite. Based on the preservation of primary periclase inclusions, we infer that periclase also existed in the groundmass, but was subsequently altered to brucite.

We suggest that CO_2 degassing in the latter stages of kimberlite emplacement into the crust is largely driven by the observed reaction between olivine and the carbonate melt. For this reaction to proceed, CO_2 should be removed (i.e. degassed), which will cause further reaction and additional degassing in response to this chemical system change (Le Chatelier's principle). Our study demonstrates that these proposed decarbonation reactions may be a commonly overlooked process in the crystallisation of monticellite and exsolution of CO_2, which may in turn contribute to the explosive eruption and brecciation processes that occur during kimberlite magma emplacement and pipe formation.

1. Introduction

Group-I (or archetypal; Mitchell, 1995) kimberlites are relatively rare and volumetrically insignificant igneous rocks that originate from great mantle depths (> 150–200 km; Clement et al., 1984; Mitchell, 1986). Kimberlite rocks are composed of two principle components: i) olivine, which is considered to be largely mantle xenocrysts (Kamenetsky et al., 2008; Brett et al., 2009; Pilbeam et al., 2013; Bussweiler et al., 2015) and a significant contributor to the high Mg# of kimberlite rocks (Mitchell, 1986) and, ii) carbonate (e.g., calcite), which is considered to be mainly of magmatic origin (Dawson, 1980; Mitchell, 1986; Armstrong et al., 2004; Wilson et al., 2007; Giuliani

* Corresponding author.
E-mail address: adam.abersteiner@utas.edu.au (A. Abersteiner).

http://dx.doi.org/10.1016/j.chemgeo.2017.06.037
Received 12 January 2017; Received in revised form 24 May 2017; Accepted 27 June 2017
Available online 29 June 2017

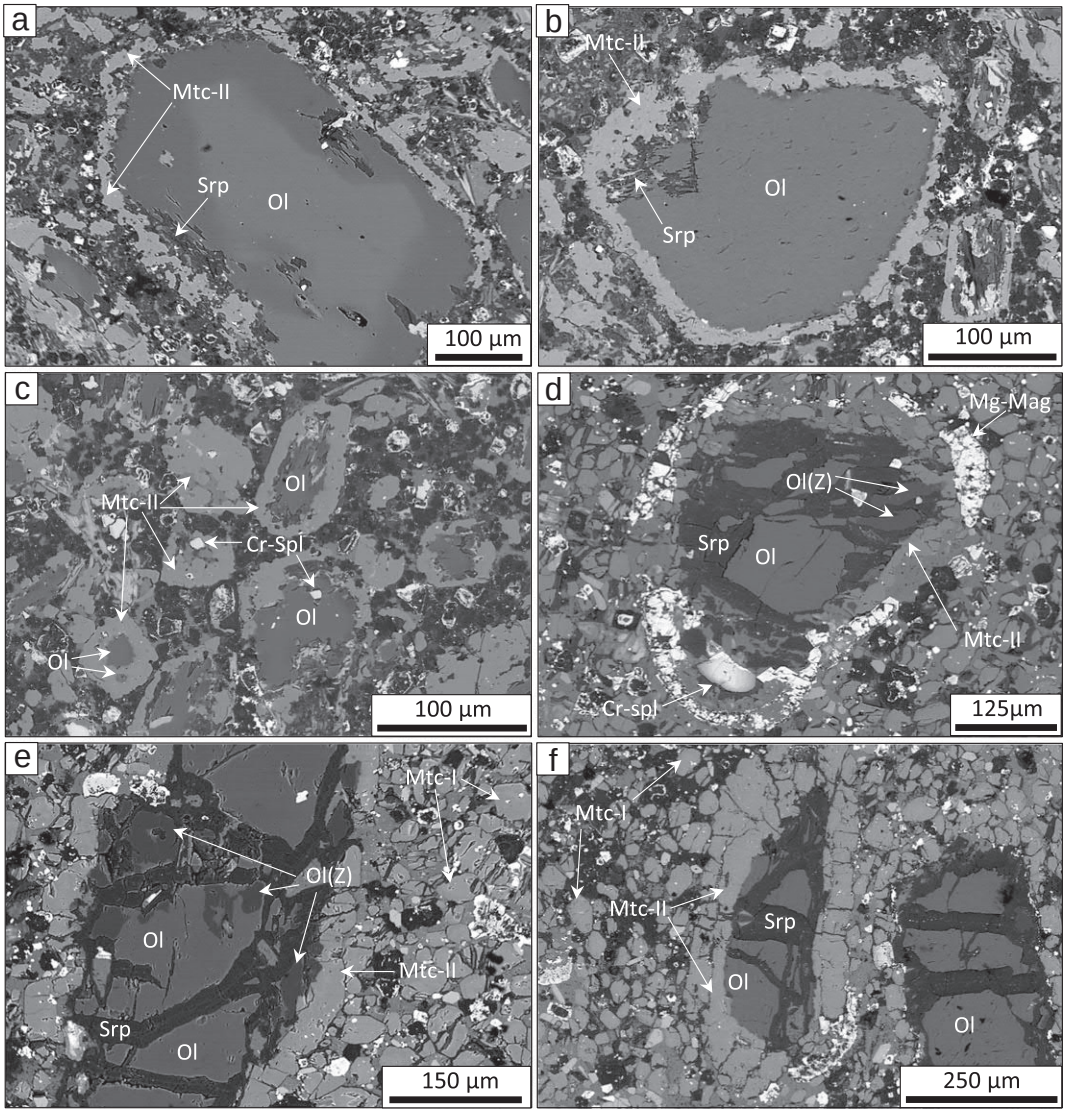

Fig. 1. Back-scattered electron (BSE) SEM images of the groundmass textures of: (a–f) Olivine (Ol) partially replaced by Mtc-II (Mtc) in sample LDC7 (a–c) and FLP1 (d–f). (c) Olivine is almost completely replaced by Mtc-II and only relic olivine and Cr-spinel (Cr-Spl) remains. (d) Monticellite-II replacing olivine is surrounded by a partial epitaxial overgrowth of Mg-magnetite (Mg-Mag). (d, e) Olivine grains in sample FLP1 exhibit patchy zoning (Ol(Z)) towards high Fo-content (> 98) along internal fractures and along the contacts with pseudomorphic Mtc-II. Srp: serpentine.

et al., 2014; Bussweiler et al., 2016; Tappe et al., 2017), but is also related to externally derived hydrothermal fluids (Exley and Jones, 1983; Podvysotskiy, 1985; Giuliani et al., 2014; Giuliani et al., 2016). Serpentine is also a major groundmass component in the majority of kimberlites where it commonly replaces minerals such as olivine, monticellite and carbonate (Skinner and Clement, 1979; Mitchell, 1986). In addition to these minerals, the kimberlite groundmass contains varying amounts of accessory components that include phlogopite, perovskite, spinel, monticellite, apatite and other minor phases (Dawson, 1980; Mitchell, 1986; Skinner, 1989).

Kimberlite rocks are no longer considered to be representative of their parental melts because: i) kimberlites are hybrid rocks that entrain significant xenogenic material (e.g., olivine; Kamenetsky et al., 2008; Brett et al., 2009; Arndt et al., 2010). ii) Kimberlite melts have been shown to react with entrained xenoliths, xenocrysts (Hunter and Taylor, 1982; Stripp et al., 2006; Buse et al., 2010; Soltys et al., 2016), cratonic lithosphere (Tappe et al., 2017) and wall rocks (Smith et al., 2004). iii) Kimberlite magmas exsolve and degas volatiles (e.g., H_2O and CO_2) during their ascent to the surface and upon emplacement (Sparks et al., 2006; Nowicki et al., 2008). iv) Kimberlite rocks are almost always altered by syn- and post-magmatic alteration by deuteric (Mitchell, 2008, 2013) and/or hydrothermal and meteoric fluids (Sparks et al., 2006; Sparks et al., 2009; Giuliani et al., 2014; Giuliani et al., 2016).

In order to constrain the petrogenesis of kimberlite melts, we examine monticellite, which occurs in the groundmass of kimberlites, exclusively within minimally altered samples in highly variable amounts, rarely up to 80 vol% (Nikishov and Nikishova, 1966; Mitchell, 1978; Skinner and Clement, 1979; Shee et al., 1991; Kampata et al., 1994; Beard et al., 1998). In this contribution, we present a detailed study of monticellite and monticellite-hosted inclusions from the Leslie (Slave Craton, Canada) and Pipe 1 (Karelian Craton, Finland) kimberlites and demonstrate the influence of monticellite crystallisation on kimberlite melt evolution and CO_2 degassing.

2. Geological setting

The Eocene-aged (53.1 ± 0.7 Ma, 2σ; Sarkar et al., 2015) Leslie kimberlite is part of the Lac de Gras kimberlite field consists of > 150 kimberlite bodies (i.e. diatremes and dykes; Nowicki et al., 2004) and is located in the east-central Archean Slave Province, Canada. The Leslie kimberlite pipe was intruded through Archean porphyritic biotite granites (Berg and Carlson, 1998; Kjarsgaard et al., 2002). The Leslie

kimberlite pipe is composed predominantly of monticellite-rich, hypabyssal facies kimberlite. Crater facies kimberlite is largely absent and only remnant volcaniclastic/tuffisitic kimberlite breccias occur along the pipe margins (Berg and Carlson, 1998; Armstrong et al., 2004; Fedortchouk and Canil, 2004).

The early Silurian-aged (430 Ma) Pipe 1 kimberlite is part of the Kupio-Kaavi kimberlite cluster consists of approximately 24 kimberlite bodies (Tyni (1997)) and is located on south-western margin of the Archean Karelian Craton in eastern Finland. The Pipe 1 kimberlite is considered the 'freshest' of the Kupio-Kaavi cluster and was intruded through basement gneisses of the Archean Karelian craton and Proterozoic allochthonous metasedimentary cover rocks which are thought to have thrusted onto the Karelian craton during Svecofennian orogeny 1.9–1.8 Ga (Kontinen et al., 1992).

3. Sample descriptions: petrography, mineralogy and geochemistry

3.1. Petrography and mineralogy

Leslie kimberlite sample (LDC7) was obtained from a section of drill core (LDC7: depth unknown) and Pipe 1 kimberlite sample (FLP1) represents a fragment of kimberlite rock derived from the surface exposure of the Pipe 1 kimberlite.

Samples LDC7 and FLP1 were examined by optical and scanning electron microscopy (SEM; see methods in Supplementary material). Both samples are representative of Group-I hypabyssal facies kimberlite and exhibit similar groundmass textures and mineralogy. Olivine is abundant (~40–50 vol%) in both samples, occurring as anhedral-to-rounded (up to 10 mm) and euhedral phenocrystic grains (< 0.1 to > 0.5 mm) which exhibit limited alteration to serpentine and carbonate (i.e. calcite) along grain rims and internal fractures (Fig. 1). The compositions of olivine and monticellite (Tables 1 and 2) were analysed by electron microprobe (EMP) and SEM-EDS (see Supplementary material for methodology). The cores of olivine grains in sample LDC7 show variable Fo (87.4–92.5 mol% in EMP; Table 1; 88–94 mol% in SEM-EDS; Fig. 2). This is consistent with analyses of olivine cores in the Leslie kimberlite by Fedortchouk and Canil (2004). Zoned overgrowths display an elevated and more narrow Fo range (91.5–93.0 mol%; Table 1). Olivine grains in sample FLP1 exhibit a relatively restricted range in Fo (90.2–90.9 mol% in EMP; Table 2). Olivine also exhibits irregularly shaped and intermittent zoning along the internal fractures and contacts with pseudomorphic monticellite (Figs. 1e, e and 2d; see Section 4 for details). These zones were analysed in sample FLP1 and are characterised by almost pure forsterite (> 98.3 mol% in EMP; Table 2).

The groundmasses of LDC7 and FLP1 contain similar mineral phases which include (in order of relative abundance) monticellite, calcite, phlogopite/kinoshitalite, brucite, spinel (Cr-spinel, MUM, Mg-magnetite, pleonaste), apatite, perovskite and Fe-Ni-Cu-sulphides (djerfisherite ($K_6Na(Fe^{2+},Cu,Ni)_{25}S_{26}Cl$)) along with abundant alteration phases (i.e. brucite and interstitial serpentine and calcite). Monticellite is a dominant groundmass mineral in both samples LDC7 (~25 vol%) and FLP1 (~40–45 vol%) occurring as discrete euhedral grains and aggregates (Fig. 3a–c) and as replacement of olivine (Figs. 1 and 3d–f; see Section 4 for details). Phlogopite/kinoshitalite is complexly zoned and commonly forms elongate (30–150 μm; Fig. 4a, b and Supplementary Fig. S1) grains and larger > 300 μm poikilitic segregations which commonly contain oikocrysts of monticellite, brucite, Fe-Mg-oxides and Cr-spinel. Brucite is a common phase in both samples and occurs as discrete round grains that range in size from 5 to 50 μm (Fig. 4a–c and Supplementary Fig. S1) and are uniformly distributed throughout the groundmass. Brucite commonly contains very thin (< 2 μm), discontinuous rims (or 'coatings') of Mg-magnetite along the internal grain margins and disseminated throughout the core (Fig. 4b and c). Cr-spinel is a more significant groundmass phase in sample FLP1 than in LDC7, where it has well developed atoll-textures (Fig. 4d and e; see Mitchell, 1986; Roeder and Schulze, 2008). Here, a euhedral zoned Cr-spinel core is surrounded by a 'lagoon' consisting of serpentine, calcite ± brucite ± phlogopite ± garnet which is in turn enclosed by a variably thick (5–50 μm) spongy rim of MUM/Mg-magnetite that parallels the shape of the Cr-spinel core exactly (Fig. 4d and e). MUM-rims around chromite in sample FLP1 are occasionally surrounded by a thin (~5 μm) epitaxial rim of Mg-magnetite (Fig. 3d). These cores are classified as titanian magnesian aluminous chromite (TIMAC; Mitchell, 1986) and are zoned towards MUM and pleonaste compositions (e.g., Fig. 4d). These atoll-spinel textures in sample LDC7 are usually poorly preserved and composed of only a thin (< 5 μm) rim of Mg-magnetite (Fig. 4e). Mg-magnetite and MUM also occur is discrete euhedral (10–50 μm and rarely up to ~200 μm) grains throughout the groundmass of both studied samples. Apatite is more common in sample LDC7 than in FLP1 where it occurs as both isolated acicular grains (< 30 μm; Fig. 4e and f) and larger (300–500 μm) segregations (Fig. 4g and h), whereas apatite in FLP1 is a minor phase that only occurs as (< 40 μm) acicular grains. Larger apatite segregations occasionally poikilitically enclose inclusions of olivine, monticellite and spinel (e.g. Fig. 4f).

Table 1
Representative electron microprobe (EMP) analyses of monticellite and olivine from the Leslie (LDC7) kimberlite.

	Monticellite							Olivine								
Grain#	1M-II	2M-II	3M-II	4M-II	5M-I	6M-I	7M-I	1C	2C	3C	3R	4C	5C	5R	6C	6R
SiO_2	37.02	37.64	37.73	37.58	37.79	37.52	37.99	40.95	41.17	40.55	40.89	40.90	40.52	41.28	40.40	40.77
Al_2O_3	0.06	0.04	0.01	0.01	0.02	0.01	< 0.01	0.01	< 0.01	0.01	0.02	0.01	0.01	0.02	0.01	0.01
Cr_2O_3	< 0.02	< 0.02	0.01	< 0.02	0.01	0.01	0.04	0.04	0.03	0.01	0.04	0.02	0.01	< 0.02	0.01	0.10
FeO[a]	2.39	2.19	2.21	2.18	1.96	1.99	2.13	7.41	8.09	9.98	8.19	8.31	10.75	6.91	12.11	8.31
NiO	0.04	0.01	0.02	0.03	0.02	< 0.02	< 0.02	0.38	0.14	0.40	0.37	0.36	0.37	0.09	0.37	0.14
MnO	0.35	0.38	0.28	0.28	0.26	0.27	0.26	0.13	0.17	0.17	0.14	0.13	0.16	0.23	0.18	0.15
MgO	23.37	23.93	24.79	24.47	24.75	24.78	24.78	51.06	50.34	48.94	50.00	50.31	48.39	51.40	46.92	50.29
CaO	34.57	34.61	34.04	34.11	33.99	34.05	34.08	0.03	0.13	0.01	0.04	0.04	0.02	0.18	0.03	0.06
Total	97.80	98.79	99.09	98.67	98.81	98.64	99.29	100.00	100.08	100.07	99.69	100.08	100.22	100.10	100.04	99.83
Mol%																
Mo	94.6	94.0	89.2	90.7	90.3	90.2	89.7	–	–	–	–	–	–	–	–	–
Ki	5.4	4.9	4.8	4.8	4.2	4.3	4.6	–	–	–	–	–	–	–	–	–
Fo	0.0	1.1	6.0	4.6	5.5	5.5	5.7	92.47	91.73	89.74	91.59	91.52	88.92	92.99	87.35	91.52
Fa	–	–	–	–	–	–	–	7.53	8.27	10.26	8.41	8.48	11.08	7.01	12.65	8.48

Monticellite: M-I = monticellite-I, M-II = monticellite-II.
Olivine: C = core, R = rim.
Mo = monticellite, Ki = kirschsteinite, Fo = forsterite, Fa = fayalite.
[a] Total iron.

Table 2
Representative electron microprobe (EMP) analyses of monticellite and olivine from the Pipe 1 (FLP1) kimberlite.

	Monticellite											Olivine						
Grain#	1M-II	2M-II	3-MII	4M-II	5M-I	5M-I(R)	6M-I	7M-I	7M-I(R)	8M-I	8M-I(R)	1C	1Z	2C	3C	3Z	4C	4Z
SiO_2	38.11	37.77	37.84	38.10	37.36	37.99	37.75	38.29	37.40	37.49	38.07	40.81	42.52	40.40	40.64	42.16	40.97	42.49
Al_2O_3	0.02	0.01	0.01	< 0.01	0.03	0.01	0.03	0.01	0.04	0.03	< 0.01	0.03	< 0.01	0.03	0.01	0.01	0.03	0.01
Cr_2O_3	0.01	0.01	0.01	0.02	0.03	0.01	0.02	< 0.02	0.01	0.01	0.01	0.03	0.01	0.05	0.07	0.01	0.02	0.01
FeO[a]	2.40	2.19	2.02	3.28	3.91	2.08	3.48	2.17	5.96	3.89	1.96	9.29	1.13	9.14	8.89	1.33	9.54	1.78
NiO	0.06	0.02	0.01	0.03	0.01	< 0.02	< 0.02	< 0.02	0.03	< 0.02	0.01	0.23	0.01	0.32	0.39	0.02	0.22	0.02
MnO	0.29	0.28	0.27	0.30	0.34	0.28	0.34	0.26	0.37	0.37	0.25	0.16	0.19	0.15	0.12	0.19	0.16	0.23
MgO	24.00	24.90	24.71	24.44	23.34	24.64	23.57	25.14	22.34	22.93	24.78	49.12	56.43	49.59	49.78	55.74	49.28	56.01
CaO	34.59	34.04	34.09	33.61	33.90	34.20	33.88	34.16	33.14	34.46	34.30	0.16	0.21	0.07	0.06	0.23	0.19	0.30
Total	99.46	99.22	98.94	99.77	98.86	99.19	99.08	100.03	99.29	99.18	99.36	99.83	100.51	99.74	99.96	99.70	100.42	100.84
Mol%																		
Mo	92.7	88.9	90.4	84.9	86.8	90.7	87.7	88.5	79.7	89.9	91.0	–	–	–	–	–	–	–
Ki	5.3	4.7	4.4	7.0	8.6	4.5	7.7	4.6	13.0	8.7	4.3	–	–	–	–	–	–	–
Fo	1.9	6.4	5.2	8.1	4.6	4.7	4.6	6.9	7.3	1.4	4.8	90.41	98.89	90.63	90.90	98.68	90.21	98.25
Fa	–	–	–	–	–	–	–	–	–	–	–	9.59	1.11	9.37	9.10	1.32	9.79	1.75

Monticellite: M-I = monticellite-I, M-II = monticellite-II, (R) = rim.
Olivine: C = core, Z = zoned region.
Mo = monticellite, Ki = kirschsteinite, Fo = forsterite, Fa = fayalite.
[a] Total iron.

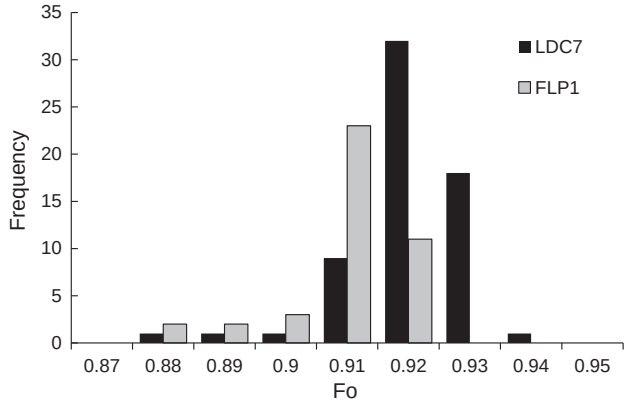

Fig. 2. Histogram of olivine core compositions in samples LDC7 (n = 63) and FLP1 (n = 41) showing the distribution of forsterite (Fo) mol%.

Euhedral perovskite (10–40 μm) is a minor mineral in both samples. Fe-Ni-Cu-sulphides and djerfisherite are disseminated throughout the groundmass and are interstitial to most other phases.

3.2. Geochemistry

The concentrations of most major elements (see Supplementary material for methodology) in samples LDC7 and FLP1 (Supplementary Table 1) are consistent with previous whole-rock analyses of the Leslie kimberlite (Fedortchouk and Canil, 2004; Nowicki et al., 2008) and Pipe 1 (O'Brien and Tyni, 1999), and are typical of kimberlites worldwide (Price et al., 2000; Le Roex et al., 2003; Becker and Le Roex, 2006; Kjarsgaard et al., 2009; Tappe et al., 2011, 2013, 2017).

Primitive mantle normalised (after Sun and McDonough, 1989) lithophile trace element patterns show enrichment in highly incompatible elements (Supplementary Fig. S2a and b) and relative depletion in heavy rare-earth elements, resulting in a negative slope (Supplementary Fig. S2c; Supplementary Table 1). These trace element patterns are characterised by large negative anomalies in Rb, K, Pb, Sr, P, Zr, Hf, Ti and to a lesser extent in Y (Supplementary Fig. S2a and b).

In addition, isotopic compositions of $\delta^{13}C$ (compared to VPDB - "Vienna Pee Dee Belemnite" standard) and $\delta^{18}O$ (compared to VSMOW – "Vienna Standard Mean Ocean Water" standard) of carbonate were analysed (see Supplementary material for methodology) and found to be $\delta^{13}C = -5.00‰$ and $\delta^{18}O = 13.69‰$ for LDC7 and $\delta^{13}C = -5.23‰$ and $\delta^{18}O = 17.90‰$ for FLP1.

4. Monticellite petrography, compositions and inclusions

4.1. Petrography of monticellite

Monticellite is a dominant groundmass phase in samples LDC7 and FLP1. The approximate mass fraction of monticellite in each sample was calculated by subtracting the CaO-content from calcite (based on CO_2-content and assuming calcite is dominantly magmatic) and apatite (based on P_2O_5-content), and assuming that perovskite is a volumetrically insignificant phase. Based on this recalculated CaO-total (which is hosted in monticellite), mass balance calculations show that monticellite comprises approximately 14.6 wt% of sample LDC7 and 25.6 wt% of sample FLP1. In our studied rocks, monticellite (Mtc) occurs as two distinct morphological types which are described below:

Mtc-I occurs as subhedral-to-euhedral microphenocrysts ranging from 10 to 150 μm in sample LDC7 (Fig. 3a) and 10–80 μm in sample FLP1 (Figs. 1e, f, 3b, c, f, 4d and f). Monticellite grains are generally uniformly distributed throughout the groundmass but also form densely packed clusters (Fig. 3a and b). The majority of monticellite grains exhibit compositional heterogeneity and zoning is usually very patchy and diffuse, which is characterised by minor variations in Fe-content (Fig. 3c; Tables 1 and 2; see Section 4.2 for details).

Mtc-II forms pseudomorphs after olivine (Figs. 1 and 3d–f). Monticellite replacing olivine is more prevalent in sample LDC7, where numerous groundmass olivine grains are partially replaced and only relic olivine remains (e.g., Figs. 1c, 3d and e).The contacts between relic olivine and pseudomorphic monticellite are usually highly irregular and jagged. Pseudomorphic monticellite sometimes contains small anhedral relic inclusions (< 20 μm) of olivine (Figs. 1c and 3e). Monticellite replaces both euhedral and anhedral-to-rounded shaped olivine grains, and in cases completely replaces some olivine grains (< 50–100 μm). These completely replaced olivine grains are distinguished from discrete groundmass grains (i.e. Mtc-I) by the presence of small relic inclusions (< 20 μm) of olivine and Cr-spinel, the absence of zoning, irregular grain boundaries and internal fracturing (Figs. 1c, 3d and e). An additional feature in sample FLP1 is discontinuous overgrowths of Mg-magnetite around Mtc-II replacing olivine (Fig. 1d).

4.2. Monticellite compositions

Both morphologies of monticellite show very similar chemical

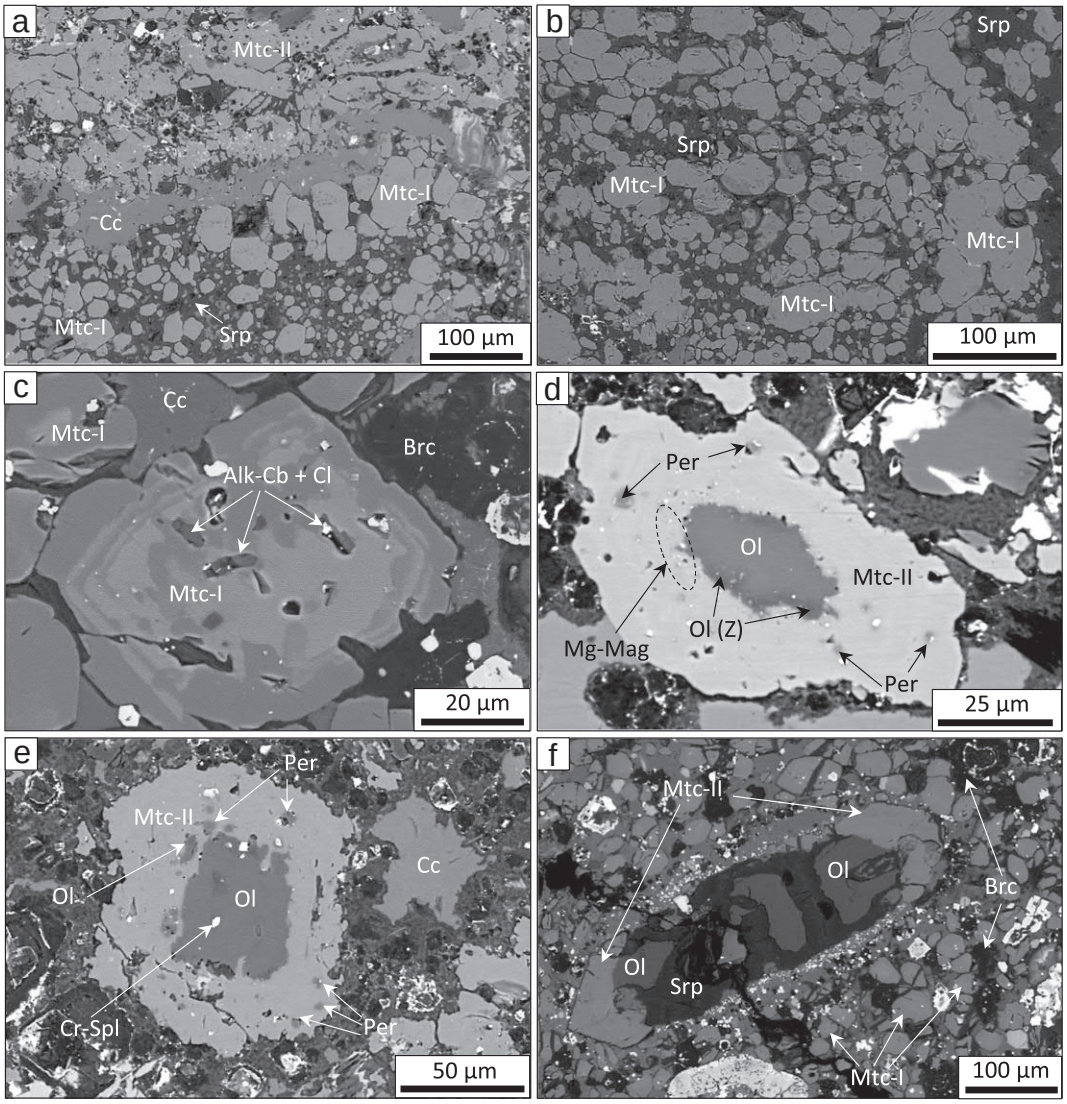

Fig. 3. Back-scattered electron (BSE) SEM images of the groundmass textures of: (a, b) Mtc-I (Mtc) grains forming clusters that are surrounded by interstitial serpentine (Srp) and/or calcite (Cc) in samples (a) LDC7 and (b) FLP1. (c) A concentrically zoned Mtc-I grain oscillating between lighter (more Fe-rich) and darker (less Fe-rich) areas in sample FLP1. This grain also contains several multiphase inclusions consisting of alkali-carbonates (Alk-Cb) and chlorides (Cl). (d–f) Olivine (Ol) replaced by Mtc-II in samples (d, e) LDC7 and (f) FLP1. Pseudomorphic Mtc-II commonly host abundant primary inclusions of periclase (Per), clusters/trails of Mg-magnetite (Mg-Mag; < 2 µm) and anhedral relics of olivine. The olivine grain in (d) is characterised by a zoning (Ol(Z)) along the contact with the pseudomorphic Mtc-II which contains elevated Fo relative to the core. Brc: Brucite.

compositions and are solid solutions of monticellite (84.9–94.6 mol%), kirschsteinite (4.2–13.0 mol%) and forsterite (1.1–8.1 mol%; Fig. 5; Tables 1 and 2), with the exception of a single pseudomorphic Mtc-II analysed in sample LDC7 (94.6 mol%: monticellite and 5.4 mol%: kirschsteinite; Table 1). Mtc-II is characterised by slightly elevated NiO (up to 0.06 wt%) compared to Mtc-I grains, which contain very low (< 0.03 wt%) NiO. The majority of Mtc-I exhibits some degree of compositional heterogeneity, which is usually patchy and diffuse. In sample FLP1, a small proportion (< 1%) of grains exhibit variable zoning patterns of both Fe-richer and Fe-poorer cores and rims (Table 2) as well as multiple zones which oscillate in Fe-content (Fig. 3c).

4.3. Inclusions in monticellite

Monticellite is a host to abundant monomineralic (i.e. crystal) and multiphase (i.e. melt) inclusions. These inclusions are randomly distributed and appear unrelated to any fracture system and are therefore interpreted to be primary. The compositions of inclusions were analysed by field emission (FE) SEM (see Supplementary material for methodology).

Monomineralic inclusions are typically round-to-euhedral in shape and range in size between 1 and 12 µm and are comprised of (in order of decreasing abundance) periclase (Figs. 3d, e and 6), perovskite, phlogopite, Fe-Mg-Al-oxides (Mg-magnetite, pleonaste). To our knowledge, this is the first confirmation of periclase occurring in kimberlites. Nikishov and Nikishova (1966) previously speculated on the presence of periclase inclusions in monticellite, but were unable to positively identify it. Periclase inclusions are typically sub-rounded in shape and range from 2 to 10 µm. EDS analyses revealed periclase to form minor solid solutions with (FeO) wüstite (Mg# ~85–90) and can be more accurately defined as ferropericlase. Furthermore, periclase inclusions in monticellite commonly occur in conjunction with Fe-Mg-oxides (Fig. 6a, c and d) that are usually too small to be accurately identified by EMP (i.e. Mg-magnetite? magnesiowüstite?). These Fe-Mg-oxides also occur as < 2 µm monomineralic inclusions that form clusters adjacent to the monticellite and olivine relic interface (Fig. 3d). Periclase inclusions are sometimes associated with other components (e.g., alkali-carbonates, chlorides, perovskite, phosphates, spinels, silicates and sulphides) which are usually concentrated, forming a

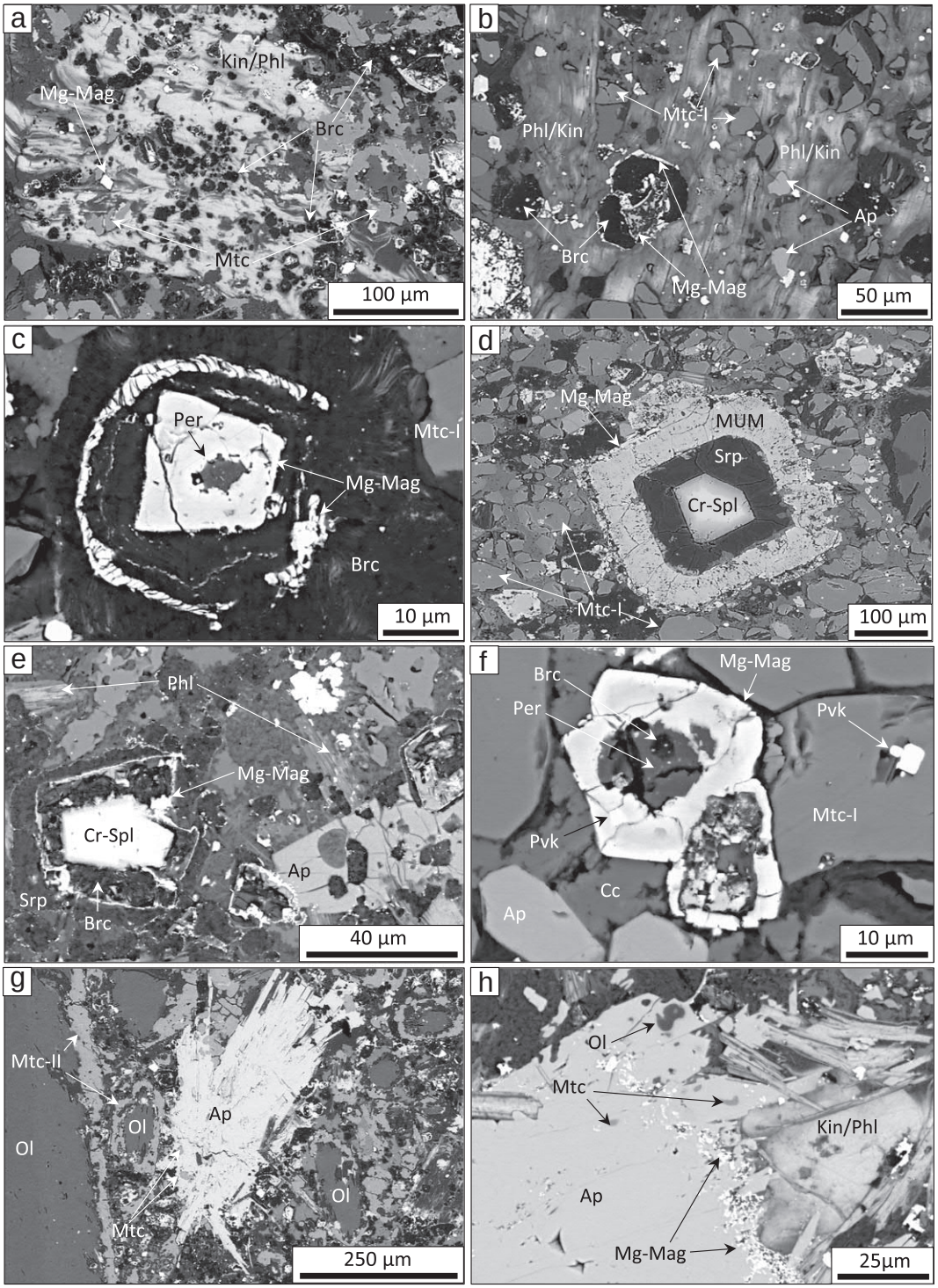

Fig. 4. Back-scattered electron (BSE) SEM images of the groundmass textures of: Zoned phlogopite/kinoshitalite (Phl/Kin) segregations in sample (a) LDC7, and (b) FLP1 poikilitically enclosing monticellite (Mtc), brucite (Brc), apatite (Ap) and Mg-Magnetite (Mg-Mag). (c) A groundmass brucite grain in sample FLP1 with inclusions of Mg-magnetite. The central Mg-magnetite inclusion contains an inclusion of periclase (Per). (d, e) Atoll-shaped grains of Cr-spinel (Cr-Spl) surrounded by a rim of: (d) magnesian ulvöspinel-magnetite (MUM) and Mg-magnetite and a lagoon infilled with serpentine (Srp) in sample FLP1, and (e) Mg-magnetite with a lagoon infilled with brucite in sample LDC7. (f) A groundmass Mg-magnetite grain with contains inclusions of periclase, brucite and perovskite (Pvk) in sample FLP1. (g) A ~350 µm apatite (Ap) segregation that contains oikocrysts of monticellite in sample LDC7. (h) A close-up of a large apatite segregation intergrown with kinoshitalite/phlogopite in sample LDC7. Apatite contains numerous oikocrysts of olivine, monticellite and Mg-magnetite.

'coating' (Fig. 6a). Periclase is replaced by brucite and disseminated Fe-Mg-oxides where fractures intersect the host monticellite grain (Fig. 6d).

Multiphase melt inclusions are almost entirely absent from grains located within the isolated monticellite clusters (Fig. 3a and b). Multiphase inclusions in monticellite exhibit a variety of shapes, ranging from rounded-to-elongate and amoeboid and are 1–15 µm in size. Approximately eighty primary multiphase inclusions were examined in sample LDC7 and FPL1. These inclusions are extremely heterogeneous in composition and contain between two and six phases (Figs. 3c, 7 and 8) which are represented in order of abundance by calcite, alkali (Na, K, Sr, Ba and some F- and V-bearing) carbonates, dolomite, periclase, Mg-

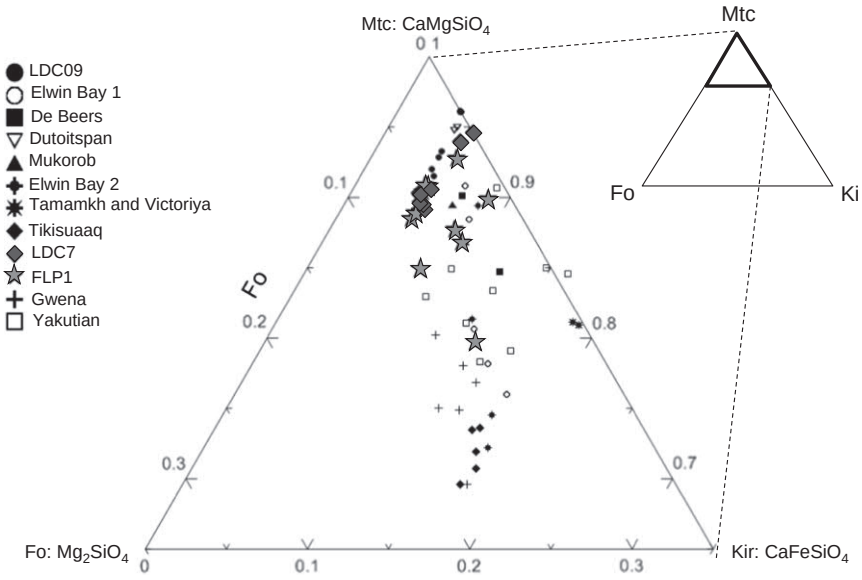

Fig. 5. Ternary diagram of representative compositions of monticellite from samples LDC7 and FLP1. Shown for comparison are compositions of monticellite from Leslie (LDC09-28.9m; Armstrong et al., 2004), Elwin Bay (1; Mitchell, 1978), De Beers (Clement et al., 1975), Dutoitspan (Snowden, 1981), Mukorob (Mitchell, 1986), Elwin Bay (2; Mitchell, 1986) kimberlites, Tamamkh and Victoriya alnöites (Nikishov et al., 1979), Tikisuaaq aillikite dyke (Tappe et al., 2009), Gwena kimberlite (Kampata et al., 1994) and Yakutian kimberlites (Egorov and Bogdanov, 1991). Mtc: monticellite, Ki: kirschsteinite, Fo: forsterite.

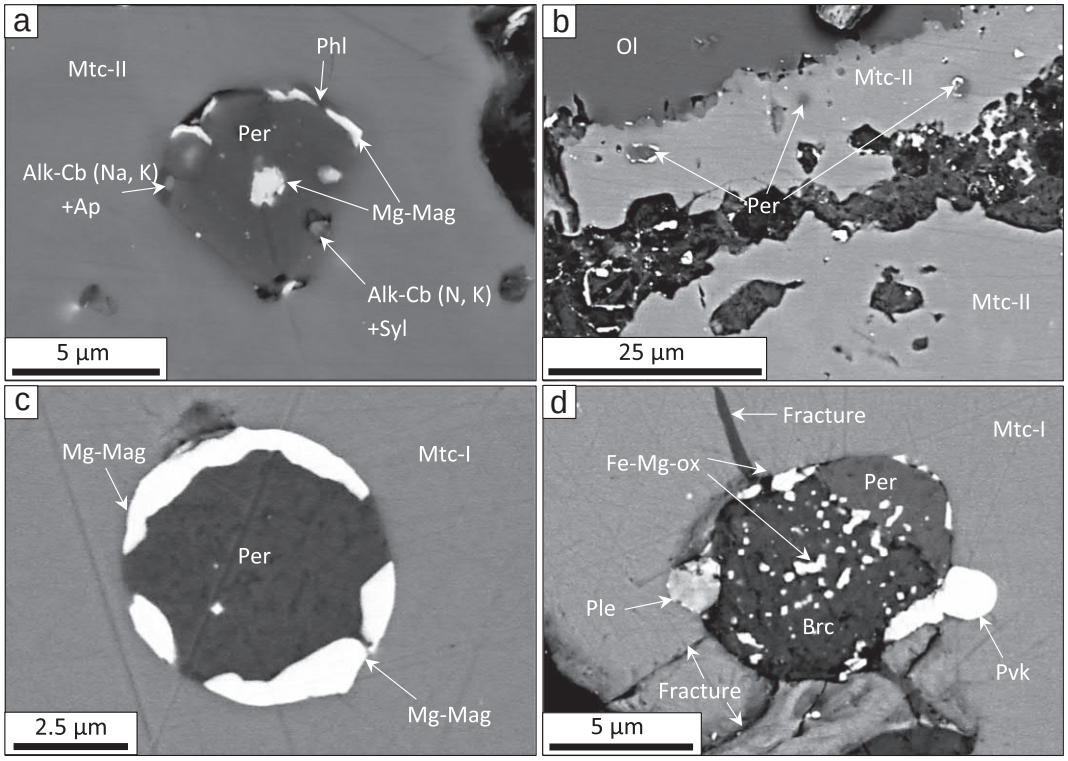

Fig. 6. Back-scattered electron (BSE) SEM images of: (a, b) Periclase inclusions in Mtc-II (Mtc) replacing olivine in sample LDC7. These inclusions are commonly accompanied by a 'coating' along the inclusion peripheries of Mg-magnetite (Mg-mag). (a) This inclusion also contains other phases such as alkali-carbonates (Alk-Cb), apatite (Ap), phlogopite (Phl) and sylvite (Syl). (c, d) Periclase inclusions in groundmass Mtc-I grains in sample FLP1. (c) Similar to LDC7, this inclusion contains a 'coating' of Mg-magnetite along the inclusion peripheries. (d) An inclusion of periclase transected by multiple fractures, exposing it to post-entrapment alteration. Periclase and brucite (Brc) co-exist, where periclase has been partially altered to mixtures of brucite and disseminated Fe-Mg-oxides (Fe-Mg-Ox). This inclusion demonstrates the incomplete transformation of periclase to brucite. Ple: Pleonaste, Pvk: perovskite.

Fe-Al-oxides (e.g., spinel: Mg-magnetite, pleonaste), F-rich apatite, forsteritic olivine, sylvite/halite (including Na-K solid solution), perovskite, phlogopite and Ni-Fe-sulphides (see Table 3).

4.3.1. Inclusions in perovskite, Mg-magnetite and calcite

Periclase and multiphase alkali (Na, K) carbonate and chloride dominated melt inclusions are present in perovskite and Mg-magnetite (Supplementary Figs. S3 and S4). Perovskite is also a common crystal inclusion phase in Mg-magnetite in sample FLP1 (Fig. 4f). Similar to monticellite, inclusions of periclase are replaced by brucite where fractures intersect the host grain (Fig. 4f). Groundmass calcite is also a host to abundant (< 3 µm) disseminated monomineralic inclusions of alkali (Na and to a lesser extent Ba, Sr) carbonates (Supplementary Fig. S5).

5. Discussion

Monticellite, although a significant groundmass mineral in some kimberlites, has remained largely neglected and poorly understood. A prominent feature in samples LDC7 and FLP1 is the presence of

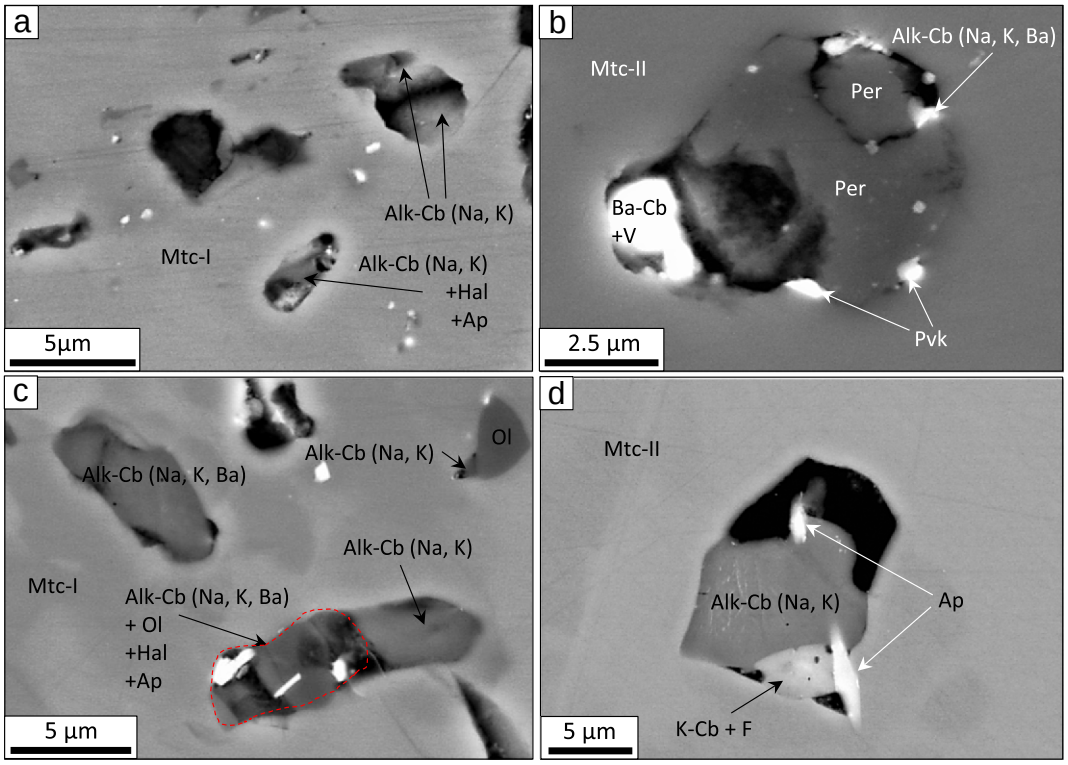

Fig. 7. Back-scattered electron (BSE) SEM images of: (a, b) primary inclusions in monticellite (Mtc) in sample LDC7. These inclusions contain daughter crystals of periclase (Per), alkali-carbonates (Alk-Cb), halite (Hal), apatite (Ap), perovskite (Pvk) and V-bearing Ba-carbonate (Ba-Cb + V). (c, d) Primary multiphase inclusions in monticellite in sample FLP1. These inclusions contain daughter crystals of: alkali-carbonates, olivine (Ol), halite (Hal), apatite (Ap) and F-bearing K-carbonate (K-Cb + F).

monticellite replacing olivine. There have been few documented occurrences of such monticellite features (also termed 'rims' or 'coronas') around olivine in kimberlites (e.g., Verhoogen, 1938; Nikishov and Nikishova, 1966; Kampata et al., 1994; O'Brien and Tyni, 1999), carbonatites (e.g., Barker and Nixon, 1989) and alnöites (Lewis, 1982). In addition, monticellite has also been reported as 'rims' around clinopyroxene and phlogopite in carbonatites (Barker and Nixon, 1989). In other studies, monticellite has been reported as a secondary phase replacing both serpentinised (e.g., Clement, 1982; Kornilova et al., 1983) and unserpentinised olivine (e.g., Tappe et al., 2009). However, there is no holistic understanding on the petrogenesis of monticellite and its different morphologies in kimberlites.

Samples LDC7 and FLP1 show both mineralogical and textural features as well as major and trace element patterns typical of hypabyssal kimberlites worldwide (Mitchell, 1986, 2008; Skinner, 1989). Previous petrographic and geochemical studies show that the Leslie (Fedortchouk and Canil, 2004; Armstrong et al., 2004; Wilson et al., 2007) and Pipe 1 kimberlites (O'Brien and Tyni, 1999) are relatively well-preserved. This is in agreement with incompatible trace element patterns which show pronounced negative Pb, Sr, Zr and Hf anomalies in our samples, indicating minimal contamination (Tappe et al., 2013), especially in comparison to many southern African kimberlites (Supplementary Fig. S2; see Le Roex et al., 2003). Samples LDC7 and FLP1 contain abundant groundmass monticellite (25 and 40–45 vol%, or ~15 and ~25 wt% respectively), which occurs as two distinct morphologies (i.e. Mtc-I: discrete groundmass grains and Mtc-II: replacing olivine). In the following sections we constrain the petrogenesis of monticellite crystallisation and its implications for kimberlite melt evolution and CO_2 degassing.

5.1. Crystallisation of monticellite

The preservation of Mtc-II suggest that monticellite crystallisation occurred in-situ after the kimberlite magma was emplaced and that the groundmass was not significantly disrupted after emplacement by any physical processes such as mechanical rounding/abrasion (e.g., olivine rounding; Reid et al., 1975; Arndt et al., 2010), explosivity or brecciation. This intact nature of the groundmass in our studied samples is further supported by other well-preserved features, such as the euhedral shapes of discrete Mtc-I and atoll-rims around Cr-spinel.

The compositional similarity between both morphologies of monticellite (Tables 1 and 2; Fig. 5) suggests that they crystallised at the same time. This crystallisation timing can be further constrained from crystal inclusions of perovskite in Mtc-I (Fig. 4f) and the interstitial growth around some Cr-spinel grains, indicating that monticellite crystallised after Cr-spinel and sometime during and/or after perovskite formed. The zoning of Cr-spinel grains from TIMAC towards MUM and pleonaste compositions is typical of archetypal kimberlites and is attributed to magma differentiation (Mitchell, 1986; Roeder and Schulze, 2008). Monticellite probably formed at the same time as Mg-magnetite/pleonaste based on abundant daughter phases of Mg-Fe-Al-spinels occurring within multiphase inclusions and as euhedral crystal inclusions in monticellite. In sample FLP1, epitaxial mantles of Mg-magnetite are sometimes overgrown around Mtc-II replacing olivine (Fig. 1d) indicating that Fe-Mg-spinel crystallisation continued after monticellite had formed. Large groundmass apatite and phlogopite segregations commonly contain oikocrysts of monticellite (Fig. 4a, b and f), indicating monticellite crystallisation occurred before and/or together with apatite and phlogopite formation. A summary of the relative crystallisation history of samples LDC7 and FLP1 is presented in Fig. 9 based on our petrographic observations.

5.2. Constraining late-stage kimberlite melt composition from melt inclusions

Melt inclusions in monticellite, perovskite and Mg-magnetite in samples LDC7 and FLP1 are characterised by alkali (Na, K, Ba, Sr)-enriched Ca-Mg-carbonates, chlorides, phosphates, spinel, silicates (e.g.

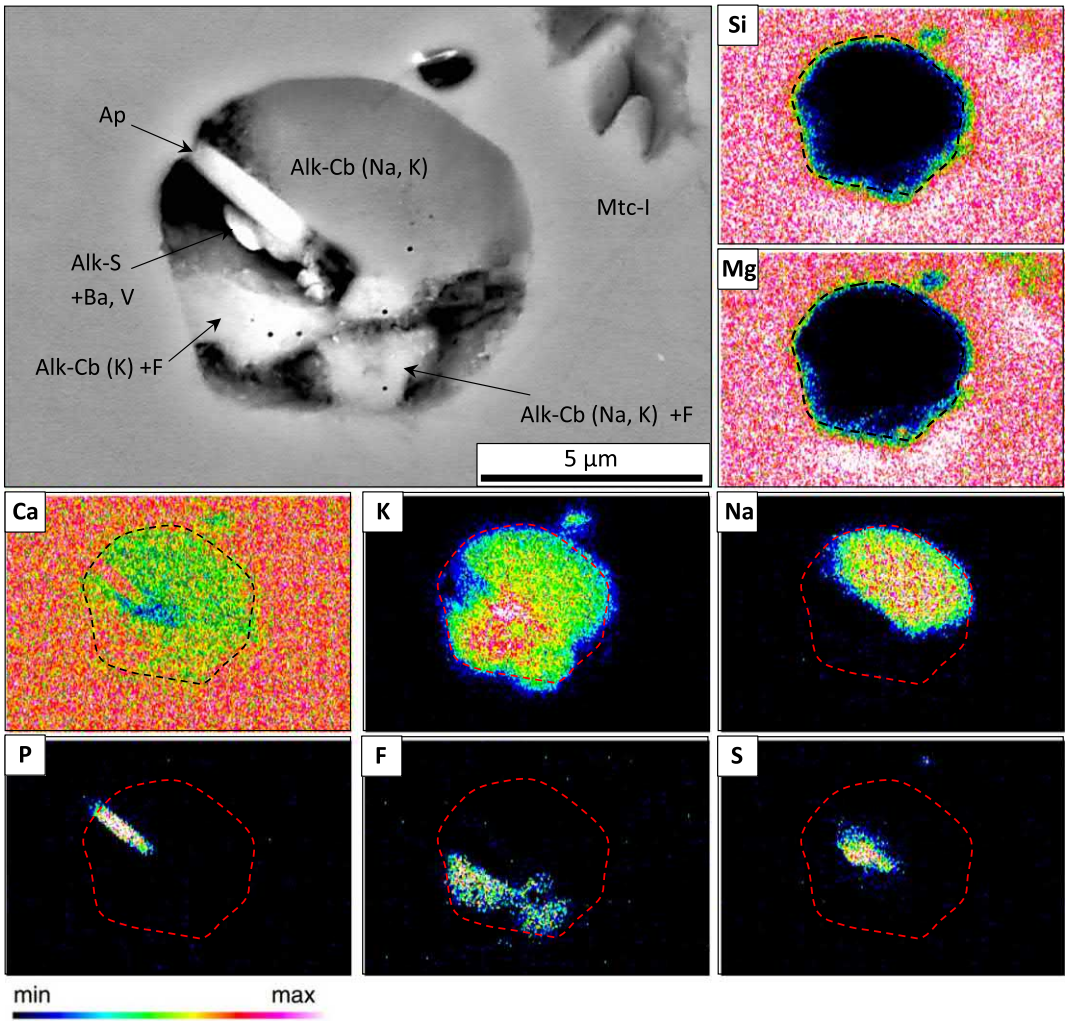

Fig. 8. Back-scattered electron SEM image and X-ray elemental map of a representative inclusion in monticellite-I (Mtc) in sample FLP1. Detected minerals include: apatite (Ap), alkali-sulphur-bearing mineral + Ba, V (Alk-S), alkali-carbonate (Alk-Cb) + F (fluorine). The black/red dashed line represents the boundary of the inclusion. (For interpretation of the references to colour in this figure legend, the reader is referred to the web version of this article.)

olivine, phlogopite) and sulphides. Previous studies of melt inclusions in olivine, Cr-spinel, perovskite and apatite from various kimberlites worldwide (Kamenetsky et al., 2009, 2012, 2013; Golovin et al., 2007; Abersteiner et al., 2016; Giuliani et al., 2016), olivine and ilmenite in kimberlitic polymict breccias (Giuliani et al., 2012) and in mantle xenolith-hosted minerals (Soltys et al., 2016) reported similar alkali-carbonate dominated, silicate-chloride-phosphate-bearing phase assemblages to the ones observed in our samples. We suggest that the melt inclusions in groundmass kimberlite minerals represent the entrapment of a variably differentiated kimberlite melt. The low-silica content in melt inclusions in monticellite, perovskite and Mg-magnetite in our samples indicates the kimberlite melt was Si-poor during groundmass crystallisation. Olivine is the dominant silicate phase in most kimberlites and estimates on the amount of its crystallisation ranges from 25 vol% (Clement, 1982; Scott-Smith, 1996; Harris et al., 2004) to ~5 vol% (Brett et al., 2009). Therefore, the perceived amount of olivine, monticellite and to a lesser extent phlogopite crystallisation from the kimberlite melt will have large implications for the initial Si-content of the initial kimberlite melt. Based on our analyses of melt inclusions, monticellite, perovskite and Mg-magnetite were crystallised from a Ca-Mg and alkali (Na, K, Ba, Sr) enriched, P-Cl-bearing, carbonate-silicate melt.

The presence of abundant Na-Ba-Sr-carbonates inclusions in groundmass calcite further confirms the alkali and alkali-earth-rich nature of the late-stage melt after differentiation of the primary kimberlite melt occurred. Alternatively, these inclusions represent relics of alkali-carbonate that survived groundmass carbonate recrystallization induced by infiltrating external fluids.

There is an unequivocal discrepancy between the whole-rock geochemistry (Supplementary Table 1), the phase assemblages observed in the kimberlite groundmass, and the compositions of primary melt inclusions in monticellite (Table 3), perovskite and Mg-magnetite. Alkalis and halogens typically reside in water-soluble minerals, therefore it is likely that the effects of low temperature alteration typically associated with kimberlite rocks (i.e. serpentinisation) could significantly modify/remove any primary crystallising alkali-carbonate, chloride and phosphate minerals in the groundmass (see Kamenetsky et al., 2014; Giuliani et al., 2016). This alludes to a proto-kimberlite melt which contains higher concentrations of alkali-carbonates, chlorides and phosphates than commonly measured in whole-rock analyses (e.g., Le Roex et al., 2003; Becker and Le Roex, 2006; Nielsen and Sand, 2008; Kjarsgaard et al., 2009). Although unconstrained in their concentration in the proto-kimberlite melt, the presence of abundant alkali-carbonates in melt inclusions in monticellite, perovskite and Mg-magnetite suggests that the carbonate component in the kimberlite melt is more complex than dolomitic/calcitic compositions.

5.3. Origin of monticellite

Petrographic and textural data indicate that olivine replacement by

Table 3
Summary of mineral phases included in multiphase inclusions in monticellite from samples FLP1 and LDC7, listed in order of decreasing abundance. Calculated distribution (%) is based on visual estimates of approximately 80 inclusions in each sample.

FLP1	Distribution (%)	LDC7	Distribution (%)
Alkali-carbonates (Na, K, Sr, Ba) ± F/V	34	Calcite $CaCO_3$	19
Calcite $CaCO_3$	11	Dolomite $CaMg(CO_3)_2$	16
Dolomite $CaMg(CO_3)_2$	10	Alkali-carbonates (Na, K, Sr, Ba)	16
F-rich apatite $Ca_5(PO_4)_3(F,Cl,OH)$	8	Mg-magnetite $MgFe_2O_4$	9
Mg-magnetite $MgFe_2O_4$	7	Spinel Fe-Al-Mg-Cr	7
Halite/sylvite NaCl/KCl	6	Olivine $(Fe,Mg)_2SiO_4$	6
Periclase MgO	5	Apatite $Ca_5(PO_4)_3(F,Cl,OH)$	6
Perovskite $CaTiO_3$	5	Periclase MgO	6
Spinel Fe-Al-Mg-Cr	5	Perovskite $CaTiO_3$	6
Olivine $(Fe,Mg)_2SiO_4$	4	Halite/sylvite NaCl/KCl	6
Phlogopite $KMg_3(AlSi_3O_{10})(F,OH)_2$	3	Sulphides Fe	3
Sulphides Ni, Fe	2		

Mtc-II resulted from an in-situ reaction between olivine and the kimberlite melt. A plausible scenario for this replacement of olivine could be attributed to a specific decarbonation reaction (i.e. release of CO_2).

$$(Fe, Mg)_2SiO_4 + CaCO_3 \rightleftharpoons Ca(Fe, Mg)SiO_4 + (Fe, Mg)O + CO_2$$

Olivine (forsterite) + Carbonate (melt) ⇌ Monticellite + Periclase + Carbon Dioxide (vapour)

(Reaction 1)

This decarbonation reaction was first examined by Sharp et al. (1986) in experimental studies in the CaO-MgO-SiO_2-CO_2 system. A similar reaction between xenocrystic olivine and magmatic calcite was speculated by Barker and Nixon (1989) for the formation of monticellite 'rims' around olivine in the Fort Portal carbonatite:

$$3Mg_2SiO_4 + 6CaCO_3 = CaMgSiO_4 + Ca_5(SiO_4)_2CO_3 + 5MgO + 5CO_2$$

Forsterite+Calcite = Monticellite + Spurrite + Periclase + Carbon Dioxide (vapour)

(Reaction 2)

In our study, we show the first direct petrographic evidence supporting such a reaction. In addition, we propose that Reaction (1) represents a simplified version of a potentially complex array of reactions that may occur between the carbonate component of the cooling kimberlite melt and olivine, many of which evolve CO_2. As previously inferred, alkali-carbonate component is significant in the kimberlite melt and therefore could also react with olivine to produce monticellite, periclase and CO_2.

$$(Mg, Fe)_2SiO_4 + Na_2Ca_2(CO_3)_3 \rightleftharpoons Ca(Fe, Mg)SiO_4 + Na_2Ca(CO_3)_2 + (Fe, Mg)O + CO_2$$

Olivine (forsterite) + Alkali-Carbonate (melt) ⇌ Monticellite + Alkali-Carbonate + Periclase + Carbon Dioxide (vapour)

(Reaction 3)

This represents one example of a potential reaction between the shortite component of a kimberlite melt and olivine. In addition to the formation of Mtc-II replacing olivine, these reactions are supported by the preservation of abundant monomineralic inclusions of periclase and Fe-Mg-oxides in monticellite, perovskite and Mg-magnetite. Alkali-carbonates, such as those produced in Reaction (3) may be preserved within melt inclusions and in the thin 'coatings' associated with inclusions of periclase (e.g., Fig. 6a).

Although petrographic and textural data supports the above reactions as a mechanism for olivine replacement by Mtc-II, the formation of groundmass Mtc-I is more ambiguous. There is ample evidence to show that some monticellite grains were formed by the complete replacement of olivine, as indicated by relics of olivine, euhedral Cr-spinel inclusions and occasionally irregular grain shapes (Figs. 1c, 3d and e). However, the origin of other Mtc-I grains, especially those which with euhedral shapes and are inclusion-free (e.g., Fig. 3a and b)

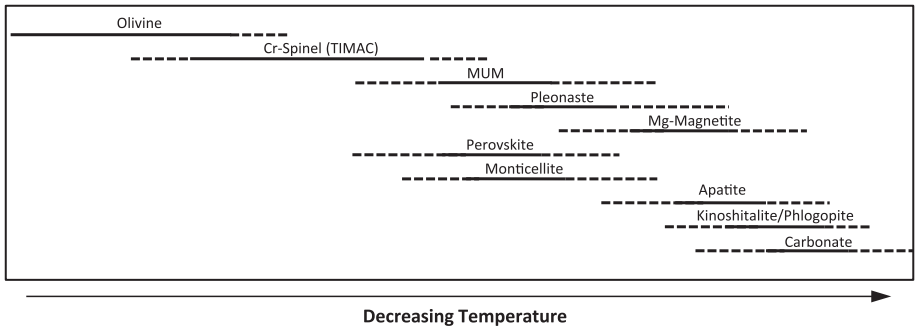

Fig. 9. Crystallisation history and relative crystallisation temperature contrasts of magmatic minerals in samples LDC7 and FLP1.

is more uncertain. These grains may have resulted from complete olivine replacement, or direct crystallisation from the melt. The presence of euhedral crystal inclusions of perovskite (Fig. 4f) and multiphase alkali-carbonate/chloride-dominated melt inclusions (Figs. 3c, 7 and 8) in some Mtc-I grains suggests that they post-date olivine crystallisation. Furthermore, Mtc-II and brucite (i.e. former periclase; see below) occur in approximately equal proportions in the groundmass. Therefore, it is unlikely that decarbonation reactions can account for all Mtc-I produced, as a higher proportion of periclase (or brucite) would be expected in the kimberlite groundmass.

Compositional heterogeneities (i.e. zoning) in Fe-content are common in many Mtc-I grains in our studied samples (e.g., Fig. 3c). Zoning of Fe-rich cores to Fe-poor margins were reported in the monticellite-rich Elwin Bay (Mitchell, 1978) and Yakutian (Monticellitovaya and Dalnaya; Egorov and Bogdanov, 1991) kimberlites, as well as in monticellite from the Tikiusaaq aillikite dykes and carbonatite intrusions (West Greenland; Tappe et al., 2009). These zoning patterns have led some authors to suggest that at least two generations of monticellite may have formed, possibly due to multiple magma intrusions or alteration during emplacement (Le Pioufle and Canil, 2012). We suggest that the compositional heterogeneities in groundmass Mtc-I support direct crystallisation from the kimberlite magma and can be explained by variation in the parental medium where other in-situ crystallising Fe-oxide phases (e.g., MUM, Mg-magnetite) were also competing for Fe.

Based on the presence of primary inclusions of periclase, we infer that brucite in the kimberlite groundmass formed as an alteration product resulting from the hydration of periclase. Such an origin for at least some of the brucite in other, more weathered kimberlites could also be invoked. Both groundmass brucite (Fig. 4a–c and Supplementary Fig. S1) and periclase inclusions (Fig. 6a–c) have similar shapes and commonly contain thin 'coatings' of Mg-magnetite along their peripheries. Brucite is a common alteration mineral in kimberlites that is thought to be preserved when MgO is in excess over SiO_2 as required by serpentine stoichiometry (Malkov, 1974; Berg, 1989). We envisage that periclase/wüstite crystallised in the groundmass of samples LDC7 and FLP1 but was subsequently altered to brucite and Fe-Mg-oxides (e.g., MUM/Mg-magnetite) during post-magmatic alteration (i.e. $MgO + H_2O \rightarrow Mg(OH)_2$; Meyer and Yang, 1962). This hydration reaction is evident in some inclusions in monticellite that were exposed to post-entrapment alteration by fractures. Such inclusions show coexisting periclase and brucite, indicating the incomplete alteration (or hydration) of periclase to brucite (Figs. 4f and 6d). It is likely that during the alteration of periclase, Fe was leached and precipitated to form the Fe-Mg-oxides which are commonly disseminated throughout brucite (Figs. 4b, c and 6d). Several groundmass brucite grains in sample FLP1 contain inclusions of Mg-magnetite, which in turn host inclusions of periclase (Fig. 4c). These probably represent relics of periclase produced during olivine dissolution (i.e. Reactions (1) and (3)). In addition, excess FeO leached during the alteration of periclase and dissolution of olivine was probably also precipitated as the MUM/Mg-magnetite atoll-rims surrounding Cr-spinel (Fig. 4d and e) and as the Mg-magnetite overgrowths around Mtc-II replacing olivine in sample FLP1 (Fig. 1d).

5.4. Implications for kimberlite petrogenesis

The degassing of CO_2 from the kimberlite magma appears instrumental for driving monticellite forming reactions. Consequently, this removal of CO_2 may facilitate further decarbonation reactions and subsequently dissolve more olivine to produce monticellite, periclase, Fe-Mg-oxides and CO_2 in response to this chemical system transformation (Le Chatelier's principle). A plausible scenario that could account for significant CO_2 removal is that the emplaced kimberlite magma was a physically open system, therefore allowing CO_2 segregation and removal from the kimberlite magma. This is exemplified by the $\delta^{13}C$ and $\delta^{18}O$ isotope values of carbonates in samples LDC7 and FLP1 which plot outside the 'mantle range' (as depicted in Demeny et al. (1998) and Giuliani et al. (2014)) and are more consistent with compositions modified by hydrothermal/meteoric fluids and degassing. We envisage that CO_2 production and removal were intrinsically coupled, and thus responsible for production of large abundances of monticellite, periclase and Fe-Mg-oxides observed. In contrast, an isolated/closed magmatic system may impede CO_2 exsolution, therefore hampering a forward reaction. If neither production nor removal of CO_2 from the kimberlite magma is sufficient to disturb the system and cause disequilibria, then the process of crystallising monticellite, periclase/Fe-Mg-oxides and CO_2 at the expense of olivine and carbonate in the kimberlite melt would be limited.

Although there is a large variability in monticellite abundances in kimberlites worldwide (e.g., Skinner and Clement, 1979; O'Brien and Tyni, 1999; Armstrong et al., 2004), the preservation of Mtc-II replacing olivine is exceptionally rare. This apparent rarity could be attributed to: i) pseudomorphic Mtc-II is unlikely to be preserved if crystallisation occurred *en route* to the surface due to physical abrasion. Furthermore, if the kimberlite magma was disrupted (e.g., brecciation, explosivity) by CO_2 degassing then these features may not be preserved in the crystallised rock; ii) monticellite is commonly overprinted by serpentinisation, whereas periclase is replaced by brucite; iii) kimberlite magmas that contain insufficient carbonate may not react significantly with olivine to produce monticellite; iv) carbonate was crystallised preferentially from the kimberlite magma instead of reacting with olivine to produce monticellite. Therefore, interplay of these factors will significantly influence the number of observed occurrences of monticellite-rich kimberlite rocks.

In addition to other commonly invoked decarbonation reactions that may occur in kimberlites (Edgar et al., 1988; Brey et al., 1991; Kamenetsky and Yaxley, 2015; Bussweiler et al., 2016), the interaction between olivine and (alkali-)carbonate in the kimberlite melt to produce monticellite (i.e. Reactions (1) and (3)) could act as a previously overlooked, yet substantial contributor to CO_2 degassing in kimberlites. Although the full volatile inventory of kimberlite magmas is never fully retained due to magma degassing *en route* to the surface and upon emplacement, CO_2 can be accommodated in groundmass carbonate (Mitchell, 1986). The preservation of olivine and groundmass calcite in our samples shows these minerals were not completely consumed during the proposed decarbonation reactions. The incomplete decomposition of carbonate melt and olivine indicates that decarbonation was stalled at some point during groundmass crystallisation, possibly due to decreased rates of CO_2 removal, the onset of carbonate formation and/or solidification.

The presence of carbonates in kimberlite rocks is inferred to provide an approximation on the minimum value of CO_2 in the host kimberlite magma (Brooker et al., 2011), however the amount of CO_2 lost is unaccountable. If CO_2 degassing is the prerequisite mechanism for monticellite formation as proposed in this study, then the observed monticellite in kimberlites could provide some estimates on the extent of CO_2 degassing.

We calculated the amount of CO_2 produced assuming that all monticellite in each sample was formed by the proposed decarbonation reactions in order to constrain a maximum estimate. Based on the approximate mass fraction of monticellite in each sample (i.e. ~14.6 wt% in LDC7 and ~25.6 wt% in FLP1), we determined that approximately ~4.03 wt% and ~7.06 wt% CO_2 was produced in LDC7 and FLP1 respectively. For a cubic metre of kimberlite magma (~3000 kg/m^3; Russell et al., 2013), we calculated that in sample LDC7, approximately ~430.7 kg of monticellite and ~118.9 kg of CO_2 (2747.0 mol) would be produced. Conversely in sample FLP1, a cubic metre of kimberlite magma would produce ~755.2 kg of monticellite and ~208.3 kg of CO_2 (4812.4 mol).

In order to calculate the volume of CO_2 produced, we employed the equation:

$$pV = nRT$$

where: p = pressure (Pa), V = volume (m^3), n = number of moles, R = gas constant (8.31441 J K^{-1} mol^{-1}), T = temperature (K). We calculated the volume of gas produced at an arbitrary upper crustal pressure and temperature of 30 MPa and 600 °C (or 873.15 K). These values lie within the crystallisation conditions estimated for other kimberlites (Kamenetsky et al., 2014 and references therein). At these selected pressure and temperature conditions, we calculated that approximately ~0.66 m^3 and ~1.16 m^3 of CO_2 would be produced from a cubic metre of kimberlite magma in samples LDC7 and FLP1 respectively. This equates to approximately ~4% in LDC7 and ~6.9% in FLP1 of the total kimberlite magma mass lost to degassing. These values are consistent with eruption models which show that kimberlite magmas should exsolve ≥ 5 wt% CO_2 (Kavanagh and Sparks, 2009).

It is important to note that these are tentative estimates, as several variables are assumed, such as the proportion of monticellite produced by decarbonation reactions and P-T conditions. However, these estimates can provide some insight into the maximum amount of CO_2 that could be produced by monticellite crystallisation.

Ultimately, the exsolution of CO_2 coupled with monticellite crystallisation could be a significant contributor to eruptive and brecciation processes that accompanied emplacement of kimberlite magma and instrumental in pipe formation. Explosive devolatisation of CO_2, along with phreatomagmatism in some cases, has been interpreted to be the dominant eruption mechanism in many Lac de Gras kimberlites (e.g., Nowicki et al., 2004; Kurszlaukis and Lorenz, 2008).

6. Conclusions

- Samples LDC7 (Leslie) and FLP1 (Pipe 1) are examples of minimally altered hypabyssal kimberlite which contain monticellite as a significant groundmass phase (25 and 40–45 vol% respectively). Monticellite (Mtc) occurs as two distinct morphological types: discrete and intergrown groundmass grains (Mtc-I), and replacement of olivine (Mtc-II).
- Monticellite, perovskite and Mg-magnetite contain abundant monocrystalline inclusions of periclase/Fe-Mg-oxides as well as multiphase (i.e. melt) inclusions dominated by alkali (Na, K, Ba, Sr)-enriched Ca-Mg-carbonates, chlorides, phosphates, spinel, silicates (e.g., olivine, phlogopite) and sulphides. These melt inclusions likely represent snapshots of a variably differentiated kimberlite melt. We infer that alkali-carbonates and chlorides are more significant component of the kimberlite melt than commonly recorded in whole-rock analyses.
- Based on petrographic and textural data, we propose that olivine replacement by monticellite resulted from an in-situ decarbonation reaction that occurred between olivine and the kimberlite melt after emplacement:

$$\text{Forsterite} + \text{Carbonate (melt)} \rightleftharpoons \text{Monticellite} + \text{Periclase} + CO_2. \quad \text{(Reaction 1)}$$

This reaction is supported by the preservation of abundant monomineralic inclusions of periclase to a lesser extent Fe-Mg-oxides in monticellite, perovskite and Mg-magnetite. We infer that periclase also crystallised in the groundmass but was subsequently altered to brucite and Fe-Mg-oxides during post-magmatic alteration.

- Degassing of CO_2 from the kimberlite magma is the driving mechanism for the proposed monticellite forming reactions. Subsequently, this removal of CO_2 may further facilitate additional decarbonation reactions to form more monticellite, periclase, Fe-Mg-oxides and CO_2 at the expensive of olivine and carbonate in the melt. These decarbonation reactions may be previously unrecognised processes in CO_2 degassing in the evolution of kimberlites and therefore may contribute to the explosive processes that occur during magma emplacement and pipe formation in the crust.

Supplementary data to this article can be found online at http://dx.doi.org/10.1016/j.chemgeo.2017.06.037.

Acknowledgements

This study forms part of A.A.'s Ph.D. We thank Yannick Bussweiler (University of Alberta) for his assistance in providing the Leslie kimberlite sample LDC7 and Christian Dietz at the Central Science Laboratory (CSL) at the University of Tasmania for his assistance with stable isotope analyses and Hugh O'Brien (Geological Survey of Finland) and Andrea Giuliani (The University of Melbourne) for their insightful discussions. This study has benefitted from the comments by two reviewers, Sebastian Tappe (University of Johannesburg), a second anonymous reviewer and the efficient editorial handling by Andrew Thomson (University College London). Financial support was provided by the Australian Research Council (Discovery grant DP130100257, 2013–2015) and University of Tasmania (New Star Professorship, 2010–2014) to V. Kamenetsky.

References

Abersteiner, A., Giuliani, A., Kamenetsky, V.S., Phillips, D., 2016. Petrographic and melt-inclusion constraints on the petrogenesis of a magmaclast from the Venetia kimberlite cluster, South Africa. Chem. Geol. http://dx.doi.org/10.1016/j.chemgeo.2016.08.029.

Armstrong, J.P., Wilson, M., Barnett, R.L., Nowicki, T., Kjarsgaard, B.A., 2004. Mineralogy of primary carbonate-bearing hypabyssal kimberlite, Lac de Gras, Slave Province, Northwest Territories, Canada. Lithos 76, 415–433.

Arndt, N.T., Guitreau, M., Boullier, A.M., Le Roex, A., Tommasi, A., Cordier, P., Sobolev, A., 2010. Olivine, and the origin of kimberlite. J. Petrol. 51, 573–602.

Barker, D.S., Nixon, P.H., 1989. High-Ca, low-alkali carbonatite volcanism at Fort Portal, Uganda. Contrib. Mineral. Petrol. 103, 166–177.

Beard, A.D., Downes, H., Hegner, E., Sablukov, S.M., Vetrin, V.R., Balogh, K., 1998. Mineralogy and geochemistry of Devonian ultramafic minor intrusions of the southern Kola Peninsula, Russia: implications for the petrogenesis of kimberlites and melilitites. Contrib. Mineral. Petrol. 130, 288–303.

Becker, M., Le Roex, A.P., 2006. Geochemistry of South African on- and off-craton, group I and group II kimberlites: petrogenesis and source region evolution. J. Petrol. 47, 673–703.

Berg, G.W., 1989. The significance of brucite in South African kimberlites. In: Ross, J. (Ed.), Kimberlite and Related Rocks: Their Mantle/Crust Setting. Diamonds and Diamond Exploration Vol. 2. Blackwell Scientific, Victoria, pp. 282–296.

Berg, G.W., Carlson, J.A., 1998. The Leslie Kimberlite Pipe of Lac de Gras, Northwest Territories, Canada: Evidence for Near Surface Hypabyssal Emplacement. Extended Abstracts Seventh International Kimberlite Conferencepp. 81–83.

Brett, R.C., Russell, J.K., Moss, S., 2009. Origin of olivine in kimberlite: phenocryst or impostor? Lithos 112S, 201–212.

Brey, G., Kogarko, L., Ryabchikov, I., 1991. Carbon dioxide in kimberlitic melts. Neues Jahrb. Mineral. Monatshefte 159–168.

Brooker, R., Sparks, R., Kavanagh, J., Field, M., 2011. The volatile content of hypabyssal kimberlite magmas: some constraints from experiments on natural rock compositions. Bull. Volcanol. 73, 959–981.

Buse, B., Schumacher, J., Sparks, R., Field, M., 2010. Growth of bultfonteinite and hydrogarnet in metasomatized basalt xenoliths in the B/K9 kimberlite, Damtshaa, Botswana: insights into hydrothermal metamorphism in kimberlite pipes. Contrib. Mineral. Petrol. 160, 533–550.

Bussweiler, Y., Foley, S.F., Prelević, D., Jacob, D.E., 2015. The olivine macrocryst problem: new insights from minor and trace element compositions of olivine from Lac de Gras kimberlites, Canada. Lithos 220-223, 238–252.

Bussweiler, Y., Stone, R.S., Pearson, D.G., Luth, R.W., Stachel, T., Kjarsgaard, B.A., Menzies, A., 2016. The evolution of calcite-bearing kimberlites by melt-rock reaction: evidence from polymineralic inclusions within clinopyroxene and garnet megacrysts from Lac de Gras kimberlites, Canada. Contrib. Mineral. Petrol. 171, 65.

Clement, C.R., 1982. A Comparative Geological Study of Some Major Kimberlite Pipes in the Northern Cape and Orange Free State. (Ph.D. Thesis) University of Cape Town, South Africa unpublished. (406 pp.).

Clement, C.R., Gurney, J.J., Skinner, E.M.W., 1975. Monticellite: An Abundant Groundmass Mineral in Some Kimberlites. Kimberlite Symposium 1, Cambridge, pp. 71–73 (Extended Abstracts).

Clement, C.R., Skinner, E.M.W., Smith, B.H.S., 1984. Kimberlite Redefined. Vol. 223 University of Chicago Press.

Dawson, J.B., 1980. Kimberlites and Their Xenoliths. Springer-Verlag, New York.

Demeny, A., Ahijado, A., Casillas, R., Vennemann, T.W., 1998. Crustal contamination and fluid/rock interaction in the carbonatites of Fuerteventura (Canary Islands, Spain): a C, O, H isotope study. Lithos 44, 101–115.

Edgar, A.D., Arima, M., Baldwin, D.K., Bell, D.R., Shee, S.R., Skinner, E.M.W., Walker, E.C., 1988. High-pressure-high-temperature melting experiments on a SiO_2-poor aphanitic kimberlite from the Wesselton mine, Kimberley, South Africa. Am. Mineral. 73, 524–533.

Egorov, K.N., Bogdanov, G.V., 1991. Monticellite from the kimberlites of Yakutia. Zapiski VMO 2, 78–87 (In Russian).

Exley, R.A., Jones, A.P., 1983. $^{87}Sr/^{86}Sr$ in kimberlitic carbonates by ion microprobe:

hydrothermal alteration, crustal contamination and relation to carbonatite. Contrib. Mineral. Petrol. 83, 288–292.
Fedortchouk, Y., Canil, D., 2004. Intensive variables in kimberlite magmas, Lac de Gras, Canada and implications for diamond survival. J. Petrol. 45, 1725–1745.
Giuliani, A., Kamenetsky, V.S., Phillips, D., Kendrick, M.A., Wyatt, B.A., Goemann, K., 2012. Nature of alkali-carbonate fluids in the sub-continental lithospheric mantle. Geology 40, 967–970.
Giuliani, A., Phillips, D., Kamenetsky, V.S., Fiorentini, M.L., Farquhar, J., Kendrick, M.A., 2014. Stable isotope (C, O, S) compositions of volatile-rich minerals in kimberlites: a review. Chem. Geol. 374-375, 61–83.
Giuliani, A., Soltys, A., Phillips, D., Kamenetsky, V.S., Maas, R., Goemann, K., Woodhead, J.D., Drysdale, R., Griffin, W.L., 2016. The final stages of kimberlite petrogenesis: petrography, mineral chemistry, melt inclusions and Sr-C-O isotope geochemistry of the Bultfontein kimberlite (Kimberley, South Africa). Chem. Geol. http://dx.doi.org/10.1016/j.chemgeo.2016.10.011.
Golovin, A.V., Sharygin, V.V., Pokhilenko, N.P., 2007. Melt inclusions in olivine phenocrysts in unaltered kimberlites from the Udachnaya–east pipe, Yakutia: some aspects of kimberlite magma evolution during late crystallization stages. Petrology 15, 168–183.
Harris, M., le Roex, A., Class, C., 2004. Geochemistry of the Uintjiesberg kimberlite, South Africa: petrogenesis of an off-craton, group I, kimberlite. Lithos 74, 149–165.
Hunter, R.H., Taylor, L.A., 1982. Instability of garnet from the mantle: glass as evidence of metasomatic melting. Geology 10, 617–620.
Kamenetsky, V.S., Yaxley, G.M., 2015. Carbonate–silicate liquid immiscibility in the mantle propels kimberlite magma ascent. Geochim. Cosmochim. Acta 158, 48–56.
Kamenetsky, V.S., Kamenetsky, M.B., Sobolev, A.V., Golovin, A.V., Demouchy, S., Faure, K., Sharygin, V.V., Kuzmin, D.V., 2008. Olivine in the Udachnaya-east kimberlite (Yakutia, Russia): types, compositions and origins. J. Petrol. 49, 823–839.
Kamenetsky, V.S., Kamenetsky, M.B., Weiss, Y., Navon, O., Nielsen, T.F.D., Mernagh, T.P., 2009. How unique is the Udachnaya-east kimberlite? Comparison with kimberlites from the Slave Craton (Canada) and SW Greenland. Lithos 112S, 334–346.
Kamenetsky, V.S., Kamenetsky, M.B., Golovin, A.V., Sharygin, V.V., Maas, R., 2012. Ultrafresh salty kimberlite of the Udachnaya-east pipe (Yakutia, Russia): a petrological oddity or fortuitous discovery? Lithos 152, 173–186.
Kamenetsky, V.S., Grutter, H., Kamenetsky, M.B., Goemann, K., 2013. Parental carbonatitic melt of the koala kimberlite (Canada): constraints from melt inclusions in olivine and Cr-spinel, and groundmass carbonate. Chem. Geol. 353, 96–111.
Kamenetsky, V.S., Golovin, A.V., Maas, R., Giuliani, A., Kamenetsky, M.B., Weiss, Y., 2014. Towards a new model for kimberlite petrogenesis: evidence from unaltered kimberlites and mantle minerals. Earth Sci. Rev. 139, 145–167.
Kampata, D.M., Nixon, P.H., Salemink, J., Demaiffe, D., 1994. Monticellite in the Gwena kimberlite (Shaba, Zaire): evidence of late-magmatic crystallization. Mineral. Mag. 58, 496–501.
Kavanagh, J., Sparks, R.S.J., 2009. Temperature changes in ascending kimberlite magma. Earth Planet. Sci. Lett. 286, 404–413.
Kjarsgaard, B.A., Wilkinson, L., Armstrong, J., 2002. Geology, Lac de Gras kimberlite field, Central Slave Province, Northwest Territories – Nunavut. Geological Survey of Canada Open File 3228 (map scale 1:250,000).
Kjarsgaard, B.A., Pearson, D.G., Tappe, S., Nowell, G.M., Dowall, D.P., 2009. Geochemistry of hypabyssal kimberlites from Lac de Gras, Canada: comparisons to a global database and applications to the parent magma problem. Lithos 112S, 236–248.
Kontinen, A., Paavola, J., Lukkarinen, H., 1992. K–Ar ages of hornblende and biotite from Late Arch ean rocks of eastern Finland. Geol. Surv. Finl. 365, 31.
Kornilova, V.P., Nikishov, K.N., Filippov, N.D., Makhoto, V.F., 1983. Association of monticellite and ore minerals in some kimberlite bodies of Yakutia. Dokl. Akad. Nauk SSSR 270, 696–700 (In Russian).
Kurszlaukis, S., Lorenz, V., 2008. Formation of "tuffisitic kimberlites" by phreatomagmatic processes. J. Volcanol. Geotherm. Res. 174, 68–80.
Le Pioufle, A., Canil, D., 2012. Iron in monticellite as an oxygen barometer for kimberlite magmas. Contrib. Mineral. Petrol. 163, 1033–1046.
Le Roex, A.P., Bell, D.R., Davis, P., 2003. Petrogenesis of group I kimberlites from Kimberley, South Africa: evidence from bulk-rock geochemistry. J. Petrol. 44, 2261–2286.
Lewis, R., 1982. Petrology of the monticellite alnoite associated with the Omaha oil field, Gallatin County, Illinois. Geol. Soc. Am. 14 (5), 265.
Malkov, B.A., 1974. Brucite in kimberlite. Dokl. Akad. Nauk SSSR 215, 157–160.
Meyer, J.W., Yang, J.C.S., 1962. Some observations in the system MgO-H_2O. Am. Mineral. 260, 707–717.
Mitchell, R.H., 1978. Mineralogy of the Elwin Bay kimberlite, Somerset Island, N.W.T., Canada. Am. Mineral. 63, 47–57.
Mitchell, R.H., 1986. Kimberlites: Mineralogy, Geochemistry and Petrology. Plenum Publishing Company, New York.
Mitchell, R.H., 1995. Kimberlites, Orangeites and Related Rocks. Plenum Press, New York.
Mitchell, R.H., 2008. Petrology of hypabyssal kimberlites: relevance to primary magma compositions. J. Volcanol. Geotherm. Res. 174, 1–8.
Mitchell, R.H., 2013. In: Paragenesis and Oxygen Isotopic Studies of Serpentine in Kimberlite. Proceedings of the 10th International Kimberlite Conference. Geological Society of India, Bangalore, pp. 1–12.
Nielsen, T.F.D., Sand, K.K., 2008. The Majuagaa kimberlite dike, Maniitsoq region, western Greenland: constraints on an Mg-rich silicocarbonatitic melt composition from groundmass mineralogy and bulk compositions. Can. Mineral. 46, 1043–1061.
Nikishov, K.N., Nikishova, V., 1966. The possibility of reaction relations between olivine and monticellite. Geochem. Int. 3, 1200–1206.
Nikishov, K.N., Poberezhskiy, V.A., Makhotko, V.F., 1979. Composition ofolivine and monticellite from monticellite alnoites of Siberia. Dokl. Akad. Nauk SSSR 224, 116–120.
Nowicki, T., Crawford, B., Dyck, D., Carlson, J., McElroy, R., Oshust, P., Helmstaedt, H., 2004. The geology of kimberlite pipes of the Ekati property, Northwest Territories, Canada. Lithos 76, 1–27.
Nowicki, T., Porritt, L., Crawford, B., Kjarsgaard, B., 2008. Geochemical trends in kimberlites of the Ekati property, Northwest Territories, Canada: insights on volcanic and resedimentation processes. J. Volcanol. Geotherm. Res. 174, 117–127.
O'Brien, H.E., Tyni, M., 1999. Mineralogy and geochemistry of kimberlites and related rocks from Finland. In: Gurney, J.J., Gurney, J.L., Pascoe, M.D., Richardson, S.H. (Eds.), Proceedings of the VIIth International Kimberlite Conference. Red Roof Design, Cape Town, pp. 625–636.
Pilbeam, L.H., Nielsen, T.F.D., Waight, T.E., 2013. Digestion fractional crystallization (DFC): an important process in the genesis of kimberlites. Evidence from olivine in the Majuagaa kimberlite, southern West Greenland. J. Petrol. 54, 1399–1425.
Podvysotskiy, V.T., 1985. Serpentine-carbonate mineralization in kimberlites. Int. Geol. Rev. 27, 810–823.
Price, S.E., Russell, J.K., Kopylova, M.G., 2000. Primitive magma from the Jericho pipe, N.W.T., Canada: constraints on primary kimberlite melt chemistry. J. Petrol. 41, 789–808.
Reid, A.M., Donaldson, C.H., Dawson, J.B., Brown, R.W., Ridley, W.I., 1975. The Igwisi Hills extrusive "kimberlites". Phys. Chem. Earth 9, 199–218.
Roeder, P.L., Schulze, D.J., 2008. Crystallization of groundmass spinel in kimberlite. J. Petrol. 49, 1473–1495.
Russell, J.K., Porritt, L.A., Hilchie, L., 2013. Kimberlite: rapid ascent of lithospherically modified carbonatitic melts. In: Pearson, D. (Ed.), Proceedings of 10th International Kimberlite Conference. Springer, New Delhi.
Sarkar, C., Heaman, L.M., Pearson, D.G., 2015. Duration and periodicity of kimberlite volcanic activity in the Lac de Gras kimberlite field, Canada and some recommendations for kimberlite geochronology. Lithos 218-219, 155–166.
Scott-Smith, B., 1996. Kimberlites. Chapter 10, Mineralogical Association of Canada Short Course Series. In: Mitchell, R.H. (Ed.), Undersaturated Alkaline Rocks: Mineralogy, Petrogenesis, and Economic Potential, Short Course. 24. pp. 217–243.
Sharp, Z.D., Essene, E.J., Anovitz, L.M., Metz, G.W., Westrum, J.E.F., Hemingway, B.S., Valley, J.W., 1986. The heat capacity of a natural monticellite and phase equilibria in the system CaO-MgO-SiO_2-CO_2. Geochim. Cosmochim. Acta 50, 1475–1484.
Shee, S.R., Clement, C.R., Skinner, E.M.W., 1991. The Petrology of the Wesselton Kimberlite Sills, Kimberley, Cape Province, South Africa. 1. Proceedings of the 5th International Kimberlite Conference, Brazil, pp. 98–114.
Skinner, E.M.W., 1989. In: Contrasting Group I and Group II Kimberlite Petrology: Towards a Genetic Model for Kimberlites. Proceedings of the Fourth International Kimberlite Conference. Geological Society of Australia Special Publication 14, Perth, Australia, pp. 528–544.
Skinner, E.M.W., Clement, C.R., 1979. Mineralogical classification of southern African kimberlites. In: Boyd, F.R., Meyer, H.O.A. (Eds.), The Mantle Sample. 2nd International Kimberlite Conference. American Geophysical Union, Washington, DC, pp. 129–139.
Smith, C.B., Sims, K., Chimuka, L., Duffin, A., Beard, A.D., Townend, R., 2004. Kimberlite metasomatism at Murowa and Sese pipes, Zimbabwe. Lithos 76 (1–4), 219–232.
Snowden, D.V., 1981. Mineralogy and Petrology of Two Kimberlites at Dutoitspan Mine, Kimberley. (M.Sc. Thesis) Rhodes Univ. Grahamstown, South Africa.
Soltys, A., Giuliani, A., Phillips, D., Kamenetsky, V.S., Maas, R., Woodhead, J., Rodemann, T., 2016. In-situ assimilation of mantle minerals by kimberlitic magmas — direct evidence from a garnet wehrlite xenolith entrained in the Bultfontein kimberlite (Kimberley, South Africa). Lithos 256-257, 182–196.
Sparks, R.S.J., Baker, L., Brown, R.J., Field, M., Schumacher, J., Stripp, G., Walters, A., 2006. Dynamical constraints on kimberlite volcanism. J. Volcanol. Geotherm. Res. 155, 18–48.
Sparks, R.S.J., Brooker, R.A., Field, M., Kavanagh, J., Schumacher, J.C., Walter, M.J., White, J., 2009. The nature of erupting kimberlite melts. Lithos 112S, 429–438.
Stripp, G.R., Field, M., Schumacher, J.C., Sparks, R.S.J., Cressey, G., 2006. Post-emplacement serpentinization and related hydrothermal metamorphism in a kimberlite from Venetia, South Africa. J. Metamorph. Geol. 24, 515–534.
Sun, S.-S., McDonough, W.F., 1989. Chemical and isotopic systematics of oceanic basalts: implications for mantle composition and processes. In: Saunders, A.D., Norry, M.J. (Eds.), Magmatism in the Ocean Basins. Geological Society Special Publication, London, pp. 313–345.
Tappe, S., Steenfelt, A., Heaman, L.M., Simonetti, A., 2009. The newly discovered Jurassic Tikiusaaq carbonatite-aillikite occurrence, West Greenland, and some remarks on carbonatite-kimberlite relationships. Lithos 112, 385–399.
Tappe, S., Pearson, D.G., Nowell, G.M., Nielsen, T.F.D., Milstead, P., Muehlenbachs, K., 2011. A fresh isotopic look at Greenland kimberlites: cratonic mantle lithosphere imprint on deep source signal. Earth Planet. Sci. Lett. 305, 235–248.
Tappe, S., Graham Pearson, D., Kjarsgaard, B.A., Nowell, G., Dowall, D., 2013. Mantle transition zone input to kimberlite magmatism near a subduction zone: origin of anomalous Nd–Hf isotope systematics at Lac de Gras, Canada. Earth Planet. Sci. Lett. 371–372, 235–251.
Tappe, S., Brand, N.B., Stracke, A., van Acken, D., Liu, C.-Z., Strauss, H., Wu, F.-Y., Luguet, A., Mitchell, R.H., 2017. Plates or plumes in the origin of kimberlites: U/Pb perovskite and Sr-Nd-Hf-Os-C-O isotope constraints from the Superior craton (Canada). Chem. Geol. http://dx.doi.org/10.1016/j.chemgeo.2016.08.019.
Tyni, M., 1997. Diamond prospecting in Finland — a review. In: Papunen, H. (Ed.), Mineral Deposits: Research and Exploration, Where Do They Meet? Balkema, Rotterdam, pp. 789–791.
Verhoogen, J., 1938. Les pipes de kimberlites de Katanga. Ann. Serv. Mines Katanga Spec. Pub. 9, 1–50.
Wilson, M.R., Kjarsgaard, B.A., Taylor, B., 2007. Stable isotope composition of magmatic and deuteric carbonate phases in hypabyssal kimberlite, Lac de Gras field, Northwest Territories, Canada. Chem. Geol. 242, 435–454.

Appendix 3.1 – Supplementary Figures

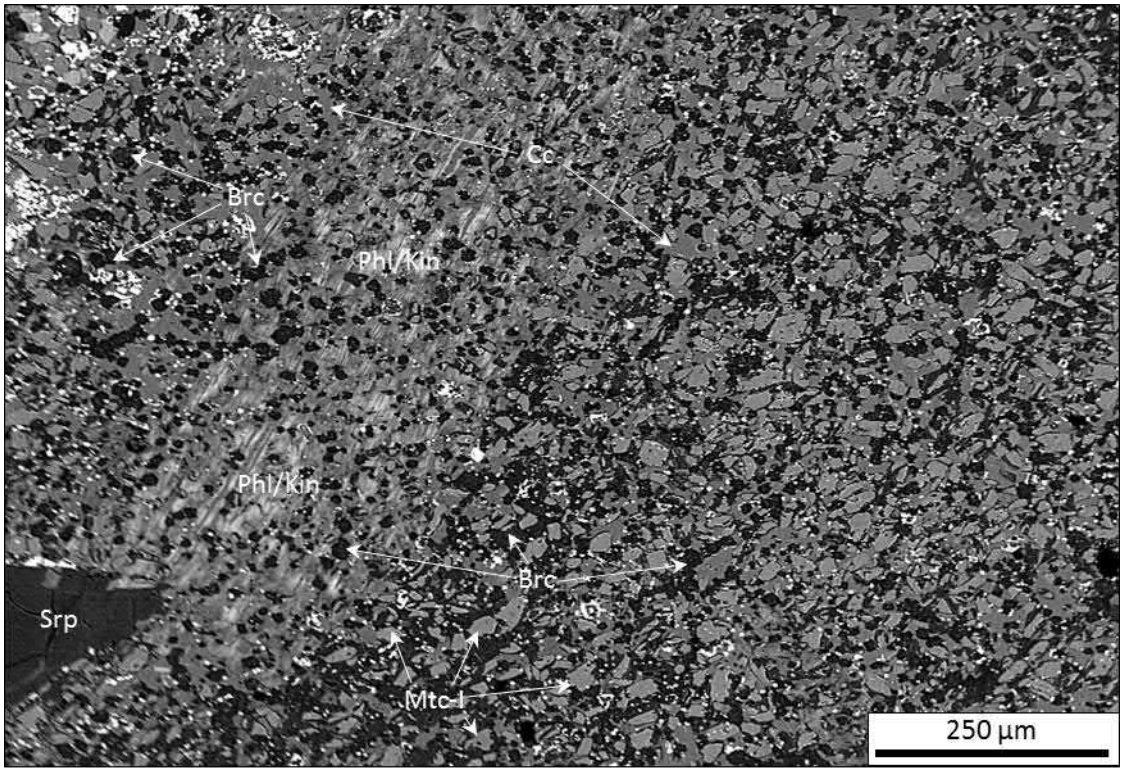

Supplementary Figure S1. Back-scattered electron (BSE) SEM images of the groundmass textures of sample LDC7 which is dominated by discrete globular grains of brucite (Brc) and Mtc-I (Mtc). The groundmass is infilled by interstitial phlogopite/kinoshitalite (Phl/Kin) and calcite (Cc). Srp: Serpentine.

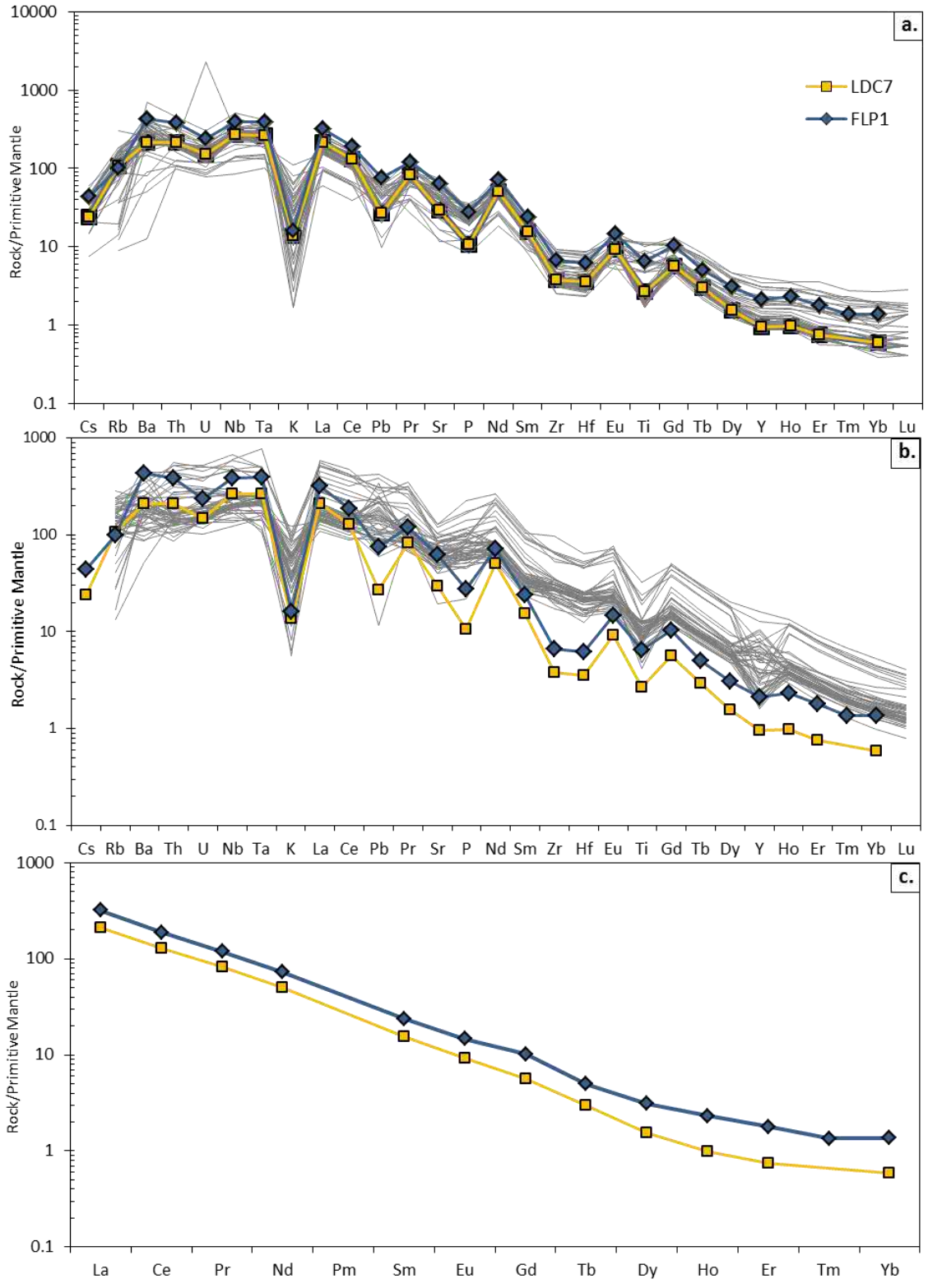

Supplementary Figure S2. Primitive mantle normalised (after Sun and McDonough, 1989) diagrams for (a, b) incompatible elements and (c) REE diagrams showing samples LDC7 and FLP1. (a, b) The background (grey) diagrams show the distribution of incompatible trace elements from various kimberlites from (a) Lac de Gras (n = 34; after Tappe et al. 2013) and Kupio-Kaavi (n = 15; after O'Brien and Tyni, 1999) and (b) southern Africa (n = 52; after le Roex et al. 2003).

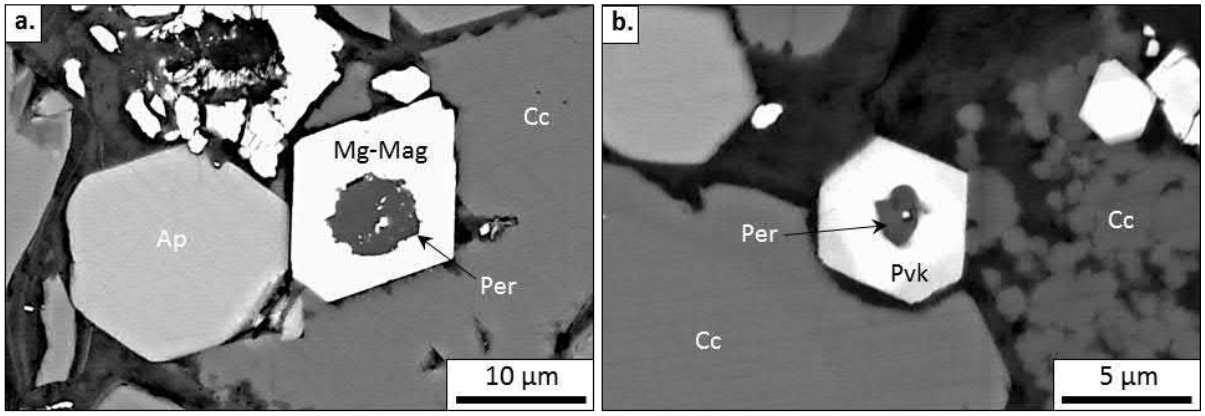

Supplementary Figure S3. Back-scattered electron (BSE) SEM images of periclase (Per) inclusions in sample FLP1 in: (a) Mg-magnetite (Mg-Mag), and (b) perovskite (Pvk). Ap: apatite, Cc: calcite.

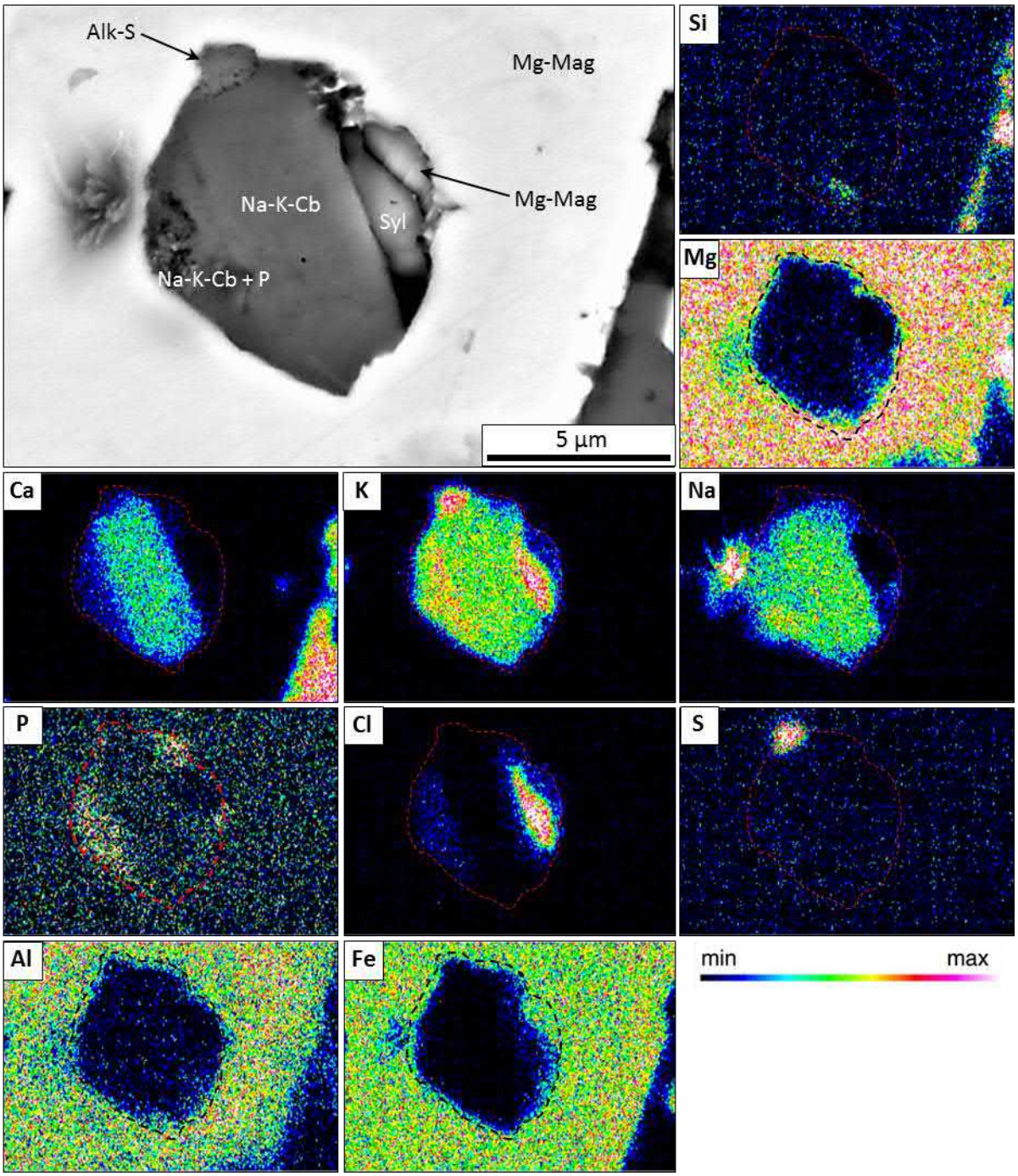

Supplementary Figure S4. Back-scattered electron SEM image and X-ray elemental map of a representative inclusion in Mg-Magnetite (Mg-Mag) in sample FLP1. Detected minerals include: Alkali-carbonates (Alk-Cb), Phosphate-bearing alkali-carbonate (Alk-Cb + P), Alkali-Sulphur-bearing mineral (Alk-S), Sylvite (Syl). The black/red dashed line represents the boundary of the inclusion.

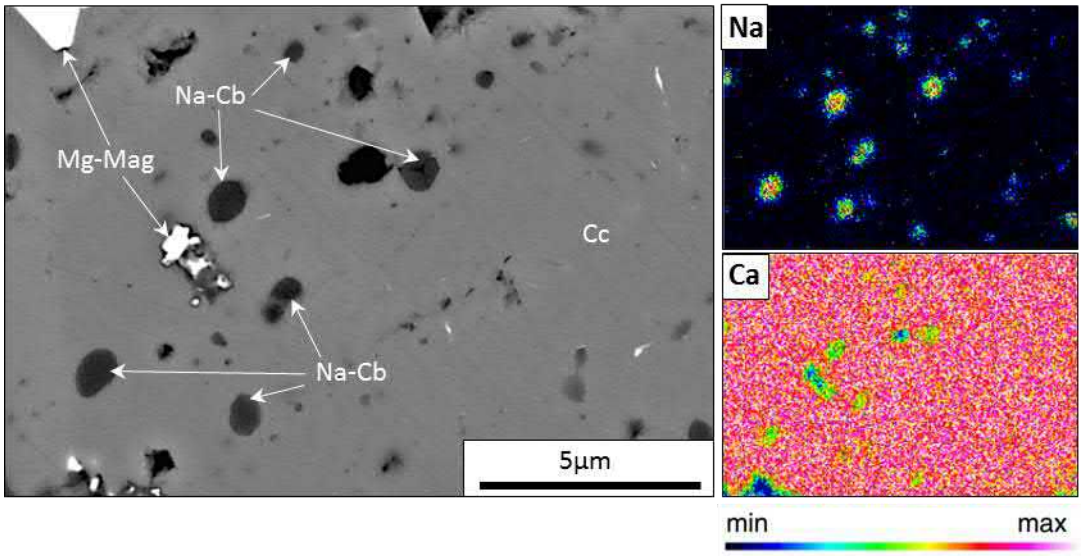

Supplementary Figure S5. Back-scattered electron SEM image and X-ray elemental map of a representative Na-carbonate (Na-Cb) inclusions in calcite (Cc) in sample FLP1. Mg-magnetite: Mg-Mag.

Appendix 3.2: Supplementary Tables

Supplementary Table S1: Major and trace element abundances in samples LDC7 and FLP1.

Sample	**LDC7**	**Pipe 1**		**LDC7**	**Pipe 1**
SiO_2	31.81	25.37	Rb	67.3	63.5
TiO_2	0.57	1.40	Ba	1482	3013
Al_2O_3	1.42	3.17	Th	18.06	32.68
FeO	8.05	10.06	U	3.15	5.04
MnO	0.17	0.23	Nb	192	276
MgO	41.39	28.46	Ta	10.8	16.3
CaO	8.20	17.43	La	145.4	219.8
Na_2O	0.05	0.18	Ce	229.4	335.8
K_2O	0.41	0.48	Pb	<5	14
P_2O_5	0.23	0.60	Pr	22.81	32.9
CO_2	2.17	6	Sr	621	1334
H_2O*	7.29	6.48	Nd	68.1	97.9
S*	0.12	0.16	Sm	6.87	10.54
Cl	0.03	0.06	Zr	42	74
Total	101.92	100.08	Hf	1.1	1.9
			Eu	1.56	2.47
F	583	2178	Gd	3.36	6.11
Co	98.8	81	Tb	0.32	0.54
Cr	2595	1362	Dy	1.14	2.28
Ni	1540	755	Y	4.3	9.5
Sc	11	19	Ho	0.16	0.38
V	68	143	Er	0.36	0.86
W	59	37	Tm	BDL	0.1
Cu	59	105	Yb	0.29	0.67
Zn	32	52	Lu	BDL	0.27

Major elements are in wt.%, trace elements in ppm.
*H_2O and S were determined by Element Analyser (see Supplementary Material for methodology)
BDL: below detection limit

Appendix 3.3: Supplementary Material – Analytical methods.

Petrographic and Inclusion Study

Specimens of LDC7 and FLP1 were prepared as thin sections and epoxy resin mounts polished using kerosene as lubricant to avoid dissolution of any water soluble phases. Initial optical petrographic and mineralogical investigations of samples were performed on Nikon Eclipse 50i POL microscope at the University of Tasmania.

Detailed examinations of major phases and inclusions in minerals were undertaken using a Hitachi SU-70 field emission SEM equipped with an Oxford AZtec XMax 80 detector at the Central Science Laboratory, University of Tasmania. A beam accelerating voltage of 15 kV was employed to produce high-resolution backscattered electron (BSE) images of minerals and energy-dispersive X-ray spectroscopy (EDS) semi-quantitative analyses and elemental maps of minerals and inclusions.

Electron Microprobe Analyses

Electron microprobe (EMP) analyses of monticellite and olivine were carried out at the Central Science Laboratory, University of Tasmania, using a Cameca SX100 electron microprobe with a beam accelerating voltage of 15 kV, beam current of 30 nA and beam diameter of 2 μm. The counting time was 20 seconds for Fe, 30 seconds for Si, Mg, 40 seconds for Mn, Cr, 60 seconds for Al, Ni, and 90 seconds for Ca. The standards were Rhodonite $MnSiO_3$ P&H (B14) for Mn, Eskolaite P&H (D12) for Cr, Nickel Oxide NiO P&H (A8) for Ni, Corundum Harvard (F6) for Al, Hematite Harvard (F3) for Fe, Augite Kakanui NMNH 122142 (J17) for Ca, Periclase UNE (G8) for Mg, and Spectrosil (D18) for Si. Detection limits (99% confidence) were <0.01 wt.% for Al and Ca, 0.01 wt.% for Si, Cr and Ni, and 0.02 wt.% for Fe and Mn. Analytical precision (1σ) was <0.01 wt.% for Al, 0.01 wt.% for Cr, Ni, Mn and Ca, 0.03 wt.% for Fe, 0.04 wt.% for Si and 0.05 wt.% for Mg.

Whole-Rock Analyses for Trace Element and Rare Earth Element Concentrations

Samples were analysed for their major and trace element concentrations in samples LDC7 and FLP1 were conducted at Intertek Minerals Laboratory (Adelaide, South Australia). Samples were prepared by pulverising 0.2g of pulverised of the selected sample and fusing with lithium borate and then dissolved by a weak acidic solution. The dissolved sample was then analysed for major (Ca, Fe, K, Mg, Mn, Na, P, Si, Ti), trace (Ba, Cr, Cs, Ga, Rb, Sc, Sn,

Sr, U, V, W), high field strength elements (HFSE; Ba, Cr, Cs, Ga, Rb, Sc, Sn, Sr, U, V, W), rare earth elements (REE; La, Ce, Pr, Nd, Sm, Eu, Gd, Tb, Dy, Ho, Er, Tm, Yb, Lu) were analysed by a combination of inductively coupled plasma optical emission spectroscopy (ICP-OES) and inductively coupled plasma mass spectrometry (ICP-MS). Samples analysing for trace elements (Ag, As, Be, Bi, Cd, Co, Cu, Ge, In, Li, Mo, Ni, Pb, Re, Sb, Se, Te, Tl, Zn) were prepared by dissolving 0.2g of sample in a 4 acid digest (HF+ HCl + HNO_3 + $HClO_4$) and then analysed by ICP-OES/ICP-MS. CO_2 and S were analysed by a carbon sulphur analyser (CSA) by igniting 0.3g of pulverised sample at high temperature in a stream of O_2. SO_2 and CO_2 produced were then measured via infra-red cells. Samples were analysed for Cl by digesting 0.2g of pulverised sample in a calcium-carbonate leach. Cl was then measured by colorimetry. Samples were analysed for F by fusing 0.2g of pulverised sample with K/Na-carbonate/Zn-oxide, then digested in deionised H_2O. F in solution was then measured via selective ion electrode. Ferrous iron was determined by digesting 0.25g of pulverised sample in sulphuric acid (H_2SO_4) and titrated to determine FeO.

Stable Isotopes

Sample preparation for stable isotope work was performed at the Central Science Laboratory (CSL) at the University of Tasmania using a MultiFlow – Isoprime100. For analysis of solid carbonate samples for either $\delta^{13}C$ or $\delta^{18}O$, the bulk rock samples were finely ground to a homogeneous and dry powder using an agate mortar. Subsample amounts accounting for approx. 100 µg of pure carbonate were placed in sealed vials and inserted into the heated sample rack (70 °C) of an Isoprime MultiFlow. The headspace was flushed with helium, after which 200 µL of 103% orthophosphoric acid were added to react as follows:

$$CaCO_3 + H_3PO_4 \leftrightarrow CaHPO_4 + CO_2 + H_2O$$

After a reaction time of 1080 min, the generated CO2 which was extracted and analysed on an Isoprime 100 continous-flow mass spectrometer. The sample gas $^{13}C/^{12}C$ and $^{18}O/^{16}O$ ratios were then converted to the conventional ‘delta notation’ as follows:

$$\delta\ [‰] = (R_{sample}/R_{standard} - 1) \times 1000$$

where "R" is the ratio of the heavy to light isotope in the sample or standard and the result is multiplied by 1000 simply to make the resulting ratio more ‘meaningful’. When analysing CO_2 different isotopic species of the same element (isotopologues) can produce a

contribution at certain masses and a correction must be made, for which we applied the following conversion (Craig correction):

$\delta\ ^{13}C = 1.067\ \delta(45/44) - 0.0338\ \delta\ ^{18}O$

and

$\delta\ ^{18}O = 1.0010\ \delta(46/44) - 0.0021\ \delta\ ^{13}C$

The data was then normalised to the Vienna Pee Dee Belemnite (VPDB) and Vienna Mean Standard Ocean Water (VSMOW) scale, respectively, using two international reference standards, NBS18 and NBS19 and two in-house reference standards (Anu M1 and Anu PRM2). The acid digestion used as sample preparation method relies on an equilibrium state rather than on a reaction proceeding to completion, for which an additional correction has to be applied. The equilibrium can be expressed as:

$\delta_{true} = (\delta_{measured} - 1000*(E-1)/E) + K * (T_{Reaction} - T_{Standard})$

being the equilibrium constant and conditions applied:

$E = 1.01025$, $K = 0.04$; $T_{Reaction} = 70\ ^oC$ and $T_{Standard} = 25\ ^oC$

Precision of the measurements, determined by repetitive analysis (n=7) of Anu PRM2 were 0.05‰ and 0.13‰ for $\delta^{13}C$ and $\delta^{18}O$ respectively. Homogeneity was assessed by repetition of a submitted sample (01-233, n=5) and resulted in standard deviation of 0.07 0/00 for $d^{13}C$ and 0.17 0/00 for $d^{18}O$ measurements.

H_2O and S Analyses

The analysis for total nitrogen, carbon, hydrogen and sulphur was determined at the Central Science Laboratory (CSL), University of Tasmania, using a Thermo Finnigan EA 1112 Series Flash Elemental Analyser. Between 0.7 and 1.7 mg of sample were weighed into tin capsules using a Sartorius SE2 ultra-microbalance with an accuracy of 0.1 microgram. Combustion of the pressed tin cups was achieved in ultra-high purity oxygen at 1000°C using tungstic oxide on alumina as an oxidising agent followed by reduced copper wires as a reducing agent. The results were calibrated using a certified sulphanilamide standard.

Chemical Geology 478 (2018) 148–163

Contents lists available at ScienceDirect

Chemical Geology

journal homepage: www.elsevier.com/locate/chemgeo

Significance of halogens (F, Cl) in kimberlite melts: Insights from mineralogy and melt inclusions in the Roger pipe (Ekati, Canada)

Adam Abersteiner[a,*], Vadim S. Kamenetsky[a], Maya Kamenetsky[a], Karsten Goemann[b], Kathy Ehrig[c], Thomas Rodemann[b]

[a] School of Physical Sciences, University of Tasmania, Hobart, Tasmania 7001, Australia
[b] Central Science Laboratory, University of Tasmania, Hobart, Tasmania 7001, Australia
[c] BHP Billiton Olympic Dam, Adelaide, SA 5000, Australia

ARTICLE INFO

Keywords:
Kimberlite
Melt inclusions
Halogens
Alkali-carbonate
Fluorine
Chlorine

ABSTRACT

The abundance and distribution of halogens (F, Cl) are rarely recorded in kimberlites and therefore their petrogenetic significance is poorly constrained. Halogens are usually present in kimberlite rocks in the structure of phlogopite and apatite, but their original concentrations are never fully retained due to the effects of alteration. To provide new constraints on the origin and evolution of halogens in kimberlites and their melts, we present a detailed study of the petrography and geochemistry of the late-Cretaceous Group-I (or archetypal) Roger kimberlite (Ekati cluster, Canada). The studied samples contain abundant anhedral-to-euhedral olivine which is set in a crystalline groundmass of monticellite, phlogopite, apatite, spinel (i.e. magnesian ulvöspinel-magnetite (MUM), Mg-magnetite, pleonaste, Cr-spinel), and perovskite along with abundant secondary alteration phases (i.e. serpentine, garnet (andradite-schlorlomite), amakinite ($(Fe^{2+}, Mg, Mn)(OH)_2$), calcite). The Roger kimberlite is characterised by the highest recorded F-content (up to 2688 ppm) of the Ekati cluster kimberlites, which is reflected by the preservation of F-rich phases, where bultfonteinite ($Ca_4(Si_2O_7)(F, OH)_2$) and fluorite commonly replace olivine.

In order to examine the composition and evolution of the kimberlite melt prior to post-magmatic processes, we studied melt inclusions in olivine, Cr-spinel, monticellite and apatite. Primary multiphase melt inclusions in Cr-spinel, monticellite and apatite and secondary inclusions in olivine are shown to contain a diversity of daughter phases and compositions that are dominated by alkali/alkali-earth (Na, K, Ba, Sr)-enriched Ca-Mg-carbonates ± F, Na-K-chlorides and sulphates, phosphates ± REE, spinel, silicates (e.g. olivine, phlogopite, (clino)humite), and sulphides. Although alkali/alkali-earth- and halogen-bearing phases are abundant in melt inclusions, they are generally absent from the kimberlite groundmass, most likely due to ubiquitous effects of syn- and/or post-magmatic alteration (i.e. serpentinisation).

Comparisons between halogens and other trace elements of similar compatibility (i.e. F/Nd and Cl/U) in the Roger kimberlite and their respective estimated primitive mantle abundances show that halogens should be a more significant component in kimberlites than typically measured. We propose that fluorine in the Roger kimberlite was magmatic and was redistributed during hydrothermal alteration by Ca-bearing serpentinising fluids to produce the observed bultfonteinite/fluorite assemblages. Based the compositions and daughter mineral assemblages in primary melt inclusions and reconstructed halogen abundances, we suggest that Cr-spinel, monticellite and apatite crystallised from a variably differentiated Si-P-Cl-F-bearing carbonate melt that was enriched in alkalis/alkali-earths and highly incompatible trace elements.

1. Introduction

Kimberlites are deeply derived magmas (> 150 km; Dawson, 1980; Clement et al., 1984; Mitchell, 1986) that can provide invaluable insights into the concentrations, distribution and behaviour of volatiles in the sub-continental lithospheric mantle (SCLM). The two principle mantle volatile components (CO_2 and H_2O) are well represented in kimberlites and have received significant attention in kimberlite literature. In kimberlitic rocks, CO_2 is hosted in carbonates and is considered to be dominantly of magmatic origin (Mitchell, 1986; Armstrong et al., 2004; Wilson et al., 2007), whereas H_2O is hosted mainly in serpentine. Different researchers have interpreted H_2O in

* Corresponding author.
E-mail address: adam.abersteiner@utas.edu.au (A. Abersteiner).

http://dx.doi.org/10.1016/j.chemgeo.2017.06.008
Received 28 February 2017; Received in revised form 9 May 2017; Accepted 6 June 2017
Available online 08 June 2017

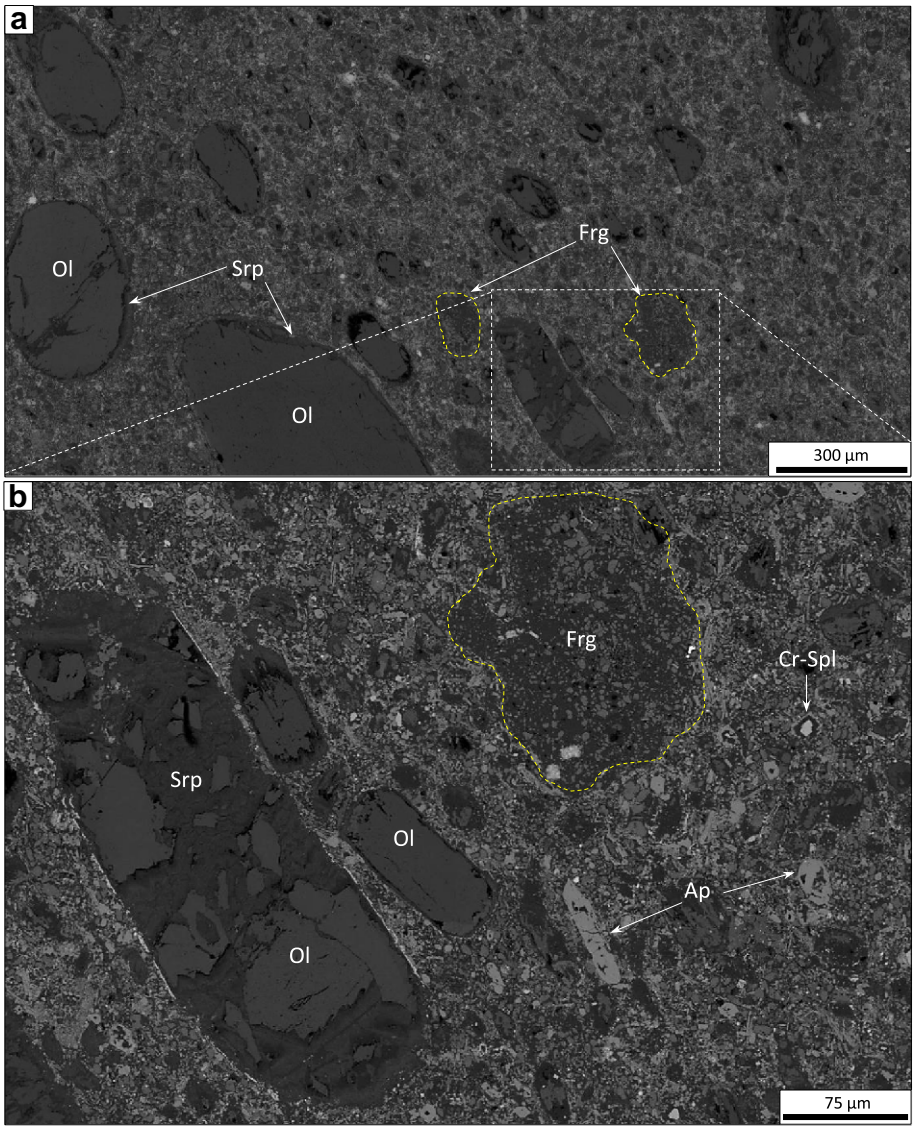

Fig. 1. (a, b) Back-scattered electron (BSE) SEM image showing groundmass textures of the Roger kimberlite. Olivine (Ol) is commonly replaced by serpentine (Srp) along rims and internal fractures. The dotted yellow lines represent the boundary of anhedral fragments (Frg; see Section 2.1) which are largely composed of chlorite/serpentine along with disseminated phlogopite and monticellite. Ap: apatite, Cr-Spl: Cr-spinel. (For interpretation of the references to colour in this figure legend, the reader is referred to the web version of this article.)

kimberlites to be either magmatic (Mitchell, 2008, 2013) or externally derived and related to alteration (Stripp et al., 2006; Sparks et al., 2009; Brooker et al., 2011; Afanasyev et al., 2014; Giuliani et al., 2014a, 2016). Compared to these extensively studied volatiles, the concentrations of halogens (e.g., F and Cl) are not routinely reported in the analyses of kimberlites and subsequently their origin in kimberlite magmas is poorly constrained. Fluorine and chlorine in magmatic systems are influential on melt viscosity, phase equilibria and the mobility of metals (Kamenetsky et al., 2007a; Tropper and Manning, 2007; Brey et al., 2009). Therefore, elucidating the halogen content of kimberlite magmas is fundamental in understanding parental melt compositions, rheology and ultimately their petrogenesis.

Fluorine and, to a lesser extent, chlorine in kimberlites are commonly substituted for OH^- in accessory groundmass minerals (i.e. phlogopite and apatite; Aoki and Kanisawa, 1979). The chlorine content of kimberlite rocks ranges from < 20 ppm to 1.91 wt% (Paul et al., 1976; Muramatsu, 1983; Becker and Le Roex, 2006; Nielsen and Sand, 2008; Nowicki et al., 2008; Kjarsgaard et al., 2009) in serpentinised kimberlites. However, the serpentine-free Udachnaya-East kimberlite (Siberia) contains exceptionally high Cl-contents (up to 6.11 wt%) which is accommodated in numerous Cl-rich groundmass phases such as halite, sylvite and djerfisherite ($K_6Na(Fe, Cu, Ni)_{25}S_{26}Cl$; Kamenetsky et al., 2004, 2007b, 2012 Sharygin et al., 2007). On the other hand, analyses of F-concentrations in kimberlites are rarer, but have been shown to be range from 210 to 7490 ppm (Paul et al., 1976; Muramatsu, 1983; Nowicki et al., 2008; Kjarsgaard et al., 2009).

Reconstructing the volatile content of kimberlite melts is often hampered by the effects of entrained and assimilated mantle and crustal rocks, degassing during ascent and emplacement, and post-emplacement alteration. Consequently, whole-rock analyses of kimberlite rocks are unlikely to produce accurate estimates of magmatic volatiles in kimberlite melts. Analyses of melt inclusions in kimberlitic minerals can provide insights into the composition of the kimberlite melt prior to post-emplacement alteration (e.g., Kamenetsky et al., 2014; Abersteiner et al., 2016; Giuliani et al., 2016). Previous studies have consistently shown that F- and Cl-bearing phases are common constituents of melt inclusions entrapped in olivine, Cr-spinel, perovskite and apatite (Kamenetsky et al., 2004; Golovin et al., 2007; Kamenetsky et al., 2009b, 2012, 2013; Mernagh et al., 2011; Abersteiner et al., 2016; Giuliani et al., 2016).

In this study, we examine a sample of hypabyssal kimberlite from the Roger pipe (Ekati, Canada). A remarkable feature of the Roger kimberlite is the presence of F-rich minerals (i.e. bultfonteinite ($Ca_4(Si_2O_7)(F, OH)_2$) and fluorite (CaF_2)) replacing olivine. In order to constrain the evolution of kimberlite melts and the origin of halogens in the Roger kimberlite, we focus on documenting the petrography and geochemistry of halogen-bearing phases and characterise melt inclusions hosted within olivine and different magmatic groundmass

minerals.

2. Petrography and geochemistry of the Roger kimberlite

2.1. Sample description

The late-Cretaceous (67.6 ± 9.1 Ma, 2σ; Lockhart et al., 2004) Roger kimberlite pipe belongs to the Ekati cluster which comprises approximately 150 bodies and is located in the Lac de Gras Kimberlite Field (Slave Province, Canada). The Roger kimberlite intruded Archean granitoids (biotite-granodiorite) in the Slave craton (Kjarsgaard et al., 2002).

Two kimberlite samples from the Roger pipe (drill hole 94–17: depth between 181 m–197 m) were analysed petrographically by optical and SEM (scanning electron microscopy; see Supplementary material for methodology). Both samples contain near identical mineralogy and are characterised by porphyritic textures that are defined by euhedral-to-anhedral olivine set in a fine-grained groundmass consisting largely of interstitial serpentine, carbonate (i.e. calcite) and to a lesser extent garnet (andradite-schlorlomite). The groundmass mineralogy is typical of hypabyssal Group-I (or archetypal; Mitchell, 1995) kimberlites (Mitchell, 1986, 2008) and contains abundant monticellite along with subordinate amounts of (in order of decreasing abundance) phlogopite, apatite, Fe-Mg-Al-Cr-spinel (i.e. magnesian ulvöspinel-magnetite (MUM), Mg-magnetite, pleonaste, Cr-spinel), perovskite, and Ni ± Fe-sulphides. The Roger sample is also characterised by abundant angular-to-irregular fragments (< 0.1–1 cm) that are pale green to creamy white in colour and completely altered, where internal structures are absent (Fig. 1). These altered fragments are dominated by amorphous chlorite and to a lesser extent serpentine and calcite along with abundant very fine (< 25 μm) disseminated grains of phlogopite, monticellite, apatite, perovskite, REE-Si-P-bearing phase (britholite? $((Ce, Ca, Th, La, Nd)_5(SiO_4, PO_4)_3(OH, F))$) and sphalerite (Fig. 1).

2.2. Petrography

Olivine is the most dominant constituent (~50 vol%), occurring as preferentially orientated anhedral-to-rounded (< 1–3 mm in length) and subhedral-to-euhedral grains (< 600 μm in length; Fig. 1). Olivine is partially-to-completely altered along rims and internal fractures to admixtures of serpentine, amakinite ($(Fe^{2+}, Mg, Mn)(OH)_2$) and carbonate (i.e. calcite; Figs. 1, and 2a and b). Olivine is also sometimes partially replaced by bultfonteinite or fluorite (Fig. 3; see Section 2.3).

Monticellite is an abundant groundmass phase (~20 vol%) that occurs as two morphological types: i) discrete subhedral-to-euhedral grains that range from 20 to 100 μm in size (Figs. 2, and 3d and e) which are occasionally interstitially grown around Cr-spinel (Fig. 2c and d), and ii) rare partial-to-complete epitaxial mantles surrounding olivine (30–50 μm in thickness) that parallel its shape (Fig. 2b).

Phlogopite is a common groundmass phase (~5 vol%) that occurs as thin (< 5–15 μm) and complexly zoned (K-rich and Ba-rich (up to 14.3 wt% Ba; kinoshitalite)) grains up to 150 μm in length that are interstitial to most other groundmass phases (Fig. 2f). Phlogopite also forms large clusters of randomly orientated grains.

Apatite is a minor phase (~2 vol%) that typically occurs as discrete subhedral-to-euhedral prismatic grains that range in size from 50 to 400 μm (Figs. 1b, and 2e and f). Apatite sometimes occurs as large (up to several millimetres) domains that cement other groundmass phases (e.g., monticellite, spinel, phlogopite; Fig. 2a). Both morphologies of apatite are identical in composition. Groundmass apatite grains are commonly complexly zoned, where semi-quantitative analyses by EDS (Fig. 4a) revealed variations in F (1.3–3.4 wt%), Sr (< 1.7 wt%) and LREE (light rare earth elements; e.g., La, Ce). Laser ablation inductively coupled plasma mass spectrometry (LA-ICPMS) analyses (n = 24; see Supplementary material for methodology) were normalised to primitive mantle values (Supplementary Fig. S1; after Sun and McDonough, 1989) and show apatite REE compositions to be significantly more enriched in LREE and strongly depleted in HREE (heavy rare earth element) concentrations. Some apatite grains are characterised by thin (< 1–2 μm) zones surrounding hosted inclusions (Fig. 2f). These zones are characterised by elevated brightness in BSE imaging and higher REE-content relative to the rest of the apatite grain.

Fe-Mg-Al-spinel (i.e. MUM, Mg-magnetite and pleonaste) constitutes ~2 vol% of the groundmass and occurs as discrete euhedral grains (10–50 μm), thin (2 μm) euhedral 'atoll-rims' around Cr-spinel (Figs. 1b, 2c and d) and as rare anhedral grain clusters around olivine. Cr-spinel is a rare groundmass phase (< 1 vol%) that occurs as euhedral grains ranging from 20 to 100 μm in size. Cr-spinel also occurs as smaller (< 40 μm) euhedral inclusions in olivine (or its alteration products; Fig. 3e and f). Groundmass Cr-spinel is characterised by chromite-rich (titanian magnesian aluminous chromite: TIMAC; Mitchell, 1986) cores that are zoned towards MUM/pleonaste rims which sometimes form atoll-structures (e.g., Mitchell, 1986; Roeder and Schulze, 2008). These atoll-structures are characterised by a zoned euhedral Cr-spinel core surrounded by a 'lagoon' consisting of common alteration phases (i.e. serpentine, calcite) that is in turn enclosed by a thin rim (< 10 μm) of Mg-magnetite/MUM ± pseudomorphic garnet that parallels the shape of the Cr-spinel core exactly (Figs. 1b, and 2c and d).

2.3. Secondary assemblage: replacement minerals

Calcite is a common matrix phase that is interstitial to most other phases. Secondary (i.e. post-magmatic) calcite is a common replacement mineral of olivine.

Garnet is a minor phase (~2 vol%) that forms solid solutions between andradite $Ca_3Fe_2Si_3O_{12}$ and schlorlomite $Ca_3(Ti^{4+}, Fe^{3+})_2(((Si, Ti)O_4)_3)$. Garnet occurs as clusters of subhedral grains interstitially throughout the groundmass (Fig. 2b and c) and epitaxial mantles around olivine that are occasionally intergrown with monticellite (Fig. 2b and c). Atoll-rims surrounding Cr-spinel are sometimes partially-to-completely replaced by garnet (Fig. 2c and d).

Amakinite is a common replacement after olivine (Fig. 3c and d) that is commonly intergrown with serpentine. Amakinite displays a mottled dark brown colour under reflected light microscope. Electron microprobe (EMP; see Supplementary material for methodology) analyses of amakinite show that the cation content of amakinite is almost ideal. Amakinite shows a narrow range in H_2O-content between 27.8 and 28.7 wt% (as calculated by stoichiometry) and MnO (0.8–1.1 wt%) with FeO and MgO contents ranging between 17.2 and 23.5 wt% and 43.9–49.9 wt% respectively (Table 1), indicating the presence of a solid solution with brucite ($Mg(OH)_2$) and pyrochroite ($Mn(OH)_2$).

Bultfonteinite (~1 vol%) is a common replacement mineral after olivine (Fig. 3a, b and e) and occasionally overprints secondary calcite replacing olivine (Fig. 3b), as well occurring as rare interstitial segregations (up to ~125 μm) throughout the groundmass. Bultfonteinite replacing olivine is distinguished from other alteration phases (e.g., serpentine, calcite) as it is a uniform pale milky green colour under reflected light microscope and usually bladed/needle-like in shape (Fig. 3a). The distribution of bultfonteinite is extremely heterogeneous, where it may be ubiquitous in some areas, but rare or absent in others. Bultfonteinite was analysed by EDS (Fig. 4b) and EMP (see Supplementary material for methodology) and shown to be relatively homogeneous with F and stoichiometric H_2O contents ranging between 8.4 and 9.4 wt% and 12.7–13.2 wt% respectively (Table 2). These compositions are similar to analyses of secondary bultfonteinite in altered basalt xenoliths entrained in the Damtshaa kimberlite (Botswana; Buse et al., 2010).

Fluorite is a rare (< 1 vol%) phase that replaces olivine along grain margins and internal fractures (Fig. 3c–f) and overprints secondary calcite replacing olivine (Fig. 3d–f), as indicated by small anhedral inclusions (< 5 μm) of serpentine/calcite. Fluorite displays a pale olive

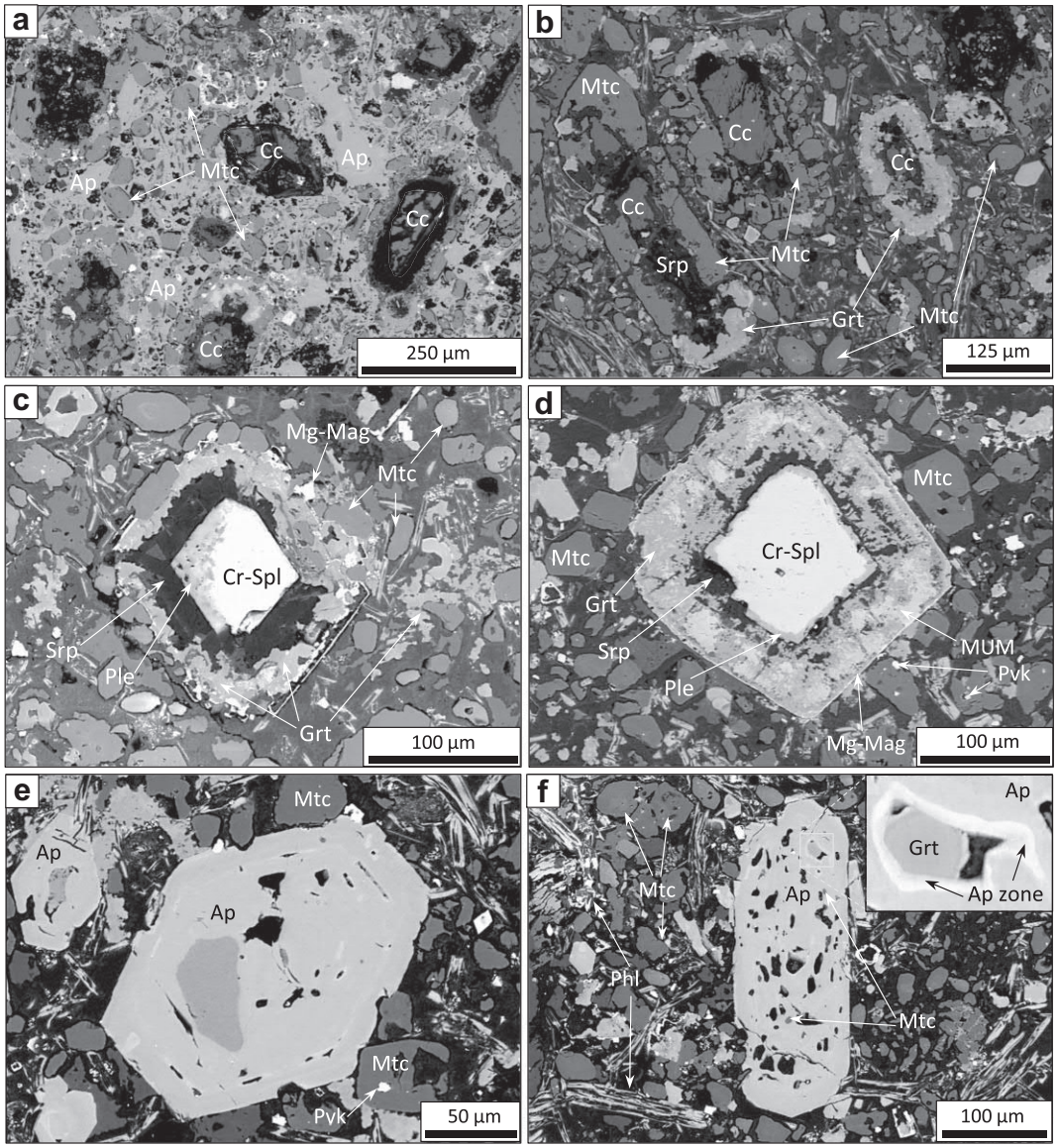

Fig. 2. Back-scattered electron (BSE) SEM images of: (a) Apatite domain cementing monticellite (Mtc) and former olivine which has been replaced by calcite (Cc). (b) Monticellite and garnet (Grt) forming partial-to-complete epitaxial mantles around altered olivine grains which have been replaced by calcite and serpentine (Srp). (c, d) Atoll-shaped Cr-spinel (Cr-Spl) grains showing pronounced zoning in the core from Cr-rich compositions to pleonaste (Ple) along the rims. The Cr-spinel core is separated by a distinct gap of serpentine that is in turn surrounded by a composite rim of magnesian ulvöspinel-magnetite (MUM; lighter colour) and garnet (darker colour) and an outermost thinner rim of Mg-magnetite (Mg-Mag). (e) Apatite grain showing pronounced zoning between darker (F-enriched) and lighter (Rare Earth Element (REE)-enriched) areas. (f) Inclusion-rich apatite grain. These inclusions are orientated parallel with the direction of the longest axis of the apatite grain. The inset in (f) shows the zoning (Ap zone) around an apatite-hosted inclusion which is characterised by elevated brightness under BSE imaging and REE-content. Cc: calcite, Phl: phlogopite, Pvk: perovskite.

green colour under reflected light microscope and forms blocky and/or bladed/needle-like shapes (Fig. 3c–f). Fluorite is also present interstitially in the groundmass as extremely rare domains up to ~400 µm in size. Fluorite replacing olivine almost never occurs in conjunction with bultfonteinite, except in one example (see Fig. 3e). Fluorite replacing olivine is usually irregularly zoned along crystal faces in contact with the groundmass which is characterised by F-depletion and O-enrichment. Analyses by EDS (Fig. 4c) and EMP (see Supplementary material for methodology) of fluorite show heterogeneities that are defined by increased O-content and subsequent F-depletion to some extent in both zoned rims (3.2–8.6 wt% O in EMP; mean: 6.9 wt%) and interior (0.7–2.1 wt% O in EMP; mean: 1.5 wt%; Table 3). The Ca-content is generally unaffected by the presence of O (Table 3). This substitution of fluorine by oxygen is reflected by a 1:4 replacement ratio, resulting in high cation totals (i.e. > 3; Fig. 5).

2.4. Major and trace element composition

The studied samples are characterised by low SiO_2 and high MgO and CaO (Table 4; see Supplementary material for methodology). These concentrations closely correlate with previous analyses of the Roger kimberlite drill core 94–17 at depths ranging from 131.9–139.7 m (Nowicki et al., 2008) and other Lac de Gras kimberlites (Kopylova and Hayman, 2008; Nowicki et al., 2008; Kjarsgaard et al., 2009; Tappe et al., 2013).

Primitive mantle normalised (after Sun and McDonough, 1989) lithophile trace element patterns show characteristic enrichment in highly incompatible elements and LREE (light rare earth elements) and depletion in HREE (heavy rare earth elements), resulting in a steep slope (Fig. 6) and large negative anomalies in Rb, K, Pb, Sr, P, Zr, Hf and Ti (Fig. 6a). In comparison to other Lac de Gras kimberlites, the Roger kimberlite exhibits the highest F-content (R10: 2263; R11: 2688 ppm) which is consistent with previous analyses (1534–2532 ppm

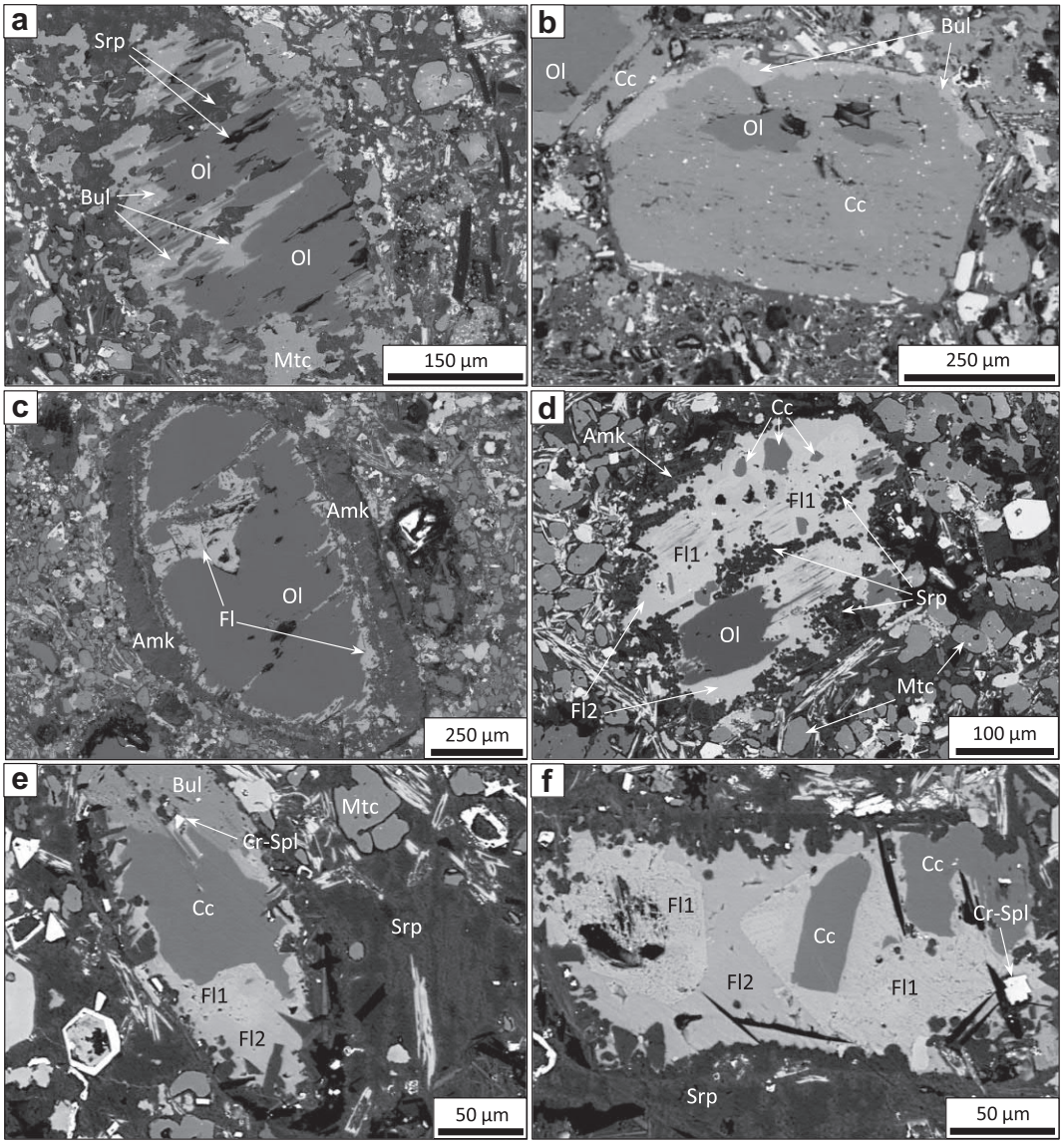

Fig. 3. Back-scattered electron (BSE) SEM images of: (a–f) olivine (Ol) showing varying degrees of replacement by fluorite (Fl), bultfonteinite (Bul) amakinite (Amk), serpentine (Srp) and calcite (Cc). (e, d, f) Fluorite is zoned between darker (elevated O-content; Fl1) and lighter (lower O-content; Fl2) areas (Table 3). (e) Olivine is replaced by both bultfonteinite and fluorite. Cr-Spl: Cr-Spinel.

F; Nowicki et al., 2008) in the same drill hole.

In addition, isotopic compositions of $\delta^{13}C$ (compared to VPDB - "Vienna Pee Dee Belemnite" standard) and $\delta^{18}O$ (compared to VSMOW – "Vienna Standard Mean Ocean Water" standard) of carbonate were analysed (see Supplementary material for methodology) and found to be $\delta^{13}C = -4.00‰$ and $\delta^{18}O = 12.02‰$ for R10 and $\delta^{13}C = -3.67‰$ and $\delta^{18}O = 11.99‰$ for R11.

3. Inclusions in kimberlite minerals

Multiphase (i.e. melt) inclusions were examined in olivine, Cr-spinel, monticellite and apatite. Inclusions in Cr-spinel, monticellite and apatite contain polycrystalline assemblages that are randomly distributed throughout their host grain and located away from any fracture system, and are therefore considered to be primary. In contrast, olivine-hosted inclusions are located along internal healed fractures and are therefore interpreted to be secondary, as defined by Roedder (1984). Inclusions were exposed in a water-free environment and analysed by field emission (FE) SEM (see Supplementary material for methodology). Despite these precautions, many inclusions still showed ubiquitous re-precipitation around their boundaries and on the host mineral surface, as illustrated in Supplementary Fig. S2. Consequently, many exposed inclusions contain large cavities/voids which were probably hosts to escaped fluids and/or water-soluble phases.

Thirteen primary melt inclusions were examined in Cr-spinel. Inclusions are typically irregularly shaped, range in size from 3 to 25 µm and contain (in order of decreasing abundance) halite/sylvite, dolomite, alkali (K, Na, Ba) carbonates, phlogopite, olivine, apatite and Fe-sulphides (Table 5; Fig. 7a).

Over one hundred primary melt inclusions were examined in monticellite. These inclusions are irregular-to-amoeboid in shape, range from 3 to 20 µm in size and dominated by (in order of decreasing abundance) Ca-Mg alkali (K, Na, Ba, Sr) carbonates (some F-bearing; Fig. 4e), sylvite/halite, phlogopite, alkali (Na, K) sulphates (e.g., arcanite (K_2SO_4)), Mg-magnetite, apatite, forsteritic olivine, humite (Fig. 4d; F-content varying between 3.5 and 4.7 wt%), unidentified alkali (Na, K, Ba) Si-REE-bearing phases, F-bearing alkali (Ba, K, Na) phosphates (Fig. 4f) and Ni-Fe-sulphides (Table 5; Fig. 7b and c). Monticellite is also host to monocrystalline inclusions of perovskite and MUM-spinel (Fig. 3e and f).

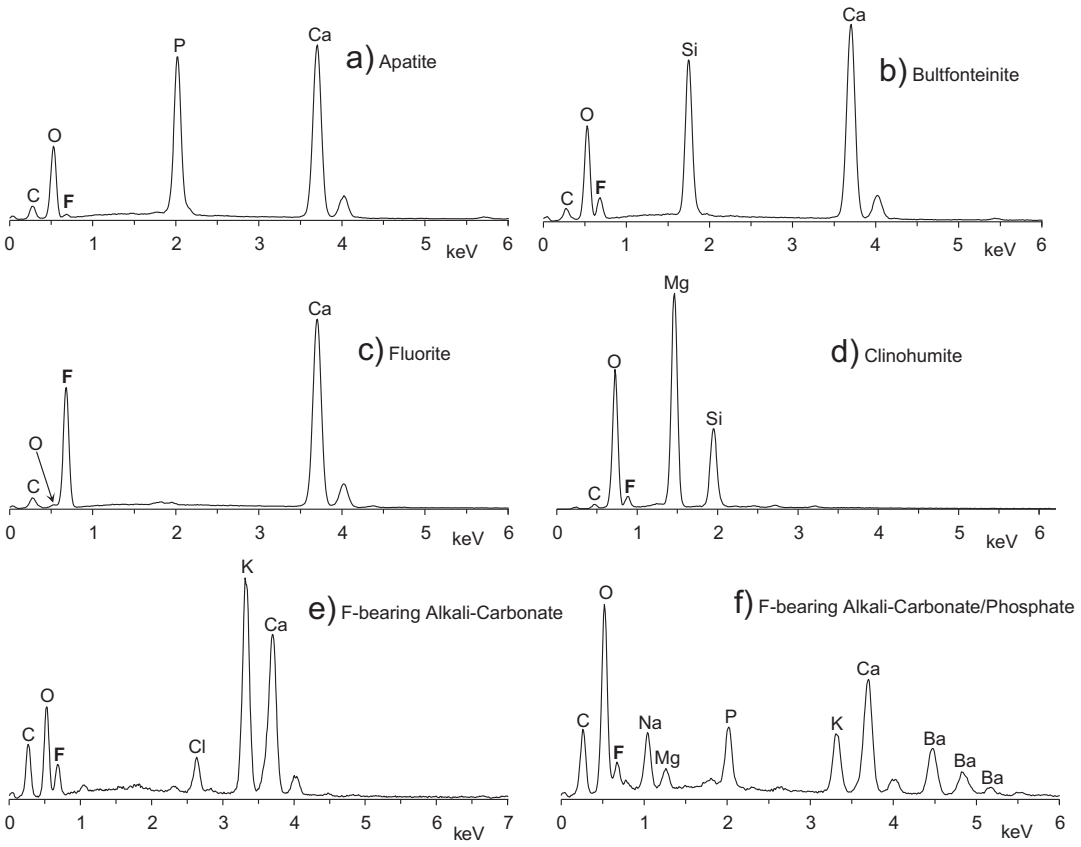

Fig. 4. Representative EDS spectrums of F-bearing phases: (a) groundmass apatite, (b, c) bultfonteinite and fluorite replacing olivine, and (d–f) F-bearing phases in melt inclusions.

Melt inclusions are particularly abundant in apatite, resulting in some grains being extremely turbid due to the quantity of inclusions. Over one hundred primary melt inclusions were examined in apatite. These inclusions are typically elongate in shape, orientated parallel with the longest apatite grain axis, range from 2 to 15 μm in length and contain (in order of abundance) Ca-Mg alkali (K, Na, Ba, Sr) carbonates (e.g., gregoryite (Na_2, K_2, Ca)$(CO_3)_2$, nyerereite $Na_2Ca(CO_3)_2$ and nyerereite-like phases, fairchildite ($K_2Ca(CO_3)_2$) and other unidentified F- and V-bearing and species), calcite, sylvite/halite, alkali (K, Ba, Na) sulphates (e.g., arcanite, aphthitalite ((K, Na)$_3$Na$(SO_4)_2$)) and Fe-Zn-sulphides, phlogopite, Mg-magnetite,, olivine/monticellite, unidentified alkali-Si-REE-bearing phases, alkali (Ba, K, Na) phosphates (e.g., Fig. 4f) including F-bearing varieties and humite (F-content of ~2.9 wt%; Table 5; Figs. 7d, e, 8 and 9). In addition, we report the occurrence of some highly unusual and rare Ba-K ± W ± V ± Mo-bearing phases as well as scheelite ($CaWO_4$) in apatite-hosted inclusions. These phases are volumetrically insignificant and further identification by EMP/Raman/LA-ICPMS was hampered by their small size, rarity and susceptibility to electron beam damage. Upon further inspection of EDS spectra of these Ba-K ± W ± V ± Mo phases and scheelite, we can clearly demonstrate that the peaks shown are more consistent with W, V and Mo than with Sr, Ba/REE and S respectively,

Table 1
Representative mineral analyses of amakinite replacing olivine. Mineral formulae calculated on a 2 O basis.

	1	2	3	4	5	6	7	8	9	10	11	Average
SiO_2	1.00	0.52	0.37	0.88	1.23	1.32	0.95	1.72	1.39	1.37	0.89	1.06
TiO_2	0.03	< 0.03	0.04	0.05	0.03	< 0.03	< 0.03	0.05	0.03	< 0.03	0.03	0.03
Al_2O_3	1.48	1.57	1.01	0.78	0.99	0.89	0.87	0.67	0.82	0.71	0.88	0.97
FeO	17.20	17.46	23.54	21.47	18.44	22.12	20.41	23.31	21.53	21.00	19.42	20.54
MnO	0.75	0.71	0.92	0.90	0.99	0.95	0.89	0.98	0.96	1.11	0.72	0.90
MgO	49.84	49.91	44.44	45.42	48.07	44.95	46.64	43.88	44.27	45.94	48.59	46.54
CaO	0.44	0.30	0.31	0.54	0.74	0.75	0.57	0.56	0.83	0.93	0.58	0.59
SO_3	0.04	< 0.03	0.12	0.38	0.67	0.69	0.59	0.61	0.68	0.44	0.45	0.43
H_2O	28.55	28.69	27.75	28.00	28.49	28.16	28.20	27.95	28.18	28.22	28.29	28.23
Total	99.32	99.17	98.51	98.41	99.65	99.83	99.12	99.74	98.69	99.72	99.85	
Si	0.011	0.006	0.004	0.010	0.013	0.014	0.010	0.019	0.015	0.015	0.009	
Ti	0.000	0.000	0.000	0.000	0.000	0.000	0.000	0.000	0.000	0.000	0.000	
Al	0.018	0.020	0.013	0.010	0.012	0.011	0.011	0.008	0.010	0.009	0.011	
Fe	0.152	0.154	0.216	0.195	0.163	0.198	0.183	0.210	0.194	0.187	0.172	
Mn	0.007	0.006	0.009	0.008	0.009	0.009	0.008	0.009	0.009	0.010	0.006	
Mg	0.785	0.785	0.726	0.736	0.756	0.716	0.745	0.704	0.711	0.731	0.768	
Ca	0.005	0.003	0.004	0.006	0.008	0.009	0.007	0.006	0.010	0.011	0.007	
S	0.000	0.000	0.001	0.003	0.005	0.006	0.005	0.005	0.005	0.003	0.004	
OH	2.011	2.018	2.030	2.029	2.006	2.006	2.016	2.007	2.027	2.008	2.002	
Total	2.996	2.986	3.004	3.006	2.974	2.958	2.988	2.964	2.981	2.966	2.982	

Table 2
Representative mineral analyses of bultfonteinite replacing olivine. Mineral formulae calculated on a 1 Si basis.

	1	2	3	4	5	6	7	8	9	Average
SiO_2	28.11	29.00	28.05	28.68	28.27	28.13	29.13	28.10	28.06	28.39
FeO	0.51	0.85	0.12	0.18	0.14	0.24	0.15	0.43	0.64	0.36
MgO	0.28	2.38	0.02	< 0.02	< 0.02	< 0.02	< 0.01	0.11	0.20	0.60
CaO	52.41	50.23	52.08	51.85	53.07	51.94	51.57	52.08	52.30	51.95
SO_3	0.44	0.43	0.01	< 0.01	< 0.01	0.04	0.01	0.12	0.52	0.22
F	8.87	8.41	9.37	8.76	9.26	9.65	9.20	9.21	9.36	9.12
H_2O	12.91	13.16	12.77	12.98	12.77	12.70	12.90	12.81	12.78	12.87
−O=F	3.73	3.54	3.94	3.69	3.90	4.06	3.87	3.88	3.94	3.84
Total	99.79	100.91	98.47	98.72	99.61	98.65	99.10	98.98	99.91	
Si	1.000	1.000	1.000	1.000	1.000	1.000	1.000	1.000	1.000	
Fe	0.015	0.122	0.001	0.001	0.000	0.001	0.000	0.006	0.010	
Mg	0.015	0.024	0.003	0.005	0.004	0.007	0.004	0.013	0.019	
Ca	1.997	1.856	1.989	1.937	2.011	1.978	1.897	1.986	1.997	
S	0.012	0.011	0.000	0.000	0.000	0.001	0.000	0.003	0.014	
F	0.997	0.917	1.058	0.966	1.081	1.097	0.998	1.036	1.055	
O	3.063	3.027	3.037	3.018	2.989	3.005	2.954	3.040	3.038	
H	5.096	5.090	4.984	4.967	4.969	4.943	4.880	5.015	5.059	
Total	12.196	12.047	12.073	11.892	12.054	12.033	11.734	12.099	12.192	

Table 3
Representative mineral analyses of fluorite replacing olivine in element wt%. R = rim, I = interior. Mineral formulae are calculated on a 1 Ca basis.

	1-R	2-R	3-R	4-R	5-R	6-R	7-R	Average-R	8-I	9-I	10-I	11-I	12-I	13-I	Average-I
Si	0.36	0.23	0.42	0.27	0.23	0.31	0.12	0.28	0.09	0.06	0.11	0.07	0.05	0.03	0.07
Fe	0.17	0.14	0.37	0.18	0.12	0.14	0.09	0.17	0.14	0.14	0.08	0.07	0.06	0.05	0.09
Mg	0.08	0.05	0.26	0.04	0.06	0.07	0.03	0.08	< 0.01	< 0.01	< 0.01	0.03	< 0.01	< 0.01	< 0.01
Ca	48.44	48.14	48.00	48.14	47.87	47.66	49.48	48.25	50.1	49.82	49.71	50.50	50.67	50.62	50.24
Sr	0.28	0.33	0.33	0.23	0.32	0.26	0.17	0.27	0.31	0.33	0.56	0.46	0.28	0.22	0.36
Na	0.11	0.08	0.09	0.10	0.10	0.10	< 0.02	0.09	< 0.02	0.04	< 0.02	0.04	0.08	0.07	0.05
F	43.64	41.62	41.72	43.76	43.03	43.64	45.49	43.27	47.00	46.20	46.41	47.33	47.02	47.20	46.86
O	7.60	8.63	6.93	7.21	7.75	6.85	3.20	6.88	1.46	2.05	1.91	1.80	0.72	0.95	1.48
Total	100.68	99.23	98.10	99.93	99.48	99.03	98.57		99.11	98.63	98.78	100.29	98.88	99.14	
Si	0.011	0.007	0.012	0.008	0.007	0.009	0.004		0.003	0.002	0.003	0.002	0.001	0.001	
Fe	0.003	0.002	0.006	0.003	0.002	0.002	0.001		0.002	0.002	0.001	0.001	0.001	0.001	
Mg	0.003	0.002	0.009	0.001	0.002	0.002	0.001		0.000	0.000	0.000	0.001	0.000	0.000	
Ca	1.000	1.000	1.000	1.000	1.000	1.000	1.000		1.000	1.000	1.000	1.000	1.000	1.000	
Sr	0.003	0.003	0.003	0.002	0.003	0.003	0.002		0.003	0.003	0.005	0.004	0.003	0.002	
Na	0.004	0.003	0.003	0.003	0.004	0.003	0.001		0.000	0.001	0.000	0.001	0.003	0.002	
F	1.901	1.824	1.834	1.918	1.896	1.932	1.939		1.979	1.956	1.970	1.977	1.958	1.967	
O	0.393	0.449	0.362	0.375	0.406	0.360	0.162		0.073	0.103	0.096	0.089	0.036	0.047	
Total	3.316	3.290	3.228	3.311	3.319	3.311	3.109		3.060	3.068	3.076	3.076	3.001	3.020	

which display overlap these elements (see Supplementary Fig. S3). In addition, to pristine multiphase inclusions, apatite also contains numerous altered inclusions that composed of serpentine and secondary garnet. Large apatite grains (> 100 μm) also contain abundant poikilitically enclosed monocrystalline inclusions of monticellite, spinel and perovskite.

Inclusions in apatite were also examined by LA-ICPMS. These inclusions are characterised by positive Na-K-Rb anomalies which are usually accompanied by increases in Ba, Li and to a lesser extent in V, Al and sometimes Zn (Supplementary Fig. S4). In addition, four multiphase inclusions in apatite were examined with Raman point analyses and point mapping (see Supplementary material for methodology). The inclusions studied are elongate in shape and translucent under reflected light where they contain between two and six optically distinguished phases, including vapour bubbles (Fig. 10; Table 6). All inclusions analysed display unique Raman spectrums, but are all dominated by sharp, intense bands ranging between 1048 and 1086 cm^{-1}, indicating the presence of carbonates (CO_3^{2-}). Only two phases were positively identified: calcite (Grain 2; Fig. 10c), which shows moderate bands at 154, 278 and 712 cm^{-1} and a major peak at 1086 cm^{-1}, and witherite ($BaCO_3$; Grain 3; Fig. 10f), which shows moderate bands 138, 152 and 690 cm^{-1} and major peaks at 1057 with a shoulder at 1060 cm^{-1}. The absence of bands at 3000–4000 cm^{-1} indicates that these carbonates are anhydrous. Other phases detected by Raman (Fig. 10; Table 6) represent unidentified carbonate phases with no database matches, likely representing solid solutions. These phases identified by Raman are in agreement with common carbonate minerals identified by SEM-EDS analyses (see above).

Melt inclusions in olivine are generally poorly preserved largely due to re-precipitation of soluble phases hosted within and/or host grain alteration. Two secondary melt inclusions were examined in olivine in healed fractures (Fig. 7f; Supplementary Fig. S5). These inclusions contain complex assemblages comprising of nyerereite, bradleyite ($Na_3Mg(PO_4)(CO_3)$), arcanite, tetraferriphlogopite ($KMg_3(Fe^{3+}Si_3O_{10})(OH, F)_2$), clinohumite (F-content varying between 6.9 and 7.9 wt%), sylvite, Mg-magnetite and apatite.

Groundmass calcite contains abundant disseminated (≤ 2 μm) monocrystalline inclusions of Ba-Sr-carbonates (witherite? strontianite? burbankite? ($(Na, Ca)_3(Sr, Ba, Ce)_3(CO_3)_5$)) and rare Fe-Ni-Cu-sulphides (Supplementary Fig. S6).

4. Discussion

The Roger kimberlite exhibits textural, mineralogical and geochemical characteristics typical of archetypal hypabyssal kimberlites from Ekati (Nowicki et al., 2008; Kjarsgaard et al., 2009) and others worldwide (Mitchell, 1986, 2008; Skinner, 1989). The presence of F-bearing minerals (i.e. fluorite, bultfonteinite) in the Roger kimberlite

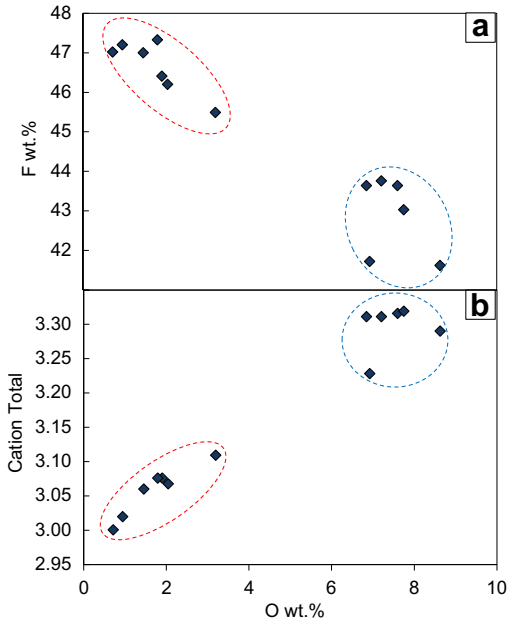

Fig. 5. (a) F wt% and (b) Cation total vs. O wt% in fluorite. Data points circled areas represent analyses of fluorite interior (red) and rims (blue; see Table 3). (For interpretation of the references to colour in this figure legend, the reader is referred to the web version of this article.)

Table 4
Major and trace element abundances in the Roger kimberlite: analyses R10 and R11.

Sample	R10	R11		R10	R11
SiO_2	28.15	28.92	Rb	5.8	57.4
TiO_2	0.88	0.87	Ba	7407	7847
Al_2O_3	4.25	3.40	Th	63.2	61.3
FeO	8.54	8.95	U	10.6	9.3
MnO	0.22	0.22	Nb	605	484
MgO	27.89	30.22	Ta	28.2	27
CaO	16.34	13.74	La	480.7	405.7
Na_2O	0.07	0.07	Ce	754	644.8
K_2O	0.12	0.33	Pb	34	28
P_2O_5	1.40	1.56	Pr	70.7	62.7
CO_2	4.28	3.43	Sr	2972	1968
H_2O^a	8.62	8.50	Nd	208	179.7
S[a]	0.11	0.09	Sm	21.2	17.6
Cl	0.06	0.02	Zr	121	118
F	0.23	0.27	Hf	3	2.9
Total	101.16	100.52	Eu	4.5	3.9
			Gd	10.2	8.8
Co	71.6	76.7	Tb	0.9	0.8
Cr	1368	1525	Dy	3.8	3.0
Ni	760	940	Li	11.5	9.5
Sc	21	20	Y	14.1	11.7
V	117	129	Ho	0.5	0.5
W	3	7	Er	1.3	1.0
Mo	1	2	Tm	0.1	0.1
Cu	81	69	Yb	0.8	0.7
Zn	52	54	Lu	0.1	0.1

Major elements are in wt%, trace elements in ppm.
[a] H_2O and S were determined by Element Analyser (see Supplementary material for methodology).

groundmass is at odds with common descriptions of kimberlite groundmass and alteration assemblages (e.g., Skinner and Clement, 1979; Dawson, 1980; Clement et al., 1984; Mitchell, 1986, 2008). To our knowledge, this is the first occurrence of significant amounts of F-rich phases occurring in a kimberlite.

In the following sections we constrain the evolution of the Roger kimberlite melt by employing petrographic observations and the compositions of primary inclusions in Cr-spinel, monticellite and apatite, and secondary inclusions in olivine. Furthermore, we investigate the possible origin(s) of halogens (F, Cl) in kimberlites (i.e. external vs. magmatic) and finally discuss the implications for the composition of the kimberlite melt.

4.1. Crystallisation and melt evolution of the Roger kimberlite

In order to constrain the evolution of the Roger kimberlite melt, we first reconstructed a relative sequence of crystallisation for the groundmass based on textures and inclusions. Crystal inclusions of Cr-spinel in the rims of olivine indicate cotectic crystallisation (Fig. 3e and f). This is consistent with studies by (Mitchell, 1986, 2008; Fedortchouk and Canil, 2004) which show olivine and Cr-spinel to be the earliest crystallising phases in kimberlites. The formation of epitaxial mantles of monticellite around olivine (Fig. 2b) and interstitial growth of discrete monticellite grains around atoll spinels indicates monticellite crystallised after olivine and spinel (Fig. 2c and d). Cr-spinel is typically zoned towards Al-Fe-rich compositions (i.e. MUM/pleonaste; Fig. 2c and d). This trend is common in archetypal kimberlites and is attributed to magma differentiation (Mitchell, 1986; Armstrong et al., 2004; Roeder and Schulze, 2008). Crystal inclusions of perovskite in monticellite (Fig. 2d and e) and apatite indicate perovskite crystallised before and/or at the same time as monticellite and apatite. Large prismatic apatite grains (up to 400 μm; Fig. 2e and f) commonly contain poikilitically enclosed inclusions of spinel, perovskite and monticellite, indicating apatite crystallisation occurred during and/or after the crystallisation of these phases. In contrast, apatite domains cementing other minerals (e.g., monticellite, phlogopite, spinel; Fig. 2a) indicate late stage crystallisation. The formation of clusters of phlogopite grains around spinel, perovskite and monticellite and interstitial calcite growth surrounding phlogopite implies that mica crystallised after spinel, perovskite and monticellite, but prior to carbonate (e.g., Fig. 2f). Interstitial calcite likely dominated the closing stages of groundmass crystallisation (e.g., Armstrong et al., 2004; Mitchell, 2008). Olivine alteration to admixtures of serpentine, amakinite, carbonate, bultfonteinite and fluorite (Figs. 1, 2a, b and 3) are interpreted to be the products of syn- and/or post-magmatic alteration (see Sections 4.2 and 4.3).

Melt inclusions in Cr-spinel, monticellite and apatite are primary and considered to represent heterogeneous trapping of kimberlite melt during groundmass crystallisation. In contrast, melt inclusions examined in olivine represents the secondary trapping of kimberlite melt at an indeterminate stage during and/or after groundmass crystallisation. Melt inclusions in olivine, Cr-spinel, monticellite and apatite contain complex daughter assemblages dominated by (in order of relative abundance) alkali (Na, K, Ba, Sr) enriched Ca-Mg-carbonates, Na-K-chlorides, alkali-sulphates, phosphates, spinel, silicates (e.g. olivine, phlogopite, (clino)humite) and sulphides (Table 5; Figs. 7–9 and Supplementary Fig. S5). Similar daughter phase compositions and assemblages have also been identified in melt inclusions in olivine, spinel, perovskite and apatite in other kimberlites worldwide (Golovin et al., 2007; Kamenetsky et al., 2009a, 2012, 2013, 2014; Mernagh et al., 2011; Abersteiner et al., 2016; Giuliani et al., 2016), as well as in olivine and ilmenite in kimberlitic polymict breccias (Giuliani et al., 2012, 2013, 2014b) and in minerals from kimberlite-hosted mantle xenoliths (Golovin et al., 2016; Soltys et al., 2016). In addition, we report the presence of several unusual and 'exotic' phases in melt inclusions which include Ba-K ± W ± V ± Mo-bearing phases, F/V-bearing carbonates, alkali-REE/phosphate-bearing phases and scheelite. Although there are appreciable concentrations of Rb, W, Mo Li and V in melt inclusion phases in apatite, there is no anomalous enrichment or depletion in these components in whole-rock compositions when compared to other kimberlites from Ekati (Nowicki et al., 2008; Tappe et al., 2013) or worldwide (Le Roex et al., 2003; Becker and Le Roex, 2006).

The differences in composition and daughter phase assemblages in

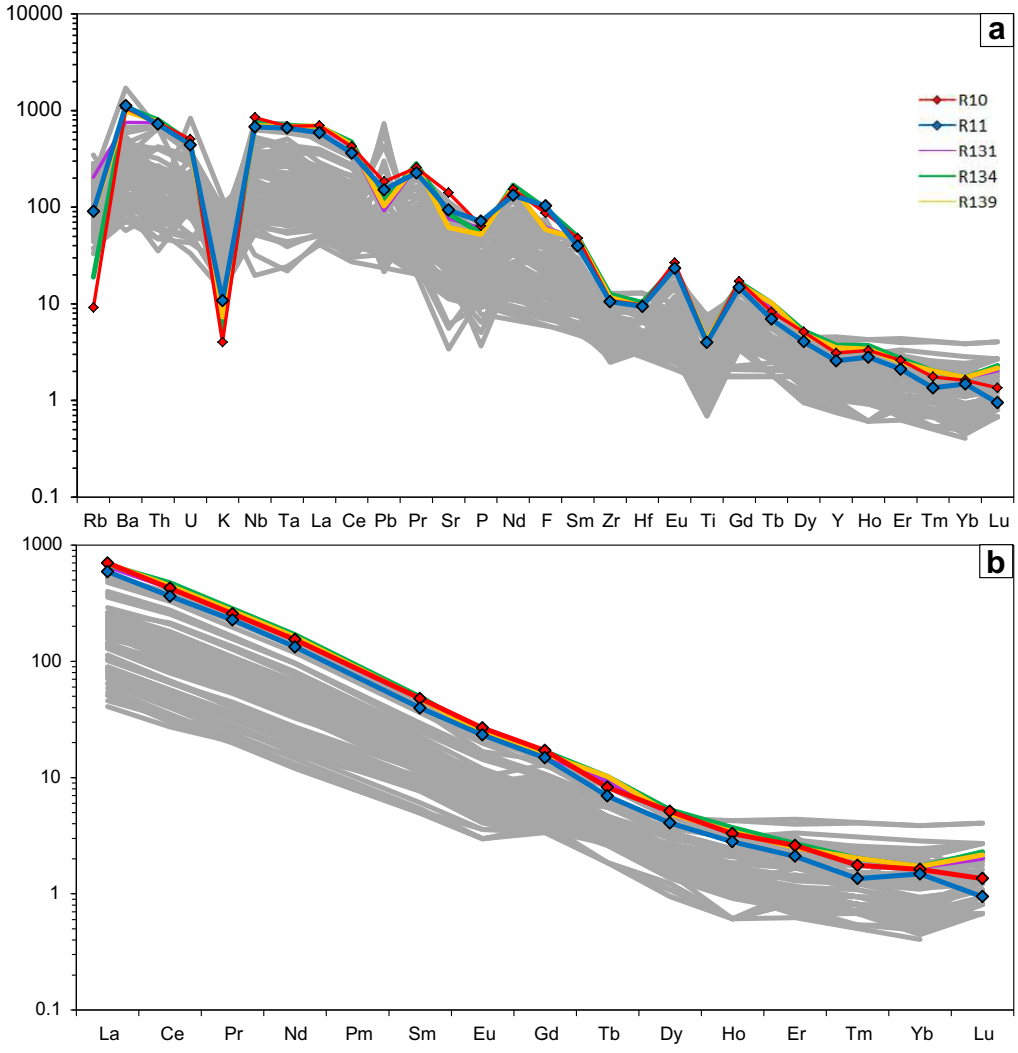

Fig. 6. (a, b) Primitive mantle normalised (after Sun and McDonough, 1989) incompatible trace element patterns of the Roger kimberlite (R10, R11) compared with Roger kimberlite analyses from the sample drill hole at depths of 131 m, 134 m and 139 m (R131, R134, R139) and other Ekati kimberlites (grey lines; Nowicki et al., 2008).

Table 5
Summary of daughter mineral phases included in Cr-spinel, monticellite and apatite listed in order of decreasing abundance.

Cr-spinel	Distribution (%)	Monticellite	Distribution (%)	Apatite	Distribution (%)
Halite/sylvite NaCl/KCl	40	Ca-Mg alkali-carbonates (K, Na, Ba, Sr) ± F	45	Ca-Mg alkali-carbonates (K, Na, Ba, Sr) ± F ± V	42
Dolomite $CaMg(CO_3)_2$	30	Sylvite/halite KCl/NaCl	25	Calcite $CaCO_3$	15
Alkali-carbonates K, Na, Ba	15	Phlogopite $KMg_3(AlSi_3O_{10})(F, OH)_2$	5	Sylvite/halite KCl/NaCl	10
Phlogopite $KMg_3(AlSi_3O_{10})(F, OH)_2$	6	Alkali-sulphates Na-K	5	Sulphates/sulphides (K-Ba-Na) + (Fe-Zn)	9
Olivine $(Mg, Fe)_2SiO_4$	5	Mg-magnetite $MgFe_2O_4$	5	Phlogopite $KMg_3(AlSi_3O_{10})(F, OH)_2$	5
Apatite $Ca_5(PO_4)_3(F, Cl, OH)$	3	Apatite $Ca_5(PO_4)_3(F, Cl, OH)$	3	Mg-magnetite $MgFe_2O_4$	5
Sulphides Fe	1	Olivine $(Mg, Fe)_2SiO_4$	3	Olivine/monticellite $(Mg, Fe)_2SiO_4/CaMgSiO_4$	5
		Humite $(Mg, Fe^{2+})_7(SiO_4)_3(F, OH)_2$	3	Alkali-Si-REE-phases Na-K-Ba-Si-REE	3
		Alkali-Si-REE-phases Na-K-Ba-Si-REE	2	Alkali-phosphate Ba-K-Na ± F	2
		Alkali-phosphate Ba-K-Na ± F	2	Humite $(Mg, Fe^{2+})_7(SiO_4)_3(F, OH)_2$	2
		Sulphides Ni, Fe	2	Ba-K ± W ± V ± Mo-phase/scheelite $CaWO_4$	2

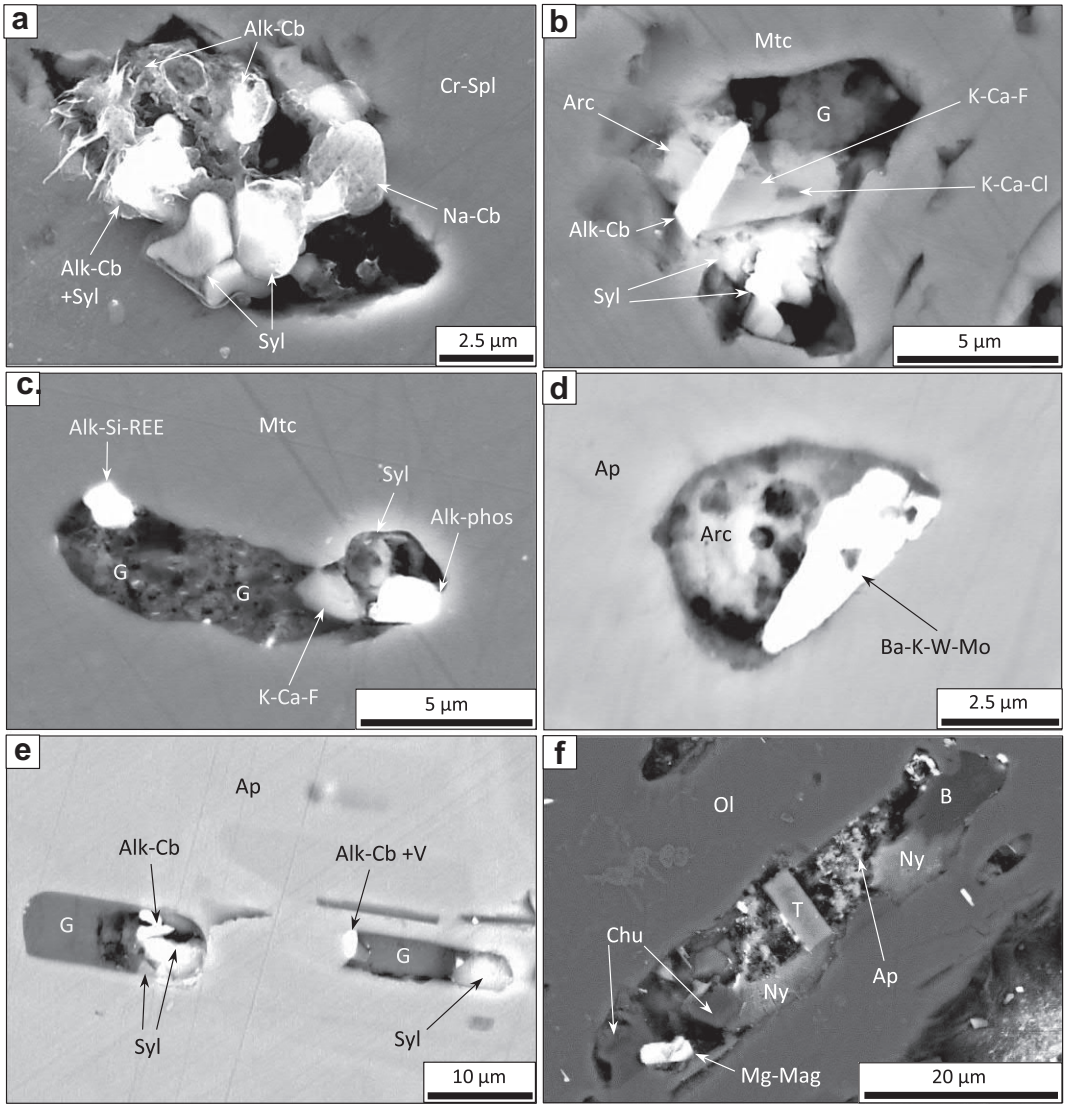

Fig. 7. Back-scattered electron (BSE) SEM images of multiphase inclusions in: (a) Cr-spinel (Cr-Spl), (b, c) monticellite (Mtc), (d, e) apatite (Ap) and (f) olivine. These multiphase inclusions host daughter phases of: (a) Alkali (Na, K) carbonate (Alk-Cb) and sylvite (Syl); (b) sylvite, alkali (Na, K, Ba) carbonates, gregoryite (G), K-Ca-F-bearing phase (K-Ca-F), Ka-Ca-Cl-bearing phase (K-Ca-Cl) and arcanite (Arc; K_2SO_4); (c) gregoryite, sylvite, K-Ca-F-bearing phase, alkali (Ba, K, Na) phosphate (Alk-phos) and an alkali (Ba, Na)-Si-REE-bearing phase (Alk-Si-REE); (d) Ba-K-W-Mo-bearing phase (Ba-K-W-Mo) and arcanite; (e) alkali (Ba, K, Na) carbonate + V, gregoryite and sylvite; (f) nyerereite (Ny), Mg-magnetite (Mg-Mag), tetraferriphologopite (T), bradleyite (B), clinohumite (Chu) and apatite (Ap).

each host mineral (Table 5) are interpreted to represent different stages of kimberlite melt entrapment, reflecting the timing of the host mineral crystallisation (Abersteiner et al., 2016). Therefore, it is likely that melt inclusions in earlier crystallising phases (i.e. Cr-spinel and monticellite) sampled a less differentiated version of the kimberlite melt, whereas melt inclusions in later forming apatite entrapped a more evolved, incompatible element-enriched kimberlite melt.

Groundmass calcite contains abundant disseminated crystal inclusions of Ba-Sr carbonates (Supplementary Fig. S6). These inclusions likely represent relics of magmatic alkali-carbonates that were recrystallised during syn- and/or post-magmatic alteration. The presence of Ba and Sr in the kimberlite melt is further signified by the partitioning of Sr into apatite and Ba into phlogopite (kinoshitalite) along with abundant Ba-Sr-bearing melt inclusion phases entrapped in olivine, Cr-spinel, monticellite and apatite.

4.2. Origin of halogens in kimberlites

The Roger kimberlite is unique amongst other Ekati kimberlites, as it contains the highest F-content (up to 2688 ppm) and large quantities of F-rich minerals (i.e. bultfonteinite, fluorite) replacing olivine. Paul et al. (1976) reported some kimberlites from central India containing even greater concentrations of fluorine (up to 7490 ppm). However, there have been no detailed petrographic studies to suggest the presence of any F-rich minerals. Our petrographic observations of the Roger kimberlite show the distribution of bultfonteinite and fluorite to be extremely heterogeneous. The difficulty in clearly identifying bultfonteinite and/or fluorite in kimberlites could account for the apparent 'rarity' of F-rich minerals in other kimberlites as they may remain largely unrecognised. In order to constrain the origin of halogens (F, Cl) in the Roger kimberlite, we examine two possible sources (i.e. magmatic vs. external).

Fluorine exists to some extent in the crystallising kimberlite melt based on its presence in groundmass apatite (~1.3–3.4 wt%) and in daughter phases in melt inclusions (i.e. apatite, phlogopite, tetraferriphlogopite and F-bearing alkali-carbonates and (clino)humite) in olivine, monticellite and apatite (e.g., Fig. 4). Trace element incompatibility studies have shown F and Nd to share similar degrees of compatibility during melting (Sun and McDonough, 1989; Workman et al., 2006). Furthermore, primitive mantle normalised patterns of

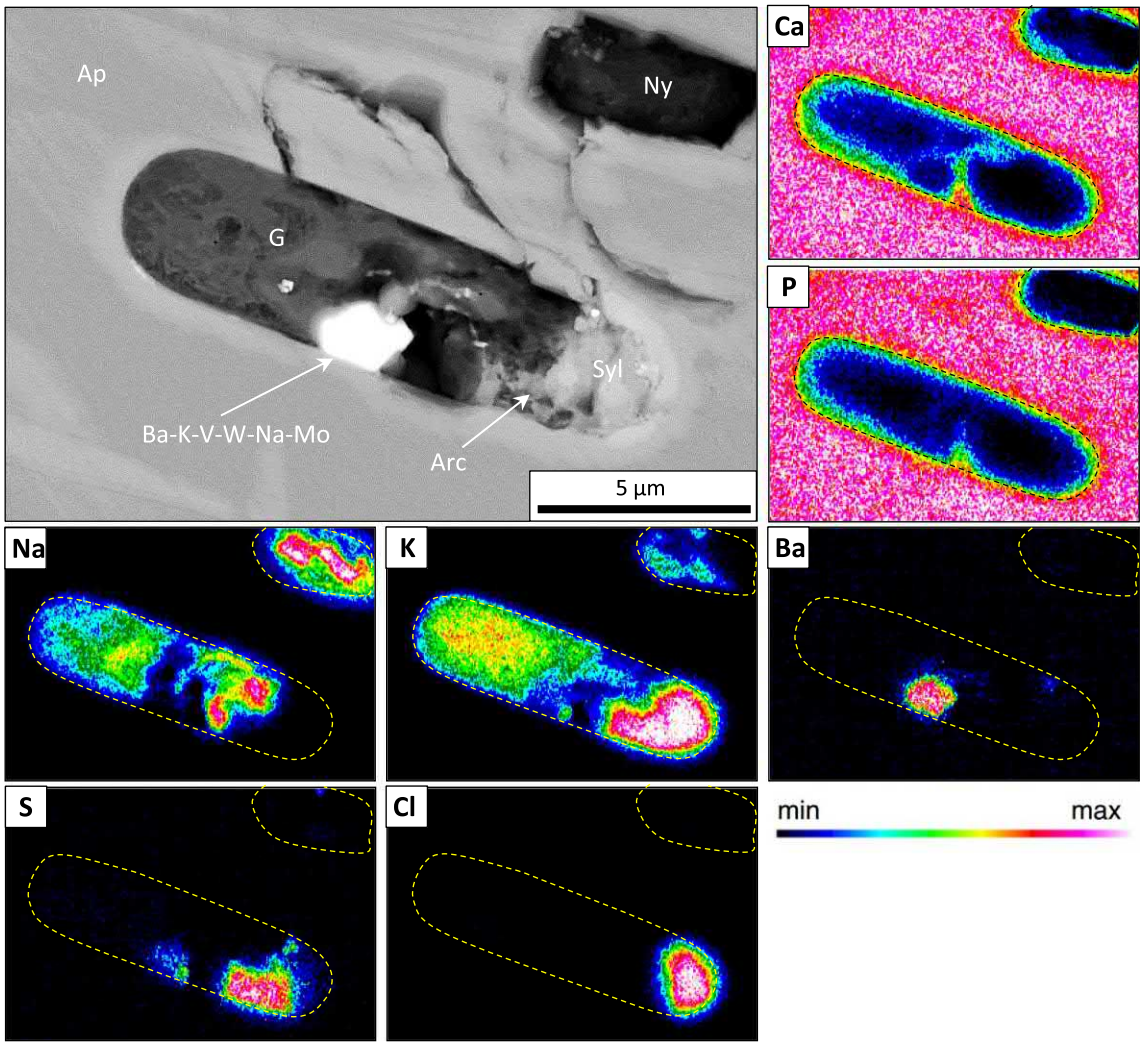

Fig. 8. Back-scattered electron SEM image and X-ray elemental map of a representative inclusion in apatite (Ap). Detected minerals include: gregoryite (G), nyerereite (Ny), arcanite (Arc), sylvite (Syl) and a Ba-K-V-W-Na-Mo-bearing phase (Ba-K-V-W-Na-Mo) phase. The dotted yellow/black line represents the boundary of the inclusion. (For interpretation of the references to colour in this figure legend, the reader is referred to the web version of this article.)

incompatible trace elements show fluorine in the Roger kimberlite to appear neither anomalously enriched nor depleted relative to Nd or Sm (Fig. 6a). Assuming that fluorine has been neither added nor removed from the kimberlite magma, we employed F/Nd ratios to produce an estimate of F concentrations in the Roger kimberlite melt. These F/Nd ratios range from ~19.2 in the primitive mantle (Sun and McDonough, 1989) to ~20.1–28.8 (Sun and McDonough, 1989; Workman et al., 2006) in mid-ocean ridge basalts (MORB), with even more variable estimates ranging between ~14.3–45.4 (Shimizu et al., 2016). On the other hand, ocean island basalt (OIB) F/Nd ratios are estimated to be ~29.9 (Sun and McDonough, 1989). Using the estimated primitive mantle F/Nd ratios (19.2) and the analysed Nd-content (1780–230 ppm) in our samples and those from Nowicki et al. (2008), we estimated the F-content of the host kimberlite melt to range between 3460 and 4420 ppm. These predicted values are notably higher than the measured whole-rock F-values from both data sets and therefore the Roger kimberlite may be a relatively close representation to 'pristine' F-concentrations in kimberlite rocks.

Chlorine is slightly more incompatible than La and Nb, but more compatible than U (Kamenetsky and Eggins, 2012). Using primitive mantle estimates of Cl (14.3; Kamenetsky and Eggins, 2012) and U (0.021; Sun and McDonough, 1989), the Cl/U ratio is ~680. Based on analysed U-contents (9.0–10.6 ppm) in both datasets for the Roger kimberlite, the estimated Cl-content is expected to range between 6120 and 7210 ppm. Similar to fluorine, these estimated Cl-values exceed the measured whole-rock Cl-content (R10: 200 ppm; R11: 600 ppm).

An alternative scenario is that alkalis/alkali-earths and halogens were derived from an external crustal or groundwater source. Contamination of kimberlites by xenoliths and/or weathering is problematic when interpreting geochemical data. In the absence of obvious petrographic evidence for crustal contamination, the Contamination Index (C·I; Clement, 1982) provides some degree of resourcefulness, where kimberlites rocks > 1 are considered 'contaminated'. Our studied samples along with those analysed by Nowicki et al. (2008) exhibit C·I values ranging between 1.05 and 1.20 which indicates 'low-level' crustal contamination. This is supported by low SiO_2 (25.4 wt %–28.9 wt%), negative Pb and Zr-Hf anomalies and steeply sloping REE patterns (La/Yb: 556–601; Table 4; Fig. 6; see Le Roex et al., 2003; Kjarsgaard et al., 2009; Tappe et al., 2013). It is noteworthy that the Roger kimberlite is the most enriched in LREEs compared to other Ekati kimberlites (Fig. 6b; see Nowicki et al., 2008; Tappe et al., 2013). Elevated Al_2O_3 levels (3.4–4.3 wt%) in the Roger kimberlite dataset indicate that there is some degree of crustal contamination present, as reflected by ln Si/Al (1.77–2.02) and Yb/Al_2O_3 (0.19–0.24) ratios (see Le Roex et al., 2003; Kjarsgaard et al., 2009; Tappe et al., 2013). However, the absence of significant crustal contamination and/or elevated fluorine in other more contaminated Ekati kimberlites makes assigning an external source of alkalis and halogens redundant.

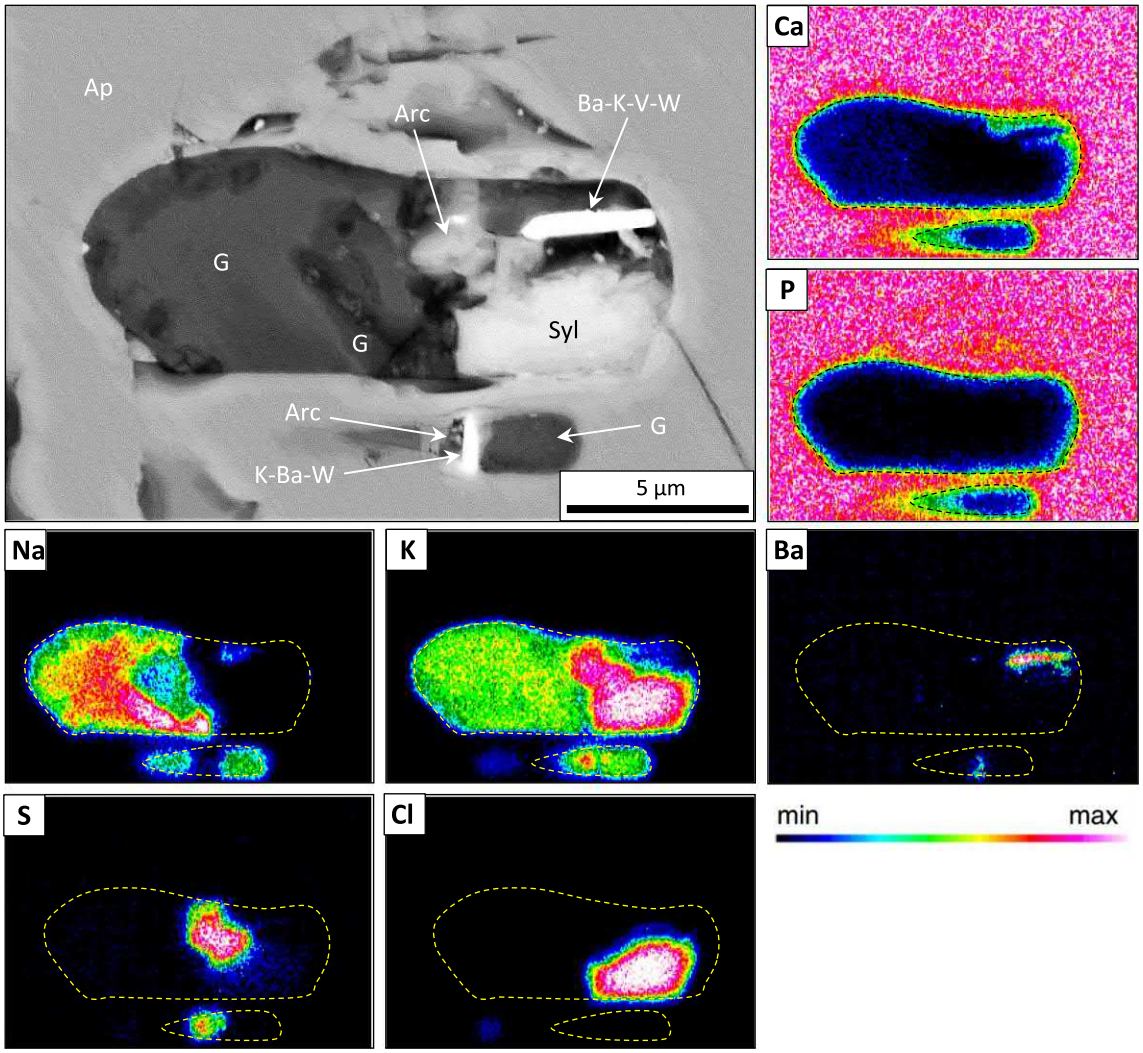

Fig. 9. Back-scattered electron SEM image and X-ray elemental map of a representative inclusion in apatite (Ap). Detected minerals include: gregoryite (G), arcanite (Arc), sylvite (Syl), a K-Ba-W-bearing phase (K-Ba-W) and a Ba-K-V-W-bearing phase (Ba-K-V-W). The dotted yellow/black line represents the boundary of the inclusion. (For interpretation of the references to colour in this figure legend, the reader is referred to the web version of this article.)

We suggest that fluorine in the Roger kimberlite was magmatically derived. Although phlogopite and apatite crystallisation accommodated some fluorine, a significant portion of fluorine remained dissolved in the late-stage residual melt. Jago and Gittins (1991) experimentally determined that F-concentrations up to 8 wt% can remain dissolved in carbonatitic ($CaCO_3$-Na_2CO_3) liquids at pressures of 1 kbar before fluorite stabilises. As deduced from melt inclusions, alkali-enriched carbonates are a significant component of the kimberlite melt and subsequently fluorine could remain dissolved at relatively low crustal depths. These halogen- and alkali/alkali-earth-enriched phase assemblages in primary melt inclusions from the Roger kimberlite minerals are analogous to the groundmass mineralogy of fresh Oldoinyo Lengai (Tanzania) natrocarbonatite lavas, which contain abundant alkali-carbonates, chlorides and F-bearing phases (e.g., Keller and Krafft, 1990; Mitchell, 1997; Zaitsev et al., 2009; Potter et al., 2016).

4.3. Constraining post-magmatic alteration

The compositions and textures of garnet (andradite-schlorlomite), amakinite, bultfonteinite and fluorite in the Roger kimberlite are consistent with a secondary origin. (Hydro)garnet is common in hydrothermally altered sediments and skarns (Deer et al., 1992) as well as in volcaniclastic and pyroclastic kimberlite rocks (Stripp et al., 2006; Willcox et al., 2015) and entrained xenoliths in kimberlites (Dawson, 1980; Buse et al., 2010). Similarly, numerous studies have documented bultfonteinite and fluorite as low-temperature hydrothermal products commonly associated with skarns (Murdoch, 1955; Henry, 1999; Ohnishi et al., 2007) and hydrothermally altered sedimentary deposits (Nyfeler et al., 1995; Bonazzi et al., 2007). In rare occurrences, bultfonteinite has been reported in altered kimberlite-hosted xenoliths (Parry et al., 1932; Chakhmouradian and Mitchell, 2001; Buse et al., 2010). Fluorite mineralisation has also been attributed to F-rich fluids in crystallising carbonatite melts (e.g., Amba Dongar, India) interacting with calcareous groundwater (Deans and Powell, 1968; Simonetti and Bell, 1995).

The formation of interstitial andradite-schlorlomite garnet is indicative of precipitation from a hydrothermal Ca-bearing serpentinising fluid (Stripp et al., 2006; Buse et al., 2010). In addition, based on the occurrence of bultfonteinite and fluorite, it is inferred that this alteration fluid was also F-bearing. Buse et al. (2010) constrained the temperature range for secondary hydrogarnet and bultfonteinite formation in basalt xenoliths from the B/K9 kimberlite (Botswana) to occur between 350 and 250 °C, which is a similar temperature range to when serpentinisation occurs (Evans, 2004; Stripp et al., 2006; Mitchell, 2008). Therefore, it is likely the observed alteration assemblages in our sample formed at similar low-temperature conditions.

Amakinite belongs to the brucite-pyrochroite group and a rare mineral in kimberlites that has only been reported in the Udachnaya-East

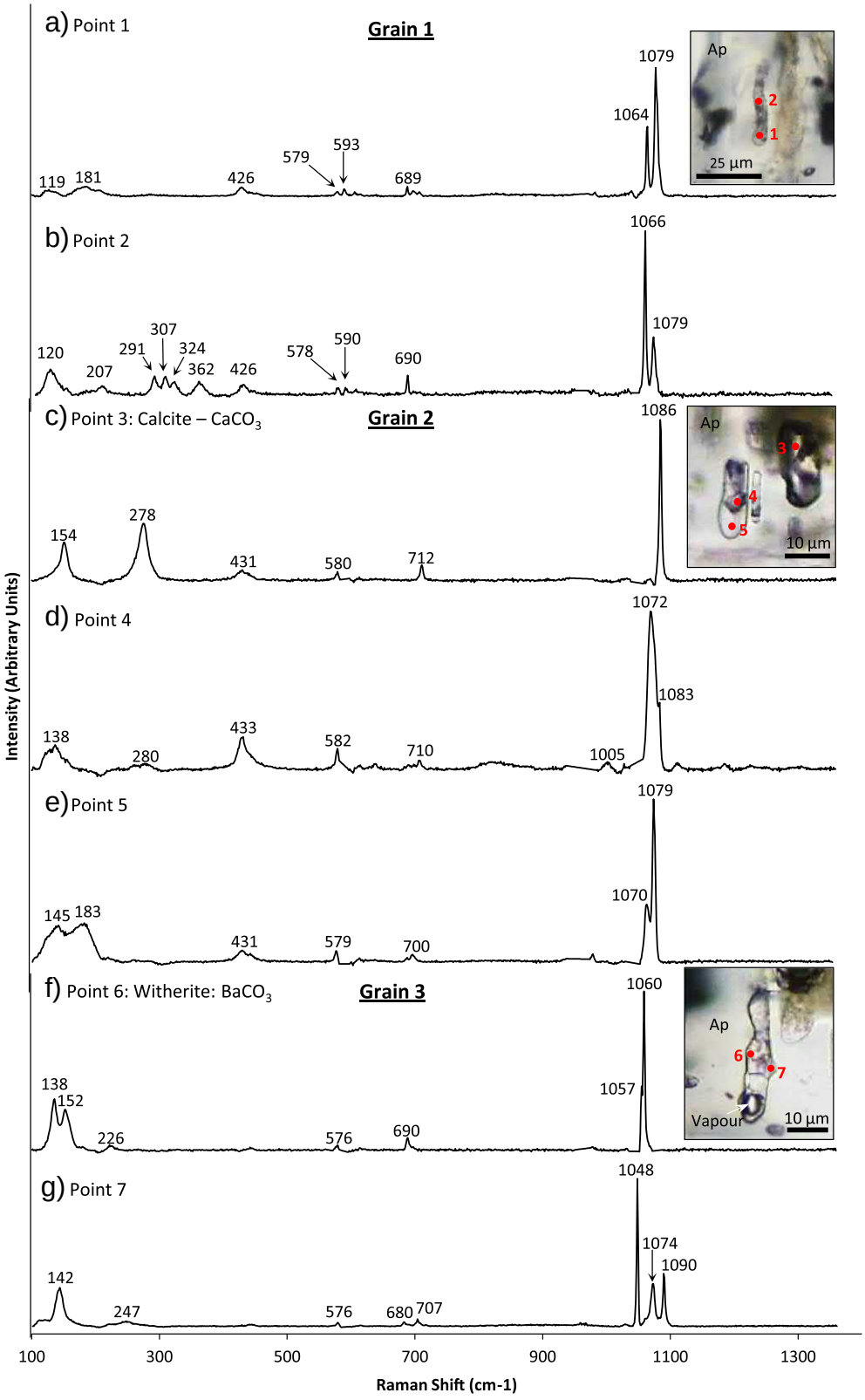

Fig. 10. Representative Raman spectra of multi-phase inclusions from apatite grains 1, 2 and 3 (Table 6) and their corresponding optical (transmitted light) images showing Raman analyses points (red dots). (For interpretation of the references to colour in this figure legend, the reader is referred to the web version of this article.)

kimberlite (Siberia) as a secondary alteration mineral commonly associated with serpentine and carbonate (Kozlov and Levshov, 1962). The MgO and H_2O-rich nature of kimberlite rocks suggests that brucite may be preserved when MgO is in excess relative to SiO_2, reflecting isochemical serpentinisation (Malkov, 1974; Berg, 1989). The preservation of amakinite indicates there was no excessive accumulation of uncompensated SiO_2 or leaching of MgO from the Roger kimberlite during alteration.

It is unlikely that kimberlite magmas retain their original halogen (F, Cl) and alkali/alkali-earth (Na, K, Ba, Sr, Rb) inventory due interactions with external fluids and volatile exsolution/degassing. This leaching of halogens and alkali/alkali-earth elements in kimberlites may be analogous to natrocarbonatite lavas, such as in Oldoinyo Lengai where fresh lavas rapidly degrade (days to months) once exposed to the

Table 6
Raman shifts for analyses points. s: strong intensity; m: medium intensity and weak intensities are unlabelled.

Sample number	Wave number										
Grain 1 – point 1	119	181			426	579/593	689		1064s	1079s	
Grain 1 – point 2	120m	207	291/307/324	362	426	578/590	690		1066s	1079s	
Grain 2 – point 3 (calcite)	154m		278m		431	580	712		1086s		
Grain 2 – point 4	138		280		433	582	710	1005	1072s	1083s	
Grain 2 – point 5	145/183m				431	579	700		1070s	1079s	
Grain 3 – point 6 (witherite)	138/152m	226				576	690		1057s	1060s	
Grain 3 – point 7	142m	247				576	680/707		1048s	1074s	1090s
Grain 4 – point 8	130m				431	580	694	997	1068s		

atmosphere and meteoric water (Zaitsev and Keller, 2006). We suggest that halogens were highly mobile during kimberlite groundmass alteration. However, the extent that other units of the Roger kimberlite pipe were affected by the mineralisation of F-rich phases is unknown. We envisage that infiltrating fluids in a physically open magmatic system interacted with carbonate and fluorine in the late-stage kimberlite melt to form a Ca-F-bearing serpentinising fluid which in turn formed the bultfonteinite and fluorite assemblages, similar to fluorite mineralisation in carbonatites (e.g., Simonetti and Bell, 1995). The presence of oxygen 'impurities' in fluorite analyses, especially in zoned areas in contact with the groundmass (up to 8.6 wt%) is likely represented by submicron inclusions of Ca-O-bearing phases (e.g. calcite) in fluorite which were probably entrapped during olivine replacement by Ca-F-rich fluids.

Our analyses of C-O isotopes in Roger kimberlite carbonates exhibit $\delta^{18}O$ higher than mantle values but $\delta^{13}C$ values typical of mantle-derived carbonate (see Giuliani et al., 2014a). These isotope values indicate the Roger kimberlite carbonates were modified by hydrothermal and/or low-temperature meteoric fluids (Giuliani et al., 2014a, 2014b). Preservation of fluorine in the Roger kimberlite is attributed to fluorine being fixed into secondary minerals (i.e. fluorite, bultfonteinite), where it was unable to be significantly leached. In contrast, chlorine is far less likely to be preserved in kimberlites as chloride minerals are highly susceptible to dissolution in water.

4.4. Comparing whole-rock and melt inclusions – implications for kimberlite melt composition

Whole-rock studies of the Roger kimberlite and other kimberlites worldwide are shown to exhibit broadly ultramafic, silicate-carbonate compositions: 17.5–35 wt% SiO_2, 20–35 wt% MgO, 12–26 wt% CaO, 5–17 wt% CO_2 (Price et al., 2000; Le Roex et al., 2003; Becker and Le Roex, 2006; Nielsen and Sand, 2008; Nowicki et al., 2008; Kjarsgaard et al., 2009). With the exception of the unserpentinised sections of the Udachnaya-East kimberlite which contains high alkali (Na_2O and K_2O up to 7 wt%) and chlorine (up to 6 wt%; Kamenetsky et al., 2004, 2012), the combined alkali/alkali-earth (i.e. Na_2O, K_2O, BaO, Sr, Rb) and halogen (i.e. F, Cl) content of most other kimberlites rarely exceeds (1 to ~2 wt%). The absence of alkali, halogen and other highly incompatible trace element bearing phases from the kimberlite groundmass is explained by their partitioning into water soluble phases (i.e. alkalis in carbonates, sulphates and phosphates, and chlorine in chlorides). Consequently, the effects of ubiquitous syn- and post-magmatic alteration (i.e. serpentinisation) likely removed these components from the groundmass (Kamenetsky et al., 2013, 2014; Giuliani et al., 2016). Giuliani et al. (2016) suggested that residual alkali- and chorine-bearing fluids are removed by infiltrating groundwater from the crystallising groundmass (i.e. released into the surrounding wall-rocks). Thereby the only direct evidence of alkali/alkali-earth and halogen-rich in altered kimberlites is from melt inclusions preserved in magmatic minerals.

The omnipresence of alkalis/alkali-earths (Na, K, Ba, Sr and to a lesser extent Rb and Li), halogens (F, Cl), phosphorus and sulphur in primary inclusions suggests that the concentrations of these components are higher (yet unconstrained) than in typical whole-rock measurements (e.g., Le Roex et al., 2003; Becker and Le Roex, 2006; Nielsen and Sand, 2008; Kjarsgaard et al., 2009) which are based on altered serpentine-bearing kimberlite samples. The paucity of SiO_2 and MgO in melt inclusions suggests that these components may be overrepresented in whole-rock analyses due to the effects of post-magmatic serpentinisation (Sparks et al., 2009; Brooker et al., 2011) and olivine accumulation (Canil and Bellis, 2008; Kamenetsky et al., 2012).

Based on the extensive studies of melt inclusions in kimberlitic minerals in our samples and others worldwide, it is evident that alkali-carbonates and chlorides are a significant component in kimberlite melts during groundmass crystallisation. Based on primary melt inclusions in Cr-spinel, monticellite and apatite, and secondary inclusions in olivine, we suggest that the kimberlite groundmass crystallised from variably differentiated Si-P-Cl-F-bearing carbonate melt enriched in alkalis/alkali-earths (Na, K, Ba, Sr) and highly incompatible trace elements. This proposed composition is in agreement with experimental studies of the Udachnaya-East kimberlite (e.g., Kamenetsky and Yaxley, 2015; Sharygin et al., 2015; Shatskiy et al., 2017) and other synthetic kimberlite systems (e.g., Canil and Bellis, 2008; Brooker et al., 2011), which have constrained an essentially silica-poor, (alkali-enriched) carbonatitic melt as a likely candidate for the primary kimberlite melt.

We suggest that the fluorine concentrations in the Roger kimberlite may be a minimum representation of its concentration in the parental melt. Analogous to the effects of fluorine in other carbonate melt systems (e.g., Jago and Gittins, 1991; Brey et al., 2009), the presence of halogens (F, Cl) in the proposed alkali-enriched Si-P-Cl-F-bearing carbonate melt for the Roger kimberlite may bear unrecognised implications for melt liquidus temperatures, rheological properties and composition.

5. Conclusions

i. The Roger kimberlite is texturally and mineralogically characteristic of hypabyssal Group-I (or archetypal) kimberlites from Ekati and worldwide, but is unique as it contains the highest F-content of the Ekati kimberlites (up to 2688 ppm) and significant amounts of F-rich minerals (i.e. bultfonteinite and fluorite) replacing olivine.
ii. Primary melt inclusions in Cr-spinel, monticellite and apatite, and secondary melt inclusions in olivine contain heterogeneous daughter phase assemblages composed of alkali/alkali-earth (Na, K, Ba, Sr)-enriched Ca-Mg-carbonates, Na-K-chlorides and sulphates, phosphates ± alkalis/REE, spinel, silicates (e.g. olivine, phlogopite, (clino)humite) and sulphides.
iii. Based on F/Nd and Cl/U ratios in the primitive mantle, we deduced that F- and Cl-concentrations should exist in higher concentrations in the Roger kimberlite melt than measured. Magmatic fluorine is evidenced by the presence of F-bearing daughter phases in melt inclusions from magmatic minerals and F-bearing groundmass minerals (e.g., apatite, phlogopite).
iv. The general paucity of alkalis/alkali-earths and halogens in kimberlites is attributed to syn- and/or post-magmatic alteration. We

suggest that fluorine was highly mobile during alteration of the Roger kimberlite but became fixed in secondary alteration minerals (i.e. bultfonteinite, fluorite) during serpentinisation.

v. Based on melt inclusions compositions and assemblages in magmatic groundmass minerals and the reconstructed halogen concentrations, we propose that a variably differentiated Si-P-Cl-F-bearing carbonate melt enriched in alkalis/alkali-earths (Na, K, Ba, Sr) and highly incompatible trace elements was parental to the Roger kimberlite.

Acknowledgements

This study forms part of A.A's Ph.D. We thank Jay Thompson (University of Tasmania) for his assistance in LA-ICPMS analyses and Christian Dietz at the Central Science Laboratory (CSL) at the University of Tasmania for stable isotope analyses. This study has benefitted from the comments by two anonymous reviewers and the efficient editorial handling by Klaus Mezger and Oliver Lord (Guest Editor). This study was supported by the Australian Research Council (ARC). Financial support was provided by the Australian Research Council (Discovery grant DP130100257, 2013–2015) and University of Tasmania (New Star Professorship, 2010–2014) to V. Kamenetsky.

Appendix A. Supplementary data

Supplementary data to this article can be found online at http://dx.doi.org/10.1016/j.chemgeo.2017.06.008.

References

Abersteiner, A., Giuliani, A., Kamenetsky, V.S., Phillips, D., 2016. Petrographic and melt-inclusion constraints on the petrogenesis of a magmaclast from the Venetia kimberlite cluster, South Africa. Chem. Geol. http://dx.doi.org/10.1016/j.chemgeo.2016.08.029.

Afanasyev, A.A., Melnik, O., Porritt, L., Schumacher, J.C., Sparks, R.S.J., 2014. Hydrothermal alteration of kimberlite by convective flows of external water. Contrib. Mineral. Petrol. 168, 1038–1055.

Aoki, K., Kanisawa, S., 1979. Fluorine contents of some hydrous minerals derived from upper mantle and lower crust. Lithos 12, 167–171.

Armstrong, J.P., Wilson, M., Barnett, R.L., Nowicki, T., Kjarsgaard, B.A., 2004. Mineralogy of primary carbonate-bearing hypabyssal kimberlite, Lac de Gras, Slave Province, Northwest Territories, Canada. Lithos 76, 415–433.

Becker, M., Le Roex, A.P., 2006. Geochemistry of South African on- and off-craton, group I and group II kimberlites: petrogenesis and source region evolution. J. Petrol. 47, 673–703.

Berg, G.W., 1989. The significance of brucite in South African kimberlites. In: Ross, J. (Ed.), Kimberlite and Related Rocks. Their Mantle/Crust Setting. Diamonds and Diamond Exploration Volume 2. Geological Society of Australia Special Publication, pp. 282–296 14.

Bonazzi, P., Bindi, L., Medenbach, O., Pagano, R., Lampronti, G.I., Menchetti, S., 2007. Olmiite, CaMn[SiO_3(OH)](OH), the Mn-dominant analogue of poldervaartite, a new mineral species from Kalahari manganese fields (Republic of South Africa). Mineral. Mag. 71, 193–201.

Brey, G.P., Bulatov, V.K., Girnis, A.V., 2009. Influence of water and fluorine on melting of carbonated peridotite at 6 and 10 GPa. Lithos 112, 249–259.

Brooker, R., Sparks, R., Kavanagh, J., Field, M., 2011. The volatile content of hypabyssal kimberlite magmas: some constraints from experiments on natural rock compositions. Bull. Volcanol. 73, 959–981.

Buse, B., Schumacher, J., Sparks, R., Field, M., 2010. Growth of bultfonteinite and hydrogarnet in metasomatized basalt xenoliths in the B/K9 kimberlite, Damtshaa, Botswana: insights into hydrothermal metamorphism in kimberlite pipes. Contrib. Mineral. Petrol. 160, 533–550.

Canil, D., Bellis, A.J., 2008. Phase equilibria in a volatile-free kimberlite at 0.1 MPa and the search for a primary kimberlite magma. Lithos 105, 111–117.

Chakhmouradian, A.R., Mitchell, R.H., 2001. Three compositional varieties of perovskite from kimberlites of the Lac de Gras field. Mineral. Mag. 65, 133–148.

Clement, C.R., 1982. A Comparative Geological Study of some Major Kimberlite Pipes in the Northern Cape and Orange Free State. University of Cape Town, Cape Town (431 pp.).

Clement, C.R., Skinner, E.M.W., Smith, B.H.S., 1984. Kimberlite Redefined. University of Chicago Presspp. 223.

Dawson, J.B., 1980. Kimberlites and Their Xenoliths. Springer-Verlag, New York (252 pp.).

Deans, T., Powell, J.L., 1968. Trace elements and strontium isotopes in carbonatites, fluorites and limestones from India and Pakistan. Nature 218, 750–752.

Deer, W.A., Howie, R.A., Zussman, J., 1992. Rock-forming Minerals, 1978-2nd ed. Longman, London.

Evans, B., 2004. The serpentinite multisystem revisited: chrysotile is metastable. Int. Geol. Rev. 46, 479.

Fedortchouk, Y., Canil, D., 2004. Intensive variables in kimberlite magmas, Lac de Gras, Canada and implications for diamond survival. J. Petrol. 45, 1725–1745.

Giuliani, A., Kamenetsky, V.S., Phillips, D., Kendrick, M.A., Wyatt, B.A., Goemann, K., 2012. Nature of alkali-carbonate fluids in the sub-continental lithospheric mantle. Geology 40, 967–970.

Giuliani, A., Kamenetsky, V.S., Kendrick, M.A., Phillips, D., Wyatt, B.A., Maas, R., 2013. Oxide, sulphide and carbonate minerals in a mantle polymict breccia: metasomatism by proto-kimberlite magmas, and relationship to the kimberlite megacrystic suite. Chem. Geol. 353, 4–18.

Giuliani, A., Phillips, D., Kamenetsky, V.S., Fiorentini, M.L., Farquhar, J., Kendrick, M.A., 2014a. Stable isotope (C, O, S) compositions of volatile-rich minerals in kimberlites: a review. Chem. Geol. 374-375, 61–83.

Giuliani, A., Phillips, D., Kamenetsky, V.S., Kendrick, M.A., Wyatt, B.A., Goemann, K., Hutchinson, G., 2014b. Petrogenesis of mantle polymict breccias: insights into mantle processes coeval with kimberlite magmatism. J. Petrol. 55, 831–858.

Giuliani, A., Soltys, A., Phillips, D., Kamenetsky, V.S., Maas, R., Goemann, K., Woodhead, J.D., Drysdale, R., Griffin, W.L., 2016. The final stages of kimberlite petrogenesis: petrography, mineral chemistry, melt inclusions and Sr-C-O isotope geochemistry of the Bultfontein kimberlite (Kimberley, South Africa). Chem. Geol. http://dx.doi.org/10.1016/j.chemgeo.2016.10.011.

Golovin, A.V., Sharygin, V.V., Pokhilenko, N.P., 2007. Melt inclusions in olivine phenocrysts in unaltered kimberlites from the Udachnaya-East pipe, Yakutia: some aspects of kimberlite magma evolution during late crystallization stages. Petrology 15, 168–183.

Golovin, A.V., Sharygin, I.S., Korsakov, A.V., 2016. Origin of alkaline carbonates in kimberlites of the Siberian craton: evidence from melt inclusions in mantle olivine of the Udachnaya-East kimberlite. Chem. Geol. http://dx.doi.org/10.1016/j.chemgeo.2016.10.036.

Henry, D.A., 1999. Cuspidine-bearing skarn from Chesney Vale. Victoria. Aust. J. Earth. Sci. 46, 251–260.

Jago, B.C., Gittins, J., 1991. The role of fluorine in carbonatite magma evolution. Nature 349, 56–58.

Kamenetsky, V.S., Eggins, S.M., 2012. Systematics of metals, metalloids, and volatiles in MORB melts: effects of partial melting, crystal fractionation and degassing (a case study of Macquarie Island glasses). Chem. Geol. 302-303, 76–86.

Kamenetsky, V.S., Yaxley, G.M., 2015. Carbonate–silicate liquid immiscibility in the mantle propels kimberlite magma ascent. Geochim. Cosmochim. Acta 158, 48–56.

Kamenetsky, M.B., Sobolev, A.V., Kamenetsky, V.S., Maas, R., Danyushevsky, L.V., Thomas, R., Pokhilenko, N.P., Sobolev, N.V., 2004. Kimberlite melts rich in alkali chlorides and carbonates: a potent metasomatic agent in the mantle. Geology 32, 845–848.

Kamenetsky, V.S., Kamenetsky, M.B., Sharygin, V.V., Golovin, A.V., 2007a. Carbonatechloride enrichment in fresh kimberlites of the Udachnaya-East pipe, Siberia: a clue to physical properties of kimberlite magmas? Geophys. Res. Lett. 34, L09316. http://dx.doi.org/10.1029/2007GL029389.

Kamenetsky, V.S., Kamenetsky, M.B., Sharygin, V.V., Faure, K., Golovin, A.V., 2007b. Chloride and carbonate immiscible liquids at the closure of the kimberlite magma evolution (Udachnaya-East kimberlite, Siberia). Chem. Geol. 237, 384–400.

Kamenetsky, V.S., Kamenetsky, M.B., Weiss, Y., Navon, O., Nielsen, T.F.D., Mernagh, T.P., 2009a. How unique is the Udachnaya-East kimberlite? Comparison with kimberlites from the Slave Craton (Canada) and SW Greenland. Lithos 112S, 334–346.

Kamenetsky, V.S., Maas, R., Kamenetsky, M.B., Paton, C., Phillips, D., Golovin, A.V., Gornova, M.A., 2009b. Chlorine from the mantle: magmatic halides in the Udachnaya-East kimberlite, Siberia. Earth Planet. Sci. Lett. 285, 96–104.

Kamenetsky, V.S., Kamenetsky, M.B., Golovin, A.V., Sharygin, V.V., Maas, R., 2012. Ultrafresh salty kimberlite of the Udachnaya-East pipe (Yakutia, Russia): a petrological oddity or fortuitous discovery? Lithos 152, 173–186.

Kamenetsky, V.S., Grutter, H., Kamenetsky, M.B., Goemann, K., 2013. Parental carbonatitic melt of the Koala kimberlite (Canada): constraints from melt inclusions in olivine and Cr-spinel, and groundmass carbonate. Chem. Geol. 353, 96–111.

Kamenetsky, V.S., Golovin, A.V., Maas, R., Giuliani, A., Kamenetsky, M.B., Weiss, Y., 2014. Towards a new model for kimberlite petrogenesis: evidence from unaltered kimberlites and mantle minerals. Earth Sci. Rev. 139, 145–167.

Keller, J., Krafft, M., 1990. Effusive natrocarbonatite activity of Oldoinyo Lengai, June 1988. Bull. Volcanol. 52, 629–645.

Kjarsgaard, B.A., Wilkinson, L., Armstrong, J., 2002. Geology, Lac de Gras kimberlite field, Central Slave Province, Northwest Territories - Nunavut, (NTS 76C, D, E, F), 1:250,000 scale color map with descriptive notes. Geol. Surv. Can. Pap. 3228.

Kjarsgaard, B.A., Pearson, D.G., Tappe, S., Nowell, G.M., Dowall, D.P., 2009. Geochemistry of hypabyssal kimberlites from Lac de Gras, Canada: comparisons to a global database and applications to the parent magma problem. Lithos 112S, 236–248.

Kopylova, M.G., Hayman, P., 2008. Petrology and textural classification of the Jericho kimberlite, northern Slave Province, Nunavut, Canada. Can. J. Earth Sci. 45, 701–723.

Kozlov, I.T., Levshov, P.P., 1962. Amakinite, a new mineral of the brucite-pyrochroite group. Zapiski VMO 91, 71–77.

Le Roex, A.P., Bell, D.R., Davis, P., 2003. Petrogenesis of group I kimberlites from Kimberley, South Africa: evidence from bulk-rock geochemistry. J. Petrol. 44, 2261–2286.

Lockhart, G., Grütter, H., Carlson, J., 2004. Temporal, geomagnetic and related attributes of kimberlite magmatism at Ekati, Northwest Territories, Canada. Lithos 77, 665–682.

Malkov, B.A., 1974. Brucite in kimberlite. Doklady Academy Science USSR 215, 157–160.
Mernagh, T.P., Kamenetsky, V.S., Kamenetsky, M.B., 2011. A Raman microprobe study of melt inclusions in kimberlites from Siberia, Canada, SW Greenland and South Africa. Spectrochim. Acta A Mol. Biomol. Spectrosc. 80, 82–87.
Mitchell, R.H., 1986. Kimberlites: Mineralogy, Geochemistry and Petrology. Plenum Publishing Company, New York (442 pp.).
Mitchell, R.H., 1995. Kimberlites, Orangeites and Related Rocks. Plenum Press, New York (410 pp.).
Mitchell, R.H., 1997. Carbonate-carbonate immiscibility, neighborite and potassium iron sulphide in Oldoinyo Lengai natrocarbonatite. Min. Mag. 61, 779–789.
Mitchell, R.H., 2008. Petrology of hypabyssal kimberlites: relevance to primary magma compositions. J. Volcanol. Geotherm. Res. 174, 1–8.
Mitchell, R.H., 2013. Oxygen Isotope Studies of Serpentine in Kimberlite, Proceedings of the 10th International Kimberlite Conference. Geological Society of India, Bangalore, pp. 1–12.
Muramatsu, Y., 1983. Geochemical investigations of kimberlites from the Kimberley area, South Africa. Geochem. J. 17, 71–86.
Murdoch, J., 1955. Bultfonteinite from Crestmore, California. Amer. Miner. 40, 505–509.
Nielsen, T.F.D., Sand, K.K., 2008. The Majuagaa kimberlite dike, Maniitsoq region, western Greenland: constraints on an Mg-rich silicocarbonatitic melt composition from groundmass mineralogy and bulk compositions. Canad. Min. 46, 1043–1061.
Nowicki, T., Porritt, L., Crawford, B., Kjarsgaard, B., 2008. Geochemical trends in kimberlites of the Ekati property, Northwest Territories, Canada: insights on volcanic and resedimentation processes. J. Volcanol. Geotherm. Res. 174, 117–127.
Nyfeler, D., Armbruster, T., Dixon, R., Bermanec, V., 1995. Nchwaningite, $Mn(^{2+})(_{2+})SiO_3(OH)_2{\cdot}H_2O$, a new pyroxene-related chain silicate from the N'chwaning mine, Kalahari manganese field, South Africa. Amer. Miner. 80, 377–386.
Ohnishi, M., Kusachi, I., Kobayashi, S., Yamakawa, J., Tanabe, M., Kishi, S., Yasuda, T., 2007. Numanoite, $Ca_4CuB_4O_6(OH)_6(CO_3)_2$, a new mineral species, the Cu analogue of borcarite from the Fuka mine, Okayama Prefecture, Japan. Can. Mineral. 45, 307–315.
Parry, J., Williams, A.F., Wright, F.E., 1932. On bultfonteinite a new fluorine-bearing hydrous calcium silicate from South Africa. Mineral. Mag. 23, 145–162.
Paul, D.K., Buckley, F., Nixon, P.H., 1976. Research paper: fluorine and chlorine geochemistry of kimberlites. Chem. Geol. 17, 125–133.
Potter, N.J., Kamenetsky, V.S., Simonetti, A., Goemann, K., 2016. Different types of liquid immiscibility in carbonatite magmas: a case study of the Oldoinyo Lengai 1993 lava and melt inclusions. Chem. Geol. http://dx.doi.org/10.1016/j.chemgeo.2016.09.034.
Price, S.E., Russell, J.K., Kopylova, M.G., 2000. Primitive magma from the Jericho Pipe, N.W.T., Canada: constraints on primary kimberlite melt chemistry. J. Petrol. 41, 789–808.
Roedder, E., 1984. Fluid inclusions. In: Reviews in Mineralogy. 12 Mineralogical Society of America.
Roeder, P.L., Schulze, D.J., 2008. Crystallization of groundmass spinel in kimberlite. J. Petrol. 49, 1473–1495.
Sharygin, V.V., Golovin, A.V., Pokhilenko, N.P., Kamenetsky, V.S., 2007. Djerfisherite in the Udachnaya-East pipe kimberlites (Sakha-Yakutia, Russia): paragenesis, composition and origin. Eur. J. Mineral. 19 (1), 51–63.
Sharygin, I., Litasov, K., Shatskiy, A., Golovin, A., Ohtani, E., Pokhilenko, N., 2015. Melting phase relations of the Udachnaya-East group-I kimberlite at 3.0–6.5 GPa: experimental evidence for alkali-carbonatite composition of primary kimberlite melts and implications for mantle plumes. Gondwana Res. 28, 1391–1414.
Shatskiy, A., Litasov, K.D., Sharygin, I.S., Ohtani, E., 2017. Composition of primary kimberlite melt in a garnet lherzolite mantle source: constraints from melting phase relations in anhydrous Udachnaya-East kimberlite with variable CO_2 content at 6.5 GPa. Gondwana Res. 28, 1391–1414.
Shimizu, K., Saal, A.E., Myers, C.E., Nagle, A.N., Hauri, E.H., Forsyth, D.W., Kamenetsky, V.S., Niu, Y., 2016. Two-component mantle melting-mixing model for the generation of mid-ocean ridge basalts: implications for the volatile content of the Pacific upper mantle. Geochim. Cosmochim. Acta 176, 44–80.
Simonetti, A., Bell, K., 1995. Nd, Pb, and Sr isotope systematics of fluorite at the Amba Dongar carbonatite complex, India: evidence for hydrothermal and crustal fluid mixing. Econ. Geol. 90, 2018–2027.
Skinner, E.M.W., 1989. Contrasting group I and group II kimberlite petrology: towards a genetic model for kimberlites. In: Glover, J.E., Harris, P.G. (Eds.), Kimberlites and Related Rocks. 4th International Kimberlite Conference. Geological Society of Australia, Perth, pp. 528–544.
Skinner, E.M.W., Clement, C.R., 1979. Mineralogical classification of southern African kimberlites. In: Boyd, F.R., Meyer, H.O.A. (Eds.), The Mantle Sample. 2nd International Kimberlite Conference. American Geophysical Union, Washington, DC, pp. 129–139.
Soltys, A., Giuliani, A., Phillips, D., Kamenetsky, V.S., Maas, R., Woodhead, J., Rodemann, T., 2016. In-situ assimilation of mantle minerals by kimberlitic magmas — direct evidence from a garnet wehrlite xenolith entrained in the Bultfontein kimberlite (Kimberley, South Africa). Lithos 256-257, 182–196.
Sparks, R.S.J., Brooker, R.A., Field, M., Kavanagh, J., Schumacher, J.C., Walter, M.J., White, J., 2009. The nature of erupting kimberlite melts. Lithos 112S, 429–438.
Stripp, G.R., Field, M., Schumacher, J.C., Sparks, R.S.J., Cressey, G., 2006. Post-emplacement serpentinization and related hydrothermal metamorphism in a kimberlite from Venetia, South Africa. J. Metamorph. Geol. 24, 515–534.
Sun, S.-S., McDonough, W.F., 1989. Chemical and isotopic systematics of oceanic basalts: implications for mantle composition and processes. In: Saunders, A.D., Norry, M.J. (Eds.), Magmatism in the Ocean Basins. Geological Society Special Publication, London, pp. 313–345.
Tappe, S., Graham Pearson, D., Kjarsgaard, B.A., Nowell, G., Dowall, D., 2013. Mantle transition zone input to kimberlite magmatism near a subduction zone: origin of anomalous Nd–Hf isotope systematics at Lac de Gras, Canada. Earth Planet. Sci. Lett. 371–372, 235–251.
Tropper, P., Manning, C.E., 2007. The solubility of fluorite in H_2O and H_2O–NaCl at high pressure and temperature. Chem. Geol. 242, 299–306.
Willcox, A., Buisman, I., Sparks, R.S.J., Brown, R.J., Manya, S., Schumacher, J.C., Tuffen, H., 2015. Petrology, geochemistry and low-temperature alteration of lavas and pyroclastic rocks of the kimberlitic Igwisi Hills volcanoes, Tanzania. Chem. Geol. 405, 82–101.
Wilson, M.R., Kjarsgaard, B.A., Taylor, B., 2007. Stable isotope composition of magmatic and deuteric carbonate phases in hypabyssal kimberlite, Lac de Gras field, Northwest Territories, Canada. Chem. Geol. 242, 435–454.
Workman, R.K., Hauri, E., Hart, S.R., Wang, J., Blusztajn, J., 2006. Volatile and trace elements in basaltic glasses from Samoa: implications for water distribution in the mantle. Earth Planet. Sci. Lett. 241, 932–951.
Zaitsev, A., Keller, J., 2006. Mineralogical and chemical transformation of Oldoinyo Lengai natrocarbonatites, Tanzania. Lithos 91, 191–207.
Zaitsev, A.N., Keller, J., Spratt, J., Jeffries, T.E., Sharygin, V.V., 2009. Chemical composition of nyerereite and gregoryite from natrocarbonatites of Oldoinyo Lengai volcano, Tanzania. Geol. Ore Depos. 51, 608–616.

Appendix 4.1: Supplementary Figures

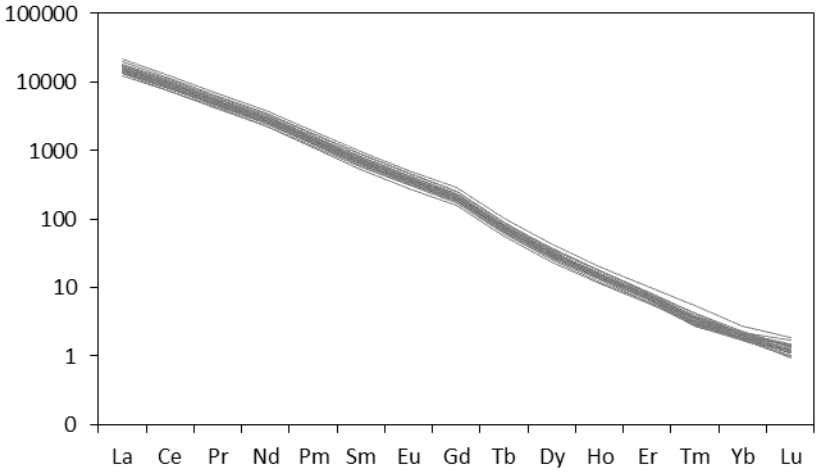

Supplementary Figure S1. Primitive mantle normalised (after Sun and McDonough, 1989) REE patterns of 24 analysed points in apatite (analysed by LA-ICP-MS) from the studied Roger kimberlite.

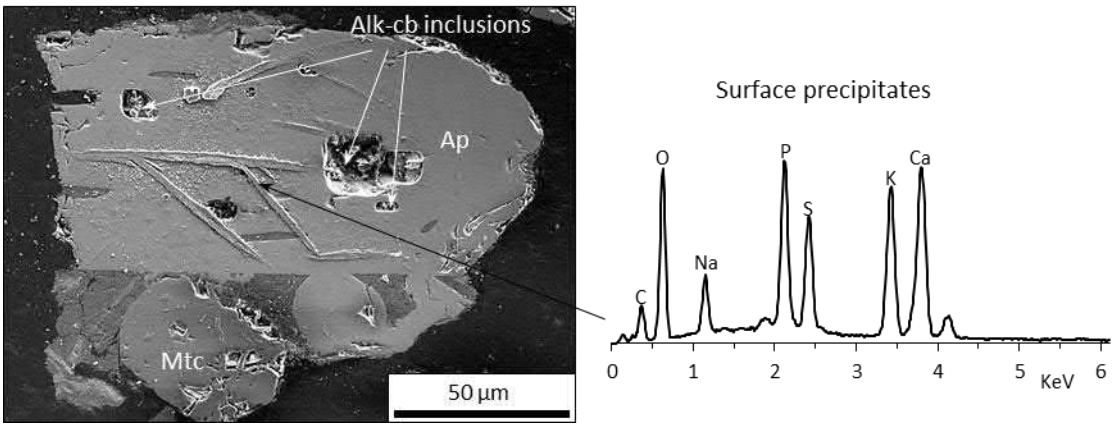

Supplementary Figure S2. Scanning electron microscope (SEM) image of exposed inclusions and surface mineral precipitates from an apatite (Ap) grain. Note the deep voids and cavities within these inclusions and recrystallised constituents from the inclusion on the apatite surface. The EDS spectrum on the right shows a qualitative representation of these surface precipitates with pronounced Na-K-S peaks and possibly Ca-peaks, although this may be attributed to background interference from the apatite. Mtc: monticellite, Alk-cb: alkali-carbonates.

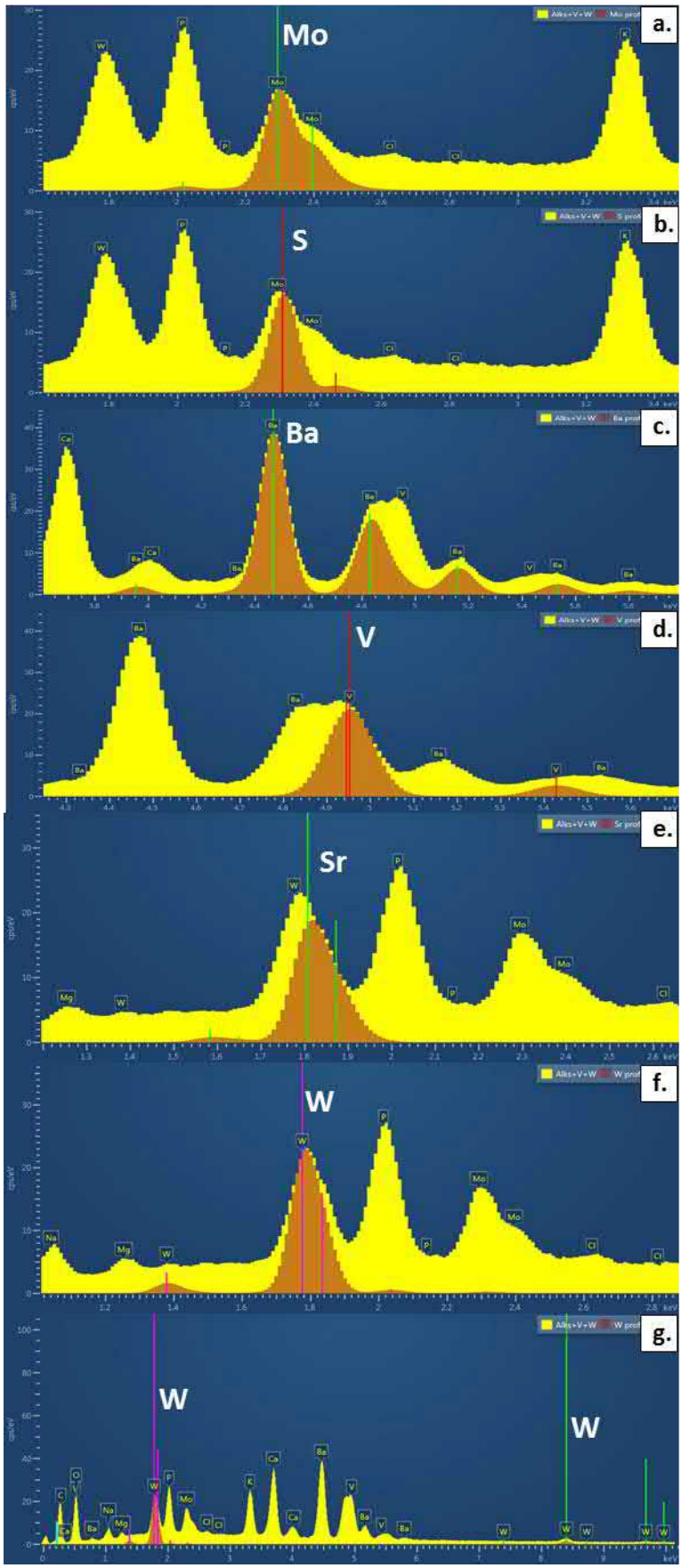

Supplementary Figure S3. Representative EDS spectra for a Ba-K + W + V + Mo phase in an apatite-hosted inclusion. (a, b) Overlap between Mo and S, where the Mo-peaks are the closest match, as indicated by a shoulder in Mo on the right. (c, d) Overlap between Ba and V, where the presence of V is observed in a shoulder alongside Ba. (e – g) Overlap between Sr and W, where the W-peaks are the closest match.

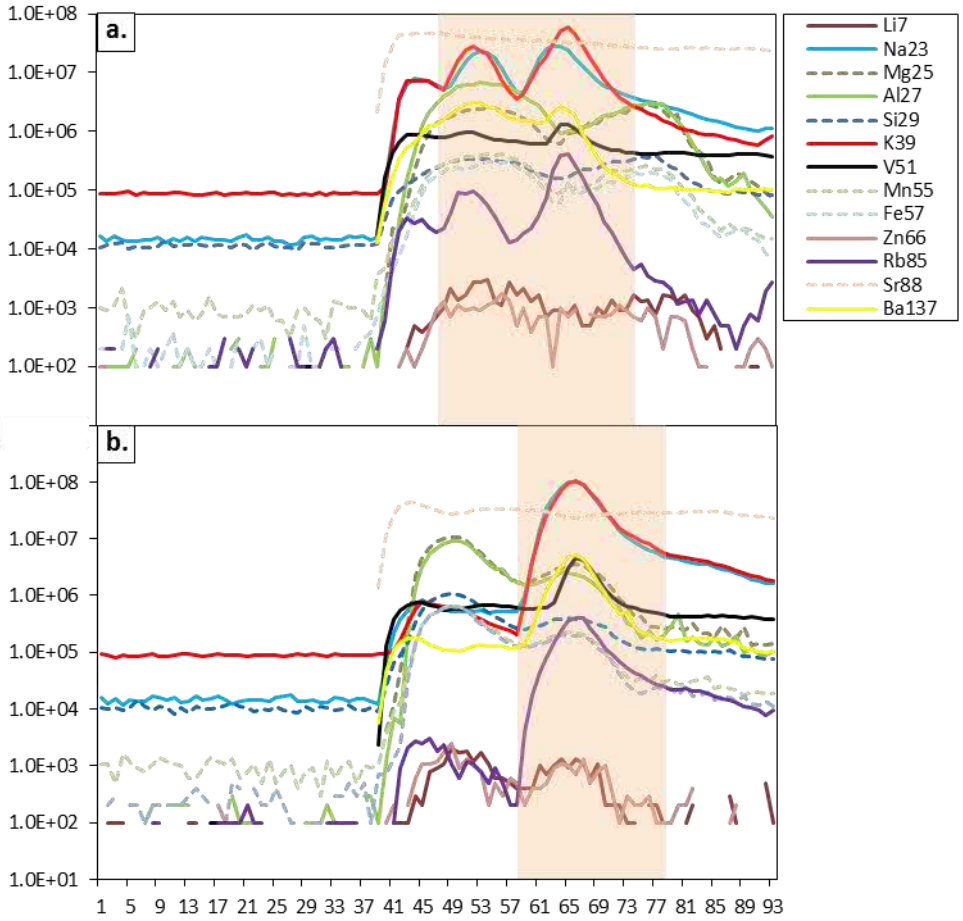

Supplementary Figure S4. Representative LA-ICPMS analyses of apatite showing ablated primary inclusions which are represented in the red shaded zone. These inclusions are characterised by positive Na-K-Rb anomalies which are usually accompanied by synchronised increases in Ba, Li and to a lesser extent in V and Al.

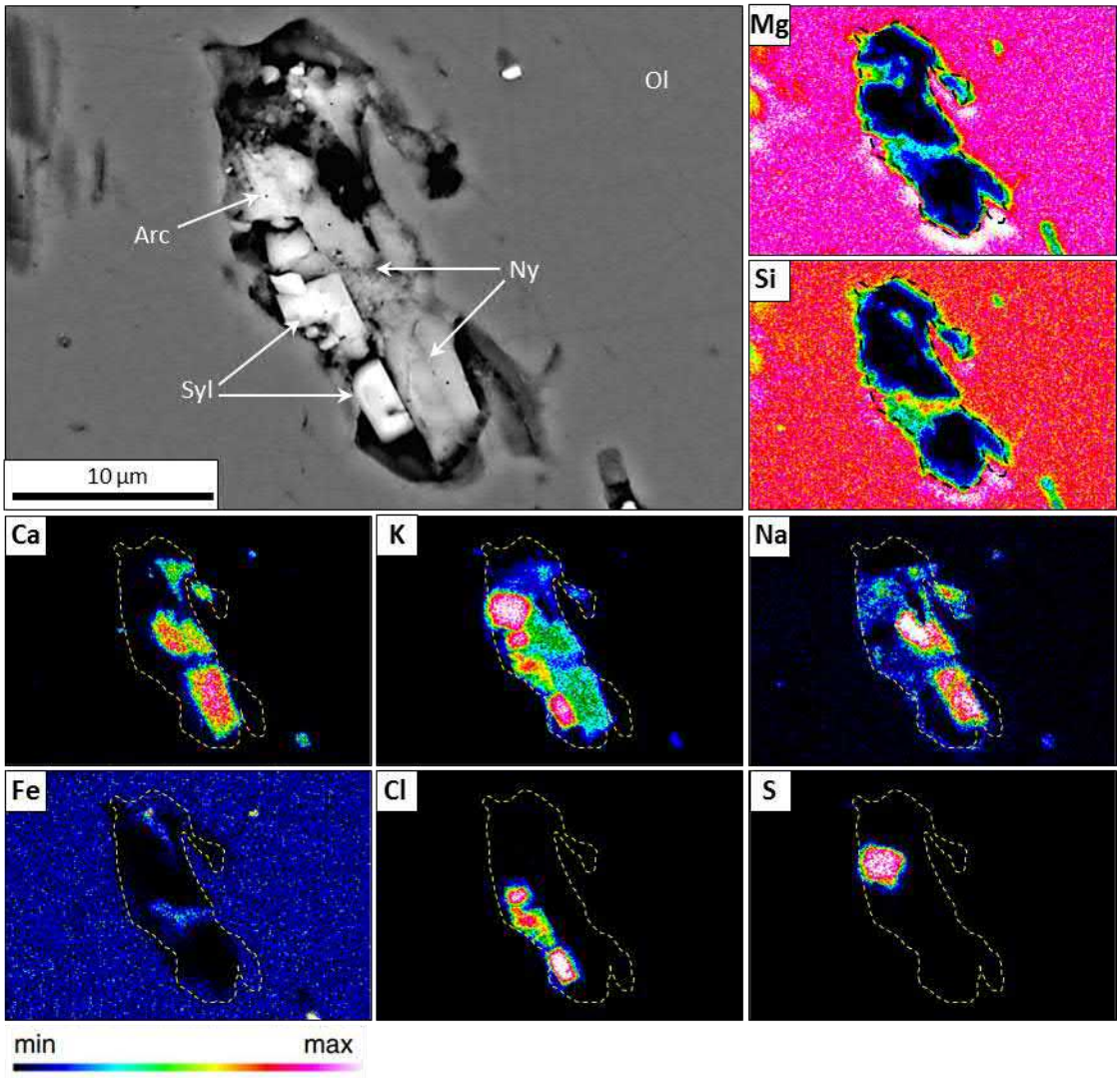

Supplementary Figure S4. Representative LA-ICPMS analyses of apatite showing ablated primary inclusions which are represented in the red shaded zone. These inclusions are characterised by positive Na-K-Rb anomalies which are usually accompanied by synchronised increases in Ba, Li and to a lesser extent in V and Al.

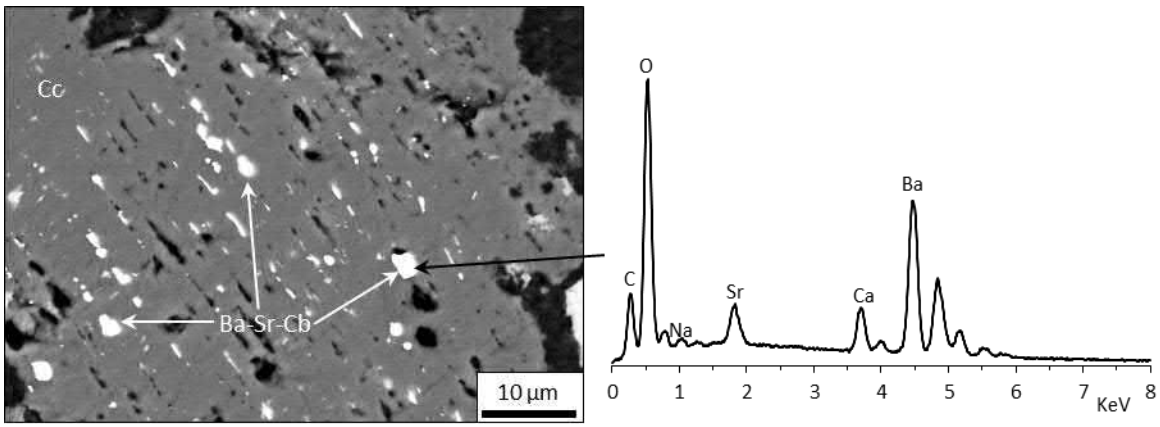

Supplementary Figure S6. Scanning electron microscope (SEM) image of groundmass calcite (Cc) with disseminated inclusions of Ba-Sr-carbonates (Ba-Sr-Cb). The EDS spectrum on the right shows a semi-quantitative representation of these Ba-Sr-carbonates.

Appendix 4.2: Supplementary Material – Analytical Methods

Petrographic and Inclusion Analyses

Specimens of the Roger kimberlite were prepared as epoxy resin rock and grain mounts polished using kerosene as lubricant to avoid dissolution of any water soluble minerals. Initial optical petrographic and mineralogical investigations of samples were performed on Nikon Eclipse 50i POL microscope at the University of Tasmania.

Detailed examinations of major phases and inclusions in minerals were performed using a Hitachi SU-70 field emission SEM equipped with an Oxford AZtec Energy XMax 80 detector at the Central Science Laboratory, University of Tasmania. A beam accelerating voltage of 15 kV was used to produce high-resolution backscattered electron (BSE) images of minerals and energy-dispersive X-ray spectroscopy (EDS) semi-quantitative analyses and elemental maps of minerals and inclusions. EDS analyses of inclusions were limited by several factors that include the inherent loss of some volatile phases upon exposure, re-precipitation of common inclusion phases (e.g., carbonates, chlorides) onto the surrounding surface and anisotropic beam scatter (see Kamenetsky et al., 2013).

Electron microprobe (EMP) analyses of major and minor elements

Electron microprobe analyses of amakinite, bultfonteinite and fluorite were carried out at the Central Science Laboratory, University of Tasmania, using a Cameca SX100 electron microprobe.

Amakinite

Analyses of amakinite were conducted using an accelerating voltage of 15 kV, beam current of 10 nA and beam size of 10 μm. The counting time was 10 seconds for Si, Al, S, 20 seconds for Mn, Ca, Mg, Fe, and 30 seconds for Ti. The off peak counting time was 6 seconds for Mg, Fe, Si, 10 seconds for S, Al, 20 seconds for Mn, Ca, and 30 seconds for Ti. Oxygen and hydrogen were calculated by stoichiometry. The standards were synthetic Rutile for Ti, natural Rhodonite for Mn and Celestine for S (all P&H Developments, UK), Hematite (Minas Gerais, Harvard 92649) for Fe, Plagioclase (Lake County, NMNH 115900) for Al, natural Wollastonite for Si, Ca, and Periclase for Mg (both University of Tasmania in house). Detection limits (99% confidence) are 0.02 wt.% for Ti, Al, Ca, S, 0.03 wt.% for Si, Mn,

0.04 wt.% for Mg, and 0.07 wt.% for Fe. Precision wt.% 1σ is 0.01 wt.% for Ti, S, 0.02 wt.% for Al, Ca, Si, 0.03 wt.% for Mn, and 0.12 wt.% for Fe, Mg.

Bultfonteinite

Analyses of bultfonteinite were conducted using an accelerating voltage of 15 kV, beam current of 20 nA and beam size of 20 µm. The counting time was 10 seconds for Si, 20 seconds for Mg, F, Ca, and 30 seconds for Fe, S. The off peak counting time was 6 seconds for Si, 10 seconds for Ca, 12 seconds for F, 20 seconds for Mg, and 30 seconds for Fe, S. Oxygen and hydrogen were calculated by stoichiometry. The same standards as for amakinite were used, plus Topaz (Topaz Valley, Utah) for F. Detection limits (99% confidence) are 0.01 wt.% for Mg, S, 0.02 wt.% for Si, Fe, 0.03 wt.% for Ca and 0.09 wt.% for F. Precision wt.% 1σ is 0.004 wt.% for S, 0.01 wt.% for Fe, Mg, 0.06 wt.% for Si, 0.09 wt.% for F and 0.11 wt.% for Ca.

Fluorite

Analyses of fluorite were conducted using an accelerating voltage of 15 kV, beam current of 20 nA and beam size of 20 µm. The counting time was 10 seconds for Si, Mg, Na, 20 seconds for F, Fe, Ca, and 30 seconds for O, Sr. The off peak counting time was 7 seconds for F, 10 seconds for Mg, Si, Na, Ca, 20 seconds for Fe, O, and 30 seconds for Sr. The standards were Jadeite for Na, Celestine for Sr (both P&H Developments, UK), Hematite (Minas Gerais, Harvard 92649) for Fe, O, natural Wollastonite for Si and Periclase for Mg (both University of Tasmania in house), and Fluorite (Astimex Standards Ltd., Toronto, Canada) for Ca, F. Detection limits (99% confidence) are 0.02 wt.% for Si, Mg, 0.03 wt.% for Fe, Ca, Sr, Na, 0.16 wt.% for F and 0.35-0.53 wt.% for O. Precision wt.% 1σ is 0.01 wt.% for Si, Fe, Mg, 0.02 wt.% for Na, Sr, 0.12 wt.% for Ca, 0.17 wt.% for F and 2.3-4.6 wt.% for O.

Raman Spectroscopic Analyses of Melt Inclusions

To circumvent the normally damaging effects caused by exposing inclusions and electron beam damage, Raman spectroscopy is a non-destructive technique capable of analysing subsurface features. However, Raman spectroscopy is limited by its ability to characterise ionically bonded materials, such as chlorides. Inclusions in apatite were characterised using a Renishaw inVia Raman microscope equipped with a 532 nm laser,

operated at 6 mW at the sample, with 1 second exposure and 5 accumulations, a 2400 l/mm grating and a 100X objective microscope.

Laser Ablation Inductively Coupled Plasma–Mass Spectrometry (LA-ICPMS) Analyses of Apatite

Trace elements of apatites were analysed by LA-ICPMS at the University of Tasmania. The instrumentation comprises ASI Resolution S155 ablation system equipped with a Coherent Compex Pro 110 ArF excimer laser. This was coupled to an Agilent 7900 quadrupole ICP-MS. Helium flow was 0.35 l/min immediately mixed with Ar after ablation flowing at a rate of 1.05 l/min. Laser ablation conditions were as follows: fluence of 4.5 J/cm^2; repetition rate of 10 Hz; ablation time of 50 seconds; 20 second delay for sample washout; beam size of 29 µm. The glass reference material NIST612 was employed as a calibration standard. Data reduction was undertaken according to the standard methods of (Longerich et al., 1996) using the NIST612 (Jochum etal., 2011) glass as a primary reference material and 43Ca as the internal standard and assuming stoichiometric proportions in apatite (39.3 wt.% Ca). The BCR-2g glass was analysed throughout the analytical session and used as a secondary reference material. Additionally a piece of the Durango apatite was measured for quality control purposes.

Whole-Rock Analyses for Trace Element and Rare Earth Element Concentrations

Samples were analysed for their major and trace element concentrations in samples R10 and R11 were conducted at Intertek Minerals Laboratory (Adelaide, South Australia). Samples were prepared by pulverising ~20g of each sample down to a particle size of 80% passing -75 µm. Subsamples were extracted from each pulverised sample for dissolution and chemical analysis. 0.2g of pulverised sample was fused with lithium borate and then dissolved by a weak acidic solution. The dissolved sample was then analysed for major (Ca, Fe, K, Mg, Mn, Na, P, Si, Ti), trace (Ba, Cr, Cs, Ga, Rb, Sc, Sn, Sr, U, V, W), high field strength elements (HFSE; Ba, Cr, Cs, Ga, Rb, Sc, Sn, Sr, U, V, W), rare earth elements (REE; La, Ce, Pr, Nd, Sm, Eu, Gd, Tb, Dy, Ho, Er, Tm, Yb, Lu) were analysed by a combination of inductively coupled plasma optical emission spectroscopy (ICP-OES) and inductively coupled plasma mass spectrometry (ICP-MS). Samples analysing for trace elements (Ag, As, Be, Bi, Cd, Co, Cu, Ge, In, Li, Mo, Ni, Pb, Re, Sb, Se, Te, Tl, Zn) were prepared by dissolving 0.2g of sample in a 4 acid digest (HF+ HCl + HNO_3 + $HClO_4$) and then analysed by ICP-OES/ICP-MS. CO_2 and S were analysed by a carbon sulphur analyser (CSA) by

igniting 0.3g of pulverised sample at high temperature in a stream of O2. SO_2 and CO_2 produced were then measured via infra-red cells. Samples were analysed for Cl by digesting 0.2g of pulverised sample in a calcium-carbonate leach. Cl was then measured by colorimetry. Samples were analysed for F by fusing 0.2g of pulverised sample with K/Na-carbonate/Zn-oxide, then digested in deionised H_2O. F in solution was then measured via selective ion electrode. Ferrous iron was determined by digesting 0.25g of pulverised sample in sulphuric acid (H_2SO_4) and titrated to determine FeO.

Stable Isotopes

Sample preparation for stable isotope work was performed at the Central Science Laboratory (CSL) at the University of Tasmania using a MultiFlow – Isoprime100. For analysis of solid carbonate samples for either $\delta^{13}C$ or $\delta^{18}O$, the bulk rock samples were finely ground to a homogeneous and dry powder using an agate mortar. Subsample amounts accounting for approx. 100 μg of pure carbonate were placed in sealed vials and inserted into the heated sample rack (70 °C) of an Isoprime MultiFlow. The headspace was flushed with helium, after which 200 μL of 103% orthophosphoric acid were added to react as follows:

$$CaCO_3 + H_3PO_4 \leftrightarrow CaHPO_4 + CO_2 + H_2O$$

After a reaction time of 1080 min, the generated CO2 which was extracted and analysed on an Isoprime 100 continous-flow mass spectrometer. The sample gas $^{13}C/^{12}C$ and $^{18}O/^{16}O$ ratios were then converted to the conventional ‘delta notation’ as follows:

$$\delta\ [‰] = (R_{sample}/R_{standard} - 1) \times 1000$$

where "R" is the ratio of the heavy to light isotope in the sample or standard and the result is multiplied by 1000 simply to make the resulting ratio more ‘meaningful’. When analysing CO_2 different isotopic species of the same element (isotopologues) can produce a contribution at certain masses and a correction must be made, for which we applied the following conversion (Craig correction):

$$\delta\ ^{13}C = 1.067\ \delta(45/44) – 0.0338\ \delta\ ^{18}O$$

and

$$\delta\ ^{18}O = 1.0010\ \delta(46/44) – 0.0021\ \delta\ ^{13}C$$

The data was then normalised to the Vienna Pee Dee Belemnite (VPDB) and Vienna Mean Standard Ocean Water (VSMOW) scale, respectively, using two international reference standards, NBS18 and NBS19 and two in-house reference standards (Anu M1 and Anu PRM2). The acid digestion used as sample preparation method relies on an equilibrium state rather than on a reaction proceeding to completion, for which an additional correction has to be applied. The equilibrium can be expressed as:

$$\delta_{true} = (\delta_{measured} - 1000*(E-1)/E) + K * (T_{Reaction} - T_{Standard})$$

being the equilibrium constant and conditions applied:

$E = 1.01025$, $K = 0.04$; $T_{Reaction} = 70$ ºC and $T_{Standard} = 25$ ºC

Precision of the measurements, determined by repetitive analysis (n=7) of Anu PRM2 were 0.05‰ and 0.13‰ for $\delta^{13}C$ and $\delta^{18}O$ respectively. Homogeneity was assessed by repetition of a submitted sample (01-233, n=5) and resulted in standard deviation of 0.07 0/00 for $d^{13}C$ and 0.17 0/00 for $d^{18}O$ measurements.

H_2O and S Analyses

The analysis for total nitrogen, carbon, hydrogen and sulphur was determined at the Central Science Laboratory (CSL), University of Tasmania, using a Thermo Finnigan EA 1112 Series Flash Elemental Analyser. Between 0.7 and 1.7 mg of sample were weighed into tin capsules using a Sartorius SE2 ultra-microbalance with an accuracy of 0.1 microgram. Combustion of the pressed tin cups was achieved in ultra-high purity oxygen at 1000°C using tungstic oxide on alumina as an oxidising agent followed by reduced copper wires as a reducing agent. The results were calibrated using a certified sulphanilamide standard.

References

Longerich, H.P., Jackson, S.E., Gunther, D., 1996. Laser ablation inductively coupled plasma mass spectrometric transient signal data acquisition and analyte concentration calculation. Journal of Analytical Atomic Spectrometry 11, 899–904

Jochum, K. P., et al. (2011), Determination of reference values for NIST SRM 610–617 glasses following ISO guidelines, Geostand. Geoanal. Res., 35, 397–429.

JOURNAL OF PETROLOGY

Journal of Petrology, 2018, Vol. 59, No. 8, 1467–1492
doi: 10.1093/petrology/egy068
Advance Access Publication Date: 9 July 2018
Original Article

OXFORD

Was Crustal Contamination Involved in the Formation of the Serpentine-Free Udachnaya-East Kimberlite? New Insights into Parental Melts, Liquidus Assemblage and Effects of Alteration

Adam Abersteiner[1]*, Vadim S. Kamenetsky[1], Alexander V. Golovin[2,3], Maya Kamenetsky[1] and Karsten Goemann[4]

[1]School of Physical Sciences, University of Tasmania, Hobart, Tasmania 7001, Australia; [2]Sobolev Institute of Geology and Mineralogy, Siberian Branch Russian Academy of Sciences, Koptyuga Pr. 3, Novosibirsk 630090, Russian Federation; [3]Diamond and Precious Metal Geology Institute, Siberian Branch Russian Academy of Sciences, Lenina Pr. 39, Yakutsk 677000, Russian Federation; [4]Central Science Laboratory, University of Tasmania, Hobart, Tasmania 7001, Australia

*Corresponding author. Present address: School of Natural Sciences, University of Tasmania, Hobart, Tasmania 7001, Australia. Telephone: +61406717535. E-mail: adam.abersteiner@utas.edu.au

Received September 14, 2017; Accepted June 21, 2018

ABSTRACT

The petrologically unique Udachnaya-East kimberlite (Siberia, Russia) is characterised by unserpentinised and H_2O-poor volcaniclastic and coherent units that contain fresh olivine, along with abundant alkali-rich carbonates, chlorides, sulphides and sulphates in the groundmass. These mineralogical and geochemical characteristics have led to two divergent models that advocate different origins. It has been suggested that the unserpentinised units from Udachnaya-East are representative of pristine unaltered kimberlite. Conversely, the alkali-chlorine-sulphur enrichment has been attributed to interactions with crustal materials and/or post-emplacement contamination by brines. The mineralogical and geochemical features and the compositions of melt inclusions in unserpentinised and serpentinised Udachnaya-East kimberlite varieties are compared in this study. Both varieties of kimberlite have similar major, compatible and incompatible trace element concentrations and primitive mantle normalised trace element patterns, groundmass textures and silicate, oxide and sulphide mineral compositions. However, these two kimberlite varieties are distinguished by: (i) the presence of unaltered olivine, abundant Na–K–Cl–S-rich minerals (i.e. chlorides, S-bearing alkali-carbonates, sodalite) and the absence of H_2O-rich phases (i.e. serpentine, iowaite ($Mg_4Fe^{3+}(OH)_8OCl{\bullet}3(H_2O)$) in unserpentinised samples, and (ii) the absence of alkali- and chlorine-enriched phases in the groundmass and characteristic olivine alteration (i.e. replacement by serpentine and/or iowaite) in serpentinised samples. In addition, melt inclusions hosted in olivine, monticellite, spinel and perovskite from unserpentinised and serpentinised kimberlite contain identical daughter phase assemblages that are dominated by alkali-carbonates, chlorides and sulphates/sulphides. This enrichment in alkalis, chlorine and sulphur in melt inclusions demonstrates that these elements were an intrinsic part of the parental magma. The paucity of alkali-carbonates and chlorides in the groundmass of serpentinised Udachnaya-East kimberlite is attributed to their instability and removal during post-emplacement alteration. All evidence previously used in support of crustal and brine contamination of the Udachnaya-East kimberlite is thoroughly evaluated. We demonstrate that 'contamination models' are inconsistent with petrographic, geochemical and melt inclusion data. Our combined data suggest that the Udachnaya-East kimberlite crystallised from an essentially H_2O-poor, Si–Na–K–Cl–S-bearing carbonate-rich melt.

Key words: alkali-carbonates; chlorides; kimberlite; melt inclusions; Udachnaya-East

INTRODUCTION

Kimberlites are relatively rare and volumetrically insignificant rocks that originated from deeply-derived magmas from depths >150 km (e.g. Dawson, 1980; Clement *et al.*, 1984; Mitchell, 1986; Pearson *et al.*, 2014). Reconstructing the parental kimberlite melt composition is a fundamental task in understanding their petrogenesis, rheology, ascent and emplacement. Although whole-rock analyses of kimberlite rocks show that they are generally ultramafic, silica-poor and volatile (H_2O, CO_2)-rich (e.g. Price *et al.*, 2000; le Roex *et al.*, 2003; Becker & Le Roex, 2006; Kjarsgaard *et al.*, 2009), these compositions cannot be regarded as an accurate reflection of their parental melt. This classical conception of kimberlite melt compositions has been challenged in the past decade by a continually growing number of petrographic and melt inclusion studies (Golovin *et al.*, 2003, 2007, 2017*a*, 2018; Kamenetsky *et al.*, 2004, 2008, 2009*a*, 2013, 2014; Abersteiner *et al.*, 2017*a*, 2017*b*, 2017*c*; Giuliani *et al.*, 2017), and experimental work (Safonov *et al.*, 2009, 2010; Sparks *et al.*, 2009; Brooker *et al.*, 2011; Russell *et al.*, 2012; Kamenetsky & Yaxley, 2015; Sharygin *et al.*, 2015, 2017) which suggest a kimberlite melt which had initially carbonatite-like and silica-poor compositions.

The Udachnaya-East kimberlite (Siberia, Russia) is the flagship example for this new alternative model, largely due to the absence of serpentine, the preservation of fresh olivine and its atypical H_2O-poor and Na–K–Cl–S-enriched groundmass mineralogy (Egorov *et al.*, 1986; Sharygin *et al.*, 2003; Kamenetsky *et al.*, 2004, 2008, 2012). This, combined with the study of melt inclusions in olivine, has led to the proposal that the Udachnaya-East kimberlite is 'uniquely fresh' and that the kimberlites originated from essentially silica–H_2O-poor, alkali-Cl-enriched carbonatitic compositions (Kamenetsky *et al.*, 2004, 2007*b*, 2009*a*, 2014; Golovin *et al.*, 2007, 2017*a*).

Analyses of the Udachnaya-East kimberlite have been complemented by additional studies of melt inclusions in olivine and primary inclusions in magmatic kimberlitic minerals (e.g. monticellite, Cr-spinel, perovskite, apatite) in other altered (i.e. serpentinised) kimberlites worldwide (e.g. Canada, Greenland, Finland, South Africa; Golovin *et al.*, 2003, 2007, 2017*a*; Kamenetsky *et al.*, 2009*a*, 2012, 2013; Mernagh *et al.*, 2011; Abersteiner *et al.*, 2017*a*, 2017*b*, 2017*c*; Giuliani *et al.*, 2017). These studies have consistently produced similar results, advocating the Si-poor and alkali-Cl–S-(and to a lesser extent P–F-) bearing carbonate-rich nature of kimberlite melts entrapped within inclusions.

This alternative model for kimberlite petrogenesis has been heavily criticised in recent studies by Kopylova *et al.* (2013, 2016) and Kostrovitskiy *et al.* (2013). These authors emphasise that the unique Na–Cl–S-enriched groundmass mineralogy of the Udachnaya-East pipe is not exceptional or representative of pristine kimberlite, but can be explained by:(i) contamination of the kimberlite magma by crustal material, and (ii) interaction with external Na–Ca–Cl brines that precipitate salts and carbonates.

Our study provides new constraints on the origin of the unusual groundmass mineralogy and composition of the Udachnaya-East kimberlite and the evolution of its parental melt. We present detailed petrographic studies along with geochemical and melt inclusion analyses from a variety of serpentinised and unserpentinised volcaniclastic and coherent kimberlite samples. This comparison aims to evaluate comprehensively whether the Na–Cl–S-enrichment in the Udachnaya-East was inherited from a magmatic (i.e. mantle-derived melt) or secondary (i.e. crustal) source.

GENERAL GEOLOGY

The Devonian (~365–367 Ma; Kinny *et al.*, 1997; Kamenetsky *et al.*, 2009*b*) Udachnaya kimberlite is part of the Daldyn-Alakit kimberlite field in the Siberian craton (Russia; Fig. 1). The Udachnaya kimberlite intruded thick (>2 km) Ordovician and Devonian limestones, dolomites, marls, siltstones and mudstones (Marshintsev, 1986; Kharkiv *et al.*, 1991, 1998; Zinchuk *et al.*, 1993). This kimberlite forms a composite twin-diatreme structure (i.e. an older eastern and younger western body) that diverges at ~250 m depth (Fig. 2; Kharkiv *et al.*, 1991; Zinchuk *et al.*, 1993). The complex nature of the Udachnaya kimberlite suggests that it formed from multiple magmatic events. The eastern and western Udachnaya kimberlite bodies are different in terms of mineralogy, petrography, composition and degree of alteration. The western body exhibits extensive alteration (i.e. serpentinisation) typical of kimberlites worldwide.

Megascopic and macroscopic study of Udachnaya-East kimberlite units

In this study we use the term kimberlite 'units' instead of 'phases' (see Kopylova *et al.*, 2016). This is because a separate 'phase' of kimberlite magmatism requires: (i) different timing of formation, and (ii) a clear boundary between the first and secondary kimberlite varieties. Scott Smith *et al.* (2013) noted in their kimberlite classification scheme that 'One phase of kimberlite may comprise one or more lithological units, lithofacies, facies and, or, facies associations, thus the terms are not synonymous'. The dating of individual kimberlite units from the Udachnaya pipe has never been conducted, even where the boundaries between the different units are clearly defined. In this study, we examined samples from kimberlite units 9 and 10 from the eastern body

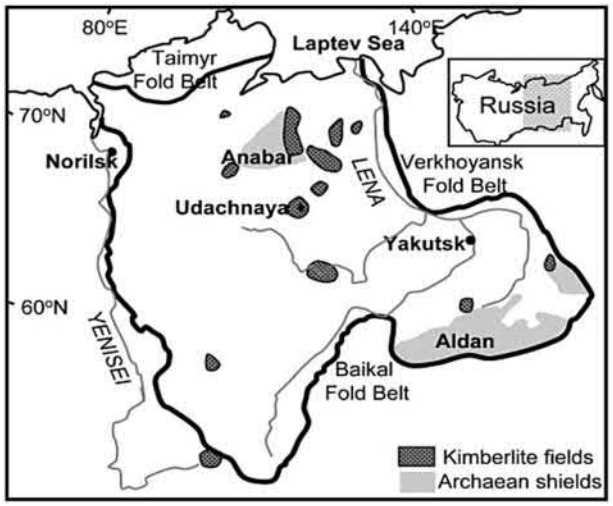

Fig. 1. Map of the Siberian Platform showing the location of the Udachnaya kimberlite and other kimberlite fields after Pearson *et al.* (1995) and Kamenetsky *et al.* (2008).

(Fig. 2). According to the classification scheme of Scott Smith *et al.* (2013), unit 9 is volcaniclastic kimberlite (VK), where fragmentation of magma occurred, whereas unit 10 is classed as coherent kimberlite (CK), where the magma did not undergo fragmentation. The classification of unit 9 depends on the individual hand sample studied; it can be classified as either olivine-rich pyroclastic kimberlite (PK; Supplementary Data Electronic Appendix 2: Fig. S1, supplementary data are available for downloading at http://www.petrology.oxfordjournals.org) or magmaclast-rich PK (Electronic Appendix 2: Fig. S2), as gravitational separation of minerals in the melt during emplacement of unit 9 has been noted (Kamenetsky *et al.*, 2012).

Xenolith-poor (> 5–15%) VK unit 9 is located in the central part of the Udachnaya-East pipe and is surrounded by xenolith-rich (> 15–50%) VK unit 8 (Fig. 2; Supplementary Data Electronic Appendix 2: Figs S3 and S4). Sometimes there are clear boundaries between kimberlite unit 9 and the very xenolith-rich (> 50–75%; Electronic Appendix 2: Fig. S5) unit 7 VK. Units 8 and 9 also contain dykes and veins (ranging in size from several cm to several metres) of xenolith-poor (>0–5%; Fig. 3a; Electronic Appendix 2; Fig. S6) CK (unit 10 in Fig. 2). Units 7 and 8 are partially serpentinised across the entire 370–640 m depth interval. Kimberlite units 9 and 10 can be separated across depth intervals 370—410, 410—500 and 500–640 m Although the textural and structural characteristics of units 9 and 10 are identical, there are various changes in groundmass mineralogy that take place at different depths (Fig. 2).

The so-called 'salty' xenolith-poor unserpentinised VK (Unit 9a in Figs 2 and 3; Supplementary Data Electronic Appendix 2: Figs S4b, S7, S8a, S9, S11b and S12b) is located between 410–500 m (± 10 m) depth. This kimberlite is characterised by the following features:

i. The absence of serpentine and very low H_2O (<0·6 wt %) content (Kamenetsky *et al.*, 2008, 2012).
ii. The presence of alkali-rich carbonates, chlorides, sulphates and sulphides in the groundmass (Table 1), which is reflected by enrichment in alkalis (Na_2O up to 6·2 wt % and K_2O up to 2·2 wt %), chlorine (up to 6·1 wt %) and sulphur (up to 0·5 wt %; Table 2; Supplementary Data Electronic Appendix 2: Figs S7b, S9b, S11c and S12b; Kamenetsky *et al.*, 2004, 2007*a*, 2012, 2014; Sharygin *et al.*, 2003, 2007; D'Eyrames *et al.*, 2017; Golovin *et al.*, 2017*b*; Kitayama *et al.*, 2017).
iii. The presence of chloride and chloride-carbonate (as well as alkali carbonates) 'nodules', which reach up to 30 cm in size (Supplementary Data Electronic Appendix 2: Figs S8–S10; Kamenetsky *et al.*, 2007*b*).
iv. The absence of cracks, caverns and cavities (Supplementary Data Electronic Appendix 2: Figs S7 and S8a) that contain secondary hydrothermal assemblages, which are common in other units of the Udachnaya-East pipe (Mikhailenko *et al.*, 2018).
v. The excellent preservation of mantle-derived lherzolite, dunite, harzburgite, eclogite and pyroxenite xenoliths (e.g. Agashev *et al.*, 2010; Doucet *et al.*, 2012; Ionov *et al.*, 2017; Supplementary Data Electronic Appendix 2: Figs S11 and S12).

It should be noted that chloride and chloride–carbonate 'nodules' occupy between 3–5 vol. % of the VK kimberlite unit (Supplementary Data Electronic Appendix 2: Fig. S8a) and the sedimentary xenolith content is ≤ 6 vol. % (Kamenetsky *et al.*, 2014). When this 'salty' kimberlite is exposed to the atmosphere, it is rapidly degraded due to the dissolution and decomposition of chlorides, alkali-carbonates and alkali-sulphates (Supplementary Data Electronic Appendix 2: Fig. S13). This same kimberlite was classified by Kopylova *et al.* (2016) into two so-called 'phases': olivine-rich pyroclastic kimberlite (PK) and magmaclast-rich PK.

Dykes and veins of xenolith-poor unserpentinised CK (unit 10 inside unit 9a in Fig. 2) are present within unserpentinised VK unit 9a at the same 410–500 m level. These CK dykes and veins share the same characteristic features (i, ii and iv) as VK unit 9a, except that the chloride and chloride-carbonate 'nodules' (iii) are absent. The high Na_2O (3·4 wt %) and Cl (0·9 wt %; Sharygin *et al.*, 2015) contents led to the formation of Na–Ca-carbonates, chlorides and alkali-sulphates in the CK units (e.g. Fig. 5 from Kitayama *et al.*, 2017).

In general, all units of kimberlite at the 410–500 m depth interval have been referred to as 'Serpentine Free Udachnaya-East' (SFUE) kimberlite by Kopylova *et al.* (2013) and Kostrovitskiy *et al.* (2013). Note that kimberlitic units 9 and 10 are partially serpentinised at depths of 370–410 and 500–640 m (Fig. 2; unit 9 b and 10). The chloride, alkali-carbonate and alkali-sulphate assemblages in the groundmass of these units are absent, along with chloride and chloride-carbonate 'nodules' in unit 9 b. In addition, voids, caverns and cracks appear,

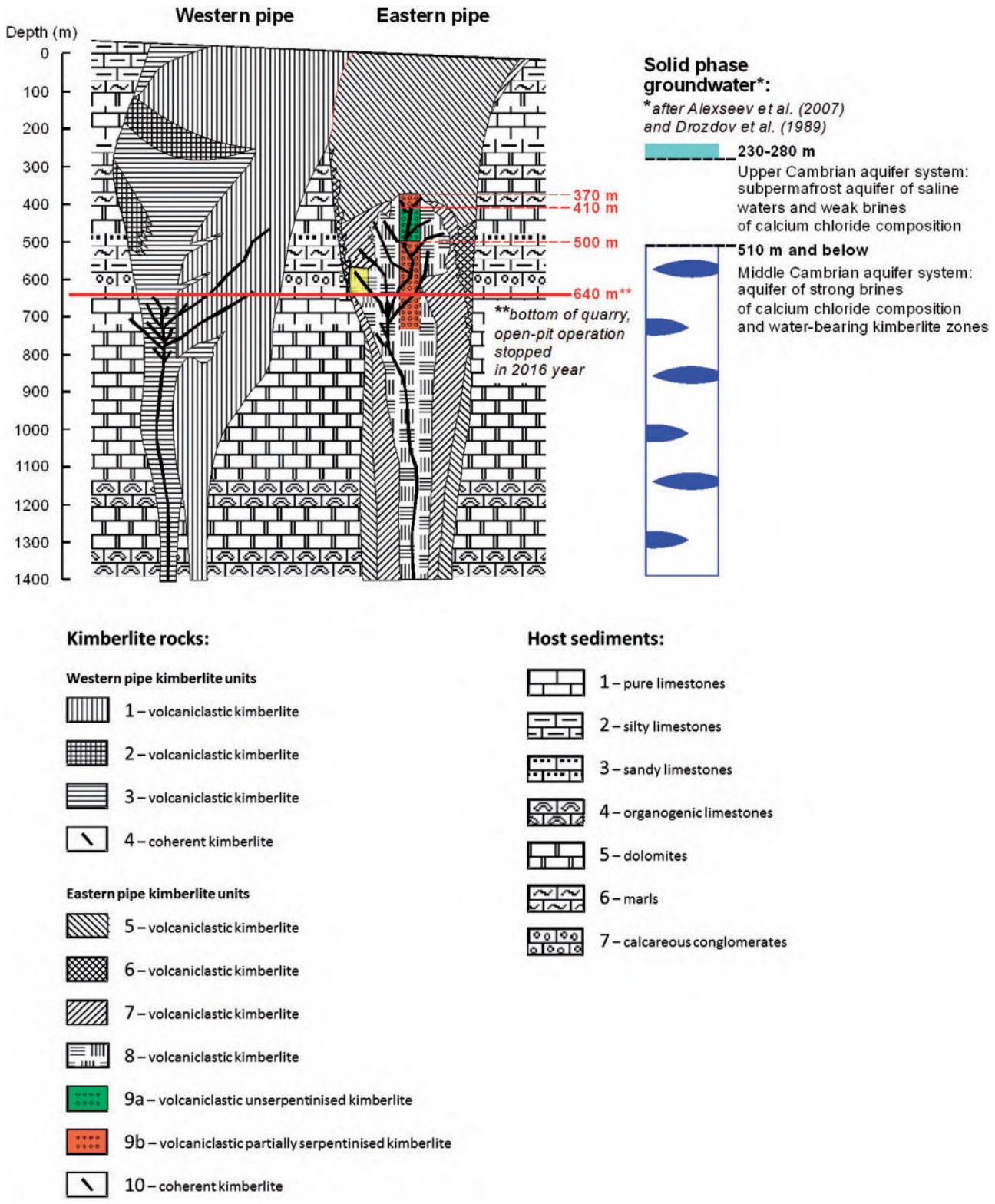

Fig. 2. Geological cross-section of the Udachnaya kimberlite pipes (edited after Golovin *et al.* (2017)). Units 1–4 = western body, which contains volcaniclastic kimberlite (units 1–3, which have well defined boundaries) and veins of coherent kimberlite (4). Units 5–10 = eastern body, which consists of volcaniclastic kimberlite (units 5–9, which have well defined boundaries) and veins of coherent kimberlite (10). Volcaniclastic kimberlite unit 9 can be divided into two types (a) and (b). Although the textural and structural characteristics of these types are identical, there are various changes in groundmass mineralogy that occur at different depths. Volcaniclastic kimberlite unit 9: (a) Green = unserpentinised 'fresh' kimberlite (see Kamenetsky *et al.*, 2012, 2014), depth = 410–500 m; (b) Orange= partially serpentinised kimberlite at 370–410 m and 500–640 m depth intervals. The upper boundary of kimberlite unit (9) is at 370 m (according to Kharkiv *et al.* (1998) and Marshintsev *et al.* (1976)). Other boundaries were constrained during 2003–2016 field work. Megascopic and macroscopic photographs of the eastern body kimberlite units are included in Supplementary Data Electronic Appendix 2 (Figs S1–S16). The area containing the two so-called 'epigenetic halite and sedimentary evaporite' units (see Kopylova *et al.* (2016)) and are indicated in yellow. Host sediments are after Alexseev (2009).

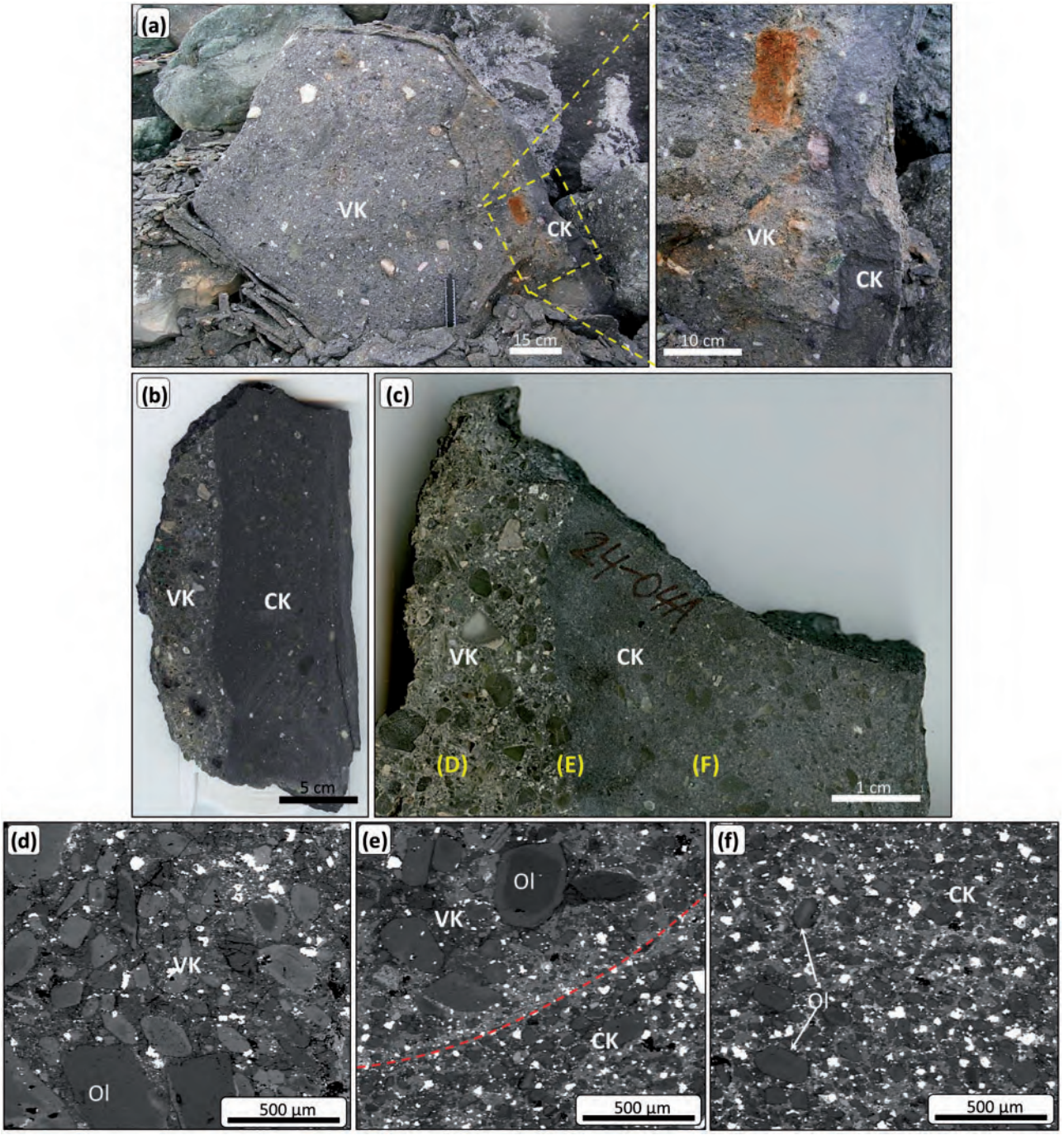

Fig. 3. (a–c) Specimens of unserpentinised volcaniclastic kimberlite (VK) cross-cut by a thin dyke (~10 cm) of coherent kimberlite (CK; sample K24–04A). The inset (top-right) shows a zoom in of this CK dyke cross-cutting VK. Panels (b) and (c) show the sharp boundary between VK and CK. Panel (c) is sample K24–04A and labels (D), (E) and (F) represent the relative positions of groundmass photographs for (d–f) which show the transition in textures from VK to CK. (d) VK, (e) boundary (defined by red-dotted line) between VK and CK, and (f) CK. CK is characterised by more uniform and fine-grained textures and a higher abundance of groundmass oxides (bright phases). Olivine: Ol.

in which hydrothermal mineral assemblages are present, which include calcite, gypsum, halite, and iowaite (Supplementary Data Electronic Appendix 2: Figs S14 and S15; Mikhailenko *et al.*, 2018).

ANALYTICAL METHODS

Eleven specimens of the Udachnaya-East (K16/05, K20–05, K28/05, K17/04, K25/04, K-U, UV-K1–15, K2–03, K24/04A, K24/04B, UV-K1–05) kimberlite were examined (Table 1).

Table 1: Summary of mineralogical similarities and differences for serpentinised and unserpentinised Udachnaya-East kimberlite samples

Sample	Depth of Sampling	Lithology	Mineralogical Similarities	Key Unique Minerals	Approximate Mineral Abundances (%)
Serpentinised Samples			Olivine, Monticellite, Phlogopite, Calcite, Perovskite, Ilmenite (macrocrysts), Mg–Ti-Magnetite, Magnesian Ulvöspinel-Magnetite (MUM), Pleonaste, Cr-Spinel, Apatite, Fe–Ni-Sulphides, Djerfisherite	Serpentine, Iowaite	Olivine: 40–50, Calcite: 15–25, Serpentine: 10–25, Spinel + Perovskite: 5–15, Monticellite: 3–4, Iowaite: 3–4, Phlogopite: 2–4, Ilmenite: 1–2, Apatite: ≤1, Sulphides: ≤1
K16/05	500–520	AC			
K-U	400–420	VK			
K17/04	480–500	VK			
K28/05	500–520	AC			
K25/04	480–500	VK			
K20-05	500–520	VK			
Unserpentinised Samples				Halite, Sylvite, Alkali (Na, K) Carbonates (including SO_4^{2-} bearing), Sodalite	Olivine: 50–60, Calcite: 10-15, Alkali-Carbonates: 10–15, Spinel + Perovskite: 5–15, Chlorides: 4–6, Sodalite: 3–5, Monticellite: 3–4, Phlogopite: 2–4, Ilmenite: 1–2, Apatite: ≤1, Sulphides: ≤1
K24/04A	480–500	CK			
K2-03	440–480	VK			
K24/04B	480–500	VK			
UV-K1-15	440–480	VK			
UV-K1-05	440–480	VK			

Depth of sampling (in metres) reflect most likely position in the mining pit for most samples as they were taken from stockpiles.
CK, coherent kimberlite; VK, volcaniclastic kimberlite; AC, autolithic clasts of kimberlite (or autoliths), hosted in VK.

Table 2: Representative whole-rock major element compositions of the Udachnaya-East kimberlite

Sample	SiO_2	TiO_2	Al_2O_3	FeO	MnO	MgO	CaO	Na_2O	K_2O	P_2O_5	Cl	LOI	Total	S	CO_2	H_2O
K16/05	26·58	1·81	1·72	8·32	0·13	30·87	13·06	0·39	0·91	0·48	0·59	13·74	98·59	n/a	9·3	4·45
K-U	31·95	1·87	2·13	9·33	0·15	35·27	8·08	0·17	0·5	0·41	0·12	9·01	98·99	0·03	4·9	4·12
K17/04	28·52	1·09	1·74	7·97	0·13	32·72	12·29	0·31	0·99	0·4	0·55	12·31	99·02	0·05	8·5	3·81
K28/05	27·79	1·67	2·08	8·57	0·16	31·37	13·33	0·37	1·29	0·56	0·40	10·91	98·50	0·19	7·3	3·64
K25/04	28·96	1·44	1·89	8·83	0·16	33·31	11·51	0·22	1·23	0·55	0·39	10·03	98·52	0·05	7·8	2·28
K20-05	27·01	0·98	1·3	7·99	0·14	33·94	13·98	0·25	0·5	0·47	0·49	11·92	98·97	0·08	10·5	1·40
K24/04A	25·88	1·75	2·27	9·86	0·2	31·54	13·96	1·08	0·86	0·82	0·08	10·41	98·70	0·06	9·9	0·56
K2-03	29·95	1·33	2·03	8·53	0·15	32·66	9·54	3·94	1·61	0·45	1·34	6·74	98·27	0·28	6·3	0·42
K24/04B	27·84	1·4	1·84	9·45	0·18	33·86	10·86	2·26	0·95	0·63	0·34	9·61	99·22	0·14	9·2	0·39
UV-K1-15	27·28	0·87	1·52	7·53	0·13	30·95	9·74	6·07	1·75	0·35	n/a	7·95	94·14	0·24	7·7	0·23
UV-K1-05	27·26	1·03	1·8	7·07	0·12	29·92	9·44	6·23	1·88	0·34	5·68	7·84	98·60	0·31	7·7	0·17

Analyses are ordered from highest H2O content through to lowest.
Major elements, Cl, S, LOI (loss on ignition), CO_2 and H_2O are in wt %.
Depth of sampling (in metres) reflect most possible position in the mining pit for most samples taken from stockpiles.
CK, coherent kimberlite; VK,volcaniclastic kimberlite; AC, autolithic clasts of kimberlite (or autoliths),hosted in VK; n/a, not available.
Source: Kamenetsky *et al.* (2012).

These samples were also analysed by Kamenetsky *et al.* (2012; see Supplementary Data Electronic Appendix 1 for methodology and complete data set) and prepared as epoxy resin rock and grain mounts polished using kerosene as lubricant to avoid dissolution of any water-soluble minerals. Phases such as alkali-carbonates and chlorides are very susceptible to dissolution and re-precipitation due to hydrous interaction (e.g. water contact and atmospheric moisture). Initial optical petrographic and mineralogical investigations of samples were performed on a Nikon Eclipse 50i POL microscope at the University of Tasmania.

Detailed examination of groundmass phases and inclusions in minerals were performed using a Hitachi SU-70 field emission (FE) scanning electron microscope (SEM) equipped with an Oxford AZtec Energy XMax 80 detector at the Central Science Laboratory, University of Tasmania. A beam accelerating voltage of 15 kV was used to produce high-resolution backscattered electron (BSE) images of minerals and energy-dispersive X-ray spectroscopy (EDS) semi-quantitative analyses and elemental maps of minerals and inclusions.

PETROGRAPHY

Samples of the Udachnaya-East (UE) kimberlite were selected based on the presence of serpentine as a replacement mineral after olivine and as an interstitial groundmass phase. Six partially serpentinised samples (K16/05, K20–05, K28/05, K17/04, K25/04, K-U) were derived from depth intervals of 480–520 m (below the SFUE) and 400–420 m (roof of the SFUE) and five unserpentinised samples (UV-K1–15, K2–03, K24/04A, K24/04B, UV-K1–05) were sourced from a depth interval of 440–500 m (within the SFUE; Table 1). The petrography of both serpentinised and unserpentinised varieties of the UE kimberlites have been extensively described in the literature (e.g. Marshintsev, 1986; Egorov *et al.*, 1991; Kharkiv *et al.*, 1991; Kamenetsky *et al.*, 2004, 2008, 2012, 2014; Kopylova *et al.*, 2013, 2016; Kostrovitskiy *et al.*, 2013; D'Eyrames *et al.*, 2017; Kitayama *et al.*, 2017).

The UE samples were analysed by optical microscopy and FE-SEM. Samples UV-K1–15, K2–03, K24/04B, UV-K1–05 (unit 9a in Fig. 2, 'salty' unserpentinised

kimberlite; see also Fig. 3 and Supplementary Data Electronic Appendix 2: Figs S4b, S7, S8a, S9, S11 and S12) and K20–05, K17/04, K25/04, K-U (unit 9 b in Fig. 2, partially serpentinised kimberlite; Electronic Appendix 2: Figs S3, S5b, S14 and S15) are texturally defined as massive VK. Samples K16/05 and K28/05 (Electronic Appendix 2: Fig. S16) are autolithic clasts (AC) of kimberlite (or autoliths) hosted in unit 9 b VK. These samples are composed of kimberlite material surrounding a fragment of sedimentary rock in the core. Sample K24/04A is representative of an unserpentinised CK dyke or vein in unit 9a (Figs 2 and 3).

Unserpentinised CK occurs as thin (5–10 cm) dykes that intrude unserpentinised VK. These are dark in colour (grey-black) and generally uniform in grain size, xenolith-poor and contain abundant fine-grained olivine (Fig. 3a–c, e and f) that are preferentially aligned, and higher abundances (up to 15 vol. %) of oxides (e.g. spinel, perovskite) than in VK. VK is generally light-grey in colour, has a macrocrystic texture (Fig. 3a–e) and contains a higher abundance of randomly orientated olivine and carbonate in the groundmass, as well as minor amounts of mantle-derived (e.g. ilmenite, clinopyroxene, garnet, and phlogopite) and crustal xenocrysts (e.g. amphibole, alkali-feldspar) and xenoliths.

Olivine is the dominant mineral (40–60 vol. %) in CK and VK from both unserpentinised and serpentinised varieties and is petrographically and geochemically similar, represented by two morphologically distinct populations which were described in detail by Kamenetsky *et al.* (2008). The first type of olivine (olivine-I) is round to ovoid in shape or occurs as angular fragments up to several millimetres in size. Large olivine grains (>0·5 mm) are less common in CK than in VK. The second type of olivine (olivine-II) forms smaller (<250 μm) euhedral grains that commonly exhibit complex zoning patterns (Figs 3, 4, 6 and 7; Supplementary Data Electronic Appendix 2: Fig. S17), reflecting variation in Fo-content and a complex crystallisation history (Kamenetsky *et al.*, 2008). The cores of both olivine types exhibit variable Fo contents (0·85–0·94 mol %) but most compositions are clustered between Fo 0·91–0·94 mol % (Fig. 5).

Both unserpentinised and serpentinised varieties of CK and VK are represented by broadly similar silicate (olivine, monticellite, phlogopite), carbonate (calcite), oxide (perovskite, macrocrystic ilmenite, Fe–Ti–Mg–Al–Cr-spinel (Mg–Ti-magnetite, magnesian ulvöspinel-magnetite (MUM), pleonaste, Cr-spinel), phosphate (apatite) and sulphide (Fe–Ni-sulphides, djerfisherite ($K_6Na(Fe^{2+}$, Cu, $Ni)_{25}S_{26}Cl$)) groundmass assemblages. A summary of the depth constraints, mineralogical similarities and differences, as well as their approximate abundances in the studied samples is presented in Table 1.

In both unserpentinised and serpentinised CK and VK kimberlite varieties, monticellite is a common groundmass phase that typically occurs as discrete subhedral to euhedral (10–70 μm) grains (Fig. 4b and Supplementary Data Electronic Appendix 2, Fig. S17a). In rare cases, monticellite is a replacement mineral after olivine in unserpentinised kimberlite (Electronic Appendix 2, Fig. S17a; Abersteiner *et al.* (2017*b*)). The distribution of monticellite is extremely heterogeneous on a millimetre scale; it may be abundant in some areas, but absent in others. Phlogopite usually occurs as clusters of microphenocrysts (<15 μm), but may also occur as larger (up to 1 mm) rare macrocrysts. Calcite is a ubiquitous phase that is interstitial to most other phases (Fig. 4c and d; Supplementary Data Electronic Appendix 2, Fig. S17a and c). Only in unserpentinised samples does calcite also form euhedral needle-like grains (Electronic Appendix 2, Fig. S17b). Euhedral perovskite and spinel range in size from 10–100 μm and are more common in CK (Fig. 3f) than in VK (Fig. 3d). Cr-spinel and Mg–Ti-magnetite usually form well-developed atoll shapes (see definition by Mitchell (1986) and Roeder & Schulze (2008)). Here, the euhedral zoned core is surrounded by an intermediate 'lagoon' (5–15 μm thick) zone composed of pleonaste and an outer thin rim (1–5 μm) of (Mg-) magnetite which parallels the shape of the core exactly (Electronic Appendix 2, Fig. S17c). These atoll-shapes show excellent preservation in unserpentinised samples. Apatite is a rare groundmass phase that occurs as acicular microphenocrysts that are 1–10 μm in size. Sulphides are minor groundmass phases that are generally amorphous and interstitial to most other groundmass phases (i.e. silicates, oxides) and range in size from 5–100 μm (Supplementary Data Electronic Appendix 2, Fig. S17d).

The unserpentinised UE kimberlite samples are mineralogically and geochemically distinguished from serpentinised samples by: (i) the absence of H_2O-rich phases in the groundmass (i.e. serpentine and iowaite ($Mg_4Fe^{3+}(OH)_8OCl{\bullet}3(H_2O)$)); (ii) the excellent preservation of euhedral olivine which has near-perfect crystal faces (Figs 4a, b and 6);(iii) the presence of groundmass halite and sylvite, which are usually interstitial to other groundmass phases (e.g. silicates, oxides, phosphates etc). In addition, there are larger irregular to semi angular shaped halite 'nodules', which are up to several centimetres across (Kamenetsky *et al.*, 2007*a*, 2007*b*). These halite nodules commonly contain bleb-like inclusions (1–60 μm in size) of sylvite (Supplementary Data Electronic Appendix 2, Fig. S18) as well as lesser amounts of calcite and/or phlogopite. (iv) The presence of abundant (up to 15 vol. %) alkali- (Na, K) carbonates (e.g. shortite ($Na_2Ca_2(CO_3)_3$), including some S-enriched (i.e. sulphate) varieties (up to 2–4·7 wt % S)) and sodalite ($Na_8Al_6Si_6O_{24}Cl_2$). In contrast, serpentinised UE samples contain varying amounts of serpentine and iowaite (~10–30 %), which replaces olivine grains along rims and fractures (Figs 4c, d, 7 and Supplementary Data Electronic Appendix 2, Figs S19 and S4). Olivine replacement is sometimes accompanied by zoning from serpentine along the olivine contact towards iowaite along the peripheries (Electronic Appendix 2, Fig. S19). Iowaite also occasionally forms large (up to 250 μm)

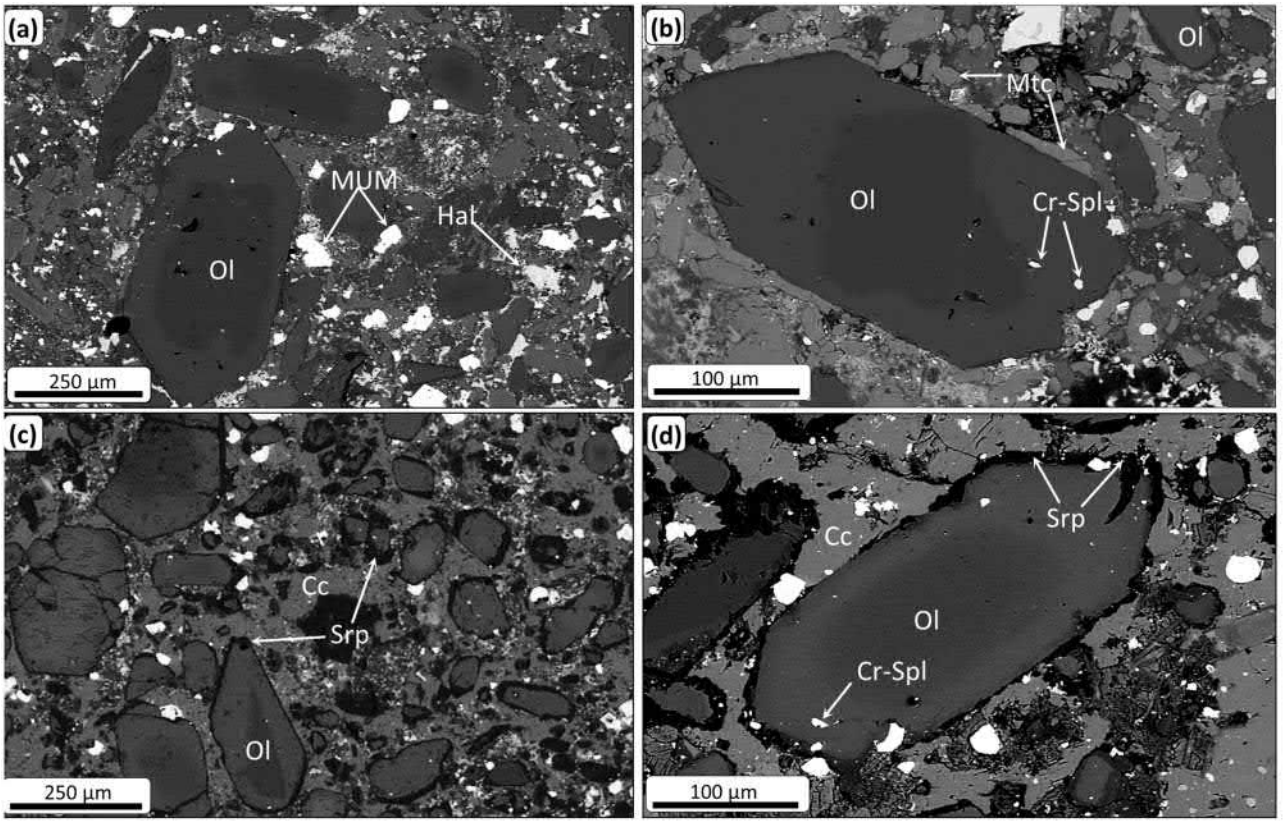

Fig. 4. Back-scattered electron (BSE) SEM images of olivine in unserpentinised (a, b) and serpentinised (c, d) VK samples. (a, b) Euhedral to anhedral olivine (Ol) with pronounced zoning and unaltered rims. The groundmass is composed of: euhedral monticellite (Mtc), interstitial alkali-carbonates (dark grey) and calcite (light grey), interstitial chlorides (e.g. halite, Hal); euhedral oxides (e.g. perovskite, magnetite, Cr-spinel, magnesian ulvöspinel-magnetite – MUM) are white. (c, d) Euhedral to anhedral olivine with pronounced zoning and serpentinised rims and fractures. The groundmass is composed of: serpentine (black), calcite (light grey) and euhedral oxides (white).

aggregates in the groundmass. Areas directly in contact or within a few millimetres of groundmass surrounding crustal xenoliths or xenocrysts are characterised by more intense serpentinisation (Electronic Appendix 2, Fig. S20). In serpentinised samples, xenocrysts of ilmenite and garnet also exhibit variably thick (25 to >100 μm) reaction rims, in which ilmenite is partially replaced by Ti–Fe–Mg-spinel and perovskite, and pyrope–almandine garnet is partially replaced by phlogopite. Although garnet xenocrysts were not observed in unserpentinised samples, ilmenite shows a stronger degree of preservation along rims where grains are surrounded by only thin (<5–10 μm) reaction rims of Ti–Fe-oxides.

GEOCHEMISTRY

The major element compositions of serpentinised and unserpentinised CK and VK are characterised by low-silica (26·6–32 wt % SiO_2), FeO_{total} (7·5–8·8 wt %) and Al_2O_3 (1·3–2·1 wt %), and moderate-to-high CaO (9·5–14 wt %) and CO_2 (6·3–10·5 wt %; Fig. 8a–c; Table 2). These compositions are consistent with whole-rock analyses of other kimberlites from Yakutia (Vasilenko *et al.*, 2002) and worldwide (O'Brien & Tyni, 1999; Price *et al.*, 2000; le Roex *et al.*, 2003; Becker & le Roex, 2006; Nowicki *et al.*, 2008; Kjarsgaard *et al.*, 2009; Tappe *et al.*, 2011, 2013, 2016). Unserpentinised samples are distinct from partially serpentinised samples as they are enriched in alkalis (K_2O up to 2·23 wt %, and Na_2O up to 6·10 wt %), chlorine (up to 6·11 wt %) and sulphur (up to 0·5 wt %; Figs 8d–h; Table 2; Kamenetsky *et al.*, 2004, 2012; Kitayama *et al.*, 2017). The absence or paucity of serpentine/iowaite in kimberlite samples is reflected by the extremely low H_2O-contents (≤0·6 wt %; average from 11 samples is 0·35 wt %; Supplementary Data Electronic Appendix 1). In contrast, partially serpentinised varieties of the UE kimberlite, along with the overwhelming majority of other localities worldwide, have extremely low Na_2O (typically <0·5 wt %) and Cl (typically <0·1 wt %, rarely higher than 1 wt %; Nowicki *et al.*, 2008) and highly variable H_2O (≥0·6 to >16 wt %; Fig. 8d–h; Shee, 1985; Mitchell, 1986; O'Brien & Tyni, 1999; Price *et al.*, 2000; Vasilenko *et al.*, 2002; le Roex *et al.*, 2003; Becker & le Roex, 2006; Kjarsgaard *et al.*, 2009; Tappe *et al.*, 2016). Overall, the Na_2O, Cl and to a lesser extent K_2O and S contents in each UE sample are directly related to the H_2O contents of each sample (i.e. degree of serpentinisation average H_2O-content is 2·5 wt % from 18 samples; Supplementary Data Electronic Appendix 1).

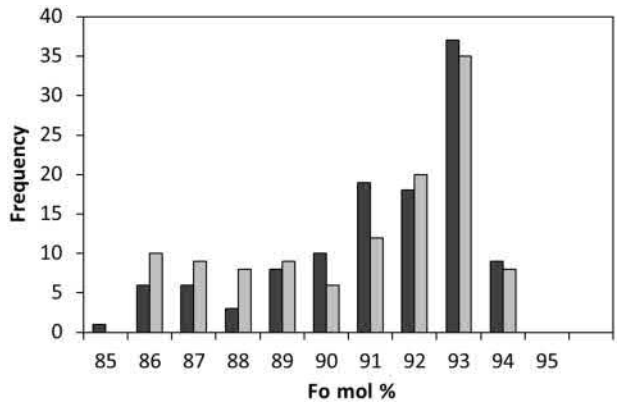

Fig. 5. Histogram of olivine core compositions from serpentinised (dark grey; n = 117) and unserpentinised (light grey; n = 117) UE kimberlite samples, showing the distribution of forsterite (Fo) mol %.

Samples with ≤0·6 wt % H_2O (i.e. unserpentinised) exhibit the greatest variability in alkali, chlorine and sulphur contents, whereas samples with 0·6–4·5 wt % H_2O (i.e. serpentinised; Supplementary Data Electronic Appendix 1) are generally significantly depleted in these elements (Fig. 8d and e; Table 2).

Primitive-mantle normalised (after Sun & McDonough, 1989) trace element diagrams show typical kimberlite enrichment in most incompatible elements and depletions in heavy rare-earth elements (HREE) and Y (Fig. 9). This is accompanied by strong negative anomalies in K, Pb, P, Ti and to a lesser extent in Ba, Sr, Zr and Hf relative to elements of similar incompatibility. Both serpentinised and unserpentinised CK and VK samples have almost identical trace elements patterns and concentrations.

INCLUSIONS IN MINERALS

Analyses of melt inclusions hosted by kimberlitic minerals provide 'snapshots' of the kimberlite melt composition prior to or during solidification of the magma and are unaffected by post-magmatic modifications of the rock. In our study, olivine-hosted melt inclusions occur along healed fractures and planes, and are, therefore, assigned a secondary origin (as defined by Roedder, 1984). Although the majority of these inclusions are isolated within the host-olivine, many are interconnected by thin channels and, therefore, modification of the original melt composition by 'necking down' is possible.

Inclusions were examined in olivine, monticellite, spinel (Cr-spinel/MUM) and perovskite in the groundmass as well as in grain separates from both unserpentinised and serpentinised samples. The compositions of inclusions were analysed by FE-SEM. Representative bulk compositions of melt inclusions cannot be accurately quantified because of: i) the potential for the loss of water-soluble phases during exposure of the inclusions during sample preparation and storage (Supplementary Data Electronic Appendix 2, Fig. S21); ii) melt inclusions in kimberlitic minerals are heterogeneous in composition; iii) analyses of exposed melt inclusions only provide a two-dimensional cross section. Therefore, qualitative reconstructions of melt inclusion compositions are based on a statistically high number of analyses.

In this study, over 150 inclusions in olivine were analysed. In addition, over 3000 inclusions have been analysed in numerous studies of olivine from the Udachnaya-East kimberlite (Golovin *et al.*, 2003, 2007, 2017*a*; Kamenetsky *et al.*, 2004, 2008, 2009*a*, 2012; Mernagh *et al.*, 2011). The majority of secondary inclusions in olivine in this study are typically round to amoeboid in shape and less than 5 μm in size (Figs 10, 11a and b). However, larger irregular-shaped inclusions may reach up to 50–150 μm or more in size (Figs 11c, d, 12 and 13). The daughter phase assemblages in olivine-hosted inclusions from both unserpentinised and serpentinised samples are virtually identical; they contain complex daughter phase assemblages of (in order of relative abundance): halite/sylvite, Ca–Mg-bearing alkali (Na, K, Ba, Sr) carbonates (e.g. commonly shortite ($Na_2Ca_2(CO_3)_3$) as well as nyerereite ($Na_2Ca(CO_3)_2$), dolomite, calcite, natrite (Na_2CO_3), strontianite ($SrCO_3$ and some S-bearing varieties), Fe–Ti–Mg–Cr–Al-spinels, alkali (Na, K)-rich sulphates (e.g. arcanite (K_2SO_4)), tetraferriphlogopite ($KMg_3Fe^{3+}Si_3O_{10}(OH)_2$), djerfisherite, Fe–Ni-sulphides, phlogopite, monticellite, perovskite, humite ($(Mg, Fe)_7(SiO_4)_3(F, OH)_2$) and apatite (Table 3; Figs 11–13). Olivine also hosts numerous euhedral inclusions (<20 μm) of spinel (MUM, Cr-spinel, magnetite), needle-shaped rutile, and perovskite, as well as rare rounded (up to 50 μm) inclusions of orthopyroxene and clinopyroxene within olivine cores.

Monticellite (Fig. 14a–c), spinel (Fig. 14d–f) and perovskite (Fig. 14g) host numerous multiphase primary inclusions (n = >30) that are typically <10 μm in size and irregular in shape. Melt inclusions in groundmass minerals are less common than in olivine, largely due to the smaller sizes of the host grain and relative abundance. Phase assemblages hosted in these inclusions are analogous to multiphase inclusions in olivine, and are dominated by: sylvite/halite, Ca–Mg-bearing alkali (Na, K)-carbonates, Fe–Mg–Ti-spinel, alkali (Na, K)-sulphates, phlogopite and perovskite (Table 3). In addition, spinel hosts numerous larger (up to 20 μm) rounded monocrystalline olivine inclusions.

Interstitial groundmass calcite hosts abundant rounded multiphase inclusions (n = >20) ranging in size from 1–50 μm in size. These inclusions are comprised of (in order of relative abundance) halite/sylvite, Ca–Mg-bearing alkali (Na, K ± S) carbonates and djerfisherite (Table 3; Fig. 14h).

DISCUSSION

Kimberlites: rock vs melt compositions

Reconstructing the composition of kimberlites is challenging as kimberlite whole-rocks can no longer be considered as representative of their parental melts. This is

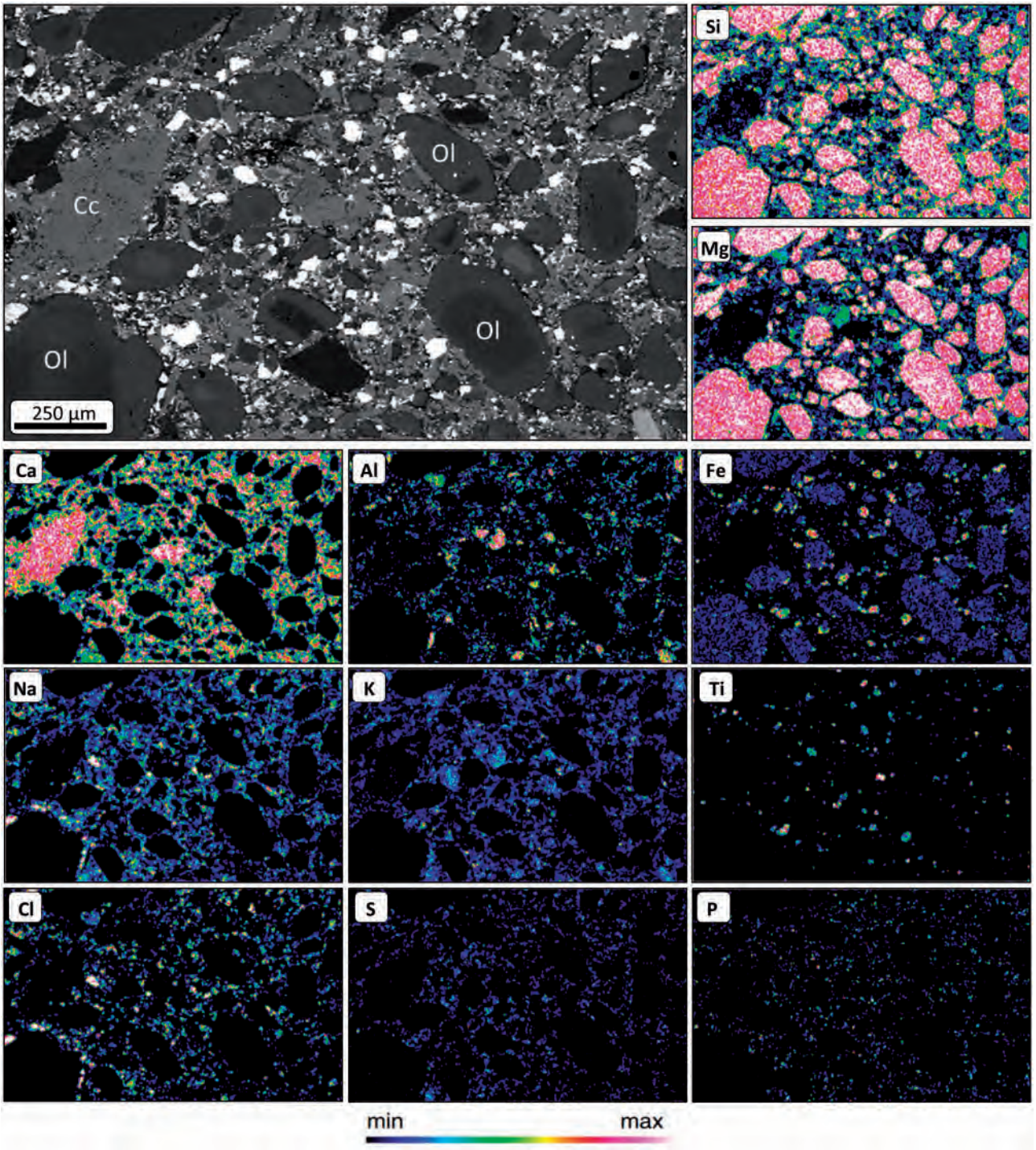

Fig. 6. Back-scattered electron SEM image and X-ray element maps of unserpentinised VK sample UV-K1–15. Olivine (Ol; Si, Fe, Mg maps) is set in a groundmass of S-bearing Na–K–Ca-carbonates (Ca, Na, K, S maps), calcite (highest intensity on Ca-map), sodalite (Al, Cl, Na maps), phlogopite (K, Al, Mg maps), chlorides (Na, K, Cl maps), apatite (P maps) and Fe–Ti-oxides (highest intensity on Fe, Ti maps).

because parental kimberlite melts are inevitably altered *en route* to the surface and upon emplacement. This includes: i) reactions between the kimberlite magma and entrained mantle and crustal material (Hunter & Taylor, 1982; Smith *et al.*, 2004; Buse *et al.*, 2010; Kamenetsky & Yaxley, 2015; Soltys *et al.*, 2016; Tappe *et al.*, 2016; Sharygin *et al.*, 2017; Stone & Luth, 2017). Furthermore, entrained xenogenic material such as mantle-derived olivine (Kamenetsky *et al.*, 2008; Brett *et al.*, 2009; Arndt *et al.*, 2010) contributes significantly to the whole-rock composition, even in so-called aphanitic varieties. ii) Volatiles (e.g. H_2O, CO_2) are exsolved and degassed during kimberlite magma ascent and emplacement (Sparks *et al.*, 2006; Nowicki *et al.*, 2008;

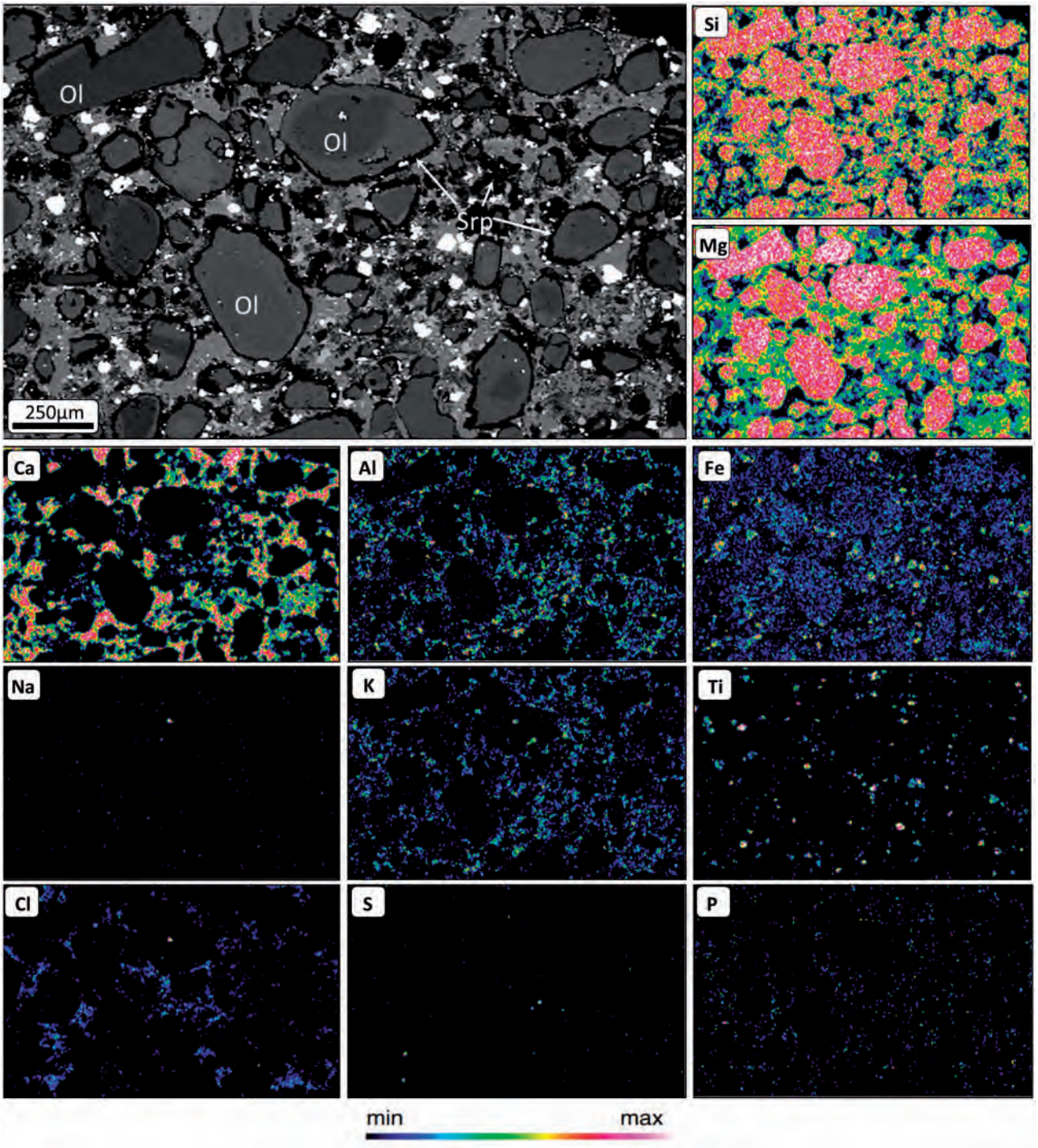

Fig. 7. Back-scattered electron SEM image and X-ray element maps of serpentinised VK sample K17–04. Olivine (Ol; Si, Fe, Mg maps) is set in a groundmass of serpentine (Srp – black; Fe, Mg, Si maps), calcite (Ca map), iowaite (Cl map), phlogopite (K, Al, Mg maps), sulphides (S map), apatite (P map) and Fe–Ti-oxides (Fe, Ti maps).

Abersteiner *et al.*, 2017*b*; Giuliani *et al.*, 2017; Shatskiy *et al.*, 2017). iii) Kimberlite rocks are commonly subject to extensive alteration by deuteric (Kopylova *et al.*, 2007; Mitchell, 2008, 2013) and/or post-emplacement hydrothermal/meteoric fluids (Sparks *et al.*, 2006, 2009; Brooker *et al.*, 2011; Afanasyev *et al.*, 2014; Giuliani *et al.*, 2014, 2017). This low-temperature modification partially overprints the primary kimberlite mineralogy and textures, in which serpentine, brucite and carbonate (e.g. calcite and dolomite) are produced (Clement, 1982; Mitchell, 1986).

Kimberlite composition (current debate)

During the last 15 years, the perception of kimberlite petrogenesis and the composition of their parental melts have diverged into two contrasting models.

The classical view is based on the whole-rock composition of kimberlite rocks and maintains that kimberlites originate from ultramafic/basic and volatile (H_2O, CO_2)-rich melts (Price *et al.*, 2000; le Roex *et al.*, 2003; Becker & le Roex, 2006; Kopylova *et al.*, 2007; Mitchell, 2008; Kjarsgaard *et al.*, 2009). Diamond resorption experiments have been used as an indicator of high volatile activity in kimberlite magmas (Fedortchouk *et al.*, 2010; Fedortchouk, 2015). However, these studies did not test these diamond resorption experiments in putative kimberlite magmas, but rather in aqueous solutions. Furthermore these studies were conducted at fixed *P–T* conditions and neglect the observation that diamonds are brought to the surface whilst being encased in their host mantle xenolith (e.g. peridotite, eclogite). In addition, the presence of phlogopite in kimberlites signifies the presence of H_2O in kimberlite melts. SEM-EDS analyses of phlogopite in the Udachnaya-East kimberlite indicate that it is generally F- and Cl-poor, and is, therefore, assumed to be dominantly H_2O-bearing. If the approximate K_2O/H_2O in phlogopite is ~2·5/3 and the average K_2O in bulk-rocks is 1·3 wt % (Table 2) and all K in the kimberlite is assumed to have partitioned into phlogopite, then the maximum estimated H_2O content corresponds to only 0·43–0·52 wt %. It is noteworthy that K in unserpentinised samples is also partitioned into groundmass alkali-carbonates and chlorides, which suggests that the amount of H_2O partitioned into phlogopite is lower. Even if there was hypothetically 10 wt % phlogopite in a kimberlite with ~3·7 wt % H_2O (based on compositions from Kopylova *et al.* 2010), the amount of H_2O hosted by phlogopite would still correspond to <1 wt %.

The alternative view does not consider whole-rock reconstructions to be representative of the parental kimberlite melt, largely due to the hybrid and contaminated nature of kimberlite rocks. This alternative approach relies on recent advancements in petrographic and melt inclusion studies of kimberlites worldwide (Golovin *et al.*, 2003, 2007, 2017*a*; Kamenetsky *et al.*, 2004, 2009*a*, 2013, 2014; Abersteiner *et al.*, 2017*a*, 2017*b*, 2017*c*; Giuliani *et al.*, 2017). These studies have suggested that kimberlite melts are depleted in SiO_2 and H_2O, and enriched in alkalis, halogens and CO_2 (i.e. carbonate) relative to whole-rock compositions. In addition, experimental studies have demonstrated the inability to successfully reproduce kimberlite melts using putative whole-rock kimberlite compositions at magma emplacement conditions (e.g. Sparks *et al.*, 2009; Brooker *et al.*, 2011; Moussallam *et al.*, 2016).

The UE kimberlite has taken the centre stage in the pursuit of genetic reconstructions and is considered the flagship 'least altered' kimberlite for testing the above opposing models. In the following sections we combine petrographic, geochemical and melt inclusion data in order to evaluate these two divergent views on the origin of the UE kimberlite and ultimately constrain the parental melt composition.

Unserpentinised and serpentinised UE kimberlite

This study examined coherent and volcaniclastic units of UE kimberlite, which are represented by both unserpentinised and partially serpentinised varieties. Regardless of their textural classification or degree of serpentinisation, both contain texturally and chemically identical olivine populations (Figs 4–7) with similar zoning patterns along with groundmass assemblages of calcite, phlogopite, Fe–Ti–Mg–Al–Cr-spinel (e.g. magnetite/Mg-magnetite, MUM, pleonaste, Cr-spinel), monticellite, perovskite, sulphides (e.g. Fe–Ni-sulphides, djerfisherite) and apatite. Daughter phase assemblages in multiphase melt inclusions hosted in olivine and groundmass minerals (spinel, monticellite, perovskite) in unserpentinised and serpentinised varieties also share a strong degree of similarity (see below). In addition, the whole-rock major element concentrations and primitive mantle normalised trace element patterns are virtually identical (Fig. 8a–c and 9; Table 2). Although there are numerous key textural, mineralogical and geochemical similarities between unserpentinised and serpentinised UE kimberlite, distinct differences are reflected by:

- Unserpentinised kimberlite contains well-preserved euhedral olivine and abundant Na–K–Cl-rich minerals (i.e. chlorides, S-bearing alkali-carbonates and sodalite) in the groundmass and H_2O-bearing phases are uncommon (≤4 vol. % phlogopite; Table 1).
- Unserpentinised kimberlite exhibits low H_2O contents (<0·6 wt %) and elevated concentrations of Na_2O (up to 6·2 wt %) and Cl (up to 6·1 wt %; Fig. 8d–h; Table 2). In contrast, serpentinised samples (i.e. serpentine–iowaite bearing) contain moderately variable H_2O (>0·6 wt % and up to 4·5 wt %), and low-Na_2O (<0·5 wt %), -Cl (<0·7 wt %) and to a lesser extent K and S concentrations (Fig. 8d–h; Table 2).

Melt inclusion perspective on kimberlite melt compositions

Melt inclusion phase assemblages from serpentinised and unserpentinised UE samples are virtually identical and dominated by (in order of relative abundance): Na–K-chlorides, Ca alkali (Na, K, Sr) carbonates, Fe–Ti–Mg–Cr–Al-spinels, Na–K-sulphates, silicates (tetraferriphlogopite, phlogopite, monticellite, humite), sulphides (Fe–Ni-bearing, djerfisherite), perovskite and apatite (Table 3; Figs 11–13). The preservation of water-soluble phases in olivine-hosted melt inclusions in serpentinised samples suggests that these inclusions were isolated from the groundmass after their entrapment.

Melt inclusions in monticellite, spinel and perovskite are interpreted to be primary as they are randomly distributed throughout their host grains and located away from fracture systems. The preservation of euhedral monticellite grains and atoll-shaped spinels suggests that these groundmass minerals crystallised *in situ*. Inclusions of Cr-spinel in olivine (Fig. 4b and d) indicate coeval crystallisation with olivine. Previous studies have shown olivine to be the earliest liquidus phase to

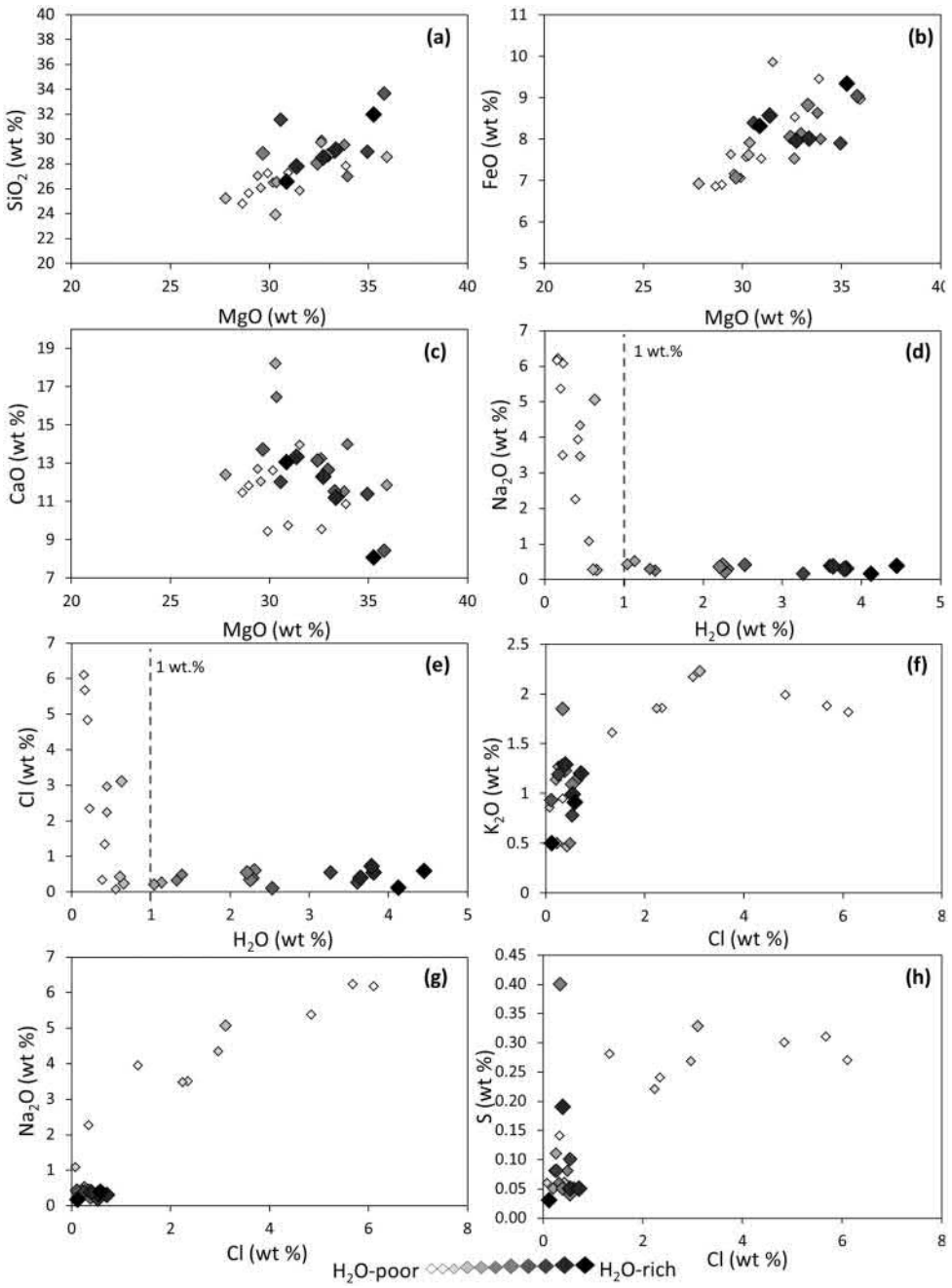

Fig. 8. Relationships in Udachnaya-East whole-rock compositions between (a–c) major element (SiO_2, FeO, CaO) oxides and MgO, (d, e) Na_2O and Cl vs H_2O, (f–h) K_2O, Na_2O and S vs Cl. Data points are arranged on a grey scale starting at white (smallest symbols), which represent the least hydrous samples, through to black (largest symbols) which indicate the most hydrous samples. The dashed grey line represents 1 wt % H_2O. Data for whole-rock compositions are presented in Table 2 and Supplementary Data Electronic Appendix 1 (see also Kamenetsky *et al.* 2012).

crystallise in kimberlites along with chromite (Mitchell, 1986, 2008; Fedortchouk & Canil, 2004). Multi-phase assemblages in primary melt inclusions in magmatic minerals are broadly similar to those in olivine (i.e. alkali-carbonate and chloride dominated; Fig. 14a–g). Therefore, primary melt inclusions provide strong evidence that alkali-carbonates and chlorides were a significant and intrinsic part of the evolved kimberlite melt during groundmass crystallisation.

Was the Udachnaya-East kimberlite contaminated?

The UE kimberlite is unique as it contains an exotic alkali-chlorine-sulphur enriched groundmass mineralogy. This has motivated a group of authors to assert that the parental magma was no different to other kimberlites worldwide (i.e. H_2O-rich, ultramafic), but was contaminated by crustal xenoliths (e.g. evaporites) and/or altered by post-emplacement sedimentary Na–Ca–Cl

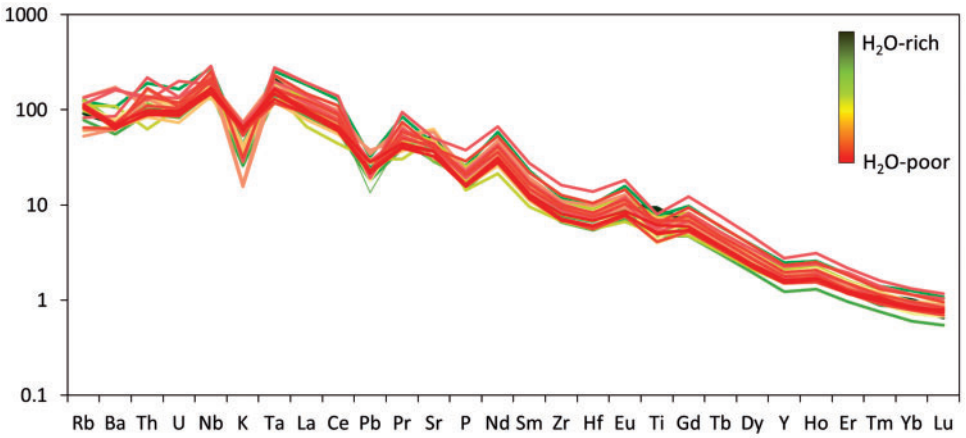

Fig. 9. Primitive mantle normalised (after Sun & McDonough, 1989) incompatible trace element patterns of the UE kimberlite. The coloured lines represent the degree of H_2O-enrichment in each sample, where dark green represents the most hydrous samples, the yellow represents intermediate, and the red represents the least hydrous. Data given are in Supplementary Data Electronic Appendix 1.

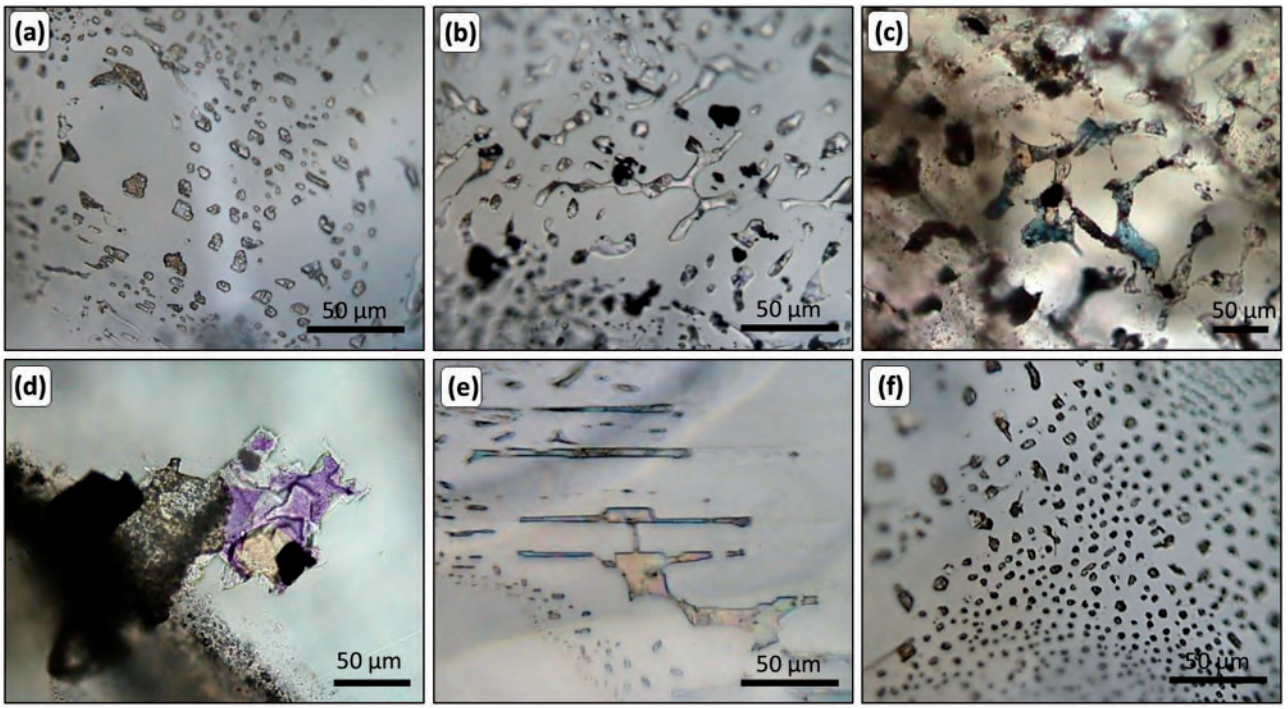

Fig. 10. Transmitted light photomicrographs showing different morphologies and abundances of micro-inclusions hosted in olivine from grain separates from serpentinised VK. Inclusions contain blue (c) and purple (d) chlorides.

brines (Kopylova *et al.*, 2013, 2016; Kostrovitskiy *et al.*, 2013). These authors have presented numerous accounts of the preservation of olivine, the low H_2O contents and origin of high alkalis, chlorine and sulphur in unserpentinised UE kimberlite rocks. Although contamination in the crust may seem like an appealing explanation for the origin of alkali-chlorine-sulphur enrichment in the UE kimberlite, the data to support these contamination models are poorly substantiated and the interpretations contain numerous contradictions (i.e. inconsistencies between successive publications, see below). In addition, previous studies of the UE kimberlite by Kopylova *et al.* (2016) are not supported by accurate designation of different kimberlite units within the pipe and the results reported are largely inconsistent with our petrographic, geochemical and melt inclusion data.

In the following sections, we demonstrate the problems associated with multiple contamination models and ultimately validate the pristine nature of the unserpentinised UE kimberlite. We combine these data with reliable field documentation of structural and textural features of individual kimberlite units and strict depth and location constraints for each kimberlite unit. A

summary of key ideas on the origin of low-H_2O, alkali-chlorine-sulphur enriched unserpentinised kimberlite by Kopylova *et al.* (2013, 2016) and Kostrovitskiy *et al.* (2013) is presented in Fig. 15.

Was crustal contamination involved?

The incorporation of country-rock xenoliths is central to the notion that magmatic assimilation caused the elevated Na, K, Cl and S contents of the UE kimberlite (Kopylova *et al.*, 2013; Kostrovitskiy *et al.*, 2013). A key argument for the non-magmatic origin of salts in the UE kimberlite, in particular large chloride 'nodules' (Kamenetsky *et al.*, 2007, 2014) is that they represent xenoliths that were entrained when the ascending magma intruded carbonate beds hosting 'karst cavities filled with epigenetic halite and gypsum and occasional sedimentary evaporites' (Kopylova *et al.*, 2016; p. 116). The resulting hybridised kimberlite melt is thought to have formed alkali-carbonates, sodalite and chlorides instead of serpentine (Kopylova *et al.*, 2013; Kostrovitskiy *et al.*, 2013). However, this magmatic assimilation model was later abandoned by Kopylova *et al.* (2016). These authors instead proposed a mechanical model for the integration and dispersal of crustal xenoliths combined with infiltrating post-emplacement crustal brines (see below) as the most influential factors controlling the composition of the UE kimberlite. Nevertheless, the entrainment of crustal halite xenoliths is contradictory to what the authors previously reported as the UE kimberlite 'does not intersect massive evaporites' (p. 77 of Kostrovitskiy *et al.* (2013)). Furthermore, there is no direct evidence for these so-called 'evaporite beds' that the UE kimberlite allegedly intruded through. Such evidence cannot be found in the reports of the open pit or underground mine, or from deep drilling (e.g. parametric and geotechnical drill holes KCC-1, 2, 3; see Figs 1 and 2 of Kamenetsky *et al.* (2014)).

Origin of alkalis, chlorine and sulphur in melt inclusions

The entrapment of secondary melt inclusions in olivine in the UE kimberlite has been employed as a principal constraint to support the alkali-chlorine-sulphur enrichment of the parental kimberlite magma (Kamenetsky *et al.*, 2004, 2009*a*, 2012, 2014). However, Kopylova *et al.* (2013) and Kostrovitskiy *et al.* (2013) advocated that these secondary inclusions in olivine resulted from explosive and thermal cracking of grains and subsequent entrapment of late residual melts and fluids that equilibrated with kimberlite melts in the subsurface. The enrichment

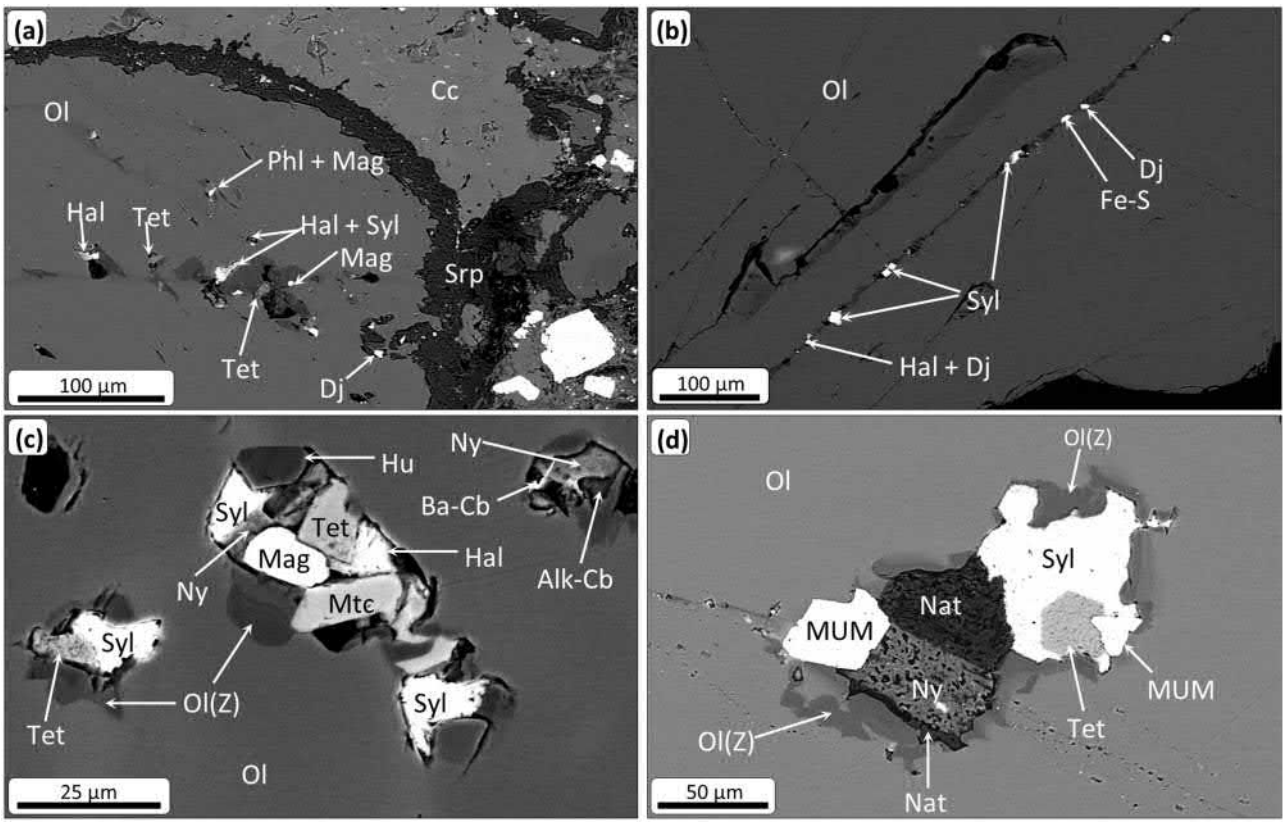

Fig. 11. Back-scattered electron (BSE) SEM images of multiphase secondary melt inclusions in olivine (Ol) from serpentinised (a, b) VK and (c, d) AC. (a, b) Trails of secondary inclusions composed of halite (Hal), tetraferriphlogopite (Tet), sylvite (Syl), phlogopite (Phl), magnetite (Mag), djerfisherite (Dj) and Fe-sulphides (Fe–S). (c, d) Large multiphase inclusions in olivine composed of tetraferriphlogopite, sylvite, nyerereite (Ny), magnetite, monticellite (Mtc), Ba-carbonate (Ba-Cb), humite (Hu), alkali (Na, K) carbonate (Alk-Cb), magnesian ulvöspinel-magnetite (MUM) and natrite (Nat). Inclusions are commonly surrounded by patchy zoning of olivine (Ol(Z)) which is characterised by an elevated Fo content.

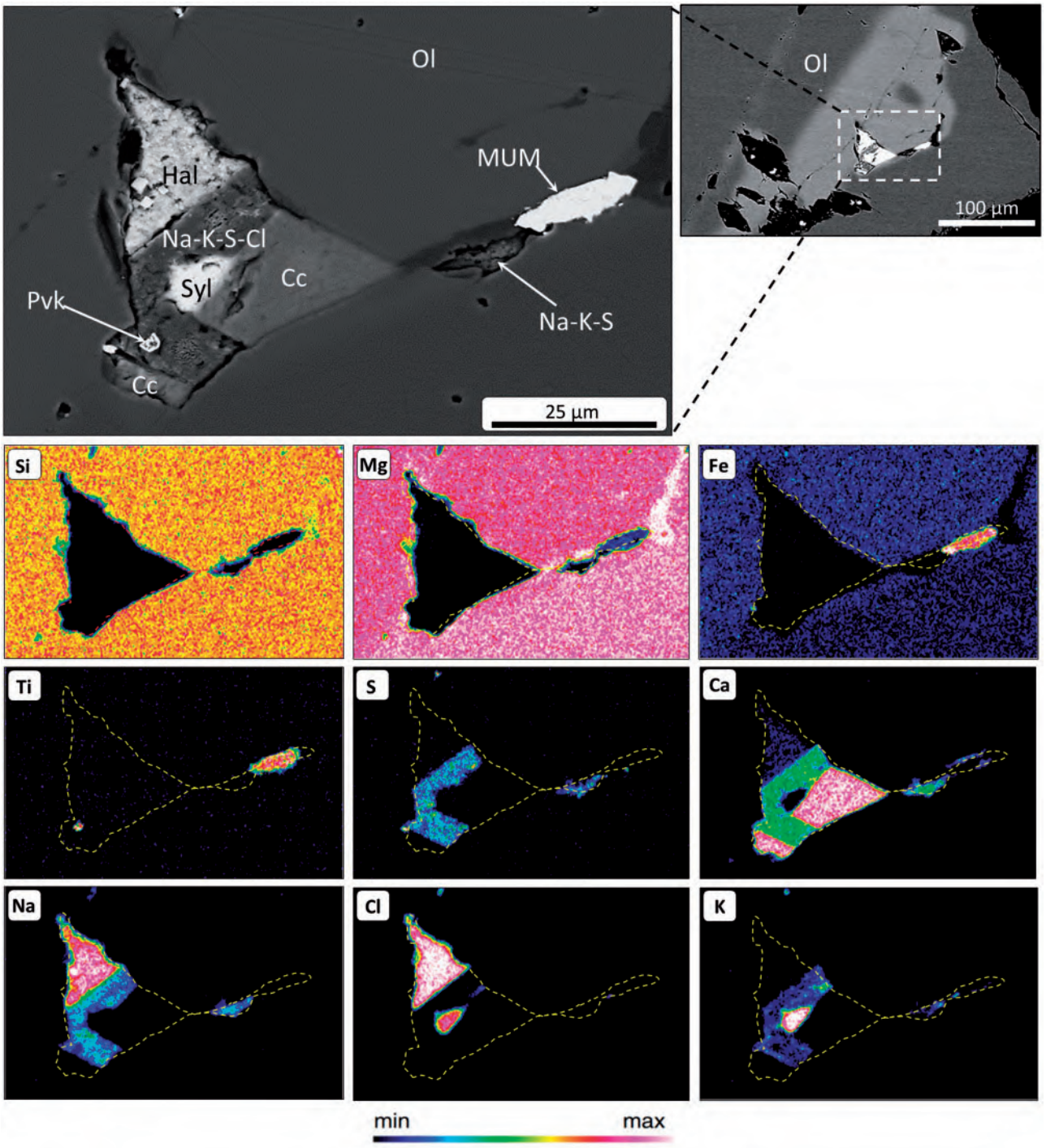

Fig. 12. Back-scattered electron SEM image and X-ray elemental maps of a secondary multiphase melt inclusion in olivine (Ol) from serpentinised AC. Detected minerals include: halite (Hal), perovskite (Pvk), calcite (Cc), sylvite (Syl), magnesian ulvöspinel-magnetite (MUM) and unidentified Na–K–S±Cl-bearing phases. The red/yellow line indicates the boundary of the inclusion.

of Na, K, Cl and S in these olivine-hosted melt inclusions was ascribed to the supposed crustal assimilation by the UE kimberlite magma (Kopylova *et al.*, 2013; Kostrovitskiy *et al.*, 2013). However, Kopylova *et al.* (2013; pp. 12) highlighted an inherent dilemma in the magmatic assimilation model, as 'this should not be appropriate for pyroclastic rocks, since the assimilation could only take place at some deeper level prior to degassing and explosive fragmentation. Only an in situ process that affected kimberlites after or during emplacement could be responsible for the correlation'. In a later study by the same authors, an alternative model was introduced for the mechanical incorporation of Na–Cl enrichment in olivine-hosted inclusions, where 'petrographic observations find such inclusions only in discrete grains in one type of PK (olivine-rich PK;

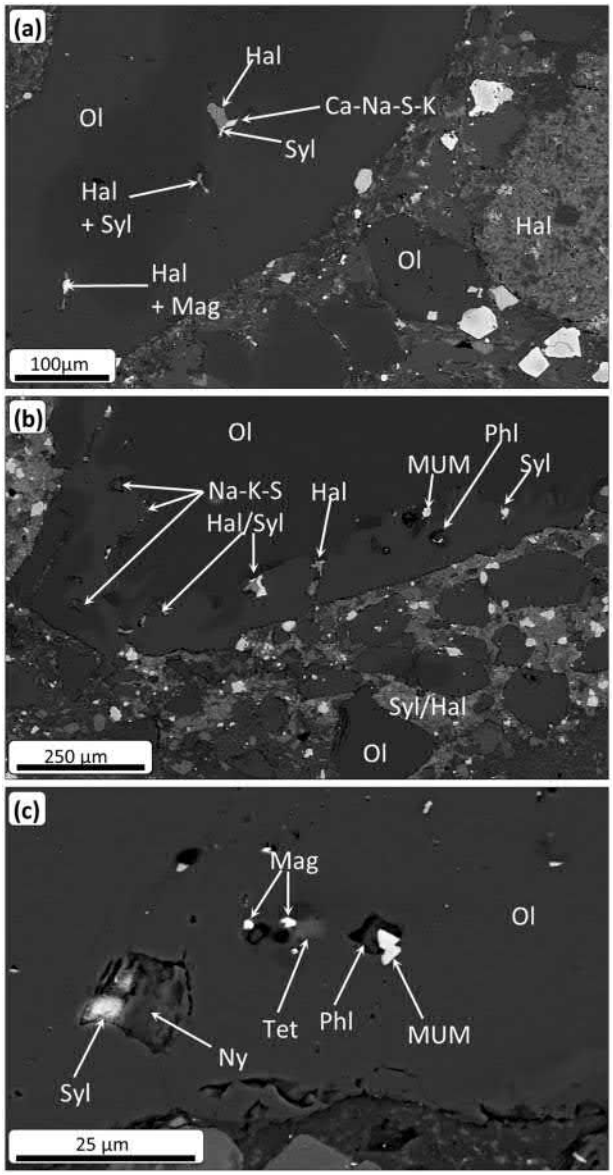

Fig. 13. Back-scattered electron (BSE) SEM images of multiphase inclusions in olivine (Ol) from unserpentinised VK. Multiphase inclusions in olivine are composed of halite (Hal), sylvite (Syl), magnetite (Mag), magnesian ulvöspinel-magnetite (MUM), phlogopite (Phl), tetraferriphlogopite (Tet), nyereereite (Ny) and unidentified Ca–Na/K–S-bearing phases.

pyroclastic kimberlite*)*, where explosive emplacement fractures olivine clasts and mixes them with salt-rich ash, which could plastically penetrate the cracks and deposit halite along the network of fractures. Halite inclusions do not occur in fractures connecting to the calcite matrix or in CK (coherent kimberlite*)* olivine*′*. (Kopylova *et al.*, 2016; p. 132).

Our study clearly demonstrates that alkali-chlorine-sulphur enrichment is not restricted to olivine-hosted secondary inclusions from 'pyroclastic' kimberlite, but is present in both CK and VK UE units at wide range of depth intervals (400–520 m). In our view, the notion of 'explosive fracturing' of olivine inadequately explains the development of secondary melt inclusions in CK (i.e. veins and dykes), which did not experience explosive fragmentation. We propose that the development of secondary melt inclusions in olivine was the result of the rapid ascent and decompression of kimberlite magma causing fracturing (Brett *et al.*, 2015) and rounding (or milling) of grains by mechanical abrasion (Reid *et al.*, 1975; Arndt *et al.*, 2010). Fractures in olivine were then penetrated by kimberlite melt (Brett *et al.*, 2015) and later sealed during olivine crystallisation (Fedortchouk & Canil, 2004; Mitchell, 2008; Brett *et al.*, 2009), forming inclusion trails (Kamenetsky *et al.*, 2008; Fig. 16). In addition, primary melt inclusions in spinel, monticellite and perovskite were entrapped *in situ* during crystallisation of the host-mineral, demonstrating that the crystallising kimberlite melt was enriched (i.e. relative to serpentinised kimberlite) in alkalis, chlorine and sulphur.

Similar alkali-halogen-sulphur enrichment trends have been indicated by melt inclusions in olivine and groundmass minerals (e.g. spinel, perovskite, apatite) in previous studies of the UE kimberlite (Golovin *et al.*, 2003, 2007, 2017*a*; Kamenetsky *et al.*, 2004, 2009*a*, 2012; Mernagh *et al.*, 2011) and other localities worldwide (e.g. Gahcho Kué, Jericho; Aaron (Kamenetsky *et al.*, 2009*a*; Mernagh *et al.*, 2011); Leslie (Kamenetsky *et al.*, 2009*a*; Abersteiner *et al.*, 2017*b*), Koala (Kamenetsky *et al.*, 2013) and Roger (Abersteiner *et al.*, 2017*c*) pipes in Canada; Pipe 1 in Finland (Abersteiner *et al.*, 2017*b*); Majuagaa dyke in West Greenland (Kamenetsky *et al.*, 2009*a*; Mernagh *et al.*, 2011); Wesselton pipe (Mernagh *et al.*, 2011), Bultfontein (Giuliani *et al.*, 2017) and Venetia (Abersteiner *et al.*, 2017*a*) kimberlites in South Africa. Previous experiments on olivine-hosted melt inclusions from Udachnaya-East and other kimberlites worldwide (e.g. Kamenetsky *et al.*, 2004, 2009, 2013, 2014; Golovin *et al.*, 2018) showed that these inclusions typically homogenise at 660–760°C at 1 atm. Upon cooling the melt separates into carbonate and chloride immiscible components and crystallises completely at 200–160°C.

The study of melt inclusions provides substantial evidence to show that alkali-chlorine-sulphur enrichment is an intrinsic feature of variably differentiated kimberlite melts, originating in the mantle. A crustal contamination model is unable to comprehensively explain the occurrence of this widespread alkali-chlorine-sulphur enrichment trend in other kimberlites that intruded diverse lithologies in different cratons.

Evidence against post-emplacement alteration by crustal brines

Another major argument against a magmatic origin for alkali-chlorine-sulphur enrichment in the groundmass of the UE kimberlite has been ascribed to interactions with crustal Na–Ca–Cl brines (Kopylova *et al.*, 2013, 2016; Kostrovitskiy *et al.*, 2013). In our view, the preservation of a water-soluble mineralogy in the presence of infiltrating fluids without olivine alteration renders such a contamination model paradoxical. The interaction

Table 3: Summary of mineral phases hosted in multiphase melt inclusions in olivine and groundmass monticellite, spinel, perovskite and calcite from serpentinised and unserpentinised Udachnaya-East kimberlite

Mineral	Ideal Formulae	Abundance (%)
Olivine		
Halite/Sylvite	NaCl/KCl	33
Alkali carbonates	Ca–Mg–Na–K–Ba–Sr ± S Shortite: $Na_2Ca_2(CO_3)_3$	28
Spinel	Fe–Ti–Mg–Cr–Al	8
Alkali-sulphates	Na–K: Arcanite (K_2SO_4)	7
Tetraferriphlogopite	$KMg_3Fe^{3+}Si_3O_{10}(OH)_2$	5
Sulphides	Fe–Ni: Djerfisherite $(K_6Na(Fe^{2+},Cu,Ni)_{25}S_{26}Cl)$	5
Phlogopite	$KMg_3(AlSi_3O_{10})(F,OH)_2$	4
Monticellite	$CaMgSiO_4$	3
Perovskite	$CaTiO_3$	3
Humite	$(Mg,Fe)_7(SiO_4)_3(F,OH)_2$	2
Apatite	$Ca_5(PO_4)_3(F,Cl,OH)$	2
Monticellite, Spinel, Perovskite		
Sylvite/Halite	KCl/NaCl	40
Alkali carbonates	Ca–Mg–Na–K	30
Fe–Mg–Ti-spinel	Fe–Mg–Ti	10
Alkali-sulphates	Na-K	10
Phlogopite	$KMg_3(AlSi_3O_{10})(F,OH)_2$	5
Perovskite	$CaTiO_3$	5
Calcite		
Halite/Sylvite	NaCl/KCl	55
Alkali-carbonates	Ca–Mg–Na–K ± S	40
Djerfisherite	$K_6Na(Fe^{2+},Cu,Ni)_{25}S_{26}Cl$	5

The abundance (%) represents the average proportion of each phase hosted within each mineral.

between the SFUE kimberlite and crustal brines is thought to have impeded serpentinisation (Kostrovitskiy *et al.*, 2013) where 'salts and alkali carbonate, rather than secondary serpentine, may have precipitated in breccia voids and replaced original groundmass minerals' (Kopylova *et al.*, 2013; p. 13). Furthermore, Kopylova *et al.* (2016) considered that 'Na-rich brines dissolve calcite and replace it with fine needles of Na-Ca carbonates' (p. 126), and 'the serpentine of the PKs (pyroclastic kimberlites) matrix (<3%) may have been replaced with secondary Na-Ca carbonate' (p. 132). However, this is in stark contrast to our petrographic observations, which show that olivine maintains near perfect euhedral crystal shapes (Fig. 4a and b) with sharp contacts with the groundmass and no textures that indicate secondary replacement by serpentine, calcite or alkali-carbonates.

It was proposed by Kopylova *et al.* (2013, 2016) and Kostrovitskiy *et al.* (2013) that the Udachnaya-West (UW) and UE intersected different aquifers with different flow rates and compositions. The aquifer in contact with the UW pipe was considered to be Ca–Cl in composition and have a low flow rate, whereas the UE pipe intersected a different aquifer that was Na–Cl in composition and had a high hydraulic pressure (Kopylova *et al.*, 2013, 2016). Nevertheless, crustal brines do not adequately explain why there is no similar ~400–500 m brine-induced 'SFUE' in the UW kimberlite, which is adjacent to UE. Furthermore, these supposed brines represent present day aquifers and cannot take into account ~360 Myr of hydrology in the host sedimentary succession, or shifting brine levels and erosion that has occurred since kimberlite emplacement.

One of the most remarkable features which is inconsistent with secondary alteration by crustal brines is the almost anhydrous (<0·6 wt %) geochemical character of the unserpentinised UE kimberlite (Fig. 8d and e; Table 2). Kopylova *et al.* (2013) and Kostrovitskiy *et al.* (2013) ascribed the low H_2O of unserpentinised UE kimberlite to high-salinity fluids which resulted from magmatic assimilation. This fluid was considered to have caused a reduction in serpentine stability and the subsequent removal of H_2O from the melt. Alternatively, Kostrovitskiy *et al.* (2013) proposed that the absence of serpentine was due a uniquely H_2O-poor primary UE melt, which was previously advocated by Kamenetsky *et al.* (2007*a*, 2009*a*, 2012). In their sudden departure from magmatic assimilation of crustal evaporite xenoliths model, Kopylova *et al.* (2016) proposed that H_2O and CO_2 were removed during explosive fragmentation of pyroclastic kimberlite, but remained in CK. This contradicts our results on the unserpentinised CK sample K24–04A (Fig. 3), which is essentially anhydrous (≤0·56 wt % H_2O) and CO_2-rich (up to 9·85 wt %; Table 2). Furthermore, the majority of kimberlite samples analysed by Kopylova *et al.* (2016) were derived from 565–585 m from mine stockpiles. This is below the SFUE depth interval and where modern brines are thought to be present (Fig. 2). Inexplicably, Kopylova *et al.* (2016) abandoned the term for the 400–500m 'SFUE' depth horizon predefined by their earlier studies (Kopylova *et al.*, 2013; Kostrovitskiy *et al.*, 2013). Not only in this study, the 'SFUE' is the only depth horizon where we observed H_2O-poor and alkali-chlorine-sulphur-enriched unserpentinised kimberlite. It is noteworthy that the majority (i.e. 24 out of 36) of analyses of SFUE kimberlite analysed by Kostrovitskiy *et al.* (2013) contain $H_2O \geq 1$ wt % (up to 5·49 wt %). These geochemical data were not supported by any petrographic images to demonstrate the absence of serpentine in the groundmass and are inconsistent with our results, which show that as H_2O-content increases (>0·6 wt %), serpentine starts to appear in the groundmass and increases in abundance with increasing H_2O-content.

We consider that unserpentinised water-soluble alkali-chlorine-sulphur-rich groundmass phases could only be preserved if the emplaced kimberlite rocks were unaffected by hydrous alteration. In this study, partially serpentinised samples were derived from 400–420m, which coincides with the roof of the SFUE, and 480–520 m, which coincides with depths at which modern brines occur (~510 m). In contrast, unserpentinised samples were derived from 440–500 m, which is above this brine horizon (Fig. 2; also see fig. 2 of Kitayama *et al.* (2017) and fig. 8 of Alexeev *et al.* (2007)) and within the SFUE defined by Kopylova *et al.* (2013) and Kostrovitskiy *et al.* (2013). Incipient serpentinisation corresponds with the complete absence of water-soluble minerals (e.g.

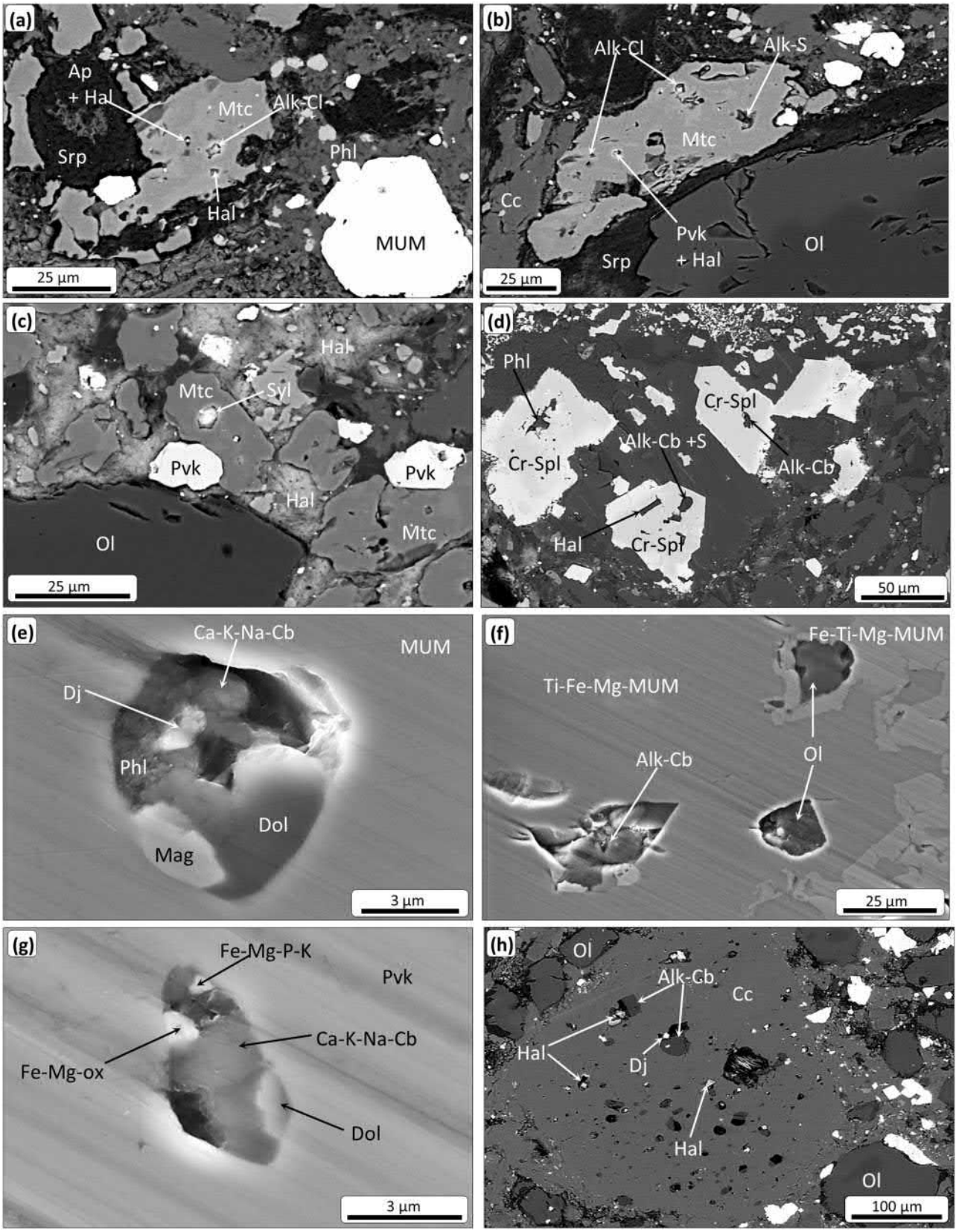

Fig. 14. Back-scattered electron (BSE; a–d and h) and secondary electron (SE; e–g) SEM images of primary multiphase melt inclusions in (a, b) monticellite from serpentinised VK, (c) monticellite from unserpentinised VK, (d) Cr-spinel (Cr-Spl) in unserpentinised VK, (e, f) magnesian ulvöspinel-magnetite (MUM) and (g) perovskite (Pvk) in unserpentinised CK, and (h) groundmass calcite (Cc) in serpentinised VK. Detected phases within inclusions include: apatite, (Ap), perovskite, alkali (Na, K) chlorides (Alk-Cl), alkali (Na, K) sulphur-bearing phases (Alk-S), phlogopite (Phl), alkali (Na, K) carbonate, halite (Hal), djerfisherite (Djer), dolomite (Dol), magnetite (Mag), Fe–Mg-oxide (Fe–Mg-ox) and unidentified Fe–Mg–P–K-bearing phases. MUM-spinel also contains monocrystalline inclusions of olivine (Ol).

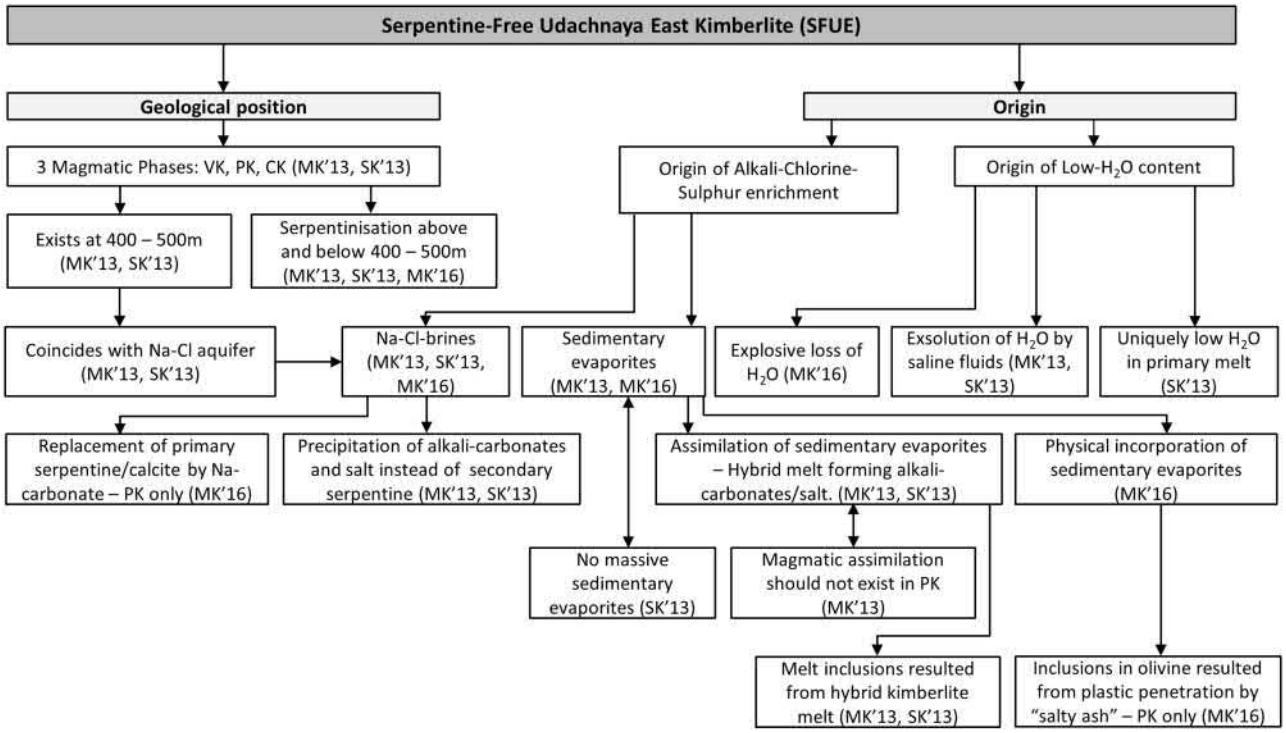

Fig. 15. Summary of the ideas presented by Kopylova *et al.* (2013, 2016; MK'13, MK'16) and Kostrovitskiy *et al.* (2013; SK'13) on the geological position and origin of the low-H_2O, alkali-chlorine-sulphur enriched unserpentinised Udachnaya-East kimberlite. VK, volcaniclastic kimberlite; PK, pyroclastic kimberlite; CK, coherent kimberlite.

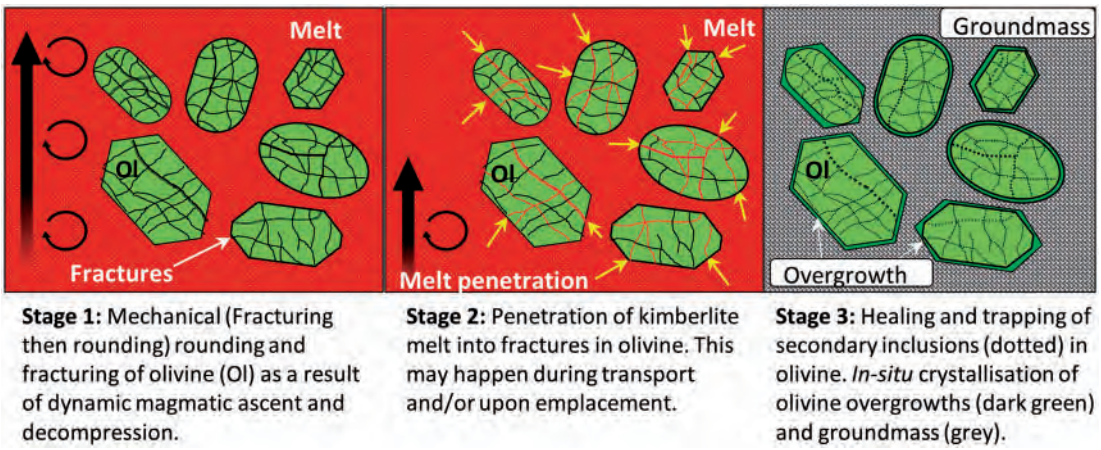

Fig. 16. Schematic diagram of the entrapment of secondary olivine-hosted inclusions. Stage (1): Fracturing of olivine during magma ascent. Stage (2): Penetration of kimberlite melt into olivine fractures during transport and, or, upon emplacement. (3) Healing and trapping of inclusions in olivine and crystallisation of olivine overgrowths around pre-existing grains.

chlorides, S-bearing alkali-carbonates) in the groundmass, which is reflected by significantly lower concentrations of Na_2O, K_2O, Cl and S (Table 2) than in unserpentinised samples. Chlorine is retained in the groundmass to some extent during serpentinisation where it is fixed in hydrothermal iowaite.

In addition, sulphur isotope and bulk S analyses have shown that groundmass sulphates and sulphides in the unserpentinised 'salty' UE kimberlite do not conform with an external brine or assimilation of country-rock origin and are instead consistent with late-stage magmatic crystallisation (D'Eyrames *et al.*, 2017; Kitayama *et al.*, 2017). It is well-established that $^{37}Cl/^{35}Cl$ ratios in crustal rocks differ only slightly from those in mantle-derived rocks and meteorites (Sharp *et al.*, 2007), whereas sulphur isotope ratios differ significantly. Sulphur isotopes were studied in: (i) VK and CK unserpentinised kimberlite units; (ii) salt-bearing sediment samples; (iii) brine containing sulphates from a depth of 750 m in a drill hole 1 km south of Udachnaya; and (iv) hydrothermal sulphides and sulphates from Udachnaya pipe. Kitayama *et al.* (2017) concluded that,

'salty kimberlites from Udachnaya-East were not contaminated by brine infiltration, hydrothermal alteration or the assimilation of known salt-rich country rocks' (p. 328). Similarly, combined Sr-, Nd- and Pb-isotopic data support a magmatic (i.e. mantle-derived) origin for chlorides and alkali-carbonates from unserpentinised kimberlite rocks (Maas *et al.*, 2005; Kamenetsky *et al.*, 2009*a*; 2014).

Perhaps the most substantial evidence against crustal brine contamination in the UE kimberlite is from melt inclusions. Primary and secondary inclusions from both unserpentinised and serpentinised samples clearly demonstrate that the kimberlite melt was already enriched in alkalis, chlorine and sulphur (Figs 11–14) prior to magma solidification and post-emplacement alteration.

Preservation of the unserpentinised Udachnaya-East kimberlite horizon

The preservation of the unserpentinised kimberlite horizon at Udachnaya-East may have one or several explanations:

(i) Unserpentinised kimberlite units are located in the central part of the pipe and thus are relatively isolated from external groundwater (Fig. 2). Furthermore, the unserpentinised kimberlite horizon is located above and below two modern aquifers (Fig. 2).

(ii) Chlorides are characterised by high thermal conductivity and plastic behaviour which can be self-sealing should fractures develop (Roxburgh, 1987). Chlorides in the UE kimberlite may have formed a protective ductile seal in the kimberlite, which prevented the ingress of water (Kamenetsky *et al.*, 2012). An example of the protective nature of chlorides is in the use of evaporites/rock salt used as disposal sites for high level nuclear waste in Germany (Roxburgh, 1987; Kim *et al.*, 1996; Kim & Grambow, 1999). In the case of Udachnaya-East, it is likely that once this chloride seal is completely breached by groundwater, the kimberlite is prone to alteration (Kamenetsky *et al.*, 2012).

Post-emplacement alteration: implications for kimberlites worldwide

The strong degree of petrographic, geochemical and melt inclusion similarity between unserpentinised and serpentinised UE kimberlite suggests that both varieties crystallised from the same magma, but were subject to different post-emplacement processes. Based on our observations of the UE kimberlite, we interpret the unserpentinised samples to represent pristine, unaltered kimberlite. In contrast, partially serpentinised samples were altered by infiltrating post-magmatic external fluids dissolving groundmass alkali-carbonates, chlorides and sulphates and instead forming secondary calcite, serpentine and iowaite. Evidence for an initially chlorine-bearing groundmass of the serpentinised kimberlite is signified by: (i) the preservation of Cl-bearing djerfisherite, which is a relatively stable mineral during post-magmatic alteration (Sharygin *et al.*, 2011), and (ii) secondary iowaite, which resulted from the release of Mg–Fe cations during olivine dissolution (Stripp *et al.*, 2006; Evans *et al.*, 2013) combining with dissolved chlorine (Kopylova *et al.*, 2016), which in our view was derived from the groundmass halite and sylvite.

The instability and rapid degradation of alkali-carbonates and chlorides in the UE unserpentinised kimberlite units could be analogous to the freshly erupted Oldoinyo Lengai (Tanzania) natrocarbonatite lavas, where significant mineralogical and compositional changes can occur within days to months upon exposure to the atmosphere (Dawson *et al.*, 1987; Dawson, 1993; Zaitsev & Keller, 2006). Alkalis are rapidly leached from the carbonatitic rocks during alteration and consequently the only evidence of the initially alkali-rich groundmass mineralogy is preserved in melt inclusions. In the case of the Kerimasi (Tanzania; Zaitsev, 2010; Guzmics *et al.*, 2011), Tinderet (Kenya; Zaitsev *et al.*, 2013) and Oka (Canada; Chen *et al.*, 2013) calciocarbonatite complexes, Na_2O and K_2O are significantly depleted in bulk-rock compositions but are highly enriched in crystal and melt inclusions hosted by groundmass phases (e.g. magnetite, apatite). The resolution to this paradox is that the emplaced carbonatite rocks crystallised from an initially alkali-rich (or natrocarbonatite) magma, but were subjected to extensive weathering and/or metasomatism (Zaitsev, 2010; Guzmics *et al.*, 2011; Chen *et al.*, 2013; Zaitsev *et al.*, 2013). A similar trend of alkali, halogen and sulphur enrichment is recorded by melt inclusions in olivine and groundmass minerals in our samples, as well as in other studies of the UE kimberlite and other localities worldwide (see above). By analogy with the alteration processes of natrocarbonatites, we consider that it is likely that alkalis, chlorine and sulphur were significantly leached from the kimberlites during syn- and/or post-emplacement alteration.

Although Oldoinyo Lengai natrocarbonatite lavas and the reconstructed melt inclusion compositions from kimberlites are inferred to be analogous, kimberlites and carbonatites generally experience different styles of eruption. In many cases, kimberlite volcanoes have highly dynamic eruptions (e.g. Skinner & Marsh, 2004; Sparks *et al.*, 2006) with explosive flows through conduits, but may also erupt weakly and form lava flows (Brown *et al.*, 2012). In contrast, the Oldoinyo Lengai natrocarbonatite lavas erupt effusively (Keller & Krafft, 1990; Kervyn *et al.*, 2008). In our view, the presence of entrained mantle silicates (e.g. olivine, orthopyroxene) in kimberlites is fundamental to CO_2 degassing and ultimately to their rapid ascent, where assimilation of silicates and decompression can cause a catastrophic reduction in carbon dioxide solubility (Brooker *et al.*, 2011; Russell *et al.*, 2012; Kamenetsky & Yaxley, 2015; Moussallam *et al.*, 2016) in the melt, or olivine may react with the carbonate component of the melt upon emplacement to liberate CO_2 (Abersteiner *et al.*, 2017*b*). The absence of mantle silicates in

Oldoinyo Lengai means that such volatile degassing or decarbonation reaction scenarios are unlikely.

Abundant alkali-chlorine-bearing multiphase inclusions hosted in groundmass calcite are primary in both serpentinised and unserpentinised samples (Fig. 14h). Groundmass calcite is generally considered to be primary magmatic (Dawson, 1980; Mitchell, 1986; Armstrong *et al.*, 2004; Wilson *et al.*, 2007; Giuliani *et al.*, 2014), but has also been ascribed to external post-magmatic fluids (Exley & Jones, 1983; Podvysotskiy, 1985; Armstrong *et al.*, 2004; Giuliani *et al.*, 2014, 2017). The remarkable compositional similarity of inclusions in magmatic groundmass calcite to melt inclusions hosted in olivine, monticellite, spinel and perovskite suggests that these calcite-hosted inclusions represent relics of the late-stage differentiated kimberlite melt that evolved towards incompatible element enriched, carbonatitic compositions, from which Si and Al were removed due to fractional crystallisation (i.e. olivine, spinel, phlogopite formation).

CONCLUSIONS

Although the composition and origin of the proto-kimberlite melt is beyond the scope of this study, we consider alkali-chlorine-sulphur enrichment (i.e. relative to serpentinised kimberlite) in melt inclusions to be a function of kimberlite melt evolution. Progressive crystallisation of silicate phases (e.g. olivine) during groundmass crystallisation removed SiO_2 and MgO from the melt, resulting in a melt shift towards carbonatitic compositions that concentrated alkalis, chlorine and sulphur. This differentiation process ultimately crystallised alkali-carbonates, chlorides, sulphates and sulphides in the UE kimberlite groundmass. The initial H_2O-contents of the parental UE kimberlite magma is ultimately dependent on whether serpentine is interpreted to be a late-magmatic (i.e. crystallises from deuteric fluids) phase or secondary product resulting from alteration. In our view, these water-soluble alkali- and chlorine-bearing phases could only be preserved if the parental magma was H_2O-poor. This implies that serpentine and iowaite in the Udachnaya-East kimberlite were formed as a secondary product (i.e. post-magmatic) due to infiltrating external fluids.

Based on the composition of the unserpentinised UE kimberlite groundmass and melt inclusions reported here, we suggest that the unserpentinised UE kimberlite is pristine and crystallised from an H_2O-poor, Si–Na–K–Cl–S-bearing, carbonate-rich melt, which could be analogous to the modern natrocarbonatite lavas observed at Oldoinyo Lengai. These results support the notion that parental proto-kimberlite melt for the Udachnaya-East was essentially anhydrous, SiO_2-poor and was dominated by carbonates and enriched in lithophile trace elements, alkalis (Na, K), halogens (Cl) and sulphur.

ACKNOWLEDGMENTS

This study forms part of A.A's Ph.D and was supported by an Australian Postgraduate Award (APA). This work has benefitted from comments by two reviewers, Geoffrey Howarth and Lucy Porritt, and efficient editorial handling by James Mungall.

FUNDING

This work was supported by Australian Research Council (ARC) Discovery grant (DP130100257, 2013–2015) and University of Tasmania (New Star Professorship, 2010–2014) to V. Kamenetsky. AVG was supported by Russian state assignment project No. 0330–2016-0006.

SUPPLEMENTARY DATA

Supplementary data are available at *Journal of Petrology* online.

REFERENCES

Abersteiner, A., Giuliani, A., Kamenetsky, V. S. & Phillips, D. (2017a). Petrographic and melt-inclusion constraints on the petrogenesis of a magmaclast from the Venetia kimberlite cluster, South Africa. *Chemical Geology* **455**, 331–341.

Abersteiner, A., Kamenetsky, V. S., Graham Pearson, D., Kamenetsky, M., Goemann, K., Ehrig, K. & Rodemann, T. (2017b). Monticellite in group-I kimberlites: Implications for evolution of parental melts and post-emplacement CO_2 degassing. *Chemical Geology* **478**, 76–88.

Abersteiner, A., Kamenetsky, V. S., Kamenetsky, M., Goemann, K., Ehrig, K. & Rodemann, T. (2017c). Significance of halogens (F, Cl) in kimberlite melts: Insights from mineralogy and melt inclusions in the Roger pipe (Ekati, Canada). *Chemical Geology* **478**, 148–163.

Afanasyev, A. A., Melnik, O., Porritt, L., Schumacher, J. C. & Sparks, R. S. J. (2014). Hydrothermal alteration of kimberlite by convective flows of external water. *Contributions to Mineralogy and Petrology* **168**, 1038–1055.

Agashev, A. M., Pokhilenko, N. P., Cherepanova, Y. V. & Golovin, A. V. (2010). Geochemical evolution of rocks at the base of the lithospheric mantle: Evidence from study of xenoliths of deformed peridotites from kimberlite of the Udachnaya pipe. *Doklady Earth Sciences* **432**, 746–749.

Alexseev, S. V. (2009). *Cryogeological Systems of the Yakutian Diamondiferous Province*. Novosibirsk: Academic Publishing House "GEO", p. 319.

Alexeev, S. V., Alexeeva, L. P., Borisov, V. N., Shouakar-Stash, O., Frape, S. K., Chabaux, F. & Kononov, A. M. (2007). Isotopic composition (H, O, Cl, Sr) of ground brines of the Siberian Platform. *Russian Geology and Geophysics* **48**, 225–236.

Armstrong, J. P., Wilson, M., Barnett, R. L., Nowicki, T. & Kjarsgaard, B. A. (2004). Mineralogy of primary carbonate-bearing hypabyssal kimberlite, Lac de Gras, Slave Province, Northwest Territories, Canada. *Lithos* **76**, 415–433.

Arndt, N. T., Guitreau, M., Boullier, A. M., le Roex, A., Tommasi, A., Cordier, P. & Sobolev, A. (2010). Olivine, and the Origin of Kimberlite. *Journal of Petrology* **51**, 573–602.

Becker, M. & le Roex, A. P. (2006). Geochemistry of South African on- and off-craton, Group I and Group II kimberlites:

petrogenesis and source region evolution. *Journal of Petrology* **47**, 673–703.

Brett, R. C., Russell, J. K. & Moss, S. (2009). Origin of olivine in kimberlite: Phenocryst or impostor? *Lithos* **112S**, 201–212.

Brett, R. C., Russell, J. K., Andrews, G. D. M. & Jones, T. J. (2015). The ascent of kimberlite: Insights from olivine. *Earth and Planetary Science Letters* **424**, 119–131.

Brooker, R., Sparks, R., Kavanagh, J. & Field, M. (2011). The volatile content of hypabyssal kimberlite magmas: some constraints from experiments on natural rock compositions. *Bulletin of Volcanology* **73**, 959–981.

Brown, R. J., Manya, S., Buisman, I., Fontana, G., Field, M., Mac Niocaill, C., Sparks, R. S. J. & Stuart, F. M. (2012). Eruption of kimberlite magmas: physical volcanology, geomorphology and age of the youngest kimberlitic volcanoes known on earth (the Upper Pleistocene/Holocene Igwisi Hills volcanoes, Tanzania). *Bulletin of Volcanology* **74**, 1621–1643.

Buse, B., Schumacher, J., Sparks, R. & Field, M. (2010). Growth of bultfonteinite and hydrogarnet in metasomatized basalt xenoliths in the B/K9 kimberlite, Damtshaa, Botswana: insights into hydrothermal metamorphism in kimberlite pipes. *Contributions to Mineralogy and Petrology* **160**, 533–550.

Chen, W., Kamenetsky, V. S. & Simonetti, A. (2013). Evidence for the alkaline nature of parental carbonatite melts at Oka complex in Canada. *Nature Communications* **4**, 2687.

Clement, C. R. (1982). *A Comparative Geological Study of Some Major Kimberlite Pipes in the Northern Cape and Orange Free State*. Cape Town: University of Cape Town, p. 431.

Clement, C. R., Skinner, E. M. W. & Scott Smith, B. H. (1984). Kimberlite re-defined, *The Journal of Geology* **32**, 223–228.

D'Eyrames, E., Thomassot, E., Kitayama, Y., Golovin, A., Korsakov, A. & Ionov, D. (2017). A mantle origin for sulfates in the unusual "salty" Udachnaya-East kimberlite from sulfur abundances, speciation and their relationship with groundmass carbonates. *Bulletin De La Société Géologique De France* **188**, 6–11.

Dawson, J. B. (1980). *Kimberlites and Their Xenoliths*. New York, NY: Springer.

Dawson, J. B. (1993). A supposed sövite from Oldoinyo Lengai, Tanzania: result of extreme ateration of alkali carbonatite lava. *Mineralogical Magazine* **57**, 93–101.

Dawson, J. B., Garson, M. S. & Roberts, B. (1987). Altered former alkalic carbonatite lava from Oldoinyo Lengai, Tanzania: inferences for calcite carbonatite lavas. *Geology* **15**, 765–768.

Doucet, L. S., Ionov, D. A., Golovin, A. V. & Pokhilenko, N. P. (2012). Depth, degrees and tectonic settings of mantle melting during craton formation: inferences from major and trace element compositions of spinel harzburgite xenoliths from the Udachnaya kimberlite, central Siberia. *Earth and Planetary Science Letters* **359–360**, 206–218.

Egorov, K. N., Kornilova, V. P., Safronov, A. F. & Filippov, N. D. (1986). Micaceous kimberlite from the Udachnaya-East pipe. *Doklady of the Academy of Sciences of the USSR* **291**, 199–202 (In Russian).

Egorov, K. N., Bogdanov, G. V., Lashkevitch, V. V., Medvedeva, T. I. & Tikhonova, G. A. (1991). Generations and physical-chemical conditions of serpentinization in kimberlite, *Proceedings of the Russian Mineralogical Society* **120**, 1–12.

Evans, B. W., Hattori, K. & Baronnet, A. (2013). Serpentinite: what, why, where? *Elements* **9**, 99–106.

Exley, R. A. & Jones, A. P. (1983). 87Sr/86Sr in kimberlitic carbonates by ion microprobe: Hydrothermal alteration, crustal contamination and relation to carbonatite. *Contributions to Mineralogy and Petrology* **83**, 288–292.

Fedortchouk, Y. (2015). Diamond resorption features as a new method for examining conditions of kimberlite emplacement. *Contributions to Mineralogy and Petrology* **170**, 36pp.

Fedortchouk, Y. & Canil, D., (2004). Intensive variables in kimberlite magmas, Lac de Gras, Canada and implications for diamond survival. *Journal of Petrology* **4**. 1725–1745.

Fedortchouk, Y., Matveev, S. & Carlson, J. A. (2010). H_2O and CO_2 in kimberlitic fluid as recorded by diamonds and olivines in several Ekati Diamond Mine kimberlites, Northwest Territories, Canada. *Earth and Planetary Science Letters* **289**, 549–559.

Giuliani, A., Phillips, D., Kamenetsky, V. S., Fiorentini, M. L., Farquhar, J. & Kendrick, M. A. (2014). Stable isotope (C, O, S) compositions of volatile-rich minerals in kimberlites: a review. *Chemical Geology* **374-375**, 61–83.

Giuliani, A., Soltys, A., Phillips, D., Kamenetsky, V. S., Maas, R., Goemann, K., Woodhead, J. D., Drysdale, R. & Griffin, W. L. (2017). The final stages of kimberlite petrogenesis: Petrography, mineral chemistry, melt inclusions and Sr-C-O isotope geochemistry of the Bultfontein kimberlite (Kimberley, South Africa). *Chemical Geology* **455**, 342–356.

Golovin, A. V., Sharygin, I. S. & Korsakov, A. V. (2017a). Origin of alkaline carbonates in kimberlites of the Siberian craton: Evidence from melt inclusions in mantle olivine of the Udachnaya-East kimberlite. *Chemical Geology* **455**, 357–375.

Golovin, A. V., Sharygin, V. V. & Pokhilenko, N. P. (2007). Melt inclusions in olivine phenocrysts in unaltered kimberlites from the Udachnaya-East pipe, Yakutia: Some aspects of kimberlite magma evolution during late crystallization stages. *Petrology* **15**, 168–183.

Golovin, A. V., Sharygin, I. S., Kamenetsky, V. S., Korsakov, A. V. & Yaxley, G. M. (2018). Alkali-carbonate melts from the base of cratonic lithospheric mantle: links to kimberlites. *Chemical Geology* **483**, 261–274.

Golovin, A. V., Sharygin, V. V., Pokhilenko, N. P., Mal'kovets, V. G., Kolesov, B. A. & Sobolev, N. V. (2003). Secondary melt inclusions in olivine from unaltered kimberlites of the Udachnaya-East pipe, Yakutia. *Doklady Earth Sciences* **388**, 93–96.

Golovin, A. V., Goryainov, S. V., Kokh, S. N., Sharygin, I. S., Rashchenko, S. V., Kokh, K. A., Sokol, E. V. & Devyatiyarova, A. S. (2017b). The application of Raman spectroscopy to djerfisherite identification. *Journal of Raman Spectroscopy* **48**, 1574–1582.

Guzmics, T., Mitchell, R. H., Szabó, C., Berkesi, M., Milke, R. & Abart, R. (2011). Carbonatite melt inclusions in coexisting magnetite, apatite and monticellite in Kerimasi calciocarbonatite, Tanzania: melt evolution and petrogenesis. *Contributions to Mineralogy and Petrology* **161**, 177–196.

Hunter, R. H. & Taylor, L. A. (1982). Instability of garnet from the mantle: glass as evidence of metasomatic melting. *Geology* **10**, 617–620.

Ionov, D. A., Doucet, L. S. & Ashchepkov, I. V. (2010). Composition of the lithospheric mantle in the siberian craton: new constraints from fresh peridotites in the Udachnaya-East kimberlite. *Journal of Petrology* **51**, 2177–2210.

Ionov, D. A., Doucet, L. S., Pogge von Strandmann, P. A. E., Golovin, A. V. & Korsakov, A. V. (2017). Links between deformation, chemical enrichments and Li-isotope compositions in the lithospheric mantle of the central Siberian craton, *Chemical Geology* **475**, 105–121.

Kamenetsky, M. B., Sobolev, A. V., Kamenetsky, V. S., Maas, R., Danyushevsky, L. V., Thomas, R., Pokhilenko, N. P. & Sobolev, N. V. (2004). Kimberlite melts rich in alkali

chlorides and carbonates: a potent metasomatic agent in the mantle. *Geology* **32**, 845–848.

Kamenetsky, V. S. & Yaxley, G. M. (2015). Carbonate–silicate liquid immiscibility in the mantle propels kimberlite magma ascent. *Geochimica et Cosmochimica Acta* **158**, 48–56.

Kamenetsky, V. S., Grütter, H., Kamenetsky, M. B. & Gömann, K. (2013). Parental carbonatitic melt of the Koala kimberlite (Canada): constraints from melt inclusions in olivine and Cr-spinel, and groundmass carbonate. *Chemical Geology* **353**, 96–111.

Kamenetsky, V. S., Kamenetsky, M. B., Golovin, A. V., Sharygin, V. V. & Maas, R. (2012). Ultrafresh salty kimberlite of the Udachnaya-East pipe (Yakutia, Russia): a petrological oddity or fortuitous discovery? *Lithos* **152**, 173–186.

Kamenetsky, V. S., Kamenetsky, M. B., Sharygin, V. V., Faure, K. & Golovin, A. V. (2007a). Chloride and carbonate immiscible liquids at the closure of the kimberlite magma evolution (Udachnaya-East kimberlite, Siberia). *Chemical Geology* **237**, 384–400.

Kamenetsky, V. S., Kamenetsky, M. B., Sharygin, V. V. & Golovin, A. V. (2007b). Carbonate-chloride enrichment in fresh kimberlites of the Udachnaya-East pipe, Siberia: a clue to physical properties of kimberlite magmas? *Geophysical Research Letters* **34**, L09316.doi.org/10.1029/2007GL029389.

Kamenetsky, V. S., Golovin, A. V., Maas, R., Giuliani, A., Kamenetsky, M. B. & Weiss, Y. (2014). Towards a new model for kimberlite petrogenesis: evidence from unaltered kimberlites and mantle minerals. *Earth-Science Reviews* **139**, 145–167.

Kamenetsky, V. S., Kamenetsky, M. B., Sobolev, A. V., Golovin, A. V., Demouchy, S., Faure, K., Sharygin, V. V. & Kuzmin, D. V. (2008). Olivine in the Udachnaya-East Kimberlite (Yakutia, Russia): types, compositions and origins. *Journal of Petrology* **49**, 823–839.

Kamenetsky, V. S., Kamenetsky, M. B., Weiss, Y., Navon, O., Nielsen, T. F. D. & Mernagh, T. P. (2009a). How unique is the Udachnaya-East kimberlite? Comparison with kimberlites from the Slave Craton (Canada) and SW Greenland. *Lithos* **112**, 334–346.

Kamenetsky, V. S., Maas, R., Kamenetsky, M. B., Paton, C., Phillips, D., Golovin, A. V. & Gornova, M. A. (2009b). Chlorine from the mantle: magmatic halides in the Udachnaya-East kimberlite, Siberia. *Earth and Planetary Science Letters* **285**, 96–104.

Keller, J. & Krafft, M. (1990). Effusive natrocarbonatite activity of Oldoinyo Lengai, June 1988. *Bulletin of Volcanology* **52**, 629–645.

Kervyn, M., Ernst, G. G. J., Klaudius, J., Keller, J., Kervyn, F., Mattsson, H. B., Belton, F., Mbede, E. & Jacobs, P. (2008). Voluminous lava flows at Oldoinyo Lengai in 2006: chronology of events and insights into the shallow magmatic system. *Bulletin of Volcanology* **70**, 1069–1086.

Kharkiv, A. D., Zinchuk, N. N. & Kruchkov, A. I. (1998). *Primary Diamond Deposits of the World (in Russian)*. Moscow: Nedra, p. 555.

Kharkiv, A. D., Zuenko, V. V., Zinchuk, N. N., Kryuchkov, A. I., Ukhanov, A. V. & Bogatykh, M. M. (1991). *Petrochemistry of Kimberlites*. Moscow: Nedra, p. 304.

Kim, J. I. & Grambow, B. (1999). Geochemical assessement of actinide isolation in a German salt repository environment. *Engineering Geology* **52**, 221–230.

Kim, J. I., Gompper, K. D., Closs, K. D., Kessler, G. & Faude, D. (1996). German approaches to closing the nuclear fuel cycle and final disposal of HLW. *Journal of Nuclear Materials* **238**, 1–10.

Kinny, P. D., Griffin, B. J., Heaman, L. M., Brakhfogel, F. F. & Spetsius, Z. V. (1997). SHRIMP U-Pb ages of perovskite from Yakutian kimberlites. *Geologiya i Geofizika* **38**, 91–99.

Kitayama, Y., Thomassot, E., Galy, A., Golovin, A., Korsakov, A., d'Eyrames, E., Assayag, N., Bouden, N. & Ionov, D. (2017). Co-magmatic sulfides and sulfates in the Udachnaya-East pipe (Siberia): a record of the redox state and isotopic composition of sulfur in kimberlites and their mantle sources. *Chemical Geology* **455**, 315–330.

Kjarsgaard, B. A., Pearson, D. G., Tappe, S., Nowell, G. M. & Dowall, D. P. (2009). Geochemistry of hypabyssal kimberlites from Lac de Gras, Canada: Comparisons to a global database and applications to the parent magma problem. *Lithos* **112**, 236–248.

Kopylova, M. G., Kostrovitsky, S. I. & Egorov, K. N. (2013). Salts in southern Yakutian kimberlites and the problem of primary alkali kimberlite melts. *Earth-Science Reviews* **119**, 1–16.

Kopylova, M. G., Matveev, S. & Raudsepp, M. (2007). Searching for parental kimberlite melt. *Geochimica et Cosmochimica Acta* **71**, 3616–3629.

Kopylova, M. G., Mogg, T. & Scott Smith, B. (2010). Mineralogy of the Snap Lake kimberlite, Northwest Territories, Canada, and compositions of phlogopite as records of its crystallization. *Canadian Mineralogist* **48**, 549–570.

Kopylova, M. G., Gaudet, M., Kostrovitsky, S. I., Polozov, A. G. & Yakovlev, D. A. (2016). Origin of salts and alkali carbonates in the Udachnaya East kimberlite: insights from petrography of kimberlite phases and their carbonate and evaporite xenoliths. *Journal of Volcanology and Geothermal Research* **327**, 116–134.

Kostrovitskiy, S. I., Kopylova, M. G., Egorov, K. N. & Yakovlev, D. A. (2013). The "exceptionally fresh" Udachnaya-East kimberlite: evidence for brine and evaporite contamination. In: Pearson, D. G., et al. (eds) *Proceedings of the 10th International Kimberlite Conference 1. Special Issue of the Journal of the Geological Society of India, Geological Society of India* **75**, 75–91.

le Roex, A. P., Bell, D. R. & Davis, P. (2003). Petrogenesis of Group I kimberlites from Kimberley, South Africa: evidence from bulk-rock geochemistry. *Journal of Petrology* **44**, 2261–2286.

Maas, R., Kamenetsky, M. B., Sobolev, A. V., Kamenetsky, V. S. & Sobolev, N. V. (2005). Sr, Nd, and Pb isotope evidence for a mantle origin of alkali chlorides and carbonates in the Udachnaya kimberlite, Siberia. *Geology* **33**, 549–552.

Marshintsev, V. K. (1986). *Vertical Heterogeneity of Kimberlite Bodies in Yakutia*. Novosibirsk: Nauka, p. 239.

Marshintsev, V. K., Migalkin, K. N., Nikolaev, N. C. & Barashkov, Y. P. (1976). Unaltered kimberlite of the Udachnaya East pipe. *Transactions (Doklady) of the USSR Academy of Sciences* **231**, 961–964.

Mernagh, T. P., Kamenetsky, V. S. & Kamenetsky, M. B. (2011). A Raman microprobe study of melt inclusions in kimberlites from Siberia, Canada, SW Greenland and South Africa. *Spectrochimica Acta Part A: Molecular and Biomolecular Spectroscopy* **80**, 82–87.

Mikhailenko, D. S., Korsakov, A. V., Rashchenko, S. V., Seryotkin, Y. V., Belakovskiy, D. I. & Golovin, A. V. (2018). Kuliginite: A new hydroxychloride mineral from Udachnaya kimberlite pipe, Yakutia. *American Mineralogist*, In press.

Mitchell, R. H. (1986). *Kimberlites: Mineralogy, Geochemistry and Petrology*. New York, NY: Plenum Publishing Company.

Mitchell, R. H. (2008). Petrology of hypabyssal kimberlites: relevance to primary magma compositions. *Journal of Volcanology and Geothermal Research* **174**, 1–8.

Mitchell, R. H. (2013). Oxygen isotope studies of serpentine in Kimberlite. In: *Proceedings of the 10th International Kimberlite Conference*. Bangalore: Geological Society of India, pp. 1–12.

Moussallam, Y., Morizet, Y. & Gaillard, F. (2016). H_2O–CO_2 solubility in low SiO_2-melts and the unique mode of kimberlite degassing and emplacement. *Earth and Planetary Science Letters* **447**, 151–160.

Nowicki, T., Porritt, L., Crawford, B. & Kjarsgaard, B. (2008). Geochemical trends in kimberlites of the Ekati property, Northwest Territories, Canada: Insights on volcanic and resedimentation processes. *Journal of Volcanology and Geothermal Research* **174**, 117–127.

O'Brien, H. E. & Tyni, M. (1999). Mineralogy and geochemistry of kimberlites and related rocks from Finland. In: Gurney, J. J., Gurney, J. L., Pascoe, M. D. & Richardson, S. H. (eds) *Proceedings of the VIIth International Kimberlite Conference*. Cape Town: Red Roof Design, pp. 625–636.

Pearson, D. G., Shirey, S. B., Carlson, R. W., Boyd, F. R., Pokhilenko, N. P. & Shimizu, N. (1995). Re-Os, Sm-Nd, and Rb-Sr isotope evidence for thick Archaean lithospheric mantle beneath the Siberian craton modified by multistage metasomatism. *Geochimica et Cosmochimica Acta* **59**, 959–977.

Pearson, D. G., Brenker, F. E., Nestola, F., McNeill, J., Nasdala, L., Hutchison, M. T., Matveev, S., Mather, K., Silversmit, G., Schmitz, S., Vekemans, B. & Vincze, L. (2014). Hydrous mantle transition zone indicated by ringwoodite included within diamond. *Nature* **507**, 221–224.

Podvysotskiy, V. T. (1985). Serpentine-carbonate mineralization in kimberlites. *International Geology Review* **27**, 810–823.

Price, S. E., Russell, J. K. & Kopylova, M. G. (2000). Primitive Magma From the Jericho Pipe, N.W.T., Canada: Constraints on Primary Kimberlite Melt Chemistry. *Journal of Petrology* **41**, 789–808.

Reid, A. M., Donaldson, C. H., Dawson, J. B., Brown, R. W. & Ridley, W. I. (1975). The Igwisi Hills extrusive "kimberlites". *Physics and Chemistry of the Earth* **9**, 199–218.

Roedder, E. (1984). Fluid inclusions. Reviews in Mineralogy. Mineralogical Society of America, 12. Book Crafters Inc., Michigan. 644 pp.

Roeder, P. L. & Schulze, D. J. (2008). Crystallization of groundmass spinel in kimberlite. *Journal of Petrology* **49**, 1473–1495.

Roxburgh, I. S. (1987). The suitability of evaporites as HLW Repositories. In: *Geology of High-Level Nuclear Waste Disposal*. Dordrecht: Springer, pp. 40–56.

Russell, J. K., Porritt, L. A., Lavallee, Y. & Dingwell, D. B. (2012). Kimberlite ascent by assimilation-fuelled buoyancy. *Nature* **481**, 352–356.

Safonov, O. G., Kamenetsky, V. S. & Perchuk, L. L. (2011). Links between carbonatite and kimberlite melts in chloride-carbonate-silicate systems: experiments and application to natural assemblages. *Journal of Petrology* **52**, 1307–1331.

Safonov, O. G., Chertkova, N. V., Perchuk, L. L. & Litvin, Y. A. (2009). Experimental model for alkalic chloride-rich liquids in the upper mantle. *Lithos* **112**, 260–273.

Scott Smith, B. H., Nowicki, T. E., Russell, J. K., Webb, K. J., Mitchell, R. H., Hetman, C. M., Harder, M., Skinner, E. M. W. & Robey, J. A. (2013). Kimberlite terminology and classification. In: Pearson, D.G., *et al.* (eds.), *Proceedings of 10th International Kimberlite Conference. Special Issue of the Journal of the Geological Society of India* **2**, 1–18.

Sharp, Z. D., Barnes, J. D., Brearley, A. J., Fischer, T., Chaussidon, M. & Kamenetsky, V. S. (2007). Chlorine isotope homogeneity of the mantle, crust and carbonaceous chondrites. *Nature* **446**, 1062–1065.

Sharygin, I. S., Golovin, A. V. & Pokhilenko, N. P. (2011). Djerfisherite in Kimberlites of the Kuoikskoe field as an indicator of enrichment of Kimberlite melts in chlorine. *Doklady Earth Sciences* **436**, 301–307.

Sharygin, V. V., Kamenetsky, V. S. & Kamenetsky, M. B. (2008). Potassium sulfides in kimberlite-hosted chloride-'nyerereite' and chloride clasts of the Udachnaya-East pipe, Yakutia, Russia. *Canadian Mineralogist* **46**, 1079–1095.

Sharygin, V. V., Golovin, A. V., Pokhilenko, N. P. & Sobolev, N. V. (2003). Djerfisherite in unaltered kimberlites of the Udachnaya-East pipe, Yakutia. *Doklady Earth Sciences* **390**, 554–557.

Sharygin, V. V., Golovin, A. V., Pokhilenko, N. P. & Kamenetsky, V. S. (2007). Djerfisherite in the Udachnaya-East pipe kimberlites (Sakha-Yakutia, Russia): paragenesis, composition and origin. *European Journal of Mineralogy* **19**, 51– 63.

Sharygin, I. S., Litasov, K. D., Shatskiy, A., Golovin, A. V., Ohtani, E. & Pokhilenko, N. P. (2015). Melting phase relations of the Udachnaya-East Group-I kimberlite at 3.0-6.5 GPa: experimental evidence for alkali-carbonatite composition of primary kimberlite melts and implications for mantle plumes. *Gondwana Research* **28**, 1391– 1414.

Sharygin, I. S., Litasov, K. D., Shatskiy, A., Safonov, O. G., Golovin, A. V., Ohtani, E. & Pokhilenko, N. P. (2017). Experimental constraints on orthopyroxene dissolution in alkali carbonate melts in the lithospheric mantle: Implications for kimberlite melt composition and magma ascent. *Chemical Geology* **455**, 44–56.

Shatskiy, A., Litasov, K. D., Sharygin, I. S. & Ohtani, E. (2017). Composition of primary kimberlite melt in a garnet lherzolite mantle source: constraints from melting phase relations in anhydrous Udachnaya-East kimberlite with variable CO_2 content at 6.5 GPa. *Gondwana Research* **45**, 208–227.

Shee, S. R. (1985). The petrogenesis of the wesselton mine kimberlites, Kimberley, Cape Province, RSA. Unpublished Ph.D. thesis, University of Cape Town, South Africa.

Skinner, E. M. W. & Marsh, J. S. (2004). Distinct kimberlite pipe classes with contrasting eruption processes. *Lithos* **76**, 183–200.

Smith, C. B., Sims, K., Chimuka, L., Duffin, A., Beard, A. D. & Townend, R. (2004). Kimberlite metasomatism at Murowa and Sese pipes, Zimbabwe. *Lithos* **76**, 219–232.

Soltys, A., Giuliani, A., Phillips, D., Kamenetsky, V. S., Maas, R., Woodhead, J. & Rodemann, T. (2016). In-situ assimilation of mantle minerals by kimberlitic magmas—direct evidence from a garnet wehrlite xenolith entrained in the Bultfontein kimberlite (Kimberley, South Africa). *Lithos* **256–257**, 182–196.

Sparks, R. S. J., Baker, L., Brown, R. J., Field, M., Schumacher, J., Stripp, G. & Walters, A. (2006). Dynamical constraints on kimberlite volcanism. *Journal of Volcanology and Geothermal Research* **155**, 18–48.

Sparks, R. S. J., Brooker, R. A., Field, M., Kavanagh, J., Schumacher, J. C., Walter, M. J. & White, J. (2009). The nature of erupting kimberlite melts. *Lithos* **112**, 429–438.

Stone, R. S. & Luth, R. W. (2017). Orthopyroxene survival in deep carbonatite melts: implications for kimberlites. *Contributions to Mineralogy and Petrology* **171**, 1–9.

Stripp, G. R., Field, M., Schumacher, J. C., Sparks, R. S. J. & Cressey, G. (2006). Post-emplacement serpentinization and related hydrothermal metamorphism in a kimberlite from Venetia, South Africa. *Journal of Metamorphic Geology* **24**, 515–534.

Sun, S.-S. & McDonough, W. F. (1989). Chemical and isotopic systematics of oceanic basalts: implications for mantle composition and processes. In: Saunders, A. D. & Norry, M. J. (eds) *Magmatism in the Ocean Basins*. London: Geological Society Special Publication, pp. 313–345.

Tappe, S., Brand, N. B., Stracke, A., van Acken, D., Liu, C.-Z., Strauss, H., Wu, F.-Y., Luguet, A. & Mitchell, R. H. (2016). Plates or plumes in the origin of kimberlites: U/Pb perovskite and Sr-Nd-Hf-Os-C-O isotope constraints from the Superior craton (Canada). *Chemical Geology* **455**, 57–83.

Tappe, S., Graham Pearson, D., Kjarsgaard, B. A., Nowell, G. & Dowall, D. (2013). Mantle transition zone input to kimberlite magmatism near a subduction zone: origin of anomalous Nd–Hf isotope systematics at Lac de Gras, Canada. *Earth and Planetary Science Letters* **371–372**, 235–251.

Tappe, S., Pearson, D. G., Nowell, G., Nielsen, T., Milstead, P. & Muehlenbachs, K. (2011). A fresh isotopic look at Greenland kimberlites: cratonic mantle lithosphere imprint on deep source signal. *Earth and Planetary Science Letters* **305**, 235–248.

Vasilenko, V. B., Zinchuk, N. N., Krasavchikov, V. O., Kuznetsova, L. G., Khlestov, V. V. & Volkova, N. I. (2002). Diamond potential estimation based on kimberlite major element chemistry. *Journal for Geochemical Exploration* **76**, 93–112.

Wilson, M. R., Kjarsgaard, B. A. & Taylor, B. (2007). Stable isotope composition of magmatic and deuteric carbonate phases in hypabyssal kimberlite, Lac de Gras field, Northwest Territories, Canada. *Chemical Geology* **242**, 435–454.

Zaitsev, A. N. (2010). Nyerereite from calcite carbonatite at the Kerimasi Volcano, Northern Tanzania. *Geology of Ore Deposits* **6**, 630–640.

Zaitsev, A. & Keller, J. (2006). Mineralogical and chemical transformation of Oldoinyo Lengai natrocarbonatites, Tanzania. *Lithos* **91**, 191–207.

Zaitsev, A., Wenzel, T., Vennemann, T. & Markl, G. (2013). Tinderet volcano, Kenya: an altered natrocarbonatite locality? *Mineralogical Magazine* **77**, 213–226.

Zinchuk, N. N., Spetsius, Z. V., Zuenko, V. V. & Zuev, V. M. (1993). *The Udachnaya Kimberlite Pipe (in Russian)*. Novosibirsk: Publishing House of the Novosibirsk University, p. 147

Appendix 5.1 - Electronic Appendix 1

Appendix 5.2 - Electronic Appendix 2

Contributions to Mineralogy and Petrology (2019) 174:8
https://doi.org/10.1007/s00410-018-1540-8

ORIGINAL PAPER

Djerfisherite in kimberlites and their xenoliths: implications for kimberlite melt evolution

Adam Abersteiner[1] · Vadim S. Kamenetsky[1] · Karsten Goemann[2] · Alexander V. Golovin[3,4] · Igor S. Sharygin[3] · Andrea Giuliani[5,6] · Thomas Rodemann[2] · Zdislav V. Spetsius[7] · Maya Kamenetsky[1]

Received: 12 June 2018 / Accepted: 4 December 2018 / Published online: 2 January 2019

Abstract

Djerfisherite ($K_6(Fe,Ni,Cu)_{25}S_{26}Cl$) occurs as an accessory phase in the groundmass of many kimberlites, kimberlite-hosted mantle xenoliths, and as a daughter inclusion phase in diamonds and kimberlitic minerals. Djerfisherite typically occurs as replacement of pre-existing Fe–Ni–Cu sulphides (i.e. pyrrhotite, pentlandite and chalcopyrite), but can also occur as individual grains, or as poikilitic phase in the groundmass of kimberlites. In this study, we present new constraints on the origin and genesis of djerfisherite in kimberlites and their entrained xenoliths. Djerfisherite has extremely heterogeneous compositions in terms of Fe, Ni and Cu ratios. However, there appears to be no distinct compositional range of djerfisherite indicative of a particular setting (i.e. kimberlites, xenoliths or diamonds), rather this compositional diversity reflects the composition of the host kimberlite melt and/or interacting metasomatic medium. In addition, djerfisherite may contain K and Cl contents less than the ideal formula unit. Raman spectroscopy and electron backscatter diffraction (EBSD) revealed that these K–Cl poor sulphides still maintain the same djerfisherite crystal structure. Two potential mechanisms for djerfisherite formation are considered: (1) replacement of pre-existing Fe–Ni–Cu sulphides by djerfisherite, which is attributed to precursor sulphides reacting with metasomatic K–Cl bearing melts/fluids in the mantle or the transporting kimberlite melt; (2) direct crystallisation of djerfisherite from the kimberlite melt in groundmass or due to kimberlite melt infiltration into xenoliths. The occurrence of djerfisherite in kimberlites and its mantle cargo from localities worldwide provides strong evidence that the metasomatising/infiltrating kimberlite melt/fluid was enriched in K and Cl. We suggest that kimberlites originated from melts that were more enriched in alkalis and halogens relative to their whole-rock compositions.

Keywords Djerfisherite · Kimberlite · Sulphides · Metasomatism · Potassium · Chlorine · Diamond

Communicated by Chris Ballhaus.

Electronic supplementary material The online version of this article (https://doi.org/10.1007/s00410-018-1540-8) contains supplementary material, which is available to authorised users.

✉ Adam Abersteiner
adam.abersteiner@utas.edu.au

[1] School of Physical Sciences, University of Tasmania, Hobart, TAS 7001, Australia

[2] Central Science Laboratory, University of Tasmania, Hobart, TAS 7001, Australia

[3] Sobolev Institute of Geology and Mineralogy, Siberian Branch Russian Academy of Sciences, Koptyuga Pr. 3, Novosibirsk 630090, Russian Federation

[4] Novosibirsk State University, Pirogova 2, Novosibirsk 630090, Russian Federation

[5] KiDs (Kimberlites and Diamonds), School of Earth Sciences, The University of Melbourne, Parkville, VIC 3010, Australia

[6] ARC Centre of Excellence for Core to Crust Fluid Systems (CCFS) and GEMOC, Department of Earth and Planetary Sciences, Macquarie University, North Ryde, NSW 2109, Australia

[7] Geo-Scientific Investigation Enterprise, ALROSA PJSC, Mirny, Yakutia, Russia

Introduction

Djerfisherite ($K_6(Fe,Ni,Cu)_{25}S_{26}Cl$) is a potassium–chlorine bearing sulphide that was first recognised in meteorites (Fuchs 1966) and later in numerous silica undersaturated terrestrial lithologies, which include alkaline ultramafic/basic and syenitic complexes, kimberlites and carbonatites (see reviews by Clarke et al. 1994; Henderson et al. 1999; Clay et al. 2014). Djerfisherite has been documented as a common accessory phase in kimberlites (Dobrovol'skaya et al. 1975; Distler et al. 1987; Spetsius et al. 1987; Clarke et al. 1994; Chakhmouradian and Mitchell 2001; Sharygin et al. 2003, 2007, 2008, 2011; Abersteiner et al. 2017b; Golovin et al. 2017a) and as daughter phase in olivine-hosted melt inclusions (Golovin et al. 2003, 2007, 2018; Sharygin et al. 2003, 2007; Kamenetsky et al. 2009a; Mernagh et al. 2011). In addition, djerfisherite has been reported in numerous kimberlite-borne mantle xenoliths and xenocrysts (e.g. eclogites, harzburgites, lherzolites; Clarke 1979; Govorov et al. 1984; Aulbach et al. 2004; Misra et al. 2004; Sharygin et al. 2007, 2012; Kamenetsky et al. 2009c; Sobolev et al. 2010; Giuliani et al. 2013; Logvinova et al. 2015; Bragagni et al. 2017) and in diamond-hosted inclusions (Bulanova et al. 1980, 1990; Logvinova et al. 2008; Hunt et al. 2012).

Although a primary origin for djerfisherite in mantle-derived xenoliths has been suggested (Govorov et al. 1984; Bragagni et al. 2017), the majority of studies propose that djerfisherite resulted from the in situ interaction between K–Cl bearing melts/fluids and primary Fe–Ni–Cu sulphides at depths coeval with kimberlite magmatism (Bulanova et al. 1990; Solovieva et al. 1997; Sharygin et al. 2012; Clay et al. 2014). In addition, the presence of djerfisherite in the groundmass of kimberlites and as a daughter phase in secondary melt inclusions in kimberlitic olivine suggests late-stage magmatic crystallisation (Dobrovol'skaya et al. 1975; Distler et al. 1987; Clarke et al. 1994; Chakhmouradian and Mitchell 2001; Golovin et al. 2003; Sharygin et al. 2003, 2007, 2011; Kamenetsky et al. 2009a; Mernagh et al. 2011; Kitayama et al. 2017). While there is a general consensus that the genesis of djerfisherite in the mantle is related to the interaction of pre-existing sulphides and K–Cl bearing melts/fluids, the composition of this hypothetical melt/fluid is poorly constrained. The presence of abundant potassium in kimberlites is indicated by the presence of groundmass phlogopite, whereas chlorine concentrations are not as well understood, as it is either extremely low (O'Brien and Tyni 1999; Kjarsgaard et al. 2009) or not routinely determined in the majority of whole-rock kimberlite analyses.

In this contribution, we examine previous occurrences of djerfisherite in kimberlites and mantle rocks and minerals from worldwide localities, as well as several new discoveries. We characterise the different morphologies and compositions of djerfisherite in different settings. Furthermore, we address the potentially different modes of djerfisherite formation and whether kimberlite melts, metasomatic fluids or contamination is involved in its genesis.

Sample descriptions and geological setting

The investigated samples include kimberlite, and mantle and crustal xenoliths, which were petrographically and mineralogically examined in detail. Djerfisherite is typically an accessory phase (i.e. usually ≤ 1 vol%) in each sample. All studied samples were examined by optical and scanning electron microscopy (SEM), with selected samples analysed further by electron microprobe (EMP), Raman spectroscopy and electron backscatter diffraction (EBSD; see Supplementary Material for details of methodology). A summary of host locality age and the petrography and mineralogy of all samples analysed in this study is presented in Table 1. These samples consist of:

1. Three mantle-derived xenoliths obtained from the mine dumps of the Bultfontein (Group I, or archetypal) kimberlite (South Africa) and comprise a spinel harzburgite, lindsleyite $[(Ba,Sr)(Ti,Cr,Fe,Mg)_{21}O_{38}]$-–mathiasite $[(K,Ca,Sr)(Ti,Cr,Fe,Mg)_{21}O_{38}]$ (LIMA)-bearing spinel lherzolite and a polymict breccia (i.e. 'failed' kimberlite intrusion; see Lawless et al. 1979; Pokhilenko 2009; Giuliani et al. 2014c).
2. A garnet harzburgite (RV1a) from the Roberts Victor orangeite (or Group II kimberlite; South Africa).
3. Nine kimberlite rock samples from the Udachnaya-East (Group I) kimberlite (Russia), which were derived from two mineralogically and geochemically distinct units (i.e. serpentine-bearing and serpentine-free kimberlite; see Egorov et al. 1986; Kopylova et al. 2013; Kostrovitskiy et al. 2013; Kamenetsky et al. 2014, 2007; Golovin et al. 2017b; Abersteiner et al. 2018).
4. Six mantle-derived xenoliths from the 'serpentine-free' horizon of the Udachnaya-East kimberlite which includes sheared peridotites, coarse-grained eclogites and a wehrlite.
5. A crustal amphibolite xenolith from the unserpentinised Udachnaya-East kimberlite.
6. Kimberlite rock samples from the Obnazhennaya and Vtorogodnitsa (Group-I) kimberlites (Russia).
7. Kimberlite rock samples from the Koala and Leslie (Group-I) kimberlites (Canada).

Table 1 Summary of location, age, sample type, petrography, mineralogy and reference(s) of samples used in this study

Locality and age of host kimberlite	Sample type	Petrography and mineralogy	References
Bultfontein kimberlite (Group I), Kaapvaal Craton (South Africa) ~84 Ma (Allsopp and Barrett 1975)	Spinel harzburgite XM1/422	Composed of porphyroblastic olivine and orthopyroxene, which are variably serpentinised along rims and fractures. Subordinate 'symplectitic' intergrowths of Cr–spinel + diopside + orthopyroxene are occasionally altered to phlogopite and spinel along with Ni-rich assemblages, which contain minor djerfisherite	Giuliani et al. (2013)
	LIMA-bearing lherzolite XM1/362	Coarse-grained lindsleyite [(Ba,Sr)$(Ti,Cr,Fe,Mg)_{21}O_{38}$]–mathiasite [(K,Ca,Sr)$(Ti,Cr,Fe,Mg)_{21}O_{38}$] (LIMA) bearing, spinel lherzolite, which contains abundant phlogopite, clinopyroxene and minor Fe–Ni (± K–Cl) sulphides	Giuliani et al. (2014c, 2018)
	Polymict breccia DU-1	Contains preferentially orientated lenses of ilmenite and minor rutile. Ilmenite-rich domains contain blebs of Fe–Cu–Ni (± K–Cl) sulphides along with grains of olivine, garnet, orthopyroxene and clinopyroxene set in a finer grained matrix of olivine, orthopyroxene, phlogopite, ilmenite and rutile	Giuliani et al. (2012, 2014c)
Roberts Victor kimberlite (Group II), Kaapvaal Craton (South Africa) 128 ± 15 Ma (Smith et al. 1985)	Garnet harzburgite RV1a	Dominated by porphyroblastic olivine along with orthopyroxene, garnet, Cr–spinel and minor clinopyroxene. Olivine and orthopyroxene are commonly replaced by serpentine and to a lesser extent calcite and phlogopite along grain boundaries. Ilmenite, magnetite, Ni–Fe–Cu–sulphides and djerfisherite are commonly disseminated interstitially between porphyroblastic rock-forming minerals	
Udachnaya-East kimberlite (Group I), Siberian Craton (Russia) ~365–367 Ma (Kamenetsky et al. 2009b; Kinny et al. 1997)	'Serpentine-free' kimberlite K1-15, K2-03, K24-04b, K24-04a, pt4a-05	Composed of abundant olivine along with (in order of relative abundance) groundmass carbonate (calcite, Na–K carbonates ± some S-bearing species), halite, sylvite, sodalite, monticellite, phlogopite, perovskite, ilmenite, spinel (e.g. Mg–Ti–magnetite, magnesian ulvöspinel–magnetite (MUM), pleonaste, chromite), apatite, Fe–Ni–sulphides, djerfisherite and rasvumite	Egorov et al. (1986); Kamenetsky et al. (2007, 2014); Kopylova et al. (2013); Kostrovitskiy et al. (2013); Golovin et al. (2017b)

Table 1 (continued)

Locality and age of host kimberlite	Sample type	Petrography and mineralogy	References
	'Serpentine-bearing' kimberlite K20-05, K28-05, K17-05, K25-04	Texturally and mineralogically similar to 'serpentine-free' samples in terms of silicate (i.e. olivine, monticellite, phlogopite), oxide (i.e. perovskite, ilmenite, spinel), phosphate (i.e. apatite) and sulphide (i.e. Fe–Ni–sulphides, djerfisherite, rasvumite) mineralogy. However, alkali (Na, K ± S) carbonates, chlorides and sodalite are absent, and serpentine and to a lesser extent iowaite [$Mg_4Fe^{3+}(OH)_8OCl \bullet 3(H_2O)$] occur in variable abundances (up to 30 vol.%) interstitially throughout the groundmass and as replacement of olivine along rims and fractures	
	Sheared peridotite UE-UV0112, UD-12	Dominated by olivine porphyroclasts and neoblasts (~ 75 vol.%) along with clinopyroxene, orthopyroxene and garnet porphyroblasts. Fe–Ni–Cu (± K–Cl) sulphide blebs (pentlandite, pyrrhotite, chalcopyrite, djerfisherite) are interstitial to the silicate minerals. These sheared peridotite xenoliths appear largely unaffected by secondary alteration due to the absence of serpentine replacing olivine or orthopyroxene	Sharygin et al. (2012)
	Eclogite UE12, UE-SS, UE-40-05-1	Composed predominantly of clinopyroxene and garnet along with minor phlogopite. Complex Fe–Ni–Cu-bearing (including djerfisherite) sulphides occur as secondary intragranular blebs hosted in clinopyroxene and garnet, as well as interstitial segregations between the rock-forming minerals. Sulphides in sample UE-SS are sometimes surrounded by discontinuous mantles of an unidentified Fe–O–Ni–Cl bearing phase(s). Other accessory phases in the eclogites include Al–Fe–Mg–Cr-spinel, sodalite and calcite	

Table 1 (continued)

Locality and age of host kimberlite	Sample type	Petrography and mineralogy	References
	Wehrlite UV01-332	Coarse grained and dominantly composed of olivine and clinopyroxene along with lesser garnet and ilmenite (Supplementary Fig. S1). Complex mineral pools occur at grain boundaries (Supplementary Fig. S1) and are composed of alkali (Na, K) carbonate, K–sulphate and blebs of ferropericlase, which are surrounded by rims of Mg–magnetite (Supplementary Fig. S1d). Minor mineral in these pools include calcite, magnetite, apatite, perovskite, northupite [$Na_3Mg(CO_3)_2Cl$], bradleyite [$Na_3Mg(PO_4)(CO_3)$], Na–K sulphate, djerfisherite and halite. Analyses of melt inclusions in silicate (i.e. olivine; Supplementary Fig. S1c) rock-forming minerals also identified compositionally similar assemblages to those in interstitial mineral pools	
Obnazhennaya and Vtorogodnitsa kimberlites (Group I), Siberian Craton (Russia) 158–170 Ma (Sun et al. 2014)	Kimberlite O-1-I, o-1-II, o-1-III, o-1-IV V-50, V-100	These kimberlites have porphyritic textures defined by larger grains of olivine, phlogopite, ilmenite and garnet in a groundmass of serpentine, calcite, dolomite, spinel, phlogopite, apatite and minor Fe–Ni–Cu sulphides and djerfisherite	Sharygin et al. (2011)
Koala kimberlite (Group I), Slave Craton (Canada) ~53 Ma (Creaser et al. 2004)	Kimberlite BHP7	Sample of coherent kimberlite probably derived from the basal hypabyssal unit of the Koala pipe (Porritt and Cas 2011). Olivine is abundant and the groundmass is composed of serpentine, carbonate (i.e. calcite, dolomite), monticellite, spinel, perovskite, phlogopite/kinoshitalite, apatite and accessory pyrochlore $(Na,Ca)_2Nb_2O_6(OH,F)$, barite, Fe–Ni–Cu sulphides and djerfisherite	
Leslie kimberlite (Group I), Slave Craton (Canada) ~53 Ma (Sarkar et al. 2015)	Kimberlite LDC7	Dominated by olivine and groundmass monticellite along with lesser calcite, phlogopite/kinoshitalite, brucite, spinel (Cr–spinel, MUM, Mg–magnetite, pleonaste), apatite, perovskite and minor Fe–Ni–Cu sulphides and djerfisherite	Bussweiler et al. 2015; Abersteiner et al. (2017b)

Djerfisherite petrography and composition

Djerfisherite in kimberlite-hosted xenoliths, kimberlite groundmass and melt inclusions hosted in kimberlitic/xenocrystic minerals show variable morphologies. Although the majority of djerfisherite grains examined are relatively homogeneous and unzoned, there are usually large compositional variations in terms of Fe–Ni–Cu ratios and to a lesser extent K and Cl content between individual djerfisherite grains or within rims surrounding other Fe–Ni–Cu sulphides. The petrography and compositions of djerfisherite are summarised in Table 2 and Supplementary Table 1, respectively (see Supplementary Data for complete EMP/EDS datasets).

Djerfisherite in mantle xenoliths: Siberian craton

Djerfisherite in sheared peridotites (samples UE-UV0112, UD-12 and samples analysed by Sharygin et al. 2012) and eclogites (samples UE12, UE-SS, UE-40-05-1) frequently forms variably thick rims (5 to > 50 µm) around Fe–Ni–Cu sulphide globules (i.e. pentlandite, pyrrhotite and chalcopyrite) hosted in porphyroclastic rock-forming minerals (Fig. 1). Djerfisherite also forms rims around sulphides interstitial to major silicate components composing these xenoliths (Figs. 2, 3). Less common are individual subhedral (i.e. semi-cubic) grains of djerfisherite that range in size between 5 and 50 µm within xenolith interstices, which were also identified in eclogite samples UE-40-05-01 and UE-SS. These djerfisherite grains are sometimes intergrown with other Fe–Ni sulphides and associated with secondary kimberlitic minerals such as phlogopite, sodalite or spinel (Fig. 4a, b).

In wehrlite sample UV01-332, djerfisherite is the only sulphide phase present within complex mineral 'pools, which are interstitial to the main silicate rock-forming minerals (Supplementary Figure S1). The mineralogy of these 'pools is presented in Table 1 (Supplementary Figure S1) and similar mineral assemblages to these 'pools were identified in secondary melt inclusions hosted in the rock-forming silicates (e.g. olivine; Supplementary Figure S1c). Djerfisherite in these pools typically forms subhedral-shaped grains, which range in size from 15 to >100 µm (Fig. 5).

Djerfisherite occurs as large bleb-to-amoeboid shaped aggregates (up to > 600 µm) in xenocrystic olivine from Vtorogodnitsa kimberlite sample V-100 (Supplementary Figure S2), where it also forms along fractures which are connected to the groundmass. In addition, djerfisherite also occurs as daughter phase in secondary multiphase melt inclusions along healed cracks in olivine in sheared peridotites from the Udachnaya-East kimberlite (Fig. 6; Sharygin et al. 2012). Daughter djerfisherite in multiphase melt inclusions typically ranges from < 5–20 µm in size. In terms of mineral chemistry, there is wide variation in Fe, Ni and Cu ratios, but Fe is regularly the most abundant in all samples (Supplementary Table 1 and Data).

Djerfisherite in mantle xenoliths: Kaapvaal craton

Djerfisherite in garnet harzburgite (sample RV1a) occurs as small (< 30 µm) disseminated grains within xenolith interstices, where it commonly occurs in textural association with spinel and other Fe–Ni–Cu sulphides. In addition, djerfisherite replaces significant portions of Fe–Ni–Cu sulphides, which are interstitial to major silicate/oxide components in this xenolith (Supplementary Figure S3).

In harzburgite sample XM1/422, djerfisherite occurs as a minor phase within nickel-rich assemblages (i.e. composed dominantly of native nickel and heazlewoodite) associated with spinel + pyroxene symplectites (Giuliani et al. 2013). In lherzolite sample XM1/362, djerfisherite is interstitial to the major xenolith components, or forms rims around other Fe–Ni sulphides (Fig. 4c) and also occurs in textural association with secondary (i.e. kimberlitic) perovskite. In polymict breccia sample DU-1, djerfisherite was identified as a daughter phase within multiphase secondary melt inclusions hosted in ilmenite together with spinel, alkali–carbonates, priderite [$(K,Ba)(Ti,Fe^{3+})_8O_{16}$], phlogopite and freudenbergite [$Na_2Fe^{3+}{}_2Ti_6O_{16}$] (Supplementary Figure S4). Similar to kimberlite-hosted mantle xenoliths from the Siberian Craton, Kaapvaal Craton samples generally show wide variation in Fe, Ni and Cu cations, where Fe is regularly the most abundant. Djerfisherite in samples XM1/362 and XM1/422 contain below average weight totals K (5.3–7.1 wt% and 4.6–7.1 wt%, respectively) and Cl (0.0 wt% and 0.6–1.1 wt%, respectively; Supplementary Table 1) and below average atoms per formula unit (a.p.f.u) with regard to K (3.4–4.4 in sample XM1/422) and Cl (< 0.1 in sample XM1/422; Supplementary Data).

Djerfisherite in kimberlites

Djerfisherite in the kimberlitic groundmass occurs either as: (1) individual and/or clusters of subhedral grains that typically range in size from 10 to > 70 µm; (2) segregations (25 to >100 µm) that are interstitial to other groundmass minerals (Fig. 7a, b), which sometimes poikilitically enclose grains of other groundmass phases (e.g. olivine, calcite, spinel and phlogopite); (3) rims surrounding aggregates of other Fe–Ni–Cu-bearing sulphides (Fig. 7c, d). The distribution of djerfisherite in kimberlites is extremely variable, being very common in some kimberlites (e.g. Leslie

Table 2 Summary of the location, sample ID, petrography and reference(s) of mantle-derived rock and mineral occurrences of djerfisherite (Dj)

Locality	Host	Sample ID	Djerfisherite petrography	References
Bultfontein (South Africa)	Spinel harzburgite	XM1/422	Dj is a minor phase in Ni-rich assemblages	Giuliani et al. (2013)
	LIMA-bearing lherzolite	XM1/362	Dj interstitial to major xenolith components + Dj rims around Fe–Ni sulphides + texturally associated with kimberlitic perovskite	Figure 4c; Giuliani et al. (2014c, 2018)
	Polymict breccia	DU-1	Dj is a daughter phase in multiphase secondary melt inclusions in ilmenite	Figure 7; Giuliani et al. (2012, 2013)
Roberts Victor (South Africa)	Garnet harzburgite	RV1a	Disseminated Dj grains within xenolith interstices + Dj rims around Fe–Ni–Cu sulphide aggregates	
Frank Smith (South Africa)	Clinopyroxene–ilmenite nodule	190/186	Dj occurs around a polysulphide bleb of pyrrhotite and pentlandite	Clarke et al. (1979)
Udachnaya-East (Russia)	Kimberlite	K1-15, K2-03, K24-04b, K24-04a, K20-05, K28-05, K17-05, K25-04	Individual groundmass grains of Dj + interstitial Dj segregations + Dj rims around Fe–Ni–Cu sulphides + Dj in secondary melt inclusions in olivine	Figure 8b–d, 13; Kamenetsky et al. (2012)
	Eclogite	UE12, UE-SS, UE-40-05-1	Dj rims around Fe–Ni–Cu sulphide globules + Dj rims around interstitial sulphide aggregates + individual grains of Dj	Figures 1, 4a,b
	Sheared peridotite	UE-UV0112, UD-12	Dj rims around Fe–Ni–Cu sulphide globules	Figures 2, 3; Sharygin et al. (2012)
	Wehrlite	UV01-332	Dj is interstitial to silicate rock-forming minerals	Figure 5
	Kimberlite olivine		Dj occurs in the groundmass of serpentine-free kimberlite breccia and monticellite kimberlite. Dj grains occur in association with magnetite, pyrrhotite or interstitial groundmass phase Dj occurs as secondary inclusions in olivine	Sharygin et al. (2003)
	Eclogite	U33/1, UX/1	Dj occurs as rims around polyphase pyrrhotite/pentlandite sulphide grains hosted in clinopyroxene	Misra et al. (2004)
	Eclogite	51/3	Dj occurs in association with chalcopyrite, pyrrhotite and pentlandite in eclogite	Sobolev et al. (2010)
	Eclogite	TV-127/7 9	Dj occurs as globular and drop-shaped inclusions in omphacite and garnet and occurs in association with chalcopyrite, pyrrhotite and pentlandite	Govorov et al. (1984)
	Garnet peridtotite	U-331	Dj occurs within the xenolith as a rock-forming mineral	Logvinova et al. (2015)
Yakutia (Russia)	Diamond		Dj occurs as daughter inclusions in diamond	Bulanova et al. (1980, 1990), Logvinova et al. (2008)
	Ilmenite nodule Garnet peridotite Eclogite Enstatite noduleOlivineKimberlite	II-1058, I1-1049R-916R-358 K-7Vt-743Vt-732	Dj intergrowth with cobalt pentlandite Dj replacement after pentlandite and chalcopyrite	Distler et al. (1987)
Vtorogodnitsa (Russia)	Kimberlite, olivine xenocryst	V-50, V-100	Individual groundmass grains of Dj + interstitial Dj segregations + Dj rims around Fe–Ni–Cu sulphides + blebs of Dj aggregates in xenocrystic olivine and along fractures + Dj in secondary melt inclusions hosted in olivine	Figure 6; Sharygin et al. (2011)
Obnazhennaya (Russia)	Kimberlite	O-1-I, o-1-II, o-1-III, o-1-IV	Dj occurs in the groundmass as individual groundmass grains + interstitial Dj segregations + Dj rims around Fe–Ni–Cu sulphides	Sharygin et al. (2011)
Koala (Canada)	Kimberlite	BHP7		Figures 9, 11
Leslie (Canada)	Kimberlite	LDC7		Figure 8a

Table 2 (continued)

Locality	Host	Sample ID	Djerfisherite petrography	References
Somerset Island(Canada)	Garnet harzburgite	JPS6A	Dj occurs as overgrowth coronae around (partly altered) pentlandite cores	Bragagni et al. (2017)
Renard (Canada)	Diamond		Diamond-hosted polymineralic inclusion containing Dj, calcite, dolomite and apatite	Hunt et al. (2012)
Lac De Gras (Canada)	Kimberlite		Dj occurs in the groundmass of kimberlites	Chakhmouradian and Mitchell (2001)
A154 (Canada)	Olivine	C229	Dj was identified as an inclusion in xenocrystic olivine	Aulbach et al. (2004)
Majuagaa Dyke (Greenland)	Olivine		Dj occurs in olivine-hosted secondary melt inclusions	Mernagh et al. (2011)

sample LDC7 and Udachnaya-East sample K24-04a/b), but rare in others (e.g. Koala sample BHP7). Furthermore, these distribution heterogeneities of djerfisherite are evident even within individual kimberlite pipes, such as Udachnaya-East, where djerfisherite is extremely variable within individual samples derived from a large range of depth intervals (~440–520 m).

Kimberlite groundmass occurrences of djerfisherite all exhibit relatively consistent K and Cl content and wide variation in Fe–Ni–Cu ratios (Supplementary Table 1 and Data). However, similar to samples XM1/422 and XM1/362, the Koala kimberlite contains djerfisherite with K and Cl contents below formula average. Some djerfisherite grains maintain ideal potassium (i.e. 6) and chlorine (i.e. 1) a.p.f.u (Supplementary Data). In some grains, compositionally '*bona fide*' (i.e. contains ideal a.p.f.u and stoichiometric K–Cl content) djerfisherite may be in direct contact with 'Cl-free' djerfisherite (Fig. 8).

Raman spectroscopy and EBSD (see Supplementary Material for methodology) were employed to determine whether these K–Cl poor sulphides in the Koala kimberlite are structurally similar to regular djerfisherite. Both forms of djerfisherite exhibit virtually identical Raman spectra. A good representation of the spectra is achieved by fitting six peaks: two strong bands with maxima between 269 and 272 and 142–144 cm^{-1}, and four weaker peaks at 120–124, 303–305, 330–340, and 348–359 cm^{-1}, respectively (Fig. 9). Some minor peak shifts and variations in band width are observed between individual measurements, but there are no consistent differences between Raman spectra of the two forms. In addition, our data are similar to djerfisherite reference material reported by Golovin et al. (2017a); Fig. 9a. The electron backscatter patterns (EBSPs) of both forms match djerfisherite (see example patterns in Supplementary Figures S5 and 6). An EBSD map of an area that contains both *'bona fide'* djerfisherite and K–Cl poor (i.e. below ideal a.p.f.u) djerfisherite shows that the sharp boundary between both forms crosscuts several grains within the assemblage (see Supplementary Figure S5d).

Djerfisherite in crustal xenoliths

Djerfisherite was identified inside a crustal xenolith fragment (sample pt4a-05) entrained in the Udachnaya-East kimberlite. Here, djerfisherite occurs as thin (< 20 µm) rims, which are sometimes associated with rasvumite (KFe_2S_3) around pyrrhotite segregations or within fractures (Supplementary Figure S7). EDS analyses have shown djerfisherite to have the following compositions: 8.7–9.2 wt% K, 1.3–1.4 wt% Cl, 44.6–49.3 wt% Fe, 0.5–1.8 wt% Ni, 4.5–8.9 wt% Cu (Supplementary Table 1 and Data).

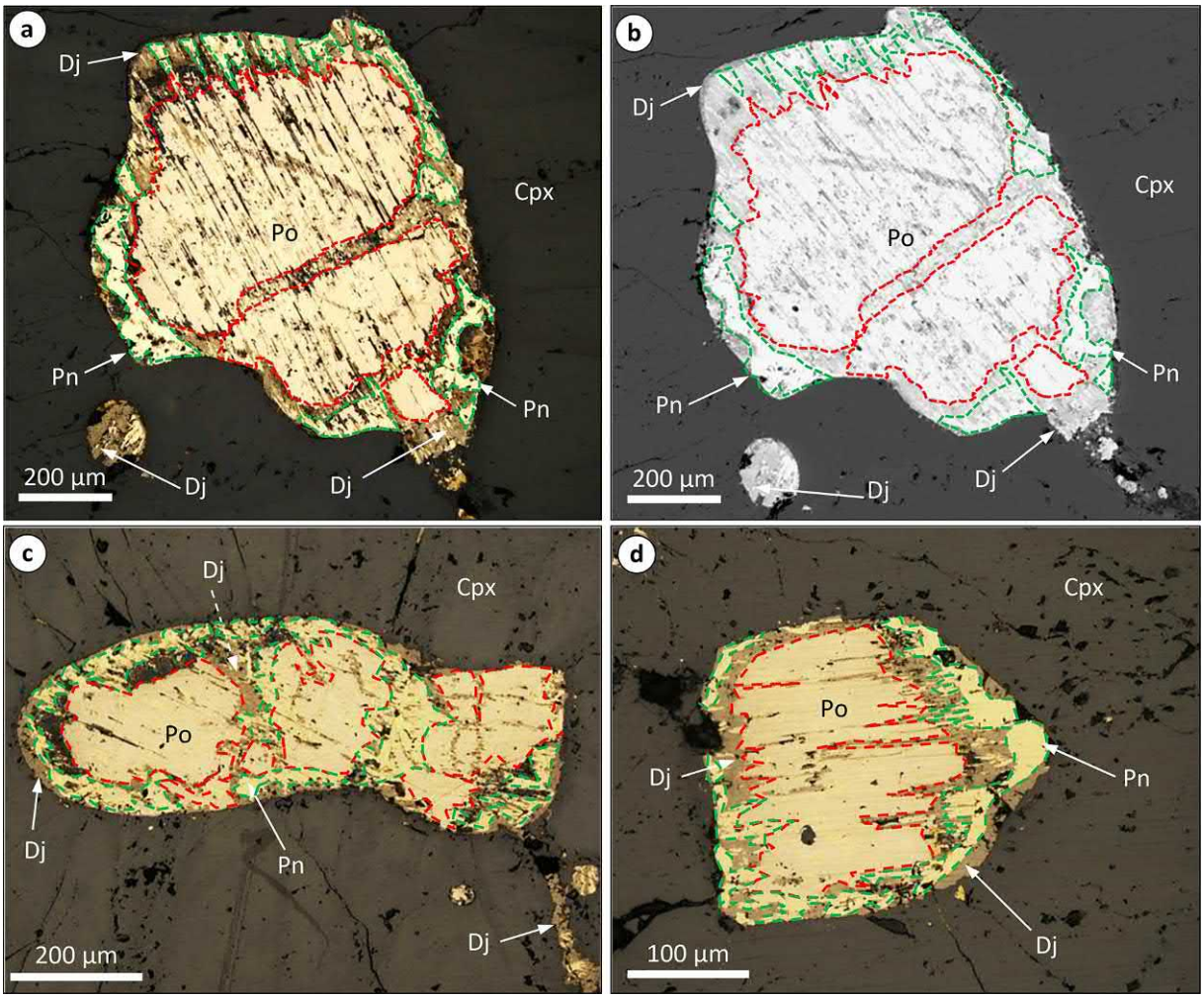

Fig. 1 Reflected-light (**a, c, d**) and backscattered electron (BSE) SEM (**b**) images showing intragranular sulphide aggregate included in rock-forming clinopyroxene (cpx) from an eclogite xenolith (sample UE-40-05-01; Udachnaya-East, Siberia). These sulphides are composed predominantly of pyrrhotite (Po—dotted red lines) and pentlandite (Pn—dotted green lines) which shows partial replacement by djerfisherite (Dj—brown/bronze colour in reflected light) along rims and fractures

Djerfisherite in melt inclusions from kimberlitic minerals

Djerfisherite occurs as a daughter phase (< 5–20 µm) in secondary multiphase melt inclusions (Fig. 10) hosted in kimberlitic olivine. Melt inclusions containing daughter djerfisherite are prominent in both serpentinised and unserpentinised varieties of the Udachnaya-East kimberlite. These olivine-hosted melt inclusions are located along healed fractures and are therefore interpreted to be secondary in origin (as defined by Roedder 1984). Daughter djerfisherite hosted in melt inclusions typically occurs in association with Ca–Mg bearing alkali (Na, K, Ba, Sr) carbonates [e.g. calcite, dolomite, nyerereite [$Na_2Ca(CO_3)_2$], shortite [$Na_2Ca_2(CO_3)_3$], strontianite [$SrCO_3$] as well as S-bearing (sulphate?) varieties], silicates (e.g. phlogopite, tetraferriphlogopite, humite, monticellite), Fe–Ti–Mg–Cr–Al spinels, chlorides (halite, sylvite), alkali (Na, K)-rich sulphates [e.g. arcanite (K_2SO_4)], phosphates (e.g. apatite) and Fe–Ni sulphides (Fig. 10). This is consistent with previously reported occurrences of djerfisherite in olivine-hosted melt inclusions (Golovin et al. 2003, 2007, 2017a, 2018; Sharygin et al. 2003, 2007; Kamenetsky et al. 2008, 2009a; Mernagh et al. 2011; Abersteiner et al. 2018).

The compositions of djerfisherite in olivine-hosted melt inclusions in samples from Udachnaya-East from this study could not be accurately quantified by EMP analyses due to their small sizes.

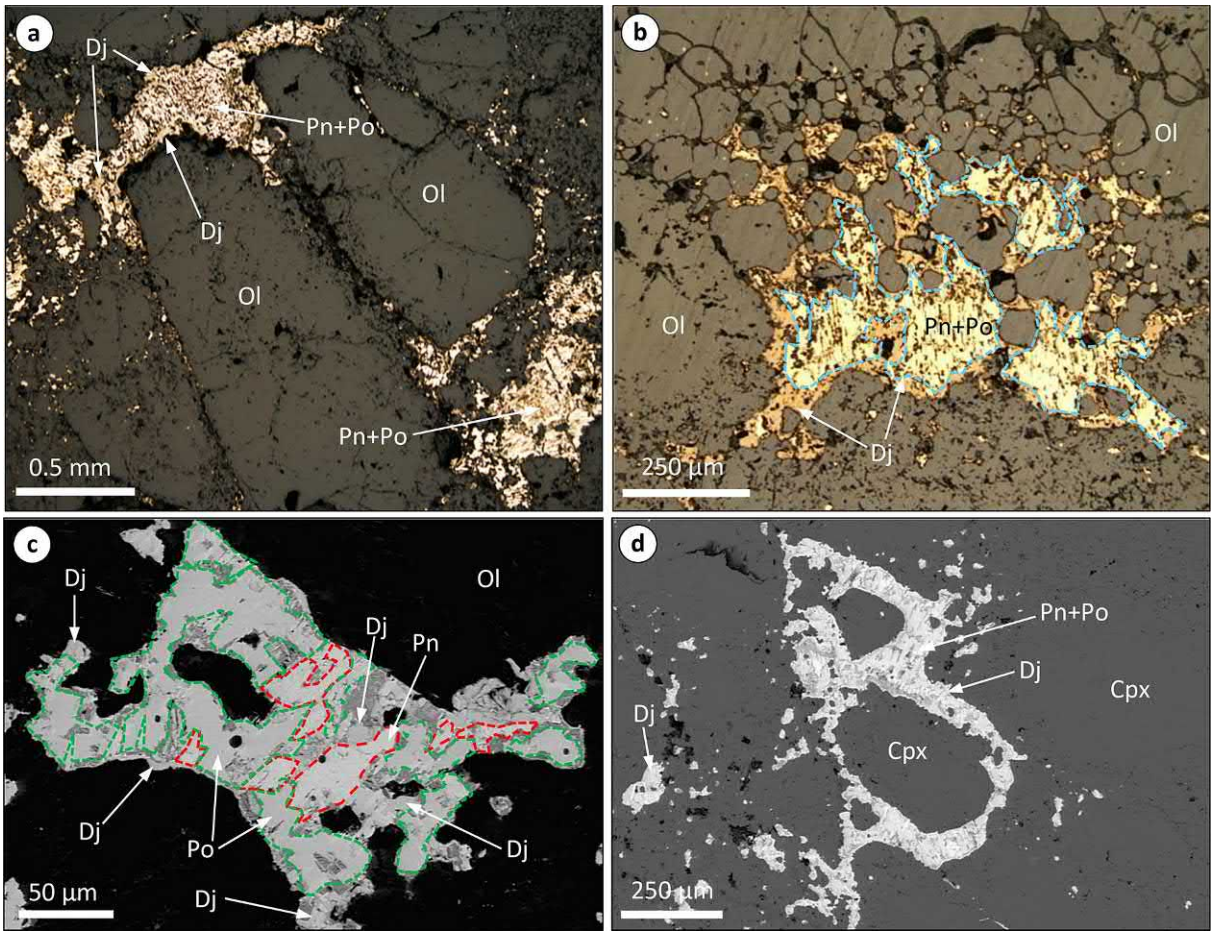

Fig. 2 Reflected light (**a, b**) and backscattered electron (BSE) SEM (**c, d**) images of intergranular sulphide segregations occurring in minerals' interstices in sheared peridotite xenoliths (samples UD1-2 and UV0112; Udachnaya-East, Siberia). Djerfisherite (Dj—brown/bronze colour in reflected light) partially replaces these Fe–Ni sulphides (pyrrhotite, Po—red dotted lines; pentlandite, Pn—green dotted lines) along rims and fractures. Sulphides are interstitial to rock-forming minerals, which suggests melt infiltration. *Ol* olivine, *Cpx* clinopyroxene. Blue dotted lines show intergrowths of pyrrhotite and pentlandite

Discussion

Our results in combination with previous studies show djerfisherite to be an accessory mineral in many kimberlites and their entrained xenoliths (i.e. mantle and crustal) and xenocrysts (e.g. olivine, diamond). The prevalence of djerfisherite in these different lithologies suggests that there is a strong link between kimberlite magmatism and djerfisherite formation. We investigate the genesis of djerfisherite and its implications for the composition and evolution of kimberlite melts.

Chemical variations in djerfisherite

Although djerfisherite is generally unzoned and homogeneous within individual grains, there is considerable compositional heterogeneity between different grains within a single sample, as well as between different host rocks and localities. In addition, djerfisherite rims surrounding Fe–Ni–Cu sulphides can exhibit wide and diffuse compositional variations in different areas of the same rim. These variations are most apparent in the three main elements (Fe, Ni, Cu; Figs. 11, 12). Iron is invariably the most abundant of these elements, where it typically ranges between ~33 and 50 wt% (Figs. 11, 12). In general, nickel is more abundant than copper in the majority of djerfisherite grains examined. Both nickel and copper display wide variations, where they can range from < 0.5 wt% through to 25 wt% Ni and 20 wt% Cu. Decrease in Fe and/or Cu in djerfisherite is usually counterbalanced by increases in Ni and vice versa. The apparent heterogeneity within djerfisherite rims surrounding other Fe–Ni–Cu sulphides may reflect the different contributions of Fe, Ni and Cu inherited from the original sulphide phase being replaced, and/or the variably differentiated (i.e. localised variations) host kimberlite melt (Dobrovolskaya and Nekrasov 1992; Zaccarini et al. 2007; Osadchii et al. 2018).

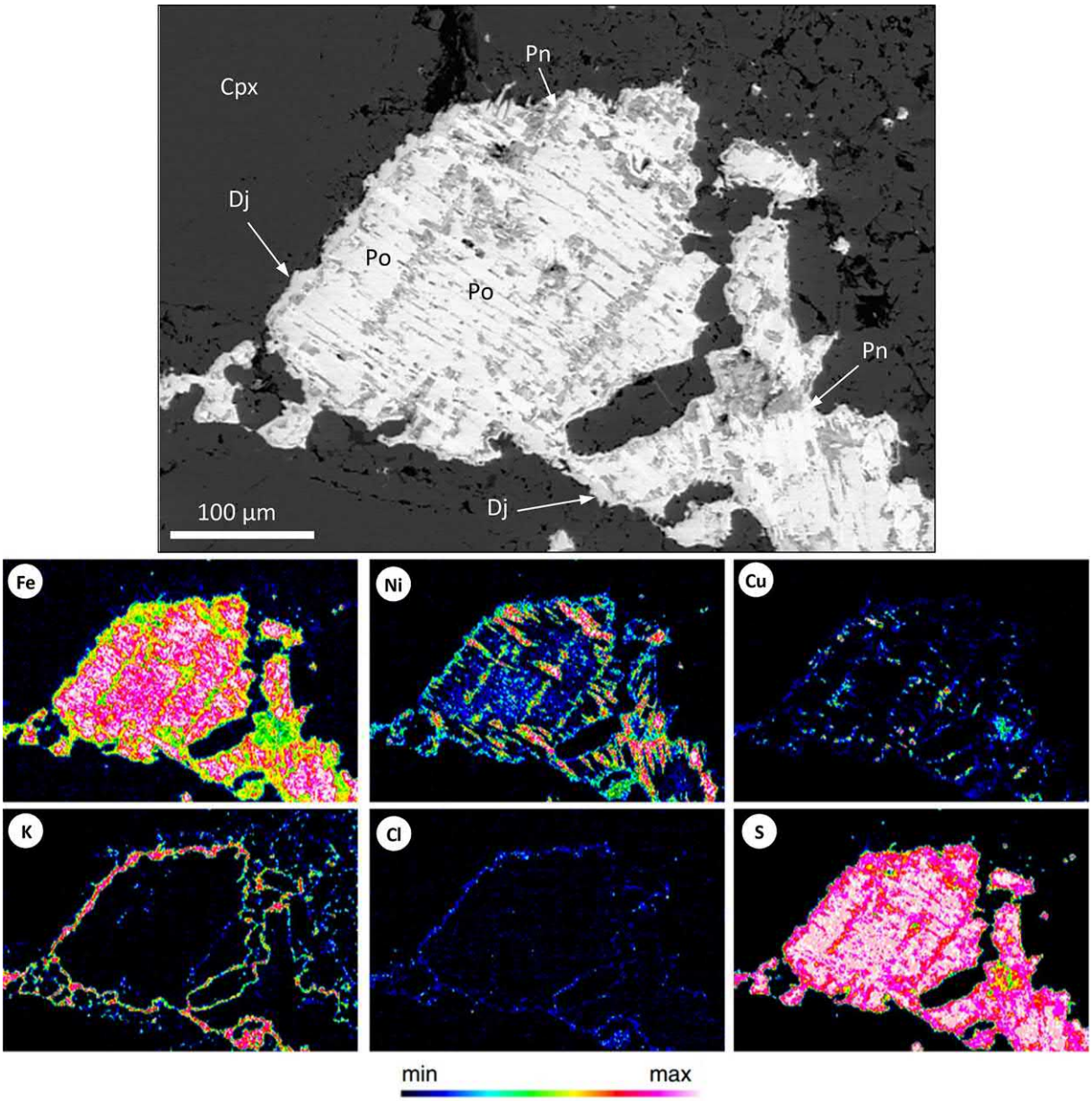

Fig. 3 Backscattered electron (BSE) SEM image and X-ray elemental maps of an intergranular sulphide segregation in a sheared peridotite xenolith (sample UD-12; Udachnaya-East, Siberia). This map demonstrates the complex zoning in Fe–Ni–Cu contents. Djerfisherite (Dj) is indicated by the presence of K–Cl–S, which occurs along the rims and fractures of this sulphide segregation. Detected minerals include: *Cpx* clinopyroxene, *Po* pyrrhotite, *Pn* pentlandite. Pentlandite is indicated by the presence of elevated (red-pink) Ni

In addition, the presence of appreciable Ni and Cu contents distinguished djerfisherite from Fe-dominated chlorbartonite ($K_6Fe_{24}S_{26}(S,Cl)$), which bears close chemical, structural and optical similarities to djerfisherite (Yakovenchuk et al. 2003).

Although there is significant scatter and overlap in djerfisherite compositions in terms of Fe–Ni–Cu ratios in each sample (Figs. 11, 12), there appears to be no distinct compositional ranges indicative of djerfisherite derived from any specific kimberlite or its entrained mantle material (i.e. xenoliths or inclusions in diamonds and olivine) setting. The only notable observation is that djerfisherite occurrences from Siberian kimberlites show the highest Cu contents (up to 20 wt%), whereas djerfisherite from South African and Canadian kimberlites contain significantly lower Cu (up to 4.1 wt%; Supplementary Table 1). These compositional variations in djerfisherite probably reflect localised variations in the composition of the crystallising kimberlite melt and/or interacting metasomatic medium (i.e. melt and/or fluid) beneath each craton. Our study confirms the earlier

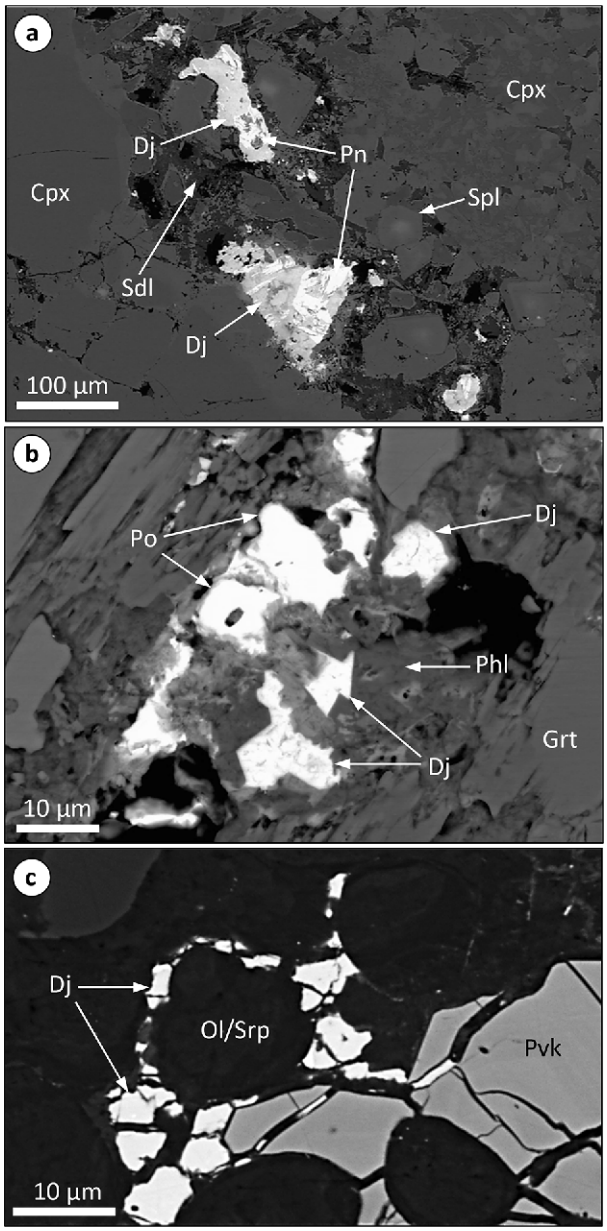

Fig. 4 Backscattered electron (BSE) SEM images of individual djerfisherite grains and as a replacement phase after other Fe–Ni–sulphides (e.g. pentlandite: Pn) in the interstices between rock-forming minerals in eclogite xenolith samples **a** UE-40-05-01 and **b** UE-SS (Udachnaya-East, Siberia), and **c** LIMA-bearing lherzolite xenolith sample XM1/362 (Bultfontein, South Africa). Djerfisherite is also aggregated with other typical groundmass kimberlite minerals, such as spinel (Spl), sodalite (Sdl), phlogopite (Phl) and perovskite (Pvk). *Cpx* clinopyroxene, *Grt* garnet

observation of Bulanova et al. (1990) that djerfisherite in ultramafic xenoliths usually has higher Ni contents, whereas djerfisherite in eclogite xenoliths is enriched in Fe and Cu. Djerfisherite from different settings (e.g. carbonatites, alkaline mafic/felsic rocks, meteorites) exhibits more restrictive ranges in terms of Fe–Ni–Cu ratios, which are usually indicative of their host rock setting (Henderson et al. 1999 and Zaccarini et al. 2007; Clay et al. 2014) and possibly mechanism of formation. Kimberlitic djerfisherite exhibits the largest variation in Fe–Ni–Cu ratios, which is probably due to their hybridised and highly variable compositions.

Is K–Cl poor 'djerfisherite' still djerfisherite?

The majority of djerfisherite grains have K contents ranging between 8.5 and 9.5 wt%. However, some djerfisherite grains display K contents below this range (e.g. Koala, XM1/362, XM1/422), which is usually accompanied by systematic decreases in, or absence of, Cl (Supplementary Table 1 and Data). Since sodium is generally extremely low in djerfisherite (< 0.3 wt%), the overall Na content appears uninfluenced by any discernible changes in K or Cl. Djerfisherite grains in the sample XM1/422 and XM1/362 are essentially Cl free and display anomalously low K contents (< 6 wt%; Supplementary Table 1 and Data). These djerfisherite grains typically have 'non-ideal' a.p.f.u totals, which are reflected by low proportions of alkalis, chlorine or Fe–Ni–Cu element totals (Fig. 11). In the Koala sample, some djerfisherite grains appear to be in contact with irregularly shaped zones which are defined by lower K–Cl, higher than average S and extremely low Cu compared to '*bona fide*' djerfisherite. These '*bona fide*' djerfisherite grains may be directly adjacent to K–Cl poor djerfisherite (Fig. 8) and both types occur within the same grain with a sharp compositional boundary.

Bona fide djerfisherite and K–Cl poor djerfisherite have almost identical Raman spectra (Fig. 9). This implies that K–Cl bonding is ionic, otherwise there would be distinct differences reflected in the Raman spectra between the two types. Therefore, only indirect effects of their removal on the structure would be visible in Raman spectra and these changes appear to be too subtle to be registered by Raman spectroscopy. The observed shifts are more likely attributed to compositional variations unrelated to K and Cl, such as variations in Co and Ni concentrations, two elements that substitute Fe in the Fe–S framework (see also Golovin et al. 2017a). The EBSD patterns of both phases also match djerfisherite (see example patterns in Supplementary Figures S5 and S6). EBSD is not sensitive enough to detect small structural changes potentially caused by the removal of K and Cl, but an EBSD map of an area that contains both regular djerfisherite and K–Cl poor djerfisherite shows that the sharp boundary between both phases crosscuts several grains in the assemblage. This confirms that both phases have the same crystal structure and growth of each grain from djerfisherite to K–Cl poor djerfisherite continued epitaxially in spite of the change in parental/interacting fluid/melt composition. An alternate scenario may be due to djerfisherite interacting with post-emplacement external fluids, thereby removing K

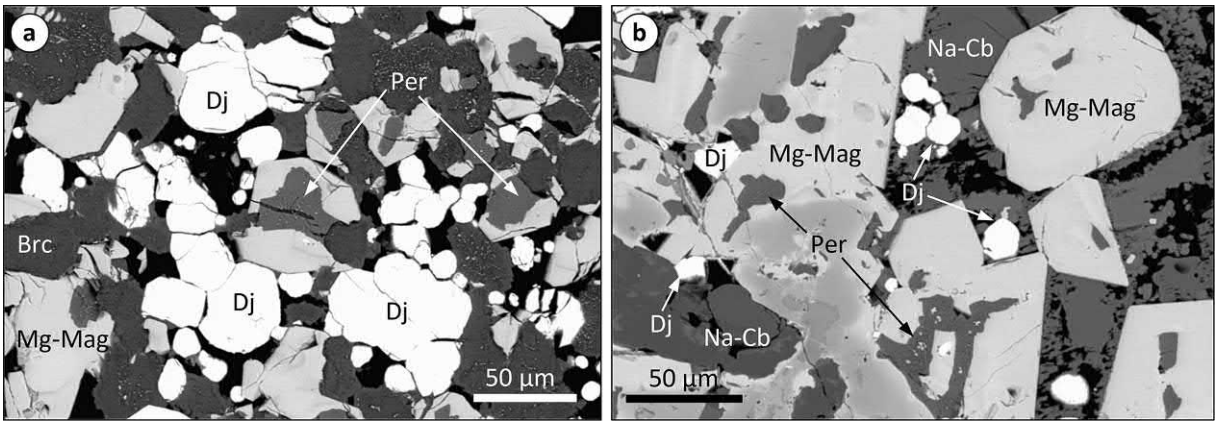

Fig. 5 Backscattered electron (BSE) SEM images of individual grains and aggregates of sub-rounded to subhedral shaped djerfisherite (Dj) from melt pools occurring in wehrlite xenolith sample UV01-332 (Udachnaya-East, Siberia; Supplementary Figure S1). Djerfisherite occurs in association with zoned Mg–magnetite (Mg–Mag), periclase (Per), brucite (Brc) and Na–carbonate (Na–Cb)

and Cl from the grain. Osadchii et al. (2018) suggested that the low Cl content in some djerfisherite occurrences may be due to Cl removal from the structure during weathering and/or sample preparation. However, Sharygin et al. (2011) suggested that djerfisherite is relatively stable during post-magmatic alteration of kimberlite rocks. Our results show that djerfisherite is preserved within a variety of kimberlite rocks and mantle xenoliths exhibiting different degrees of serpentinisation. Therefore, it is likely that changes in the K–Cl content of djerfisherite occurred during crystal growth and/or metasomatism, and not due to alteration fluids. The instability of K and Cl in djerfisherite may be analogous to high temperature > 800 °C and pressure (up to 3GPa) experiments, which showed that djerfisherite decomposes into KCl and intermediate K-bearing sulphide solid solutions (Sharygin et al. 2016). Other unclassified K-bearing and/or Cl-poor sulphides reported in different kimberlites and kimberlite-hosted rocks (e.g. Clarke 1979; Czamanske et al. 1981; Pasteris 1982; Lorand and Grégoire 2006) may also be a variety of K–Cl poor djerfisherite.

Origin of djerfisherite

Djerfisherite in kimberlites and kimberlite-hosted xenoliths/xenocrysts predominantly occurs as the partial-to-complete replacement of pre-existing Fe–Ni–Cu sulphides. This has been commonly attributed to metasomatism (Clarke 1979; Spetsius et al. 1987; Bulanova et al. 1990; Misra et al. 2004; Sharygin et al. 2007, 2012) of pre-existing sulphides by kimberlitic melt(s)/fluid(s) that were enriched in K and Cl. The presence of alkalis and halogens in the mantle is evidenced by:

1. Fluid microinclusions in fibrous diamonds (Navon et al. 1988; Izraeli et al. 2001; Klein-BenDavid et al. 2007; Zedgenizov et al. 2007; Logvinova et al. 2008).
2. Daughter inclusions of djerfisherite in diamond-hosted inclusions (Bulanova et al. 1980, 1990; Logvinova et al. 2008; Hunt et al. 2012) and mantle olivine and ilmenite (Fig. 6; Supplementary Figs. S1c and S4; Sharygin et al. 2003; Kamenetsky et al. 2009a, c; Mernagh et al. 2011; Golovin et al. 2017a, 2018).
3. In wehrlitic sample (UV01-332), djerfisherite occurs as subrounded-to-subhedral shaped grains within complex mineral pools composed of periclase and alkali (Na, K) carbonates, and is interstitial to major rock-forming phases (Fig. 5; Supplementary Fig. S1). These mineral pools are interpreted to be unaffected by serpentinisation (i.e. alteration of periclase forms brucite; see Supplementary Fig. S1) and are therefore interpreted to be pristine magmatic in origin (i.e. crystallised 'melt pools'). The timing of formation of these melt pools cannot be confidently assigned, but were likely coeval with xenolith entrainment in the kimberlite magma or represent kimberlite melt penetration that en route to the surface.
4. The presence of hydrous K-bearing minerals (e.g. phlogopite, amphibole) in mantle xenoliths suggested that potassic metasomatism occurred in the upper mantle (e.g. Reid et al. 1975; Dawson and Smith 1977; Gurney and Harte 1980; Erlank et al. 1987; Misra et al. 2004; Araújo et al. 2009; Giuliani et al. 2012).

Experimental studies have shown that djerfisherite forms at a relatively narrow range of temperatures and pressures (i.e. 350–650 °C) at 1 atmosphere pressure (Clarke 1979) and 470 °C at 0.1 GPa (Gorbachev and Nekrasov 1980). This corresponds to crustal emplacement conditions of kimberlite magmas. On the other hand, the high pressure stability of djerfisherite is still poorly constrained. Sharygin et al. (2016) conducted experiments on djerfisherite between 600 and 1200 °C at 3 GPa (i.e. within the diamond stability

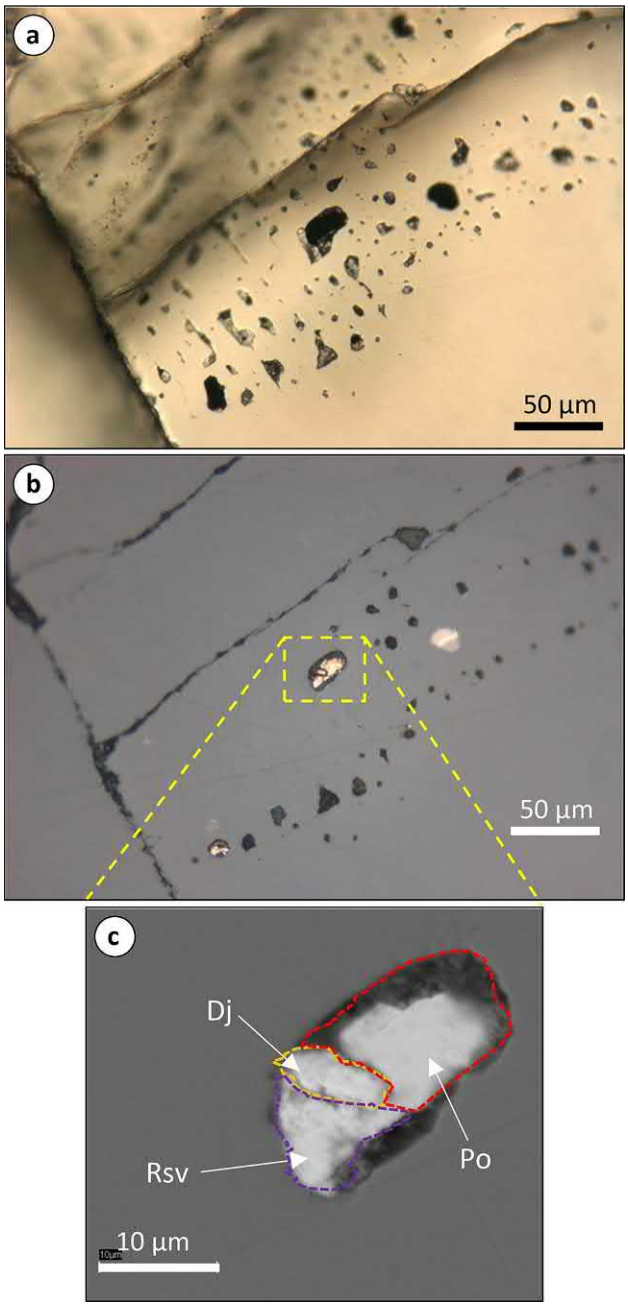

Fig. 6 **a** Transmitted-light and **b** reflected-light microscope images, and **c** backscattered electron SEM image of secondary melt inclusion in olivine from sheared peridotite xenolith sample 89-03-1 (Udachnaya-East, Russia). *Dj* djerfisherite—orange dotted line, *Rsv* rasvumite—purple dotted line, *Po* pyrrhotite—red dotted line

field). These experiments showed that between 600 and 800 °C and at 3GPa, djerfisherite decomposes to KCl + Cl-free K-sulphides and at higher temperatures the K-phases are absent. Therefore, it is unlikely that djerfisherite is a stable in situ phase that formed in the deep mantle. However, these experiments do not fully take into account all parameters of mantle conditions, such as oxygen fugacity or the possible existence of H_2O and K–Cl bearing fluids. It is noteworthy that djerfisherite may be stable within some lithospheric mantle occurrences, such as in spinel harzburgite (sample XM1/422) which was equilibrated at 700 °C (Giuliani et al. 2013; i.e. within the djerfisherite stability field). e. In the following section, we identify two key mechanisms for djerfisherite formation from kimberlite melts/fluids:

1. The majority of djerfisherite occurrences are as replacement rims along the peripheries or internal fractures of other Fe–Ni–Cu sulphides (Figs. 1, 2, 3, 4, 7; Supplementary Figures S3 and S7). However, these djerfisherite rims around Fe–Ni–Cu sulphides are unlikely to represent a stable in situ configuration that would survive for long at mantle depths. It is possible that mantle metasomatism involving K–Cl rich kimberlitic melts/fluids reacted with precursor Fe–Ni–Cu sulphides at mantle depths close to the timing of, or during kimberlite magma ascent. Djerfisherite aggregates hosted in xenocrystic olivine from kimberlite sample V-100 (Supplementary Fig. S2) probably formed due to the complete replacement of pre-existing Fe–Ni–Cu sulphides due to infiltrating metasomatic kimberlite melts/fluids. In addition, kimberlite melt penetration is evident in mantle-derived xenoliths where secondary kimberlitic minerals such as phlogopite, spinel, sodalite and perovskite are present and interstitial to major xenolith constituents (Fig. 4). The presence of djerfisherite in diamonds and mantle xenolith minerals may be attributed to decompression fracturing during rapid kimberlite magma ascent (Brett et al. 2015), where these fractures may have facilitated pathways for kimberlite melt infiltration, which was then able to react with precursor Fe–Ni–Cu sulphides. Therefore, it is possible that djerfisherite in diamonds and mantle xenoliths may have formed after their entrainment into the ascending kimberlite magma. Furthermore, we found djerfisherite and rasvumite in fractures and along rims of pyrrhotite grains in a crustal xenolith (sample pt4a-05) hosted in the Udachnaya-East kimberlite (Supplementary Figure S7). In our view, this crustal fragment was permeated by the host kimberlite melt, where minerals such as sodalite crystallised from the melt directly and/or as a replacement of pre-existing minerals. Precursor sulphides (i.e. pyrrhotite) in the xenolith were in turn partially replaced by djerfisherite and rasvumite along rims and fractures due to interaction with this kimberlite melt.
2. The second origin for djerfisherite is the direct crystallisation from the kimberlite melt. Analyses of a kimberlite-hosted garnet harzburgite from Somerset Island (Canada) by Bragagni et al. (2017) found coronae (i.e. overgrowths) of djerfisherite surrounding Fe–Ni sulphides contain more radiogenic $^{187}Os/^{188}Os$ composi-

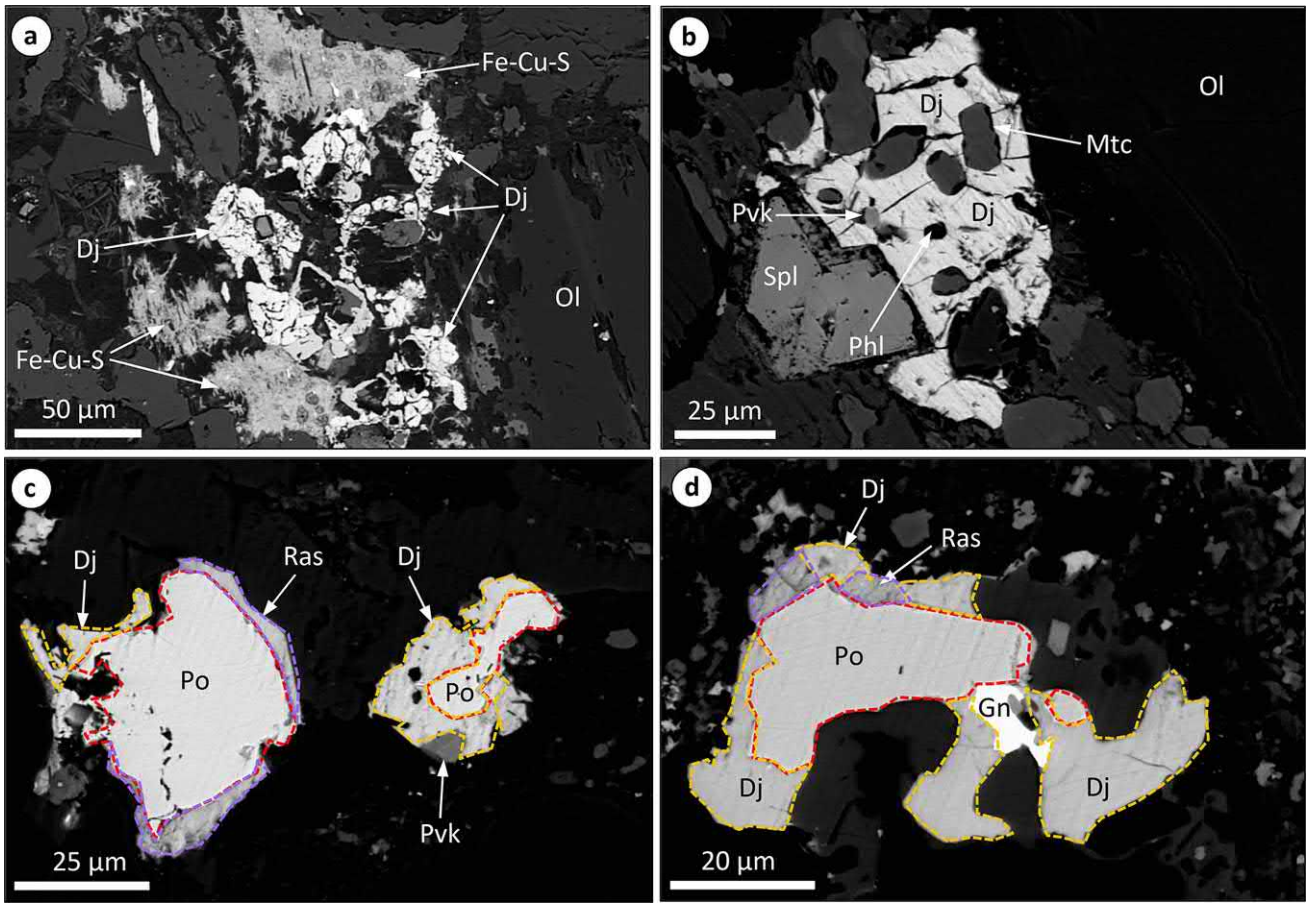

Fig. 7 Backscattered electron (BSE) SEM images of djerfisherite (Dj—orange dotted lines) in the groundmass of the **a** Leslie (Canada), and **b**–**d** Udachnaya-East kimberlites (Siberia). **a, b** Djerfisherite segregations are interstitial to surrounding groundmass phases and contain poikilitically enclosed inclusions of phlogopite (Phl), perovskite (Pvk) and monticellite (Mtc). **c, d** Rims of djerfisherite and rasvumite (Ras—purple dotted lines) partially replace pyrrhotite (Po—red dotted lines) along its rims. *Ol* olivine, Fe–Cu–S Fe–Cu–sulphide, *Spl* spinel, *Gn* galena

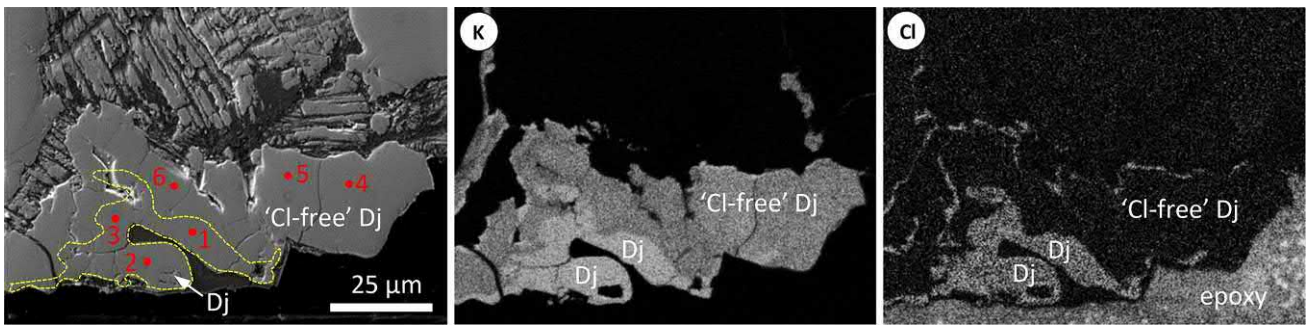

Fig. 8 Secondary electron (SE) SEM image and X-ray elemental map of djerfisherite (Dj) zoned between Cl-bearing '*bona fide*' djerfisherite and 'Cl-free' djerfisherite from the groundmass of the Koala kimberlite (Canada). These zones are in sharp contact with each other. The red numbered points represent locations of Raman analyses, which are shown in Fig. 9. 1, 2, 3—'*bona fide*' djerfisherite; 4, 5, 6—'Cl-free' djerfisherite

tions. This isotopic signature is distinct from the 'older' sulphide cores and consistent with direct crystallisation of djerfisherite after kimberlite melt penetration. Furthermore, djerfisherite typically forms the subhedral shapes or segregations, which poikilitically enclose other magmatic groundmass minerals (e.g. olivine, cal-

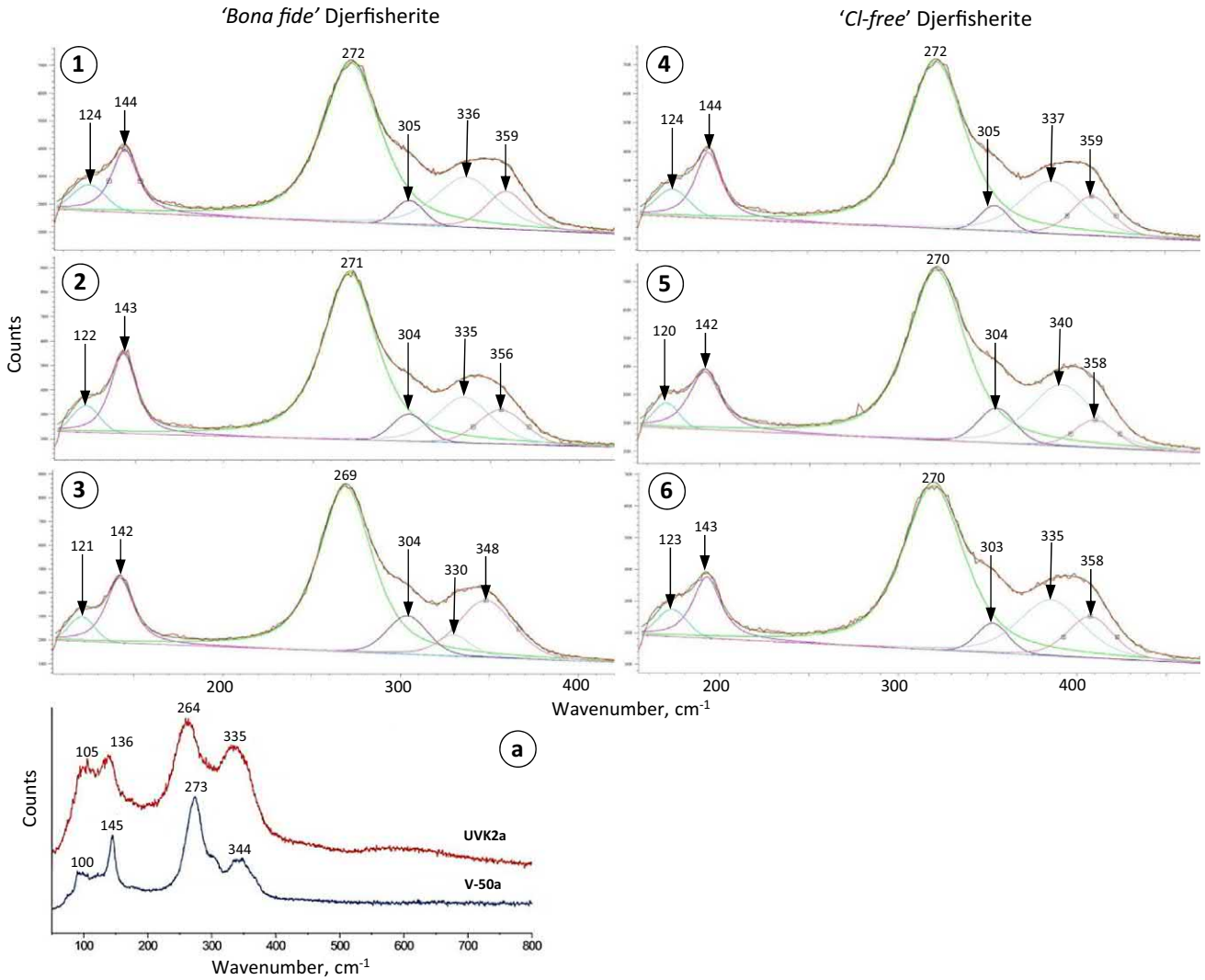

Fig. 9 Representative Raman spectra of Cl-bearing and Cl-free djerfisherite from the Koala kimberlite (see analyses locations in Fig. 8) with six (individually coloured) fitting peaks shown. Both forms of djerfisherite exhibit near identical Raman peaks. **1**–**3** '*bona fide*' djerfisherite, **4**–**6** '*Cl-free*' djerfisherite. **a** Comparison of Raman spectra from the Udachnaya-East (UVK2a) and Vtorogodnitsa (V-50a) kimberlites from Golovin et al. (2017a)

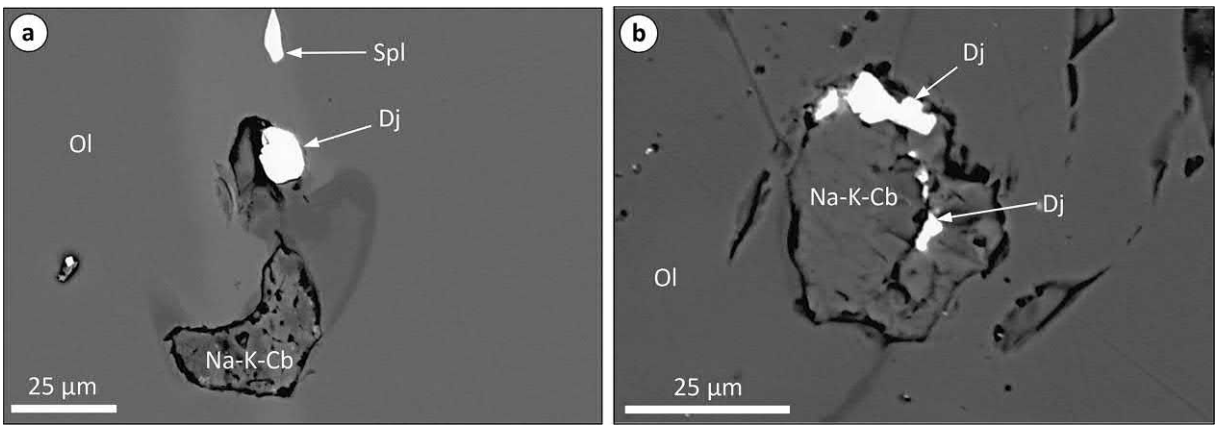

Fig. 10 Backscattered electron (BSE) SEM images of secondary melt inclusions in olivine (Ol) from the Udachnaya-East kimberlite (Siberia). These inclusions host daughter phases of alkali (Na, K) carbonates (Na–K Cb) and djerfisherite (Dj). *Spl* spinel

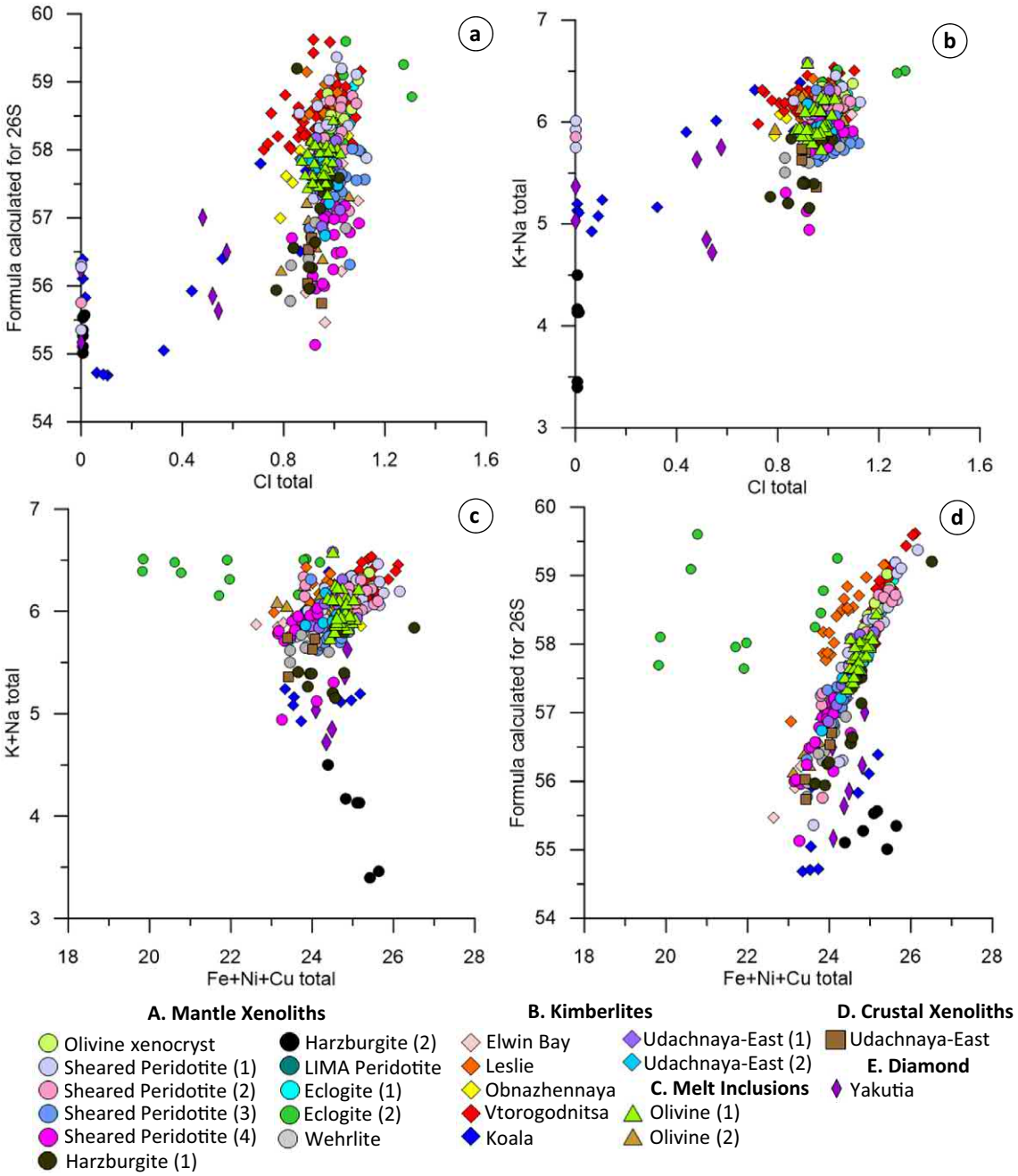

Fig. 11 Compositional variation diagrams (atoms per formula unit) of **a** Cl vs. total calculated for 26S, **b** Cl vs. K + Na, **c** Fe + Ni + Cu vs. K + Na and **d** Fe + Ni + Cu vs. total calculated for 26S for djerfisherite in: (A) kimberlite-hosted mantle xenoliths: inclusion in xenocrystic olivine (sample V-100); Udachnaya-East sheared peridotite (1) sulphide globules, (2) individual sulphide segregations, (3) polysulphide segregations in rock-forming interstices and (4) secondary melt inclusions in olivine (Supplementary Data; Sharygin et al. 2012); Roberts Victor (sample RV1a) garnet harzburgite (1); Bultfontein (sample XM1/422) spinel harzburgite (2); Bultfontein LIMA-bearing peridotite (sample XM1/362); Udachnaya-East eclogite (1; sample UE12); Yakutian eclogites (2; Bulanova et al. 1990); Udachnaya-East wehrlite (sample UV01-322). (B) Kimberlite groundmass: Elwin Bay (Clarke et al. 1994); Leslie (sample LDC7); Obnazhennaya and Vtorogodnitsa (Supplementary Data; Sharygin et al. 2011); Koala (sample BHP7); Udachnaya-East (1—Sharygin et al. 2003, 2007; 2). (C) Melt inclusions in kimberlitic olivine (1—Golovin (2004); 2—Udachnaya-East, this study). (D) Crustal xenolith in the Udachnaya-East kimberlite (sample pt4a-05). (E) Kimberlite-hosted diamond (Bulanova et al. 1990)

cite, spinel and phlogopite; Fig. 7a, b) indicating late-stage precipitation from the kimberlite melt. However, the complete replacement of pre-existing Fe–Ni–Cu sulphides by djerfisherite should not be excluded. Secondary melt inclusions hosted in olivine contain daughter djerfisherite, which indicates direct crystallisation from

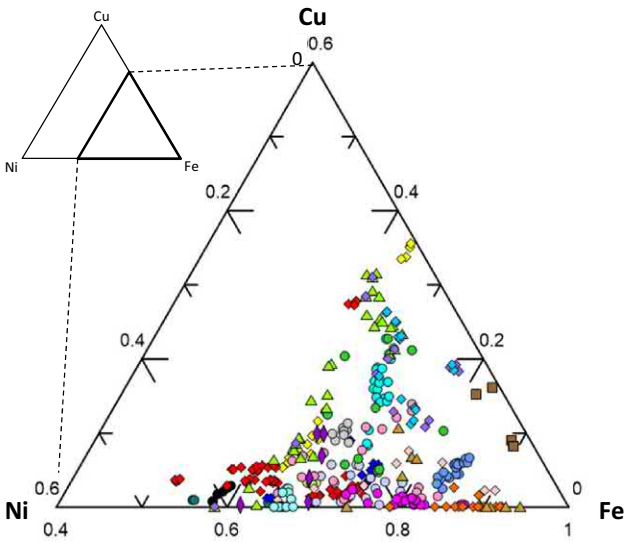

Fig. 12 Ternary of diagram of Fe, Ni and Cu compositions of djerfisherite (refer to Fig. 11 for legend)

entrapped kimberlite melts (e.g. Fig. 10). The enrichment of K–Cl in this entrapped kimberlite melts/fluids is further substantiated by its association with alkali (Na, K) carbonates and salts (halite, sylvite). This primary origin of djerfisherite bears similarities to other djerfisherite occurrences from different lithologies, such as in the Guli Dunite Complex (Russia), where djerfisherite is thought to have formed as a primary mineral during late-stage fractionation of alkali-enriched residual melts (Zaccarini et al. 2007).

In addition, the presence of djerfisherite in meteorites shows it to be a primary phase, which formed during solar nebula condensation in unequilibrated E chondites (Clay et al. 2014). The extensive variety of processes for djerfisherite formation in extra-terrestrial and terrestrial settings suggests that this sulphide has the potential to be a useful tracker for examining K and Cl in mantle evolution.

Significance of K–Cl enrichment in the kimberlite melt

The presence of groundmass djerfisherite (Fig. 7a, b) and djerfisherite as a replacement mineral after precursor Fe–Ni–Cu sulphides (Fig. 7c, d) in kimberlite rocks provides strong evidence that the parental kimberlite melt contained K and Cl in some abundance. Reconstructing the composition of parental kimberlite melts employing whole-rock compositions is challenging, largely due to the overprinting effects of post-magmatic alteration (Sparks et al. 2006, 2009; Stripp et al. 2006; Afanasyev et al. 2014; Giuliani et al. 2014a, 2017; Kamenetsky et al. 2014), entrainment of mantle and crustal xenoliths and xenocrysts (e.g. olivine; Kamenetsky et al. 2008; Brett et al. 2009; Arndt et al. 2010; Giuliani 2018; Soltys et al. 2018) and interactions with entrained material (Hunter and Taylor 1982; Smith et al. 2004; Buse et al. 2010; Sharygin et al. 2015, 2017b; Soltys et al. 2016; Tappe et al. 2016). The pursuit in identifying the true nature of parental kimberlite melt compositions has resulted in two divergent views. The classic view of kimberlite petrogenesis maintains that they derived from ultramafic/basic, ultrapotassic and volatile (H_2O, CO_2)-rich compositions (Price et al. 2000; le Roex et al. 2003; Becker and le Roex 2006; Kjarsgaard et al. 2009; Kopylova et al. 2013). These compositions are based heavily on whole-rock reconstructions, which are unable to fully discriminate the full masking effects of alteration and contamination. Alternatively, numerous petrographic and melt inclusions studies (Golovin et al. 2007, 2017b, 2018; Kamenetsky et al. 2009b, 2013, 2014; Abersteiner et al. 2017a, b, c, 2018; Giuliani et al. 2017) and experimental works (e.g. Sparks et al. 2009; Brooker et al. 2011; Russell et al. 2012; Kamenetsky and Yaxley 2015) have advocated that parental kimberlite melt compositions had formerly more characteristics of carbonate or silicate–carbonate melts enriched in alkalis (Na, K) and halogens (F, Cl) relative to whole-rock compositions. However, the extent of this enrichment remains uncertain. The paucity of alkali- and halogen-rich phases in the kimberlite groundmass is commonly attributed to their incorporation into water-soluble phases (e.g. carbonates, halides) where they are highly susceptible to degradation and removal during hydrous alteration (i.e. serpentinisation), such as the alkali–carbonate and chloride-rich groundmass mineralogy of the Udachnaya-East kimberlite (Kopylova et al. 2013; Kamenetsky et al. 2014). Furthermore, alkalis and halogens concentrated in the residual kimberlite melt/fluid could be released into the surrounding wall rocks (Smith et al. 2004; Giuliani et al. 2017) or expelled as a fluid/gas phase during ascent and/or emplacement (Stamm and Schmidt 2017; Soltys et al. 2018).

The continually growing list of djerfisherite (see Table 2 and Supplementary Table 1), rasvumite and other K-rich sulphide (e.g. Clarke et al. 1977; Clarke 1979; Pasteris 1982; Lorand and Grégoire 2006; Sharygin et al. 2008) occurrences in various kimberlites and kimberlite-hosted xenoliths and xenocrysts strongly favours a former host medium that was alkali and halogen enriched, such as the carbonate or silicate–carbonate parental kimberlite melt model. Furthermore, recent S-isotope studies by d'Eyrames et al. (2017) and Kitayama et al. (2017) demonstrated that "*kimberlites preserve a unique population of djerfisherites (Cl- and K-rich sulphides) with* $\delta^{34}S$ *values within the mantle range*". The preservation of djerfisherite in kimberlites, even after post-magmatic alteration, provides strong evidence of a former mantle-derived K–Cl bearing source. This

K–Cl signature in djerfisherite therefore requires a formerly alkali–halogen enriched source, such as in the carbonate or carbonate–silicate parental kimberlite melt model.

Conclusions

- Djerfisherite is extremely diverse in composition with regard to Fe:Ni:Cu ratios, where heterogeneities are possibly linked to localised variations in the interacting metasomatic medium and/or host kimberlite melt/fluid, rather than any particular settings.
- Djerfisherite may contain lower than average K and Cl contents, which results in below average a.p.f.u. Raman spectroscopy and EBSD analyses show these djerfisherite grains still maintain the same crystal structure as *'bona fide'* djerfisherite.
- Two key mechanisms for djerfisherite genesis are identified: (1) precursor Fe–Ni–Cu sulphides reacting with metasomatic K–Cl rich melts/fluids in the mantle or the transporting kimberlite melt to form djerfisherite; and (2) direct crystallisation of djerfisherite from the kimberlite melt.
- Although an accessory phase, djerfisherite is an important tracer for K and Cl in kimberlite magmas and the mantle. Other alkali- and chlorine-enriched phases (e.g. alkali–carbonates, halides), which are inferred to have previously existed in the groundmass of kimberlites, were probably removed during post-magmatic alteration. It is suggested that the parental kimberlite melts were formerly carbonate or carbonate–silicate in composition and enriched in alkalis and halogens relative to whole rock.

Acknowledgements The constructive comments by Keith Putirka and the five anonymous reviewers contributed to improving this manuscript and are gratefully acknowledged. This study has benefited from the efficient editorial handling by Chris Ballhaus. This study forms part of A.A's Ph.D. and was supported by the Australian Postgraduate Award (APA). We thank Sergei Kostrovitsky for sharing wehrlite sample UV01-332. This is contribution 1232 from the ARC Centre of Excellence for Core to Crust Fluid Systems (http://www.ccfs.mq.edu.au) and 1271 in the GEMOC Key Centre (http://www.gemoc.mq.edu.au). This work was supported by funding by Australian Research Council (ARC) Discovery Grant (DP130100257, 2013–2015) and University of Tasmania (New Star Professorship, 2010–2014) to V. Kamenetsky. AVG and IS were supported by the Russian state assignment project No 0330-2019-0009 and Russian Foundation for Basic Research (Grant no. 16-35-60052 mol_a_dk). AG receives funding from the ARC through a DECRA fellowship (Grant no. DE-150100009).

References

Abersteiner A, Giuliani A, Kamenetsky VS, Phillips D (2017a) Petrographic and melt-inclusion constraints on the petrogenesis of a magmaclast from the Venetia kimberlite cluster, South Africa. Chem Geol 455:331–341. https://doi.org/10.1016/j.chemgeo.2016.08.029

Abersteiner A, Kamenetsky VS, Pearson DG, Kamenetsky M, Goemann K, Ehrig K, Rodemann T (2017b) Monticellite in group-I kimberlites: implications for evolution of parental melts and post-emplacement CO 2 degassing. Chem Geol 478:76–88. https://doi.org/10.1016/j.chemgeo.2017.06.037

Abersteiner A, Kamenetsky VS, Kamenetsky M, Goemann K, Ehrig K, Rodemann T (2017c) Significance of halogens (F, Cl) in kimberlite melts: insights from mineralogy and melt inclusions in the Roger pipe (Ekati, Canada). Chem Geol 478:148–163. https://doi.org/10.1016/j.chemgeo.2017.06.008

Abersteiner A, Kamenetsky VS, Golovin AV, Kamenetsky M, Goemann K (2018) Was crustal contamination involved in the formation of the serpentine-free Udachnaya-East kimberlite? New insights into parental melts, liquidus assemblage and effects of alteration. J Petrol. https://doi.org/10.1093/petrology/egy068

Afanasyev AA, Melnik O, Porritt L, Schumacher JC, Sparks RSJ (2014) Hydrothermal alteration of kimberlite by convective flows of external water. Contrib Mineral Petrol 168:1038–1055. https://doi.org/10.1007/s00410-014-1038-y

Araújo DP, Griffin WL, Reilly SY (2009) Mantle melts, metasomatism and diamond formation: insights from melt inclusions in xenoliths from Diavik. Slave Craton Lithos 112(2):675 – 682. https://doi.org/10.1016/j.lithos.2009.06.005

Arndt NT, Guitreau M, Boullier AM, le Roex A, Tommasi A, Cordier P, Sobolev A (2010) Olivine, and the origin of kimberlite. J Petrol 51:573–602. https://doi.org/10.1093/petrology/egp080

Aulbach S, Griffin WL, Pearson NJ, O'Reilly SY, Kivi K, Doyle BJ (2004) Mantle formation and evolution, slave craton: constraints from HSE abundances and Re–Os isotope systematics of sulfide inclusions in mantle xenocrysts. Chem Geol 208:61–88. https://doi.org/10.1016/j.chemgeo.2004.04.006

Becker M, le Roex AP (2006) Geochemistry of South African on- and off-craton, group i and group ii kimberlites: petrogenesis and source region evolution. J Petrol 47:673–703. https://doi.org/10.1093/petrology/egi089

Bragagni A, Luguet A, Fonseca ROC, Pearson DG, Lorand JP, Nowell GM, Kjarsgaard BA (2017) The geological record of base metal sulfides in the cratonic mantle: a microscale $^{187}Os/^{188}Os$ study of peridotite xenoliths from Somerset Island, Rae craton (Canada). Geochim Cosmochim Acta 216:264–285. https://doi.org/10.1016/j.gca.2017.04.015

Brett RC, Russell JK, Moss S (2009) Origin of olivine in kimberlite: phenocryst or impostor? Lithos 112S: 201–212. https://doi.org/10.1016/j.lithos.2009.04.030

Brett RC, Russell J, Andrews G, Jones T (2015) The ascent of kimberlite: insights from olivine. Earth Planet Sci Lett 424:119–131. https://doi.org/10.1016/j.epsl.2015.05.024

Brooker R, Sparks R, Kavanagh J, Field M (2011) The volatile content of hypabyssal kimberlite magmas: some constraints from experiments on natural rock compositions. Bull Volcanol 73:959–981. https://doi.org/10.1007/s00445-011-0523-7

Bulanova GP, Shestakova OE, Leskova NV (1980) Djerfisherite in diamond-hosted sulfide inclusions. Dokl Acad Sci USSR 255:430–433

Bulanova GP, Spetsius ZV, Leskova NV (1990) Sulphides in diamonds and xenoliths from Yakutian kimberlite pipes. Nauka, Novosibirsk, 120 pp (In Russian)

Buse B, Schumacher J, Sparks R, Field M (2010) Growth of bultfonteinite and hydrogarnet in metasomatized basalt xenoliths in the B/K9 kimberlite, Damtshaa, Botswana: insights into hydrothermal metamorphism in kimberlite pipes. Contrib Mineral Petrol 160:533–550. https://doi.org/10.1007/s00410-010-0492-4

Bussweiler Y, Foley SF, Prelević D, Jacob DE (2015) The olivine macrocryst problem: new insights from minor and trace element

compositions of olivine from Lac de Gras kimberlites, Canada. Lithos 220-223:238–252. https://doi.org/10.1016/j.lithos.2015.02.016
Chakhmouradian AR, Mitchell RH (2001) Three compositional varieties of perovskite from kimberlites of the Lac de Gras field. Mineral Mag 65:133–148
Clarke DB (1979) Synthesis of nickeloan djerfisherite and the origin of potassic sulphides at the Frank Smith mine. In: The mantle sample: inclusions in kimberlites and other volcanics. Proc Second Int Kimberlite Conf 2 pp 300–307
Clarke DB, Pe GG, Mackay RM, Gill KR, O'Hara MJ, Gard JA (1977) A new potassium-iron nickel sulphide from a nodule in kimberlite. Earth Planet Sci Lett 35:421–428
Clarke DB, Mitchell RH, Chapman CAT, MacKay RM (1994) Occurrence and origin of djerfisherite from the Elwin Bay kimberlite, Somerset Island, Northwest Territories. Can Mineral 32:815–823
Clay PL, O'Driscoll B, Upton BGJ, Busemann H (2014) Characteristics of djerfisherite from fluid-rich, metasomatized alkaline intrusive environments and anhydrous enstatite chondrites and achondrites. Am Miner 99:1683–1693. https://doi.org/10.2138/am.2014.4700
Creaser RA, Grütter H, Carlson J, Crawford B (2004) Macrocrystal phlogopite Rb–Sr dates for the Ekati property kimberlites, Slave Province, Canada: evidence for multiple intrusive episodes in the paleocene and eocene. Lithos 76(1–4):399–414. https://doi.org/10.1016/j.lithos.2004.03.039
Czamanske GK, Erd RC, Leonard BF, Clark JR (1981) Bartonite, a new potassium iron sulfide mineral. Am Miner 66:369–375
d'Eyrames E, Thomassot E, Kitayama Y, Golovin A, Korsakov A, Ionov D (2017) A mantle origin for sulfates in the unusual "salty" Udachnaya-East kimberlite from sulfur abundances, speciation and their relationship with groundmass carbonates. Bull Geol Soc Fr 187:67–74. https://doi.org/10.1051/bsgf/2017007
Dawson JB, Smith JV (1977) The MARID (mica-amphibole-rutile-ilmenitediopside) suite of xenoliths in kimberlite. Geochim Cosmochim Acta 41:309–333. https://doi.org/10.1016/0016-7037(77)90239-3
Distler VV, Ilupin IP, Laputina IP (1987) Sulfides of deep-seated origin in kimberlites and some aspects of copper-nickel mineralization. Int Geol Rev 29(4):456–464. https://doi.org/10.1080/00206818709466163
Dobrovol'skaya MG, Tsepin AI, Ilupin IP, Ponomarenko AI (1975) Djerfisherite from Yakutia kimberlites. In: Tatarinov PM (ed) Minerals and parageneses of endogenic deposits (in Russian). Nauka, Leningrad, pp 3–11
Dobrovolskaya M, Nekrasov IY (1992) Phase relations in systems containing alkali metals (in Russian). Dokl Earth Sci 322:373–377
Egorov KN, Kornilova VP, Safronov AF, Filippov ND (1986) Micaceous kimberlite from the Udachnaya-East pipe. Dokl Acad Sci USSR 291:199–202 (In Russian)
Erlank AJ, Waters FG, Hawkesworth CJ, Haggerty SE, Allsopp HL, Rickard RS, Menzies M (1987) Evidence for mantle metasomatism in peridotite nodules from the kimberley pipes, South Africa. In: Menzies MA, Hawkesworth CJ (eds) Mantle Metasomatism. Academic Press, London, pp 221–311
Fuchs LH (1966) Djerfisherite, alkali copper–iron sulfide: a new mineral from enstatite chondrites. Science 153:166–167
Giuliani A, Kamenetsky VS, Phillips D, Kendrick MA, Wyatt BA, Goemann K (2012) Nature of alkali-carbonate fluids in the subcontinental lithospheric mantle. Geology 40:967–970. https://doi.org/10.1130/g33221.1
Giuliani A, Kamenetsky VS, Kendrick MA, Phillips D, Goemann K (2013) Nickel-rich metasomatism of the lithospheric mantle by pre-kimberlitic alkali-S–Cl-rich C–O–H fluids. Contrib Mineral Petrol 165:155–171. https://doi.org/10.1007/s00410-012-0801-1
Giuliani A, Phillips D, Kamenetsky VS, Fiorentini ML, Farquhar J, Kendrick MA (2014a) Stable isotope (C, O, S) compositions of volatile-rich minerals in kimberlites: a review. Chem Geol 374–375:61–83. https://doi.org/10.1016/j.chemgeo.2014.03.003
Giuliani A, Phillips D, Maas R, Woodhead JD, Kendrick MA, Greig A, Armstrong RA, Chew D, Kamenetsky VS, Fiorentini ML (2014b) LIMA U–Pb ages link lithospheric mantle metasomatism to Karoo magmatism beneath the kimberley region, South Africa. Earth Planet Sci Lett 401:132–147. https://doi.org/10.1016/j.epsl.2014.05.044
Giuliani A, Phillips D, Kamenetsky VS, Kendrick MA, Wyatt BA, Goemann K, Hutchinson G (2014c) Petrogenesis of mantle polymict breccias: insights into mantle processes coeval with kimberlite magmatism. J Petrol 55:831–858. https://doi.org/10.1093/petrology/egu008
Giuliani A, Soltys A, Phillips D, Kamenetsky VS, Maas R, Goemann K, Woodhead JD, Drysdale R, Griffin WL (2017) The final stages of kimberlite petrogenesis: petrography, mineral chemistry, melt inclusions and Sr-C-O isotope geochemistry of the Bultfontein kimberlite (Kimberley, South Africa). Chem Geol 455:342–356. https://doi.org/10.1016/j.chemgeo.2016.10.011
Giuliani A, Woodhead JD, Phillips D, Maas R, Davies GR, Griffin WL (2018) Titanates of the lindsleyite–mathiasite (LIMA) group reveal isotope disequilibrium associated with metasomatism in the mantle beneath Kimberley (South Africa). Earth Planet Sci Lett 482:253–264. https://doi.org/10.1016/j.epsl.2017.11.014
Golovin AV (2004) Melt evolution features during crystallisation of kimberlites (Udachnaya-East pipe, Yakutia) and basanites (Bele pipe, Khakasia) based on study of melt inclusions. PhD dissertation, UIGGM SD RAS, Novosibirsk, pp 240 **(In Russian)**
Golovin AV, Sharygin VV, Pokhilenko NP, Malkovets VG, Kolesov BA, Sobolev NV (2003) Secondary melt inclusions in olivine from unaltered kimberlites of the Udachnaya-East Pipe, Yakutia. Dokl Earth Sci 388:93–96
Golovin AV, Sharygin VV, Pokhilenko NP (2007) Melt inclusions in olivine phenocrysts in unaltered kimberlites from the Udachnaya-East pipe, Yakutia: some aspects of kimberlite magma evolution during late crystallisation stages. Petrology 15(2):168–183. https://doi.org/10.1134/s086959110702004x
Golovin AV, Goryainov SV, Kokh SN, Sharygin IS, Rashchenko SV, Kokh KA, Sokol EV, Devyatiyarova AS (2017a) The application of Raman spectroscopy to djerfisherite identification. J Raman Spectrosc 48:1574–1582. https://doi.org/10.1002/jrs.5143
Golovin AV, Sharygin IS, Korsakov AV (2017b) Origin of alkaline carbonates in kimberlites of the Siberian craton: evidence from melt inclusions in mantle olivine of the Udachnaya-East kimberlite. Chem Geol 455:357–375. https://doi.org/10.1016/j.chemgeo.2016.10.036
Golovin AV, Sharygin IS, Kamenetsky VS, Korsakov AV, Yaxley GM (2018) Alkali-carbonate melts from the base of cratonic lithospheric mantle: links to kimberlites. Chem Geol 483:261–274. https://doi.org/10.1016/j.chemgeo.2018.02.016
Gorbachev NS, Nekrasov IY (1980) Genesis of synthetic and natural potassium sulfides. Dokl Acad Sci USSR. Earth Sci Sect 251:126–129.
Govorov I, Blagodareva N, Kiryukhina N, Khar'kiv A, Shcheglov A (1984) Primary potassium minerals in deep-seated eclogites of Yakutia. Int Geol Rev 26:1290–1294. https://doi.org/10.1080/00206818409466649
Gurney JJ, Harte B (1980) Chemical variations in upper mantle nodules from Southern African kimberlites. Phil Trans R Soc Lond Ser A 297:273–293. https://doi.org/10.1098/rsta.1980.0215
Henderson CMB, Kogarko LN, Plant DA (1999) Extreme closed system fractionation of volatile-rich, ultrabasic peralkaline melt inclusions and the occurrence of djerfisherite in the Kugda alkaline complex, Siberia. Mineral Mag 63:433–438. https://doi.org/10.1180/002646199548529

Hunt L, Stachel T, McCandless TE, Armstrong J, Muelenbachs K (2012) Diamonds and their mineral inclusions from the Renard kimberlites in Quebec. Lithos 142–143:267–284. https://doi.org/10.1016/j.lithos.2012.02.022

Hunter RH, Taylor LA (1982) Instability of garnet from the mantle: glass as evidence of metasomatic melting. Geology 10:617–620. https://doi.org/10.1130/0091-7613(1982)10%3C617:IOGFTM%3E2.0.CO;2

Izraeli ES, Harris JW, Navon O (2001) Brine inclusions in diamonds: a new upper mantle fluid. Earth Planet Sci Lett 187:323–332. https://doi.org/10.1016/S0012-821X(01)00291-6

Kamenetsky VS, Yaxley GM (2015) Carbonate–silicate liquid immiscibility in the mantle propels kimberlite magma ascent. Geochim Cosmochim Acta 158:48–56. https://doi.org/10.1016/j.gca.2015.03.004

Kamenetsky VS, Kamenetsky MB, Sharygin VV, Golovin AV (2007) Carbonate-chloride enrichment in fresh kimberlites of the Udachnaya-East pipe, Siberia: a clue to physical properties of kimberlite magmas? Geophys Res Lett 34:L09316. https://doi.org/10.1029/2007GL029389

Kamenetsky VS, Kamenetsky MB, Sobolev AV, Golovin AV, Demouchy S, Faure K, Sharygin VV, Kuzmin DV (2008) Olivine in the Udachnaya-East Kimberlite (Yakutia, Russia): types, compositions and origins. J Petrol 49:823–839. https://doi.org/10.1093/petrology/egm033

Kamenetsky VS, Kamenetsky MB, Weiss Y, Navon O, Nielsen TFD, Mernagh TP (2009a) How unique is the Udachnaya-East kimberlite? Comparison with kimberlites from the Slave Craton (Canada) and SW Greenland. Lithos 112S:334–346. https://doi.org/10.1016/j.lithos.2009.03.032

Kamenetsky VS, Maas R, Kamenetsky MB, Paton C, Phillips D, Golovin AV, Gornova MA (2009b) Chlorine from the mantle: magmatic halides in the Udachnaya-East Kimberlite, Siberia. Earth Planet Sci Lett 285:96–104. https://doi.org/10.1016/j.epsl.2009.06.001

Kamenetsky VS, Kamenetsky M, Sobolev AV, Golovin AV, Sharygin VV, Pokhilenko NP, Sobolev NV (2009c) Can pyroxenes be liquidus minerals in the kimberlite magma? Lithos 112S:213–222. https://doi.org/10.1016/j.lithos.2009.03.040

Kamenetsky VS, Kamenetsky MB, Golovin AV, Sharygin VV, Maas R (2012) Ultrafresh salty kimberlite of the Udachnaya-East pipe (Yakutia, Russia): a petrological oddity or fortuitous discovery? Lithos 152:173–186. https://doi.org/10.1016/j.lithos.2012.04.032

Kamenetsky VS, Grutter H, Kamenetsky MB, Goemann K (2013) Parental carbonatitic melt of the Koala kimberlite (Canada): constraints from melt inclusions in olivine and Cr-spinel, and groundmass carbonate. Chem Geol 353:96–111. https://doi.org/10.1016/j.chemgeo.2012.09.022

Kamenetsky VS, Golovin AV, Maas R, Giuliani A, Kamenetsky MB, Weiss Y (2014) Towards a new model for kimberlite petrogenesis: evidence from unaltered kimberlites and mantle minerals. Earth Sci Rev 139:145–167. https://doi.org/10.1016/j.earscirev.2014.09.004

Kinny PD, Griffin BJ, Heaman LM, Brakhfogel FF, Spetsius ZV (1997) SHRIMP U-Pb ages of perovskite from Yakutian kimberlites. Geologiya i geofizika 38:91–99

Kitayama Y, Thomassot E, Galy A, Golovin A, Korsakov A, d'Eyrames E, Assayag N, Bouden N, Ionov D (2017) Co-magmatic sulfides and sulfates in the Udachnaya-East pipe (Siberia): a record of the redox state and isotopic composition of sulfur in kimberlites and their mantle sources. Chem Geol 455:315–330. https://doi.org/10.1016/j.chemgeo.2016.10.037

Kjarsgaard BA, Pearson DG, Tappe S, Nowell GM, Dowall DP (2009) Geochemistry of hypabyssal kimberlites from Lac de Gras, Canada: comparisons to a global database and applications to the parent magma problem. Lithos 112S:236–248. https://doi.org/10.1016/j.lithos.2009.06.001

Klein-BenDavid O, Izraeli ES, Hauri E, Navon O (2007) Fluid inclusions in diamonds from the Diavik mine, Canada and the evolution of diamond-forming fluids. Geochim Cosmochim Acta 71:723–744. https://doi.org/10.1016/j.gca.2006.10.008

Kopylova MG, Kostrovitsky SI, Egorov KN (2013) Salts in southern Yakutian kimberlites and the problem of primary alkali kimberlite melts. Earth Sci Rev 119(0):1–16. https://doi.org/10.1016/j.earscirev.2013.01.007

Kostrovitskiy SI, Kopylova MG, Egorov KN, Yakovlev DA (2013) The exceptionally fresh Udachnaya-East Kimberlite: evidence for brine and evaporite contamination. In: Pearson DG et al (eds), Proceedings of the 10th international kimberlite conference pp 75–91

Lawless PJ, Gurney JJ, Dawson JB (1979) Polymict peridotites from the bultfontein and de beers mines, Kimberly, South Africa. In: Boyd FR, Meyer HOA (eds) The mantle sample. 2nd international kimberlite conference. American Geophysical Union pp 145–155. https://doi.org/10.1029/SP016p0145

le Roex AP, Bell DR, Davis P (2003) Petrogenesis of group i kimberlites from Kimberley, South Africa: evidence from bulk-rock geochemistry. J Petrol 44:2261–2286. https://doi.org/10.1093/petrology/egg077

Logvinova AM, Wirth R, Fedorova EN, Sobolev NV (2008) Nanometre-sized mineral and fluid inclusions in cloudy Siberian diamonds: new insights on diamond formation. Eur J Mineral 20:317–331. https://doi.org/10.1127/0935-1221/2008/0020-1815

Logvinova AM, Taylor LA, Fedorova E, Yelisseyev A, Wirth R, Howarth G, Reutsky VN, Sobolev NV (2015) A unique diamondiferous peridotite xenolith from the Udachnaya kimberlite pipe, Yakutia: role of subduction in diamond formation. Russ Geol Geophys 56:306–320. https://doi.org/10.1016//j.rgg.201

Lorand JP, Grégoire M (2006) Petrogenesis of base metal sulphide assemblages of some peridotites from the Kaapvaal craton (South Africa). Contrib Mineral Petrol 151:521–538. https://doi.org/10.1007/s00410-006-0074-7

Mernagh TP, Kamenetsky VS, Kamenetsky MB (2011) A Raman microprobe study of melt inclusions in kimberlites from Siberia, Canada, SW Greenland and South Africa. Spectrochim Acta Part A Mol Biomol Spectrosc 80:82–87. https://doi.org/10.1016/j.saa.2011.01.034

Misra KC, Anand M, Taylor LA, Sobolev NV (2004) Multi-stage metasomatism of diamondiferous eclogite xenoliths from the Udachnaya kimberlite pipe, Yakutia, Siberia. Contrib Mineral Petrol 146:696–714. https://doi.org/10.1007/s00410-003-0529-z

Navon O, Hutcheon ID, Rossman GR, Wasserburg GJ (1988) Mantle-derived fluids in diamond micro-inclusion. Nature 335:784–789. https://doi.org/10.1038/335784a0

O'Brien HE, Tyni M (1999) Mineralogy and geochemistry of kimberlites and related rocks from Finland. In: Proceedings of the 7th international kimberlite conference, Geological Survey of Finland pp 626–636

Osadchii VO, Voronin MV, Baranov AV (2018) Phase equilibria in the KFeS2–Fe–S system at 300–600 °C and bartonite stability. Contrib Mineral Petrol https://doi.org/10.1007/s00410-018-1464-3

Pasteris JD (1982) Evidence of potassium metasomatism in mantle xenoliths: EOS Transactions (abstract). Am Geophys Union 63:462

Pokhilenko NP (2009) Polymict breccia xenoliths: evidence for the complex character of kimberlite formation. Lithos 112:934–941. https://doi.org/10.1016/j.lithos.2009.06.019

Porritt LA, Cas RAF (2011) The influence of complex intra- and extravent processes on facies characteristics of the Koala Kimberlite, NWT, Canada: volcanology, sedimentology and intrusive

processes. Bull Volcanol 73:717–735. https://doi.org/10.1007/s00445-011-0452-5
Price SE, Russell JK, Kopylova MG (2000) Primitive magma from the Jericho pipe, N.W.T, Canada: constraints on primary kimberlite melt chemistry. J Petrol 41:789–808. https://doi.org/10.1093/petrology/41.6.789
Reid AM, Donaldson CH, Brown RW, Ridley WI, Dawson JB (1975) Mineral chemistry of peridotite xenoliths from the Lashaine volcano, Tanzania. Phys Chem Earth 9:525–543. https://doi.org/10.1016/0079-1946(75)90037-3
Roedder E (1984) Fluid inclusions: reviews in mineralogy, vol 12. Mineralogical Society of America, Book Crafters Inc., Michigan, p 644
Russell JK, Porritt LA, Lavallee Y, Dingwell DB (2012) Kimberlite ascent by assimilation-fuelled buoyancy. Nature 481:352–356. https://doi.org/10.1038/nature10740
Sarkar C, Heaman LM, Pearson DG (2015) Duration and periodicity of kimberlite volcanic activity in the Lac de Gras kimberlite field, Canada and some recommendations for kimberlite geochronology. Lithos 218–219:155–166. https://doi.org/10.1016/j.lithos.2015.01.017
Sharygin VV, Golovin AV, Pokhilenko NP, Sobolev NV (2003) Djerfisherite in unaltered kimberlites of the Udachnaya-East pipe, Yakutia. Dokl Earth Sci 390:554–557
Sharygin VV, Golovin AV, Pokhilenko NP, Kamenetsky VS (2007) Djerfisherite in the Udachnaya-East pipe kimberlites (Sakha-Yakutia, Russia): paragenesis, composition and origin. Eur J Mineral 19:51–63. https://doi.org/10.1127/0935-1221/2007/0019-0051
Sharygin VV, Kamenetsky VS, Kamenetsky MB (2008) Potassium sulfides in kimberlite-hosted chloride-'nyerereite' and chloride clasts of the Udachnaya-East pipe, Yakutia, Russia. Can Mineral 46:1079–1095. https://doi.org/10.3749/canmin.46.4.1079
Sharygin IS, Golovin AV, Pokhilenko NP (2011) Djerfisherite in Kimberlites of the Kuoikskoe field as an indicator of enrichment of Kimberlite melts in chlorine. Dokl Earth Sci 436:301–307. https://doi.org/10.1134/s1028334x11020255
Sharygin IS, Golovin AV, Pokhilenko NP (2012) Djerfisherite in xenoliths of sheared peridotite in the Udachnaya-East pipe (Yakutia): origin and relationship with kimberlitic magmatism. Russ Geol Geophys 53:247–261. https://doi.org/10.1016/j.rgg.2012.02.003
Sharygin IS, Litasov KD, Shatskiy A, Golovin AV, Ohtani E, Pokhilenko NP (2015) Melting phase relations of the Udachnaya-East Group-I kimberlite at 3.0–6.5 GPa: experimental evidence for alkali-carbonatite composition of primary kimberlite melts and implications for mantle plumes. Gondwana Res 28:1391–1414. https://doi.org/10.1016/j.gr.2014.10.005
Sharygin IS, Litasov KD, Sharygin VV, Shatskiy A, Ohtani E (2016) Genesis of djerfisherite in kimberlite-hosted mantle xenoliths. In: Goldschmidt conference 2016 **(Abstract: 2812)**
Sharygin IS, Litasov KD, Shatskiy A, Safonov OG, Golovin AV, Ohtani E, Pokhilenko NP (2017b) Experimental constraints on orthopyroxene dissolution in alkali carbonate melts in the lithospheric mantle: implications for kimberlite melt composition and magma ascent. Chem Geol 455:44–56. https://doi.org/10.1016/j.chemgeo.2016.09.030
Smith CB, Allsopp HL, Kramers JD, Hutchinson G, Roddick JC (1985) Emplacement ages of Jurassic-Cretaceous South African kimberlites by the Rb–Sr method on phlogopite and whole-rock samples. Trans Geol Soc S Afr 88:249–266
Smith CB, Sims K, Chimuka L, Duffin A, Beard AD, Townend R (2004) Kimberlite metasomatism at Murowa and Sese pipes. Zimb Lithos 76:219–232. https://doi.org/10.1016/j.lithos.2004.03.009
Sobolev VN, Taylor LA, Snyder GA, Jerde EA, Neal CR, Sobolev NV (2010) Quantifying the effects of metasomatism in mantle xenoliths: constraints from secondary chemistry and mineralogy in Udachnaya Eclogites, Yakutia. Int Geol Rev 41:391–416. https://doi.org/10.1080/00206819909465149
Solovieva LV, Egorov KN, Markova ME, Kharkiv AD, Popolitov KE, Barankevich VG (1997) Mantle metasomatism and melting in deep-seated xenoliths from the Udachnaya pipe, their possible relationship with diamond and kimberlite formation. Russ Geol Geophys 38:182–204
Soltys A, Giuliani A, Phillips D, Kamenetsky VS, Maas R, Woodhead J, Rodemann T (2016) In-situ assimilation of mantle minerals by kimberlitic magmas—direct evidence from a garnet wehrlite xenolith entrained in the Bultfontein kimberlite (Kimberley, South Africa). Lithos 256–257:182–196. https://doi.org/10.1016/j.lithos.2016.04.011
Soltys A, Giuliani A, Phillips D (2018) A new approach to reconstructing the composition and evolution of kimberlite melts: a case study of the archetypal Bultfontein kimberlite (Kimberley, South Africa). Lithos 304–307:1–15. https://doi.org/10.1016/j.lithos.2018.01.027
Sparks RSJ, Baker L, Brown RJ, Field M, Schumacher J, Stripp G, Walters A (2006) Dynamical constraints on kimberlite volcanism. J Volcanol Geotherm Res 155:18–48. https://doi.org/10.1016/j.jvolgeores.2006.02.010
Sparks RSJ, Brooker RA, Field M, Kavanagh J, Schumacher JC, Walter MJ, White J (2009) The nature of erupting kimberlite melts. Lithos 112S:429–438. https://doi.org/10.1016/j.lithos.2009.05.032
Spetsius ZV, Bulanova GP, Leskova NV (1987) Djerfisherite and its genesis in kimberlitic rocks. Dokl Acad Sci USSR 293:199–202
Stamm N, Schmidt MW (2017) Asthenospheric kimberlites: volatile contents and bulk compositions at 7 GPa. Earth Planet Sci Lett 474:309–321. https://doi.org/10.1016/j.epsl.2017.06.037
Stripp GR, Field M, Schumacher JC, Sparks RSJ, Cressey G (2006) Post-emplacement serpentinization and related hydrothermal metamorphism in a kimberlite from Venetia, South Africa. J Metamorph Geol 24:515–534. https://doi.org/10.1111/j.1525-1314.2006.00652.x
Sun J, Liu C-Z, Tappe S, Kostrovitsky SI, Wu F-Y, Yakovlev D, Yang Y-H, Yang J-H (2014) Repeated kimberlite magmatism beneath Yakutia and its relationship to Siberian flood volcanism: insights from in situ U–Pb and Sr–Nd perovskite isotope analysis. Earth Planet Sci Lett 404:283–295. https://doi.org/10.1016/j.epsl.2014.07.039
Tappe S, Brand NB, Stracke A, van Acken D, Liu C-Z, Strauss H, Wu F-Y, Luguet A, Mitchell RH (2016) Plates or plumes in the origin of kimberlites: U/Pb perovskite and Sr–Nd–Hf–Os–C–O isotope constraints from the Superior craton (Canada). Chem Geol 45:57–83. https://doi.org/10.1016/j.chemgeo.2016.08.019
Yakovenchuk VN, Pakhomovsky YA, Men'shikov YP, Ivanyuk GY, Krivovichev SV, Burns PC (2003) Chlorbartonite, K6Fe24S26(Cl,S), a new mineral species from a hydrothermal vein in the Khibina massif, Kola Peninsula, Russia: description and crystal structure. Can Mineral 41:503–511
Zaccarini F, Thalhammer OAR, Princivalle F, Lenaz D, Stanley CJ, Garuti G (2007) Djerfisherite in the guli dunite complex, polar siberia: a primary or metasomatic phase? Can Mineral 45:1201–1211. https://doi.org/10.2113/gscanmin.45.5.120
Zedgenizov DA, Rege S, Griffin WL, Kagi H, Shatsky VS (2007) Composition of trapped fluids in cuboid fibrous diamonds from the Udachnaya kimberlite: LAM-ICPMS analysis. Chem Geol 240:151–162. https://doi.org/10.1016/j.chemgeo.2007.02.003

Appendix 6.1 - Analytical Methods

Petrographic and Inclusion Study

All studied samples were prepared as thin sections and/or epoxy resin mounts. Preliminary analyses of sample mineralogy and textures were carried out by optical microscopy on a Nikon Eclipse 50i POL microscope at the University of Tasmania.

Scanning Electron Microscopy

Detailed examination of minerals and hosted inclusions were conducted using a Hitachi SU-70 field emission scanning electron microscope (SEM) equipped with an Oxford AZtec energy dispersive x-ray spectrometry (EDS) and electron backscatter diffraction (EBSD) system at the Central Science Laboratory, University of Tasmania. A beam accelerating voltage of 15 kV was employed with a Hitachi photo-diode backscattered electron (BSE) detector and an Oxford XMax80 EDS detector to produce high-resolution BSE images of minerals and semi-quantitative EDS analyses and element maps of minerals and inclusions. EBSD was performed at 20 kV accelerating voltage using an Oxford HKL NordlysNano camera. EBSD maps were processed using the HKL Channel5 Tango package.

BSE images of djerfisherite from Obnazhennaya and Vtorogodnitsa kimberlites, and Udachnaya-East sheared peridotites and melt inclusions in olivine were obtained by a JEOL 6380LA and LEO 1430 VP SEM coupled with an INCA Energy 350 (Oxford Instruments) EDS system at the Sobolev Institute of Geology and Mineralogy, Siberian Branch, Russian Academy of Sciences (Novosibirsk).

Raman

The Raman spectra were recorded on a Renishaw inVia spectrometer with StreamLineHR, using a Helium–neon laser at 633nm with a power setting of 200 μW at the sampling spot, a 50x (NA 0.75) objective, 120 s exposure time and a 1800 l/mm grating resulting in a spectral range of 104-1325 cm-1 and resolution of about 1 cm-1.

Electron Microprobe

Bultfontein, UE12, Koala

Electron microprobe analyses of djerfisherite were carried out at the Central Science Laboratory, University of Tasmania, using a Cameca SX100 electron microprobe.

Analyses of djerfisherite were conducted using an accelerating voltage of 15 kV, beam current of 10 nA and beam size of 10 μm. The counting time was 10 seconds for Si, Mg, 20 seconds for K, Na, Cu, Ni, Co, 30 seconds for Fe, Mn, Cl, S and 40 seconds for Ca. The background counting time was 10 seconds for Si, Mg, 12 seconds for Cu, Ni, 16 seconds for K, Na, 24 seconds for Fe, Mn, Cl, S and 30 seconds for Ca. The calibration standards were Marcasite for Fe and S, Bustamite for Mn, Tugtupite for Cl, Cuprite for Cu, Pentlandite for Ni (all Astimex Standards Ltd, Toronto, Canada), Anorthoclase Kakanui USNM133868 for Na, Olivine San Carlos USNM111312/444 for Mg, Microcline USNM143966 for K (all

Jarosewich et al. 1980), Clinopyroxene Delegate (University of Tasmania in-house) for Ca and Si, and Co metal for Co. Detection limits (99% confidence) are 0.01 wt.% for Cl, S, 0.02 wt.% for K, Ca, Si, Mg, 0.03 wt.% for Fe, Mn, Na, 0.05 wt.% for Co, and 0.06 wt.% for Cu, Ni.

Reference:

Jarosewich, E., Nelen, J.A., Norberg, J.A., 1980. Reference Samples for Electron Microprobe Analysis. Geostandards Newsletter 4, 43-47.

Obnazhennaya, Vtorogodnitsa

The chemical composition of djerfisherite from the Obnazhennaya and Vtorogodnitsa kimberlites were determined on a JEOL JXA-8100 microprobe at the Sobolev Institute of Geology and Mineralogy, Siberian Branch, Russian Academy of Sciences (Novosibirsk). Analyses of djerfisherite were conducted using an accelerating voltage of 20 kV, beam current of 10 nA and beam size of 2 μm. The counting time was 10 seconds on each analytical line. The calibration standards were FeS (pyrrhotite) for Fe and S; $CuFeS_2$ (chalcopyrite) for Cu, Fe-Ni-Co alloy for Co and Ni, orthoclase for K, albite for Na, and chlorapatite for Cl.

Udachnaya-East Sheared Peridotites

The chemical composition of djerfisherite from the Udachnaya-East sheared peridotites were determined on a Camebax-Micro and a JEOL JXA-8100 at the Sobolev Institute of Geology and Mineralogy, Siberian Branch, Russian Academy of Sciences (Novosibirsk). Analyses of djerfisherite were conducted using an accelerating voltage of 20 kV, beam current of 10 and 15 nA and beam size of 2 μm. The calibration standards were FeS (pyrrhotite) for Fe and S, $CuFeS_2$ (chalcopyrite) for Cu, Fe-Ni-Co alloy for Co and Ni, orthoclase for K, albite for Na, and chlorapatite for Cl.

Electronic Appendix 6.2 – Supplementary Data

Appendix 6.3: Supplementary Figures

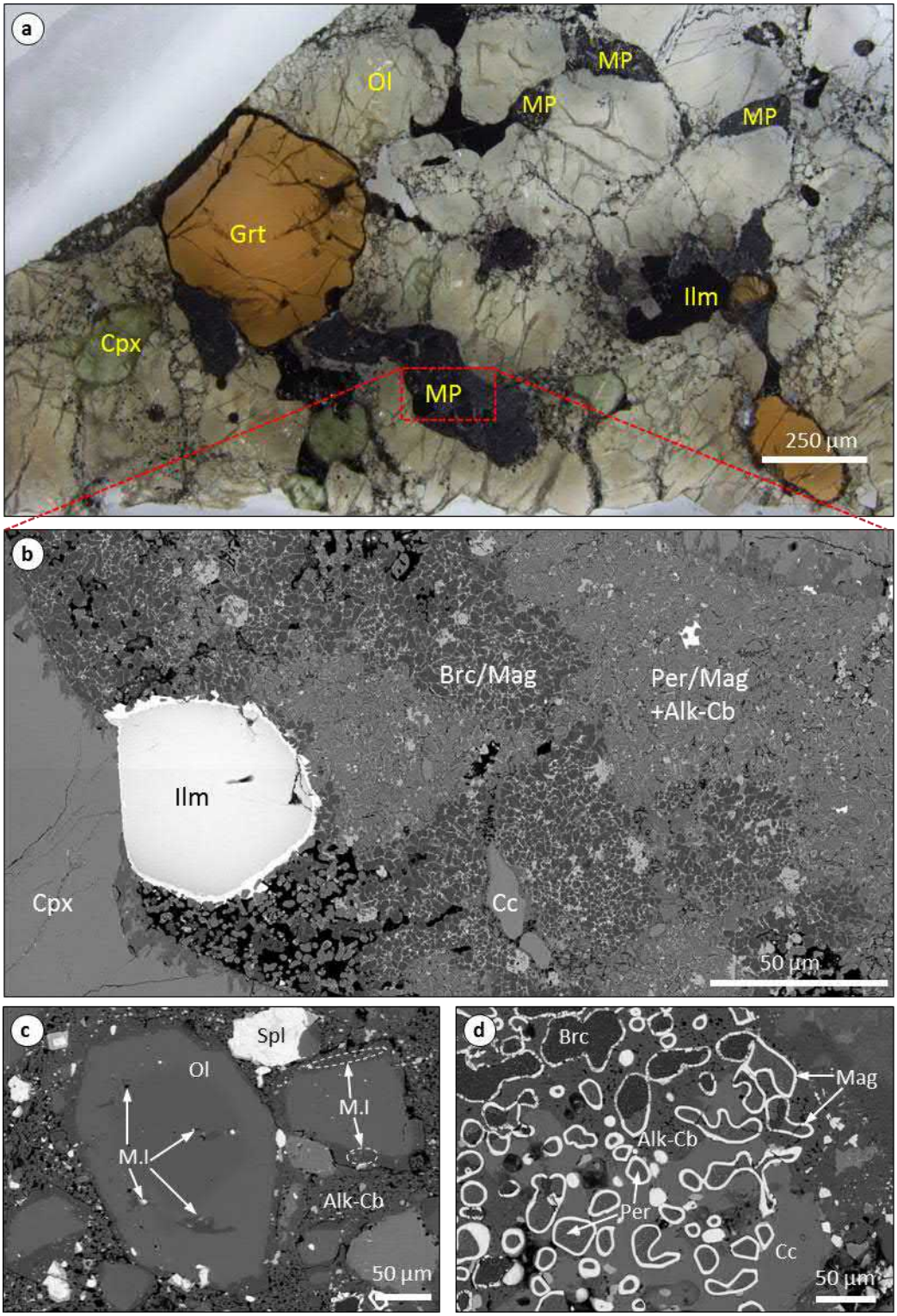

Supplementary Figure S1. (a) Reflected-light optical image of wehrlitic xenolith sample UV01-332 (Udachnaya-East, Siberia) showing groundmass textures, mineralogy and the location of 'melt pools' (MP – see Discussion). Cpx: clinopyroxene, Ol: olivine, Grt: garnet. (b – d) Backscattered electron (BSE) SEM images of: (b) a melt pool located between rock-forming mineral interstices. (c) Location of melt inclusions (M.I) hosted in olivine. (d) Bleb-shaped ferropericlase (Per) and brucite (Brc) surrounded by rims of Mg-magnetite (Mag). Ilm: ilmenite, Cc: calcite, Spl: spinel, Alk-Cb: alkali-carbonate – see Figure 5 for detailed images of djerfisherite in the melt pools.

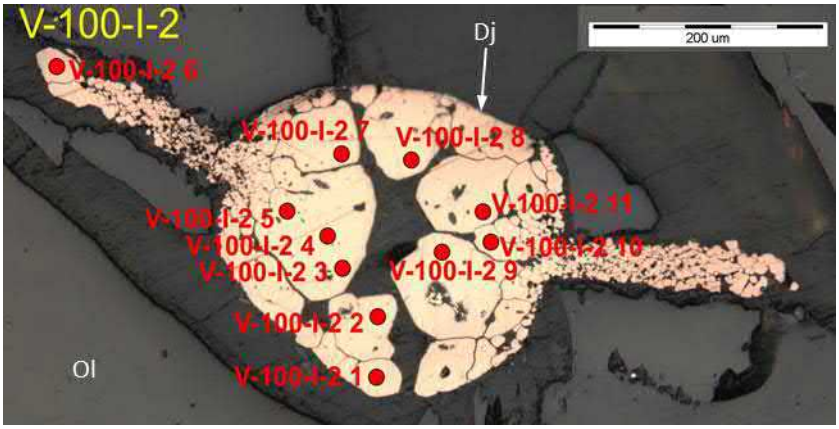

Supplementary Figure S2. Reflected light image of djerfisherite (Dj) inclusion in xenocrystic olivine (Ol) from the Vtorogodnitsa pipe (sample V-100). Analyses points are displayed in Supplementary Data.

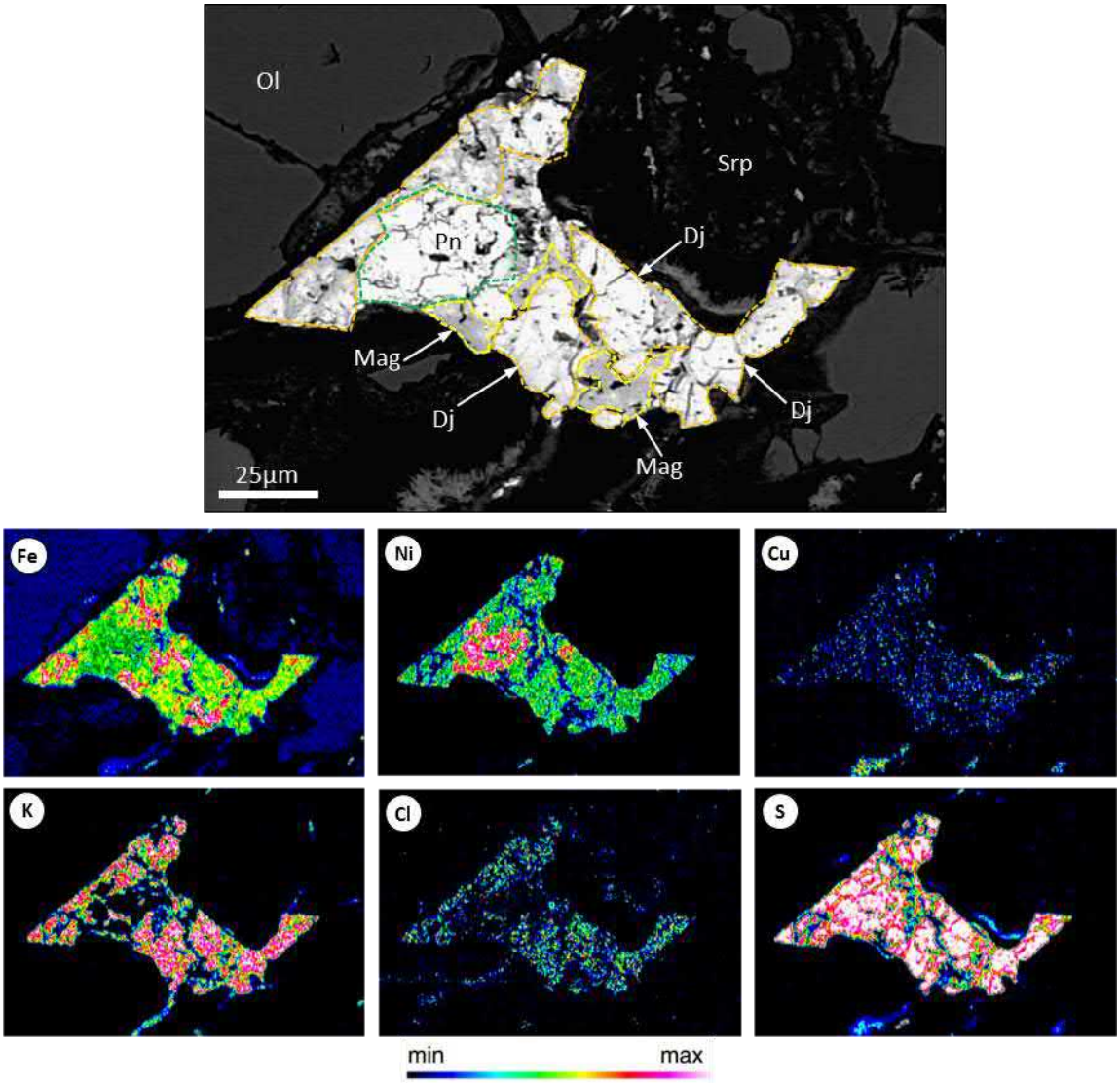

Supplementary Figure S3. Back-scattered electron (BSE) SEM image and X-ray elemental maps of an intergranular sulphide segregation in garnet harzburgite xenolith sample RV1a. This sulphide shows complex zoning between pentlandite (Pn – green dotted lines), magnetite (Mag – yellow dotted lines) and djerfisherite (Dj – orange dotted lines), which is indicated by the presence of K-Cl-S. Ol: olivine, Srp: serpentine.

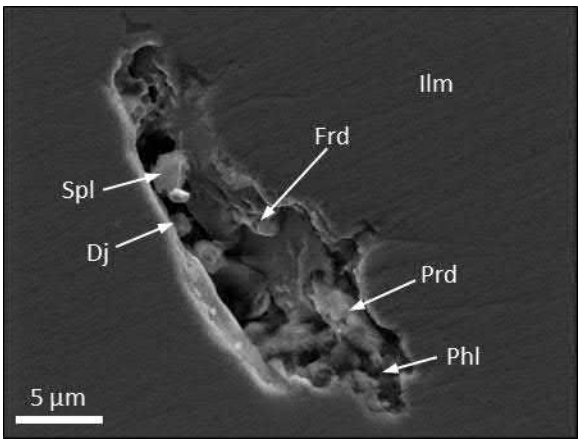

Supplementary Figure S4. Secondary electron (SE) SEM images of a multiphase inclusion hosted in ilmenite (Ilm) in mantle polymict breccia sample DU-1 (Bultfontein, South Africa). Detected minerals in the inclusion include: djerfisherite (Dj), spinel (Spl), freudenbergite (Frd), priderite (Prd) and phlogopite (Phl).

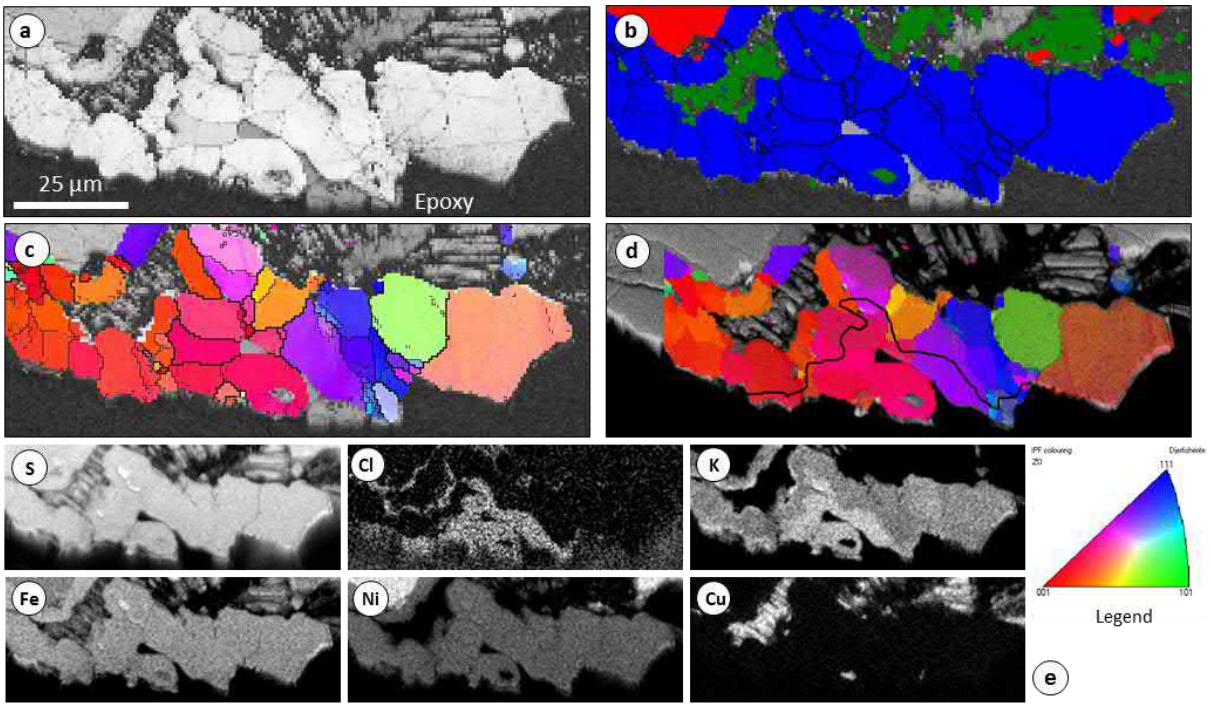

Supplementary Figure S5. Secondary electron (SE) SEM images of a multiphase inclusion hosted in ilmenite (Ilm) in mantle polymict breccia sample DU-1 (Bultfontein, South Africa). Detected minerals in the inclusion include: djerfisherite (Dj), spinel (Spl), freudenbergite (Frd), priderite (Prd) and phlogopite (Phl).

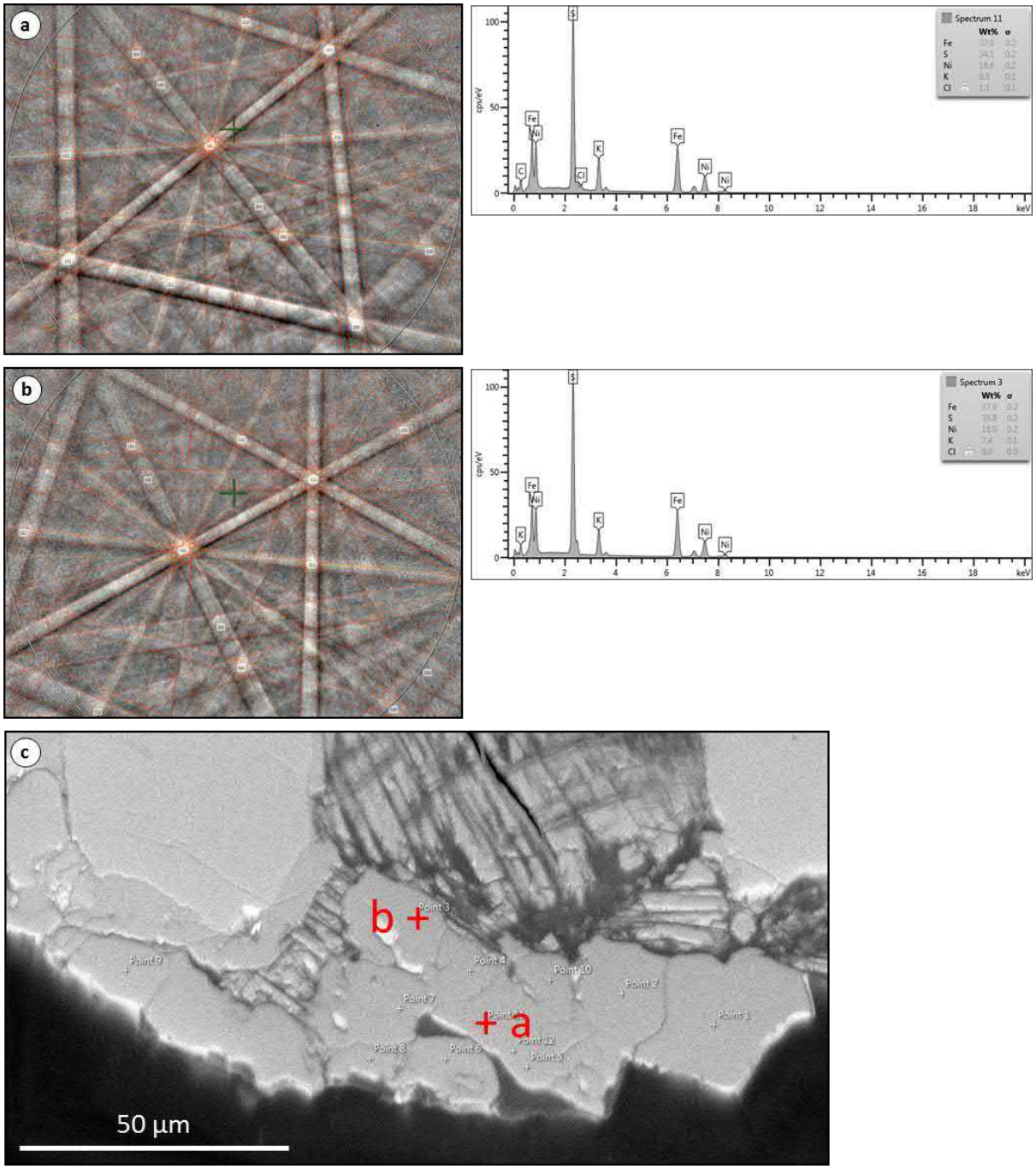

Supplementary Figure S6. (a) Indexed electron backscatter pattern (EBSP) and corresponding energy dispersive x-ray spectrum (EDS) with semi-quantitative analysis for djerfisherite in Koala kimberlite, 11 bands indexed, mean angular deviation (MAD) 0.27, grain orientation 253.2; 33.9; 46.3º relative to surface normal. (b) EBSP and EDS for K-Cl poor phase, 11 bands indexed as djerfisherite, MAD 0.20, orientation 255.4; 28.9; 29.7º. (c) Forescattered electron (FSE) image with point locations, see also Fig. 8.

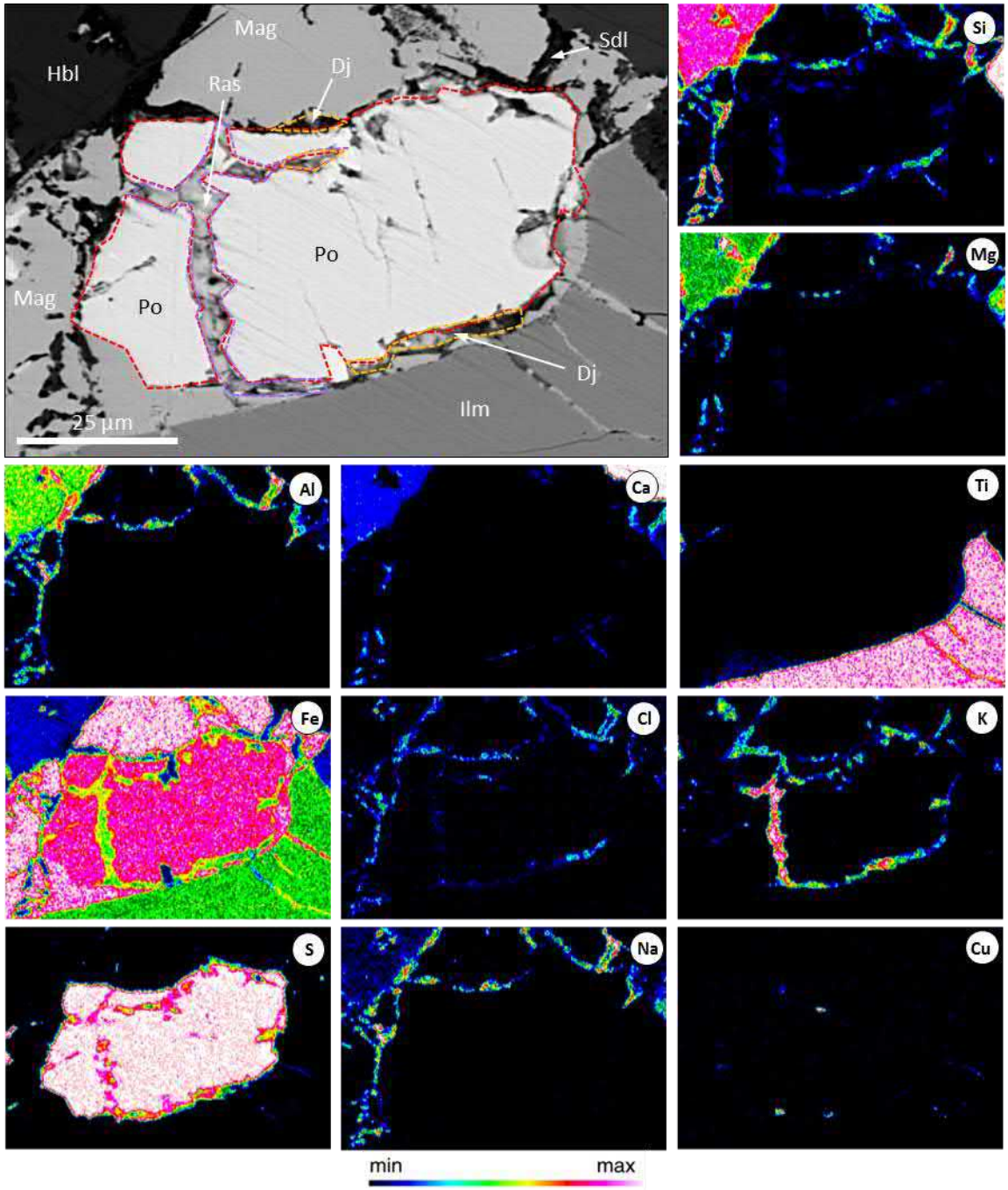

Supplementary Figure S7. Backscattered electron (BSE) SEM image and X-ray elemental maps of djerfisherite (Dj – orange dotted lines) and rasvumite (Ras – purple dotted lines) partially replacing pyrrhotite (Po – red dotted lines) along rims and fractures in crustal amphibolite xenolith (pt4a-05) from the Udachnaya-East kimberlite (Siberia). Djerfisherite is indicated by the presence of K-Cl-S, whereas rasvumite is indicated by elevated (red-pink) K and the absence of Cl. Ilm: ilmenite, Mag: magnetite, Hbl: hornblende, Sdl: sodalite.

Appendix 6.4: Supplementary Tables

Supplementary Table S1: Summary of djerfisherite composition range (wt.%) in kimberlites and kimberlite-borne xenoliths and xenocrysts from Siberia, South Africa and Canada.

Sample	Locality	K	Cl	Fe	Ni	Cu	Reference
Siberia (Russia)							
Eclogite (UE12)	Udachnaya-East	9.3 – 9.5	1.4 – 1.5	37.7 – 39.9	5.6 – 10.7	4.6 – 12.7	
Wehrlite (UV01-332)	Udachnaya-East	8.7 – 9.2	1.2 – 1.5	37.2 – 38.6	11.0 – 12.7	4.8 – 6.2	
Olivine xenocryst (V-100)	Vtorogodnitsa	9.3 – 9.5	1.3 – 1.5	37.6 – 38.5	15.7 – 16.2	1.8 – 2.0	Sharygin et al. (2011)
Djerfisherite hosted in olivine (Sheared Peridotite)	Udachnaya-East	8.1 – 9.4	1.2 – 1.6	40.0 – 47.7	6.5 – 13.9	0.2 – 1.3	Sharygin et al. (2012)
S-globules (Sheared Peridotite)	Udachnaya-East	8.7 – 9.6	0.0 – 1.5	36.7 – 43.5	9.6 – 16.0	0.2 – 7.2	Sharygin et al. (2012)
S-segregations (Sheared Peridotite)	Udachnaya-East	9.0 – 9.8	0.0 – 1.5	35.1 – 45.2	6.4 – 18.1	0.6 – 7.8	Sharygin et al. (2012)
S-segregations in grain interstices (Sheared Peridotite)	Udachnaya-East	8.9 – 9.6	1.3 – 1.6	43.7 – 47.4	4.6 – 10.3	0.4 – 3.7	Sharygin et al. (2012)
Djerfisherite in eclogite	Yakutian kimberlites	9.3 – 10.1	1.3 – 1.8	35.2 – 43.2	4.3 – 13.1	2.7 – 13.0	Bulanova (1990)
Djerfisherite in diamond	Yakutian kimberlites	7.4 – 9.3	0 – 0.8	35.5 – 39.6	13.7 – 22.2	0.2 – 5.7	Bulanova (1990)
Kimberlite	Udachnaya-East	8.9 – 9.4	1.3 – 1.5	32.6 – 43.4	1.9 – 23.1	0.1 – 17.6	Sharygin et al. (2003)
Kimberlite	Udachnaya-East	9.0 – 3.4	1.2 – 1.4	37.0 – 42.4	2.2 – 7.5	6.2 – 14.9	Sharygin et al. (2007)
Kimberlite	Obnazhennaya	8.5 – 9.3	1.1 – 1.5	35.1 – 37.2	0.4 – 17.0	3.0 – 20.0	Sharygin et al. (2011)
Kimberlite	Vtorogodnitsa	9.9 – 9.7	1.0 – 1.5	28.5 – 41.5	6.1 – 24.4	0.7 – 15.8	Sharygin et al. (2011)
Crustal Xenolith (pt4a-05)	Udachnaya-East	8.7 – 9.2	1.3 – 1.4	44.6 – 49.3	0.5 – 1.8	4.5 – 8.9	
Secondary melt Inclusions in kimberlitic olivine	Udachnaya-East	9.4 – 10.8	1.2 – 1.8	38.0 – 50.6	2.8 – 14.3	0.0 – 6.0	
Secondary melt inclusions in kimberlitic olivine	Udachnaya-East	8.9 – 9.3	1.2 – 1.4	32.6 – 38.8	3.8 – 23.1	0.1 – 17.8	Golovin (2004)
South Africa							
Spinel Harzburgite (XM1/422)	Bultfontein	4.6 – 7.1	0.6 – 1.1	33.3 – 34.2	21.5 – 24.3	0.4 – 1.6	
LIMA-bearing Spinel Lherzolite (XM1/362)	Bultfontein	5.3 – 7.1	0.0	27.0 – 35.4	17.5 – 21.6	0.3 – 0.5	
Garnet Harzburgite (RV1a)	Roberts Victor	8.0 – 9.9	1.2 – 1.4	35.4 – 37.2	17.1 – 19.1	0.0 – 1.4	
Clinopyroxene-ilmenite nodule	Frank Smith	4.8 – 9.1	0.0 – 1.4	39.6 – 42.2	11.1 – 14.5	1.8 – 3.5	Clarke (1979)
Canada							
Kimberlite (BHP7)	Koala	7.9 – 9.2	0.1 – 1.3	39.5 – 40.9	10.5 – 11.9	2.0 – 3.2	
Kimberlite (LDC7)	Leslie	7.9 – 9.8	1.2 – 1.4	40.1 – 50.3	2.3 – 11.1	0.0 – 1.4	
Kimberlite	Elwin Bay	9.0 – 9.6	1.3 – 1.6	36.7 – 47.4	3.9 – 18.9	0.5 – 4.1	Clarke et al. (1994)
Garnet Harzburgite (JPS6A)*	Somerset Island	9.5, 9.6	N/A	37.5, 38.4	18.0, 17.5	1.1, 1.2	Bragagni et al. (2017)

*Analyses of only 2 djerfisherite grains. N/A: not available.

Lithos 324–325 (2019) 297–314

Contents lists available at ScienceDirect

Lithos

journal homepage: www.elsevier.com/locate/lithos

Composition and emplacement of the Benfontein kimberlite sill complex (Kimberley, South Africa): Textural, petrographic and melt inclusion constraints

Adam Abersteiner [a,*], Vadim S. Kamenetsky [a], Karsten Goemann [b], Andrea Giuliani [c,d], Geoffrey H. Howarth [e,f], Montgarri Castillo-Oliver [d], Jay Thompson [a], Maya Kamenetsky [a], Alexander Cherry [a]

[a] ARC Centre of Excellence in Ore Deposits (CODES), School of Natural Sciences, University of Tasmania, Hobart, Tasmania 7001, Australia
[b] Central Science Laboratory, University of Tasmania, Hobart, Tasmania 7001, Australia
[c] KiDs (Kimberlites and Diamonds), School of Earth Sciences, The University of Melbourne, Parkville 3010, Victoria, Australia
[d] ARC Centre of Excellence for Core to Crust Fluid Systems (CCFS) and GEMOC, Department of Earth and Planetary Sciences, Macquarie University, North Ryde 2109, NSW, Australia
[e] Department of Geological Sciences, University of Cape Town, Rondebosch 7701, South Africa
[f] Department of Geology, University of Georgia, Athens, GA, 30602, USA.

ARTICLE INFO

Article history:
Received 6 August 2018
Accepted 16 November 2018
Available online 19 November 2018

Keywords:
Benfontein
Kimberlite
Sill
Magma Differentiation
Atoll-Spinel
Melt Inclusion

ABSTRACT

The Benfontein kimberlite is a renowned example of a sill complex and provides an excellent opportunity to examine the emplacement and evolution of intrusive kimberlite magmas. We have undertaken a detailed petrographic and melt inclusion study of the Benfontein Upper, Middle and Lower sills. These sills range in thickness from 0.25 to 5 m. New perovskite and baddeleyite U/Pb dating produced ages of 85.7 ± 4.4 Ma and 86.5 ± 2.6 Ma, respectively, which are consistent with previous age determinations and indicate emplacement coeval with other kimberlites of the Kimberley cluster.

The Benfontein sills are characterised by large variations in texture (e.g., layering) and mineral modal abundance between different sill levels and within individual samples. The Lower Sill is characterised by carbonate-rich diapirs, which intrude into oxide-rich layers from underlying carbonate-rich levels. The general paucity of xenogenic mantle material in the Benfontein sills is attributed to its separation from the host magma during flow differentiation during lateral spreading. The low viscosity is likely responsible for non-explosive emplacement of the Benfontein sills, while the rhythmic layering is attributed to multiple magma injections.

The Benfontein sills are marked by the excellent preservation of olivine and groundmass mineralogy, which is composed of monticellite, spinel, perovskite, baddeleyite, ilmenite, apatite, calcite, dolomite along with secondary serpentine and glagolevite [$NaMg_6[Si_3AlO_{10}](OH,O)_8 \cdot H_2O$]. This is the first time glagolevite is reported in kimberlites. Groundmass spinel exhibits atoll-textures and is composed of a magnesian ulvöspinel – magnetite (MUM) or chromite core, surrounded by occasional pleonaste and a rim of Mg-Al-magnetite. We suggest that pleonaste crystallised as a magmatic phase, but was resorbed back into the residual host melt and/or removed by alteration.

Analyses of secondary inclusions in olivine and primary inclusions in monticellite, spinel, perovskite, apatite and interstitial calcite are largely composed of Ca-Mg carbonates and, to a lesser extent, alkali-carbonates and other phases. These inclusions probably represent the entrapment of variably differentiated parental kimberlite melts, which became progressively more enriched in carbonate, alkalis, halogens and sulphur during crystal fractionation. Carbonate-rich diapirs from the Lower Sill contain more exotic phase assemblages (e.g., Ba-Fe titanate, barite, ancylite, pyrochlore), which probably result from the extreme differentiation of residual kimberlite melts followed by physical separation and isolation from the parental carbonate-rich magma. It is likely that any alkali or halogen rich minerals crystallising in the groundmass were removed from the groundmass during syn−/post-magmatic alteration, or in the case of Na, remobilised to form secondary glagolevite. The Benfontein sill complex

* Corresponding author.
E-mail address: adam.abersteiner@utas.edu.au (A. Abersteiner).

https://doi.org/10.1016/j.lithos.2018.11.017

therefore provides a unique example of how the composition of kimberlites may be modified after magma emplacement in the upper crust.

1. Introduction

Kimberlite magmas are usually emplaced in the Earth's crust as subvertical composite pipes, which can be further divided into crater and diatreme facies, and root zone (i.e. dykes and sills; Dawson, 1971; Hawthorne, 1975; Mitchell, 1986, Sparks, 2013). Dykes commonly occur as sub-vertical tabular bodies (Mitchell, 1986) that can transect kimberlite pipes (e.g., Clement, 1982; Moss et al., 2009), and their emplacement can predate (e.g., Moss et al., 2009; Nowicki et al., 2004) or postdate (e.g., Ranger et al., 2018) pipe formation, or be completely un-associated with pipes (e.g., Andrews and Emeleus, 1975). In contrast, kimberlite sills are relatively rare as they are usually distal to the main kimberlite diatremes and their exposure on the surface is extremely fortuitous. In South Africa, notable sill complexes include Benfontein (Dawson and Hawthorne, 1973; Howarth and Taylor, 2016; McMahon and Haggerty, 1984; Mitchell, 1994), Wesselton Water Tunnels (Clement, 1982; Hawthorne, 1968; Mitchell, 1984; Shee et al., 1991; White et al., 2012), Mayeng, Kamfersdam, Trentham, Saltpetrepan and Karolusdrift (Hawthorne, 1968; Mitchell, 1986 and references therin). Other occurrences of kimberlite sills in the world include Iramba Plateau (Tanzania; Mannard, 1962), Wessels (Zimbabwe; Hawthorne, 1968), Amon (Canada; Tappe et al., 2014), Wemindji (Canada; Zurevinski and Mitchell, 2011), Pyramidefjeld (Greenland; Andrews and Emeleus, 1975) and Iron Mountain (USA; Coopersmith et al., 2003).

Sills, unlike other kimberlite zones (i.e. diatreme, crater), are typically coherent in texture (Scott Smith et al., 2013), non-brecciated, generally contain low quantities of xenogenic (i.e. crustal and mantle) material, and commonly retain the original kimberlite mineralogy. In addition, kimberlite sills are renowned for preserving unique features such as magmatic sedimentation (e.g., layering) and flow textures (Dawson and Hawthorne, 1973; Hawthorne, 1968; Shee et al., 1991; White et al., 2012; Zurevinski and Mitchell, 2011). These characteristics render sills excellent candidates for examining the original composition, evolution and physical properties of kimberlite magmas.

The Benfontein kimberlite is a world-class example of a sill complex that preserves well-defined magmatic stratification defined by alternating of layers enriched in oxide, carbonate-phosphate and silicate minerals, respectively (Dawson and Hawthorne, 1973; Hawthorne, 1968; McMahon and Haggerty, 1984). One of the most prominent features in the Benfontein sills is the presence of carbonate-rich diapirs that originate from carbonate layers and intrude layers rich in oxide minerals (Dawson and Hawthorne, 1973). The Benfontein sills have been largely neglected for >20 years until Howarth and Taylor (2016) examined the compositions of olivine grains from this locality. In this contribution, we revisit the genesis of the Benfontein sills by presenting: i) detailed petrography and geochronology in order to gain new insights into its emplacement and relationship to adjacent Kimberley cluster kimberlites, and ii) examine the groundmass mineralogy and melt inclusions hosted within olivine and groundmass minerals to constrain the composition and evolution of the parental kimberlite melt.

2. Geological setting and previous work

The Benfontein kimberlite sill complex is located approximately 8 km south-east of Kimberley (South Africa; Fig. 1) at the edge of a major kimberlite cluster that strikes NW-SE through Kimberley (Dawson and Hawthorne, 1973). The sill complex intruded the Carboniferous Dwyka Group shales and is situated directly beneath the Jurassic Karoo dolerite sills, which forms a 'cap-rock' to the Benfontein sills in most areas (Dawson and Hawthorne, 1973). Kimberlite magmas spread out horizontally in response to the permeability barrier represented by the Karoo dolerite sills, thus generating the sill complex (Fig. 2). A similar model was proposed by Shee et al. (1991) for the development of the adjacent Wesselton Water Tunnel Sills (Kimberley, South Africa). U-Pb dating of perovskite from the Benfontein sill produced emplacement ages of 86.0 ± 2.7 Ma (Batumike et al., 2008) and 88.0 ± 3.0 Ma (Wu et al., 2010), in agreement with geochronological constraints on the emplacement of the other Kimberley kimberlites (i.e. ~80–90 Ma; Allsopp and Barrett, 1975; Batumike et al., 2008; Fitch and Miller, 1983). Palaeo-stratigraphic reconstructions based on entrained crustal-xenoliths in the neighbouring Kimberley cluster pipes have estimated that up to 850 m of cover rock was removed by post-emplacement erosion (Hanson et al., 2009), therefore indicating an approximate emplacement depth of the sill-complex ~850 m below the original surface.

The sill complex is subdivided into three distinct laterally spreading units, which are referred to as the Lower, Middle and Upper Sills (Dawson and Hawthorne, 1973; Fig. 2). The thickness of these sills is variable, where the Lower Sill is the thinnest (0.25–0.5 m), the Middle Sill is between 1.5 and 2 m (Fig. 2) and the Upper Sill is between 2 and 5 m (Dawson and Hawthorne, 1973). These sills are characterised by well-defined layering and cross lamination, which probably resulted from multiple injections of kimberlite magma (Dawson and Hawthorne, 1973). Layering is generally carbonate-rich and accompanied by abundant: i) olivine, ii) olivine-spinel-perovskite, and/or iii) spinel-perovskite. These layers show mineral grading, which is reflected by systematic changes in the concentrations of olivine, spinel, perovskite and interstitial calcite, serpentine and phlogopite (Dawson and Hawthorne, 1973). In addition, calcite-rich horizons (5 mm–20 cm thick) are present near the Upper and Middle Sill contacts. Upward migrating carbonate-rich diapirs were observed in the Lower Sill where calcite-rich horizons are overlain by denser oxide-rich (e.g., spinel and perovskite) layers (Dawson and Hawthorne, 1973).

Thirteen samples of the Benfontein kimberlite sills were analysed. Samples JJG-BEN1, JJG-BEN2, JJG-2241A, JJG-2241B (Middle Sill) and 173/33/K18/276 (Lower Sill) were obtained from the John J. Gurney

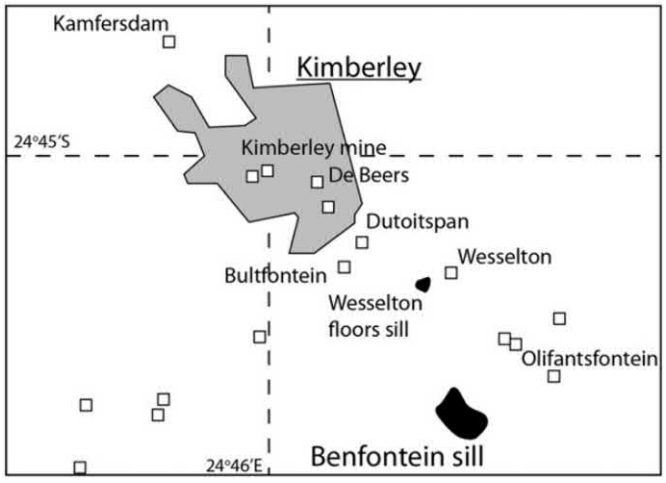

Fig. 1. Location of the Benfontein sill complex and surrounding kimberlite pipes (squares) and sills (black shading) in the Kimberley region (South Africa; after Howarth et al., 2016).

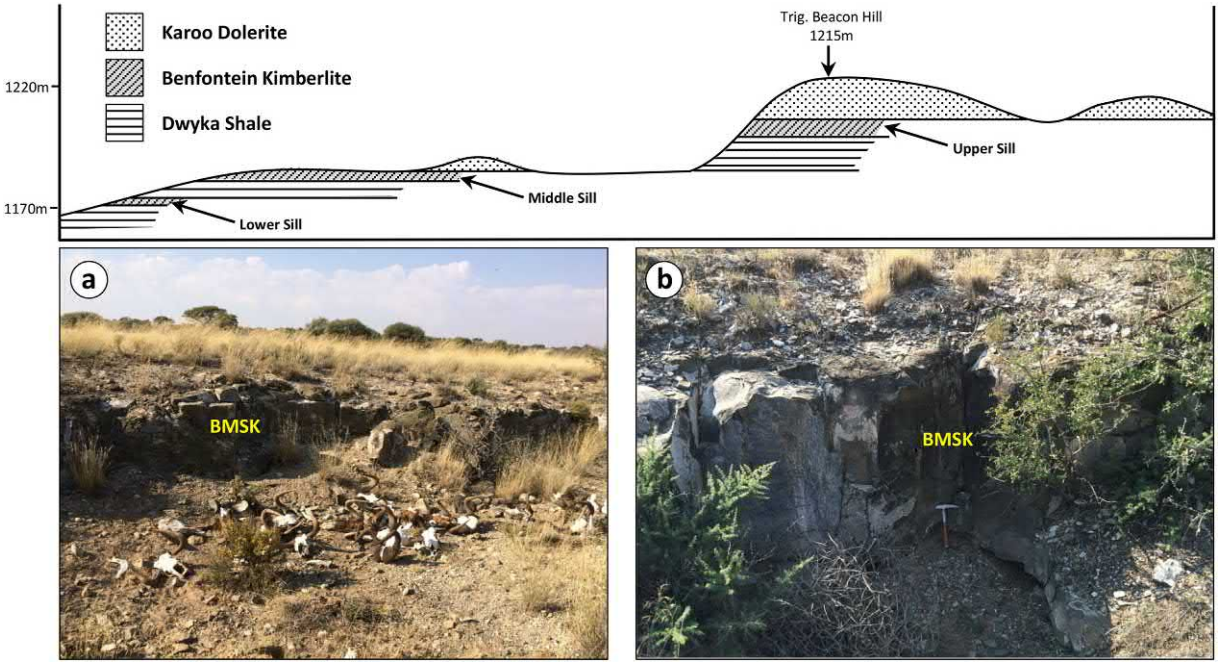

Fig. 2. Cross-section of the Benfontein kimberlite sill complex modified after Fig. 2 in Dawson and Hawthorne (1973). (a, b) Outcrop of the Benfontein Middle Sill kimberlite (BMSK).

Upper Mantle Research Collection at the University of Cape Town (South Africa). In addition, the following samples were collected during field work in 2015: Upper Sill (BUSK-1, BUSK-2), Middle Sill (BMSK-1, BMSK-3) and Lower Sill (BLS, BLSK-2, BLSK-4, BLSK-5). A summary of sample location, mineralogy, textures and structures is presented in Table 1.

3. Results

3.1. Petrography

While layering is one of the most conspicuous features of the Benfontein kimberlite sills, macro- and microscopic textures and mineral modal abundances are extremely heterogeneous between different sill levels and even within individual samples. Layering is defined by variable abundances of silicate, oxide, phosphate and carbonate minerals and, to a lesser extent, grain size variations, and their thickness varies between one mm and several cm. Layers are subdivided into four types based on their dominant constituents: (i) oxide-rich layers, which are composed dominantly of spinel and to a lesser extent perovskite, along with rare baddeleyite and ilmenite, (ii) olivine-rich layers, with abundant olivine and/or monticellite, (iii) apatite-rich layers, and (iv) carbonate-rich (i.e. calcite and dolomite) layers and veins, including calcite-rich diapirs in the Lower Sill. In the following sections we report textural and petrographic details of each sample examined in this study.

3.1.1. Upper Sill

Sample BUSK-1 is characterised by diffuse to well-defined layering, which includes zones enriched in oxides-olivine and calcite-apatite (Fig. 3a). A single crustal shale xenolith (~4 cm in length) is

Table 1
Summary of the location, mineralogy, textures and structures each Benfontein kimberlite sill sample.

Location	Sample	Mineralogy	Textures and Structures	Reference
Upper Sill	BUSK-1	Olivine, spinel (MUM, chromite), perovskite, baddeleyite, ilmenite, apatite, serpentine, calcite	Well-defined alternating oxide-olivine and calcite-apatite rich layering. Calcite laths	Fig. 3
	BUSK-2	Olivine, monticellite, spinel, apatite, perovskite, baddeleyite, kinoshitalite/phlogopite Calcite, serpentine, glagolevite, rutile, ankerite, siderite.	Massive. Porphyritic (defined by olivine).	Supplementary Fig. 2
Middle Sill	JJG-BEN1 JJG-BEN2	Olivine, MUM-spinel, perovskite, ilmenite, baddeleyite, apatite, serpentine, glagolevite, calcite, dolomite, barite.	Diffuse mineral grading between olivine and oxide rich layers.	Fig. 4
	BMSK-1 BMSK-3a BMSK-3b	Olivine, MUM-spinel, perovskite, baddeleyite, apatite, serpentine, calcite, Fe-Cu-sulphides, glagolevite, barite.	Massive. Porphyritic (defined by olivine). Fibrous calcite veins.	Fig. 5
	JJG-2241A JJG-2241B	Olivine, MUM-spinel, perovskite, apatite, serpentine, glagolevite, calcite.	Massive. Porphyritic (defined by olivine). Olivine-phlogopite-ilmenite xenolith fragments	
Lower Sill	173/33/K18/276 BLSK-5	MUM-spinel, perovskite, baddeleyite, apatite, calcite, dolomite, chlorite, ankerite, siderite, barite.	Calcite-rich diapirs,oxide cumulate layers, calcite laths, load casts.	Fig. 7
	BLS	Olivine, MUM-spinel, perovskite, baddeleyite, apatite, calcite, serpentine, barite, Nb-rutile, fluorobritholite.	Well-defined layering (oxide-olivine and apatite rich layers)	Fig. 8
	BLSK-2	Olivine, MUM-spinel, perovskite, apatite, serpentine, chlorite, calcite, dolomite.	Massive olivine cumulate. Porphyritic (defined by olivine)	Fig. 9
	BLSK-4	MUM-spinel, perovskite, baddeleyite, calcite, serpentine.	Massive oxide cumulate.	Supplementary Fig. 6

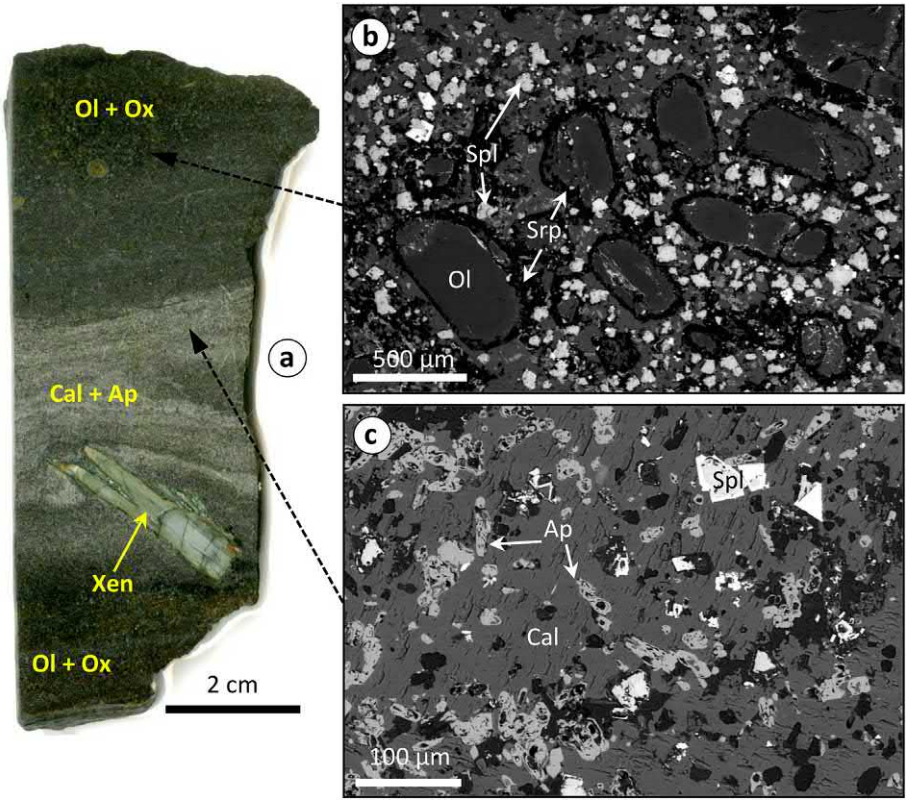

Fig. 3. (a) Hand-specimen photograph of Benfontein Upper Sill kimberlite sample BUSK-1. This sample is characterised by dark olivine and oxide (Ol + Ox) dominated zones (or layering) and lighter calcite and apatite (Cal + Ap) rich zones. The calcite rich zones form weakly defined and diffuse layering. A crustal shale xenolith (Xen) is superimposes onto surrounding calcite and apatite rich layers, causing deformation of layering. (b, c) Back-scattered electron (BSE) SEM images of image (a) showing: (b) olivine (Ol) and spinel (Spl) dominated zones, and (c) apatite (Ap) and calcite (Cal) rich zones. Srp: serpentine.

superimposed onto the magmatic layering, which wraps around this xenolith (Fig. 3a). A prominent feature of this sample is the presence of abundant calcite laths. These calcite laths are randomly orientated and evenly distributed throughout the sample (i.e. occur in oxide-olivine and calcite-apatite zones), range in size from ~3 mm to 1 cm in length, and are interstitial to most groundmass minerals. Olivine grains occur as smaller subhedral-to-subrounded (100 μm – 1 mm in size) and as larger rounded grains (up to several millimetres in size). Olivine grains are partially replaced along rims and internal fractures by serpentine and to a lesser extent calcite and rare magnetite (Fig. 3b). Groundmass minerals vary significantly in proportion on a millimetre scale and consist of euhedral oxide phases (i.e. spinel, perovskite, baddeleyite), apatite and interstitial serpentine and calcite. The sample is traversed by a single horizontal zone ~ 4–5 cm in thickness (Fig. 3a), with a weakly layering texture and preferential crystallographic orientation of poikilitic calcite and apatite grains (Fig. 3c).

Sample BUSK-2 shows massive porphyritic texture and contains abundant (40–50 vol%) rounded olivine grains that are typically 100–500 μm in size, with rare crystals up to 5 mm in size (Supplementary Fig. S1). Olivine grains are partially replaced by serpentine and to a lesser extent calcite and a Na-Mg-Si-Al-bearing mineral (SEM-EDS) along rims and internal fractures. This mineral occurs throughout the sill complex as complex intergrowths with serpentine and is classified as the chlorite-group mineral, glagolevite [$NaMg_6[Si_3AlO_{10}](OH,O)_8 \cdot H_2O$] (Supplementary Fig. S1c; Krivovichev et al., 2004). The groundmass is composed of abundant (~15–20 vol%) atoll-spinel. Spinel grains exhibit varying degrees of alteration (Supplementary Fig. S1b), where the outermost rims are commonly discontinuous and the core show uneven partial replacement by unidentified Fe-rich and Si-Al-bearing phases (e.g., chlorite), and occasionally rutile and ankerite/siderite. In addition, monticellite is very abundant (10–15 vol%) in the groundmass where it occurs as single grains as well as tightly packed aggregates around olivine (Supplementary Figs. S1b, c). Other common groundmass minerals include apatite and perovskite, whereas baddeleyite and poikilitic kinoshitalite/phlogopite are scarce. Calcite and to a lesser extent serpentine ± glagolevite occur as common interstitial phases in the groundmass. To our knowledge, this is the first occurrence of glagolevite documented in the groundmass of kimberlites.

3.1.2. Middle Sill

Samples JJG-BEN1 and JJG-BEN2 exhibit excellent rhythmic layering defined by alternating olivine-rich and oxide-rich layers. These layers range from 2 to 15 mm in thickness and show graded mineral contacts (Fig. 4). Olivine is largely fresh, typically subrounded-to-subhedral in shape, ranges from 100 μm to 1 mm in size and shows some preferential grain alignment with longest axes parallel to the direction of layering. Oxide-dominated layers are composed mostly of atoll-spinel along with lesser perovskite, ilmenite and baddeleyite. Both the olivine and oxide rich layers host moderate contents (5 vol%) of apatite along with abundant interstitial calcite, dolomite, serpentine and lesser magnetite and barite.

Samples BMSK-1, BMSK-3a and BMSK-3b are all massive and porphyritic in texture due to the occurrence of olivine (>100 μm) grains. Olivine is unevenly distributed, whereas in some areas it forms tightly packed clusters or trails with graded contacts, and is rare or absent in other areas of the same sample (Fig. 5). Olivine is completely replaced by serpentine and/or calcite (Fig. 5c). These samples are also transected by veins (between 2 and 8 mm thick) of fibrous calcite, which shows sharp boundaries with the kimberlite (Fig. 5b). Fragments of the kimberlite groundmass are sometimes entrained within these calcite veins (Supplementary Fig. S2). In addition, calcite veins host sporadic patches (<30–50 μm) of disseminated barite and magnetite as well as euhedral crystals (<50 μm) of bultfonteinite ($Ca_4(Si_2O_7)(F, OH)_2$). The groundmass is composed of abundant atoll-spinel and apatite (10–20 vol%)

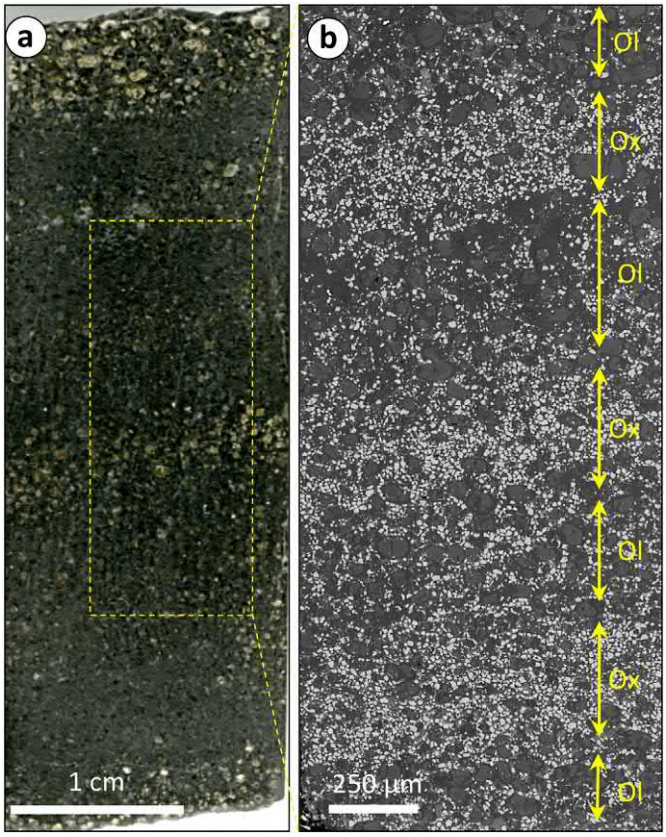

Fig. 4. (a) Hand-specimen photograph of Benfontein Middle Sill kimberlite sample JJG-BEN1. Parallel cumulate layering is indicated by alternating zones of green/yellow grains (olivine – Ol) and dark (i.e. oxide – Ox) rich zones. (b) Back-scattered electron (BSE) SEM image zoom in of image (a) showing distinct olivine (dark grains) and oxide (light grains) rich parallel layering.

along with subordinate perovskite, baddeleyite, Fe-Cu-sulphides and interstitial calcite, serpentine and glagolevite.

Samples JJG-2241A and JJG-2241B exhibit massive, porphyritic textures and contain abundant rounded and subhedral-to-euhedral fresh olivine grains ranging between 150 μm and 2 mm in size. The groundmass consists of fine-grained serpentine, glagolevite (Fig. 6) and interstitial calcite along with abundant (15 vol%) apatite, lesser (5–10 vol %) atoll-spinel, and rare perovskite. In addition, these samples contain fragments (up to 1 mm) of fine-grained olivine-phlogopite-ilmenite aggregates (Supplementary Fig. S3). Ilmenite along the xenoliths is mantled by MUM-spinel, while phlogopite is rimmed by a thin layer (<30 μm) of kinoshitalite (i.e. Ba-rich phlogopite). These olivine-phlogopite-ilmenite aggregates probably represent fragments of larger peridotite xenoliths (e.g., Dawson and Hawthorne, 1973).

3.1.3. Lower Sill

Samples 173/33/K18/276, BLS, BSLK-4 and BLSK-5 are characterised by the presence of carbonate diapirs, which intrude into oxide-rich layers from underlying carbonate-rich layers (Figs. 7a, b). Carbonate diapirs may still be connected to the main calcite layer by a thin neck. Detached and connected diapirs are locally abundant and occur in swarms of elongated bodies that range in length from 1 mm through to a few centimetres in length (Figs. 7a, b). Empty vugs occur in the cores of some diapirs. Carbonate diapirs are commonly composed of tightly packed clusters of randomly orientated calcite laths that range from 200 μm to ~2 mm in length. The spacing between these calcite laths is usually infilled by calcite, dolomite (Figs. 7c – e) and minor ankerite/siderite.

The groundmass of the oxide-rich layers also contains abundant calcite laths similar to those in the carbonate diapirs (Fig. 7f). Groundmass minerals (e.g., spinel) in close proximity to these calcite diapirs are characterised by more intense alteration to Fe-Ti-Si-Mg-bearing phases and to a lesser extent ankerite/siderite, barite and magnetite (Supplementary Figs. S4). This alteration zone surrounding carbonate diapirs is visible in hand specimen where it is characterised by patchy brown-coloured haloes (Figs. 7a, b).

Sample BLS does not host carbonate diapirs but consists of thin (1–3 mm) alternating oxide-olivine and apatite-rich layers (Fig. 8). These layers form sharp contacts with each other, without any apparent mineral grading. Oxide-olivine layers contain a relatively high modal abundance of apatite (up to 15 vol%) in the matrix, whereas apatite-rich layers are almost devoid of oxides and olivine. In some areas of the groundmass, spinel is partially replaced by barite (Supplementary Fig. S5), Nb-rutile, magnetite and fluorobritholite $(REE)_5(SiO_4,PO_4)_3(OH,F)$.

Carbonate diapirs and layering are absent from sample BLSK-2 and BLSK-4. These samples exhibit massive and porphyritic textures, with dominant olivine and oxide minerals in samples BLSK-2 and oxide minerals in BLSK-4, respectively (up to 70 vol% in both samples; Supplementary Fig. S6). Olivine in sample BLSK-2 forms partially altered, rounded and subhedral-to-euhedral grains, which range from 150 μm to 3 mm in size (Supplementary Fig. S6c). The groundmass is composed of abundant spinel, perovskite and apatite along with interstitial calcite and serpentine. In sample BLSK-4, olivine is completely absent and the groundmass is fine-grained and dominated by well-preserved atoll-shaped spinels, lesser perovskite, baddeleyite (Supplementary Fig. S6d), apatite and interstitial calcite and serpentine.

3.2. Compositions of olivine and oxide minerals

Olivine sizes (see Section3.1) are extremely variable throughout the Benfontein samples and exhibit core compositions ranging between Fo of 88–91 mol% (SEM-EDS; Supplementary Tables 2 S1). This range is consistent with previous analyses of olivine cores from the Benfontein sills (Fo: 88–93 mol%; Arndt et al., 2010; Dawson and Hawthorne, 1973; Giuliani, 2018; Howarth and Taylor, 2016).

Spinel is the most abundant oxide phase in the Benfontein kimberlite sills, and occurs in the following forms: i) individual euhedral grains within the groundmass, which are sometimes intergrown with perovskite, baddeleyite and apatite, ii) mantles surrounding ilmenite macrocrysts, iii) crystal inclusions hosted in olivine (Howarth and Taylor, 2016), and iv) a daughter phase in melt inclusions hosted in magmatic minerals (see Section5.3). Individual groundmass spinel grains typically form atoll-shaped structures (see definitions by Mitchell, 1986; Roeder and Schulze, 2008), which range in size from 40 to 250 μm (Figs. 9a – d). Atoll-spinels are characterised by a homogeneous euhedral core of Mg-Al-titanomagnetite (or magnesian ulvöspinel – magnetite: MUM), or less commonly Fe-Mg-chromite (or titanian magnesian aluminous chromite – TIMAC; Mitchell, 1986) (Fig. 10; Supplementary Tables 2 S2 – S4). Zoning in these spinel cores was only identified in the Upper Sill, where grains are diffusely zoned from TIMAC cores to MUM along the peripheries (Supplementary Tables 2 S2). This zoning pattern is consistent with magmatic Trend 1 (Fig. 10), as defined by (Mitchell, 1986). These compositions are consistent with previous analyses of spinels from the Benfontein sills by (Boctor and Boyd, 1981; Gaspar and Wyllie, 1984; Jones and Wyllie, 1985; Roeder and Schulze, 2008). The euhedral spinel core is usually mantled by a variably thick (~3–30 μm) zone (or 'lagoon') composed of fine-grained intergrowths of serpentine, chlorite and calcite, which is in turn enclosed by a thin (2–10 μm) epitaxial rim of Mg-Al-Ti-magnetite. This outermost rim mirrors the shape of the spinel core exactly (Figs. 9a – d), which is considered to reflect growth in crystallographic continuity with the core (Mitchell, 1986). In some atoll-spinels, the 'lagoon' zone is partially-to-completely infilled by Al-rich (i.e., pleonaste) spinel (Figs. 9a, b). It is noteworthy that pleonaste is only preserved within

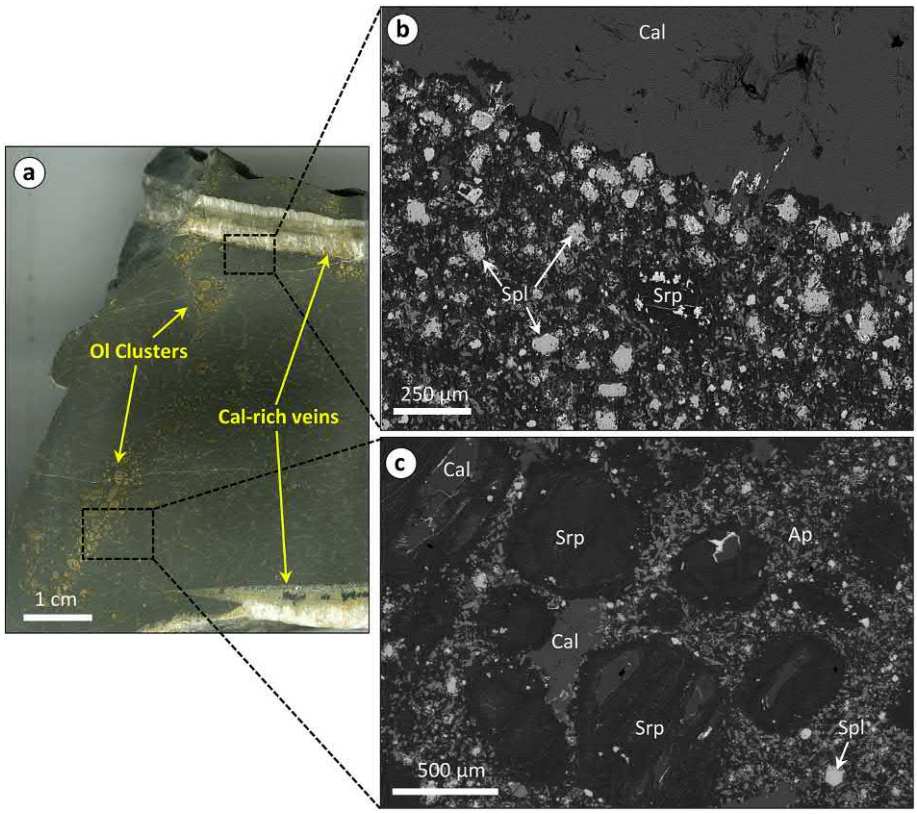

Fig. 5. (a) Hand-specimen photograph of Benfontein Middle Sill kimberlite sample BMSK-3. This sample is characterised by cross-cutting fibrous calcite (Cal) rich veins and randomly distributed olivine (Ol) clusters/trails which show moderate size-grading. (b, c) Back-scattered electron (BSE) SEM images of: (b) the edge of the calcite vein cross-cutting the groundmass, and (c) olivine dominated cluster, where grains are completely replaced by serpentine (Srp) and calcite. Spl: spinel, Ap: apatite.

atoll-spinels that are located in the least altered (i.e., serpentinised) areas of the groundmass. In addition, fretted contacts between MUM core and pleonaste (Fig. 9b) suggest partial resorption of the core before overgrowth. The preservation of TIMAC cores through to pleonaste is analogous to spinel zoning Trend 3 (high-Cr to high-Al; as defined by Roeder and Schulze, 2008; Fig. 10). In addition, the Mg-Al-magnetite outer rim and pleonaste zones of atoll-spinels are sometimes intergrown with perovskite, baddeleyite and apatite (Figs. 9a – c).

MUM-spinel typically forms mantles around partially resorbed ilmenite macrocrysts (Fig. 9d; Supplementary Fig. S3). The ilmenite core is anhedral-to-amoeboid in shape and enriched in MgO (up to 17.33 wt%; Supplementary Table 2 S3). The mantle of MUM-spinel typically adopts the shape of the ilmenite core and, similar to atoll spinel, is rimmed by a serpentine-calcite lagoon followed by a magnetite rim.

Perovskite commonly occurs in conjunction with spinel, where it occurs as complexly zoned euhedral grains up to 150 μm in size (Figs. 9e, f). Perovskite grains are sometimes mantled by a thin (1–3 μm) outer rim, which is characterised by elevated light rare earth element (LREE) contents. Primitive mantle normalised (N) (after Sun and McDonough (1989)) REE patterns of perovskite cores show homogeneous compositions and characteristic enrichment in LREEs and depletion in heavy (H)REEs, resulting in a steep slope (La_N: 11560–14,770 vs. Lu_N: 8–15 Supplementary Fig. S7). These compositions are consistent with previous analyses of Benfontein perovskite (see Fig. 2 of Jones and Wyllie, 1984) and other adjacent Kimberley kimberlites (e.g., Dutoitspan – Ogilvie-Harris et al., 2009; Bultfontein – Giuliani et al., 2017; Supplementary Fig. S7).

4. Geochronology

Baddeleyite is an extremely rare mineral in kimberlites and may be primary magmatic (Scatena-Wachel and Jones, 1984) or xenocrystic (Schärer et al., 1997). We examine the reliability of U-Pb dating of kimberlitic baddeleyite by comparing it with perovskite.

4.1. Perovskite

The majority of perovskite grains have U (161–292 ppm) and widely variable Th contents (852–14,607 ppm) (Supplementary Table 2 S5) consistent with analyses of Benfontein perovskite by Wu et al. (2010). All analyses of perovskite plot away from the Concordia curve due to the presence of "common lead". Although the majority of perovskite analyses overlap, there is a sufficient spread in $^{238}U/^{206}Pb$ (21.66–46.46) and $^{207}Pb/^{206}Pb$ (0.34–0.62) to generate a robust linear regression ($n = 49$, MSWD = 0.53, probability of fit = 0.997) corresponding to an intercept age of 85.7 ± 4.4 Ma (2 s.d.), and an upper intercept of $^{207}Pb/^{206}Pb = 0.865$ (Supplementary Fig. S8).

4.2. Baddeleyite

Baddeleyite grains have U (107–249 ppm) contents and are almost completely devoid of Th (1–7 ppm; Supplementary Table 2 S6). These U and Th concentrations are typical for baddeleyite grains reported in other kimberlite pipes (Sun et al., 2018). Approximately half of baddeleyite analyses overlap and plot on or near the Concordia curve. Similar/identical lower intercept ages are obtained regardless if the upper intercept is anchored or not (see Supplementary Tables 1). This indicates no significant Pb loss due to alteration of baddeleyite, which is consistent with the freshness of baddeleyite grains estimated by optical microscopy. A regression through the data points ($^{238}U/^{206}Pb$ = 14.34–77.24; $^{207}Pb/^{206}Pb$ = 0.04–0.69) returns an intercept age of 86.5 ± 2.6 Ma and an upper intercept of $^{207}Pb/^{206}Pb = 0.868$ ($n = 21$, MSWD = 1.6, probability of fit = 0.040; Supplementary Fig. S8). The

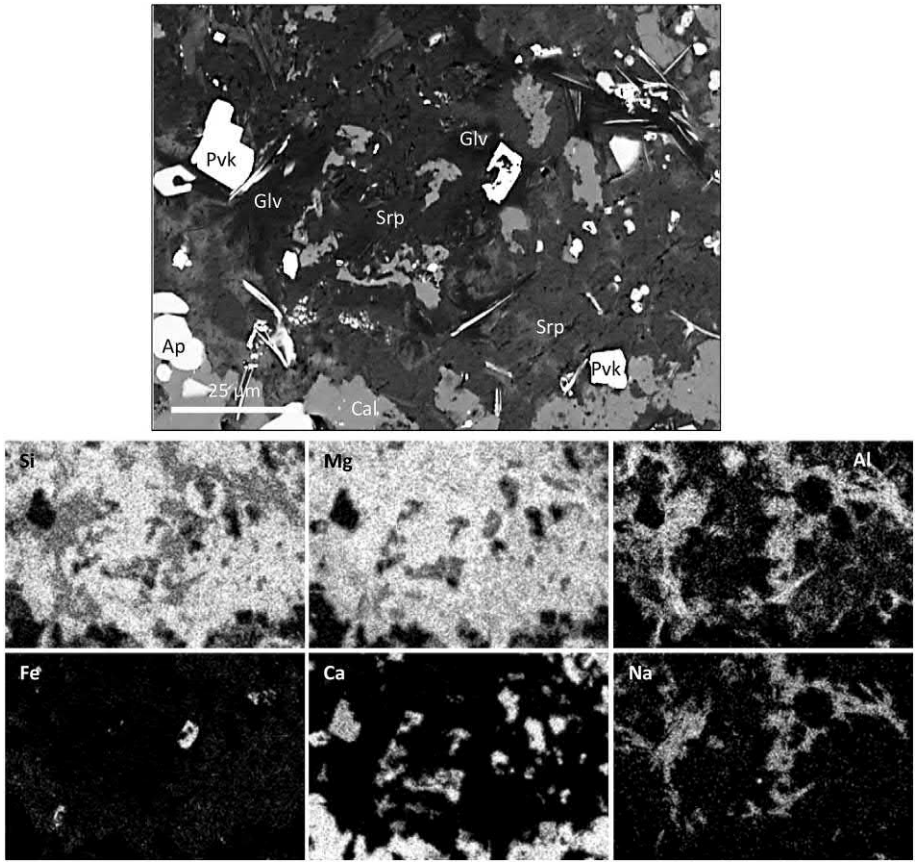

Fig. 6. Back-scattered electron (BSE) SEM images and X-ray elemental maps of interstitial glagolevite (Glv) and serpentine (Srp) intergrowths in the groundmass of sample JJG-2241A. The presence of glagolevite is signified by elevated Na coupled with Al. Pvk: perovskite, Ap: apatite, Cal: calcite.

indistinguishable of ages determined for baddeleyite and perovskite confirm that baddeleyite can be reliably dated in kimberlites.

5. Inclusions

Monomineralic (i.e. crystal) and multiphase (i.e. crystallised melt) inclusions were examined in olivine, spinel, perovskite, monticellite, apatite and carbonate (i.e. calcite, dolomite) from the Upper, Middle and Lower sills. Melt inclusions hosted in olivine occur as trails that are aligned along healed fractures, and are therefore secondary in origin (e.g., Roedder, 1984). On the other hand, melt inclusions in oxides, monticellite and apatite exhibit variable shape, are distributed randomly (i.e. not associated to any fracture system), and are therefore interpreted to be primary in origin.

5.1. Olivine

Multiphase melt inclusions in olivine are extremely rare. This is partly due to the poor preservation (i.e. partial-to-complete serpentinisation) or absence of olivine in some samples from the Upper and Lower sills. In addition, well-preserved olivine grains from Middle Sill samples JJG-2241A and JJG-2241B and Lower Sill sample BLS are relatively free of inclusions. Twenty-five secondary melt inclusions in olivine were characterised in these samples. These inclusions are irregularly-shaped and range from 1 to 15 μm in size (Supplementary Fig. S9). They are composed of (in order of decreasing abundance) calcite, phlogopite, MUM-spinel, magnetite, dolomite, apatite and alkali (Na, K) carbonates. Olivine is also host to numerous crystal inclusions of euhedral chromite grains, which occurs as isolated inclusions (Howarth and Taylor, 2016).

5.2. Oxides

Over one hundred multiphase inclusions were examined in spinel and to a lesser extent in perovskite from the Upper, Middle and Lower sills. These inclusions are typically irregular in shape and range in size from <3–20 μm, and host between two to six individual phases (Fig. 11, Supplementary Fig. S10). These inclusions are composed of (in order of decreasing abundance): carbonates (e.g., calcite, dolomite, siderite, magnesite), including alkali-bearing (Na, K, Ba, Sr) varieties (nyerereite [$Na_2Ca(CO_3)_2$], fairchildite [$K_2Ca(CO_3)_2$], witherite [$BaCO_3$] and other unidentified Na-K ± Ba-Sr ± F-bearing varieties), phosphates ((fluor)apatite and an Na-Mg-bearing variety, possibly bradleyite [$Na_3Mg(PO_4)(CO_3)$]), phlogopite/kinoshitalite, Fe-Cu-Pb-bearing sulphides, djerfisherite ($K_6Na(Fe^{2+},Cu,Ni)_{25}S_{26}Cl$), halite/sylvite, forsteritic olivine (Fo: ~86–89 mol%; SEM-EDS), fluorite, sulphates (barite and unidentified Na-K-bearing varieties), perovskite, kimzeyite ($Ca_3(Zr,Ti)_2(Si,Al,Fe^{3+})_3O_{12}$ – as also reported by Mitchell, 1994) and other unidentified alkali-Ti-Fe-Cu-Zn-bearing oxides minerals (Table 2). Numerous exposed inclusions contain cavities/voids, which probably represent escaped fluid/gas phases and/or plucked-out minerals.

Monocrystalline inclusions in oxides are relatively rare. Spinel cores occasionally contain inclusions of forsteritic olivine, while perovskite and rutile are less common. Atoll-spinel grains where pleonaste is preserved contain rare inclusions of forsteritic olivine or baddeleyite within pleonaste.

5.3. Monticellite and apatite

Inclusions in monticellite are extremely rare. These inclusions are subrounded-to-irregular in shape and generally <4 μm in size and only

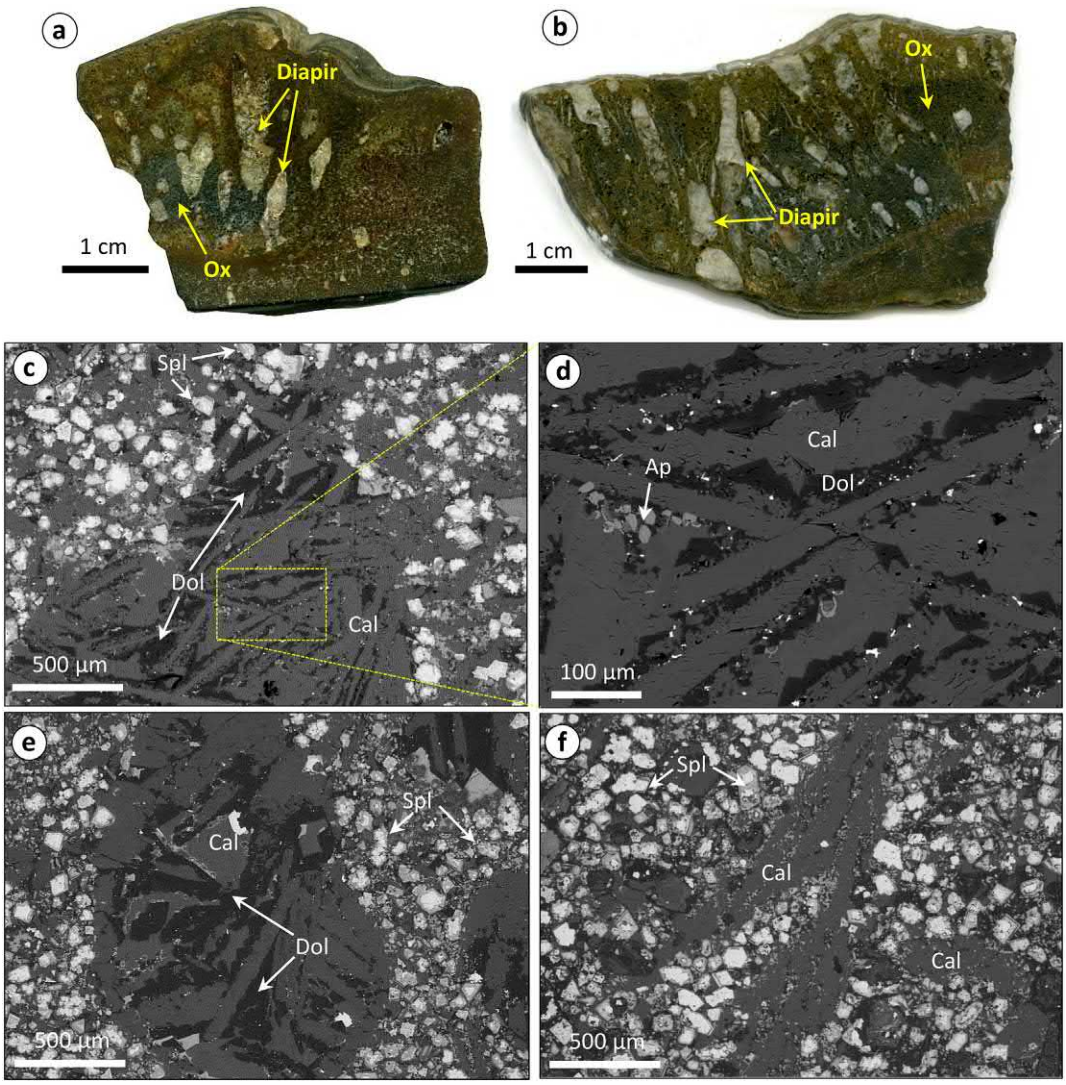

Fig. 7. Hand-specimen photograph of Benfontein Lower Sill kimberlite samples (a) BLSK-5, and (b) 173/33/K18/276. These samples are characterised by parallel aligned calcite (Cal) rich diapirs which superimpose onto oxide (Ox) rich layers. Patchy brown discolouration around these diapirs is characterised by more intense groundmass alteration. (d – f) Back-scattered electron (BSE) SEM images of: (c, e) carbonate diapir composed of calcite laths and interstitial dolomite (Dol). (d) Close up image of image pane (c) showing calcite laths. (e) Spinel (Spl) grains are altered to admixtures of Fe-Ti-Si-Mg-bearing (e.g., chlorite) phases and show minor deformation along the contact with the diapir. Diapirs are composed of randomly orientated calcite laths. The voids between these laths are infilled by dolomite (Dol). (f) The oxide (i.e. spinel) rich groundmass located away from diapirs. These areas also contain abundant individual calcite laths. Ap: apatite.

contain one or two phases, including periclase, Mg-magnetite, olivine, perovskite, apatite, witherite, kimzeyite and Fe-Cu-K-sulphides (perhaps rasvumite; KFe_2S_3) (Supplementary Fig. S11).

Although apatite is a common groundmass mineral throughout the Benfontein sill complex, inclusions hosted within apatite are extremely rare and generally <2–4 μm in size. Inclusions in apatite were only identified in samples BLS, BUSK-1 and BUSK-2; however, due to their small sizes individual phases could not be confidently identified. SEM-EDS analyses of these inclusions indicate the presence of (in order of relative abundance) abundant Ca and Mg, moderate Na, K, Mg, Fe, Al and Si, and minor Zn. It is noteworthy that the abundance of Ca may be due to interference with the host apatite.

5.4. Carbonate

Carbonate diapirs and interstitial groundmass calcite both contain abundant inclusions. The majority of the inclusions in the carbonate diapirs are restricted to the dolomitic parts or located along the dolomite and calcite lath boundary. The interior of calcite laths is generally devoid of inclusions. Inclusions in the carbonate diapirs are extremely variable in shape and range from euhedral to amoeboid. The sizes of these inclusions are between <2 μm through to several hundred μm, however, the majority of inclusions are <25 μm across. These inclusions consist of individual grains or mineral assemblages and are composed of (in order of decreasing abundance) barite, Ba-Fe-titanate ($(K,Ba)_{1-2}(Fe,Cr,Al)_{1-2}(Ti,Nb)_{6-7}O_{16}$), LREE-bearing ancylite ($Sr(REE)(CO_3)_2(OH).H_2O$), alkali (Na, K, Ba, Sr) carbonates, (fluor)apatite, Fe-Cu-sulphides (e.g., chalcopyrite and pyrite/pyrrhotite), Nb-rutile, phlogopite, fluorite, bultfonteinite ($Ca_4(Si_2O_7)(F, OH)_2$), kimzeyite, U- or Ba-bearing pyrochlore, sylvite (KCl) and other unidentified REE ± Ca ± F-bearing phases (Fig. 12; Table 3).

Interstitial groundmass calcite hosts abundant isolated or disseminated swarms of crystal inclusions that range in size from <1 to ~50 μm. In addition, numerous <10 μm-large multiphase inclusions occur in groundmass calcite. Both crystal and multiphase inclusions are composed of (in order of decreasing abundance) dolomite, alkali (Sr, Ba, Na, K) carbonates (e.g., strontianite, shortite [$Ca_2Na_2(CO_3)_3$], fairchildite, witherite and other unidentified Na-K ± Ba-Sr ± F-bearing varieties), barite, apatite, bultfonteinite, fluorite, Na-K chlorides (sylvite, halite) and humite ($(Mg,Fe)_7(SiO_4)_3(F,OH)_2$; Fig. 13).

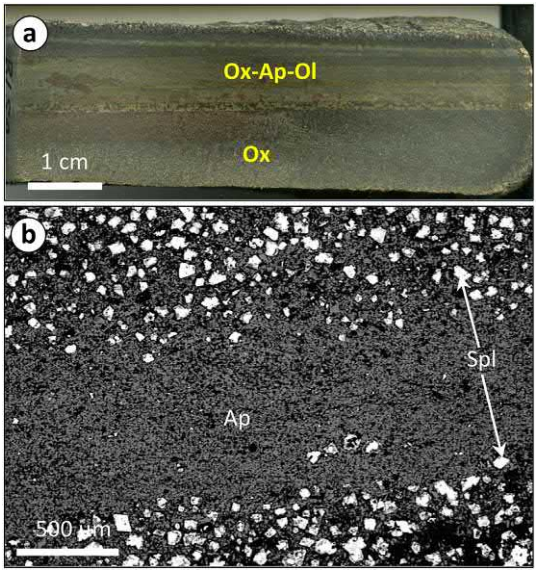

Fig. 8. (a) Hand-specimen photograph of Benfontein Lower Sill kimberlite sample BLS. (b) Back-scattered electron (BSE) SEM images of a apatite (Ap) rich layer between two (upper and lower) spinel (Spl) rich layers.

6. Discussion

6.1. Emplacement and differentiation of a low viscosity magma

There is a general scarcity of detailed studies of kimberlite sills, largely due to their apparent rarity and uneconomic diamond content. Previous studies of kimberlite sill complexes (e.g., Benfontein – Dawson and Hawthorne, 1973; Mitchell, 1994; Wesselton – Shee et al., 1991; White et al., 2012; Wemindji – Zurevinski and Mitchell, 2011; Amon – Tappe et al., 2014) have shown the kimberlites to be very rich in carbonates (e.g. calcite, dolomite), contain features characteristic of magmatic sedimentation (i.e., layering, cross-bedding) and preserve carbonate diapirs. These features, combined with evolved compositions of constituent minerals (i.e. olivine rims, spinel, phlogopite) and occurrence of exotic minerals mainly as inclusions in carbonates (e.g., barite, Ba-Fe titanate, REE-rich carbonates, Nb-rutile, Ce-monazite) have led previous authors to interpret these sills to be the products of extensive magmatic differentiation either during ascent or upon emplacement (Mitchell, 1994; Shee et al., 1991; Tappe et al., 2014; White et al., 2012; Zurevinski and Mitchell, 2011). The Benfontein sills can therefore provide useful insights into the magmatic evolution of kimberlites.

The presence of layering in the Benfontein sills is a strong indication of extensive fractional crystallisation of the parental magma. Crystal-liquid separation led to the gravitational settling of minerals (e.g., silicates, oxides and apatite) as they formed, resulting in the formation of cumulate layers (e.g., Dawson and Hawthorne, 1973). The preservation of these layers suggests that the parental magma to these sills was emplaced quiescently compared to the highly dynamic and explosive processes (e.g., fluidisation) that typically form volcaniclastic deposits infilling kimberlite diatremes (Clement, 1982; Dawson, 1971; Kurszlaukis and Lorenz, 2008; Nowicki et al., 2004; Sparks et al., 2006). The presence of monticellite has been invoked to be the product of decarbonation (i.e. degassing) of kimberlite magmas, which can exsolve significant quantities of CO_2 (Abersteiner et al., 2017b; Lim et al., 2018). Thus, abundant groundmass monticellite, including the presence of grain clusters around olivine (Supplementary Fig. S1b, c) in sample BUSK-2 indicates some post-emplacement degassing in the Upper Sill may have occurred.

Mantle xenoliths and xenocrysts in the Benfontein sill complex are scarce and do not exceed more than a few millimetres in size, with the majority <1 mm, which contrasts to the larger size of mantle-derived xenoliths (on the order of ≥10 cm and up to 1 m) reported in other Kimberley area kimberlites (Dawson et al., 2001; Lawless et al., 1979). This indicates that entrained mantle solids were likely removed from the parental magma during transport (Dawson and Hawthorne, 1973). This process may have occurred due to a combination of: (i) mechanical separation of dense mantle-derived solids from the more buoyant melt component *en route* to the surface during the ascent of kimberlites in dykes (Fig. 14). (ii) Flow differentiation upon sill formation during the lateral spreading of the magma into the country rock shales (Fig. 14). The presence of mantle-derived olivine (Howarth and Taylor, 2016) as well as mantle micro-xenoliths (Supplementary Fig. S3; Dawson and Hawthorne, 1973) indicates that only the finest grained fraction of entrained mantle material was transported and incorporated in the Benfontein sills. The removal of significant mantle-derived xenogenic cargo likely resulted in a magma enriched in carbonate melt. This process may have enhanced the buoyancy and decreased the viscosity of the magma, thus fostering magma mobility and formation of a large sill complex (known exposure area of the sills is ~4.5 km *E*-W and ~2.5 km N-S; Dawson and Hawthorne, 1973).

The low viscosity of the Benfontein parental magma, combined with crystal fractionation, was probably instrumental in the formation of magmatic layering. The earliest stage of crystallisation in the Benfontein kimberlite is signified by euhedral-shaped olivine overgrowths around xenocrystic olivine. The entrapment of euhedral crystal inclusions of chromite in this magmatic olivine (Howarth and Taylor, 2016) indicates cotectic crystallisation (e.g., Fedortchouk and Canil, 2004; Mitchell, 1986, 2008). This was then followed by the crystallisation of the remaining groundmass assemblage (e.g., spinel, perovskite, monticellite, apatite, phlogopite, baddeleyite), calcite laths and interstitial carbonate. The in situ crystallisation of the groundmass minerals suspended in a low viscosity melt (or slurry) resulted in the formation of cumulate textures and layering (e.g., Figs. 4, 8). In contrast, other areas of the Benfontein sills (e.g., sample BMSK-3; Fig. 5a) appear to have crystallised as poorly mixed olivine-rich slurries. Similar features were observed in the Benfontein sills by Dawson and Hawthorne (1973; i.e., Plate 4B) where a layered kimberlite was cross-cut by a later injection of magma. This suggests that different magma injections experienced varying levels of differentiation. The presence of rhythmic layering (e.g., samples JJG-BEN1 and BLS; Figs. 4 and 8) suggests that cumulate layers may have formed due to multiple injections of the same magma and/or magmas of similar composition into the sill.

Carbonate diapirs crystallised as late-stage features from the residual carbonatitic melt, which is consistent with the enrichment in interstitial carbonate in this and other kimberlites worldwide (e.g., Armstrong et al., 2004; Giuliani et al., 2017; Mitchell, 2008; Soltys et al., 2018b; Tappe et al., 2014). Dawson and Hawthorne (1973) attributed carbonate diapirism to large density and viscosity differences between partly solid oxide- and underlying carbonate-rich layers, whereby low density carbonate melts migrated upwards into the denser oxide-rich layer. This demonstrates that the groundmass was semi-consolidated (or slurry state) and the residual component was dominantly carbonatitic melt, which can have extremely low viscosity (e.g., Allan and Andrew, 1983). The low viscosity of the magma is further signified by the presence of a 'floating' fragment of shale in sample BUSK-1 (Fig. 3a) where the carbonate-rich layers appear to wrap around the shale fragment.

6.2. Comparison to the Wesselton kimberlite sills

The Wesselton kimberlite sills are located <10 km (Fig. 1) from Benfontein and were dated at 88.6 ± 0.8 Ma by perovskite U-Pb geochronology (Smith, 1983). This age is consistent with our new and previous calculated ages of the Benfontein sills (e.g., Supplementary Fig. S8) and adjacent Kimberley area pipes (see above).The Wesselton kimberlite sills were probably formed in a similar way whereby kimberlite

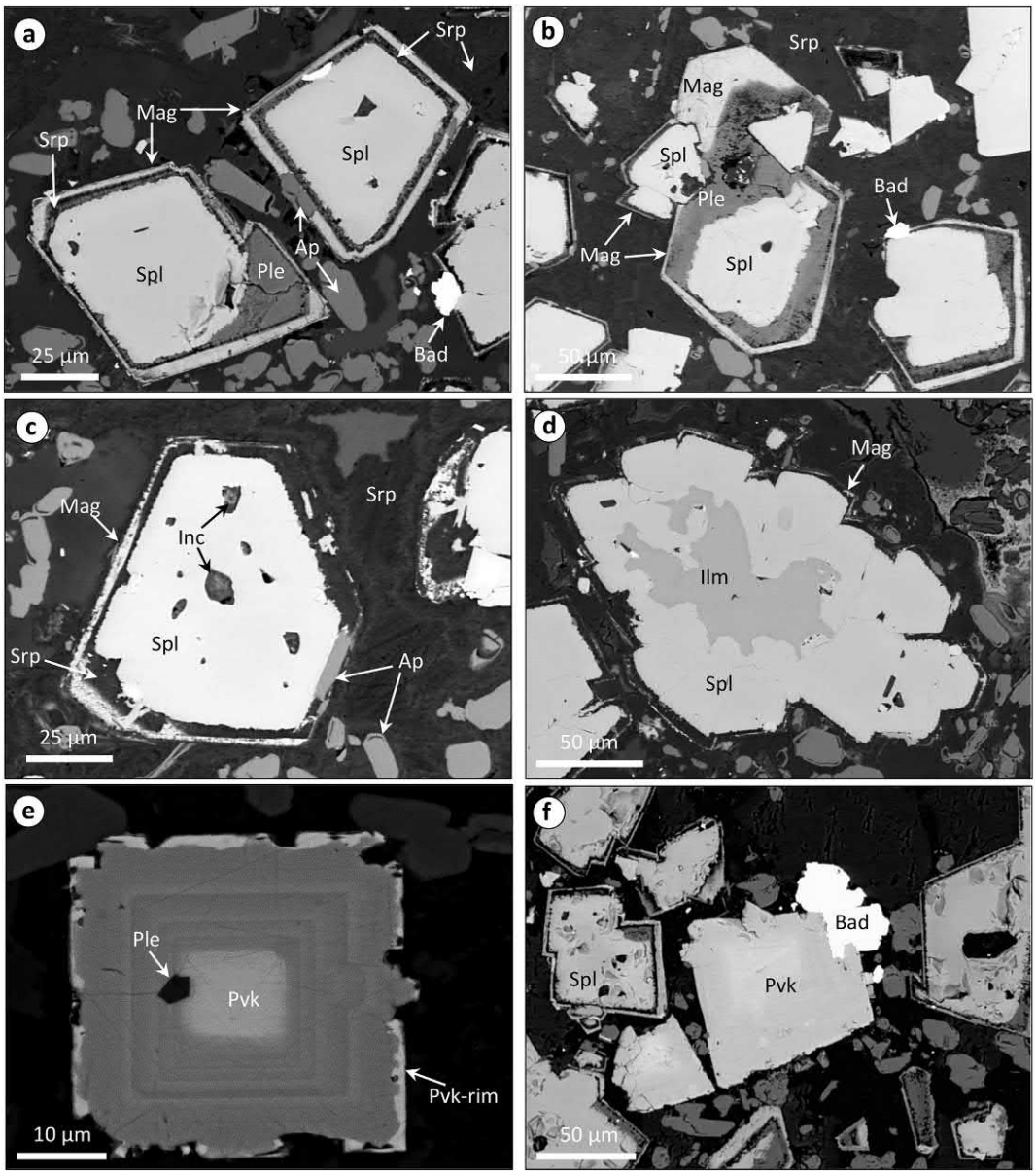

Fig. 9. Back-scattered electron (BSE) SEM images of: (a, b) Euhedral atoll-spinel (Spl; magnesian ulvospinel – magnetite) surrounded by an intermediate 'lagoon' zone which is composed of serpentine (Srp) and/or pleonaste (Ple). This lagoon is in turn mantled by a rim of Mg-Al magnetite (Mag). The outer rims of atoll-spinel grains are sometimes intergrown with apatite (Ap) or baddeleyite (Bad). (b) The MUM-spinel core is partially resorbed and forms fretted boundaries with pleonaste. (c) Atoll-spinel where pleonaste is absent and the 'lagoon' zone is occupied by serpentine. (d) Atoll-spinel overgrowth around a partially resorbed ilmenite (Ilm) core. (e) Complexly zoned perovskite grain which is characterised by oscillatory zoning in BSE imaging. The perovskite core is mantled by a light rare earth element (LREE) enriched perovskite rim. (d) Euhedral perovskite (Pvk) intergrown with an irregularly-shaped baddeleyite grain. Inc.: inclusion.

magmas intruded laterally into Dwyka shales in response to the permeability barrier represented by a Karoo dolerite sill (Shee et al., 1991). Therefore, the Wesselton sills can provide an excellent opportunity to compare potential variations in the parental magma composition and differentiation processes in two closely related sill complexes.

These kimberlites share a close similarity in terms of textures (e.g., magmatic sedimentation) and mineralogy chemistry (spinel - Mitchell, 1984; White et al., 2012; ilmenite - Shee et al., 1991; White et al., 2012; perovskite Jones and Wyllie, 1984, 1985; this study; Supplementary Fig. S7), Sr isotope ratios (Woodhead et al., 2009) and relative abundance of magmatic carbonate (Dawson and Hawthorne, 1973; Shee et al., 1991; White et al., 2012). The only notable mineralogical difference is that phlogopite is rare or absent at Benfontein but is a common groundmass constituent in the Wesselton sills (Mitchell, 1984; White et al., 2012), which is reflected by distinct differences in whole-rock K_2O content (<0.15 wt% in Benfontein; Dawson and Hawthorne, 1973; and 0.55–3.49 wt% in Wesselton; White et al., 2012). This suggests that phlogopite was either fractionated from the Benfontein kimberlite magma (e.g., during flow differentiation), or the Benfontein and Wesselton kimberlites crystallised from distinctly different parental melts, especially with respect to K_2O and possibly H_2O contents.

Both the Benfontein and Wesselton kimberlite sills are interpreted to have resulted from multiple magma injections (Dawson and Hawthorne, 1973; Shee et al., 1991; White et al., 2012), which probably gave rise to the sill complexes and large diversity of magmatic sedimentary structures. In addition, the Wesselton kimberlite sills are considered to predate the formation of the main Wesselton diatreme (Shee et al., 1991). The formation of Wesselton sill complex, including the feeder dyke(s) probably created the conduit pathways in the crust for ensuing intrusions of more turbulent pulses of kimberlite magma, which formed the main diatreme. Kimberlites emplaced by successive pulses of magma (e.g., Field and Scott Smith, 1999; Moss et al., 2009;

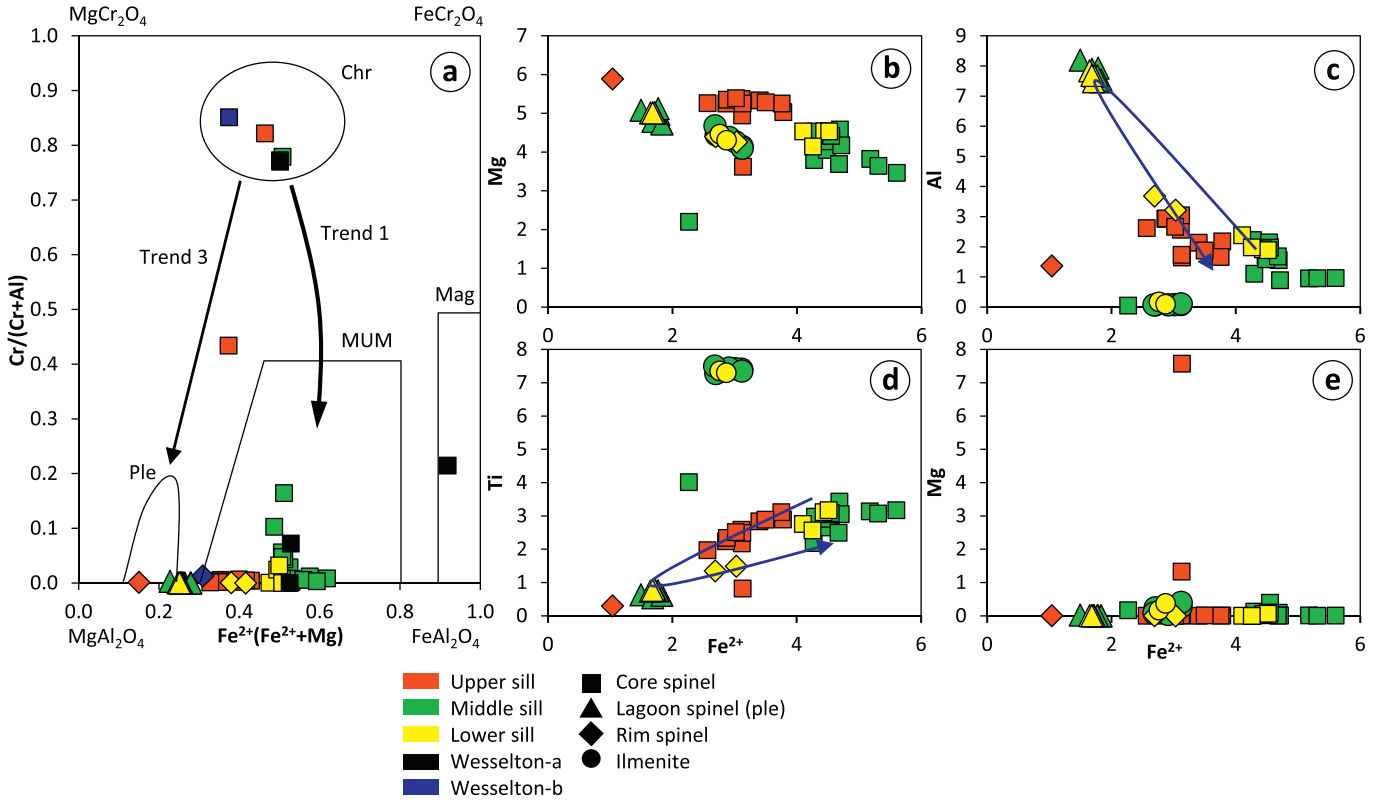

Fig. 10. (a) Cr/(Cr + Al) vs. $Fe^{2+}/(Fe^{2+}+Mg^{2+})$ of atoll-spinel grains from the Benfontein Sill Complex and spinel cores from the Wesselton kimberlite sill (a: Mitchell, 1994, b: White et al., 2012). Bivariate plots of Fe^{2+} vs: (b) Mg, (c) Al, (d) Ti, and (e) Cr (atomic proportions based on 24 oxygens). BLSK: Benfontein Lower Sill kimberlite, BMSK: Benfontein Middle Sill kimberlite, BUSK: Benfontein Upper Sill kimberlite, Chr: chromite, Ple: pleonaste, MUM: magnesian ulvöspinel-magnetite, Mag: magnetite, Ilm: ilmenite core. The blue line represents spinel compositional trends from core to rim.

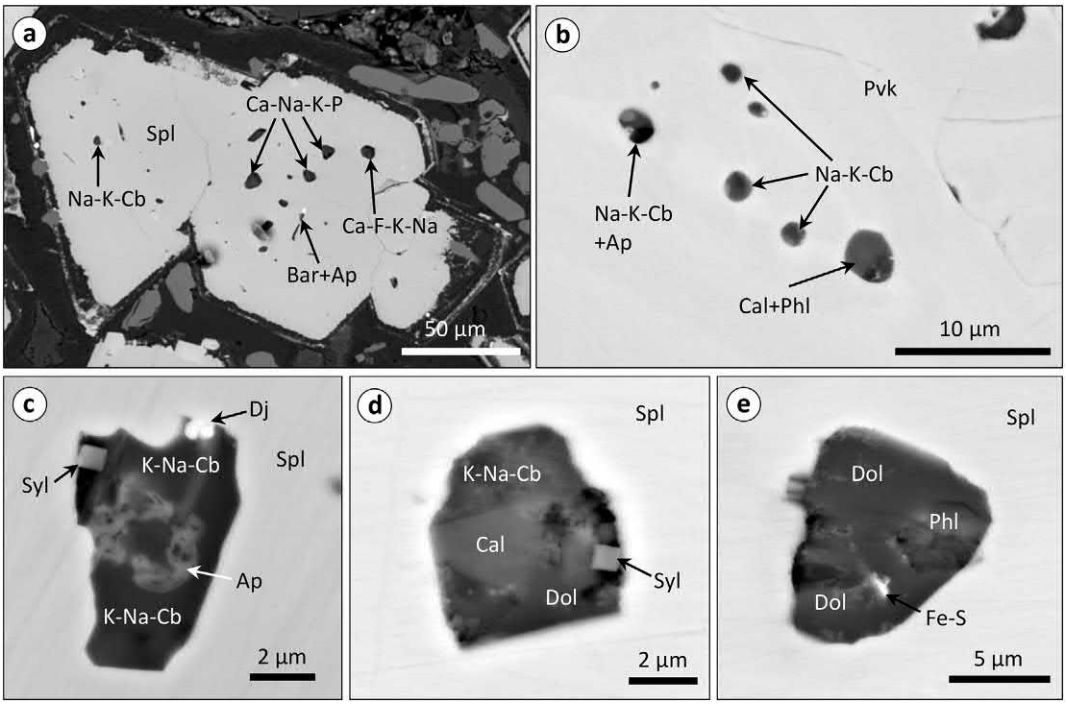

Fig. 11. Back-scattered electron (BSE) SEM images of multiphase melt inclusions in: (a, c – e) atoll-spinel (Spl) Mg-Al titanomagnetite cores, and (b) perovskite. These multiphase inclusions host daughter phases of: Alkali (Na, K) carbonates (Cb), apatite (Ap), barite (Bar), phlogopite (Phl), calcite (Cal), dolomite (Dol), djerfisherite (Dj), sylvite (Syl), Fe-sulphides (Fe-S) as well as unidentified Ca-Na-K-P and Ca-F-K-Na phases.

Table 2
Summary of daughter mineral phases included in atoll-spinel cores from the Benfontein Kimberlite Sill Complex, listed in order of decreasing abundance.

Mineral	Ideal Formula	Abundance (%)
Carbonates	Calcite ($CaCO_3$) Dolomite ($CaMg(CO_3)_2$) Nyerereite – $Na_2Ca(CO_3)_2$ Fairchildite $K_2Ca(CO_3)_2$ Witherite ($BaCO_3$) Siderite ($FeCO_3$) Magnesite ($MgCO_3$)	66
Phosphates	(Fluor)apatite ($Ca_5(PO_4)_3(F,Cl,OH)$) Na-K-bearing (Bradleyite? – $Na_3Mg(PO_4)(CO_3)$)	12
Phlogopite/ kinoshitalite	$KMg_3AlSi_3O_{10}(F,OH)_2$/(Ba,K)(Mg,Mn,Al) $_3Si_2Al_2O_{10}(OH)_2$	6
Sulphides	Fe-Cu-Pb-bearing ± K Djerfisherite $K_6Na(Fe^{2+},Cu,Ni)_{25}S_{26}Cl$	3
Olivine	$(Mg, Fe)_2SiO_4$	3
Chlorides	Halite (NaCl) Sylvite (KCl)	3
Fluorite	CaF_2	2
Sulphates	Barite ($BaSO_4$) Unidentified Na-K-bearing	2
Baddeleyite	ZrO	2
Perovskite	$CaTiO_3$	1
Kimzeyite	$Ca_3(Zr,Ti)_2(Si,Al,Fe^{3+})3O_{12}$	<1

Table 3
Summary of inclusion phases hosted in carbonate diapirs from the Benfontein Kimberlite Lower Sill, listed in order of decreasing abundance.

Mineral	Ideal Formula	Abundance (%)
Barite	$BaSO_4$	40
Barium iron titanate	$(K,Ba)_{1-2}(Fe,Cr,Al)_{1-2}(Ti,Nb)_{6-7}O_{16}$)	15
Ancylite	$Sr(REE)(CO_3)_2(OH).H_2O$	15
Alkali-carbonates	Na-K-Ba-Sr-bearing	10
(Fluro)apatite	$(Ca_5(PO_4)_3(F,Cl,OH))$	6
Sulphides	Chalcopyrite($CuFeS_2$), Pyrrhotite/ Pyrite (FeS)	6
(Nb)Rutile	$(Nb)TiO_2$	4
Phlogopite	$KMg_3AlSi_3O_{10}(F,OH)_2$	2
Fluorite	CaF_2	1
Bultfonteinite	$Ca_4(Si_2O_7)(F, OH)_2$	1
Kimzeyite	$Ca_3(Fe,Al,Ti)_2(Zr,Si)_3O_{12}$	<1
U-/Ba-pyrochlore	$(U,Ca,Ce)_2(Nb,Ta)_2O_6(OH,F)$ / $(Ba,Sr)(Nb,Ti)_2(O,OH)_7$	<1
Sylvite	KCl	<1

Sparks et al., 2006) are inferred to condition the mantle conduit, which favours the ascent to the surface of later kimberlite magmas (Giuliani et al., 2016). In contrast, the formation of the Benfontein kimberlite sill complex does not appear to have been succeeded by any additional dynamic kimberlite magmatism that penetrated the Karoo dolerite sill to form diatreme structures.

Based on the spatial proximity and similar emplacement age of the Benfontein and Wesselton sill complexes, it is likely that the Kimberley area experienced phases of less energetic kimberlite activity whereby ascending kimberlite magmas failed to breach the Karoo dolerite sill and instead propagated out laterally into the Dwyka shales (Dawson and Hawthorne, 1973; Shee et al., 1991; Fig. 14). The present day exposure of the Benfontein and Wesselton sills along with other rare kimberlite sill occurrences worldwide is extremely fortuitous, given their vertically insignificant dimensions (e.g., the Amon kimberlite sill is between 0.2 and 1 m in thickness; Tappe et al., 2014). In addition, kimberlite sills do not appear to laterally extend more than a few kilometres. Therefore, it is likely that large fractions of kimberlite magma may not reach the surface, but stall in the crust (and mantle – e.g., polymict breccias; see Giuliani et al., 2012; Lawless et al., 1979) because they are not energetic enough to breach through and traverse permeability barriers, such as dolerite sills that are present in southern Africa. Therefore, other kimberlites may have shared a similar emplacement style as the Benfontein and Wesselton kimberlite sills, but remain undiscovered as they were rapidly eroded or still under cover.

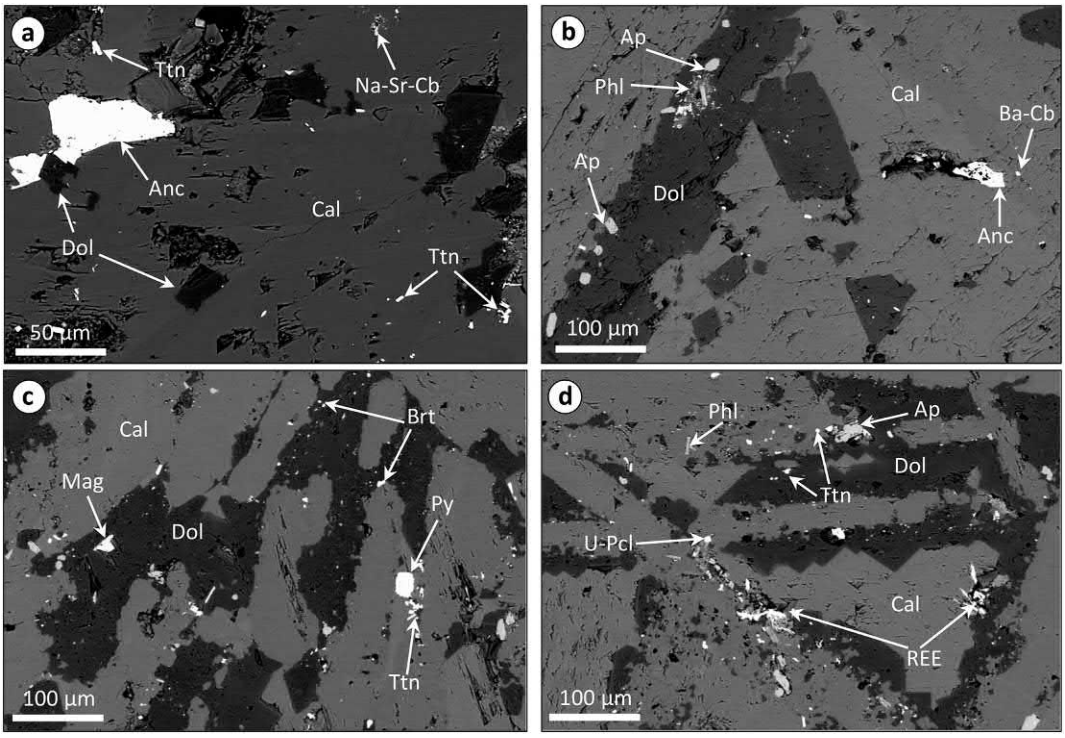

Fig. 12. Back-scattered electron (BSE) SEM images of inclusions in calcite (Cal) diapirs from the Lower Sill. These diapirs are composed of elongated calcite laths and rhombohedral dolomite (Dol). Detected phases include: Ancylite (Anc: $SrCe(CO_3)_2(OH)•(H_2O)$), barium iron titanate (Ttn; $(K,Ba)_{1-2}(Fe,Cr,Al)_{1-2}(Ti,Nb)_{6-7}O_{16}$), Na-Sr-Ba-carbonates (Cb), apatite (Ap), phlogopite (Phl), magnetite (Mag), pyrite (Py), barite (Brt), Uranopyrochlore (U-Pcl) and unidentified rare earth element bearing phases (REE).

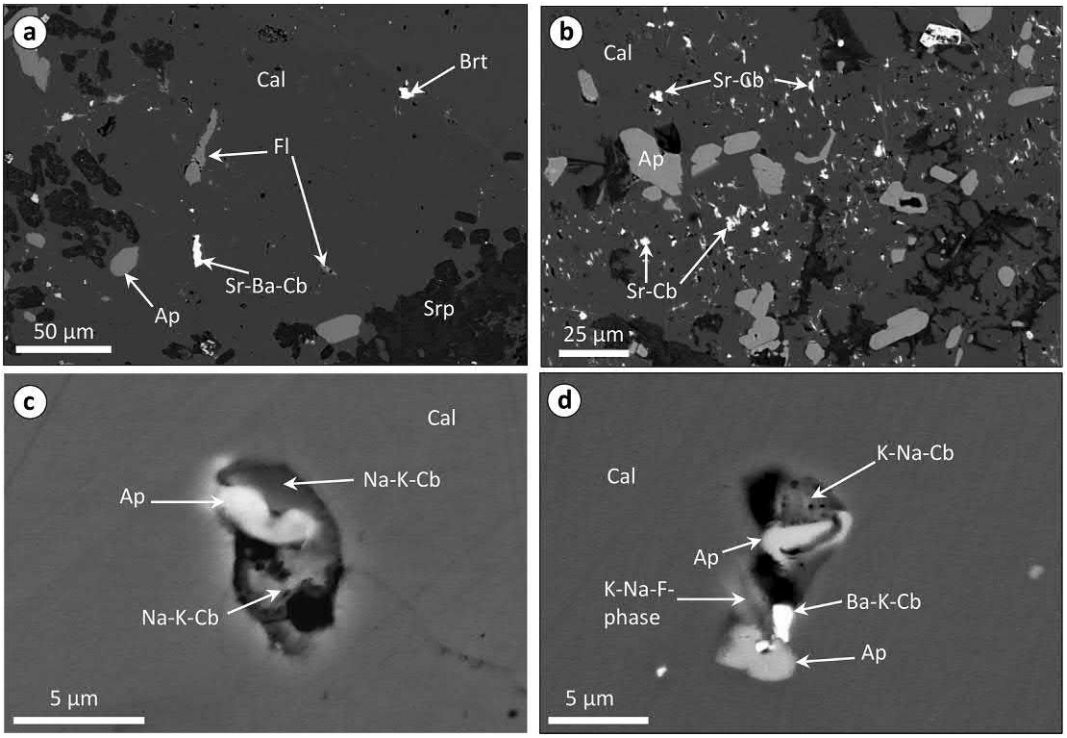

Fig. 13. Back-scattered electron (BSE) SEM images of inclusions in interstitial groundmass calcite (Cal). (a, b) Crystal and disseminated inclusions of apatite (Ap), fluorite (Fl), Sr-Ba-carbonates (Cb) and barite (Brt). (c, d) Multiphase inclusions composed of apatite, Na-K-Ba-carbonates and unidentified K-Na-F-phases. Srp: serpentine.

6.3. Evolution of the parental kimberlite magma

Reconstructing kimberlite petrogenesis is hampered as the melts parental to kimberlite rocks are commonly subject to extensive modification and hybridisation by:

i) Entrainment and interaction with mantle and crustal material (Buse et al., 2010; Hunter and Taylor, 1982; Smith et al., 2004; Soltys et al., 2016). The presence of abundant olivine in kimberlite rocks can significantly influence whole-rock compositions (Kjarsgaard et al., 2009; le Roex et al., 2003; Price et al., 2000; Soltys et al., 2018a). The majority of olivine in kimberlites has either ascribed a xenocrystic origin derived from disaggregated mantle rocks (Giuliani, 2018 and references therein).

ii) Degassing and exsolution of volatiles *en route* to the surface and upon emplacement (Abersteiner et al., 2017b; Brooker et al., 2011; Giuliani et al., 2014; Kamenetsky and Yaxley, 2015; Sparks et al., 2006).

iii) Syn- and post-magmatic alteration by C-O-H-bearing fluids, which can overprint the primary mineralogy and replace it with abundant serpentine and carbonates (Clement, 1982; Giuliani et al., 2014, 2017; Mitchell, 1986; Sparks, 2013). Therefore, the presence of serpentine can contribute to the elevated MgO, SiO_2 and H_2O content of kimberlites (Sparks et al., 2009).

Consequently, the majority of kimberlite occurrences are inevitably affected by the above processes and therefore cannot be considered accurate reflections of their original melt compositions. To circumvent these problems, we present new insights into the evolution of the parental kimberlite melt that formed the Benfontein sills through: i) the compositional evolution of atoll-spinels, and ii) the composition of melt inclusions entrapped in olivine and magmatic groundmass minerals (i.e. monticellite, spinel, perovskite, apatite and carbonate).

6.3.1. The origin of atoll-spinels

The term 'atoll-spinel' was first adopted by Mitchell and Clarke (1976) to describe groundmass spinel (e.g., titanomagnetite – chromite) grains surrounded by a 'lagoon' zone, which is in turn surrounded by an outer rim of Ti-free magnetite (Figs. 9a – d). The lagoon is typically occupied by fine-grained mixtures of secondary serpentine and/or calcite (Figs. 9a, c, d). Although atoll-shaped spinels have been documented in numerous kimberlites worldwide (e.g., Abersteiner et al., 2017a, 2018; Armstrong et al., 1997; Mitchell, 1986; Mitchell and Clarke, 1976; O'Brien and Tyni, 1999; Pasteris, 1980, 1983; Roeder and Schulze, 2008; Shee, 1985), there is no clear agreement on their origin. Previous studies have attributed the formation of atoll-spinels to: (i) resorption of a former 'intermediate' spinel phase (e.g., Mg-MUM – Mitchell and Clarke, 1976; or pleonaste – Pasteris, 1980, 1983), which generated the 'lagoon' zone. (ii) Primary growth, whereby skeletal (or cruciform) morphologies were due to rapidly changing crystallisation conditions (Armstrong et al., 1997). (iii) Absence of spinel crystallisation within atoll 'lagoon' due to a lack of necessary chemical constituents and/or spinel immiscibility (Roeder and Schulze, 2008). Roeder and Schulze (2008) further speculated that the 'lagoon' zone was occupied by an oxide-silicate kimberlite melt or immiscible fluid phase.

Benfontein samples 177/33/K18/276, BLSK-2 and BLSK-4 contain some of the best-preserved atoll-spinels from the examined suite. The most obvious feature of atoll-spinels is their well-preserved euhedral habit of both cores and rims, which suggests in situ crystallisation. In the following sections we consider two possible origins for atoll-spinels: 1) atoll-spinels are primary growth features, and 2) atoll-spinels formed due to resorption (i.e. alteration) of a former magmatic phase.

In the first scenario, the shape of atolls bear similarities to the various complex skeletal, hopper, vermiform and chain growth structures typically observed in Cr-rich spinels in rapidly quenched mid-ocean ridge basalt (MORB; Roeder et al., 2001) and ophiolites (Christiansen and Olesen, 1990). The uniform (i.e. unzoned) compositions in the majority of atoll-spinel cores from the Benfontein sills are interpreted to represent homogenisation due to slow rates of cooling (Roeder and Schulze, 2008). Slow cooling is, however, at odds with the rapid cooling required to form the various skeletal, vermiform, hopper and chain structures in Cr-spinel from MORB. In addition, Mitchell (2008) observed that kimberlitic spinels never form the skeletal-to-cruciform

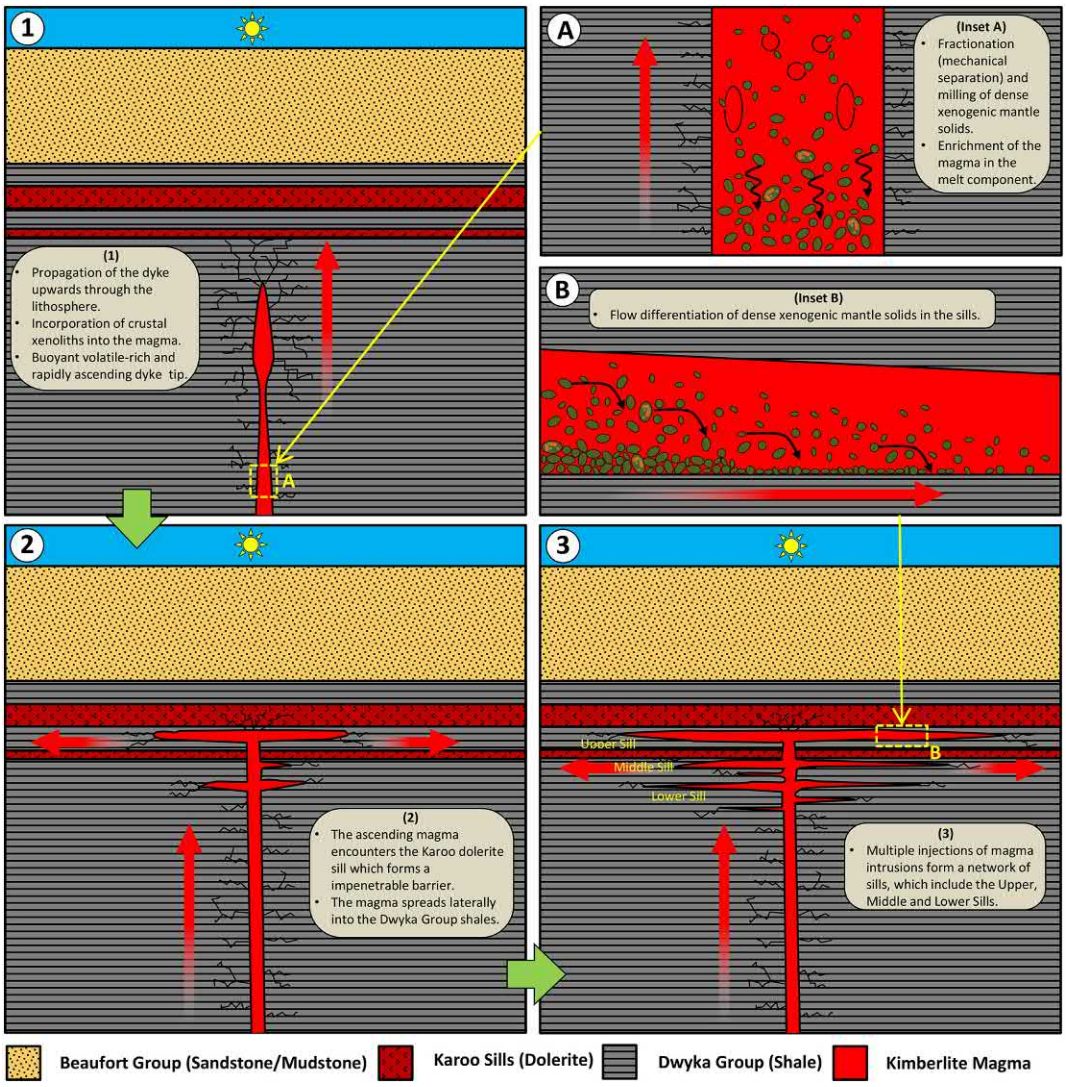

Fig. 14. Schematic diagram of the formation of the Benfontein kimberlite sill complex. Stage 1: Rapid ascent of the kimberlite magma through the lithosphere, where fracturing and incorporation of surrounding wall-rocks occurs. Inset A shows fractionation of the kimberlite magma en route to the surface, where dense entrained mantle solids (i.e. xenoliths and xenocrysts) become mechanically separated from the magma, resulting in enrichment of a more buoyant and low viscosity melt component of the magma. Stage 2: The ascending magma encounters the Karoo dolerite sill, which forms an impenetrable barrier and causes the rising magma to spread laterally into the Dwyka Group shales. Stage 3: Over multiple episodes of magma injection(s), the resulting sill complex composing of multiple tiers (e.g., Upper, Middle and Lower) are formed. Inset B shows that the most fractionated (i.e. melt) components of the magma propagates the furthest. During sill formation, heavier components (i.e. mantle-derived solids) are removed by flow differentiation.

crystals. The primary growth model also negates the occurrence of pleonaste partially-to-completely occupying the lagoon zone in atoll spinels from various localities (e.g., Benfontein – Figs. 9a, b; De Beers – South Africa; Pasteris, 1983; Pipe 1 – Finland; O'Brien and Tyni, 1999; Udachnaya-East – Russia; Abersteiner et al., 2018).

The second model attributes the formation of the lagoon zone to resorption of a former magmatic phase. This scenario implies that the former phase was highly unstable, but existed long enough for the epitaxial magnetite rim to form before being removed (Mitchell, 1986). In the Benfontein sills, the atoll-spinel cores sometimes transition to pleonaste along a sharp boundary and are in crystallographic continuity with each other (Figs. 9a, c). This pleonaste partially-to-completely occupies the gap between core and outer Mg-Al-magnetite rim. The crystallographic continuity of pleonaste with spinel core and outer rim, along with the presence of sporadic crystal inclusions of olivine and baddeleyite within the pleonaste zone suggests pleonaste crystallised in situ from a kimberlite melt. In addition, pleonaste occurs as primary crystal inclusions in perovskite in the Benfontein (Fig. 9e) and Venetia kimberlites (Abersteiner et al., 2017a), which further substantiates a magmatic origin. Pleonaste only appears to be preserved in samples which have experienced minimal alteration (i.e. serpentinisation) and is best preserved when the outer rim is continuous. In more altered samples of the Benfontein sills (e.g., samples BMSK-3, BLSK-5, or areas in close proximity to carbonate diapirs), pleonaste is largely to completely resorbed, thereby producing the characteristic 'lagoon' zone, which is composed of secondary alteration minerals (e.g., serpentine, chlorite, calcite; Figs. 9a, c, d). This suggests that pleonaste was a highly unstable phase and susceptible to alteration by external fluids and/or assimilation back into residual carbonate-rich kimberlite melts due to changing conditions (see below). We present a schematic diagram showing the formation of atoll-spinel structures in Fig. 15, showing the different stages of magmatic growth from MUM/chromite cores, to pleonaste and then to Mg-Al-magnetite rims, and resorption of pleonaste to form atoll structures.

Although magmatic pleonaste is the most likely phase that previously occupied the lagoon zone of atoll-spinels, the mechanism causing the abrupt changes from MUM/chromite cores to pleonaste and then finally transitioning to Mg-Al-magnetite is not fully understood. Pasteris (1983) speculated that in the Kimberley kimberlites the Al content of kimberlite melts was governed by the crystallisation of phlogopite and

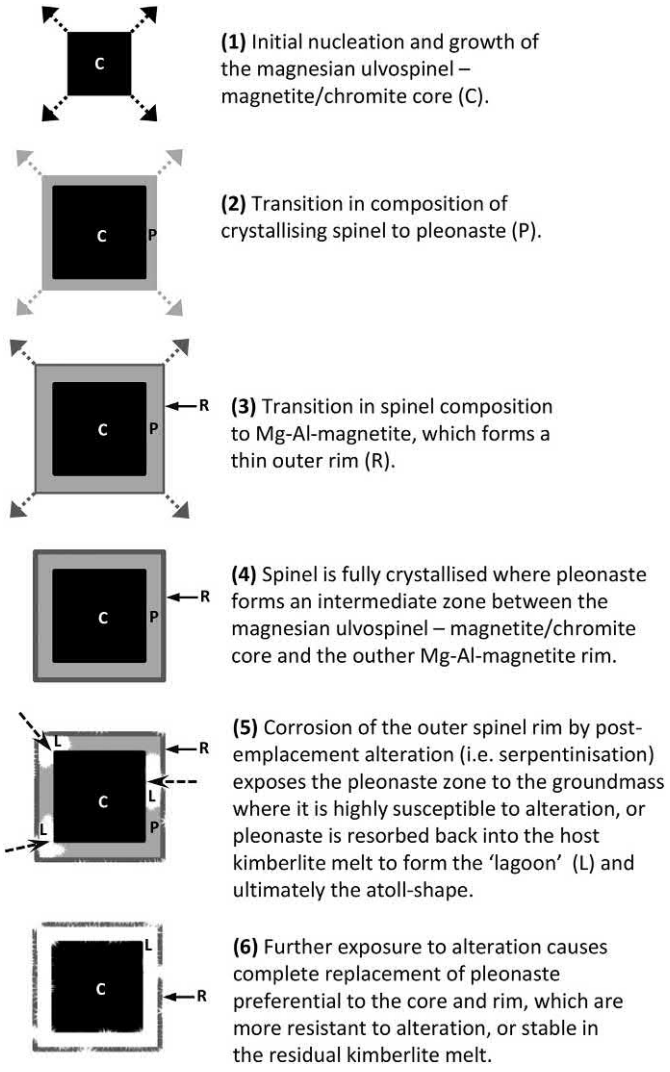

Fig. 15. Schematic diagram of the growth of spinel and the alteration processes that lead to atoll-textures.

low-Al spinel and that during ascent phlogopite became unstable and aluminium was preferentially partitioned into Al-rich spinel (or pleonaste). The in situ crystallisation of pleonaste could also be attributed to a combination of changes in the parental melt composition due to crystallisation and decreasing temperature. The early crystallisation of olivine and chromite followed by MUM spinel and perovskite (e.g., Mitchell, 1986, 2008; Soltys et al., 2018b) likely caused a significant removal of TiO_2, Cr_2O_3, FeO and MgO from the melt with consequent enrichment in Al and pleonaste supersaturation. The sudden transition to pleonaste stability may have also partially caused resorption of the spinel core, thereby producing the rugged contacts observed in Benfontein spinel (Fig. 9b). Pleonaste (and, in other localities, phlogopite) crystallisation depleted the residual melt in Al, thus rendering Mg-Al-magnetite the stable spinel phase in residual kimberlite melts and locally leading to pleonaste resorption.

6.3.2. Evolution of the Benfontein kimberlite

The study of inclusions hosted in kimberlitic minerals has been demonstrated to be an informative approach for constraining the compositional evolution of parental kimberlite melts (Abersteiner et al., 2017a, 2017b, 2018; Giuliani et al., 2017; Golovin et al., 2007, 2018; Kamenetsky et al., 2014 and references therein). Inclusions typically represent the heterogeneous trapping of kimberlitic melt and/or solid phases during crystallisation of constituent groundmass minerals, therefore providing 'snapshots' of the kimberlite magma at a particular stage of its evolution. Once entrapped within the host mineral, these inclusions are isolated from post-magmatic processes (e.g., serpentinisation).

In general, primary melt inclusions hosted in magmatic spinel, perovskite, monticellite, apatite along with secondary melt inclusions in olivine are generally composed of (in order of decreasing abundance) Ca-Mg carbonates, alkali (Na, K, Ba, Sr) carbonates, phosphates (e.g., apatite), Fe-Mg-Ti-Al-oxides (e.g., spinel, perovskite), silicates (e.g., phlogopite), Fe-rich sulphides, Na-K-chlorides, Ca-F-rich phases (e.g., fluorite), Ba-Na-K-sulphates along with other minor phases enriched in incompatible trace elements (Tables 2, 3). The compositions of these melt inclusions are consistent with the continually growing list of studies of melt inclusions hosted in kimberlitic minerals (e.g., olivine, spinel, perovskite, monticellite, apatite; see above references), olivine and ilmenite in mantle polymict breccias (i.e. failed kimberlites at mantle depths; Giuliani et al., 2012) and minerals from other kimberlite-borne mantle xenoliths (Golovin et al., 2007; Soltys et al., 2016) from localities worldwide, which show similar enrichment in these phases. These studies of melt inclusions in kimberlitic minerals suggest that the parental kimberlite melts formerly contained higher abundances of alkalis, halogens, sulphur and CO_2, and were more depleted in silica, magnesium and H_2O than what measured in kimberlite rocks. In addition, the presence of periclase inclusions in monticellite in the Upper Sill suggests possible decarbonation reactions between olivine and the carbonate component of the kimberlite melt, which produced monticellite, periclase and CO_2 (vapour) in response to magma degassing (Abersteiner et al., 2017b).

Interstitial groundmass calcite contains abundant inclusions of Ba-Sr-carbonates along with lesser Na-K-carbonates, barite and other Ca-F-rich phases (e.g., apatite, bultfonteinite, fluorite), Na-K-chlorides and humite (Fig. 13). These inclusions probably represent late-stage enrichment in alkalis and halogens in the residual kimberlite melt. In contrast, carbonate diapirs in the Lower Sill contain inclusion assemblages enriched in other phases (e.g., barite, Ba-Fe-titanate, ancylite, Nb-rutile, kimzeyite and urano/bariopyrochlore; Fig. 12; Table 3), and are compositionally distinct from inclusions in groundmass minerals from the Benfontein sills and other kimberlites worldwide (see above). The presence of these phases reflects enrichment in LREEs, HFSEs, alkalis and alkali-earths (Ba, Sr, Na, K, Ca, Mg), halogens (F, Cl) and other incompatible trace elements in the melt that generate the diapirs (Table 3). Similar inclusion assemblages were previously reported in previous studies of carbonate diapirs from the Benfontein, Wesselton and Wemindji kimberlite sills (Mitchell, 1994; Scatena-Wachel and Jones, 1984; Zurevinski and Mitchell, 2011), which suggests that these phases formed as a late-stage product during sill formation. We interpret these carbonate-rich diapirs to be foci of late-stage kimberlite melt enrichment whereby extensive melt differentiation concentrates CO_2, alkalis/alkali-earths, halogens, REEs, phosphorus and other incompatible trace elements into high enough abundances to crystallise these exotic phases. This late-stage enrichment in REEs of residual kimberlite melts is also evidenced by the presence of thin REE-rich rims around perovskite cores (Fig. 9e). This residual REE-enrichment may be due to insufficient crystallisation of perovskite, perhaps because abundant precipitation of spinel and ilmenite depleted the melt in Ti, an essential constituent of perovskite. The anomalous enrichment in incompatible trace elements recorded in the carbonate-rich diapirs also stems from the mobility of residual carbonate-rich melt fractions, which were 'squeezed out' from carbonate layers into overlying oxide-rich layers due to density contrasts induced by the settling of oxide minerals (see also Dawson and Hawthorne, 1973). These changes in density may be amplified by the pressure induced by the overburden of crustal rocks (≥850 m; Hanson et al., 2009) overlying the sill complex. As magma pressure declined, the overlying crustal rocks may cause compaction of the semi-consolidated kimberlite magma. This may lead to the physical squeezing of the residual carbonate melt fraction and the formation

of carbonate diapirs in the Lower Sill. These small scale carbonate-rich diapirs resulting from extensive differentiation and physical separation of kimberlite magma could potentially segregate at larger scales to form carbonatitic melts. One example is the co-occurrence of kimberlite dykes with carbonatite sheets at Tikiusaaq (West Greenland; Tappe et al., 2014). Similar to the formation of the Benfontein kimberlite sills, fractionation of mantle-derived constituents (e.g., olivine, xenoliths) from kimberlite magmas in the shallow mantle and/or crust could lead to the formation of carbonate-rich (or carbonatitic) liquids.

Carbonate-diapirs may appear to be effective scavengers of residual melt components (i.e. alkalis, halogens, REEs etc), which were otherwise widely distributed throughout the magma system. The scarce enrichment in alkalis, halogen and sulphur in the groundmass of kimberlites is attributed to syn−/post-magmatic alteration (i.e. serpentinisation), where infiltrating external fluids can readily dissolve and remove the host phases. This could be analogous to modern day eruptions of alkali-carbonate and chloride bearing natrocarbonatitic lavas from Oldoinyo Lengai (Tanzania), where rapid mineralogical and compositional changes occur within days to months upon interaction with the atmosphere (Dawson, 1993; Zaitsev and Keller, 2006). If alkali- and halogen-rich minerals were crystallised in the groundmass, then they were probably highly unstable and rapidly leached by contact with syn−/post-magmatic external/residual fluids. This process is observed when alkali- and halogen-bearing inclusions are exposed during sample preparation, where interactions with water or the atmosphere causes fast degradation and recrystallisation. Na in the groundmass of the Benfontein kimberlite may have been remobilised due to hydrothermal fluids led to the formation of glagolevite. However, a crustal-derived source of Na from the present day hydrology should not be excluded, as the Benfontein sills are located within an area where saltpans are extremely widespread. This is a tenuous assumption, as Cl-bearing minerals should be expected.

In addition, Howarth and Taylor (2016) documented two distinct populations of xenocrystic olivine in the Benfontein sills, which were assigned different mantle origins and classified to as Type 1 and Type 2 olivine. These authors noted that Type 1 olivine (i.e. sourced from refertilised dunite) were characterised by exceptionally Na-rich (up to 560 ppm) and Ca-rich (up to 800 ppm) cores. Howarth and Taylor (2016) attributed this Na-Ca enrichment to early-stage metasomatism at the base of SCLM by an alkali-bearing carbonate-silicate (or possibly carbonatitic) melt, which was a likely precursor to kimberlite magmatism. This interpretation is consistent with our analyses of melt inclusions, which demonstrate that alkali-carbonates were an intrinsic part of the parental kimberlite melt, likely originating in the mantle.

7. Summary

The lack of mantle cargo in the Benfontein sills suggests that the parental magma underwent substantial fractionation prior to emplacement, most probably during sill formation. Consequently, the kimberlite magma was enriched in the carbonated melt component, which probably resulted in more buoyant and lower viscosity magma. A unique feature is the presence of carbonate-rich diapirs in the Lower Sill, which probably formed due to density contrasts and/or compaction of the sills. Other kimberlite sill complexes such as Wesselton (Shee et al., 1991; White et al., 2012), Wemindji (Zurevinski and Mitchell, 2011) and Amon (Tappe et al., 2014) also exhibit similar structural and petrographic features to those of the Benfontein kimberlite. This indicates that crystal/solid fractionation and carbonate enrichment in the melt may be common processes in the development of kimberlite sills.

Petrographic data for atoll-spinels from the Benfontein sills show that pleonaste occurs in crystallographic continuity with MUM/chromite core and Mg-Al magnetite rim, along with the occurrence of crystal inclusions of olivine/baddeleyite in pleonaste, demonstrating that pleonaste was a primary magmatic phase. We propose that pleonaste persisted for long enough in composite spinel grains to act as a substrate for the growth of the outer magnetite rim. Pleonaste became highly unstable in the residual melt and/or during post-magmatic alteration, and was then altered to secondary phases (e.g., serpentine, calcite). This process is common in serpentinised samples from the Benfontein complex as well as in the majority of kimberlites worldwide.

Analyses of secondary melt inclusions in olivine and primary melt inclusions in groundmass monticellite, oxides and apatite are shown to be broadly composed of Ca-Mg carbonates and, to a lesser extent, alkali-carbonates, phosphates, oxides, silicates, sulphides, alkali-sulphates and halides. The compositions of these inclusions suggest that the melt parental to the Benfontein sills was probably more enriched in alkalis, halogens, S and other minor trace elements, compared to whole-rock compositions (Dawson and Hawthorne, 1973; Hawthorne, 1968). In addition, interstitial groundmass calcite hosts inclusion assemblages similar to those in melt inclusions from olivine and groundmass minerals, whereas carbonate diapirs contain exotic assemblages of minerals (e.g., Ba-Fe titanate, barite, ancylite, pyrochlore) that are rare or absent in kimberlites. Inclusions in carbonate diapirs are highly enriched in LREEs, HFSEs, alkalis and halogens, and probably represent the final products of extensive kimberlite melt differentiation. The absence or rarity of alkali and halogen bearing phases in the groundmass of the Benfontein sills (or kimberlites in general) is attributed to their remobilisation and removal during syn−/post-magmatic alteration. The preservation of secondary glagolevite in the groundmass of the Benfontein sills suggests that dissolved Na from the kimberlite groundmass and/or Na-brines became partially fixed into low-temperature minerals during serpentinisation.

Acknowledgements

This study forms part of A.A's Ph.D and was supported by an Australian Postgraduate Award (APA). This work has benefitted from comments by two reviewers, Shannon Zurevinski and Sebastian Tappe, and efficient editorial handling by Nelson Eby. We thank Martin Giger (University of Cape Town) and acknowledge the John J. Gurney Upper Mantle Research Collection at the University of Cape Town for providing access to samples JJG-BEN1, JJG-BEN2, JJG-2241A, JJG-2241B and 173/33/K18/276. A.G. would like to thank Jock Robey for leading the 2015 field campaign in the Kimberley area, when the remaining samples for this study were collected; Ashton Soltys for his support during field work including provision of the photos in Figure 2; and the De Beers Group for providing access to the Benfontein farm. This work was supported by funding by from the Australian Research Council (ARC) Discovery grant (DP130100257, 2013-2015) and University of Tasmania (New Star Professorship, 2010-2014) to V. Kamenetsky. A.G. acknowledges funding from the ARC through a DECRA fellowship (grant n. DE-150100009). This is contribution Systems number: 1128 from the ARC Centre of Excellence for Core to Crust Fluid Systems (www.ccfs.mq.edu.au) and GEMOC number:1268 from the GEMOC Key Centre (www.gemoc.mq.edu.au).

Appendix A. Supplementary data

Supplementary data to this article can be found online at https://doi.org/10.1016/j.lithos.2018.11.017.

References

Abersteiner, A., Giuliani, A., Kamenetsky, V.S., Phillips, D., 2017a. Petrographic and melt-inclusion constraints on the petrogenesis of a magmaclast from the Venetia kimberlite cluster, South Africa. Chem. Geol. 455, 331–341.

Abersteiner, A., Kamenetsky, V.S., Graham Pearson, D., Kamenetsky, M., Goemann, K., Ehrig, K., Rodemann, T., 2017b. Monticellite in group-I kimberlites: Implications for evolution of parental melts and post-emplacement CO 2 degassing. Chem. Geol. 478, 76–88.

Abersteiner, A., Kamenetsky, V.S., Golovin, A.V., Kamenetsky, M., Goemann, K., 2018. Was crustal contamination involved in the formation of the serpentine-free Udachnaya-

East kimberlite? New insights into parental melts, liquidus assemblage and effects of alteration. J. Petrol. 59, 1467–1492.
Allan, H.T., Andrew, S., 1983. Properties of Carbonatite Magma and Processes in Carbonatite Magma Chambers. J. Geol. 91, 437–447.
Allsopp, H.L., Barrett, D.R., 1975. Rb-Sr age determinations on south African kimberlite pipes. Phys. Chem. Earth 9, 605–617.
Andrews, J.R., Emeleus, C.H., 1975. Structural aspects of kimberlite dyke and sheet intrusion in south-West Greenland. Phys. Chem. Earth 9, 43–50.
Armstrong, K.A., Roederr, P.L., Helmstaedt, H.H., 1997. Composition of spinels in the C14 kimberlite, Kirkland Lake, Ontario. Russ. Geol. Geophys. 38, 454–466.
Armstrong, J.P., Wilson, M., Barnett, R.L., Nowicki, T., Kjarsgaard, B.A., 2004. Mineralogy of primary carbonate-bearing hypabyssal kimberlite, Lac de Gras, Slave Province, Northwest Territories, Canada. Lithos 76, 415–433.
Arndt, N.T., Guitreau, M., Boullier, A.M., le Roex, A., Tommasi, A., Cordier, P., Sobolev, A., 2010. Olivine, and the Origin of Kimberlite. J. Petrol. 51, 573–602.
Batumike, J.M., Griffin, W.L., Belousova, E.A., Pearson, N.J., O'Reilly, S.Y., Shee, S.R., 2008. LAM-ICPMSU-Pb dating of kimberlitic perovskite: Eocene-Oligocene kimberlites from the Kundelungu Plateau, D.R. Congo. Earth Planet. Sci. Lett. 267, 609–619.
Boctor, N., Boyd, F.R., 1981. Oxide minerals in a layered kimberlite-carbonate sill from Benfontein, South Africa. Contrib. Mineral. Petrol. 76, 253–259.
Brooker, R., Sparks, R., Kavanagh, J., Field, M., 2011. The volatile content of hypabyssal kimberlite magmas: some constraints from experiments on natural rock compositions. Bull. Volcanol. 73, 959–981.
Buse, B., Schumacher, J., Sparks, R., Field, M., 2010. Growth of bultfonteinite and hydrogarnet in metasomatized basalt xenoliths in the B/K9 kimberlite, Damtshaa Botswana: insights into hydrothermal metamorphism in kimberlite pipes. Contrib. Mineral. Petrol. 160, 533–550.
Christiansen, F.G., Olesen, N.O., 1990. Large skeletal chromites in the Vourinos ophiolite, Greece. Bull. Geol. Soc. Den. 38, 33–42.
Clement, C.R., 1982. A comparative geological study of some major kimberlite pipes in the Northern Cape and Orange Free State. Ph.D Thesis. University of Cape Town, Cape Town.
Coopersmith, H.G., Mitchell, R.H., Hausel, W.D., 2003. Kimberlites and Lamproites of Colorado and Wyoming, USA. In: Field Excursion Guidebook for the 8th International Kimberlite Conference. Geological Survey of Canada, p. 24.
Dawson, J.B., 1971. Advances in kimberlite geology. Earth-Sci. Rev. 7, 187–214.
Dawson, J.B., 1993. A Supposed Sövite from Oldoinyo Lengai, Tanzania: result of Extreme Alteration of Alkali Carbonatite Lava. Mineral. Mag. 57, 93–101.
Dawson, J.B., Hawthorne, J.B., 1973. Magmatic sedimentation and carbonatitic differentiation in kimberlite sills at Benfontein, South Africa. J. Geol. Soc. 129, 61–85.
Dawson, J., Hill, P., Kinny, P., 2001. Mineral chemistry of a zircon-bearing, composite, veined and metasomatised upper-mantle peridotite xenolith from kimberlite. Contrib. Mineral. Petrol. 140, 720–733.
Fedortchouk, Y., Canil, D., 2004. Intensive Variables in Kimberlite Magmas, Lac de Gras, Canada and Implications for Diamond Survival. J. Petrol. 45, 1725–1745.
Field, M., Scott Smith, B.H., 1999. Contrasting geology and near-surface emplacement of kimberlite pipes in southern Africa and Canada. In: Gurney, J.J., Gurney, J.L., Pascoe, M.D., Richardson, S.H. (Eds.), 7th International Kimberlite Conference. Red Roof Design, Cape Town, pp. 214–237.
Fitch, F.J., Miller, J.A., 1983. K-Ar age of the east peripheral kimberlite at De Beers Mine, Kimberley, R.S.a. Geol. Mag. 120, 505–512.
Gaspar, J.C., Wyllie, P.J., 1984. The alleged kimberlite-carbonatite relationship: evidence from ilmenite and spinel from Premier and Wesselton Mines and the Benfontein Sill, South Africa. Mineral. Petrol. 85, 133–140.
Giuliani, A., 2018. Insights into kimberlite petrogenesis and mantle metasomatism from a review of the compositional zoning of olivine in kimberlites worldwide. Lithos 312-313, 322–342.
Giuliani, A., Kamenetsky, V.S., Phillips, D., Kendrick, M.A., Wyatt, B.A., Goemann, K., 2012. Nature of alkali-carbonate fluids in the sub-continental lithospheric mantle. Geology 40, 967–970.
Giuliani, A., Phillips, D., Kamenetsky, V.S., Fiorentini, M.L., Farquhar, J., Kendrick, M.A., 2014. Stable isotope (C, O, S) compositions of volatile-rich minerals in kimberlites: a review. Chem. Geol. 374-375, 61–83.
Giuliani, A., Phillips, D., Kamenetsky, V.S., Goemann, K., 2016. Constraints on kimberlite ascent mechanisms revealed by phlogopite compositions in kimberlites and mantle xenoliths. Lithos 240-243, 189–201.
Giuliani, A., Soltys, A., Phillips, D., Kamenetsky, V.S., Maas, R., Goemann, K., Woodhead, J. D., Drysdale, R., Griffin, W.L., 2017. The final stages of kimberlite petrogenesis: Petrography, mineral chemistry, melt inclusions and Sr-C-O isotope geochemistry of the Bultfontein kimberlite (Kimberley, South Africa). Chem. Geol. 455, 342–356.
Golovin, A.V., Sharygin, V.V., Pokhilenko, N.P., 2007. Melt inclusions in olivine phenocrysts in unaltered kimberlites from the Udachnaya-East pipe, Yakutia: some aspects of kimberlite magma evolution during late crystallization stages. Petrology 15, 168–183.
Golovin, A.V., Sharygin, I.S., Kamenetsky, V.S., Korsakov, A.V., Yaxley, G.M., 2018. Alkali-carbonate melts from the base of cratonic lithospheric mantle: Links to kimberlites. Chem. Geol. 483, 261–274.
Hanson, E.K., Moore, J.M., Bordy, E.M., Marsh, J.S., Howarth, G., Robey, J.V.A., 2009. Cretaceous erosion in Central South Africa: evidence from upper-crustal xenoliths in kimberlite diatremes. S. Afr. J. Geol. 112, 125–140.
Hawthorne, J.B., 1968. Kimberlite sills. Trans. Geol. Soc. South Africa 71, 291–311.
Hawthorne, J.B., 1975. Model of a kimberlite pipe. Phys. Chem. Earth 9, 1–15.
Howarth, G.H., Taylor, L.A., 2016. Multi-stage kimberlite evolution tracked in zoned olivine from the Benfontein sill, South Africa. Lithos 262, 384–397.
Hunter, R.H., Taylor, L.A., 1982. Instability of garnet from the mantle: glass as evidence of metasomatic melting. Geology 10, 617–620.
Jones, A.P., Wyllie, P.J., 1984. Minor elements in perovskite from kimberlite and the distribution of rare earth elements: an electron probe study. Earth Planet. Sci. Lett. 69, 128–140.
Jones, A.P., Wyllie, P.J., 1985. Paragenetic Trends of Oxide Minerals in Carbonate-rich Kimberlites, with New analyses from the Benfontein Sill, South Africa. J. Petrol. 26, 210–222.
Kamenetsky, V.S., Yaxley, G.M., 2015. Carbonate–silicate liquid immiscibility in the mantle propels kimberlite magma ascent. Geochim. Cosmochim. Acta 158, 48–56.
Kamenetsky, V.S., Golovin, A.V., Maas, R., Giuliani, A., Kamenetsky, M.B., Weiss, Y., 2014. Towards a new model for kimberlite petrogenesis: evidence from unaltered kimberlites and mantle minerals. Earth-Sci. Rev. 139, 145–167.
Kjarsgaard, B.A., Pearson, D.G., Tappe, S., Nowell, G.M., Dowall, D.P., 2009. Geochemistry of hypabyssal kimberlites from Lac de Gras, Canada: Comparisons to a global database and applications to the parent magma problem. Lithos 112S, 236–248.
Krivovichev, S.V., Armbruster, T., Organova, N.I., Burns, P.C., Seredkin, M.V., Chukanov, N. V., 2004. Incorporation of sodium into the chlorite structure: the crystal structure of glagolevite, $Na(Mg,Al)_6[Si_3AlO_{10}](OH,O)_8$. Am. Mineral. 89, 1138–1141.
Kurszlaukis, S., Lorenz, V., 2008. Formation of "Tuffisitic Kimberlites" by phreatomagmatic processes. J. Volcanol. Geotherm. Res. 174, 68–80.
Lawless, P.J., Gurney, J.J., Dawson, J.B., 1979. Polymict peridotites from the bultfontein and de Beers Mines, Kimberly, South Africa. In: Boyd, F.R., Meyer, H.O.A. (Eds.), The Mantle Sample. 2nd International Kimberlite Conference. American Geophysical Union, pp. 145–155.
Lim, E., Giuliani, A., Phillips, D., Goemann, K., 2018. Origin of complex zoning in olivine from diverse diamondiferous kimberlites and tectonic settings: Ekati (Canada), Alto Paranaiba (Brazil) and Kaalvallei (South Africa). In: Proceedings of the 11th International Kimberlite Conference. Petrology, Mineralogy and (In Press). https://doi.org/10.1007/s00710-018-0607-6.
Mannard, G.W., 1962. The Singida kimberlite pipes, Tanganyika. Ph.D. thesis. McGill University, Montreal, Quebec.
McMahon, B.M., Haggerty, S.E., 1984. The Benfontein kimberlite sills; magmatic reactions and high intrusion temperatures. Am. J. Sci. 284, 893–941.
Mitchell, R.H., 1984. Mineralogy and origin of carbonate-rich segregations in a composite kimberlite sill. Neues Jahrbuch Mineralogie 150, 185–197.
Mitchell, R.H., 1986. Kimberlites: Mineralogy, Geochemistry and Petrology. Plenum Publishing Company, New York.
Mitchell, R.H., 1994. Accessory rare earth, strontium, barium and zirconium minerals in the Benfontein and Wesselton calcite kimberlites, South Africa. In: Proceedings of 5th international kimberlite conference (Meyer, HOA & Leonardos, OH), CPRM Brasilia special Publication 1/a, pp. 115-128.
Mitchell, R.H., 2008. Petrology of hypabyssal kimberlites: Relevance to primary magma compositions. J. Volcanol. Geotherm. Res. 174, 1–8.
Mitchell, R.H., Clarke, D.B., 1976. Oxide and sulphide mineralogy of Peuyuk kimberlite, Somerset Island, N.W.T., Canada. Contrib. Mineral. Petrol. 56, 157–172.
Moss, S., Russell, J.K., Brett R.,C., Andrews, G.D.M., 2009. Spatial and temporal evolution of kimberlite magma at A154N, Diavik, Northwest Territories, Canada. Lithos 112S, 541–552.
Nowicki, T., Crawford, B., Dyck, D., Carlson, J., McElroy, R., Oshust, P., Helmstaedt, H., 2004. The geology of kimberlite pipes of the Ekati property, Northwest Territories, Canada. Lithos 76, 1–27.
O'Brien, H.E., Tyni, M., 1999. Mineralogy and Geochemistry of Kimberlites and Related Rocks from Finland. In: Proceedings of the 7th International Kimberlite Conference. Geological Survey of Finland, 625–636.
Ogilvie-Harris, R.C., Field, M., Sparks, R.S.J., Walter, M.J., 2009. Perovskite from the Dutoitspan kimberlite, Kimberley, South Africa: implications for magmatic processes. Mineral. Mag. 73 (6), 915–928.
Pasteris, J.D., 1980. Opaque oxide phases of the De Beers Pipe kimberlite Kimberely, South Africa) and their petrologic significance. Ph.D. thesis, Yale University.
Pasteris, J.D., 1983. Spinel zonation in the De Beers Kimberlite, South Africa: possible role of phlogopite. Can. Mineral. 21, 41–58.
Price, S.E., Russell, J.K., Kopylova, M.G., 2000. Primitive Magma from the Jericho Pipe, N.W. T., Canada: Constraints on primary Kimberlite Melt Chemistry. J. Petrol. 41, 789–808.
Ranger, I.M., Heaman, L.M., Pearson, D.G., Muntener, C., Zhuk, V., 2018. Punctuated, long-lived emplacement history of the Renard 2 kimberlite, Canada, revealed by new high precision U-Pb groundmass perovskite dating. Mineral. Petrol. https://doi.org/10.1007/s00710-018-0629-0.
Roeder, P.L., Schulze, D.J., 2008. Crystallization of Groundmass Spinel in Kimberlite. J. Petrol. 49, 1473–1495.
Roeder, P.L., Poustovetov, A., Oskarsson, N., 2001. Growth forms and composition of chromian spinel in MORB magma: Diffusion controlled crystallization of chromian spinel. Can. Mineral. 39, 397–416.
le Roex, A.P., Bell, D.R., Davis, P., 2003. Petrogenesis of Group I Kimberlites from Kimberley, South Africa: evidence from Bulk-rock Geochemistry. J. Petrol. 44, 2261–2286.
Schärer, U., Corfu, F., Demaiffe, D., 1997. U-Pb and Lu-Hf isotopes in baddeleyite and zircon megacrysts from the Mbuji-Mayi kimberlite: constraints on the subcontinental mantle. Chem. Geol. 143, 1–16.
Scott Smith, B.H., Nowicki, T.E., Russell, J.K., Webb, K.J., Mitchell, R.H., Hetman, C.M., Harder, M., Skinner, E.M.W., Robey, J.A., 2013. Kimberlite Terminology and Classification. In: Pearson, D.G., et al. (Eds.), Proceedings of 10th International Kimberlite Conference. Special Issue of the Journal of the Geological Society of India Vol. 2, pp. 1–18.
Shee, S.R., 1985. The Petrogenesis of the Wesselton Mine kimberlites, Kimberley, Cape Province, RSA. Unpublished Ph.D. thesis. University of Cape Town, South Africa.
Shee, S.R., Clement, C.R., Skinner, E.M.W., 1991. The petrology of the Wesselton kimberlite sills, Kimberley, Cape Province, South Africa. In: Meyer, H.O.A., Leonardos, O.H. (Eds.), Kimberlites, Related Rocks and Mantle Xenoliths. 5th International Kimberlite Conference. CPRM Special Publication, Araxa, Brazil, pp. 98–114.

Smith, C.B., 1983. Rubidium-strontium, Uranium-lead, Samarium-neodymium Isotopic Studies of Kimberiite and Selected mantle-derived Xenoliths. Unpublished Ph.D. thesis. University of Witwatersrand, Johannesburg, South Africa.
Smith, C.B., Sims, K., Chimuka, L., Duffin, A., Beard, A.D., Townend, R., 2004. Kimberlite metasomatism at Murowa and Sese pipes, Zimbabwe. Lithos 76, 219–232.
Soltys, A., Giuliani, A., Phillips, D., Kamenetsky, V.S., Maas, R., Woodhead, J., Rodemann, T., 2016. In-situ assimilation of mantle minerals by kimberlitic magmas — Direct evidence from a garnet wehrlite xenolith entrained in the Bultfontein kimberlite (Kimberley, South Africa). Lithos 256-257, 182–196.
Soltys, A., Giuliani, A., Phillips, D., 2018a. A new approach to reconstructing the composition and evolution of kimberlite melts: a case study of the archetypal Bultfontein kimberlite (Kimberley, South Africa). Lithos 304-307, 1–15.
Soltys, A., Giuliani, A., Phillips, D., 2018b. Crystallisation sequence and magma evolution of the De Beers dyke (Kimberley, South Africa). In: Proceedings of the 11th International Kimberlite Conference. Petrology, Mineralogy and https://doi.org/10.1007/s00710-018-0588-5 (In Press).
Sparks, R.S.J., 2013. Kimberlite Volcanism. Annu. Rev. Earth Planet. Sci. 41, 497–528.
Sparks, R.S.J., Baker, L., Brown, R.J., Field, M., Schumacher, J., Stripp, G., Walters, A., 2006. Dynamical constraints on kimberlite volcanism. J. Volcanol. Geotherm. Res. 155, 18–48.
Sparks, R.S.J., Brooker, R.A., Field, M., Kavanagh, J., Schumacher, J.C., Walter, M.J., White, J., 2009. The nature of erupting kimberlite melts. Lithos 112, 429–438.
Sun, S.-S., McDonough, W.F., 1989. Chemical and isotopic systematics of oceanic basalts: Implications for mantle composition and processes. In: Saunders, A.D., Norry, M.J. (Eds.), Magmatism in the Ocean Basins. Geological Society Special Publication, London, pp. 313–345.
Sun, J., Tappe, S., Kostrovitsky, S.I., Liu, C.-Z., Skuzovatov, S.Y., Wu, F.-Y., 2018. Mantle sources of kimberlites through time: a U-Pb and Lu-Hf isotope study of zircon megacrysts from the Siberian diamond fields. Chem. Geol. 479, 228–240.
Tappe, S., Kjarsgaard, B.A., Kurszlaukis, S., Nowell, G.M., Phillips, D., 2014. Petrology and Nd–Hf Isotope Geochemistry of the Neoproterozoic Amon Kimberlite Sills, Baffin Island (Canada): evidence for Deep Mantle Magmatic activity Linked to Supercontinent Cycles. J. Petrol. 55, 2003–2042.
White, J.L., Sparks, R.S.J., Bailey, K., Barnett, W.P., Field, M., Windsor, L., 2012. Kimberlite sills and dykes associated with the Wesselton kimberlite pipe, Kimberley, South Africa. S. Afr. J. Geol. 115, 1–32.
Woodhead, J., Hergt, J., Phillips, D., Paton, C., 2009. African kimberlites revisited: in situ Sr-isotope analysis of groundmass perovskite. Lithos 112S, 311–317.
Wu, F.-Y., Yang, Y.-H., Mitchell, R.H., Li, Q.-L., Yang, J.-H., Zhang, Y.-B., 2010. In situ U-Pb age determination and Nd isotopic analysis of perovskites from kimberlites in southern Africa and Somerset Island, Canada. Lithos 115, 205–222.
Zaitsev, A., Keller, J., 2006. Mineralogical and chemical transformation of Oldoinyo Lengai natrocarbonatites, Tanzania. Lithos 91, 191–207.
Zurevinski, S., Mitchell, R., 2011. Highly evolved hypabyssal kimberlite sills from Wemindji, Quebec, Canada: insights into the process of flow differentiation in kimberlite magmas. Contrib. Mineral. Petrol. 161, 765–776.

Appendix 7.1 – Electronic Appendix – Geochronology Data

Appendix 7.2 – Electronic Appendix – Supplementary Tables

Appendix 7.3 – Analytical Techniques

Analytical Techniques

3.1 Petrographic and Geochemical Analyses

Specimens of the Benfontein kimberlite were prepared as epoxy resin rock chip mounts and polished using kerosene as lubricant to avoid dissolution of any water-soluble minerals. Optical examination of the samples was performed on a Nikon Eclipse 50i POL microscope at the University of Tasmania.

Detailed studies of groundmass phases and inclusions in minerals were performed using a Hitachi SU-70 field emission (FE) scanning electron microscope (SEM) equipped with an Oxford AZtec Energy XMax 80 detector at the Central Science Laboratory, University of Tasmania. A beam accelerating voltage of 15 kV was used to produce high-resolution backscattered electron (BSE) images of minerals and energy-dispersive X-ray spectroscopy (EDS) semi-quantitative analyses and elemental maps of minerals.

The major oxide compositions of spinel and ilmenite were measured at the Central Science Laboratory, University of Tasmania using a JEOL JXA-8530F Plus field emission electron microprobe with a beam accelerating voltage of 15 kV, beam current of 40 nA and beam size of 1 µm. The on peak and off peak counting time was 20 seconds for Mg, Al, Si, Cr, Mn, Fe, Ni, Zn and V, and 80 seconds for Ca and Ti. The calibration standards were Rutile for Ti, Rhodonite for Mn, Nickel Oxide for Ni, Chromite Tiebaghi NMNH 117075 for Cr, Al, Fe, Mg, Gahnite Brazil NMNH 145883 for Zn, Wollastonite UNE for Si, Ca and Calcium Vanadate $Ca_3(VO_4)_2$ JEOL for V. Detection limits (99% confidence) were <0.01 wt.% for Ti and Ca, 0.01 wt.% for Si, Al, V, Cr, Mn and Mg, 0.02 wt.% for Fe and Ni, and 0.03 wt.% for Zn.

3.2 U-Pb Geochronology

Uranium-Th-Pb geochronology and trace element (including rare earth elements - REE) analyses of perovskite and baddeleyite from samples JJG-BEN1 and JJG-BEN2 were conducted on an Agilent 7900 quadrupole ICPMS coupled to a Coherent COMPex Pro 110 utilising an ArF excimer laser operating at the 193 nm wavelength and a pulse width of ~20 ns at the University of Tasmania. A RESOlution/Laurin Technic S155 constant geometry ablation cell was used for analyses and ablations were done in pure helium flowing at 0.35 l/min and immediately mixed with argon flowing at 1.05 l/min. Perovskite was prepared as grain mounts, whereas baddeleyite was analysed *in situ* in the groundmass from rock-chip mounts. Perovskite and baddeleyite were ablated with a 19 µm spot size, 5 Hz and 1.94 J/cm^2 laser fluence. Measured isotopes were: ^{29}Si, ^{39}K, ^{43}Ca, ^{49}Ti, ^{56}Fe, ^{89}Y, ^{91}Zr, ^{93}Nb, ^{139}La, ^{140}Ce, ^{141}Pr, ^{146}Nd, ^{147}Sm, ^{153}Eu, ^{157}Gd, ^{159}Tb, ^{163}Dy, ^{165}Ho, ^{166}Er, ^{169}Tm, ^{169}Yb, ^{172}Yb,

^{175}Lu, ^{178}Hf, ^{181}Ta, ^{202}Hg, ^{204}Pb, ^{206}Pb, ^{207}Pb, ^{208}Pb, ^{232}Th, ^{235}U, ^{238}U). The FC-1 baddeleyite (Paces and Miller Jr, 1993) and 91500 zircon (Horstwood et al., 2016) were employed as primary standards for calibration of Pb/U ratios, and to correct for down hole Pb/U fractionation and instrument drift of baddeleyite and perovskite analyses, respectively. Previous attempts to analyse perovskite using LA-ICPMS employed zircon standards for U-Pb calibration (e.g., Batumike et al., 2008; Cox and Wilton, 2006; Wu et al., 2010) due to its similar fractionation characteristics. In addition, the Phalaborwa baddeleyite (Heaman, 2009), Temora zircon (Black et al., 2003) and a sample of perovskite from the Oka Carbonatite, previously dated by LA-ICP-MS (Cox and Wilton, 2006), were analysed as unknowns (see Supplementary Tables 1 for a comparison of published and calculated ages). "Common Pb" compositions (i.e., ^{207}Pb/^{206}Pb) in Tera-Wasserburg charts for both perovskite and baddeleyite were unanchored and obtained from regressions through the data points, with age calculations performed using Isoplot (Ludwig, 2012).

The intervals for each time-resolved ablation signal were chosen based on high and consistent counts in ^{43}Ca and ^{49}Ti (perovskite only) and ^{91}Zr (baddeleyite only), as well as stable signals for ^{238}U, ^{232}Th, and radiogenic Pb-isotopes. Elevated counts of ^{39}K and ^{56}Fe in any analyses were excluded, as they are interpreted to represent intersected inclusions or mixing with other phases. To minimise any down hole Pb/U fractionation differences between zircon and perovskite, only the first 10 seconds of each analysis were integrated. The data were reduced using an in-house excel spreadsheet. Further details including error propagations are found in Halpin et al. (2014) and Thompson et al. (2018). The complete processed dataset, including excluded analyses is presented in Supplementary Tables 1.

References:

Black, L.P., Kamo, S.L., Allen, C.M., Aleinikoff, J.N., Davis, D.W., Korsch, R.J., Foudoulis, C., 2003. TEMORA 1: a new zircon standard for Phanerozoic U–Pb geochronology.Chemical Geology 200, 155-170.

Cox, R.A., Wilton, D.H.C., 2006. U–Pb dating of perovskite by LA-ICP-MS: An example from the Oka carbonatite, Quebec, Canada. Chemical Geology 235, 21-32.

Halpin, J.A., Jensen, T., McGoldrick, P., Meffre, S., Berry, R.F., Everard, J.L., Calver, C.R., Thompson, J., Goemann, K., Whittaker, J.M., 2014. Authigenic monazite and detrital zircon dating from the Proterozoic Rocky Cape Group, Tasmania: Links to the Belt-Purcell Supergroup, North America. Precambrian Research 250, 50-67.

Heaman, L.M., 2009. The application of U–Pb geochronology to mafic, ultramafic and alkaline rocks: An evaluation of three mineral standards. Chemical Geology 261, 43-52.

Horstwood, M.S.A., Košler, J., Gehrels, G., Jackson, S.E., McLean, N.M., Paton, C., Pearson, N.J., Sircombe, K., Sylvester, P., Vermeesch, P., Bowring, J.F., Condon, D.J., Schoene, B., 2016.

Community-Derived Standards for LA-ICP-MS U-(Th-)Pb Geochronology - Uncertainty Propagation, Age Interpretation and Data Reporting. Geostandards and Geoanalytical Research 40, 311-332.

Ludwig, K.R., 2012. User's manual for Isoplot 3.75: A Geochronological Toolkit For Microsoft Excel, Berkeley Geochronology Centre, Special Publication No. 5.

Thompson, J.M., Meffre, S., Danyushevsky, L., 2018. Impact of air, laser pulse width and fluence on U–Pb dating of zircons by LA-ICPMS. Journal of Analytical Atomic Spectrometry 33, 221-230.

Appendix 7.4 – Supplementary Figures

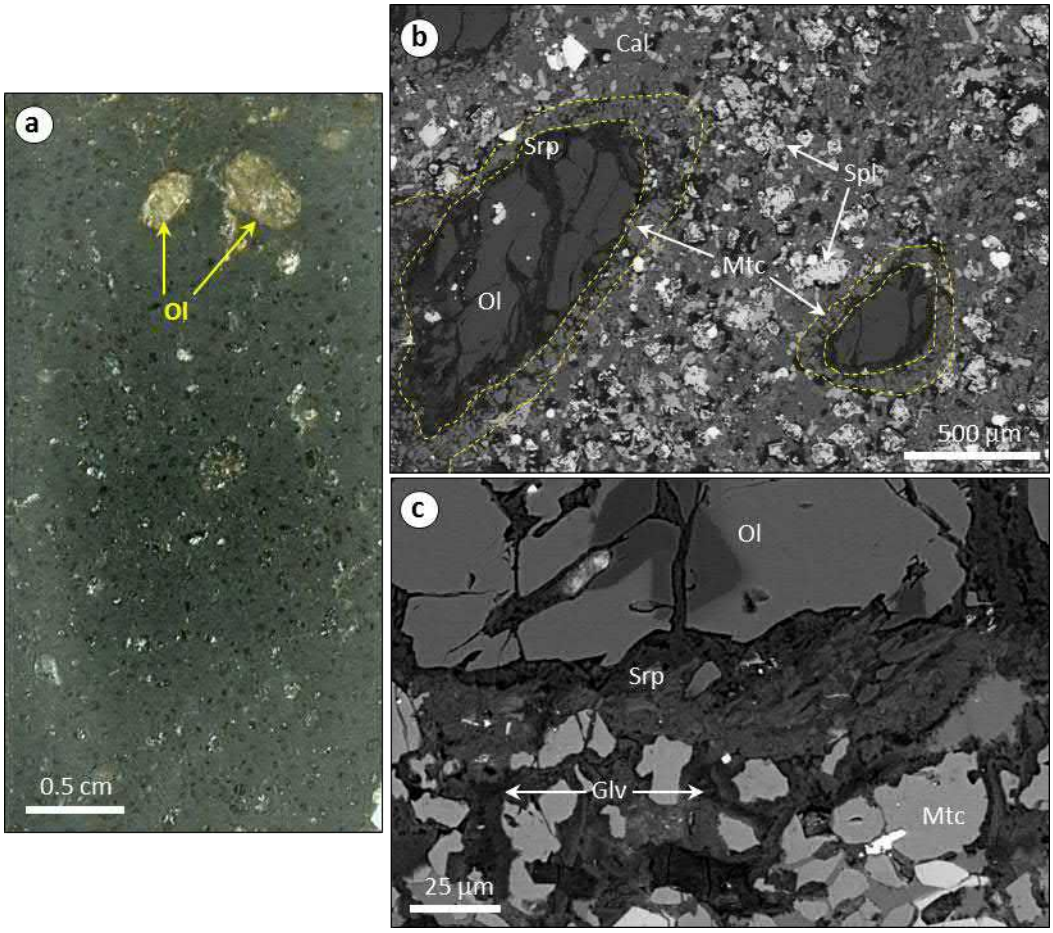

Supplementary Figure S1. (a) Hand-specimen photograph of Benfontein Upper Sill kimberlite sample BUSK-2. (b, c) Back-scattered electron (BSE) SEM images of groundmass textures. Olivine (Ol) is partially altered to serpentine (Srp) along rims and fractures. Monticellite (Mtc) is a common groundmass mineral that forms large grain clusters around olivine (image pane b – defined by yellow line). Atoll-spinel (Spl) is very abundant and evenly distributed throughout the groundmass. Cal: calcite, Glv: glagolevite.

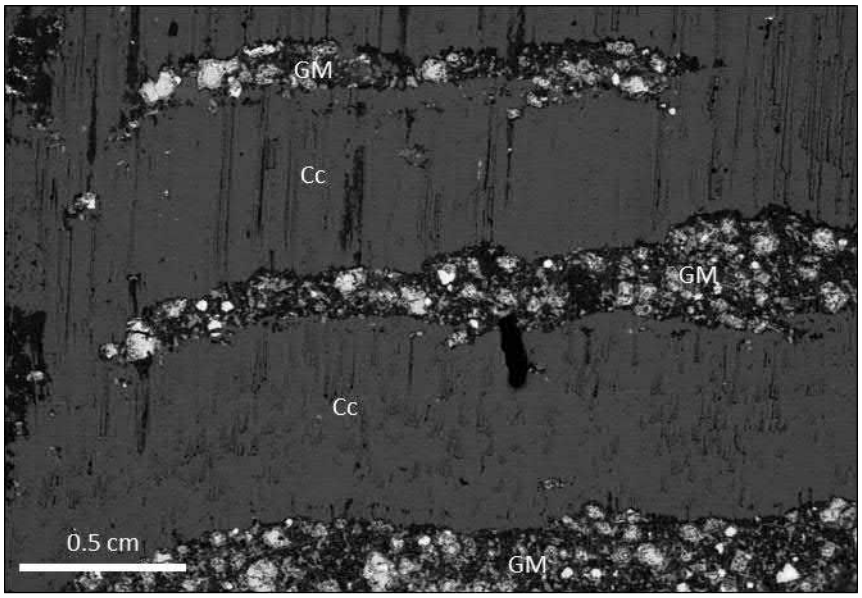

Supplementary Figure S2. Back-scattered electron (BSE) SEM image of isolated anhedral fragments of the kimberlite groundmass (GM) suspended in fibrous calcite (Cc) veins in sample BMSK-1. The groundmass is composed of oxides (bright) and interstitial serpentine (dark).

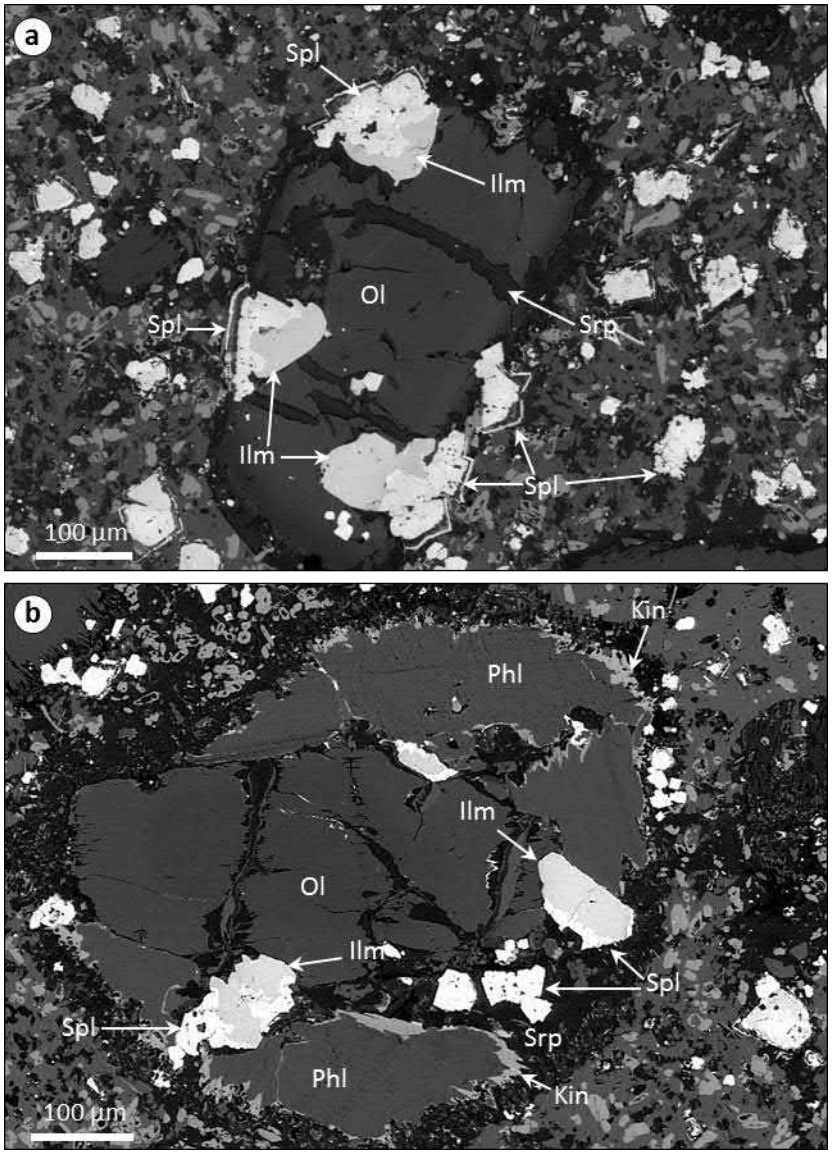

Supplementary Figure 3. Back-scattered electron (BSE) SEM images of olivine grains from samples JG-2241 series. (a, b) Olivine is partially serpentinised and contains large (up to 100 µm) inclusions of ilmenite, which are mantled by Mg-Al titanomagnetite along the sides closest to the groundmass. These spinels forms atoll shapes along the contacts with the groundmass. (b) Olivine is partially surrounded by phlogopite which forms large blocky grains around the olivine periphery. These phlogopite grains are mantled by a thin rim (<20 µm) of kinoshitalite.

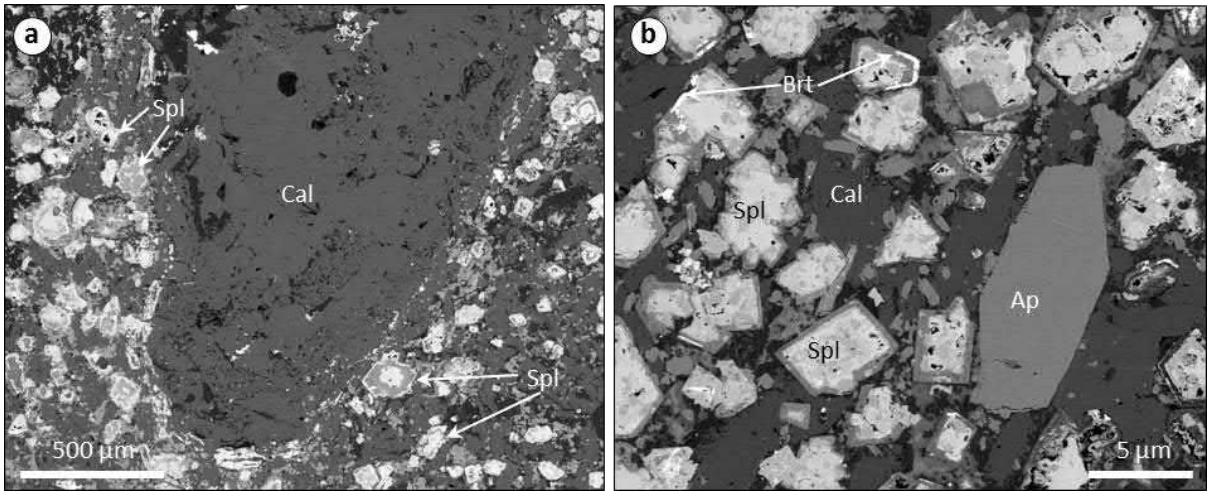

Supplementary Figure 4. (a,b) Back-scattered electron (BSE) SEM images of altered spinel (Spl) to admixtures of Fe-Ti-Si-Mg-bearing phases (sample BLSK5), which are represented by lighted shades of grey. Brt: barite, Ap: apatite, Cal: calcite.

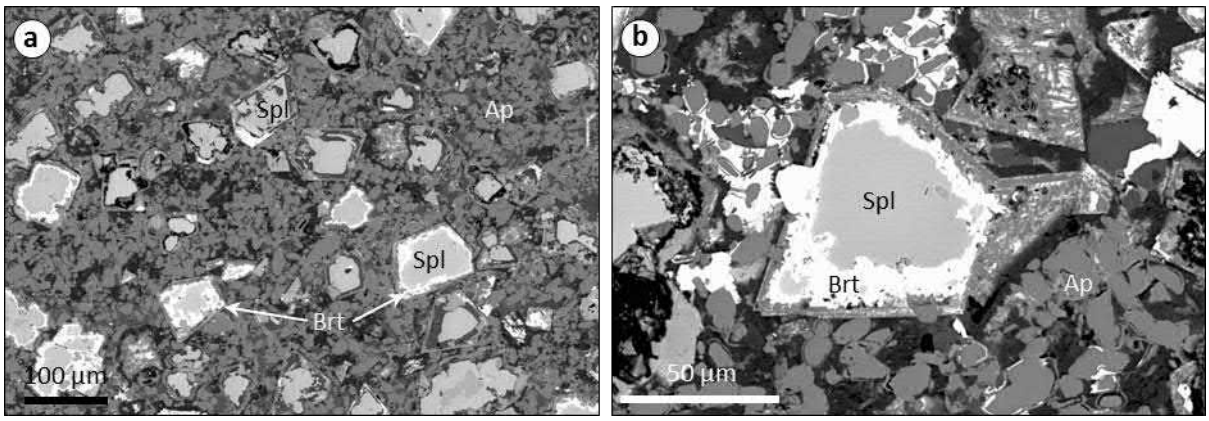

Supplementary Figure 5. Back-scattered electron (BSE) SEM image of: (a, b) barite (Brt) replacing atoll-spinel (Spl) cores in sample BLS. Ap: apatite.

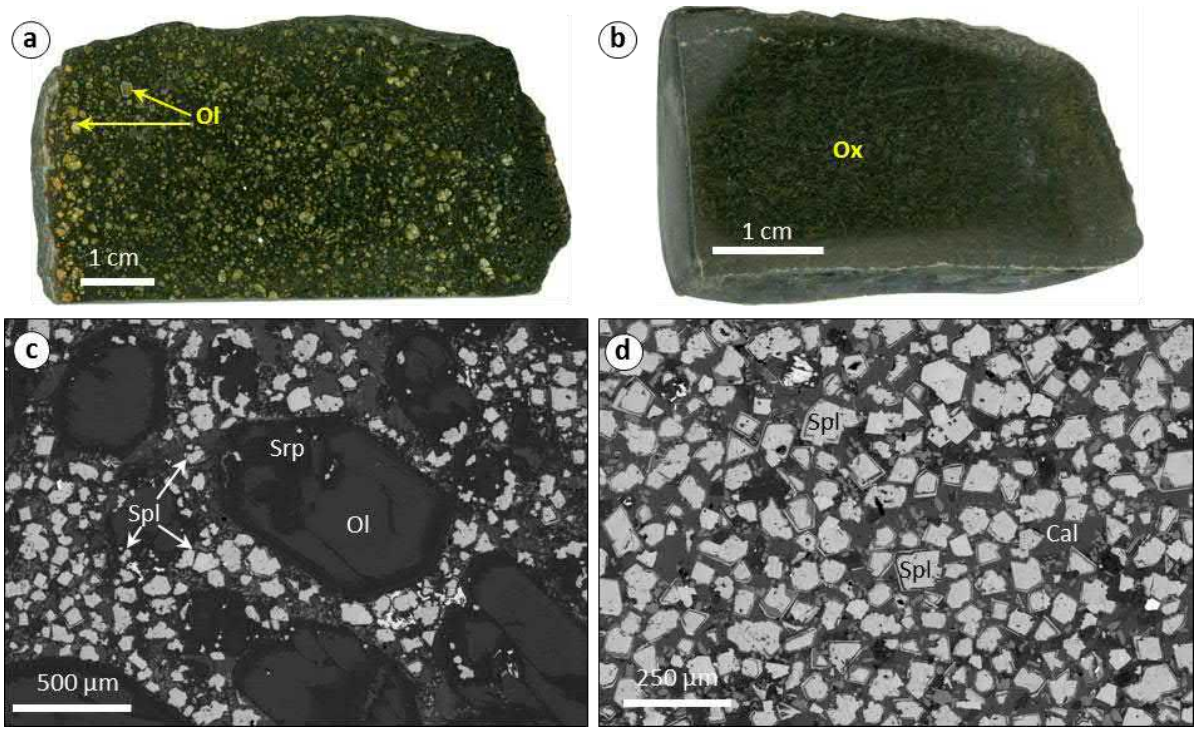

Supplementary Figure 6. Hand-specimen photograph of Benfontein Lower Sill kimberlite samples (a) BLSK-2, and (b) BLSK-4. (a) Sample BLSK-2 is an olivine (Ol) and oxide cumulate, and (b) sample BLSK-4 is an oxide cumulate and olivine is rare/absent. (c, d) Back-scattered electron (BSE) SEM images of: (c) Olivine (Ol) and oxide (i.e. atoll-spinel; Spl) rich groundmass of sample BLSK-2. Olivine is partially replaced by serpentine (Srp) along rims and internal fractures. (d) Oxide (i.e. spinel) dominated groundmass in sample BLSK-4. Oxide minerals in both BLSK-2 and BLSK-4 are well-preserved.

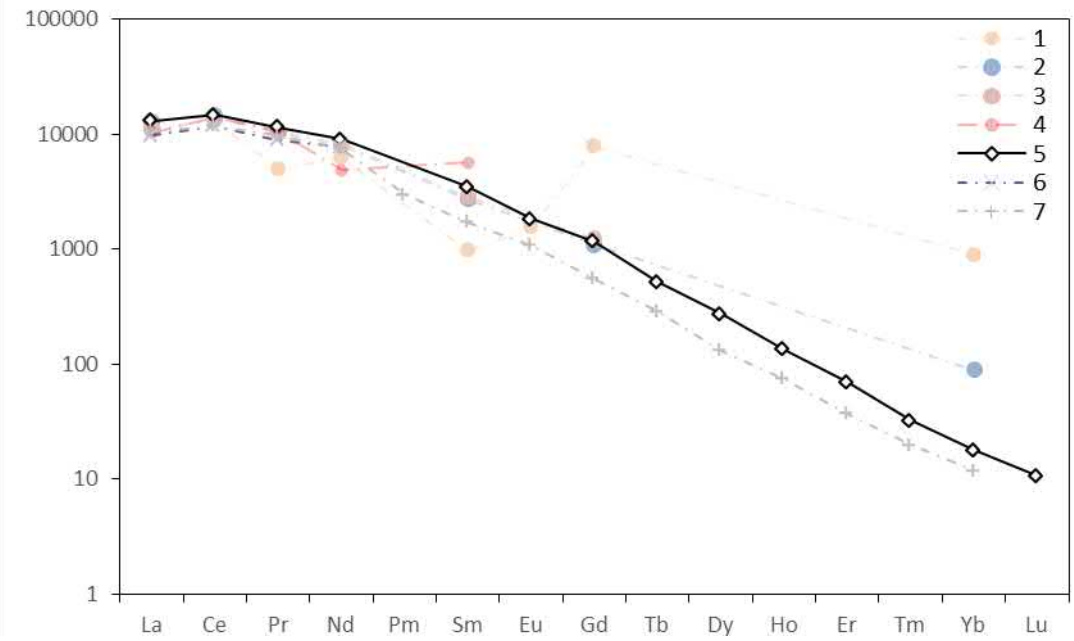

Supplementary Figure 7. Primitive mantle normalised (after Sun and McDonough, 1989) rare earth element (REE) patterns of perovskite from: (1) Benfontein sills (Boctor and Boyd, 1981), (2, 3) Benfontein sills and Wesselton, respectively (Jones and Wyllie,1984), (4) Wesselton sills (Mitchell, 1994), (5) Benfontein sills (this study; average of 50 perovskite grain analyses), (6) Dutoitspan (Ogilvie-Harris et al., 2009), (7) Bultfontein (Giuliani et al., 2017).

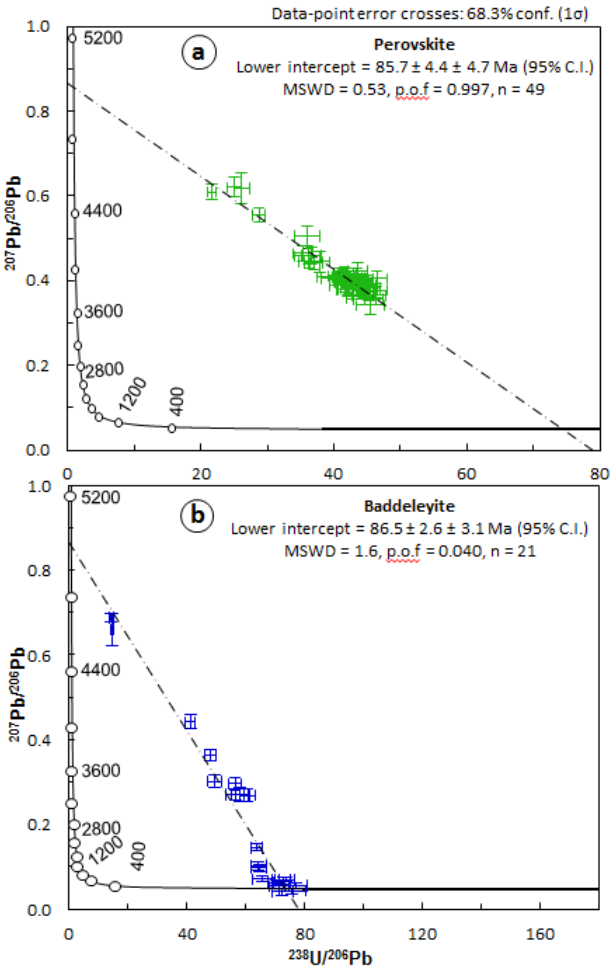

Supplementary Figure 8. U-Pb Tera-Wasserburg concordia plots for (a) perovskite, and (b) baddeleyite from samples JJG-BEN1 and JJG-BEN2. The 207Pb/206Pb intercepts for both perovskite and baddeleyite are unanchored. Reported uncertainties are given as ± 2 C.I. (confidence interval) and include systematic uncertainties. Excluded data points in baddeleyite (b) are displayed in Supplementary Material.

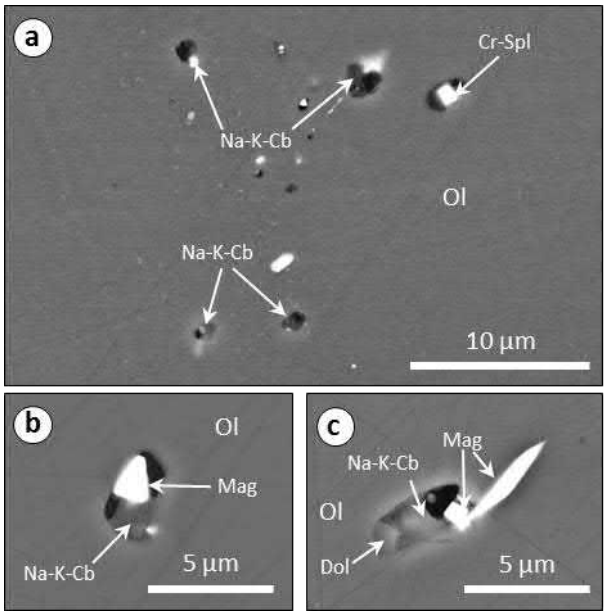

Supplementary Figure 9. Back-scattered electron (BSE) SEM images of secondary melt inclusions in olivine (Ol) from the Middle Sill sample JJG-2241. Detected phases include: Cr-spinel (Cr-Spl), Na-K-carbonates (Cb), magnetite (Mag), dolomite (Dol).

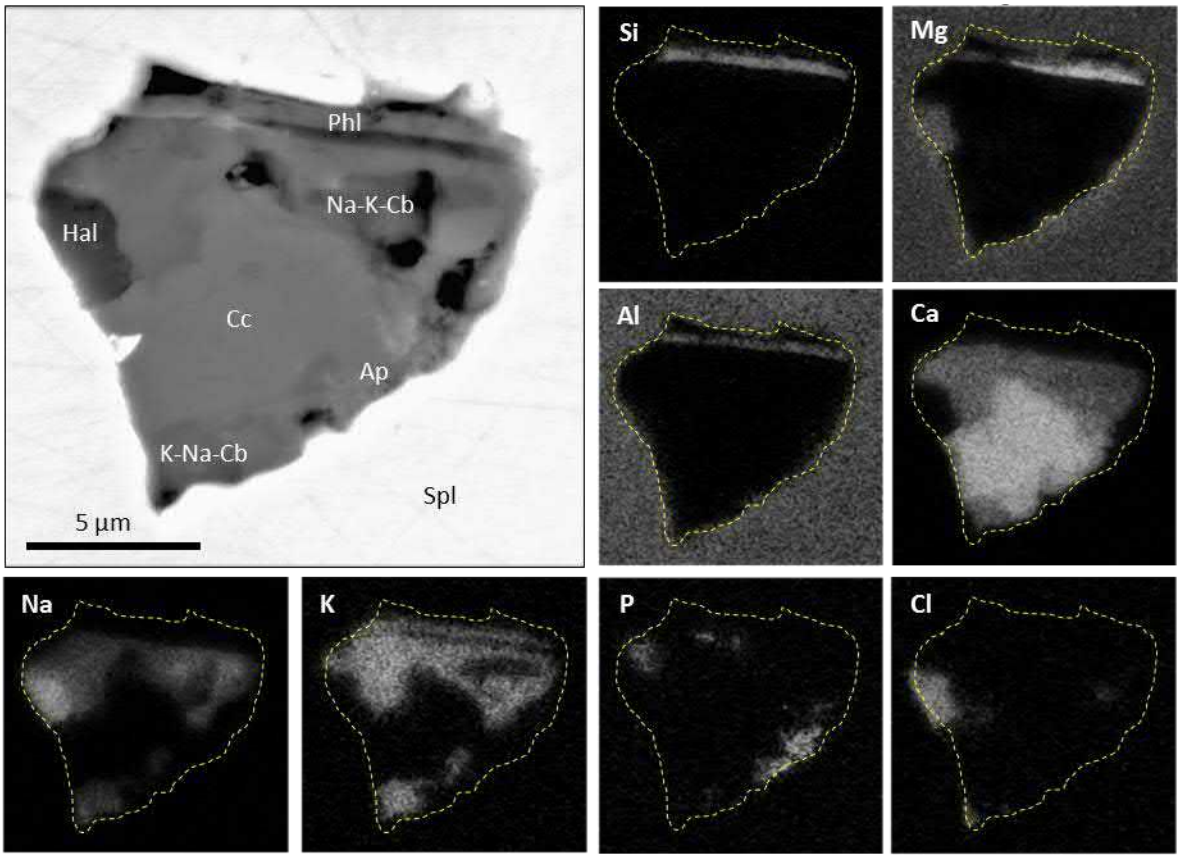

Supplementary Figure 10. Back-scattered electron (BSE) SEM images and X-ray elemental maps of a representative inclusion in Mg-Al titanomagnetite atoll-spinel (Spl). Detected minerals include: Halite (Hal), phlogopite (Phl), alkali (Na, K) carbonate (Cb), calcite (Cc) and apatite (Ap). The dotted yellow line represents the boundary of the inclusion.

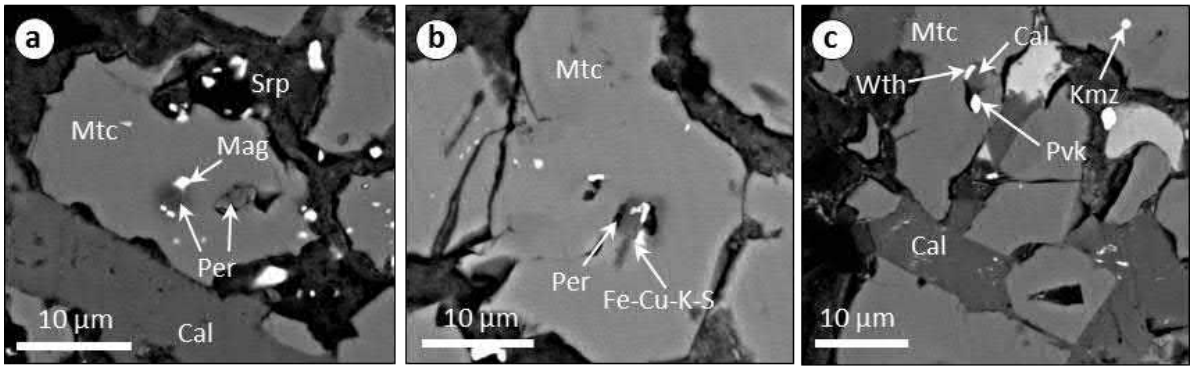

Supplementary Figure 11. Back-scattered electron (BSE) SEM images of inclusions in monticellite (Mtc). Monocrystalline inclusions of: (a) periclase and Mg-magnetite (Mag), and (c) kimzeyite (Kmz; $Ca_3(Zr,Ti)_2((Si,Al,Fe^{3+})O_4)_3$). (b, c) Multiphase inclusions which hosts daughter phases of: periclase (Pe), Fe-Cu-K-sulphide (S; rasvumite? KFe_2S_3), perovskite (Pvk), calcite (Cal) and witherite (Wth).

Lithos 336–337 (2019) 310–325

Contents lists available at ScienceDirect

Lithos

journal homepage: www.elsevier.com/locate/lithos

Polymineralic inclusions in kimberlite-hosted megacrysts: Implications for kimberlite melt evolution

Adam Abersteiner [a,*], Vadim S. Kamenetsky [a,b], Karsten Goemann [c], Alexander V. Golovin [d,e], Igor S. Sharygin [d], D. Graham Pearson [f], Maya Kamenetsky [a], Marina A. Gornova [g]

[a] School of Natural Sciences, University of Tasmania, Hobart, Tasmania 7001, Australia
[b] Institute of Volcanology and Seismology, Far East Branch, Russian Academy of Sciences, 683006 Petropavlovsk-Kamchatsky, Russia
[c] Central Science Laboratory, University of Tasmania, Hobart, Tasmania 7001, Australia
[d] Sobolev Institute of Geology and Mineralogy, Siberian Branch of Russian Academy of Sciences, Koptyuga Pr. 3, Novosibirsk 630090, Russian Federation
[e] Novosibirsk State University, Pirogova 2, Novosibirsk 630090, Russian Federation
[f] Department of Earth and Atmospheric Sciences, University of Alberta, 1-26 Earth Sciences Building, Edmonton, Alberta T6G 2E3, Canada
[g] A.P. Vinogradov Institute of Geochemistry, Siberian Branch of RAS, Irkutsk 650033, Russia

ARTICLE INFO

Article history:
Received 15 February 2019
Accepted 1 April 2019
Available online 5 April 2019

Keywords:
Megacryst
Clinopyroxene
Olivine
Polymineralic inclusion
Kimberlite
Micro melt inclusion

ABSTRACT

Megacrysts are large (cm to >20 cm in size) mantle-derived crystals, which are commonly entrained by kimberlite magmas, comprising of olivine, orthopyroxene, clinopyroxene, phlogopite, garnet, ilmenite and zircon as common phases. Numerous studies have shown megacrysts to contain polymineralic inclusions, which have been interpreted to represent entrapped kimberlite melt. To constrain the origin of these inclusions in megacrysts and their relationship to kimberlite magmatism, we present a detailed petrographic and geochemical study of clinopyroxene and olivine megacrysts and their hosted inclusions from the Diavik, Jericho, Leslie (Slave Craton, Canada) and Udachnaya-East (Siberian Craton, Russia) kimberlites. The studied megacrysts are between 1 and 3 cm in size and representative of both the Cr-rich and Cr-poor suites. Megacrysts contain two types of inclusions:

i. Large (<0.5–5 mm in size) round-to-irregular shaped polymineralic inclusions, which are composed of minerals similar to the host kimberlite groundmass, and consist of olivine, calcite, spinel, perovskite, phlogopite and apatite (± serpentine, alkali-carbonates, alkali-chlorides, barite).
ii. Swarms/trails of 'micro melt inclusions' (MMI; <1–5 μm in size), which surround polymineralic inclusions, veins and fractures, thereby forming a 'spongy' texture. MMIs generally contain multiphase assemblages similar to polymineralic inclusions as well as various additional phases, such as alkali-carbonates or alkali-chlorides, which are typically absent in polymineralic inclusions and the surrounding kimberlite groundmass.

Textural and geochemical evidence suggests that polymineralic inclusions in megacrysts crystallised from kimberlite melt, which infiltrated along fracture/vein networks. The polymineralic inclusion assemblages resulted from disequilibria reactions between the host megacryst and infiltrating kimberlite melt, which was likely enhanced by rapidly changing conditions during magmatic ascent. The connectivity of polymineralic inclusions to the kimberlite groundmass via network veins/fractures suggests that they are susceptible to infiltrating post-emplacement fluids. Therefore, the vast majority of polymineralic inclusions are unlikely to represent 'pristine' entrapped kimberlite melt. In contrast, MMIs are isolated within megacrysts (i.e. not connected to fractures/veins and therefore shielded from post-magmatic fluids) and probably represent entrapped remnants of the variably differentiated kimberlite melt, which was more enriched in alkalis-Cl-S-CO_2 than serpentinised polymineralic inclusions and the host rocks exposed at Earth's surface as kimberlites.

1. Introduction

Kimberlite magmas commonly entrain abundant mantle and crustal xenoliths and xenocrysts spanning the entire lithosphere. This xenogenic cargo is usually comprised of large (1–>20 cm) crystals of garnet, clinopyroxene, orthopyroxene, olivine, ilmenite, phlogopite

* Corresponding author.
E-mail address: adam.abersteiner@utas.edu.au (A. Abersteiner).

https://doi.org/10.1016/j.lithos.2019.04.004
0024-4937/

and zircon (Gurney et al., 1979; Harte and Gurney, 1981), which were termed 'megacrysts' to avoid genetic connotations (Dawson, 1980). Megacrysts are subdivided into two geochemically discrete suites (Cr-poor and Cr-rich; Bell and Moore, 2004; Eggler et al., 1979; Shee and Gurney, 1979), where the Cr-poor variety is invariably the most common in the majority of kimberlite localities (Harte and Gurney, 1981; Hops et al., 1992). Thermobarometric estimates suggest that megacrysts originate from within the sub-continental lithospheric mantle (SCLM), or the lithosphere-asthenosphere boundary, where they equilibrated over a large wide of pressures (~30–70 kbar) and temperatures (~650 °C and up to 1400 °C; Bussweiler et al., 2016, 2018; De Bruin, 2005; Gurney et al., 1979; Harte and Gurney, 1981; Hops et al., 1992; Kargin et al., 2017; Kopylova et al., 2009; Kostrovitsky et al., 2004; Nimis and Taylor, 2000).

Despite the ubiquity of megacrysts in kimberlites, there is no complete understanding of their origin and their relationship to kimberlite magmas. A common explanation is that megacrysts are genetically related to kimberlite (or 'proto-kimberlite') magmas and crystallised from a melt (e.g., kimberlitic) at depth prior to, or coeval with kimberlite magmatism (Bell and Moore, 2004; Hops et al., 1992; Kostrovitsky et al., 2004; Moore and Lock, 2001; Schulze et al., 2001). Radiogenic isotope (Sr-Nd-Hf) data (Kopylova et al., 2009; Malarkey et al., 2010; Nowell et al., 2004) and the close timing of megacryst formation with its entrainment into kimberlite magma (Kinny et al., 1989; Kopylova et al., 2009) suggests a genetic link to the host kimberlite, or similar source region. Another interpretation is that megacrysts have a multi-stage metasomatic origin, where they are the reaction product of kimberlitic (or 'proto-kimberlitic') melts and lithospheric mantle, occurring close to the timing of megacryst entrainment into the kimberlite magma (Bussweiler et al., 2018; Kargin et al., 2017; Kopylova et al., 2009; Pivin et al., 2009). However, trace element modelling indicates that megacrysts originated from melts compositionally distinct from kimberlite (Davies et al., 2001; Merry and le Roex, 2007). More recently, textural, compositional and isotopic data suggests megacrysts are concomitant with failed kimberlite intrusions and are the result of interactions between percolating melts and depleted mantle (Bussweiler et al., 2018).

Studies of polymineralic inclusions entrapped in megacrysts were previously employed in order to constrain their origin. Megacryst-hosted inclusions are largely composed of phlogopite, serpentine, olivine, calcite, spinel (Araújo et al., 2009; Bussweiler et al., 2016; Pivin et al., 2009; Schulze, 1985; van Achterbergh et al., 2002, 2004;) and in a rare case 'glass' (Howarth and Büttner, 2019). Early studies suggested that these inclusions represent the liquid from which megacryst minerals crystallised (Schulze, 1985). Whereas other authors have emphasised the xenocrystic nature of megacrysts in kimberlite magmas and attributed the formation of megacryst-hosted inclusions to the entrapment of kimberlite melt infiltrating along fractures (Araújo et al., 2009; Bussweiler et al., 2016; Howarth and Büttner, 2019; van Achterbergh et al., 2004). Inclusions preserved in kimberlite-hosted megacrysts may therefore present insights into the nature of the kimberlite melts that entrained them.

In this study, we present detailed petrographic, geochemical and inclusion analyses of clinopyroxene megacrysts from the Diavik, Jericho, Leslie kimberlites (Canada), and olivine and clinopyroxene megacrysts from the Udachnaya-East kimberlite (Russia). We characterise and compare inclusions between these different megacrysts in order to constrain the composition and evolution of the host kimberlite melt and its relationship to megacryst minerals.

2. Geological setting

2.1. Udachnaya-east

The Devonian-aged Udachnaya pipe (~365–367 Ma; Kamenetsky et al., 2009c; Kinny et al., 1997) is located in the Daldyn kimberlite field in the Siberian craton (Yakutia, Russia). The Udachnaya kimberlite has a composite twin-diatreme body (i.e. Eastern and Western) that was emplaced in thick (>2 km) Ordovician and Devonian sedimentary rocks (e.g., limestones, dolomites, marls, siltstones and mudstones; Alexseev, 2009; Drozdov and Sukhov, 2008). The Udachnaya-East body (this study) consists of volcaniclastic and coherent kimberlite, and is characterised by 'fresh' (or unserpentinised) olivine at the 400–500 m depth horizon (also termed Serpentine Free Udachnaya-East, or 'SFUE'; Abersteiner et al., 2018; Kamenetsky et al., 2007; Kopylova et al., 2013; Kostrovitskiy et al., 2013). The groundmass of Udachnaya-East serpentine-bearing and SFUE kimberlite units are both characterised by olivine, monticellite, phlogopite, perovskite, ilmenite, Mg-Ti-magnetite, magnesian ulvöspinel-magnetite (MUM), pleonaste, Cr-spinel, apatite, Fe-Ni-sulphides, djerfisherite ($K_6(Fe,Ni,Cu)_{25}S_{26}Cl$) and interstitial calcite. However, these two kimberlite units mineralogically differ from each other, where serpentinised samples contain serpentine and iowaite ($Mg_4Fe^{3+}(OH)_8OCl\cdot 3(H_2O)$), whereas SFUE samples contain alkali-chlorides, alkali-carbonates and sodalite (see Abersteiner et al., 2018; Kamenetsky et al., 2014b; Kopylova et al., 2013; Kostrovitskiy et al., 2013). The SFUE horizon also hosts diverse and well-preserved mantle xenoliths (e.g., peridotites, eclogites, pyroxenites; Agashev et al., 2010, 2013; Doucet et al., 2012; Ionov et al., 2017; Sharygin et al., 2012). Although mantle xenoliths are well documented in Udachnaya-East, there are few studies documenting megacryst minerals (e.g., Agashev et al., 2006; Solov'eva et al., 2008).

2.2. Diavik A154N

The Eocene-aged A154N pipe (~56 ± 0.7 Ma; Graham et al., 1999) is located in the Diavik kimberlite cluster in the Slave Craton (North West Territories, Canada). This kimberlite was emplaced in Archean granitoids and micaceous meta-sediments (Graham et al., 1999). The A154N kimberlite is a steep-sided carrot-shaped body and is composed of graded pyroclastic and stratified volcaniclastic kimberlite, and volcaniclastic kimberlite and coherent magmatic dykes at depth (Graham et al., 1999; Moss et al., 2008). Hypabyssal rocks consist of macrocrystic olivine and phlogopite, along with spinel, perovskite, phlogopite, monticellite, serpentine and calcite (Graham et al., 1999). Detailed descriptions of the A154N kimberlite are presented in Moss et al. (2008, 2009). The A154N kimberlite is host to mantle xenoliths of lherzolite, peridotite, wehrlite and eclogite and along with megacrysts of garnet, ilmenite, olivine, orthopyroxene and clinopyroxene (Araújo et al., 2009; Graham et al., 1999; Kopylova et al., 2009; Moss et al., 2009).

2.3. Jericho

The Jurassic-aged Jericho pipe (~173 ± 1.3 Ma; Heaman et al., 2006) is located in a small kimberlite cluster ~150 km north of the main Lac de Gras kimberlite field in the Slave Craton (Cookenboo, 1999). The Jericho kimberlite was emplaced in Archean granitoids, which are overlain by Devonian limestones, mudstones and sandstones (Cookenboo, 1999; Kopylova and Hayman, 2008). The kimberlite was emplaced as three steep-sided pipes, which are composed of three distinct types of kimberlite that are distinguished by their colour, texture, mantle xenolith and xenocryst content, and degree of alteration (Cookenboo, 1999; Kopylova and Hayman, 2008; Price et al., 2000). The groundmass of the Jericho kimberlite is characterised by olivine, monticellite, spinel, perovskite, ilmenite, apatite, phlogopite along with fine-grained serpentine and calcite (see Cookenboo (1999) and Kopylova and Hayman (2008) for detailed descriptions). In addition, this kimberlite is host to abundant mantle xenoliths, which includes eclogite, peridotite, megacrystalline websterite and ilmenite-garnet wehrlite, along with both low-Cr and high-Cr suites of megacrysts (e.g., garnet, orthopyroxene, clinopyroxene, ilmenite, olivine; Kopylova et al., 1999, 2009; Smart et al., 2009).

2.4. Leslie

The Eocene-aged Leslie kimberlite (53 ± 0.7 Ma, Sarkar et al., 2015) is in the Ekati property, which is located in the Lac de Gras kimberlite field in the Slave Craton. The Leslie kimberlite was emplaced in Archean porphyritic biotite granites (see Berg and Carlson, 1998; Kjarsgaard et al., 2002). The Leslie pipe is a hypabyssal kimberlite composed of abundant monticellite along with subordinate amounts of calcite, phlogopite, brucite, spinel, apatite, perovskite, Fe-Ni-Cu-sulphides and djerfisherite (Abersteiner et al., 2017a; Berg and Carlson, 1998; Bussweiler et al., 2015). To our knowledge, there are no detailed reports of mantle xenoliths or megacrysts from the Leslie kimberlite.

3. Analytical methods

Specimens of the megacrysts and kimberlite from Udachnaya-East, A154N, Jericho and Leslie were prepared as epoxy resin rock chip mounts and polished using kerosene as lubricant to avoid dissolution of any water-soluble minerals. In addition, megacryst (sample DVK_CD_01) from the A154N kimberlite were prepared as thin sections using a non-aqueous lubricant. Optical petrography was performed on a Nikon Eclipse 50i POL microscope at the University of Tasmania.

Detailed examinations of groundmass phases and inclusions in minerals were performed using a Hitachi SU-70 field emission (FE) scanning electron microscope (SEM) equipped with an Oxford AZtec Energy XMax 80 detector at the Central Science Laboratory, University of Tasmania. A beam accelerating voltage of 15 kV was used to produce high-resolution backscattered electron (BSE) images of minerals and energy-dispersive X-ray spectroscopy (EDS) semi-quantitative analyses and elemental maps of minerals.

The major element compositions of clinopyroxene and olivine megacrysts (Supplementary Tables S1, 2), as well as phlogopite (Supplementary Table S3) in polymineralic inclusions within megacrysts were measured at the Central Science Laboratory, University of Tasmania using a JEOL JXA-8530F Plus field emission electron microprobe with a beam accelerating voltage of 15 kV. For clinopyroxene, a beam current of 30 nA and beam size of 5 μm was employed. The on peak and off peak counting time was 40 s for Mg, Al, Ti, Ni, 30 s for Cr, Mn, and 20 s for Na, Si, Ca and Fe. The calibration standards were TiO_2 P&H for Ti, Rhodonite $MnSiO_3$ P&H for Mn, Eskolaite P&H for Cr, Nickel Oxide NiO P&H for Ni, Hematite Harvard for Fe, Olivine San Carlos NMNH 111312-44 for Mg, Diopside Natural Bridge NMNH 117733 for Ca, Si, Anorthoclase Kakanui, NMNH 133868 for Na, and Plagioclase Lake County NMNH 115900 for Al. Detection limits (99% confidence) were 0.01 wt% for Si, Al, Mg, Ca, Na, Cr, Mn and 0. 02 wt% for Fe. For olivine, a beam current of 300 nA and beam size of 2 μm was employed. The peak counting time was 60 s for all elements and off peak counting time was 60 s for Ca, Cr, Mn, Al and Ni. The calibration standards were Rhodonite $MnSiO_3$ P&H for Mn, Eskolaite P&H for Cr, Nickel Oxide NiO P&H for Ni, Olivine San Carlos NMNH 111312-44 for Si, Fe, Mg, Plagioclase Lake County NMNH 115900 for Al, and Wollastonite UNE for Ca. Detection limits (99% confidence) were 0.01 wt% for Al and Ca, 0.02 wt% for Cr and 0.03 wt% for Ni and Mn. For phlogopite a beam current of 10 nA and beam size of 10 μm was employed. The on peak and off peak counting time was 40 s for Sr, 30 s for F, Ni, Ba, 20 s for Na, Mg, Al, Ti, Cr, Mn and 10 s for Si, P, S, Cl, K, Ca and Fe. The calibration standards were topaz for F, jadeite P&H for Na, olivine San Carlos NMNH 111312-44 for Mg, plagioclase Lake Country NMNH for Al, wollastonite UNE for Si and Ca, fluor-apatite P&H for P, Celestine $SrSO_4$ P&H for S, tugtupite astimex for Cl, orthoclase P&H for K, rutile TiO_2 P&H for Ti, eskolaite P&H for Cr, rhodonite MnSiO3 P&H for Mn, hematite Harvard for Fe, nickel oxide NiO P&H for Ni, $SrTiO_3$ P&H for Sr, barite $BaSO_4$ P&H for Ba. Detection limits (99% confidence) were 0.01 wt% for Ti, Al, Mg, Ca, K, 0.02 wt% for Cr, Na, P, S and Cl, 0.03 wt% for Si, Ni, Mn and Ba, 0.04 wt% for Fe, Sr and F.

Trace elements (including rare earth elements – REE) of clinopyroxene megacrysts (Supplementary Tables S4, S5) were also analysed by LA-ICPMS at the University of Tasmania using an Agilent 7900 quadrupole ICPMS coupled to a Coherent COMPex Pro 110 utilising an ArF excimer laser operating at the 193 nm wavelength and a pulse width of ~20 ns. Helium flow was 0.35 l/min immediately mixed with Ar after ablation flowing at a rate of 1.05 l/min. Laser ablation conditions were as follows: fluence of 4.8 J/cm^2; repetition rate of 5 Hz; ablation time of 63 s; 23 s delay (7 s background measurement) for sample washout; beam size of 74 μm. Data reduction was undertaken according to the standard methods of (Longerich et al., 1996) using the NIST612 (Jochum et al., 2011) glass as a primary reference material. The BCR-2 g and GSD-1 g glass were analysed throughout the analytical session and used as a secondary reference material (see Supplementary Table S4). Silica measured by EMP was used as an internal standard for reducing major element LA-ICMPS data (Supplementary Table S6). Apart from CaO and MgO, which show minor variations (0.7–3.3 relative percent), all elements show close correlation to EMP data.

4. Megacryst petrography

4.1. Udachnaya-east

Clinopyroxene megacrysts from the Udachnaya-East kimberlite were collected as individual crystals with thin rinds of kimberlite groundmass attached (UV-IG), and as crystal fragments (UV9774-cpx, UV-AVG). All samples were collected from mine dumps, which represent different sections of the kimberlite body. Sample UV9774-cpx was derived from the unserpentinised volcaniclastic unit of the Udachnaya-East kimberlite, whereas sample UV-IG and UV-AVG are from a serpentinised volcaniclastic unit. Clinopyroxene sample UV-IG is sub-rounded and elongated (2.5 cm in size across the longest axis). Sample UV-AVG is ovoid and 7 cm across the longest axis (Fig. 1a). However, due to the strong degree of alteration of inclusions, this sample was not considered for further geochemical analyses. Sample UV9774-cpx represents broken angular fragments, which range in size from 0.3–1.5 cm. Megacryst UV9774-cpx exhibits variably thick (>300 μm) reaction rims composed of fine-grained intergrowths of phlogopite with minor tetraferriphlogopite ($KMg_3Fe^{3+}Si_3O_{10}(OH)_2$). In addition, sample UV9774-ol represents broken fragments (0.3–1.5 cm in size) of a single olivine megacryst from a mine dump of the unserpentinised Udachnaya-East kimberlite.

4.2. Diavik A154N

Clinopyroxene megacryst samples (A154-27 and A154-27B) from the A154N kimberlite were analysed in-situ from cut sections of kimberlite drill core. The megacrysts are typically rounded and elongated in shape and range from a centimetre to a few centimetres in size. The rims of megacrysts are usually replaced by fine-grained intergrowths of serpentine, phlogopite, calcite along with disseminated Cu-Fe-sulphides.

4.3. Jericho

Clinopyroxene megacryst samples from the Jericho kimberlite were analysed in-situ from cut sections of two kimberlite drill cores (JER03 and JER06). Clinopyroxene megacrysts are typically rounded and elongated in shape and range from 0.5 to >4 cm in size (Fig. 1b, c). The rims of megacrysts are usually replaced by fine-grained intergrowths of serpentine, phlogopite, calcite along with disseminated barite.

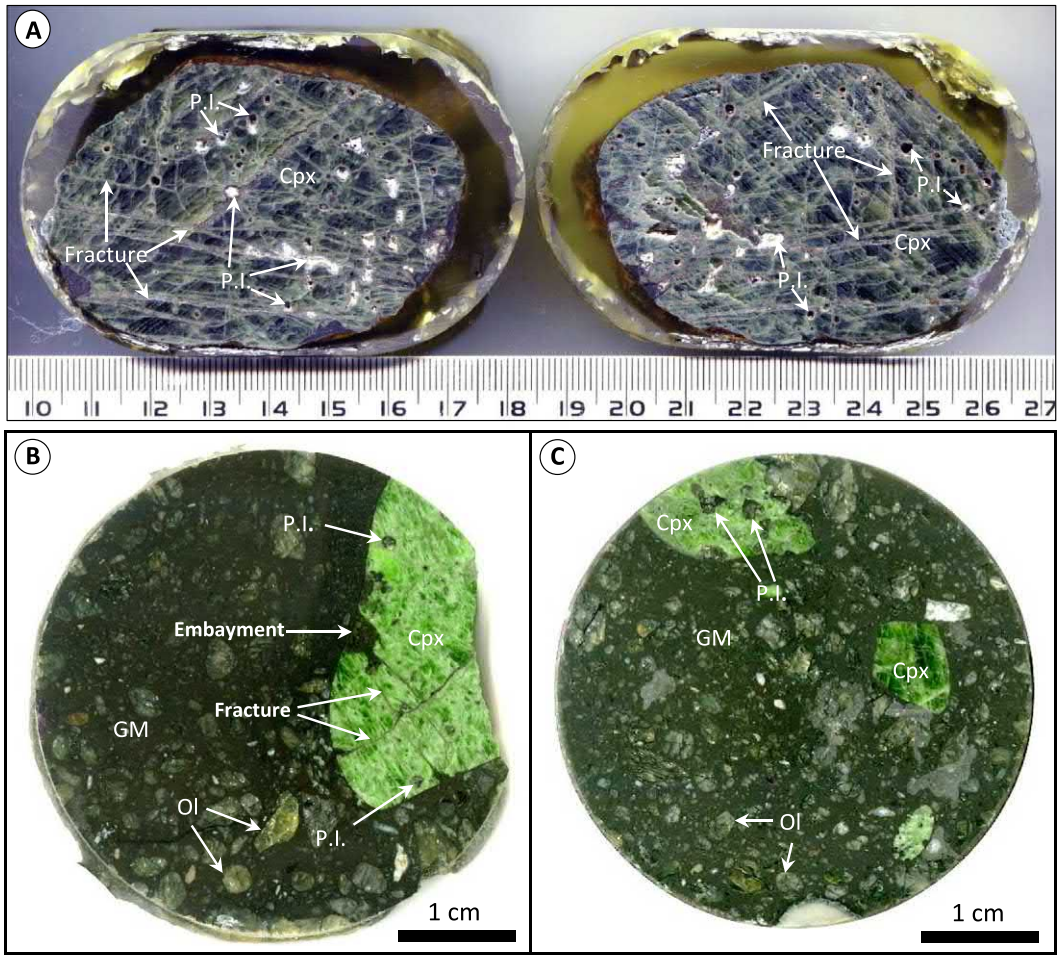

Fig. 1. (A) Polished cross-section of clinopyroxene sample UV-AVG. The sample is traversed by abundant networks of fractures/veins and populated by abundant polymineralic inclusions (P.I.), which are irregular-to-rounded in shape (dark and/or white holes) and located at the intersections of these fractures/veins. These polymineralic inclusions are highly altered, resulting in the presence of holes. (B, C) Polished sections of drill core exposing clinopyroxene megacrysts (Cpx) in sample Jer03. Polymineralic inclusions (P.I.) are abundant as generally dark grey rounded inclusions in clinopyroxene megacrysts. GM: fine-grained kimberlite groundmass, Ol: olivine.

4.4. Leslie

Fragments of clinopyroxene megacryst from the Leslie kimberlite were collected from crushed kimberlite drill core (LDC7). Samples were prepared as epoxy mounts containing fragments of clinopyroxene megacrysts, which range from 2 to 5 mm in size. The rims of megacrysts are usually replaced by fine-grained intergrowths of serpentine, phlogopite, calcite along with disseminated barite.

5. Megacryst chemistry

5.1. Udachnaya-east

Clinopyroxene samples UV9774-cpx and UV-IG are compositionally homogeneous and exhibit Mg# (Mg/(Mg + Fe) × 100) of 88.0 and 89.2 respectively, which is comparatively lower than Canadian clinopyroxene megacrysts (see below). Clinopyroxene sample UV9774-cpx has low Cr_2O_3 (0.30 wt%), minor Al_2O_3 (1.79 wt%) and Na_2O (1.48 wt%; Fig. 2; Table 1; Supplementary Table S1). Similarly, clinopyroxene sample UV-IG has low Cr_2O_3 (0.59 wt%), minor Al_2O_3 (1.73 wt%) and Na_2O (1.37 wt%; Fig. 2; Table 1; Supplementary Table S1). Both clinopyroxene megacrysts are classified as Cr-poor diopside. The single olivine megacryst analysed is forsteritic (Mg# 85.6) and contains low NiO (0.17 wt%), MnO (0.16 wt%) and CaO (0.03 wt%; Supplementary Table S2).

5.2. Diavik A154N

Clinopyroxene megacrysts from A154-27 and A154-27B are compositionally similar and represented by a narrow range in Mg# (92.0–92.5), low Cr_2O_3 (0.65–0.96 wt%), minor Al_2O_3 (1.32–1.55 wt%) and Na_2O (0.98–1.36 wt%; Fig. 2; Table 1; Supplementary Table S1), and are classified as Cr-poor diopside.

5.3. Jericho

Clinopyroxene is represented by two compositionally distinct populations. JER03 samples are represented by a narrow Mg# range of 88.8–89.8 along with moderate Cr_2O_3 (1.11–1.47 wt%), Al_2O_3 (2.17–2.49 wt %) and Na_2O (1.96–2.21 wt%; Table 1; Supplementary Table S1), and are classified as Cr-rich diopside. JER06 samples are represented by slightly higher Mg# range of 0.5–90.9 along with moderate Cr_2O_3 (1.23–1.27 wt%), Al_2O_3 (1.72–1.97 wt%) and Na_2O (1.53–1.70 wt%; Fig. 2; Table 1; Supplementary Table S1), and are also classified as Cr-rich diopside.

5.4. Leslie

The average Mg# of clinopyroxene megacrysts (LDC7) is 92.2 (n = 6) and contains moderate Cr_2O_3(0.98 wt%), minor Al_2O_3 (1.18 wt%) and

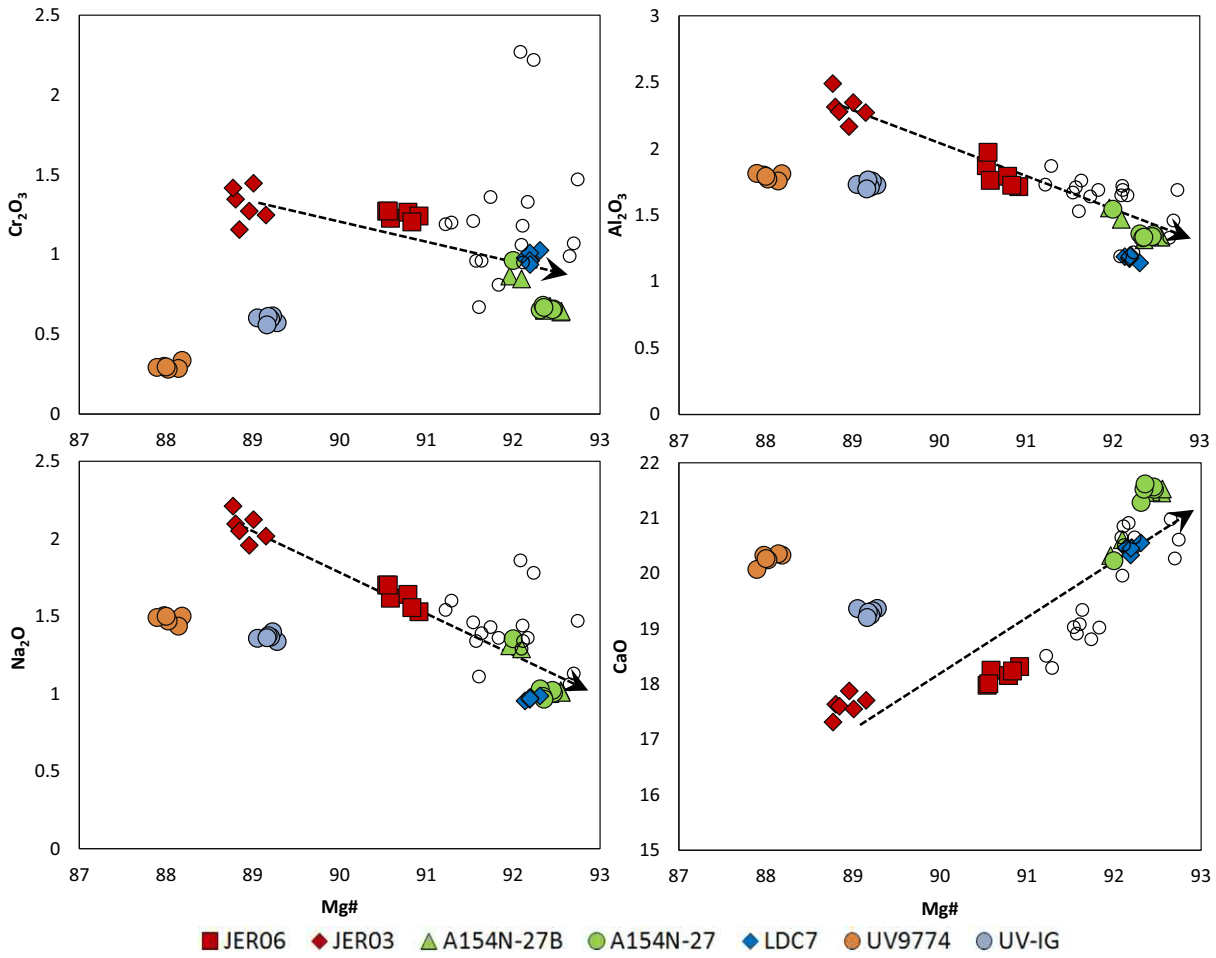

Fig. 2. Major and minor element (see Supplementary Table S1) co-variation of Mg# vs. oxide (wt%) diagrams for clinopyroxene megacryst grains from Jericho (Jer06, Jer03), A154N (A154-27, A154-27B), Leslie (LDC7) and Udachnaya-East (UV9774-cpx, UV-IG). The dotted black arrow indicates the geochemical trend of Canadian megacrysts. The clear circles are representative electron microprobe (EMP) compositions of other kimberlite-hosted clinopyroxene megacrysts from the Slave Craton from Bussweiler et al. (2018).

Na_2O (0.97 wt%; Fig. 2; Table 1; Supplementary Table S1), and are classified as Cr-rich diopside.

5.5. Rare earth elements

Chondrite normalised (after Sun and McDonough, 1989) rare earth element (REE; Fig. 3; Supplementary Table S5) patterns from clinopyroxene megacrysts from Udachnaya-East, A154N, Jericho and Leslie all show a strong degree of similarity and are typically characterised by high concentrations of Pr and Nd, whereas middle and heavy REEs are strongly fractionated relative to light REEs (Pr/Lu_N = ~31 – UV9774-cpx; ~43 – UV-IG; ~107 – A154-27; ~84 – A154-27B; ~36 – JER06; ~28 – JER03; ~89 – LDC7). These REE patterns are consistent with clinopyroxene megacrysts worldwide (Bussweiler et al., 2018; Eggler et al., 1979; Kostrovitsky et al., 2004).

6. Inclusions in megacrysts

6.1. Polymineralic inclusions

Megacryst minerals host abundant polymineralic inclusions (also previously termed 'globules' and 'melt inclusions'; Araújo et al., 2009; Bussweiler et al., 2016; Howarth and Büttner, 2019; van Achterbergh et al., 2002, 2004), which are typically round-to-amoeboid or irregular in shape and range from <0.5 to 2 mm in size (Figs. 1, 4–6; Supplementary Fig. S1). Some polymineralic inclusions hosted in clinopyroxene and olivine megacrysts from the Udachnaya-East kimberlite reach up to 5 mm across (Fig. 4). Polymineralic inclusions are generally located at the intersections of fracture and vein networks (Figs. 1, 4–6; including at cleavage plane intersections in clinopyroxene), which traverse megacryst grains and are usually connected to the kimberlite groundmass (Figs. 1, 5b, e). Polymineralic inclusions in megacrysts contain one of two types of mineral assemblages, which are reminiscent of the host kimberlite groundmass (Table 2):

1) Carbonate-silicate inclusions: These inclusions were identified in all Canadian samples (A154N, Jericho and Leslie) as well as in Udachnaya-East clinopyroxene sample UV-IG. These inclusions are largely composed of euhedral phlogopite (rarely zoned to Ba-rich

Table 1
Average electron microprobe (EMP) compositions (wt%) of clinopyroxene megacrysts from samples JER06, JER03, A154-27, A154-27B, LDC7, UV9774-cpx and UDE-IG (see Supplementary Table 1 for complete dataset).

No. analyses	JER06 6	JER03 6	A154-27 6	A154-27B 6	LDC7 6	UV9774-cpx 6	UDE-IG 6
SiO_2	55.47	55.43	55.39	55.31	54.98	55.27	55.29
TiO_2	0.14	0.25	0.22	0.23	0.08	0.17	0.26
Al_2O_3	1.81	2.31	1.38	1.39	1.18	1.55	1.73
Cr_2O_3	1.25	1.31	0.71	0.72	0.98	0.26	0.59
FeO	3.31	3.75	2.58	2.58	2.71	3.59	4.17
NiO	0.05	0.03	0.03	0.03	0.05	0.03	0.06
MnO	0.11	0.12	0.08	0.08	0.08	0.09	0.13
MgO	18.12	16.87	17.41	17.43	17.97	16.74	19.30
CaO	18.16	17.61	21.29	21.14	20.44	20.95	17.00
Na_2O	1.62	2.08	1.06	1.10	0.97	1.29	1.37

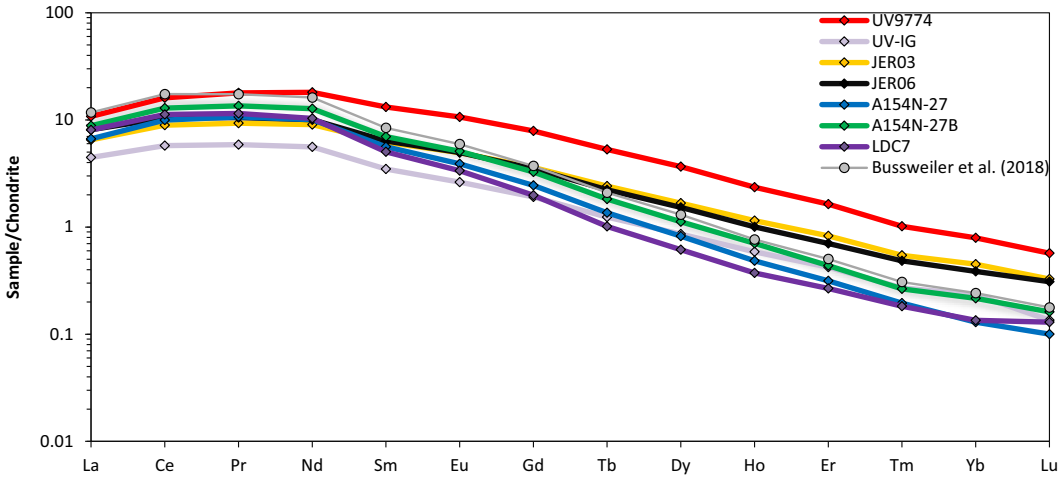

Fig. 3. Average chondrite normalised (after Sun and McDonough, 1989) rare earth element (REE) patterns of clinopyroxene megacrysts from the Udachnaya-East (UV9774-cpx, UV-IG), Jericho (Jer03, Jer06), A154N (A154-27, A154-27B) and Leslie (LDC7) kimberlites (see Supplementary Table S5). The grey line represents average chondrite normalised REE patterns of other kimberlite-hosted clinopyroxene megacrysts from the Slave Craton from Bussweiler et al. (2018).

kinoshitalite along rims), acicular olivine (also termed "spinifex"; van Achterbergh et al., 2002) (Fo_{88}) along with interstitial calcite and serpentine. Olivine crystals are sometimes surrounded by thin zoned rims of more Fe-rich olivine (Supplementary Fig. S2). In addition, these polymineralic inclusions contain subordinate amounts of euhedral chromite, MUM-spinel, apatite, perovskite and Ni-sulphides (Table 2). It is noteworthy that interstitial calcite occasionally contains micro-inclusion (<5 μm) clusters of Ba-Sr- and Na-carbonates (Fig. 7). These mineral assemblages are consistent throughout the majority of polymineralic inclusions. In addition, interstitial and euhedral-shaped barite crystals are common in polymineralic inclusions in clinopyroxene megacrysts from Jericho and Leslie. Some inclusions such as UV-IG and UV-AVG are characterised by the presence of small holes (Fig. 1a; Supplementary Fig. S1), which may indicate the presence of a former fluid or water-soluble phases. Clinopyroxene megacrysts from the Jericho kimberlite also preserve monomineralic inclusions of orthopyroxene (enstatite). These orthopyroxene inclusions are up to 2 mm in size and sometimes occur in conjunction with polymineralic inclusions. Orthopyroxene is partially altered to serpentine as well as partially replaced by typical polymineralic inclusion phases listed above (Fig. 5c).

2) Alkali-carbonate-chloride-silicate inclusions: This mineral assemblage was only identified in polymineralic inclusions in megacryst samples UV9774-cpx and UV9774-ol from the Udachnaya-East kimberlite. Inclusions are composed of skeletal-shaped olivine (Fo_{88}), euhedral zoned phlogopite-tetraferriphlogopite, interstitial shortite ($Na_2Ca_2(CO_3)_3$), pectolite ($NaCa_2Si_3O_8(OH)$), halite/sylvite, Ba-Sr-carbonate and djerfisherite (Fig. 5f; Supplementary Fig. S3; Table 2). In addition, olivine inside one clinopyroxene-hosted polymineralic inclusion is partially replaced by tetraferriphlogopite and an unidentified admixture of K-Cl-S-bearing Mg-Fe-silicate (serpentine?). Similar to UV-IG, some polymineralic inclusions contain holes (Fig. 4).

The contacts between polymineralic inclusions and the host clinopyroxene grain are characterised by subtle zoning (i.e. decrease in brightness in BSE imaging in zoned areas), which are generally defined by varying degrees of elevated Si, Ti and Mg# and lower Cr, Al and Na contents (Fig. 8c, d; Supplementary Table S1). In addition, the contact between clinopyroxene megacrysts and polymineralic inclusions from Udachnaya-East are sometimes marked by a thin rim (<25 μm) of Cr-bearing omphacite ($(Ca,Na)(Mg,Fe^{2+},Al)Si_2O_6$; Supplementary Fig. S3).

6.2. Micro melt inclusions

Polymineralic inclusions are commonly surrounded by a by a densely populated halo of micro inclusions, which form a 'sponge-like' rim (Figs. 5b, 6, 8; Araújo et al., 2009; Bussweiler et al., 2016).

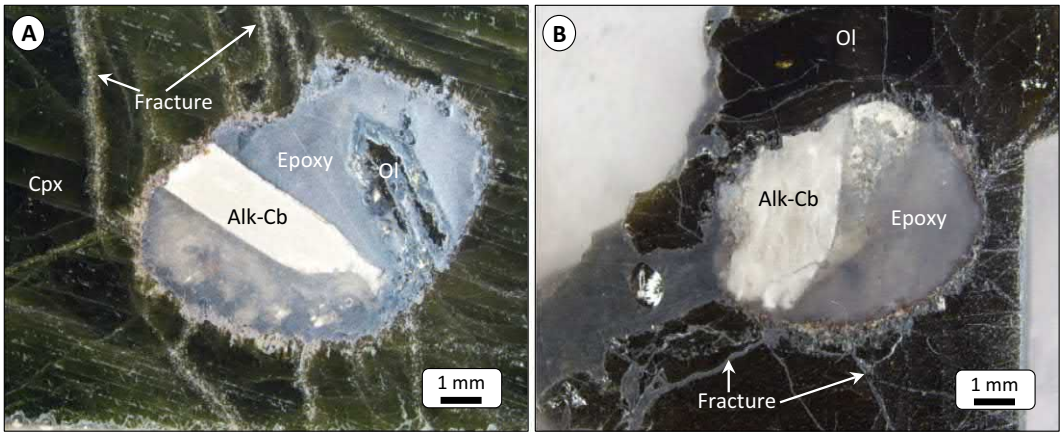

Fig. 4. Optical binocular images of polymineralic inclusions in (A) clinopyroxene (cpx) megacryst sample UV-9774-cpx, and (B) olivine (ol) megacryst sample UV-9774-ol. Holes are infilled by epoxy. Alk-Cb: alkali-carbonate.

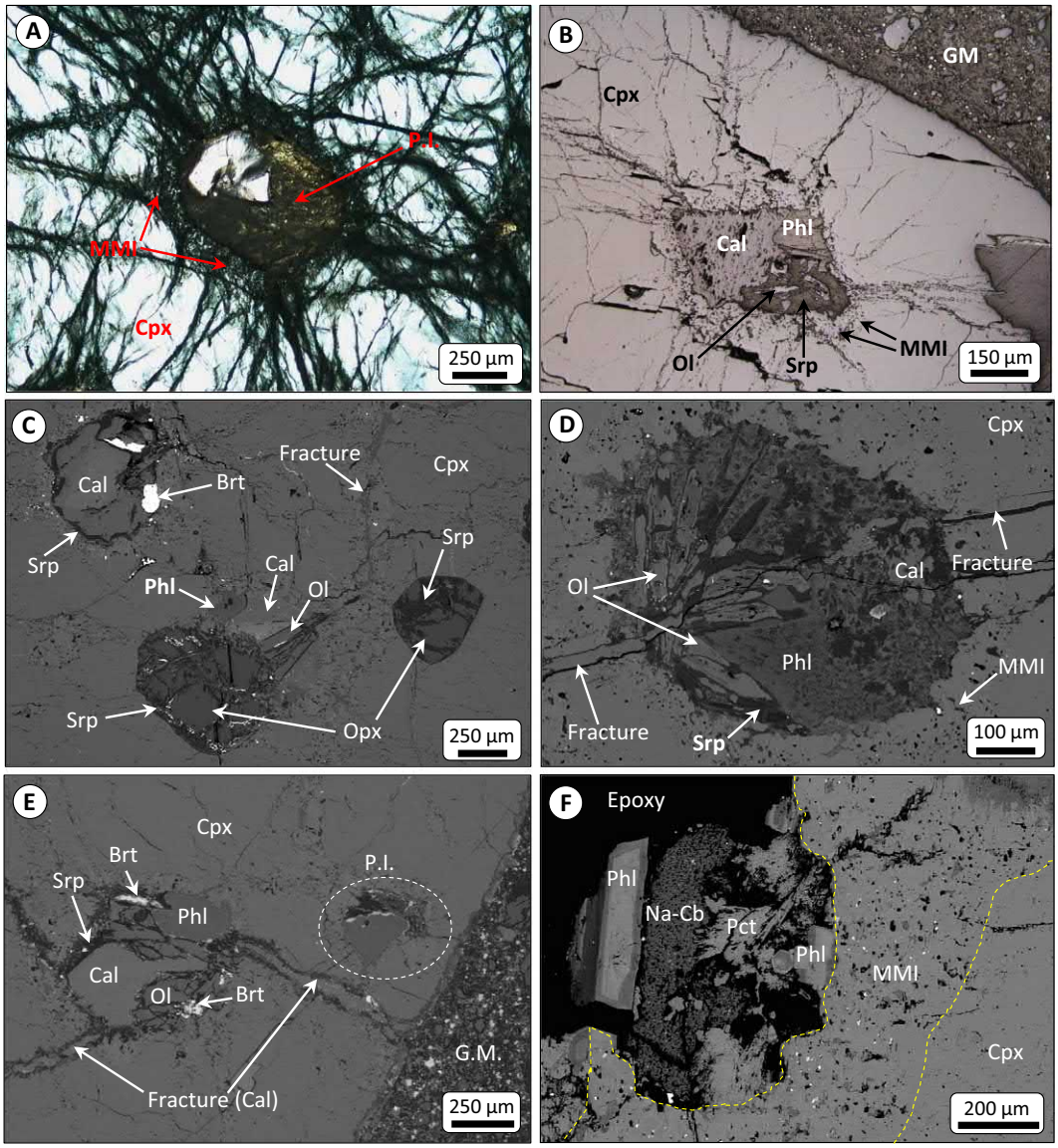

Fig. 5. (A) Transmitted light, and (B) reflected light microscope image of polymineralic inclusions (P.I.) hosted in a clinopyroxene (Cpx) megacryst from A154N sample DVK_CD_01 (previously studied by Bussweiler et al., 2016). (C – F) Back-scatter electron (BSE) SEM images of polymineralic inclusions in clinopyroxene megacrysts from samples (C) Jer03, (D) A154-27B, (E) LDC7, and (F) UV9774-cpx. Polymineralic inclusions are typically located at intersections of fractures or veins, which are usually filled with calcite (Cal). These fractures are usually connected to the host kimberlite groundmass (e.g., panel E). The interface of the clinopyroxene grain in contact with polymineralic inclusions are usually densely populated by abundant micro melt inclusions (MMI –<5 μm in size), which forms a spongy texture outlined by a yellow dotted line in panel (panel F). (F) Phlogopite grains in polymineralic inclusions are zoned from phlogopite (Phl) interiors to darker tetraferriphlogopite rims. Srp: serpentine, Ol: olivine, Brt: barite, Opx: orthopyroxene, Na-Cb: Na-carbonate, Pct: pectolite, GM: groundmass.

Table 2
Types of polymineralic melt inclusions, their mineralogy (in order of decreasing relative abundance) and the samples that they are found in.

Type	Carbonate-silicate inclusions	Alkali-carbonate-chloride-silicate inclusions
Sample	JER03, JER06, A154-27(+B), LDC7, UV-IG	UV9774-cpx, UV9774-ol
Mineralogy	Phlogopite	Olivine
	Serpentine	Phlogopite
	Calcite	Tetraferriphlogopite
	Olivine	Shortite
Decreasing	Spinel (chromite, MUM)	Pectolite
Abundance	Apatite	Halite/Sylvite
	Perovskite	Ba-Sr carbonates
	Ni-sulphides	K-Cl-S-bearing Mg-Fe-Silicate
	±Ba-Sr-Na carbonates	Djerfisherite
	±Barite	

These spongy rims also occur around network fractures/veins traversing the host megacryst grain. These micro inclusion spongy rims are notably more common and radiate further from polymineralic inclusions/fractures/veins in clinopyroxene than in olivine. The micro-inclusions composing these spongy rims are typically round-to-amoeboid in shape, range from <1–5 μm in size (rarely up to 10–20 μm; Figs. 8, 9). In addition, micro-inclusion (≤1 μm in size) trails also occur as swarms orientated along healed fracture planes and are generally isolated from any polymineralic inclusions or major fracture networks. These micro-inclusions are classified as secondary in origin (as defined by Roedder, 1984) and collectively referred to as 'micro melt inclusions' (MMIs).

In general, exposed MMIs are also polymineralic and commonly host multiple 'daughter' phases comprised of mineral assemblages similar to those in polymineralic inclusions (most notably phlogopite and serpentine). In addition, numerous MMIs contain phases enriched in Ca-Na-K and to a lesser extent P, Cl, S and rarely F.

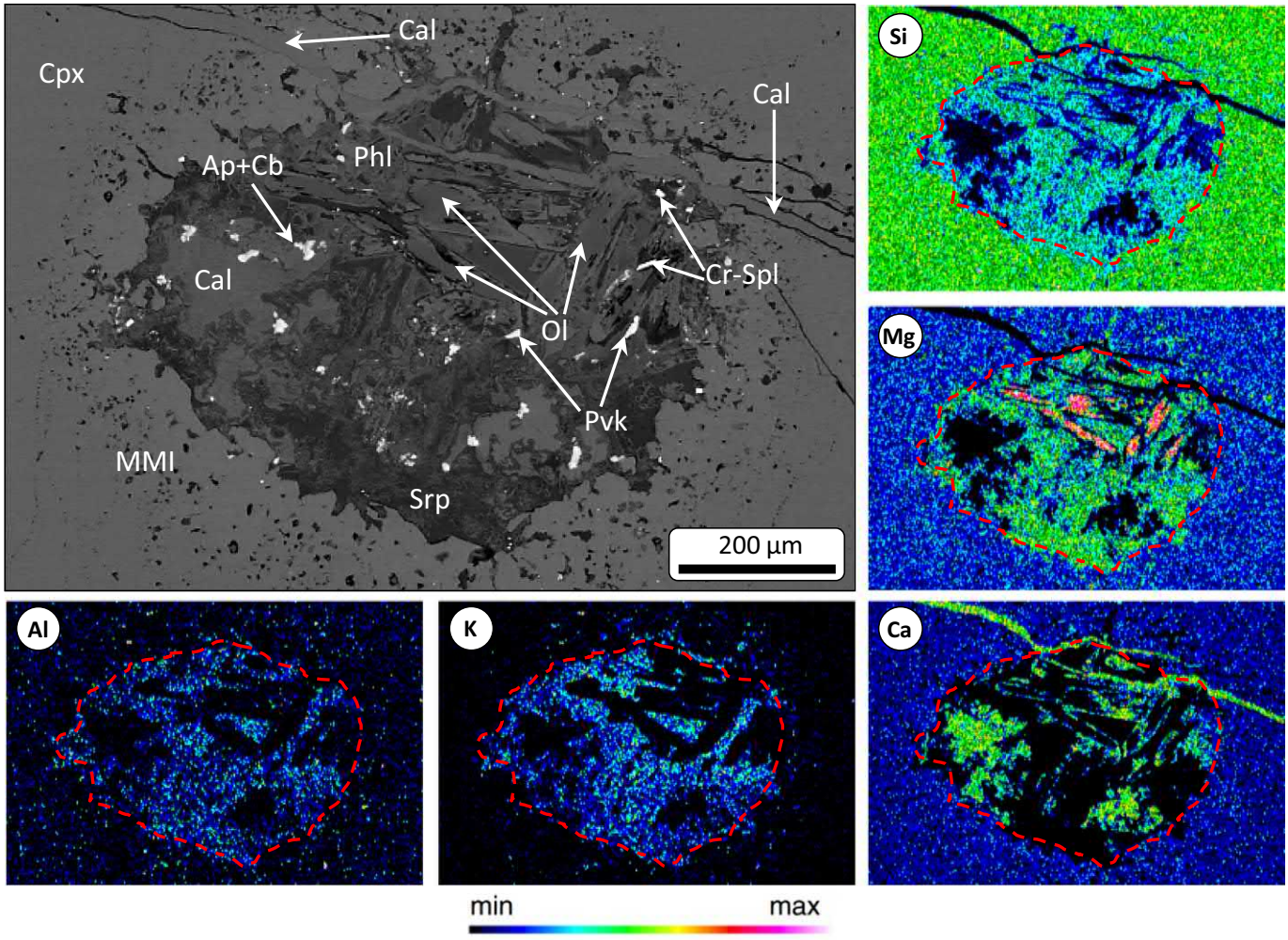

Fig. 6. Back-scatter electron (BSE) SEM image and X-ray elemental map of a polymineralic inclusion in a clinopyroxene (Cpx) megacryst from sample A154-27B. Detected minerals include olivine (Ol), calcite (Cal), serpentine (Srp), phlogopite (Phl), apatite (Ap), Ba-Na-carbonate (Cb), perovskite (Pvk) and Cr-spinel (Cr-Spl). Clinopyroxene surrounding the polymineralic inclusion exhibits characteristic "spongy-texture" and is populated by abundant micro melt inclusions (MMI).

Although accurate identification for the majority of these phases could not be confidently assigned due to their small size, some of phases may include Na-K-Ba carbonates, Na-K chlorides, apatite, alkali-sulphates, Fe-Ni-sulphides and rare feldspathoids (nepheline, leucite and kalsilite) and amphibole (i.e. richterite?; Figs. 8, 9). These alkali-halogen-S enriched MMIs occur consistently throughout all studied megacryst samples and are generally only preserved where the MMI is completely isolated (i.e. not transected by any vein or fracture network). MMI trails were also examined by LA-ICPMS. Dense clusters of inclusions close to the polished surface were targeted and their presence was indicated by a combination of synchronised positive anomalies in alkalis (Na, K, Ba, Rb, Sr, Cs), LREEs, S, Cl, Nb, Ta, U, Th, P and Al in time-resolved ablation signals (Supplementary Figs. S4, S5). Numerous inclusions were intersected at different depths during analyses, as indicated by multiple positive spikes in the above elements.

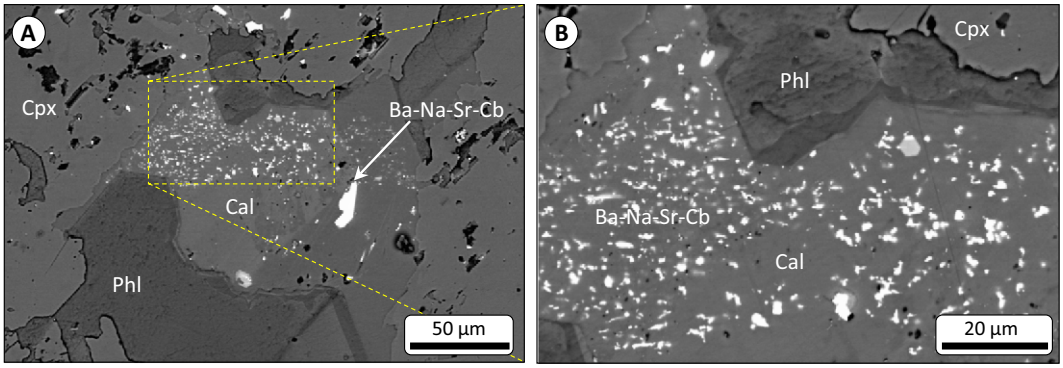

Fig. 7. (A, B) Back-scatter electron (BSE) SEM images of interstitial calcite (Cal) inside a polymineralic inclusion hosted in a clinopyroxene (Cpx) megacryst from sample Jer03. Calcite is densely populated by micro-inclusions (1–20 µm in size) of Ba-Na-Sr-bearing carbonates (Cb). Inset (B) shows a close up of these Ba-Na-Sr-carbonate inclusion swarms. Phl: phlogopite.

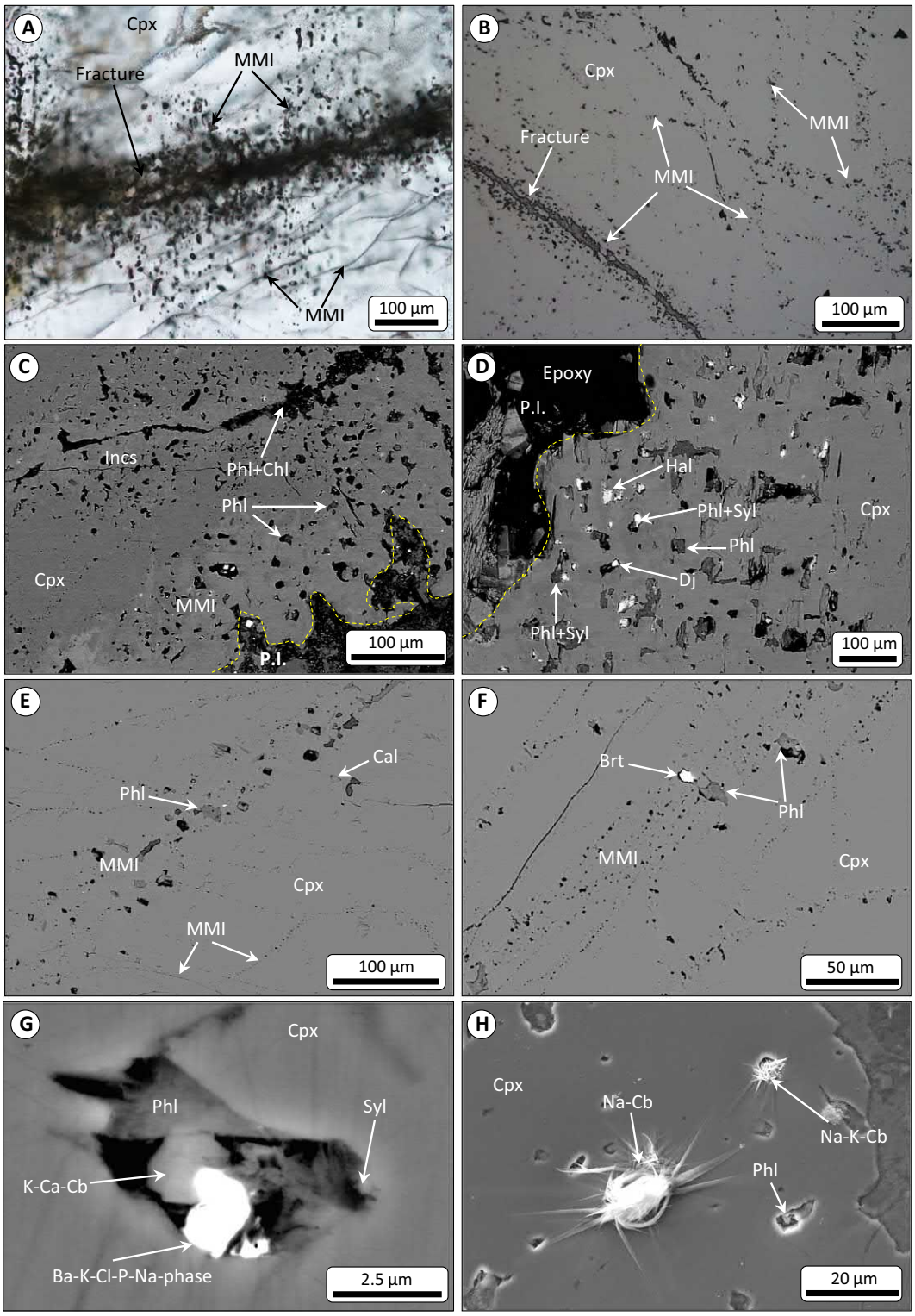

Fig. 8. (A) Transmitted light, and (B) reflected light microscope image of fracture networks and radiating micro melt inclusions (MMI) trails traversing a clinopyroxene (Cpx) megacryst from A154N (sample DVK_CD_01). Back-scatter electron (BSE) SEM images of (C, D) MMIs hosted in the "spongy-textured" zone surrounding polymineralic inclusions (P.I. – the boundary is indicated by the dotted yellow line) in clinopyroxene (Cpx) megacrysts from samples (C) A154-27B and (D) UV9774-cpx. (E – H) Exposed inclusion trails traversing host clinopyroxene megacrysts from samples (E, G) LDC7, (F) Jer06, (G) and (H) A154-27. Due to the small sizes of most MMIs (<5 µm), identification of individual phases could not be accurately determined. Some MMIs are polymineralic e.g., image panel (G) and other inclusions show evidence of re-precipitation of soluble phases on the surface (e.g., panel H). Subtle zoning is present in the spongy areas in (C) and (D), which is evident by minor differences in contrast under BSE imaging. Phl: phlogopite, Chl: chlorite, Hal: halite, Syl: sylvite, Dj: djerfisherite, Cal: calcite, Brt: barite, Cb: carbonate.

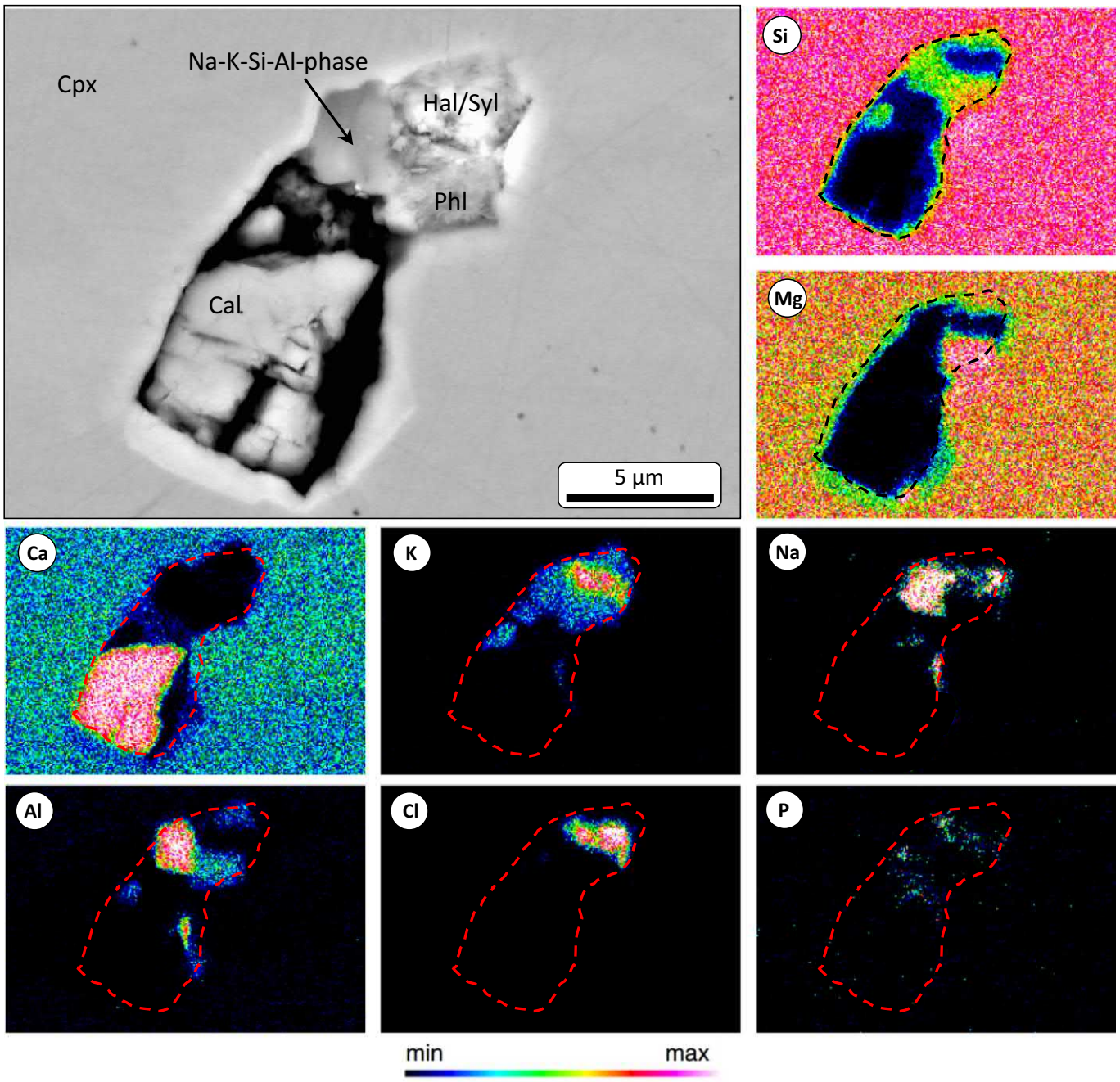

Fig. 9. Back-scatter electron (BSE) SEM image and X-ray elemental map of a micro melt inclusion hosted in a clinopyroxene (Cpx) megacryst from sample A154-27. Detected minerals include calcite (Cal), phlogopite (Phl), halite (Hal), sylvite (Syl) and an unidentified Na-K-Si-Al-bearing phase.

6.3. Composition of phlogopite in polymineralic melt inclusions

Phlogopite is one of the most common and compositionally complex minerals hosted in polymineralic inclusions and MMIs. Phlogopite in polymineralic inclusions can exhibit a variety of zoning patterns, such as thin (<10 µm) Ba-rich rims (i.e. kinoshitalite; e.g., sample Jer03; Supplementary Fig. S6; Supplementary Table S3) or may contain several discrete zones, which are characterised by decreasing TiO_2, Al_2O_3 and increasing FeO from core to rim, where it may also be surrounded by an outmost rim of tetraferriphlogopite (i.e. Al-free phlogopite; Supplementary Figs. S3, 6b; Supplementary Table S3). It is noteworthy that tetraferriphlogopite was only observed in megacryst-hosted polymineralic inclusions from Udachnaya-East. In general, phlogopite has a high Mg# (~0.86–0.94; Supplementary Table S3), whereas tetraferriphlogopite is characterised by lower Mg# ~0.77–0.82.

The compositions of phlogopite in polymineralic inclusions from each locality are characterised by minor variations (generally in the order of <1–2 wt%) in Cr_2O_3, FeO, MgO, K_2O and Na_2O contents (Fig. 10; Supplementary Table S3). BaO is generally very low (<~0.2 wt%) or negligible in phlogopite and tetraferriphlogopite, along with halogens, where Cl is <0.1 wt% and F is generally <~0.5–1 wt%, except for a single phlogopite grain in sample Jer03, which contains up to 3.6 wt% F (Fig. 10a; Supplementary Table S3).

Phlogopite in polymineralic inclusions from clinopyroxene megacrysts in sample A154-27B is characterised by slightly lower K_2O (average = ~8.27 wt%, n = 9) contents than ideal phlogopite (Supplementary Table S3). In general, phlogopite appears poorly preserved

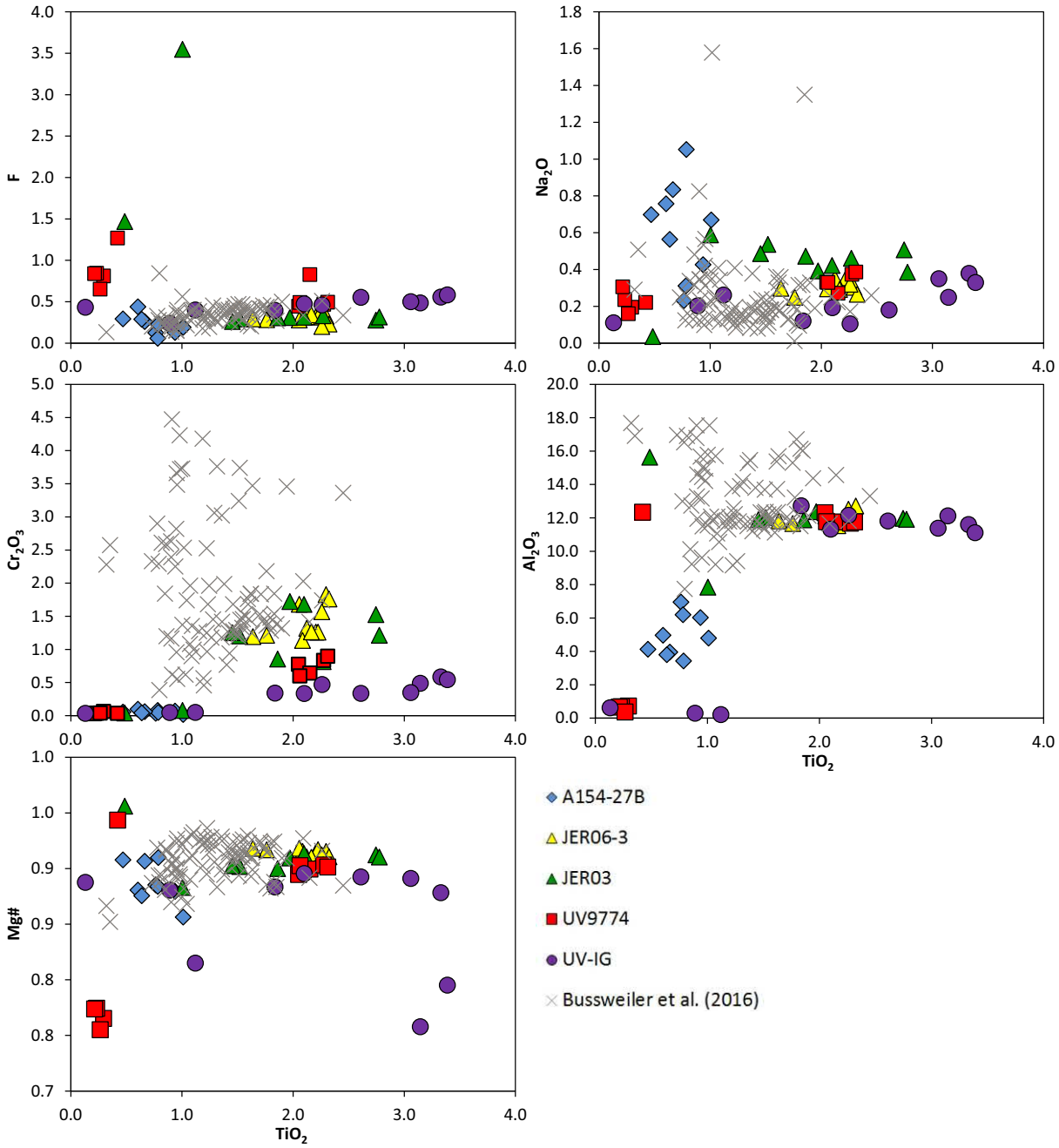

Fig. 10. Major and minor (EMPA) oxide *co*-variation diagrams for phlogopite inclusions in megacryst-hosted polymineralic inclusions. This data includes data (grey crosses) from other phlogopite inclusions hosted in megacrysts from Lac de Gras kimberlites (Canada; Bussweiler et al., 2016).

in polymineralic inclusions in this sample, as indicated by the absence of crystal shape and mottled appearance, signifying alteration (Supplementary Fig. S7).

7. Discussion

The Canadian clinopyroxene megacrysts in the present study display a distinct geochemical trend where increasing Mg# is accompanied by increasing CaO-content and decreasing Cr_2O_3, Al_2O_3 and Na_2O (Fig. 2). Although these megacrysts were derived from different kimberlite pipes (Jericho, A154N and Leslie) with different ages, their compositions (Fig. 2; Table 1; Supplementary Table S1, S5) are consistent with previous studies of Slave Craton clinopyroxene megacrysts (e.g., Bussweiler et al., 2016, 2018; Kopylova et al., 2009). Clinopyroxene megacrysts from Udachnaya-East (Russia) exhibit their own distinct geochemical signature in terms of major elements (Table 1; Supplementary Table S1), which falls outside of the Slave trend (Fig. 2), but shows some compositional overlap with clinopyroxene megacrysts from southern Africa (Boyd et al., 1984; Merry and le Roex, 2007; Shee and Gurney, 1979). Furthermore, Udachnaya-East clinopyroxene megacrysts are the most enriched in the majority of REEs (Fig. 3). However, regardless of locality, all studied megacrysts display almost identical REE patterns (Fig. 3). This suggests that clinopyroxene megacrysts were likely derived from a chemically similar source and/or common process, and the minor chemical differences between localities may reflect their regional heterogeneities in the mantle (Bell and Moore, 2004; Harte, 1983).

7.1. Polymineralic melt inclusions in megacrysts

Numerous studies have documented the presence of polymineralic inclusions hosted within megacrysts, however, these inclusions are not considered to be cognate (Araújo et al., 2009; Bussweiler et al., 2016; Howarth and Büttner, 2019; van Achterbergh et al., 2004). Polymineralic inclusions have been commonly attributed to kimberlite melt infiltration along network veins and fractures traversing the host megacryst. This is strongly supported in our studied samples, where polymineralic inclusions in kimberlite-hosted megacrysts (i.e. clinopyroxene, olivine) commonly contain minerals reminiscent of the host kimberlite groundmass, where they typically consist of olivine, serpentine, spinel (chromite, MUM), perovskite, phlogopite, apatite, calcite and barite (Table 2; see also Araújo et al., 2009; Bussweiler et al., 2016; Howarth and Büttner, 2019; van Achterbergh et al., 2002, 2004). This is also exhibited in the unique alkali-carbonate, silicate, chloride mineralogy hosted within polymineralic inclusions in megacryst samples UV9774-cpx and UV9774-ol, which are almost identical to the surrounding kimberlite groundmass.

7.1.1. Model for polymineralic melt inclusion formation

In the following sections, we present a three stage model for the: 1) infiltration of kimberlite melt and interaction with the host megacryst, 2) crystallisation of kimberlite melt in megacrysts, and 3) alteration of inclusions in megacrysts.

7.1.1.1. Stage 1: Kimberlite melt infiltration and interaction with the host megacryst. Clinopyroxene exhibits good cleavage, which represents defects in the crystal lattice. These cleavage planes are marked by networks of fractures/veins, which are usually connected to the kimberlite groundmass (Figs. 1, 5b, e). The presence of network fractures and veins connected to the kimberlite groundmass were fundamental pathways for the ingress of kimberlite melt into megacrysts (Figs. 1, 4, 5, 8). Kimberlite melt was most likely infiltrated along crystal defects, such as cleavage planes. Furthermore, additional fracturing of megacrysts probably occurred after their entrainment into the kimberlite magma, where rapid decompression during magmatic ascent led to the development of cracks (e.g., Brett et al., 2015). Additional propagation of fractures in megacrysts could develop due to the expansion of crystalline inclusions (e.g., orthopyroxene, garnet) during decompression. Alternatively, these fractures could also develop during explosive kimberlite emplacement. The entrapment of kimberlite melt in polymineralic inclusions is commonly attributed to the process of 'necking down' (as described by Roedder, 1984; see also Araújo et al., 2009; Bussweiler et al., 2016), where infiltrating kimberlite melt percolated along "*fractures and cleavage planes by dissolution and recrystallization. Surface reduction then results in the entrapment of discrete inclusions that may coalesce to form larger, rounded inclusions*" (Bussweiler et al., 2016). We adopt this model, where polymineralic inclusions developed due to the convergence of infiltrating kimberlite melt at fracture/vein junctions and coalescing (and expanding) by dissolving the host megacryst. Furthermore, the larger fractures/veins that facilitated kimberlite melt infiltration do not appear to have healed, but still connect polymineralic inclusions in megacrysts to the surrounding kimberlite groundmass (i.e. open system; Figs. 1, 5b, e). These fractures/veins were probably widened due to dissolution reactions induced by the percolating kimberlite melt, which then crystallised, effectively sealing these fracture and vein networks. Based on the connectivity of polymineralic inclusions to the kimberlite groundmass, we do not consider them to be completely isolated systems.

Polymineralic inclusions, fractures and veins are typically surrounded by a halo of dense micro melt inclusion (MMI) clusters (Figs. 5, 6, 8), which radiate outwards into the host megacryst. This halo of MMIs (or 'reaction rim') was interpreted by Bussweiler et al. (2016) to be the product of CO_2 exsolution, which was driven by disequilibria reactions between the infiltrating kimberlite melt and host megacryst. Furthermore, the entrapped kimberlite melt may have expanded within the host megacryst, thereby creating radiating networks of micro-fractures around polymineralic inclusions and thus creating pathways for MMIs to form. This process was likely enhanced by rapidly changing temperature and pressure conditions during kimberlite magma ascent. This disequilibrium between the infiltrating kimberlite melt and host megacryst is evident geochemically and mineralogically as:

i) Zoning in the spongy reaction rim surrounding polymineralic inclusions in clinopyroxene megacrysts that is characterised by elevated Si, Ti and Mg# and lower Cr, Al and Na contents (Figs. 8c, d; Supplementary Table S1). This suggests diffusion occurred between the host megacryst and infiltrating kimberlite melt. Furthermore, Sr-isotope ratios in host megacrysts were shown to be less radiogenic than carbonate in polymineralic inclusions (Bussweiler et al., 2016; van Achterbergh et al., 2002). This suggests that the host megacryst was in isotopic disequilibria with the infiltrating kimberlite melt. The overlap in Sr-isotopic signature between carbonate in polymineralic inclusions and carbonate from the host kimberlite (Bussweiler et al., 2016) supports melt infiltration of host kimberlite at depth. It is noteworthy that the Sr-isotopic signature of polymineralic inclusions may be modified by secondary processes (i.e. infiltrating fluids) due to their interconnectivity with the kimberlite groundmass (see Stage 3 below).
ii) A discontinuous reaction rim of omphacite in sample UV9774-cpx occurs at the boundary between polymineralic inclusions (typically hosted Na-carbonate; Supplementary Fig. S3) and the clinopyroxene megacryst host probably formed as a result of extensive interaction with the sodic component of the infiltrating kimberlite melt. van Achterbergh et al. (2002) interpreted the occurrence of irregular reaction rims of orthopyroxene intergrown with the host clinopyroxene along the polymineralic inclusion boundary to be exolution features. In addition, Bussweiler et al. (2016) attributed kelyphitic (i.e. fine-grained intergrowths of orthopyroxene, spinel, olivine, phlogopite and glass) rims at the interface between polymineralic inclusions and host Cr-pyrope to be the products of interaction between the infiltrating melt and host megacryst (Bussweiler et al., 2016).

Polymineralic inclusions in megacrysts may also have a hybrid nature due to the partial-to-complete dissolution and replacement of crystal inclusions of phases such as orthopyroxene or garnet. This was observed in partially resorbed orthopyroxene inclusions, which are surrounded and partly replaced by typical polymineralic inclusion minerals (Fig. 5c). Orthopyroxene dissolution is commonly attributed to its instability within ascending kimberlite melts (Brett et al., 2015; Bussweiler et al., 2015; Kamenetsky et al., 2013; Kamenetsky and Yaxley, 2015; Luth, 2009; Pilbeam et al., 2013; Sharygin et al., 2015, 2017), in particular with the carbonate melt component (Kamenetsky et al., 2009a). It is likely that the carbonatitic component of the kimberlite melt had the greatest propensity to infiltrate megacrysts along fractures due to its low viscosity and wetting properties of carbonatitic melts (Allan and Andrew, 1983).

7.1.1.2. Stage 2: Crystallisation of the kimberlite melt in megacrysts. The wide diversity in minerals observed in polymineralic inclusions in kimberlite-hosted megacrysts (Araújo et al., 2009; Bussweiler et al., 2016; van Achterbergh et al., 2002, 2004) is attributed to the heterogeneous trapping of variably differentiated kimberlite melt. Furthermore, the exposed (i.e. polished) surfaces only represent a random two-dimensional cross-section of the inclusion (see also Bussweiler et al. (2016) and Kamenetsky et al. (2013)).

Based on the precipitation of early kimberlitic liquidus minerals such as olivine and chromite (Fedortchouk and Canil, 2004; Mitchell, 1986, 2008) in polymineralic inclusions, kimberlite melt infiltration into

megacryst minerals probably occurred at a stage coeval with magmatic ascent. Polymineralic inclusions contain a suite of minerals that are typical in the groundmass of kimberlites, spanning the entire evolutionary trend. Olivine is occasionally zoned towards more Fe-rich rims, indicating the entrapped melt pockets within polymineralic inclusions evolved towards more Fe-rich compositions. Perovskite commonly occurs in polymineralic inclusions and is commonly inferred to have crystallised after olivine and spinel, but prior to carbonates in kimberlites (Mitchell, 1972). The presence of MUM-spinel suggests that spinel compositions probably evolved in response to melt differentiation (i.e. removal of Cr by chromite crystallisation; Mitchell, 1986; Roeder and Schulze, 2008). Phlogopite grains typically exhibit more complex zoning trends. In sample Jer03, phlogopite is surrounded by thin rims of kinoshitalite, which is a typical late-stage phase in kimberlites (Mitchell, 2008; Soltys et al., 2018; Tappe et al., 2014). In addition, in samples UV9774-cpx and UV-IG, phlogopite exhibits multiple discrete zones, that are characterised by increasing Mg and decreasing Ti and Fe from core to rim (Supplementary Table S3). This ultimately results in a sharp transition to an outer rim of tetraferriphlogopite. The presence of tetraferriphlogopite overgrowths around Al-bearing phlogopite was interpreted to be the result of significant changes in melt chemistry (e.g., removal of Al) and redox conditions, which caused a hiatus in phlogopite crystallisation (Mitchell, 1986). Minerals such as apatite, barite and carbonate (Armstrong et al., 2004; Giuliani et al., 2017; Mitchell, 2008; Soltys et al., 2018) are commonly considered as late-stage products of kimberlite crystallisation. Although polymineralic inclusions exhibit many mineralogical similarities to the kimberlite groundmass, these assemblages are probably the result of hybridisation between the infiltrating kimberlite melt and assimilation of host megacryst and its inclusions (e.g., Bussweiler et al., 2016). This is a microscale example of the highly reactive nature of kimberlite melts with their entrained mantle cargo.

7.1.1.3. Stage 3: Alteration of polymineralic melt inclusions. The connectivity of polymineralic inclusions through network fractures/veins to the host kimberlite groundmass (e.g., Figs. 1, 5b, e) in the majority of megacrysts provides strong evidence that these inclusions remained an open system even after crystallisation from the kimberlite melt. The groundmass of kimberlites is almost always modified by deuteric (i.e. late-stage magmatic; e.g., Mitchell, 1986, 2013) and/or external fluids (e.g., Giuliani et al., 2014, 2017; Sparks et al., 2006, 2009; Stripp et al., 2006), which results in the formation of secondary assemblages (e.g., serpentine, brucite, calcite) that can overprint primary kimberlite minerals (e.g., olivine). It is likely that secondary fluids permeated along the same fracture and vein networks that facilitated kimberlite melt infiltration. This probably resulted in the formation of interstitial secondary serpentine and/or calcite as well as the partial-to-complete replacement of primary phases such as olivine in the majority of polymineralic inclusions and their associated fracture/vein networks (Fig. 5b–e). Taking into account this, the host megacryst may have provided some degree of shielding from the effects of secondary alteration.

In addition, previous analyses of the $\delta^{18}O$ (relative to standard mean ocean water) and $\delta^{13}C$ (relative to Peedee belemnite) signatures of carbonate-rich polymineralic inclusions hosted in clinopyroxene megacrysts from the A154N kimberlite gave +14.2‰ and − 2.1‰ respectively (van Achterbergh et al., 2002). The combined melt compositions observed in polymineralic inclusions and their corresponding isotopic signature was interpreted by van Achterbergh et al. (2002) to represent altered ocean floor peridotites that were crustally contaminated. These C-O isotope values fall well outside the isotopic range of mantle carbonates (e.g., Deines, 2002). Modification of C-O isotopes in this system could be attributed to: i) open system Rayleigh fractionation (e.g., Tappe et al., 2017), and/or ii) secondary alteration by the ingress of serpentinising fluids. Similarly, in-situ analyses of $^{87}Sr/^{86}Sr$ ratios of carbonate-rich polymineralic inclusions in clinopyroxene and garnet have shown values to range from 0.7049–0.7067 and 0.7061–0.7071 respectively (Bussweiler et al., 2018; van Achterbergh et al., 2002), which display clear disequilibrium with their host megacrysts.

The effects of secondary alteration of polymineralic inclusions are most pronounced in the mineralogical differences displayed between polymineralic inclusions from samples UV9774-cpx/UV9774-ol (Figs. 4, 5f; Supplementary Fig. S3), which are from serpentine-free kimberlite, and UV-IG (Supplementary Fig. S1) and UV-AVG, which is from serpentinised kimberlite. Samples UV9774-cpx and UV9774-ol are dominated by water-soluble phases, such as alkali-carbonates and chlorides. Interestingly, olivine in the polymineralic inclusion UV9774 is partially replaced by minor K-Cl-S-bearing Mg-Fe-silicate, which is interpreted to be a serpentine mineral. However, the presence of serpentine in these polymineralic inclusions is at odds with the host megacrysts being derived from the serpentine-free unit of the Udachnaya-East kimberlite, which is interpreted to have been unaffected by post-emplacement serpentinisation, based on the preservation of fresh olivine, alkali-carbonates and alkali-chlorides in the groundmass of kimberlite rocks (Abersteiner et al., 2018; Kamenetsky et al., 2012, 2014b). The presence of holes (Figs. 1a, 4) in these polymineralic inclusions suggests there was the loss of a former phase. Furthermore, the exposure of these megacrysts in the mine dumps may have exposed them to subaerial weathering. Therefore, these megacryst inclusions may not have been pristinely preserved. Alternatively, we suggest that serpentine in these polymineralic inclusions may be a product of the complex dissolution reactions that occur between the infiltrating kimberlite melt and host megacryst. Furthermore, the presence of phlogopite in polymineralic inclusions suggests that water to some extent was also entrapped in the polymineralic inclusion, where it may have exsolved during the later stages of crystallisation and cause deuteric alteration of olivine.

In contrast, in sample UV-IG, serpentine is an abundant constituent in polymineralic inclusions and alkali-carbonates and alkali-chlorides are absent. This megacryst was derived from a serpentinised unit of the Udachnaya-East kimberlite, where the groundmass is devoid of alkali-carbonate and alkali-chloride minerals. This suggests that the same post-emplacement fluids, which removed alkali-carbonates and alkali-chlorides from the kimberlite groundmass surrounding sample UV-IG, also permeated the megacryst, resulting in similar secondary (i.e. serpentinised) mineral assemblages. Apart from samples UV9774-cpx and UV9774-ol, it appears that all other polymineralic inclusions analysed in other megacrysts from this study were also affected by post-emplacement serpentinisation. Therefore, these polymineralic inclusions cannot be considered 'pristine magmatic'.

7.2. Micro melt inclusions – insights into the kimberlitic melt?

Disequilibria reactions involving assimilation of host megacrysts along with chemical modification by post-magmatic alteration means that polymineralic inclusions should be carefully evaluated when trying to elucidate the initial composition of the kimberlite melt that entrained and infiltrated them. However, the abundant MMIs composing the spongy rims surrounding polymineralic inclusions and fractures/veins (Figs. 8, 9), as well as along healed fractures traversing megacrysts (Fig. 8b, e, f) are generally isolated (i.e. not connected to any fractures or the kimberlite groundmass). Unlike polymineralic inclusions, the fractures that formed MMIs were probably thin enough that they were able to heal (i.e. recrystallise clinopyroxene or olivine) and entrap small pockets of melt due to the aforementioned process of 'necking down'. However, not all MMIs appear completely isolated (i.e. some MMIs are still connected by micro-fractures to polymineralic inclusions/larger fractures/veins), which suggests that the amount of the host megacryst dissolved may have exceeded the amount precipitated during healing.

MMIs are considered to represent small pockets of variably differentiated kimberlite melt, which were entrapped during ascent of the host magma. Many phases hosted within isolated MMIs are similar to those

in polymineralic inclusions (e.g., phlogopite, calcite and serpentinised varieties) and should be treated with caution, as their compositions may have been modified by diffusion of elements from the host megacryst, kimberlite melt hybridisation and/or post-magmatic alteration due to connectivity to the polymineralic inclusion via microfractures. However, numerous other isolated MMIs contain additional phases, which include Na-K-Ba carbonates, Na-K chlorides, alkali-sulphates, Fe-Ni-sulphides and rare feldspathoids (nepheline, leucite and kalsilite) and amphibole were identified in MMIs in all megacryst samples. With the exception of samples UV9774-cpx and –ol, the majority of these phases are absent or extremely rare in polymineralic inclusions and host kimberlite groundmass.

The alkali-Cl-S-CO_2 bearing phases in MMIs bear striking compositional similarity to secondary melt inclusions reported in kimberlitic olivine (Abersteiner et al., 2017b; Giuliani et al., 2017; Golovin et al., 2007, 2018; Kamenetsky et al., 2004, 2009b; Mernagh et al., 2011), zircon and ilmenite megacrysts from kimberlites (Kamenetsky et al., 2014a, 2014b), olivine and ilmenite in mantle polymict breccias (i.e. 'failed kimberlites' stalled at mantle depths; Giuliani et al., 2012) and minerals from other kimberlite-borne mantle xenoliths (Abersteiner et al., 2019; Golovin et al., 2017, 2018; Sharygin et al., 2013; Soltys et al., 2016). However, the presence of other unique minerals such as feldspathoids and amphibole in MMIs are atypical in both the groundmass of kimberlites, polymineralic inclusions in megacrysts as well as other inclusions reported in other mantle-derived minerals (e.g., olivine, garnet, ilmenite, zircon; only a single study reported feldspathoids in ilmenite megacrysts; Kamenetsky et al., 2014a). These MMIs swarms/trails may therefore also represent the hybridised product of variably differentiated kimberlite melt, which interacted with the host megacryst. Furthermore, the small size and large surface area to volume ratio means that the compositions of MMIs may have been more greatly influenced by the leaching of elements from the host megacryst than larger polymineralic inclusions. Despite these apparently hybridised compositions of MMIs, the alkali-Cl-S-CO_2 enriched minerals in MMIs consistently occur in clinopyroxene and olivine megacrysts from numerous kimberlite localities worldwide. This suggests that the processes of their entrapment were identical and that the parental kimberlite melt, which infiltrated megacrysts, was probably more enriched in alkalis (especially Na), Cl, S than in kimberlite rocks exposed at the surface, which typically contain extremely low concentrations of these elements (Kjarsgaard et al., 2009; le Roex et al., 2003; Tappe et al., 2011). However, due to the heterogeneity and volumetrically small sizes of MMIs, reconstructing the potential concentrations of these components cannot be confidently performed. In the case of polymineralic inclusions and the host kimberlite, the majority of alkalis-Cl-S was probably removed by serpentinising fluids due to their incorporation into water-soluble phases (i.e. carbonates, chlorides).

8. Conclusions

- Kimberlite-hosted megacrysts commonly contain polymineralic inclusions, which host compositionally diverse mineral assemblages that span the entire kimberlite evolutionary trend and are broadly similar to their host kimberlite groundmass. Polymineralic inclusions are usually located at the intersections of fractures/veins/cleavage plane networks, and are considered to have formed due to primitive or ascending kimberlite melt infiltrating megacrysts along these crystal defects. Moreover, crystalline inclusions themselves produce additional cracks in the sample, probably due to expansion of the inclusion during decompression.
- Significant disequilibria existed between megacrysts and the infiltrating kimberlite melt, which caused partial dissolution of the host megacryst. This process was probably enhanced by the rapidly changing pressure and temperature conditions during magmatic ascent. This dissolution of the host megacryst and expansion of the entrapped kimberlite melt within the host megacryst probably resulted in the formation of swarms of micro melt inclusions (MMIs) around polymineralic inclusions, fractures and veins, as well as producing diffuse zoning in the megacryst along the contacts with polymineralic inclusions.
- The kimberlite melt, which crystallised as polymineralic inclusions and MMIs interacted with the host megacryst to produce a hybridised melt.
- Polymineralic inclusions remained open system after crystallisation due to connectivity with the kimberlite melt via network fractures/veins, which facilitated percolating external fluids. This resulted in secondary alteration of polymineralic inclusions with the exception of two relatively well-preserved megacryst samples (UV9774-cpx/UV9774-ol), which were derived from a non-serpentinised kimberlite unit from Udachnaya-East, all other studied megacryst-hosted polymineralic inclusions appear to exhibit more intense degrees of alteration by secondary fluids. Therefore, the majority of polymineralic inclusions in megacrysts cannot be considered pristine magmatic.
- Many MMIs were entrapped and isolated within the host megacryst due to 'necking down', where small fractures connected to them were later healed. Therefore, MMIs in many cases, but not all, were shielded from the effects of secondary alteration. MMIs are compositionally analogous to secondary melt inclusions hosted in kimberlitic olivine, as well as other kimberlite-borne mantle xenocrysts. Such MMIs preserve remnants of variably differentiated kimberlite melt that was modified by interaction with the host megacrysts and was probably more enriched in alkalis-Cl-S-CO_2 than serpentinised polymineralic inclusions and kimberlite rocks.

Acknowledgements

This study forms part of A.A's Ph.D and was supported by an Australian Postgraduate Award (APA) and the Max Banks Research Scholarship in Earth Sciences. This work was supported by funding from the Institute of Volcanology and Seismology, Far East Branch, Russian Academy of Sciences. AVG and ISS were supported by Russian Science Foundation (project No. 18-77-10062). This article has benefitted from the comments by Marc Norman, Geoffrey Howarth, Sebastian Tappe, Yannick Bussweiler and the efficient editorial handling by Andrew Kerr.

Appendix A. Supplementary data

Supplementary data to this article can be found online at https://doi.org/10.1016/j.lithos.2019.04.004.

References

Abersteiner, A., Kamenetsky, V.S., Graham, D.P., Kamenetsky, M., Goemann, K., Ehrig, K., Rodemann, T., 2017a. Monticellite in group-I kimberlites: implications for evolution of parental melts and post-emplacement CO2 degassing. Chem. Geol. 478, 76–88.

Abersteiner, A., Kamenetsky, V.S., Kamenetsky, M., Goemann, K., Ehrig, K., Rodemann, T., 2017b. Significance of halogens (F, Cl) in kimberlite melts: insights from mineralogy and melt inclusions in the Roger pipe (Ekati, Canada). Chem. Geol. 478, 148–163.

Abersteiner, A., Kamenetsky, V.S., Golovin, A.V., Kamenetsky, M., Goemann, K., 2018. Was crustal contamination involved in the formation of the serpentine-free Udachnaya-East kimberlite? New insights into parental melts, liquidus assemblage and effects of alteration. J. Petrol. 59, 1467–1492.

Abersteiner, A., Kamenetsky, V.S., Goemann, K., Golovin, A.V., Sharygin, I.S., Giuliani, A., Rodemann, T., Spetsius, Z.V., Kamenetsky, M., 2019. Djerfisherite in kimberlites and their xenoliths: implications for kimberlite melt evolution. Contrib. Mineral. Petrol. 174 (8), 22.

Agashev, A.M., Pokhilenko, N.P., Mal'kovets, V.G., Sobolev, N.V., 2006. Sm-Nd isotopic system in garnet megacrysts from the Udachnaya kimberlite pipe (Yakutia) and petrogenesis of kimberlites. Dokl. Earth Sci. 407, 491–494.

Agashev, A.M., Pokhilenko, N.P., Cherepanova, Y.V., Golovin, A.V., 2010. Geochemical evolution of rocks at the base of the lithospheric mantle: evidence from study of xenoliths of deformed peridotites from kimberlite of the Udachnaya pipe. Dokl. Earth Sci. 432, 746–749.

Agashev, A.M., Ionov, D.A., Pokhilenko, N.P., Golovin, A.V., Cherepanova, Y., Sharygin, I.S., 2013. Metasomatism in lithospheric mantle roots: constraints from whole-rock and mineral chemical composition of deformed peridotite xenoliths from kimberlite pipe Udachnaya. Lithos 160–161, 201–215.

Alexseev, S.V., 2009. Cryogeological Systems of the Yakutian Diamondiferous Province. Academic Publishing House "GEO", Novosibirsk, p. 319.
Allan, H.T., Andrew, S., 1983. Properties of carbonatite magma, processes in carbonatite magma chambers. J. Geol. 91, 437–447.
Araújo, D.P., Griffin, W.L., O'Reilly, S.Y., 2009. Mantle melts, metasomatism and diamond formation: insights from melt inclusions in xenoliths from Diavik, Slave Craton. Lithos 112, 675–682.
Armstrong, J.P., Wilson, M., Barnett, R.L., Nowicki, T., Kjarsgaard, B.A., 2004. Mineralogy of primary carbonate-bearing hypabyssal kimberlite, Lac de Gras, Slave Province, Northwest Territories, Canada. Lithos 76, 415–433.
Bell, D.R., Moore, R.O., 2004. Deep chemical structure of the southern African mantle from kimberlite megacrysts. S. Afr. J. Geol. 107, 59–80.
Berg, G.W., Carlson, J.A., 1998. The Leslie kimberlite pipe of Lac de Gras, Northwest Territories, Canada: evidence for near surface hypabyssal emplacement. Extended Abstracts 7th International Kimberlite Conference, Cape Town, pp. 81–83.
Boyd, F.R., Dawson, J.B., Smith, J.V., 1984. Granny Smith diopside megacrysts from the kimberlites of the Kimberley area and Jagersfontein, South Africa. Geochim. Cosmochim. Acta 48, 381–384.
Brett, R.C., Russell, J.K., Andrews, G.D.M., Jones, T.J., 2015. The ascent of kimberlite: Insights from olivine. Earth Planet. Sci. Lett. 424, 119–131.
Bussweiler, Y., Foley, S.F., Prelević, D., Jacob, D.E., 2015. The olivine macrocryst problem: New insights from minor and trace element compositions of olivine from Lac de Gras kimberlites, Canada. Lithos 220-223, 238–252.
Bussweiler, Y., Stone, R.S., Pearson, D.G., Luth, R.W., Stachel, T., Kjarsgaard, B.A., Menzies, A., 2016. The evolution of calcite-bearing kimberlites by melt-rock reaction: evidence from polymineralic inclusions within clinopyroxene and garnet megacrysts from Lac de Gras kimberlites, Canada. Contrib. Mineral. Petrol. 171, 65.
Bussweiler, Y., Pearson, D.G., Stachel, T., Kjarsgaard, B.A., 2018. Cr-rich megacrysts of clinopyroxene and garnet from Lac de Gras kimberlites, Slave Craton, Canada – implications for the origin of clinopyroxene and garnet in cratonic lherzolites. Mineral. Petrol. 112, 583–596.
Cookenboo, H., 1999. Emplacement history of th Jericho (JD-1) kimberlite pipe. Northern Canada Proceedings of the VIIth International Kimberlite Conference, pp. 125–133.
Davies, G.R., Spriggs, A.J., Nixon, P.H., 2001. A non-cognate origin for the Gibeon Kimberlite Megacryst Suite, Namibia: implications for the origin of Namibian Kimberlites. J. Petrol. 42, 159–172.
Dawson, J.B., 1980. Kimberlites and their Xenoliths. Springer-Verlag, New York.
De Bruin, D., 2005. Multiple compositional megacryst groups from the Uintjiesberg and Witberg kimberlites, South Africa. S. Afr. J. Geol. 108, 233–246.
Deines, P., 2002. The carbon isotope geochemistry of mantle xenoliths. Earth Sci. Rev. 58, 247–278.
Doucet, L.S., Ionov, D.A., Golovin, A.V., Pokhilenko, N.P., 2012. Depth, degrees and tectonic settings of mantle melting during craton formation: inferences from major and trace element compositions of spinel harzburgite xenoliths from the Udachnaya kimberlite, Central Siberia. Earth Planet. Sci. Lett. 359-360, 206–218.
Drozdov, A.V., Sukhov, S.S., 2008. A variety of natural systems of industrial groundwater on siberian platform. Water Res. 3, 264–273.
Eggler, D.H., McCallum, M.E., Smith, C.B.H., 1979. Megacryst assemblages in kimberlite from northern Colorado and southern Wyoming: petrology, geothermometry-barometry, and areal distribution. In: Boyd, F.R., Meyer, H.O.A. (Eds.), The Mantle Sample: Inclusion in Kimberlites and Other Volcanics. American Geophysical Union, pp. 213–226.
Fedortchouk, Y., Canil, D., 2004. Intensive variables in Kimberlite Magmas, Lac de Gras, Canada and implications for diamond survival. J. Petrol. 45, 1725–1745.
Giuliani, A., Kamenetsky, V.S., Phillips, D., Kendrick, M.A., Wyatt, B.A., Goemann, K., 2012. Nature of alkali-carbonate fluids in the sub-continental lithospheric mantle. Geology 40, 967–970.
Giuliani, A., Phillips, D., Kamenetsky, V.S., Fiorentini, M.L., Farquhar, J., Kendrick, M.A., 2014. Stable isotope (C, O, S) compositions of volatile-rich minerals in kimberlites: a review. Chem. Geol. 374-375, 61–83.
Giuliani, A., Soltys, A., Phillips, D., Kamenetsky, V.S., Maas, R., Goemann, K., Woodhead, J.D., Drysdale, R., Griffin, W.L., 2017. The final stages of kimberlite petrogenesis: Petrography, mineral chemistry, melt inclusions and Sr-C-O isotope geochemistry of the Bultfontein kimberlite (Kimberley, South Africa). Chem. Geol. 455, 342–356.
Golovin, A.V., Sharygin, V.V., Pokhilenko, N.P., 2007. Melt inclusions in olivine phenocrysts in unaltered kimberlites from the Udachnaya-East pipe, Yakutia: some aspects of kimberlite magma evolution during late crystallization stages. Petrology 15, 168–183.
Golovin, A.V., Sharygin, I.S., Korsakov, A.V., 2017. Origin of alkaline carbonates in kimberlites of the Siberian craton: evidence from melt inclusions in mantle olivine of the Udachnaya-East kimberlite. Chem. Geol. 455, 357–375.
Golovin, A.V., Sharygin, I.S., Kamenetsky, V.S., Korsakov, A.V., Yaxley, G.M., 2018. Alkali-carbonate melts from the base of cratonic lithospheric mantle: links to kimberlites. Chem. Geol. 483, 261–274.
Graham, I., Burgess, J.L., Bryan, D., Ravenscroft, P.J., Thomas, E., Doyle, B.J., Hopkings, R., Armstrong, K.A., 1999. Exploration history and geology of the Diavik kimberlites. Lac de Gras, Northwest Territories, Canada. In: Gurney, K.A., et al. (Eds.), Proceedings of the 7th International Kimberlite Conference, Cape Town, pp. 262–279.
Gurney, J.J., Jakob, W.R.O., Dawson, J.B., 1979. Megacrysts from the Monastery kimberlite pipe, South Africa. In: Boyd, F.R., Meyer, H.O.A. (Eds.), The Mantle Sample: Inclusions in Kimberlites and Other Volcanics. American Geophysical Union, pp. 227–243.
Harte, B., 1983. Mantle peridotites and processes - the kimberlite sample. In: Hawkesworth, C.J., Norry, M.J. (Eds.), Continental Basalt and Mantle Xenoliths. Shiva, Nantwich, pp. 46–91.
Harte, B., Gurney, J.J., 1981. The mode of formation of the Cr poor megacrystic suites from kimberlites. J. Geol. 89, 749–753.
Heaman, L.M., Creaser, R.A., Cookenboo, H.O., Chacko, T., 2006. Multi-stage modification of the northern slave mantle lithosphere: evidence from zircon- and diamond-bearing eclogite xenoliths entrained in Jericho Kimberlite, Canada. J. Petrol. 47, 821–858.
Hops, J.J., Gurney, J.J., Harte, B., 1992. The jagersfontein Cr-poor megacryst suite — towards a model for megacryst petrogenesis. J. Volcanol. Geotherm. Res. 50, 143–160.
Howarth, G.H., Büttner, S.H., 2019. New constraints on archetypal South African kimberlite petrogenesis from quenched glass-rich melt inclusions in olivine megacrysts. Gondwana Res. 68, 116–126.
Ionov, D.A., Doucet, L.S., Pogge von Strandmann, P.A.E., Golovin, A.V., Korsakov, A.V., 2017. Links between deformation, chemical enrichments and Li-isotope compositions in the lithospheric mantle of the central Siberian craton. Chem. Geol. 475, 105–121.
Jochum, K.P., Ulrike, W., Stoll, B., Kuzmin, D., Yang, Q., Raczek, I., Jacob, D.E., Stracke, A., Birbaum, K., Frick, D.A., Günther, D., Enzweiler, J., 2011. Determination of reference values for NIST SRM 610–617 glasses following ISO guidelines. Geostand. Geoanal. Res. 35, 397–429.
Kamenetsky, V.S., Yaxley, G.M., 2015. Carbonate–silicate liquid immiscibility in the mantle propels kimberlite magma ascent. Geochim. Cosmochim. Acta 158, 48–56.
Kamenetsky, M.B., Sobolev, A.V., Kamenetsky, V.S., Maas, R., Danyushevsky, L.V., Thomas, R., Pokhilenko, N.P., Sobolev, N.V., 2004. Kimberlite melts rich in alkali chlorides and carbonates: a potent metasomatic agent in the mantle. Geology 32, 845–848.
Kamenetsky, V.S., Kamenetsky, M.B., Sharygin, V.V., Golovin, A.V., 2007. Carbonate-chloride enrichment in fresh kimberlites of the Udachnaya-East pipe, Siberia: a clue to physical properties of kimberlite magmas? Geophys. Res. Lett. 34, L09316.
Kamenetsky, V.S., Kamenetsky, M.B., Sobolev, A.V., Golovin, A.V., Sharygin, V.V., Pokhilenko, N.P., Sobolev, N.V., 2009a. Can pyroxenes be liquidus minerals in the kimberlite magma? Lithos 112S, 213–222.
Kamenetsky, V.S., Kamenetsky, M.B., Weiss, Y., Navon, O., Nielsen, T.F.D., Mernagh, T.P., 2009b. How unique is the Udachnaya-East kimberlite? Comparison with kimberlites from the Slave Craton (Canada) and SW Greenland. Lithos 112S, 334–346.
Kamenetsky, V.S., Maas, R., Kamenetsky, M.B., Paton, C., Phillips, D., Golovin, A.V., Gornova, M.A., 2009c. Chlorine from the mantle: magmatic halides in the Udachnaya-East kimberlite, Siberia. Earth Planet. Sci. Lett. 285, 96–104.
Kamenetsky, V.S., Kamenetsky, M.B., Golovin, A.V., Sharygin, V.V., Maas, R., 2012. Ultrafresh salty kimberlite of the Udachnaya-East pipe (Yakutia, Russia): a petrological oddity or fortuitous discovery? Lithos 152, 173–186.
Kamenetsky, V.S., Grutter, H., Kamenetsky, M.B., Goemann, K., 2013. Parental carbonatitic melt of the Koala kimberlite (Canada): constraints from melt inclusions in olivine and Cr-spinel, and groundmass carbonate. Chem. Geol. 353, 96–111.
Kamenetsky, V.S., Belousova, E.A., Giuliani, A., Kamenetsky, M.B., Goemann, K., Griffin, W.L., 2014a. Chemical abrasion of zircon and ilmenite megacrysts in the Monastery kimberlite: implications for the composition of kimberlite melts. Chem. Geol. 383, 76–85.
Kamenetsky, V.S., Golovin, A.V., Maas, R., Giuliani, A., Kamenetsky, M.B., Weiss, Y., 2014b. Towards a new model for kimberlite petrogenesis: evidence from unaltered kimberlites and mantle minerals. Earth Sci. Rev. 139, 145–167.
Kargin, A.V., Sazonova, L.V., Nosova, A.A., Lebedeva, N.M., Tretyachenko, V.V., Abersteiner, A., 2017. Cr-rich clinopyroxene megacrysts from the Grib kimberlite, Arkhangelsk province, Russia: Relation to clinopyroxene–phlogopite xenoliths and evidence for mantle metasomatism by kimberlite melts. Lithos 292-293, 34–48.
Kinny, P.D., Compston, W., Bristow, J.W., Williams, I.S., 1989. Archaean mantle xenocrysts in a Permian kimberlite: two generations of kimberlitic zircon in Jwaneng DK2, southern Botswana. In: Glover, J.E., Harris, P.G. (Eds.), Kimberlites and Related Rocks. (Ed.), 4th International Kimberlite Conference. Geological Society of Australia, Perth, pp. 833–842.
Kinny, P.D., Griffin, B.J., Heaman, L.M., Brakhfogel, F.F., Spetsius, Z.V., 1997. SHRIMP U-Pb ages of perovskite from Yakutian kimberlites. Geol. Geofiz. 38, 91–99.
Kjarsgaard, B.A., Wilkinson, L., Armstrong, J., 2002. Geology, Lac de Gras kimberlite field, Central Slave Province, Northwest Territories - Nunavut, (NTS 76C, D, E, F), 1: 250,000 scale color map with descriptive notes Geological Survey of Canada, Open File 3228.
Kjarsgaard, B.A., Pearson, D.G., Tappe, S., Nowell, G.M., Dowall, D.P., 2009. Geochemistry of hypabyssal kimberlites from Lac de Gras, Canada: comparisons to a global database and applications to the parent magma problem. Lithos 112S, 236–248.
Kopylova, M.G., Hayman, P., 2008. Petrology and textural classification of the Jericho kimberlite, northern Slave Province, Nunavut, Canada. Can. J. Earth Sci. 45, 701–723.
Kopylova, M.G., Russell, J.K., Cookenboo, H., 1999. Petrography and chemistry of the Jericho kimberlite (Slave Craton, Northern Canada). Proceedings of the VIIth International Kimberlite Conference, pp. 468–479.
Kopylova, M.G., Nowell, G.M., Pearson, D.G., Markovic, G., 2009. Crystallization of megacrysts from protokimberlitic fluids: Geochemical evidence from high-Cr megacrysts in the Jericho kimberlite. Lithos 112, 284–295.
Kopylova, M.G., Kostrovitsky, S.I., Egorov, K.N., 2013. Salts in southern Yakutian kimberlites and the problem of primary alkali kimberlite melts. Earth Sci. Rev. 119, 1–16.
Kostrovitskiy, S.I., Kopylova, M.G., Egorov, K.N., Yakovlev, D.A., 2013. The Exceptionally Fresh Udachnaya-East Kimberlite: evidence for Brine and Evaporite Contamination. In: Pearson, D.G., et al. (Eds.), Proceedings of the 10th International Kimberlite Conference. Geological Society of India, Bangalore, pp. 75–91.
Kostrovitsky, S.I., Malkovets, V.G., Verichev, E.M., Garanin, V.K., Suvorova, L.V., 2004. Megacrysts from the Grib kimberlite pipe (Arkhangelsk Province, Russia). Lithos 77, 511–523.
le Roex, A.P., Bell, D.R., Davis, P., 2003. Petrogenesis of group I kimberlites from Kimberley, South Africa: evidence from bulk-rock geochemistry. J. Petrol. 44, 2261–2286.
Longerich, H.P., Jackson, S.E., Gunther, D., 1996. Laser ablation inductively coupled plasma mass spectrometric transient signal data acquisition and analyte concentration calculation. J. Anal. Atom. Spectrom. 11, 899–904.

Luth, R.W., 2009. The activity of silica in kimberlites, revisited. Contrib. Mineral. Petrol. 158, 283–294.
Malarkey, J., Pearson, D.G., Kjarsgaard, B.A., Davidson, J.P., Nowell, G.M., Ottley, C.J., Stammer, J., 2010. From source to crust: tracing magmatic evolution in a kimberlite and a melilitite using microsample geochemistry. Earth Planet. Sci. Lett. 299, 80–90.
Mernagh, T.P., Kamenetsky, V.S., Kamenetsky, M.B., 2011. A Raman microprobe study of melt inclusions in kimberlites from Siberia, Canada, SW Greenland and South Africa. Spectrochim. Acta A Mol. Biomol. Spectrosc. 80, 82–87.
Merry, M., le Roex, A., 2007. Megacryst suites from the Lekkerfontein and Uintjiesberg kimberlites, southern Africa: evidence for a non-cognate origin. S. Afr. J. Geol. 110, 597–610.
Mitchell, R.H., 1972. Composition of perovskite in kimberlite. Amer. Miner. 57, 1748–1753.
Mitchell, R.H., 1986. Kimberlites: Mineralogy, Geochemistry and Petrology. Plenum Publishing Company, New York.
Mitchell, R.H., 2008. Petrology of hypabyssal kimberlites: Relevance to primary magma compositions. J. Volcanol. Geotherm. Res. 174, 1–8.
Mitchell, R.H., 2013. Oxygen isotope studies of serpentine in kimberlite. Proceedings of the 10th International Kimberlite Conference. Geological Society of India, Bangalore, pp. 1–12.
Moore, A.E., Lock, N.P., 2001. The origin of mantle-derived megacrysts and sheared peridotites-evidence from kimberlites in the northern Lesotho - Orange Free State (South Africa) and Botswana pipe clusters. S. Afr. J. Geol. 104, 23–38.
Moss, S., Russell, J.K., Andrews, G.D.M., 2008. Progressive infilling of a kimberlite pipe at Diavik, Northwest Territories, Canada: insights from volcanic facies architecture, textures, and granulometry. J. Volcanol. Geotherm. Res. 174, 103–116.
Moss, S., Russell, J.K., Brett, R.C., Andrews, G.D.M., 2009. Spatial and temporal evolution of kimberlite magma at A154N, Diavik, Northwest Territories, Canada. Lithos 112S, 541–552.
Nimis, P., Taylor, W.R., 2000. Single clinopyroxene thermobarometry for garnet peridotites. Part I. Calibration and testing of a Cr-in-Cpx barometer and an enstatite-in-Cpx thermometer. Contrib. Mineral. Petrol. 139, 541–554.
Nowell, G.M., Pearson, D.G., Bell, D.R., Carlson, R.W., Smith, C.B., Kempton, P.D., Noble, S.R., 2004. Hf Isotope systematics of kimberlites and their megacrysts: new constraints on their source regions. J. Petrol. 45, 1583–1612.
Pilbeam, L.H., Nielsen, T.F.D., Waight, T.E., 2013. Digestion fractional crystallization (DFC): an important process in the genesis of kimberlites. evidence from olivine in the Majuagaa Kimberlite, Southern West Greenland. J. Petrol. 54, 1399–1425.
Pivin, M., Féménias, O., Demaiffe, D., 2009. Metasomatic mantle origin for Mbuji-Mayi and Kundelungu garnet and clinopyroxene megacrysts (Democratic Republic of Congo). Lithos 112, 951–960.
Price, S.E., Russell, J.K., Kopylova, M.G., 2000. Primitive magma from the Jericho Pipe, N.W.T., Canada: constraints on primary kimberlite melt chemistry. J. Petrol. 41, 789–808.
Roedder, E., 1984. Fluid Inclusions. Book Crafters Inc., Michigan.
Roeder, P.L., Schulze, D.J., 2008. Crystallization of groundmass spinel in kimberlite. J. Petrol. 49, 1473–1495.
Sarkar, C., Heaman, L.M., Pearson, D.G., 2015. Duration and periodicity of kimberlite volcanic activity in the Lac de Gras kimberlite field, Canada and some recommendations for kimberlite geochronology. Lithos 218-219, 155–166.
Schulze, D., 1985. Evidence for primary kimberlitic liquids in megacrysts from kimberlites in Kentucky, USA. J. Geol. 93, 75–79.
Schulze, D.J., Valley, J.R., Bell, D.R., Spicuzza, M.J., 2001. Oxygen isotope variations in Cr-poor megacrysts from kimberlite. Geochim. Cosmochim. Acta 65, 4375–4384.
Sharygin, I.S., Golovin, A.V., Pokhilenko, N.P., 2012. Djerfisherite in xenoliths of sheared peridotite in the Udachnaya-East pipe (Yakutia): origin and relationship with kimberlitic magmatism. Russ. Geol. Geophys. 53, 247–261.
Sharygin, I.S., Golovin, A.V., Korsakov, A.V., Pokhilenko, N.P., 2013. Eitelite in sheared peridotite xenoliths from Udachnaya-East kimberlite pipe (Russia) – a new locality and host rock type. Eur. J. Mineral. 25, 825–834.
Sharygin, I.S., Litasov, K.D., Shatskiy, A., Golovin, A.V., Ohtani, E., Pokhilenko, N.P., 2015. Melting phase relations of the Udachnaya-East Group-I kimberlite at 3.0–6.5 GPa: Experimental evidence for alkali-carbonatite composition of primary kimberlite melts and implications for mantle plumes. Gondwana Res. 28, 1391–1414.
Sharygin, I.S., Litasov, K.D., Shatskiy, A., Safonov, O.G., Golovin, A.V., Ohtani, E., Pokhilenko, N.P., 2017. Experimental constraints on orthopyroxene dissolution in alkali carbonate melts in the lithospheric mantle: Implications for kimberlite melt composition and magma ascent. Chem. Geol. 455, 44–56.
Shee, S.R., Gurney, J.J., 1979. The mineralogy of xenoliths from Orapa, Botswana. In: Boyd, F.R., Meyer, H.O.A. (Eds.), The Mantle Sample: Inclusions in Kimberlites and Other Volcanics. American Geophysical Union, pp. 37–49.
Smart, K.A., Heaman, L.M., Chacko, T., Simonetti, A., Kopylova, M., Mah, D., Daniels, D., 2009. The origin of high-MgO diamond eclogites from the Jericho Kimberlite, Canada. Earth Planet. Sci. Lett. 284, 527–537.
Solov'eva, L.V., Lavrent'ev, Y.G., Egorov, K.N., Kostrovitskii, S.I., Korolyuk, V.N., Suvorova, L.F., 2008. The genetic relationship of the deformed peridotites and garnet megacrysts from kimberlites with asthenospheric melts. Russ. Geol. Geophys. 49, 207–224.
Soltys, A., Giuliani, A., Phillips, D., Kamenetsky, V.S., Maas, R., Woodhead, J., Rodemann, T., 2016. In-situ assimilation of mantle minerals by kimberlitic magmas — Direct evidence from a garnet wehrlite xenolith entrained in the Bultfontein kimberlite (Kimberley, South Africa). Lithos 256-257, 182–196.
Soltys, A., Giuliani, A., Phillips, D., 2018. Crystallisation sequence and magma evolution of the De Beers dyke (Kimberley, South Africa). Mineral. Petrol. 112, 503–518.
Sparks, R.S.J., Baker, L., Brown, R.J., Field, M., Schumacher, J., Stripp, G., Walters, A., 2006. Dynamical constraints on kimberlite volcanism. J. Volcanol. Geotherm. Res. 155, 18–48.
Sparks, R.S.J., Brooker, R.A., Field, M., Kavanagh, J., Schumacher, J.C., Walter, M.J., White, J., 2009. The nature of erupting kimberlite melts. Lithos 112S, 429–438.
Stripp, G.R., Field, M., Schumacher, J.C., Sparks, R.S.J., Cressey, G., 2006. Post-emplacement serpentinization and related hydrothermal metamorphism in a kimberlite from Venetia, South Africa. J. Metamorph. Geol. 24, 515–534.
Sun, S.-S., McDonough, W.F., 1989. Chemical and isotopic systematics of oceanic basalts: implications for mantle composition and processes. In: Saunders, A.D., Norry, M.J. (Eds.), Magmatism in the Ocean Basins. Geological Society Special Publication, pp. 313–345.
Tappe, S., Pearson, D.G., Nowell, G., Nielsen, T., Milstead, P., Muehlenbachs, K., 2011. A fresh isotopic look at Greenland kimberlites: cratonic mantle lithosphere imprint on deep source signal. Earth Planet. Sci. Lett. 305, 235–248.
Tappe, S., Kjarsgaard, B.A., Kurszlaukis, S., Nowell, G.M., Phillips, D., 2014. Petrology and Nd–Hf isotope geochemistry of the Neoproterozoic Amon Kimberlite Sills, Baffin Island (Canada): evidence for deep mantle magmatic activity linked to supercontinent cycles. J. Petrol. 55, 2003–2042.
Tappe, S., Romer, R.L., Stracke, A., Steenfelt, A., Smart, K.A., Muehlenbachs, K., Torsvik, T.H., 2017. Sources and mobility of carbonate melts beneath cratons, with implications for deep carbon cycling, metasomatism and rift initiation. Earth Planet. Sci. Lett. 466, 152–167.
van Achterbergh, E., Griffin, B.J., Ryan, C.G., O'Reilly, S.Y., Pearson, N.J., Kivi, K., Doyle, B.J., 2002. Subduction signature for quenched carbonatites from the deep lithosphere. Geology 30, 743–746.
van Achterbergh, E., Griffin, W.L., Ryan, C.G., O'Reilly, S.Y., Pearson, N.J., Kivi, K., Doyle, B.J., 2004. Melt inclusions from the deep Slave lithosphere: implications for the origin and evolution of mantle-derived carbonatite and kimberlite. Lithos 76, 461–474.

Appendix 8.1 Supplementary Figures

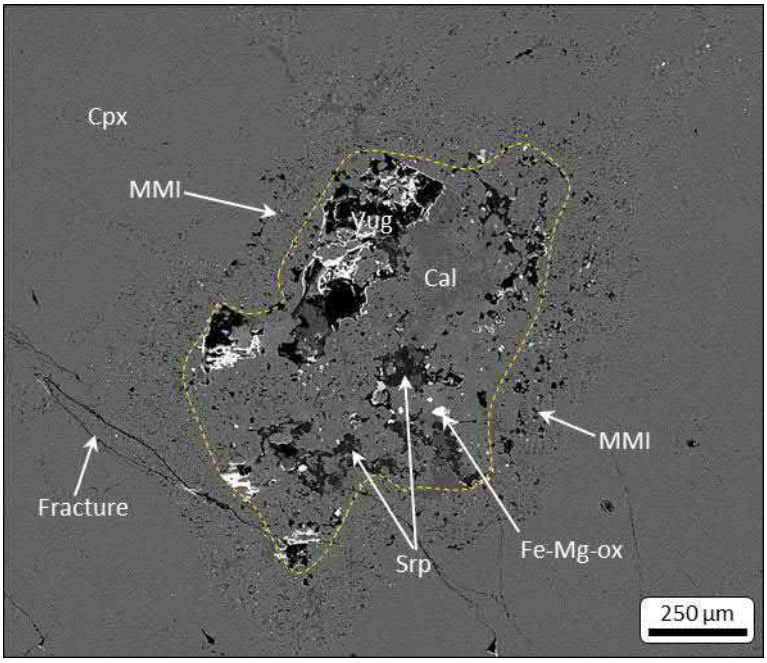

Supplementary Figure S1. Back-scatter electron (BSE) SEM images of a polymineralic inclusion (shaped marked by yellow dotted line) in sample clinopyroxene (Cpx) sample UV-IG. MMI: melt micro inclusions (<5 µm in size), which forms a "spongy" texture around the polymineralic melt inclusion, Cal: calcite, Srp: serpentine, Ox: oxide. Completely black areas represent vugs. The bright interstitial patches surrounding vugs is due to charging.

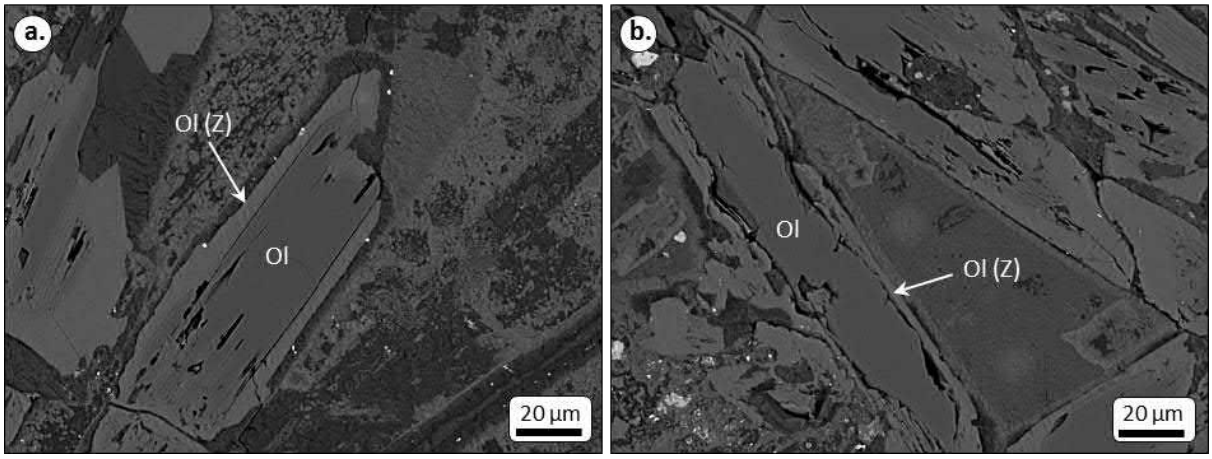

Supplementary Figure S2. Back-scatter electron (BSE) SEM images of olivine (Ol) surrounded by thin zoned rims of more Fe-rich olivine (Ol (Z)) in clinopyroxene-hosted polymineralic inclusions from sample A154-27B.

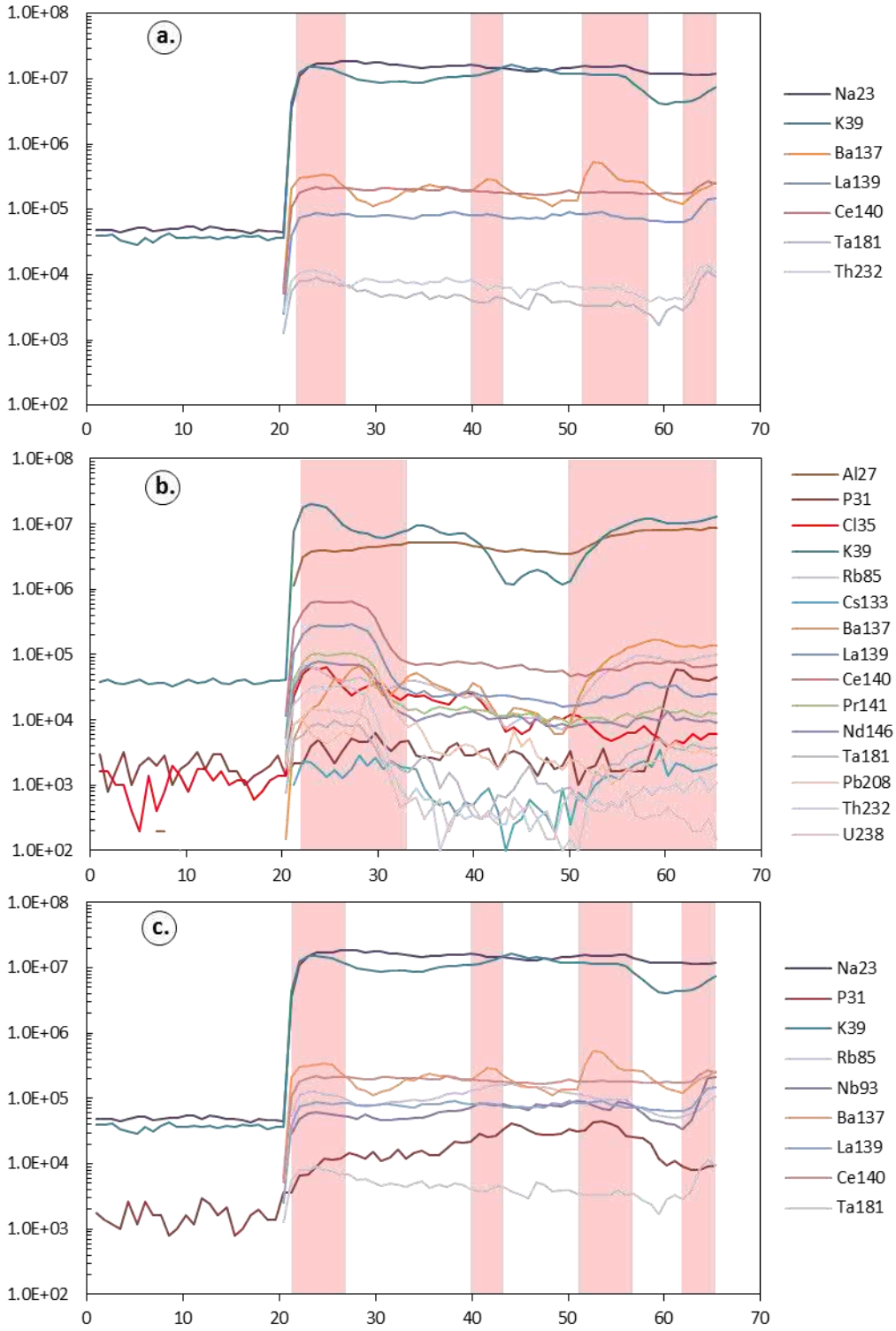

Supplementary Figure S3. Representative LA-ICP-MS analyses of (a) olivine (UV9774-ol) and (b, c) clinopyroxene (UV9774-cpx) megacrysts, showing ablated melt micro inclusion trails, which are represented in the red shaded zone. These inclusions are extremely heterogeneous in size and composition, which is reflected by positive anomalies in elements such as alkalis (Na, K, Ba, Rb, Cs), light rare earth elements (LREE), Cl, Nb, Ta, U, Th, P and Al. These positive anomalies usually occur in synchronisation with two or more other elements.

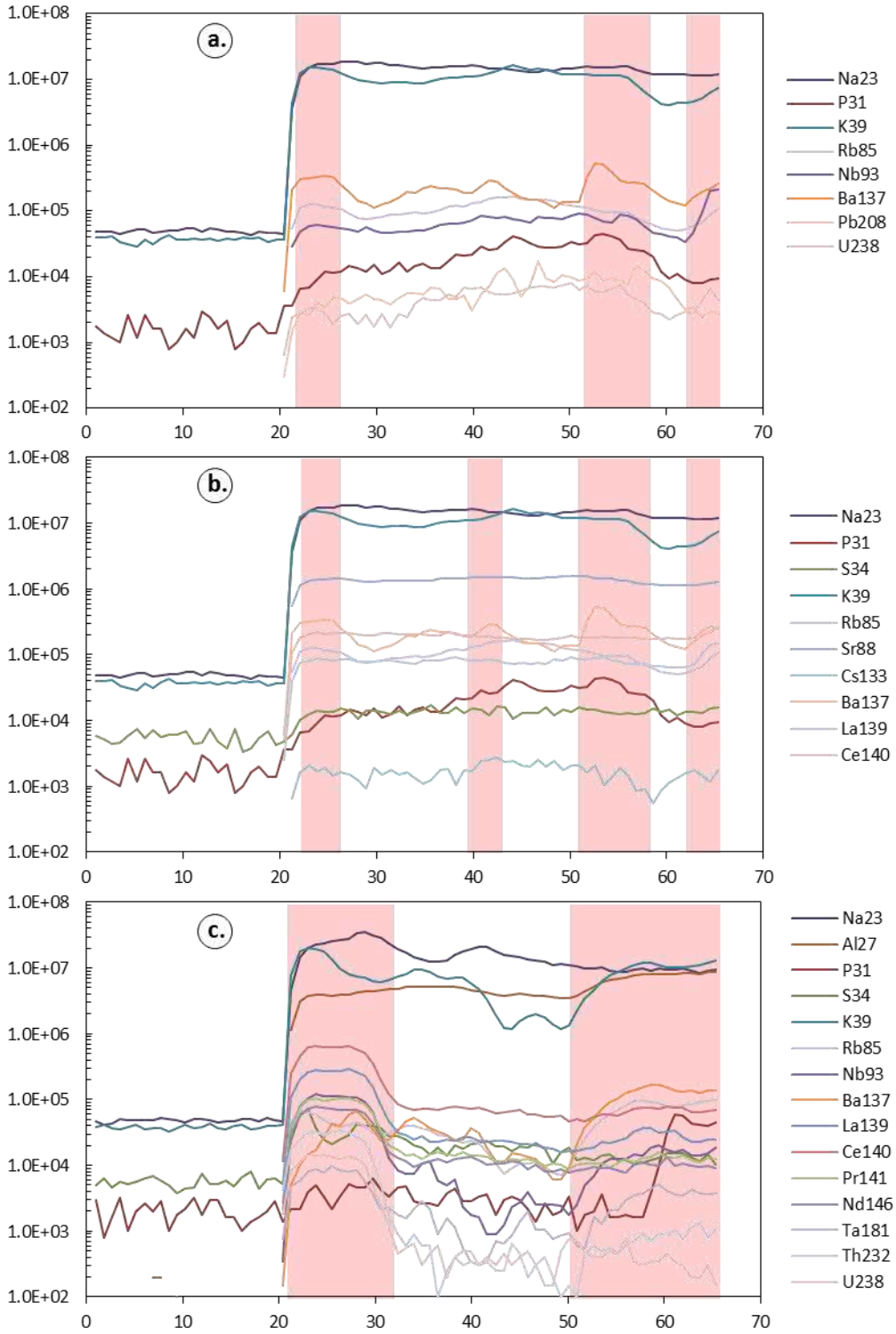

Supplementary Figure S4. Representative LA-ICP-MS analyses of clinopyroxene megacrysts from samples (a) LDC7, (b) JER03-1 and (c) A154-27, showing ablated melt micro inclusion trails, which are represented in the red shaded zone. These inclusions are extremely heterogeneous in size and composition, which is reflected by positive anomalies in elements such as alkalis (Na, K, Ba, Rb, Cs), light rare earth elements (LREE), S, Cl, Nb, Ta, U, Th, P and Al. These positive anomalies usually occur in synchronisation with two or more other elements.

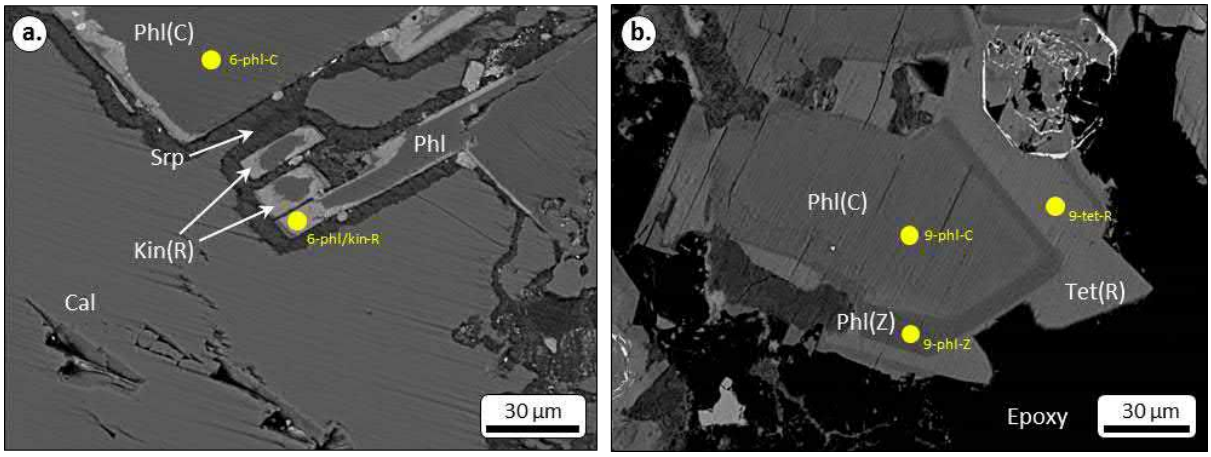

Supplementary Figure S5. Back-scatter electron (BSE) SEM images of zoned phlogopite inclusions in polymineralic inclusions in samples (a) JER03 and (b) UV9774-cpx. Analyses points (yellow) are shown in Supplementary Table S3. Cal: calcite, serpentine: Srp, Phl: phlogopite, Kin: kinoshitalite, Tet: tetraferriphlogopite, C: core, Z: intermediate zone, R: rim.

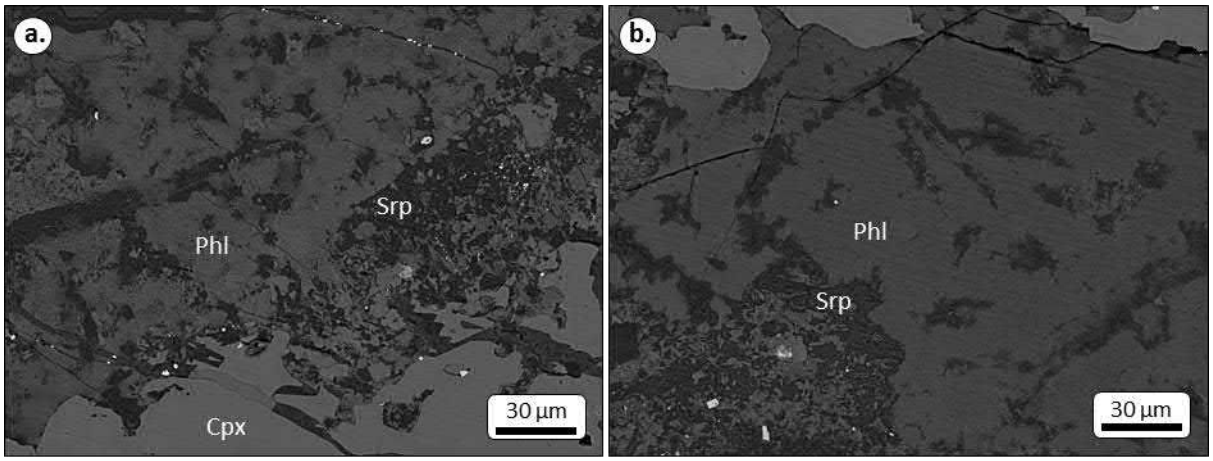

Supplementary Figure S6. Back-scatter electron (BSE) SEM images of phlogopite (Phl) in clinopyroxne-hosted (Cpx) polymineralic inclusions from sample A154-27B. Note the absence of crystal shape of phlogopite, mottled appearance and serpentinised (Srp) edges.

Appendix 8.2: Electronic Appendix – Supplementary Tables (EMPA)

Appendix 8.3: Electronic Appendix – Supplementary Tables (LA-ICPMS)

Lithos 358–359 (2020) 105405

Contents lists available at ScienceDirect

Lithos

journal homepage: www.elsevier.com/locate/lithos

Research Article

A genetic story of olivine crystallisation in the Mark kimberlite (Canada) revealed by zoning and melt inclusions

Adam Abersteiner [a,b,*], Vadim S. Kamenetsky [a,c], Karsten Goemann [d], Bruce A. Kjarsgaard [e], Thomas Rodemann [d], Maya Kamenetsky [a], Kathy Ehrig [f]

[a] School of Natural Sciences and Centre of Excellence in Ore Deposits (CODES), University of Tasmania, Hobart, Tasmania 7001, Australia
[b] Institute of Volcanology and Seismology, Far East Branch, Russian Academy of Sciences, 683006 Petropavlovsk-Kamchatsky, Russia
[c] Institute of Experimental Mineralogy RAS, Chernogolovka 142432, Russia
[d] Central Science Laboratory, University of Tasmania, Hobart, Tasmania 7001, Australia
[e] Geological Survey of Canada, 601 Booth Street, Ottawa, ON K1A 0E8, Canada
[f] BHP Olympic Dam, Adelaide, SA 5000, Australia

ARTICLE INFO

Article history:
Received 22 November 2019
Received in revised form 20 January 2020
Accepted 28 January 2020
Available online 30 January 2020

Keywords:
Kimberlite
Olivine
Zoning
Melt inclusion
Lac de Gras or Slave Craton

ABSTRACT

Elucidating the composition of primary kimberlite melts is essential to understanding the nature of their source, petrogenesis, rheology, transport and ultimately the origin of diamonds. Kimberlite rocks are typically comprised of abundant olivine (~25–60 vol%), which occurs as individual grains of variable size and morphology, and includes xenocrysts and zoned phenocrysts. Zoning patterns and inclusions in olivine can be used to decipher the petrogenetic history of kimberlites, starting from their generation in the mantle through to emplacement in the crust. This study examines well-preserved, euhedral, zoned olivine crystals from the Mark kimberlite (Lac de Gras, Canada). Olivine typically consists of xenocrystic cores, which are homogeneous in composition but vary widely between grains ($Fo_{88.1–93.6}$). These cores are in turn surrounded by (in order of crystallisation) magmatic rims and Mg-rich rinds ($Fo_{95.3–98.1}$). In addition, we document a new type of olivine zone ('outmost rind') that overgrows Mg-rich rinds.

Crystal and melt/fluid inclusions are abundant in olivine and preserve a record of kimberlite melt evolution. For the first time in the studies of kimberlite olivine, we report primary melt inclusions hosted in Mg-rich olivine rinds. In addition, we observe that pseudosecondary melt/fluid inclusions are restricted to interior olivine zones (cores, rims) and are considered to have formed prior to rind formation. Pseudosecondary melt/fluid inclusions are inferred to have been entrapped at depth, as evidenced by measured densities in thermometric experiments of CO_2 and decrepitation haloes, indicating a minimum entrapment pressure of ~200–450 MPa (or ~6–15 km). Both primary and pseudosecondary melt inclusions in olivine have daughter minerals dominated by Ca—Mg— and K-Na-Ba-Sr-bearing carbonates, K-Na-chlorides along with subordinate silicates (e.g., phlogopite, monticellite), Fe-Mg-Al-Ti-spinel, perovskite, phosphates and sulphates/sulphides and periclase. In addition to phases reported in primary melt inclusions, pseudosecondary melt inclusions contain more diverse and exotic daughter mineral assemblages, where they contain phases such as tetraferriphlogopite Ba- or K-sulphates, kalsilite and Na-phosphates. The daughter mineral assemblages are consistent with a silica-poor, alkali dolomitic carbonatite melt. We demonstrate that the different types of inclusions in olivine can assist in constraining the timing of multi-stage olivine growth and the composition of the crystallising melt.

The large variance in olivine zoning patterns, morphologies and Ni distribution (i.e. both coupling with and decoupling from Fo) indicates that olivine in the studied Mark kimberlite samples represent an accumulation of olivine, where olivine was derived from successive stages of the ascending magma and/or from multiple, but related pulses of magma. Primary and pseudosecondary melt/fluid inclusions in olivine indicate that a variably differentiated silica-poor, halogen-bearing, alkali-dolomitic melt crystallised and transported olivine in the Mark kimberlite.

1. Introduction

Kimberlites are ultramafic, silica-poor and volatile-rich ($CO_2 \pm H_2O$) igneous rocks that originate from the most deeply-derived magmas on Earth. Reconstructing the composition of the melt that gives rise to

* Corresponding author.
E-mail addresses: adam.abersteiner@utas.edu.au, adamba1742@gmail.com (A. Abersteiner).

https://doi.org/10.1016/j.lithos.2020.105405
0024-4937/

kimberlite rock is challenging, as there is uncertainty regarding the melt evolution *en route* to the surface, extent of contamination and volatile loss, and the effects of deuteric and post-emplacement alteration. Olivine is a key (~25 to 60 vol%; Brett et al., 2009; Clement et al., 1984; Giuliani, 2018; Kamenetsky et al., 2008; Mitchell, 2008) component of kimberlite rocks and is subdivided into two types on the basis of grain size and texture; these are larger (>0.5 mm) anhedral-to-rounded macrocrysts and smaller (<1 mm) euhedral phenocrysts (Mitchell, 1986; Moore, 1988). Olivine in kimberlites is usually zoned (Arndt et al., 2010; Boyd and Clement, 1977; Bussweiler et al., 2015; Howarth and Gross, 2019; Howarth and Taylor, 2016; Kamenetsky et al., 2008; Lim et al., 2018; Nielsen and Sand, 2008; Pilbeam et al., 2013) and therefore can provide invaluable insights into magma evolution starting from its formation in the mantle to its emplacement in the upper crust (see Giuliani, 2018). Furthermore, the evolutionary story of zoned olivine is reinforced by the study of crystal, melt and fluid inclusions (Abersteiner et al., 2018a, 2018b, 2018c, 2019; Golovin et al., 2007; Kamenetsky et al., 2004; Kamenetsky et al., 2008, 2009, 2012, 2013, 2014; Mernagh et al., 2011).

Earlier studies have attempted to reconstruct the nature of kimberlite melts using secondary inclusions entrapped along planar fractures, which were subsequently healed during olivine growth (e.g., Abersteiner et al., 2018b, 2018c; Giuliani et al., 2017; Golovin et al., 2007; Kamenetsky et al., 2004; Kamenetsky et al., 2014). However, the exact timing of melt entrapment in these inclusions is difficult to constrain, as this may occur at any stage or across multiple events, ranging from the timing of olivine cracking in the mantle through to ascent and emplacement in the crust (Brett et al., 2015). We present textural data to show that these inclusion trails in Mark kimberlite olivine are pseudosecondary (as defined by Roedder, 1984) in origin, like in most kimberlite studied to date. In contrast, there is a paucity of studies of primary (i.e. entrapped during crystal growth) melt inclusions in kimberlitic olivine (Giuliani et al., 2017), reflecting the difficulty in their identification and preservation in the magmatic overgrowths, which can be mechanically and chemically abraded during transport and/or serpentinisation.

This study of fresh olivine in the Mark kimberlite (Lac de Gras, Canada) provides new insights into different stages of olivine crystallisation and resorption, as well as the parental melt composition through the study of olivine zones, and primary and pseudosecondary melt/fluid and crystal inclusions. Our results demonstrate that olivine in the Mark kimberlite was crystallised from and transported by a silica-poor, halogen-bearing, alkali-dolomitic melt.

2. Sample description

The diamondiferous Mark kimberlite is located in the Lac de Gras kimberlite field, which is situated in the Archean Slave Province (Canada; Fig. 1). The kimberlite is a small (~100 - 150 m in diameter, based on geophysical interpretation) hypabyssal (coherent) body, which is poorly exposed in small outcrops and intruded cordierite porphyroblastic metagreywackes of the Yellowknife Supergroup (Davis and Kjarsgaard, 1997). No drill core data is available, which precludes understanding if this is in-fill of an open pipe, or, represents a blind plug. A Rb—Sr isochron age determination using macrocrystic phlogopite grains produced an age of ~47.5 ± 0.5 Ma (Davis and Kjarsgaard, 1997).

Multiple samples of outcrop and float were collected from the Mark kimberlite. For this study, we used the freshest sample (KIA93-K136), which is characterized by a macrocrystic texture (Fig. 2) dominated by abundant macrocrystic olivine (55 vol%), along with lesser amounts of macrocrystic phlogopite (with kinoshitalite rims), Cr-pyrope,

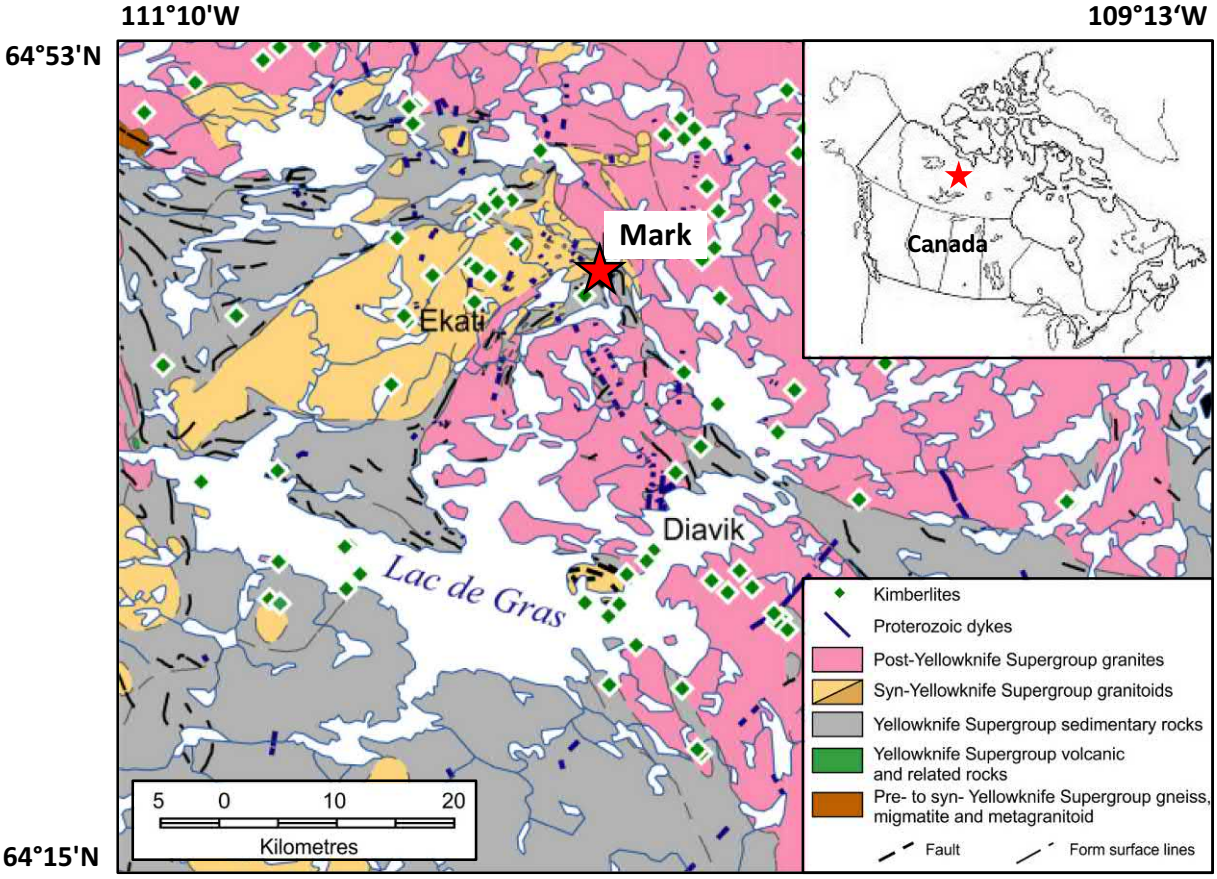

Fig. 1. Geological map of the central Slave Province showing the location of the Mark kimberlite in the Lac de Gras area (modified after Kjarsgaard et al., 2002).

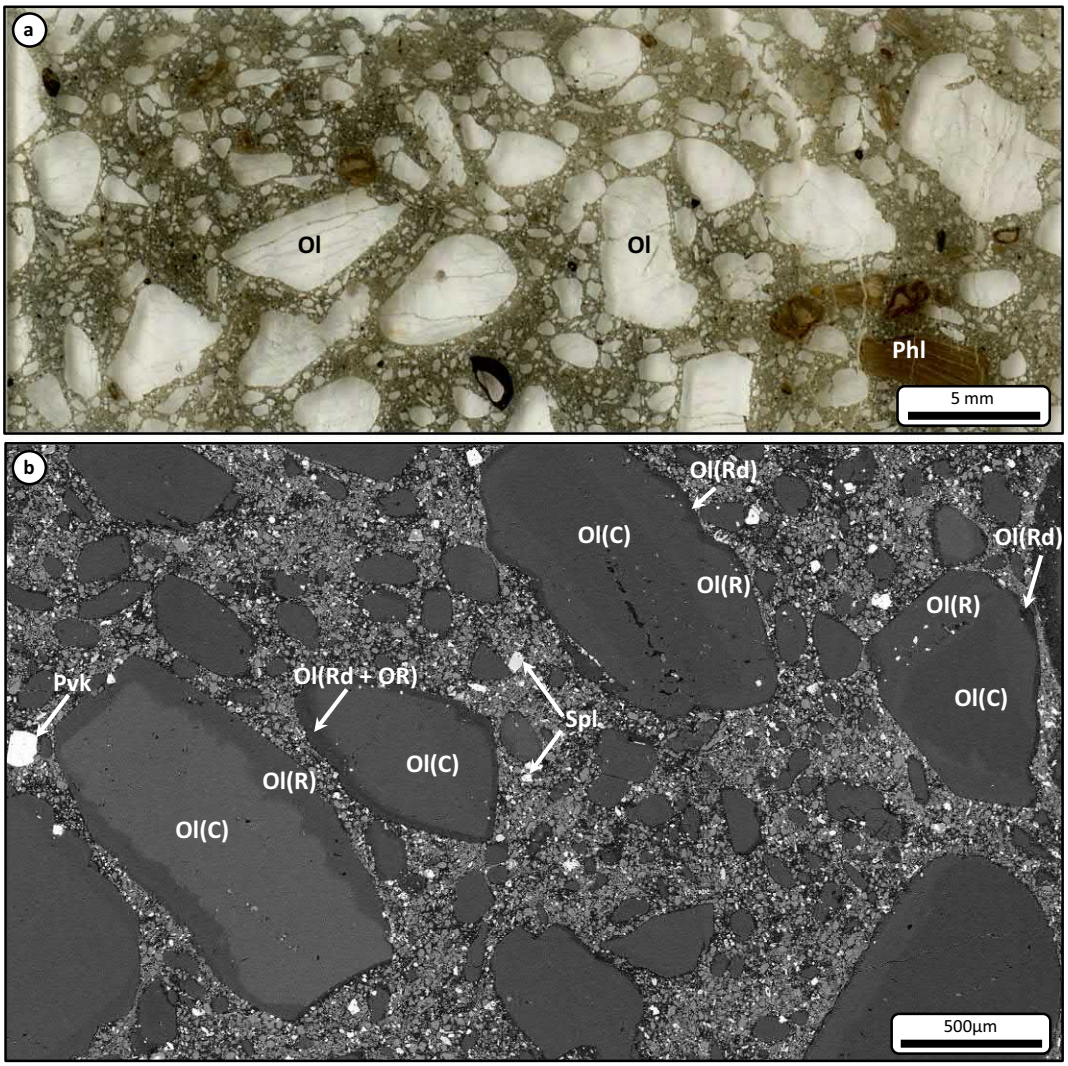

Fig. 2. (a) Optical photomicrograph in plane-polarised light of a thin section of the Mark kimberlite showing the distribution and morphology of macroscopic minerals. Ol: olivine, Phl: phlogopite. (b) Back-scattered electron (BSE) SEM images of the general groundmass petrography of the Mark kimberlite. Olivine grains exhibit a wide variety of zoning patterns, usually from brighter cores (C) towards darker (more Mg-rich) rims (R), which are in turn occasionally mantled by a Mg-rich rind (Ol(Rd)). Some grains exhibit opposite zoning (i.e. rims are more Fe-rich, or are brighter in BSE-imaging than the core). The contact between the olivine rinds and interior zones (cores, rims) can be uneven or contain embayments. Subhedral-to-euhedral monticellite (light grey) dominates the matrix along with subordinate perovskite (Pvk) and spinel (Spl). OR: outmost rind.

Cr-diopside and rare Mg-ilmenite. The groundmass is fine-grained (<1 mm) and consists of abundant monticellite (~20 vol%) along with euhedral olivine (micro)phenocrysts, zoned spinel (i.e. composed of titanian magnesian aluminous chromite (TIMAC; Mitchell, 1986) or chromite cores through to magnesian ulvöspinel magnetite (MUM) with overgrowth by pleonaste (and occasionally a thin rim of Mg-magnetite)), perovskite, apatite, kinoshitalite and Cu-Fe-sulphides, along with minor interstitial serpentine, brucite (~5–8 vol%) and carbonate (~4 vol%; i.e. calcite and rare witherite).

3. Olivine petrography and compositions

The petrography and composition of olivine were studied using an optical microscope, a scanning electron microscope (SEM) equipped with energy dispersive X-ray spectrometry (EDS) and an electron microprobe (EMP; see Supplementary Material for methodology). Analyses of olivine were conducted on one thin section, two grain mounts and nine polished rock chip mounts.

Olivine grains occur as: i) large (0.3–1.5 cm) rounded-to-anhedral macrocrysts and/or angular fragments, and ii) smaller (50 μm–2 mm) subhedral-to-euhedral (micro)phenocrysts (Figs. 2–6). The majority of olivine is fresh with insignificant or no replacement by secondary phases (i.e. serpentine/carbonate) along grain margins or internal fractures. Some olivine is occasionally partially replaced by rims of monticellite (Supplementary Fig. S1), similar to those described in the nearby Leslie kimberlite (Abersteiner et al., 2018a). In addition, some olivine grains contain embayments that are infilled with interlocking clusters (or mosaics) of euhedral re-crystallised olivine grains (or tablets) that vary widely in size from 10 to 200 μm (Supplementary Fig. S2). Individual olivine grains within these clusters exhibit different extinction angles under cross-polarised light due to their different orientations. Similar features were described in kimberlitic olivine from localities worldwide (Arndt et al., 2010; Brett et al., 2009; Cordier et al., 2015).

Despite recent advances attempting to present a comprehensive model to categorise the different compositional zones in kimberlitic olivine (see review by Giuliani, 2018), zoning patterns in olivine from the Mark kimberlite demonstrate that there are additional complications in the application of existing olivine terminology to different kimberlite localities. In this study, we adopt the most recent terminology presented by Lim et al. (2018) and Giuliani (2018). The majority of olivine in the studied Mark kimberlite exhibit distinct compositional variations, as observed in BSE-imaging (Figs. 2–6). Euhedral olivine crystals are usually zoned, where they consist of a core, which is generally homogenous in

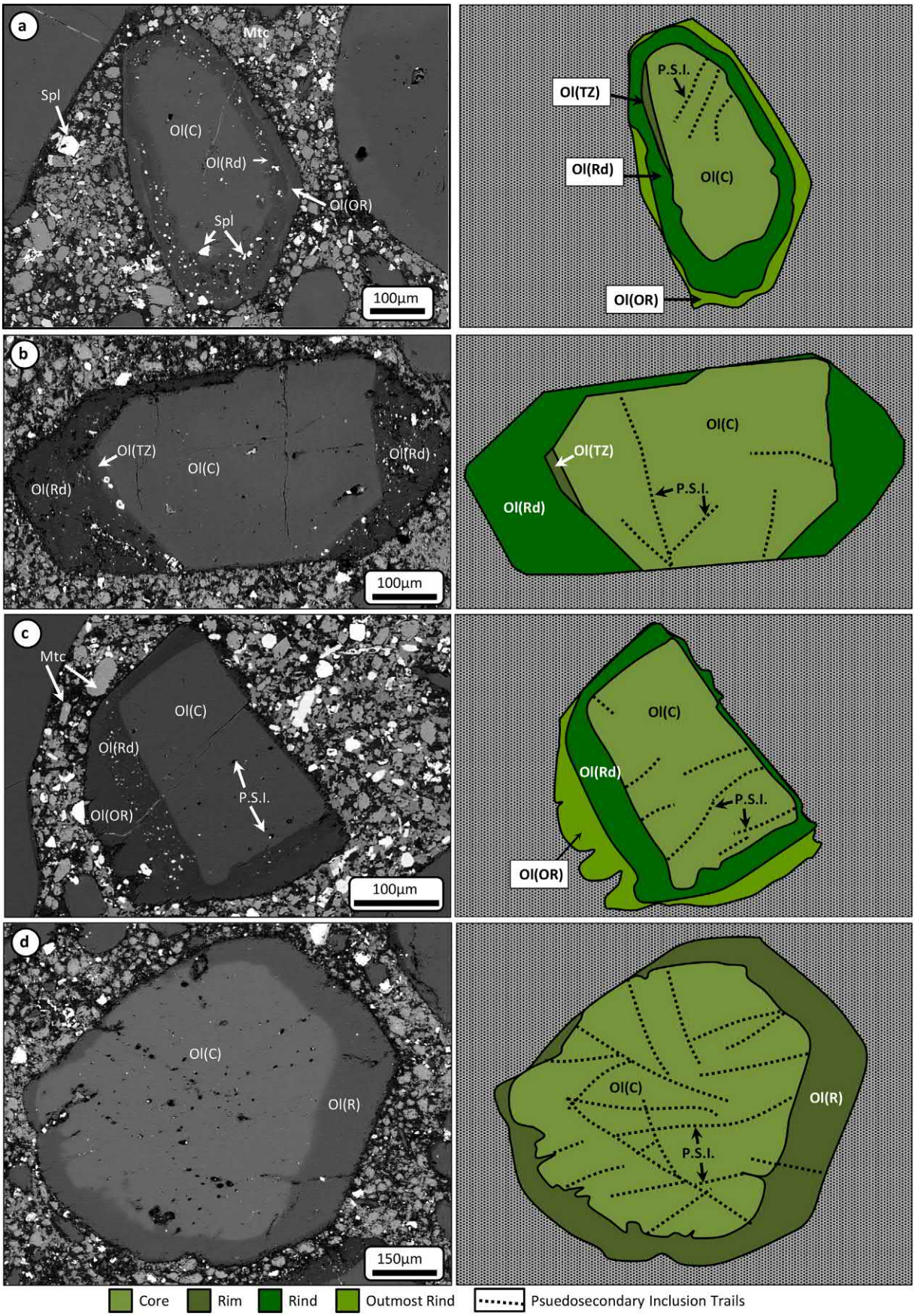

Fig. 3. Back-scattered electron (BSE) scanning electron microscope (SEM) images and schematic diagrams of zoned olivine (Ol) grains. C: core, TZ: transitional zone, R: rim, Rd: rind, OR: outmost rind, P.S.I.: pseudosecondary inclusion trails, Mtc: monticellite. Olivine cores may be surrounded by any combination of zones, but they will always occur in a specific order (i.e. core – rim – rind –outmost rind).

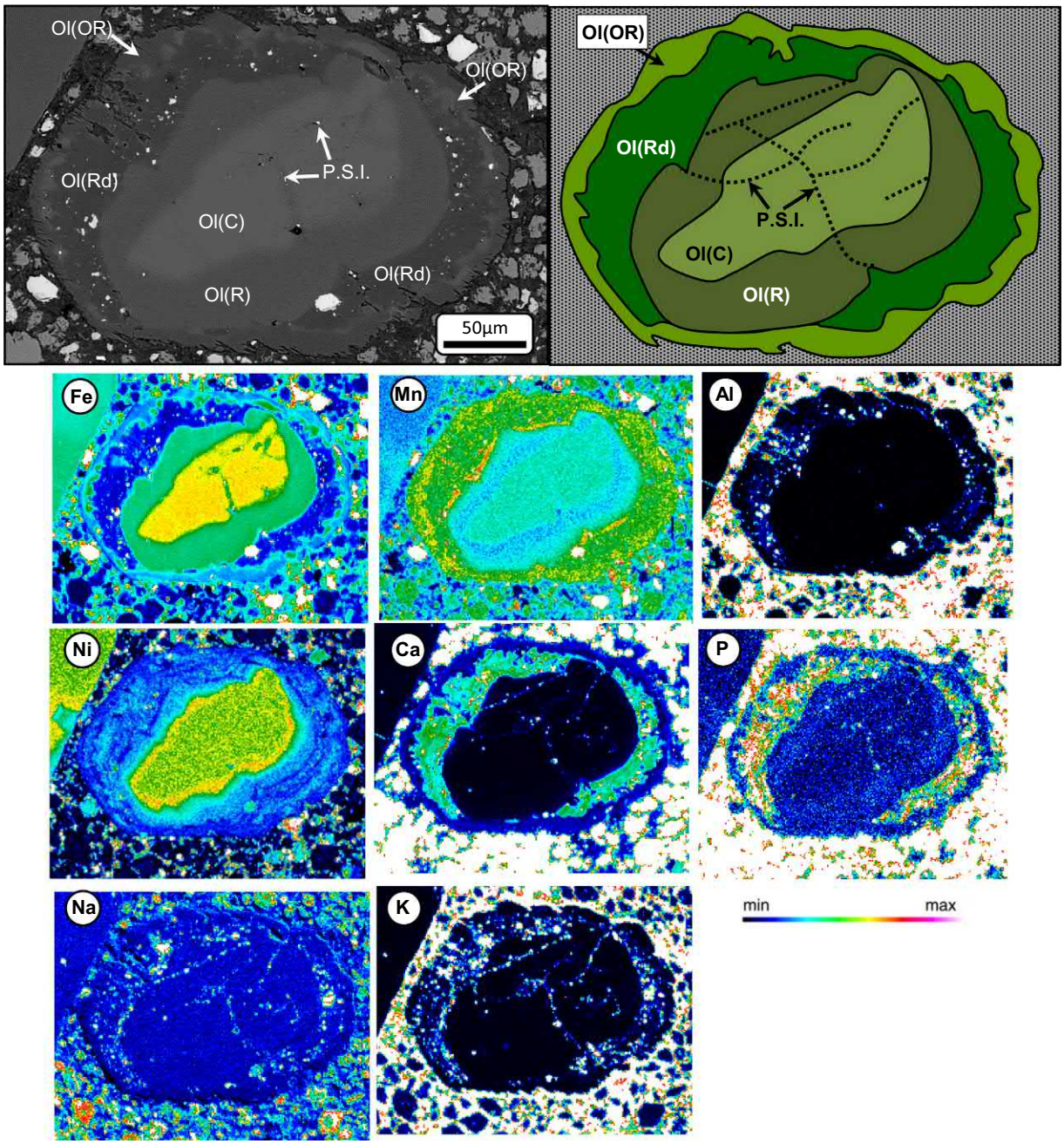

Fig. 4. Back-scattered electron (BSE) scanning electron microscope (SEM) image and schematic diagram of a zoned olivine (Ol) grain (core: C, and rim: R), which is surrounded by an Mg-rich rind (Rd). Electron microprobe (EMP) X-ray element maps show the rind to be enriched in P, Ca, Mn and depleted in Fe, Ni relative to the core. The compositional (wt%) range for each element map is: Fe: 0–8, Mn: 0–0.4, Al: 0–1, Ni: 0–0.5, Ca: 0–3, P: 0–0.1, Na: 0–0.3, K: 0–0.5. In addition, the olivine grain contains abundant primary melt inclusions (P.I.) within the rind, as well as trails of pseudosecondary secondary melt inclusions (P.S·I) that traverse the olivine interior (core and rims) and are terminated at rind or outmost rind interface. These inclusions are marked by enrichments in Na, K, P, Ca, Al and depletions in Si, Mg. These inclusions are likely represented by minerals such as alkali-carbonates, phosphates, spinel and monticellite. OR: outmost rind.

composition, but exhibit variability between grains (Fig. 7; Supplementary Table S1). The core may also contain a diffuse transitional zone which occurs along the margins between core and outer zones (Figs. 5, 6b). It is noteworthy that zones termed 'transitional' or 'internal' ('transitional zone' herein), which have been described in zoned olivine worldwide (Cordier et al., 2015; Howarth and Taylor, 2016; Lim et al., 2018; Pilbeam et al., 2013) are extremely rare features in the studied Mark kimberlite samples. The core is in turn typically concentrically surrounded by 'outer zones', which are comprised of rims and rinds. Previously, olivine rinds were interpreted to represent the final stage of olivine crystallisation from the late-stage kimberlite melt (Bussweiler et al., 2015; Giuliani, 2018; Lim et al., 2018). However, we present evidence of a previously undocumented type of olivine zone, which occasionally overgrows these rinds ('outmost rinds' herein; Figs. 2–6).

In general, there is large variability in zoning patterns in Mark kimberlite olivine. The 'outer zones' may be present in any combination surrounding olivine cores, but strictly follow a specific sequence of crystallisation (i.e. rim to rind to outmost rind; Figs. 2–6). In addition, the thicknesses of these zones (including presence of oscillatory zoning)

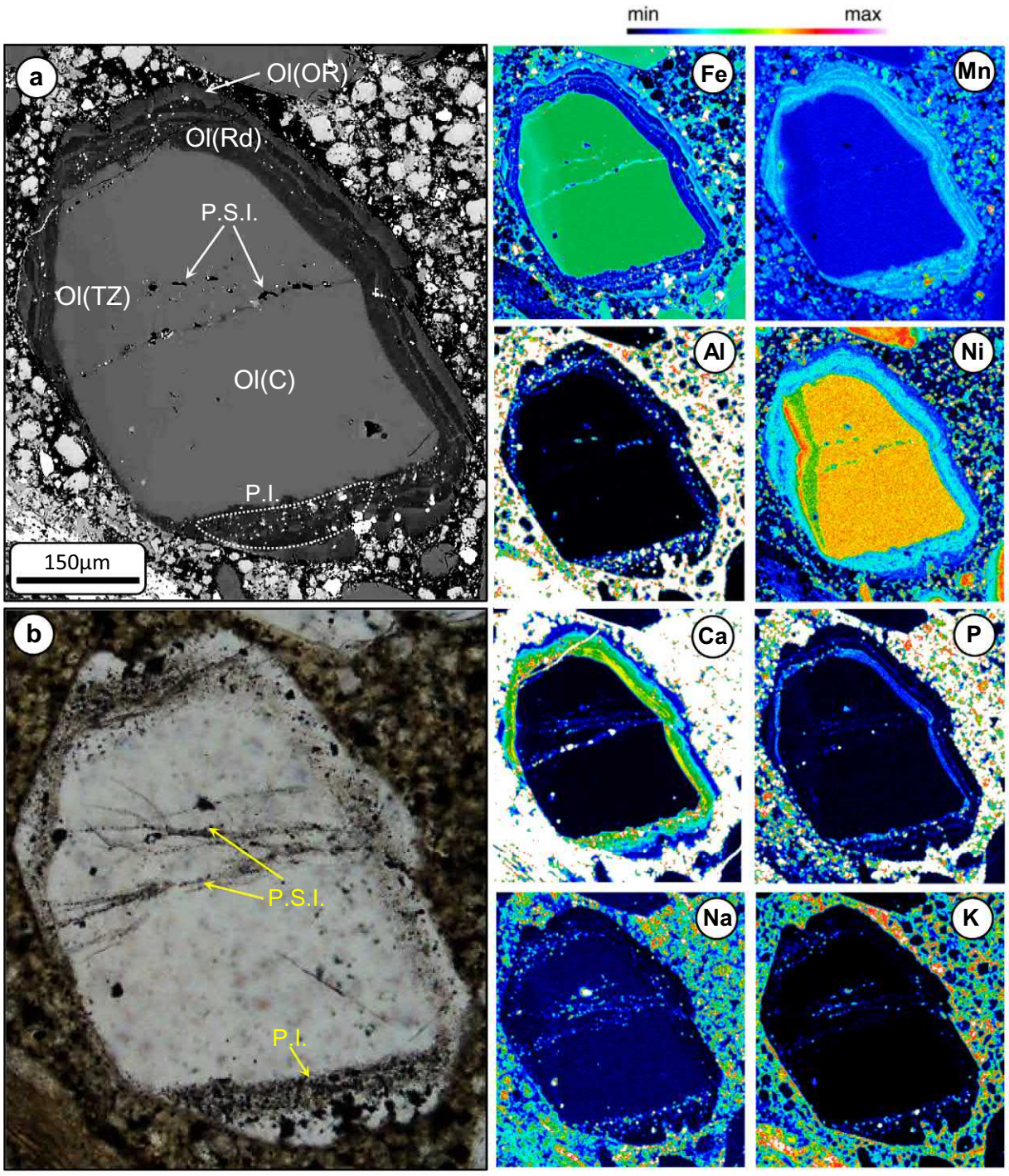

Fig. 5. (a) Back-scattered electron (BSE) scanning electron microscope (SEM), and (b) optical plane-polarised light images of a zoned olivine (Ol) grain (core: C, and partial transitional zone: TZ), which is surrounded by an Mg-rich rind (Rd) that is oscillatory zoned (~3 distinct zones alternating between more Mg- and Fe-rich compositions), as well as an outmost rind (OR). Electron microprobe (EMP) X-ray element maps show the rind to be enriched in P, Ca, Mn and depleted in Fe, Ni relative to the core. The compositional (wt%) range for each element map is: Fe: 2–15, Mn: 0–1, Al: 0–0.8, Ni: 0–0.4, Ca: 0–2.5, P: 0–0.4, Na: 0–0.3, K: 0–2. In addition, the olivine grain contains abundant primary melt inclusions (P.I.) within the rind, as well as trails of pseudosecondary secondary melt inclusions (P.S.I), which traverse the olivine interior (core and rim) and are terminated at the rind or outmost rind interface. These inclusions are marked by enrichments in Na, K, P, Ca, Al and depletions in Si, Mg. These inclusions are likely represented by minerals such as alkali-carbonates, phosphates, spinel and monticellite.

and their distribution throughout the studied samples appear completely random and dependent of how the sample was cut.

3.1. Cores

Olivine cores are highly variable in shape, ranging from ovoid, anhedral, angular and subhedral (Figs. 2–6), and are relatively homogeneous in composition. However, there is variation between olivine core compositions in terms of Fo-content ($Mg/(Mg + Fe^{2+}) \times 100$), ranging from 88.1–93.6 mol%. In addition, CaO is very low (0.01–0.05 wt%), along with low MnO (0.08–0.17 wt%) and moderate NiO (0.23–0.40 wt%; Fig. 7; Supplementary Table S1). These compositions are consistent with previously documented compositions of olivine cores from other Lac de

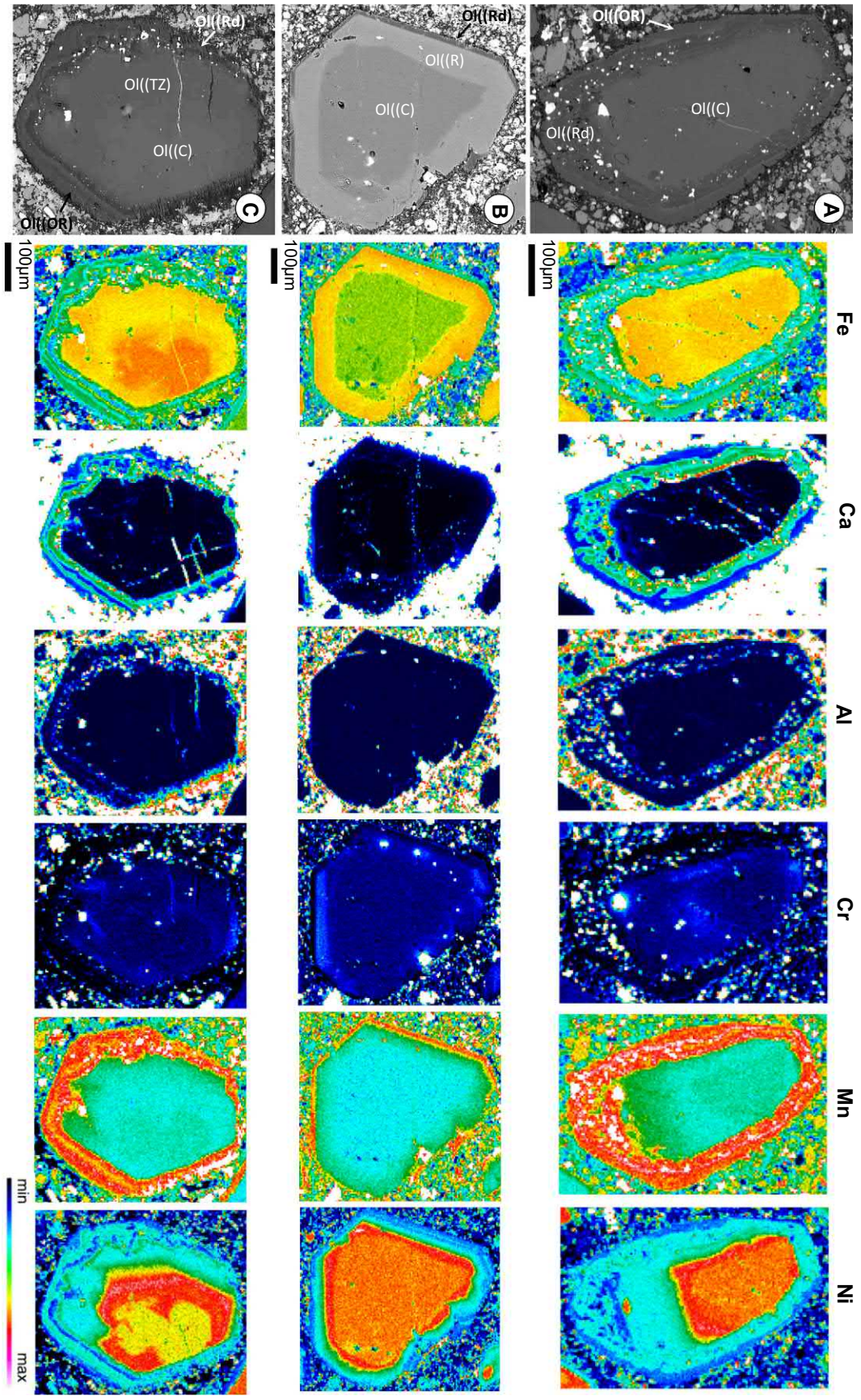

Fig. 6. Back-scattered electron (BSE) scanning electron microscope (SEM) of zoned olivine (Ol) grains. (a, c) show normal zoning (i.e. rims contain less Fe than core), and (b) shows opposite zoning (i.e. rims contain more Fe than the core). All grains are surrounded by Mg-rich rinds (Rd). The transitional zone (TZ) in (c) is marked by subtle increases to more Mg-rich and less Fe compositions. The compositional (wt%) range for each element map is: Fe: 0–10, Ca: 0–2, Al: 0–2, Cr: 0–0.5, Mn: 0–0.3, Ni, 0–0.4. Grain (a) also features in Fig. 2a. C: core, R: rim, OR: outmost rind.

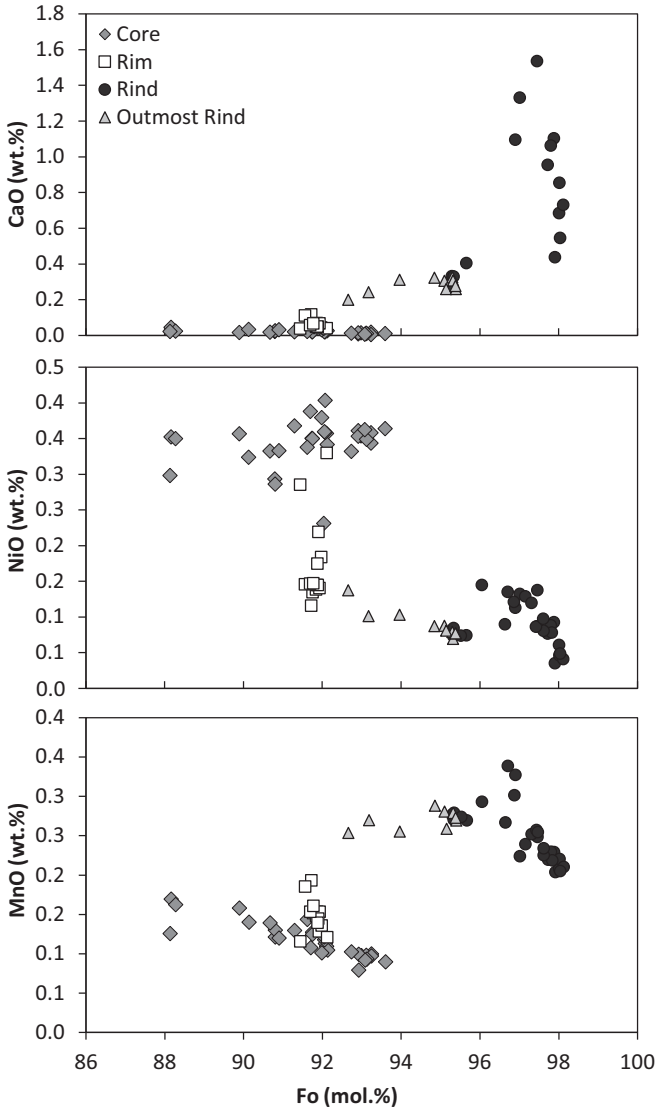

Fig. 7. Bivariate plots of Fo (mol.%) vs: CaO, NiO, and MnO (wt%) for cores (grey diamonds), rims (white squares), rinds (black circles) and outmost rinds (grey triangles).

Gras kimberlites (Brett et al., 2009; Bussweiler et al., 2015; Lim et al., 2018). Olivine cores with higher Fe-contents (i.e. Mg# <89; Figs. 2b, 3d) are rare in the Mark kimberlite and constitute less than 5% of analysed olivine grains. Olivine cores are rarely marked by the presence of thin (<30–40 μm) transitional zones, which occur discontinuously along the boundary with the outer zones surrounding the core (Figs. 3b, 5, 6c). These transitional zones appear gradational/diffuse and compositionally intermediate between the core and outer zones (e.g., increasing Mg-content relative to the core). Fig. 6c represents a rare example of a relatively wide (~50–200 μm) transitional zone enveloping an olivine core.

Upon closer inspection of olivine grains using EMP X-ray element maps, olivine cores were revealed to be relatively inhomogeneous in terms of Ni-content and distribution. Figs. 4-6 shows that Fo and Ni in distribution patterns in olivine cores can be variable: they can be coupled (Fig. 5) or strongly decoupled, Ni-content may be constant despite changing Fo (Fig. 4) or the distribution of Ni can form shapes (e.g., subhedral-to-euhedral) that do not resemble the Fo-defined core shape (Fig. 6). Similar decoupling patterns between Fo and Ni were described in zoned kimberlitic olivine from localities worldwide (Bussweiler et al., 2015; Cordier et al., 2015; Howarth et al., 2016, 2019; Kamenetsky et al., 2008; Sobolev et al., 2015).

3.2. Rims

Olivine rims were identified surrounding the cores of approximately 60% of grains and vary widely in thickness from 10 to 150 μm. The contacts between cores and rims are occasionally marked by sharp and unevenly-shaped boundaries, or embayments (Fig. 2b, 3–5; Supplementary Fig. S2). Less common are <10 μm diffuse boundaries (Figs. 2b, 3–6). These rims are marked by a narrow Mg-range ($Fo_{91.4–92.1}$) with moderately higher CaO (0.04–0.11 wt%), MnO (0.12–0.19 wt%) and lower NiO (0.12–0.33 wt%) than olivine cores (Fig. 7; Supplementary Table S1). Rim compositions of essentially fixed Fo-content with variable minor element concentrations are typical of olivine rim compositions in kimberlites at other localities worldwide (Arndt et al., 2010; Brett et al., 2015; Bussweiler et al., 2015; Howarth et al., 2016; Kamenetsky et al., 2008; Lim et al., 2018).

3.3. Rinds

Approximately 10% of olivine grains are surrounded by a variably thick (10–200 μm) rind, which has sharp contacts with cores or rims of olivine grains (Figs. 2b, 3–6, 8, 9; Supplementary Figs. S3–5). However, some rinds show uneven or embayed boundaries at the contacts with interior olivine zones. Two distinct types of rinds were identified: a) thin (<~70 μm) rinds that commonly exhibit oscillatory zoning (Fig. 8d) on a 1–5 μm scale (Figs. 3a, 5, 6a, c, 9), and b) thicker (~50–200 μm) rinds that are homogenous in composition (Figs. 3b, c, 4, 8a). Both types of olivine rinds are distinctive in BSE-images due to their high Mg-content ($Fo_{95.3–98.1}$). Furthermore, these Mg-rinds are characterized by higher CaO (0.26–1.73 wt%) and MnO (0.20–0.34 wt%) with lower NiO (0.04–0.14 wt%) concentrations as compared to core or rim compositions (Fig. 7; Supplementary Table S1). Similar Ca and Mg enrichments were observed in olivine rinds from kimberlite localities worldwide (Bussweiler et al., 2015; Howarth and Taylor, 2016; Kamenetsky et al., 2008; Lim et al., 2018; Nielsen and Sand, 2008; Pilbeam et al., 2013; Soltys et al., 2018), however, oscillatory zoning is rarely reported.

3.4. Outmost rinds

In addition, approximately 50% of olivine grains with rinds also exhibit a newly documented type of zoning (i.e. outmost rinds). They are variably thick (>10–70 μm) and characterized by elevated Fe-content (Fig. 2; $Fo_{92.7–95.4}$), lower CaO (0.20–0.33 wt%) and MnO (0.25–0.29 wt%), and similar NiO (0.07–0.14 wt%) as compared with Mg-rich rind compositions (Figs. 2-6, 9; Supplementary Table S1). Outmost rinds may exhibit either thin (<10 μm) diffusive, or sharp contacts with rinds. It is noteworthy that outmost rinds were only documented surrounding Mg-rich olivine rinds, but not cores or rims. Only in a few examples where olivine rinds have been partially abraded that outmost rinds are in direct contact with rims (e.g., Fig. 4).

4. Inclusions in olivine

The compositions of inclusions in olivine were examined by SEM-EDS and Raman spectroscopy (see Supplementary Material for methodology). In addition, LA-ICPMS traverses of olivine grains were performed in order to detect trace elements in melt inclusions in different olivine zones and in inclusion trails/clusters. A summary of melt and crystal inclusion mineral assemblages and their relative abundances is presented in Table 1.

4.1. Crystal inclusions

Olivine cores occasionally host large (100–300 μm in size) crystal inclusions of Cr-diopside, enstatite and Cr-pyrope. Cores of some olivine phenocrysts and olivine rims usually contain euhedral inclusions of

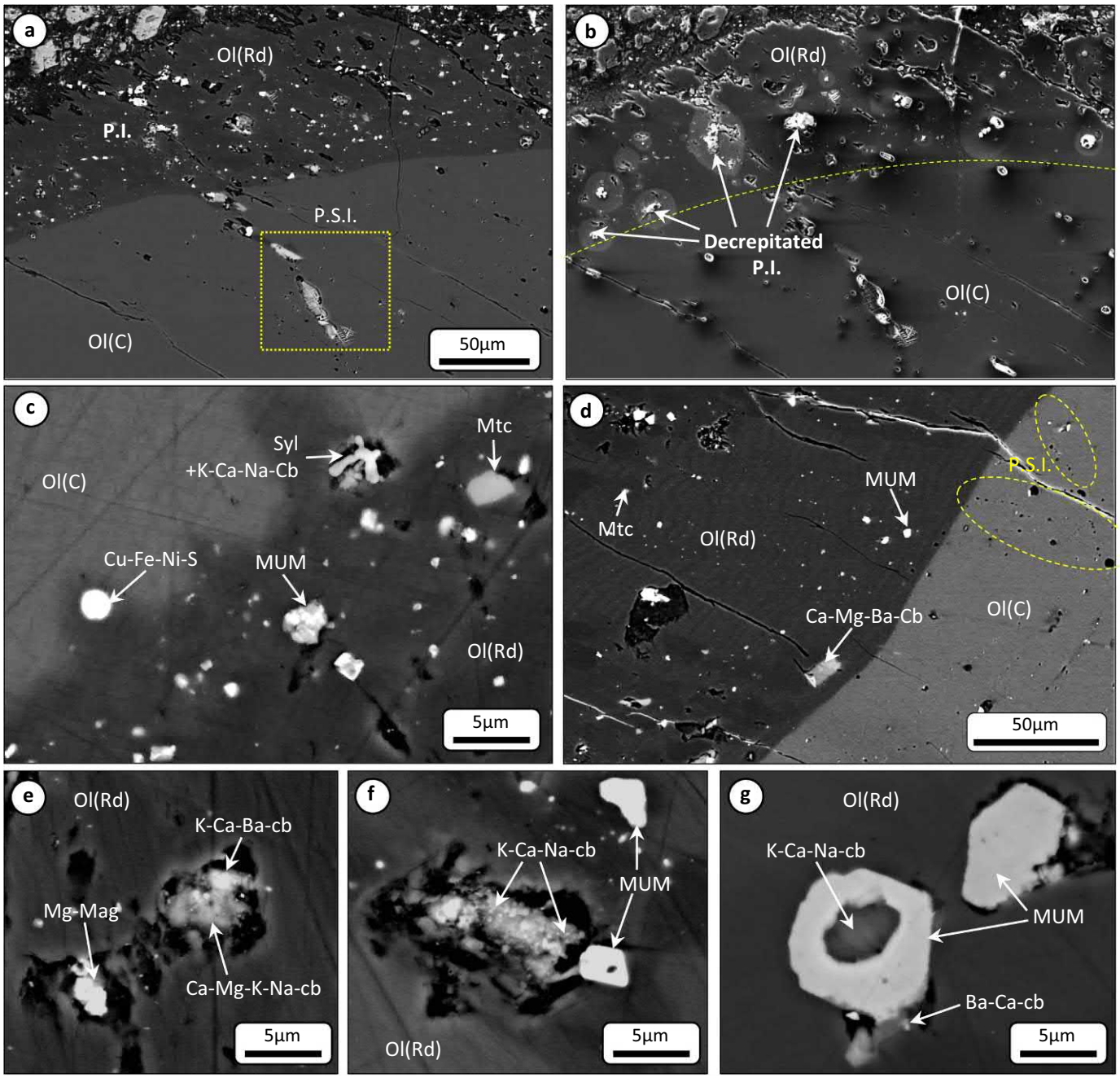

Fig. 8. (a, c–g) Back-scattered electron (BSE) and (b) secondary electron SEM images of: (a, b) relationship between pseudosecondary melt inclusion trails and primary melt inclusions in olivine (Ol). Pseudosecondary inclusion trails traverse the olivine core (C) and terminate at the rind (Rd) interface. The olivine rind is populated by abundant melt and crystal inclusions (predominantly spinel and monticellite). The yellow inset box in image panel (a) is depicted in detail in Fig. 10b. Image (b) shows that exposed melt inclusions containing water-soluble phases such as alkali-carbonates and –chlorides are commonly decrepitated and recrystallised on the polished surface around the inclusion. (c–g) Primary crystal (e.g., monticellite: Mtc, Mg-magnetite: Mg-Mag, magnesian ulvöspinel magnetite: MUM, periclase: Per, Cu-Fe-Ni-sulphides: S) and polycrystalline melt inclusions (e.g., carbonates: Cb, sylvite: Syl) in olivine rinds. Image (d) shows micrometre oscillatory zoning in the rind, as well as the relative position of pseudosecondary melt inclusion trails (P.S.I.) in the olivine core. Image (g) shows an inclusion of K-Ca-Na-carbonate hosted within a MUM spinel inclusion in an olivine rind. (For interpretation of the references to colour in this figure legend, the reader is referred to the web version of this article.)

Cr-spinel, TIMAC and less commonly MUM-spinel that range between 5 and 40 µm in size. The Mg-rich rinds are usually populated by abundant small crystal inclusions (1–10 µm) of euhedral spinel (MUM, pleonaste, Mg-magnetite), which usually occur as clusters or may show some preferential alignment parallel with the olivine margin (Figs. 3–5, 8, 9, 10a). In addition, Mg-rich rinds also contain small (2–10 µm) crystal inclusions of monticellite, along with minor perovskite and periclase, and rare apatite and phlogopite (Figs. 4, 5, 8). The outmost rinds are distinguished by a complete absence of inclusions (Figs. 3–5).

4.2. Melt/fluid inclusions

Olivine hosts two types of multiphase inclusions based on textural evidence: i) primary melt inclusions, which are restricted to Mg-rich rinds (Figs. 3–5, 8). These inclusions are randomly distributed (i.e. not associated with any fractures) or aligned parallel with growth zonation (Fig. 10a), and ii) trails of pseudosecondary melt/fluid inclusions (Figs. 2–5, 7; Supplementary Fig. S6), which occur in healed fractures within olivine cores, transitional zones and rims, and are usually

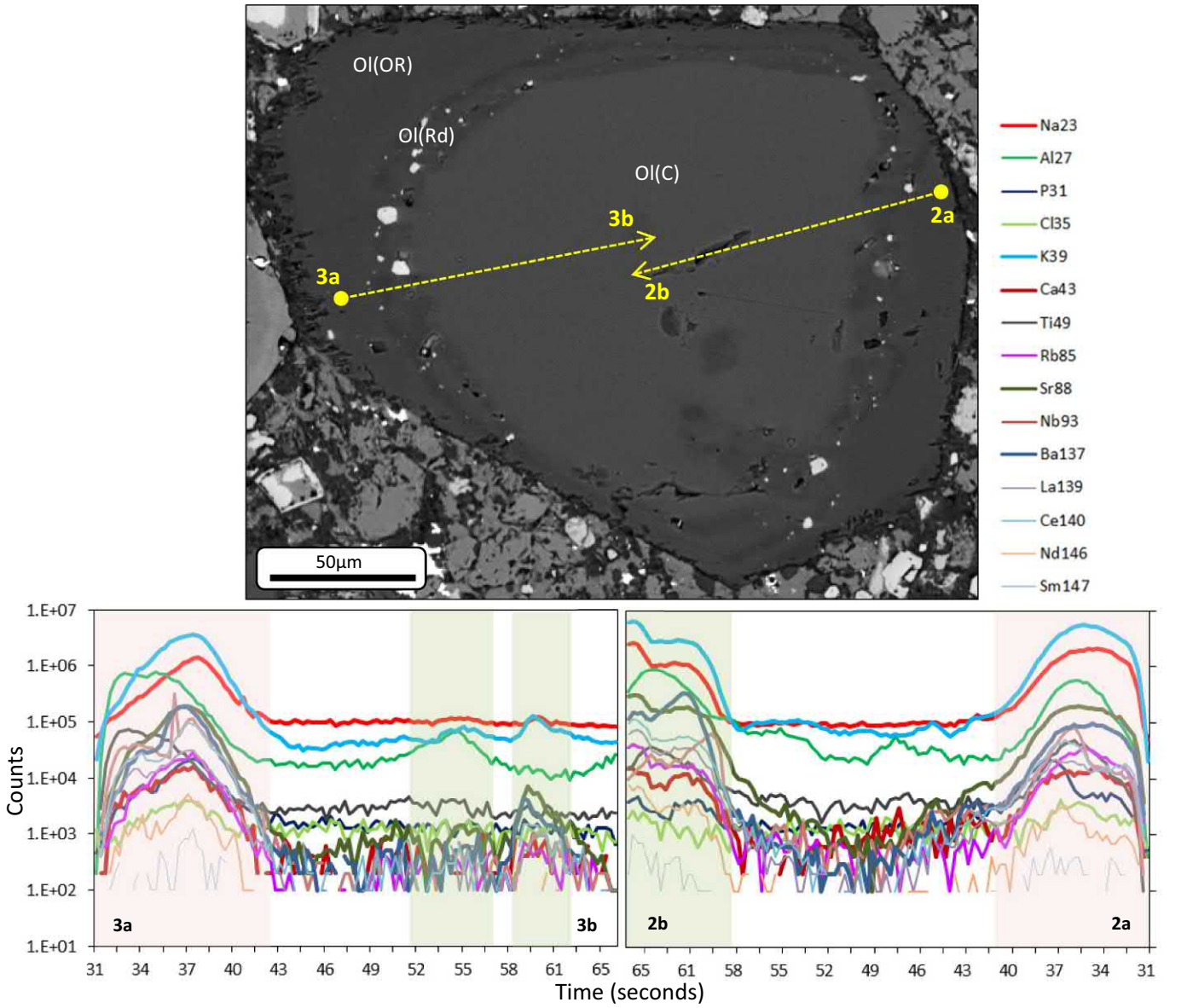

Fig. 9. Back-scattered electron (BSE) SEM image and representative LA-ICPMS traverses of a zoned olivine (Ol) grain from the Mark kimberlite, showing ablated inclusions in rinds (Rd), as well as in the olivine core (C: unshaded zone). Inclusions in the core are interpreted to be pseudosecondary in origin. Inclusions are heterogeneous in composition and reflected by positive anomalies in elements, such as alkalis/alkali-earths (Ca, Na, K, Ba, Rb, Cs), light rare earth elements (LREEs), Al, P and Nb. These positive anomalies usually occur in synchronisation of two or more of these elements. The appearance of inclusions in the outmost rind (OR) may be due to the spot size of the laser during analyses overlapping with the rind zone. The yellow arrows show the direction of the laser analyses. The red shaded zone in the laser ablation traverse represents primary inclusions hosted in the olivine rind and the green shaded zone represents pseudosecondary inclusion trails. (For interpretation of the references to colour in this figure legend, the reader is referred to the web version of this article.)

terminated at the rind or rim interface (Figs. 3–5, 10). EMPA X-ray element maps (Figs. 4, 5) reveal that olivine in healed fractures is compositionally distinct (i.e. more Fe-rich) from the olivine rinds, where the trails usually terminate. Pseudosecondary melt inclusions are therefore interpreted to have been entrapped prior to the Mg-rich rinds. It is noteworthy that the origin of some melt/fluid inclusion trails (i.e. pseudosecondary or secondary) occurring in olivine cores and rims cannot often be confidentially distinguished, especially in fractured grains or rind-free grains.

Primary melt inclusions are irregular in shape and range from 2 to 15 µm in size (Figs. 4, 5, 8). These inclusions are polycrystalline (i.e. contain 2 to >7 daughter phases) and comprised of (in order of decreasing abundance) Ca—Mg— (e.g., calcite, dolomite, Mg-calcite) and alkali (K, Na, Ba, Sr) carbonates (±F) (e.g., fairchildite ($K_2Ca(CO_3)_2$), gregoryite ($(Na_2,K_2,Ca)CO_3$), zemkorite ($(Na,K)_2Ca(CO_3)_2$), witherite ($BaCO_3$)) sylvite/halite, spinel (typically individual Mg-magnetite or MUM grains, which are occasionally zoned towards pleonaste rims), phlogopite, monticellite and rare perovskite, apatite and Fe—Cu sulphides (Table 1).

Pseudosecondary melt inclusions (Figs. 3–5, 7, 10) in olivine cores and rims are polycrystalline and are broadly similar in daughter phase assemblages and phase compositions to primary melt inclusions, although inclusions are typically larger and compositionally more diverse (~2 to >8 daughter phases). Pseudosecondary melt inclusions are occasionally interconnected by thin channels (Supplementary Fig. S6), which can cause modification of the entrapped melt by 'necking down' (see Roedder (1984) for definition). These inclusions are irregular-to-amoeboid (usually elongated) in shape, range from 5 to 50 µm in size. However, pseudosecondary melt inclusions contain more diverse and exotic daughter mineral phases, which includes magnesite, tetraferriphlogopite, Ba- or K-sulphates (e.g., barite, arcanite), kalsilite, Na-phosphates (bradleyite ($Na_3Mg(PO_4)(CO_3)$),

Table 1
Summary of mineral phases hosted in multiphase primary and pseudosecondary melt inclusions in olivine, as well as types of crystal inclusions hosted in different olivine zones. Minerals are listed in order of decreasing relative abundance.

Melt inclusions				Crystal inclusions					
				Zone					
Primary	Abundance (%)	Pseudosecondary	Abundance (%)	Core	Abundance (%)	Rim	Abundance (%)	Rind	Abundance (%)
Ca-Mg ± K-Na-Ba-Sr Carbonates	42	Ca-Mg-Fe ± K-Na-Ba-Sr ± F Carbonates	40	Cr-Diopside	50	TIMAC/MUM	100	Mg-magnetite/MUM	70
Sylvite/Halite	18	Sylvite/Halite	22	Cr-Garnet	30			Monticellite	14
Mg-magnetite/MUM	18	Calcite	15	Enstatite	12			Pleonaste	10
Phlogopite	9	Tetraferriphlogopite/Phlogopite	6	Phlogopite	7			Periclase	3
Monticellite	9	Mg-magnetite/MUM	4	Fe-Ni-Sulphides	1			Perovskite	2
Perovskite	2	Apatite	3					Phlogopite	1
Apatite	2	Barite	2						
Fe-Cu-Sulphides	<1	Perovskite	2						
		Arcanite ($K_2(SO_4)$)	2						
		Monticellite	2						
		Kalsilite	1						
		Cu-Fe-Sulphides	1						
		Bradleyite ($Na_3Mg(PO_4)(CO_3)$)	<1						
		Periclase	<1						
		Unidentified REE-Nb-Zr phase	<1						

Cu-Fe-sulphides and an unidentified rare earth element (REE)-Nb-Zr phase (Table 1).

4.2.1. Raman analyses of inclusions

Raman spectroscopy detected numerous other unidentified phases in the primary and psuedosecondary melt inclusions, which all display unique intense spectra bands between 1081 and 1104 cm^{-1} and 984–996 cm^{-1}, indicating the presence of carbonate (CO_3^{2-}) and sulphate (SO_4^{2-}) phases, respectively (Supplementary Table S2; Fig. 11; Supplementary Figs. S7). In addition, olivine cores and rims contain preferentially aligned swarms of small (1–5 μm) rounded fluid inclusions (Fig. 10a). The fluid phase was confirmed by Raman spectroscopy to be CO_2 (Supplementary Table S2). These CO_2 inclusions are sometimes surrounded by decrepitation haloes (Fig. 10a). CO_2 inclusions homogenize (see Supplementary Material for methodology) into a liquid over a range of temperatures (~25–30 °C), which corresponds to fluid densities of 0.77–0.47 g/cm^3 (see Roedder (1984)).

4.2.2. Laser ablation analyses of inclusions

Zoned olivine grains containing inclusion-rich Mg-rich rinds and clusters/trails of primary and pseudosecondary melt/fluid inclusions in the cores and rims were examined by LA-ICPMS traverses, which were conducted across from the olivine grain margin through to the core (Fig. 9; Supplementary Figs. S3–5). The presence of primary and pseudosecondary melt/fluid inclusions was indicated by synchronised positive anomalies in alkalis and alkali-earths (Na, Ca, K, Ba, Sr, Rb; e.g., carbonates, chlorides, phlogopite, tetraferriphlogopite), P (i.e. phosphates), Ti (e.g., spinel), Nb and light rare earth elements (LREEs) in time-resolved ablation signals.

4.3. Potassium and sodium contents of inclusions

Both primary and pseudosecondary melt inclusions contain abundant carbonate and chloride daughter minerals (Figs. 8–10). The ratios of Ca-K-Na of exposed melt/fluid inclusions (acquired by SEM-EDS), calculated in atomic abundances and normalised to 100 (see Fig. 12), demonstrate that the majority of Ca-K-Na carbonate minerals display significant compositional scatter. This may be due to mixtures of intergrown phases, analytical limitations (e.g., X-ray excitation at depth or secondary X-ray fluorescence, or how the sample was cut), decrepitation and recrystallisation of exposed phases (Supplementary Figs. S8–11) and/or the presence of solid solution minerals (e.g., gregoryite, zemkorite). Atmospheric moisture interaction commonly results in the recrystallisation of water-soluble phases, such as alkali-carbonates and chlorides, on the surface around inclusions. Recrystallisation results in the formation of new hydrous alkali phases (e.g., kalicnite ($K(HCO_3)$), nahcolite ($Na(HCO_3)$) and trona ($Na_3(HCO_3)(CO_3)•2(H_2O)$) (Supplementary Figs. S8–11). Furthermore, these recrystallised K- or Na-rich minerals results in appearance of almost pure K and Na endmembers and as such are not plotted on the Ca-K-Na ternary plots (Fig. 12).

In addition, the Ca-K-Na ratios acquired by LA-ICPMS traverses of zoned olivine exhibit a similar compositional trend to SEM-EDS data, but are skewed towards the Ca endmember. The higher Ca-content of inclusions (i.e. primary and pseudosecondary) analysed by LA-ICPMS may be attributed to the ablation of other Ca-rich phases (e.g., calcite, dolomite) hosted within inclusions, as well as the host Mg-rich olivine rind (up to 1.73 wt% CaO).

In general, potassium is the most dominant element in daughter alkali-carbonates and -chlorides, where K-rich minerals (e.g., fairchildite, gregoryite, sylvite) are far more common than Na-rich minerals. The SEM-EDS calculated K/Na ratios (excluding analyses of compositional endmembers) for primary and pseudosecondary melt inclusions is 2.3 ($n = 29$) and 2.2 ($n = 80$), respectively. This is in agreement with LA-ICPMS analyses of olivine-hosted inclusions,

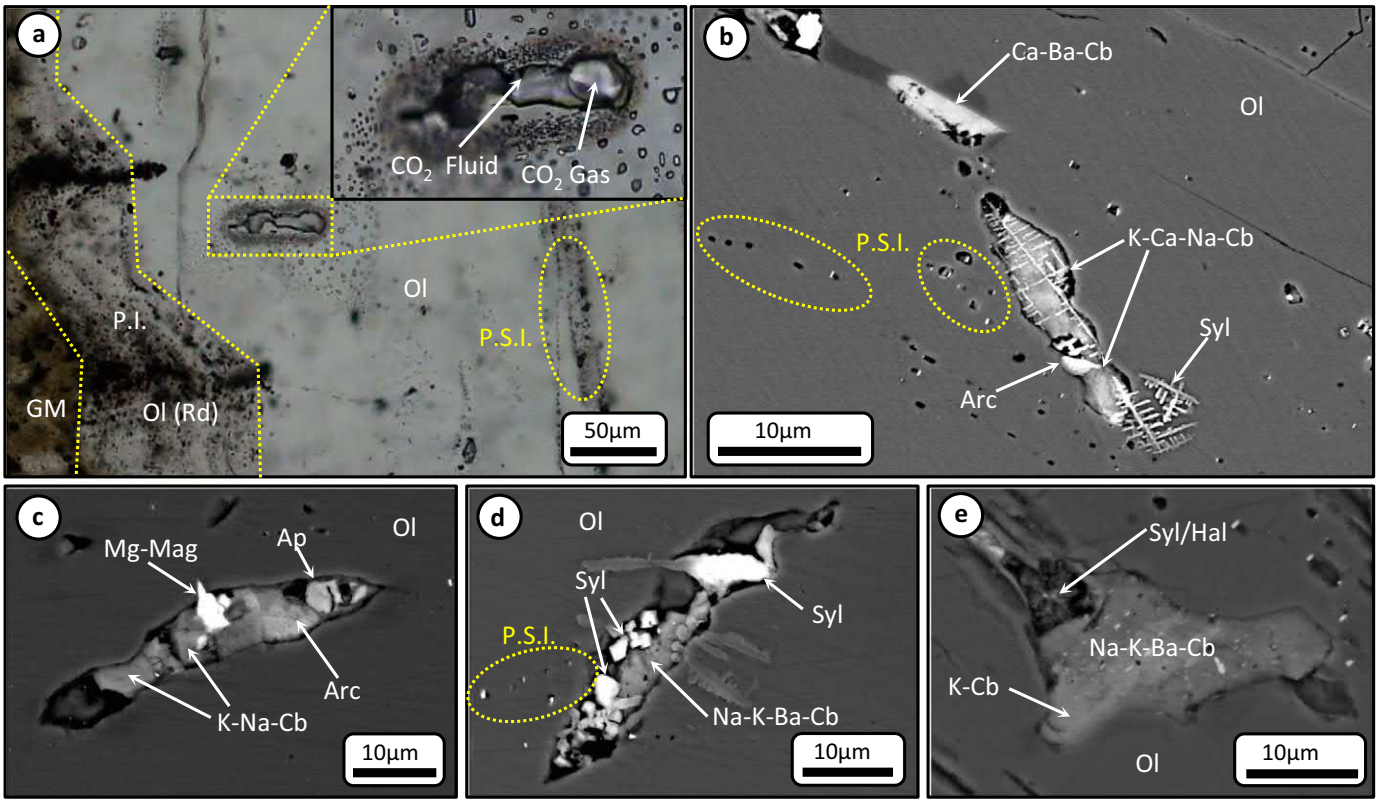

Fig. 10. (a) Optical photomicrograph in plane-polarised light of pseudosecondary melt/fluid inclusion (P.S.I.) trails aligned along healed fracture planes in olivine (Ol) and primary inclusions (P.I.), which are located in the rind zone (Rd). Primary melt inclusions (P.I.) are orientated parallel with the olivine rind zone. Olivine hosts a multiphase inclusions containing bubbles of CO_2. The inclusions in (a) is surrounded by a decrepitation halo. (b–e) Back-scattered electron (BSE) scanning electron microscope (SEM) images of individual pseudosecondary polycrystalline melt inclusions and inclusion trails in olivine. Detected phases include: apatite (Ap), calcite (Cal), Mg-magnetite (Mg-Mag), alkali (Ca, K, Na, Ba, Sr) carbonates (Cb), sylvite (Syl), halite (Hal) arcanite (Arc). GM: Groundmass.

which have a K/Na ratio of 1.8. Similarly, the SEM-EDS calculated K/Na ratio of mixed Na—K chlorides is 3.9 ($n = 12$).

5. Discussion

5.1. Olivine as a petrogenetic indicator

The variable, but high Fo (88.1–93.6 mol%), low CaO (<0.05 wt%) and high NiO (0.23–0.40 wt%; Fig. 7; Supplementary Table S1), along with rounded-to-angular shapes and/or resorbed margins, and presence of lithospheric mantle mineral inclusions (e.g., enstatite, Cr-pyrope and Cr-diopside) support a xenocrystic origin for olivine cores, deriving from peridotites in the SCLM (Arndt et al., 2010; Brett et al., 2009; Bussweiler et al., 2015; Kamenetsky et al., 2008; Howarth et al., 2016; Sobolev et al., 2015). The characteristic composition of olivine rims (constant Mg#, with variable Ni, Mn and Ca; Fig. 7; Supplementary Table S1) surrounding olivine cores, along with crystal inclusions of euhedral TIMAC spinel indicate that rims represent the earliest stage of magmatic olivine crystallisation (e.g., Arndt et al., 2010; Brett et al., 2009; Fedortchouk and Canil, 2004; Kamenetsky et al., 2008). Trails of pseudosecondary melt/fluid inclusions traversing olivine cores and rims, and terminating at the interface with Mg-rich olivine rinds, indicates that there was melt trapping prior to Mg-rich rind formation.

The Mg-rich rinds surrounding olivine cores/rims in the Mark kimberlite can be remarkably thick compared to olivine from other kimberlite localities (Bussweiler et al., 2015; Howarth and Taylor, 2016; Lim et al., 2018; Soltys et al., 2018). The presence of abundant Fe^{3+}-rich spinel as inclusions in olivine rinds indicates that the evolving kimberlite melt shifted towards more oxidising conditions (Bussweiler et al., 2015; Howarth and Taylor, 2016), therefore driving the co-precipating olivine rinds towards high-Mg (up to $Fo_{98.1}$; Fig. 7; Supplementary Table S1) compositions. The abundance of crystal and melt inclusions within Mg-rich rinds, along with their sharp contacts (Figs. 3–6, 8, 9) with interior olivine zones and oscillatory zoning, suggests that there was an episode of rapid crystallisation. Previously, olivine rinds were interpreted to represent the final stage of olivine crystallisation (Bussweiler et al., 2015; Giuliani, 2018; Lim et al., 2018). However, we recorded an additional episode of olivine growth, which is represented by the 'outmost rind' (Figs. 3–6, 9) and characterized by decreasing MgO, CaO and MnO content and absence of inclusions as compared to the Mg-rich rinds. However, the origin of the outmost rinds requires further explanation.

The sharp and uneven boundaries and embayments that occur between different olivine zones (e.g., cores-rims, rims-rinds, rinds-cores; Figs. 2–6, 8, 9) indicate that olivine: i) experienced continuous processes of mechanical abrasion, which occurred during magmatic ascent (e.g., Brett et al., 2015; Jones et al., 2014; Kamenetsky and Yaxley, 2015). ii) Multiple stages of chemical resorption by the host kimberlite melt, which were followed by new stages of olivine crystallisation. This includes olivine which underwent different evolutionary processes due to changing magma compositions and conditions such as decarbonation reactions, as evidenced by monticellite rims around olivine (see Abersteiner et al., 2018a), and magma oxidation, which is evidenced by Mg-rich rinds (see Bussweiler et al., 2015; Howarth and Taylor, 2016). In addition, the intermediate transitional zones (Figs. 3b, 5, 6c) that occur between olivine cores and rims/rinds, suggest that some olivine grains experienced some degree of partial diffusive re-equilibration between cores and rims, or with the host kimberlite melt (e.g., Howarth et al., 2016, 2019; Lim et al., 2018; Pilbeam et al., 2013).

The apparent random distribution of olivine grains with different morphologies and zoning patterns (i.e. rim, rind, outmost rind), monticellite rims around olivine (Supplementary Fig. S1) and

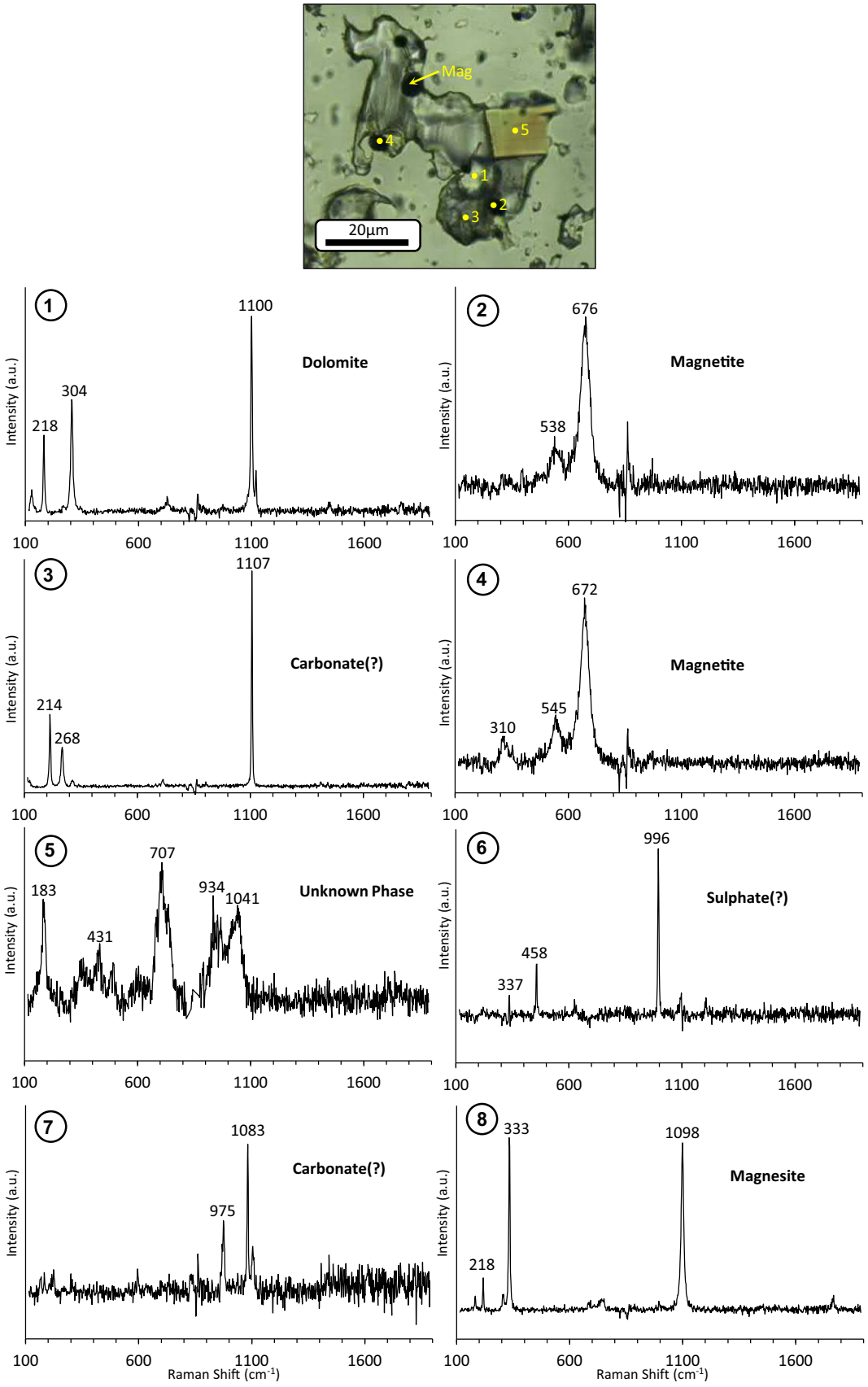

Fig. 11. Representative Raman spectra of an olivine-hosted pseudosecondary melt inclusion and the corresponding optical (transmitted light) image. Points 1–5 (yellow dots) represent visible, identifiable phases, whereas points 6–8 represent interior (not visible) phases (see 'Inclusion 1' in Supplementary Table S2). Mag: magnetite, a.u.: arbitrary units. (For interpretation of the references to colour in this figure legend, the reader is referred to the web version of this article.)

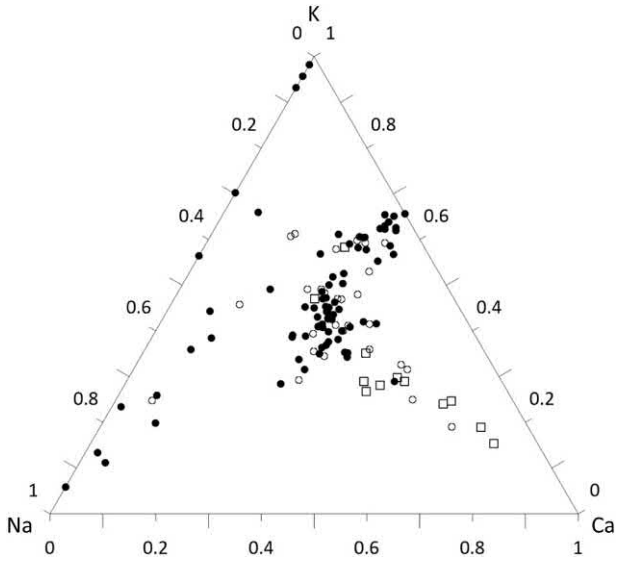

Fig. 12. Ternary diagram showing the compositions of alkali (Ca-K-Na) carbonates in primary melt inclusions (clear circles; $n = 29$) and pseudosecondary melt inclusions (shaded circles; $n = 80$) in olivine. The compositions were acquired by SEM-EDS and were calculated in atomic abundances and normalised to 100. In addition, LA-ICPMS analyses (clear squares; $n = 12$) of primary and pseudosecondary melt inclusions in olivine were similarly recalculated to atomic abundances and normalised to 100.

re-crystallisation features (i.e. mosaics; Supplementary Fig. S2) suggest that the studied Mark kimberlite represents an accumulation of olivine crystals. In addition, the wide variations in Ni distribution patterns in Mark kimberlite olivine further support the notion that olivine in the studied samples do not represent a single population formed by fractional or equilibrium crystallisation of a single melt. In general, the variations in olivine cores and rims in the Mark kimberlite sample are the product of mechanical magma mixing and accumulation of previously crystallised olivine that formed at different depths within the ascending kimberlite magma column or from successive pulses of magma (see also Mitchell, 2008).

5.2. Kimberlite melt evolution recorded by inclusions

Melt/fluid inclusion trails traversing cores and rims, and terminating at the boundary with Mg-rich olivine rinds (Figs. 3–5) present clear petrographic evidence that these inclusions are pseudosecondary in origin. This discovery suggests that previously documented 'secondary' melt/fluid inclusion trails in olivine (e.g., Abersteiner et al., 2018a, 2018b, 2018c, 2019; Giuliani et al., 2017; Golovin et al., 2007; Kamenetsky et al., 2004; Kamenetsky et al., 2008, 2009, 2012, 2013, 2014; Mernagh et al., 2011) could also potentially be pseudosecondary in origin, but were misidentified due to the lack of obvious textural relationships between inclusion trails and olivine zones due to serpentinisation and/or abrasion of magmatic olivine overgrowths (e.g., rinds). Previous attempts to constrain parental kimberlite melt compositions using 'secondary' melt/fluid inclusions in kimberlitic olivine have proved problematic due to the lack of timing constraints, as their entrapment may have occurred at any stage during transport or upon emplacement. It is envisaged that the melt/fluid inclusions in Mark kimberlite olivine cores and rims were encapsulated at depth (i.e. prior to final magma emplacement), as indicated by decrepitation haloes (Fig. 10a) surrounding some of these inclusions. Changes in external pressure (i.e. decompression) caused outward crack propagation from these inclusions into the host olivine crystal, thereby forming decrepitation haloes (see Roedder, 1984). The estimated fluid densities (0.47–0.77 g/cm^3) of decrepitated CO_2 inclusions correspond to a minimum entrapment pressure of ~200–450 MPa (see Figs. 8–7 and 8-8 of Roedder, 1984), or lithospheric depth of approximately ~6–15 km depth. However, it is possible that these fluids were entrapped in olivine at even greater depths (e.g., Golovin et al., 2018). This implies that pseudosecondary melt inclusions in olivine are unrelated to late-stage processes or products of extensive kimberlite melt differentiation. The absence of decrepitation features surrounding melt inclusions in Mg-rich olivine rinds, coupled with the entrapment of crystal inclusions of common groundmass phases (i.e. MUM, Mg-magnetite, pleonaste, monticellite, perovskite and periclase) indicates that there were no significant changes in pressure and that olivine rinds crystallised as in-situ features, after the kimberlite magma was emplaced in the upper crust.

Both primary and pseudosecondary melt inclusions in olivine share similar, but not identical daughter mineral assemblages, that are dominated by Ca—Mg (e.g., calcite, dolomite) and alkali/alkali-earth (K-Na-Ba-Sr) carbonates (e.g., fairchildite, gregoryite, zemkorite, witherite), K—Na chlorides and subordinate silicates (e.g., phlogopite, monticellite) and lesser oxides, phosphates and Fe-Cu-sulphides. This compositional and mineralogical similarity between primary and pseudosecondary melt inclusions demonstrates that these two different generations of inclusions sampled the same or a similar composition melt, which maintained relatively high alkali abundances with consistent K:Na ratios (i.e. average ~2.4 across all alkali-carbonate and –chloride daughter minerals). The extensive variations in proportions of daughter minerals is largely attributed to heterogeneous melt trapping, but also in the case of pseudosecondary inclusions, different timings of melt/fluid entrapment, as well as the process of 'necking down', which can modify the original melt/fluid composition.

There is distinct compositional and mineralogical disparity between the Mark kimberlite groundmass and melt/fluid inclusions, where diverse alkali/alkali-earth (K, Na, Ba, Sr) and halogen (Cl, F) rich phases (e.g., carbonates, chlorides, sulphates and phosphates), which are common in melt inclusions, are notably absent from the groundmass. The apparent absence of these alkali/alkali-earth- or halogen-rich phases in the kimberlite groundmass is commonly attributed to volatile exsolution and/or dissolution by late-stage and/or post-magmatic fluid-related processes (Abersteiner et al., 2018c; Giuliani et al., 2017; Kamenetsky et al., 2014). The rapid degradation of inclusions was evident throughout the study, where water-soluble carbonates and chlorides frequently recrystallised and re-precipitated (e.g., formation of new phases: kalicinite, nahcolite, trona) on the surface of polished samples (Fig. 8b; Supplementary Figs. S8–11) due to interactions with atmospheric moisture.

In general, the silica-poor and carbonate-dominated, and alkali-halogen enriched compositions of primary and pseudosecondary melt inclusions hosted in Mark kimberlite olivine are identical to other studies of olivine-hosted melt inclusions from kimberlite localities worldwide (e.g., Abersteiner et al., 2018a, 2018b, 2018c, 2019; Giuliani et al., 2017; Golovin et al., 2007, 2018; Kamenetsky et al., 2004, 2012, 2013, 2014; Mernagh et al., 2011). Therefore, the geochemical and mineralogical features of olivine-hosted melt in the Mark kimberlite are not anomalous, but typical of kimberlites globally. The notion that melt/fluid inclusions in the Mark kimberlite sampled a variably differentiated silica-poor, halogen-bearing, alkali (K > Na) dolomitic melt is in agreement with previous studies which suggest that kimberlites may have originated from melts which had a "carbonatite-like" affinity (Dawson, 1971; Kamenetsky, 2016; Kamenetsky et al., 2004, 2013, 2014; Nielsen and Sand, 2008; Pilbeam et al., 2013). In summary, our study of olivine-hosted primary melt inclusions reinforces that alkalis and halogens preserved in pseudosecondary melt/fluid inclusions do not necessarily represent residual melt products entrapped after extensive differentiation, but were a more significant and intrinsic part of the melt that transported olivine and formed the Mark kimberlite.

6. Conclusions

We present a detailed petrographic and geochemical study of olivine, its zoning patterns and hosted inclusions from a well-preserved

hypabyssal sample of the Mark kimberlite (Canada). This data places new constraints on the petrogenesis of kimberlitic olivine and the composition of the parental melt.

1) Olivine in the Mark kimberlite is well-preserved (i.e. negligible-to-minor serpentinisation of rims and internal fractures) and exhibits zoning, which is characterized by a xenocrystic core, which can include an intermediate transitional zone, along with a magmatic rim, a Mg-rich rind and an outmost rind. Outmost rinds are a previously undocumented episode of olivine growth from the late-stage kimberlite melt. Magmatic olivine zones can occur in any combination, but follow a sequence of crystallisation (core → rim → rind → outmost rind). The morphological diversity of olivine grains, as well as sharp and uneven boundaries/embayments and diffuse contacts between different olivine zones suggest there was a complex interplay of mechanical and chemical abrasion processes.
2) Olivine zoning is marked by systematic changes in Fo, Ca, Cr and Mn. However, Ni distribution is highly variable and can show either positive or negative coupling with Fo.
3) The wide variation in olivine core and rim zoning patterns, morphologies and Ni distribution patterns suggests that Mark kimberlite olivine was not derived from a single melt batch, but represents the accumulation of olivine derived from different pulses of magma, as well as olivine crystallised at variable depths from the kimberlite.
4) The Mg-rich rinds and outmost rinds represent near surface crystallisation from late-stage and relatively oxidised kimberlite melt.
5) Melt/fluid inclusion trails occurring along healed fractures in olivine cores and rims terminate along the rim and/or Mg-rich olivine rind interface. Therefore, these melt/fluid inclusions are interpreted to be pseudosecondary in origin and were likely formed prior to rim or rind formation. In addition, for the first time primary multiphase melt inclusions were identified in the Mg-rich magmatic rinds of kimberlitic olivine.
6) Estimated fluid densities of CO_2 in pseudosecondary melt/fluid inclusions constrained a minimum entrapment pressure of these inclusions to be ~200–450 MPa, which corresponds to ~6–15 km depth. However, it is envisaged that these inclusions were entrapped at much greater depths.
7) Primary and pseudosecondary melt inclusions contain compositionally identical mineral phases, dominated by Ca—Mg— and K-Na-Ba-Sr-bearing carbonates, K-Na-chlorides along with subordinate silicates (e.g., phlogopite, monticellite,), Fe-Mg-Al-Ti-oxides (including periclase and perovskite), phosphates and sulphides. The pseudosecondary inclusions can also contain tetraferriphlogopite, kalsilite and sulphates. Based on these melt inclusion compositions, it is suggested that olivine in the Mark kimberlite was crystallised from and transported by a variably differentiated silica-poor, halogen-bearing, alkali-dolomitic melt.

Supplementary data to this article can be found online at https://doi.org/10.1016/j.lithos.2020.105405.

Acknowledgements

This study forms part of A.A's Ph.D and was supported by an Australian Postgraduate Award (APA) and the Max Banks Research Scholarship in Earth Sciences. This work has benefitted from comments by two anonymous reviewers and efficient editorial handling by Greg Shellnutt. The constructive comments of Nicholas Arndt, Troels Nielsen and Dennis Brown contributed to improving this manuscript and are gratefully acknowledged. We thank James Tolley from CODES (UTas) for his assistance in LA-ICPMS data acquisition, and Jon Carlson (Dominion Diamond Mines) for his assistance in acquiring petrographic and geological data. This work was supported by funding from the Institute of Volcanology and Seismology, Far East Branch, Russian Academy of Sciences.

References

Abersteiner, A., Kamenetsky, V.S., Pearson, D.G., Kamenetsky, M., Goemann, K., Ehrig, K., Rodemann, T., 2018a. Monticellite in group-I kimberlites: implications for evolution of parental melts and post-emplacement CO_2 degassing. Chem. Geol. 478, 76–88.
Abersteiner, A., Kamenetsky, V.S., Kamenetsky, M., Goemann, K., Ehrig, K., Rodemann, T., 2018b. Significance of halogens (F, Cl) in kimberlite melts: insights from mineralogy and melt inclusions in the Roger pipe (Ekati, Canada). Chem. Geol. 478, 148–163.
Abersteiner, A., Kamenetsky, V.S., Golovin, A.V., Kamenetsky, M., Goemann, K., 2018c. Was crustal contamination involved in the formation of the serpentine-free Udachnaya-East kimberlite? New insights into parental melts, liquidus assemblage and effects of alteration. J. Petrol. 59, 1467–1492.
Abersteiner, A., Kamenetsky, V.S., Goemann, K., Giuliani, A., Howarth, G.H., Castillo-Oliver, M., Thompson, J., Kamenetsky, M., Cherry, A., 2019. Composition and emplacement of the Benfontein kimberlite sill complex (Kimberley, South Africa): textural, petrographic and melt inclusion constraints. Lithos 324-325, 297–314.
Arndt, N.T., Guitreau, M., Boullier, A.M., Le Roex, A., Tommasi, A., Cordier, P., Sobolev, A., 2010. Olivine, and the origin of kimberlite. J. Petrol. 51, 573–602.
Boyd, F.R., Clement, C.R., 1977. Compositional zoning of olivines in kimberlite from the De Beers mine, Kimberley, South Africa: International Kimberlite Conference. Extended Abstr. 2 (1), 39–41.
Brett, R.C., Russell, J.K., Moss, S., 2009. Origin of olivine in kimberlite: phenocryst or impostor? Lithos 112S, 201–212.
Brett, R.C., Russell, J.K., Andrews, G.D.M., Jones, T.J., 2015. The ascent of kimberlite: insights from olivine. Earth Planet. Sci. Lett. 424, 119–131.
Bussweiler, Y., Foley, S.F., Prelević, D., Jacob, D.E., 2015. The olivine macrocryst problem: new insights from minor and trace element compositions of olivine from Lac de Gras kimberlites, Canada. Lithos 220–223, 238–252.
Clement, C.R., Skinner, E.M.W., Smith, B.H.S., 1984. Kimberlite redefined. J. Geol. 92, 223–228.
Cordier, C., Sauzeat, L., Arndt, N.T., Boullier, A.-M., Batanova, V., Barou, F., 2015. Metasomatism of the lithospheric mantle immediately precedes kimberlite eruption: new evidence from olivine composition and microstructures. J. Petrol. 56, 1775–1796.
Davis, W.D., Kjarsgaard, B.A., 1997. A Rb - Sr isochron age for a kimberlite from the recently discovered Lac de Gras field, Slave Province, Northwest Canada. J. Geol. 105, 503–509.
Dawson, J.B., 1971. Advances in kimberlite geology. Earth Sci. Rev. 7, 187–214.
Fedortchouk, Y., Canil, D., 2004. Intensive variables in kimberlite magmas, Lac de Gras, Canada and implications for diamond survival. J. Petrol. 45 (9), 1725–1745.
Giuliani, A., 2018. Insights into kimberlite petrogenesis and mantle metasomatism from a review of the compositional zoning of olivine in kimberlites worldwide. Lithos 312–313, 322–342.
Giuliani, A., Soltys, A., Phillips, D., Kamenetsky, V.S., Maas, R., Goemann, K., Woodhead, J.D., Drysdale, R., Griffin, W.L., 2017. The final stages of kimberlite petrogenesis: petrography, mineral chemistry, melt inclusions and Sr-C-O isotope geochemistry of the Bultfontein kimberlite (Kimberley, South Africa). Chem. Geol. 455, 342–356.
Golovin, A.V., Sharygin, V.V., Pokhilenko, N.P., 2007. Melt inclusions in olivine phenocrysts in unaltered kimberlites from the Udachnaya-East pipe, Yakutia: some aspects of kimberlite magma evolution during late crystallisation stages. Petrology 15, 168–183.
Golovin, A.V., Sharygin, I.S., Kamenetsky, V.S., Korsakov, A.V., Yaxley, G.M., 2018. Alkali-carbonate melts from the base of cratonic lithospheric mantle: links to kimberlites. Chem. Geol. 483, 261–274.
Howarth, G.H., Gross, J., 2019. Diffusion-controlled and concentric growth zoning revealed by phosphorous in olivine from rapidly ascending kimberlite magma, Benfontein, South Africa. Geochim. Cosmochim. Acta 266, 292–306.
Howarth, G.H., Taylor, L.A., 2016. Multi-stage kimberlite evolution tracked in zoned olivine from the Benfontein sill, South Africa. Lithos 262, 384–397.
Jones, T.J., Russell, J.K., Porritt, L.A., Brown, R.J., 2014. Morphology and surface features of olivine in kimberlite: implications for ascent processes. Solid Earth 5, 313–326.
Kamenetsky, V.S., 2016. Comment on: "the ascent of kimberlite: Insights from olivine" by Brett R.C. et al. [Earth Planet. Sci. Lett. 424 (2015) 119–131]. Earth Planet. Sci. Lett. 440, 187–189.
Kamenetsky, V.S., Yaxley, G.M., 2015. Carbonate–silicate liquid immiscibility in the mantle propels kimberlite magma ascent. Geochim. Cosmochim. Acta 158, 48–56.
Kamenetsky, M.B., Sobolev, A.V., Kamenetsky, V.S., Maas, R., Danyushevsky, L.V., Thomas, R., Pokhilenko, N.P., Sobolev, N.V., 2004. Kimberlite melts rich in alkali chlorides and carbonates: a potent metasomatic agent in the mantle. Geology 32, 845–848.
Kamenetsky, V.S., Kamenetsky, M.B., Sobolev, A.V., Golovin, A.V., Demouchy, S., Faure, K., Sharygin, V.V., Kuzmin, D.V., 2008. Olivine in the Udachnaya-East Kimberlite (Yakutia, Russia): types, compositions and origins. J. Petrol. 49, 823–839.
Kamenetsky, V.S., Kamenetsky, M.B., Weiss, Y., Navon, O., Nielsen, T.F.D., Mernagh, T.P., 2009. How unique is the Udachnaya-East kimberlite? Comparison with kimberlites from the Slave Craton (Canada) and SW Greenland. Lithos 112S, 334–346.
Kamenetsky, V.S., Kamenetsky, M.B., Golovin, A.V., Sharygin, V.V., Maas, R., 2012. Ultrafresh salty kimberlite of the Udachnaya-East pipe (Yakutia, Russia): a petrological oddity or fortuitous discovery? Lithos 152, 173–186.
Kamenetsky, V.S., Grutter, H., Kamenetsky, M.B., Goemann, K., 2013. Parental carbonatitic melt of the Koala kimberlite (Canada): constraints from melt inclusions in olivine and Cr-spinel, and groundmass carbonate. Chem. Geol. 353, 96–111.
Kamenetsky, V.S., Golovin, A.V., Maas, R., Giuliani, A., Kamenetsky, M.B., Weiss, Y., 2014. Towards a new model for kimberlite petrogenesis: evidence from unaltered kimberlites and mantle minerals. Earth Sci. Rev. 139, 145–167.

Kjarsgaard, B.A., Wilkinson, L., Armstrong, J., 2002. Geology, Lac de Gras Kimberlite Field, Central Slave Province, Northwest Territories - Nunavut: Geological Survey of Canada, Open File 3228 Map Scale 1:250,000.

Lim, E., Giuliani, A., Phillips, D., Goemann, K., 2018. Origin of complex zoning in olivine from diverse, diamondiferous kimberlites and tectonic settings: Ekati (Canada), Alto Paranaiba (Brazil) and Kaalvallei (South Africa). Mineral. Petrol. 112, 539–554.

Mernagh, T.P., Kamenetsky, V.S., Kamenetsky, M.B., 2011. A Raman microprobe study of melt inclusions in kimberlites from Siberia, Canada, SW Greenland and South Africa. Spectrochim. Acta A Mol. Biomol. Spectrosc. 80, 82–87.

Mitchell, R.H., 1986. Kimberlites: Mineralogy, Geochemistry and Petrology. Plenum Publishing Company, New York, p. 442.

Mitchell, R.H., 2008. Petrology of hypabyssal kimberlites: relevance to primary magma compositions. J. Volcanol. Geotherm. Res. 174, 1–8.

Moore, A.E., 1988. Olivine: a monitor of magma evolutionary paths in kimberlites and olivine melilitites. Contrib. Mineral. Petrol. 99, 238–248.

Nielsen, T.F.D., Sand, K.K., 2008. The Majuagaa kimberlite dike, Maniitsoq region, West Greenland: constraints on an Mg-rich silicocarbonatitic melt composition from groundmass mineralogy and bulk compositions. Can. Mineral. 46, 1043–1061.

Pilbeam, L.H., Nielsen, T.F.D., Waight, T.E., 2013. Digestion fractional crystallization (DFC): an important process in the genesis of kimberlites. Evidence from Olivine in the Majuagaa Kimberlite, Southern West Greenland. J. Petrol. 54, 1399–1425.

Roedder, E., 1984. Fluid inclusions. Michigan, Book Crafters Inc., Mineralogical Society of America. Rev. Mineral. 12, 644.

Sobolev, N.V., Sobolev, A.V., Tomilenko, A.A., Kovyazin, S.V., Batanova, V.G., Kuz'min, D.V., 2015. Paragenesis and complex zoning of olivine macrocrysts from unaltered kimberlite of the Udachnaya-East pipe, Yakutia: relationship with the kimberlite formation conditions and evolution. Russ. Geol. Geophys. 56, 260–279.

Soltys, A., Giuliani, A., Phillips, D., 2018. Crystallisation sequence and magma evolution of the De Beers dyke (Kimberley, South Africa). Mineral. Petrol. 112, 503–518.

Chapter 9 Appendices:

Appendix A: Analytical Techniques

Detailed studies of olivine and its inclusions were performed using a Hitachi SU-70 field emission (FE) scanning electron microscope (SEM) equipped with an Oxford AZtec Energy XMax 80 detector at the Central Science Laboratory, University of Tasmania. A beam accelerating voltage of 15 kV was used to produce high-resolution backscattered electron (BSE) images of minerals and energy-dispersive X-ray spectroscopy (EDS) semi-quantitative analyses and elemental maps of minerals.

Additional details on EMPA point measurements and X-ray mapping

Point measurements and x-ray element mapping of olivine were performed at the Central Science Laboratory, University of Tasmania, using a JEOL JXA-8530F Plus field emission electron microprobe.

Point Measurements

A beam accelerating voltage of 15 kV, a beam current of 300 nA and beam size of 2 µm were used. The trace elements Al, Cr, Ca, Mn and Ni were acquired by wavelength -dispersive x-ray spectrometry (WDS, one element per spectrometer) counting for 60 seconds on peaks and backgrounds using the following settings:

Element/ Line	WDS crystal	peak position	background high	background low	PHA baseline	PHA window	PHA Gain	PHA bias	PHA mode	dead time
Al Kα	TAP	90.53	94.38	85.63	0.7	9.3	32	1654	INTE	1.28
Ca Kα	PETL	107.61	109.76	104.31	1.5	3.9	8	1705	DIFF	1.39
Cr Kα	PETL	73.20	76.01	70.86	0.7	9.3	8	1677	INTE	1.38
Mn Kα	LiFL	146.24	150.54	142.24	0.7	9.3	32	1697	INTE	1.23
Ni Kα	LIFL	115.25	118.25	112.65	0.7	9.3	32	1668	INTE	1.26

Primary calibration standards were natural corundum (Harvard H126097, McGuire et al., 1992) for Al, natural wollastonite (in-house) for Ca, synthetic eskolaite Cr2O3 (99.99%, P&H Developments, UK) for Cr, natural rhodonite (Broken Hill, Australia, P&H Developments, UK) for Mn, and synthetic NiO (99.99%, P&H Developments, UK) for Ni.

The major elements Si, Mg, and Fe were acquired simultaneously with the WDS elements above using a Thermo UltraDry Extreme 30 mm^2 EDS detector with a total counting time of 90 seconds, time constant of 4000 ns and dead time of around 30%. Net intensities were extracted using the Filter Fit algorithm in Thermo Pathfinder 1.3. The calibration standard for all three elements was San Carlos Olivine (NMNH 111312-44; Jarosewich et al., 1980; Batanova et al., 2015). 3 points on this standard were acquired before and after the samples using the full method with all trace elements.

All data was acquired and processed using the Probe For EPMA package by Probe Software, Inc. (Eugene, OR, USA) and the default matrix corrections (Armstrong/Love Scott, LINEMU). Oxygen was calculated by stoichiometry and included in the matrix correction.
Detection limits, precision, and San Carlos Olivine data are given in Table DR 1.

X-Ray Element Mapping

X-ray element maps were acquired by WDS on the same instrument using an accelerating voltage of 20 kV, a beam diameter of 2 µm and a beam current of 70 nA in the first pass (Mg, Fe, Si) and 300 nA in the second and third pass (Al, Ca, Cr, Mn, Ni, Na, K, P). Fe, Si, K and P were measured on 2 WDS in parallel:

Spectrometer	1	2	3	4	5
Pass 1, 70 nA	Mg Kα, TAP	Fe Kα, LIFL	Si Kα, PETL	Si Kα, PETL	Fe Kα, LIFL
Pass 2, 300 nA	Al Kα, TAP	Mn Kα, LiFL	Ca Kα, PETL	Cr Kα, PETL	Ni Kα LIFL
Pass 3, 300 nA	P Kα, PETJ	K Kα, PETL	P Kα, PETL	Na Kα, TAPL	K Kα, PETL

The dwell time per pixel was 200 ms. The maps were quantified using the same calibration standards, software and matrix correction as above and the Mean Atomic Number background correction (Donovan & Tingle 1996) to correct for continuum background. Several additional point measurements were performed in different zones of the olivine to confirm compositional features observed in the map.

Raman Spectroscopy

The Raman spectra were recorded on a Renishaw inVia spectrometer with StreamLineHR, using a Helium–neon laser at 532nm with a power setting of 800 mW at the sampling spot, a 100x objective and a 1800 l/mm grating resulting in a spectral range of 115-1887 cm^{-1}. For 2D Raman maps, the following settings were employed: 10 accumulations at 1 s

exposure time. For 3D Raman maps, the following settings were employed: 3 accumulations at 1 s exposure time. 3D map data was reduced using direct classic least squares (DCLS) method.

Microthermometry

Thermometric experiments of olivine-hosted fluid inclusions were performed in air using a Linkam MDS 600 heating stage on an Olympus BX51 microscope equipped with an Olympus DP11 digital camera.

References

Batanova, V. G., Sobolev, A. V., and Kuzmin, D. V., 2015, Trace element analysis of olivine: High precision analytical method for JEOL JXA-8230 electron probe microanalyser: Chemical Geology, v. 419, p. 149-157, https://doi.org/10.1016/j.chemgeo.2015.10.042.

Donovan, J. J. and Tingle, T. N., 1996, An improved mean atomic number background correction for quantitative microanalysis: Journal of the Microscopy Society of America, v. 2, p. 1-7, https://doi.org/10.1017/S1431927696210013.

Jarosewich, E., Nelen, J. A., and Norberg, J. A., 1980, Reference samples for electron microprobe analysis: Geostandards Newsletter, v. 4, p. 43-47, https://doi.org/10.1111/j.1751-908X.1980.tb00273.x.

McGuire, A. V., Francis, C. A., and Dyar, M. D., 1992, Mineral standards for electron microprobe analysis of oxygen: American Mineralogist, v. 77, p. 1087-1091.

Appendix B: Supplementary Figures

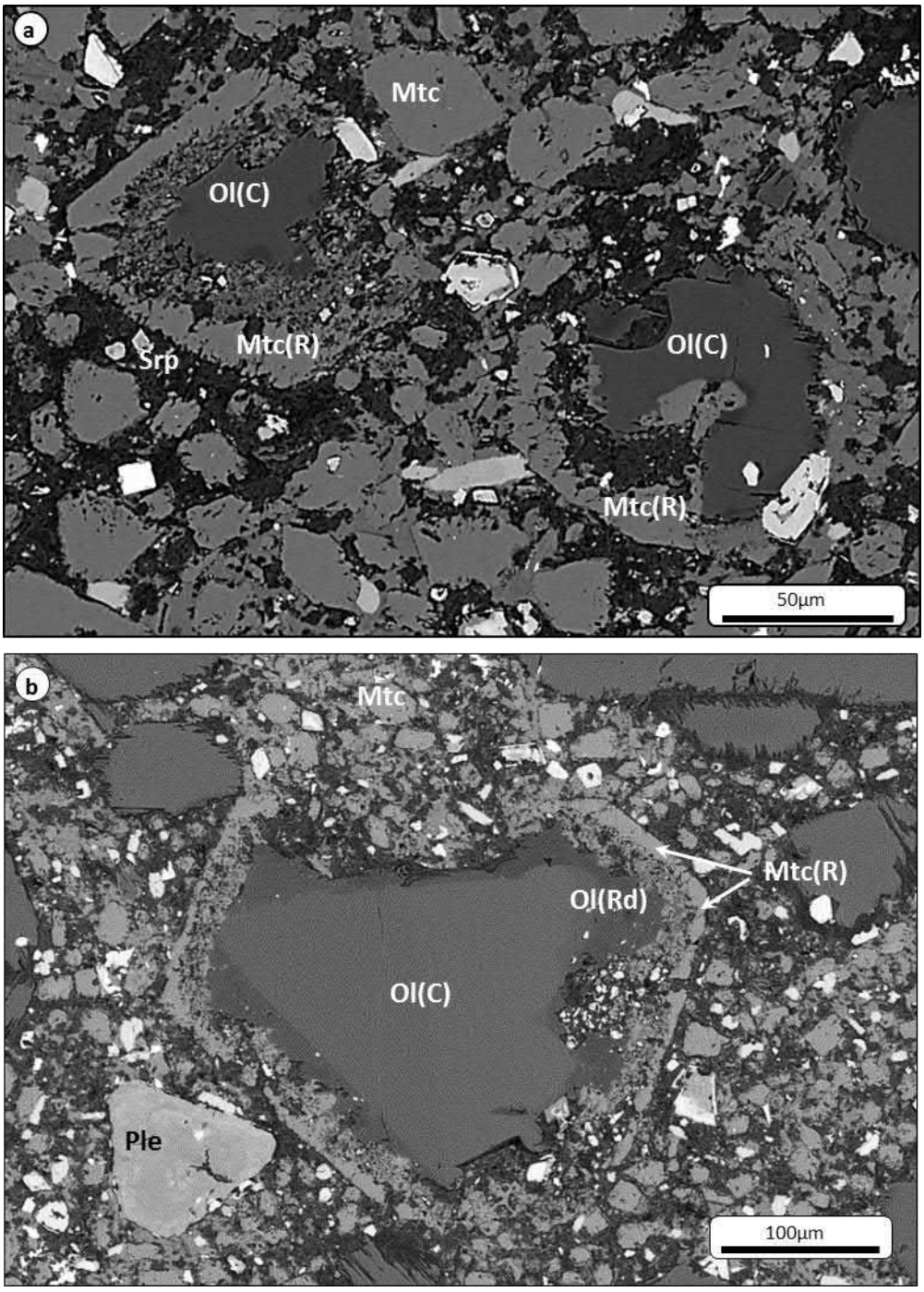

Supplementary Figure 1. (a, b) Back-scattered electron (BSE) SEM images of olivine (Ol) grains (Cores – C) partial and/or overgrowth by a rim of monticellite (Mtc(R)). The kimberlite groundmass is dominated by subhedral-to-euhedral monticellite (Mtc) grains. Srp: serpentine.

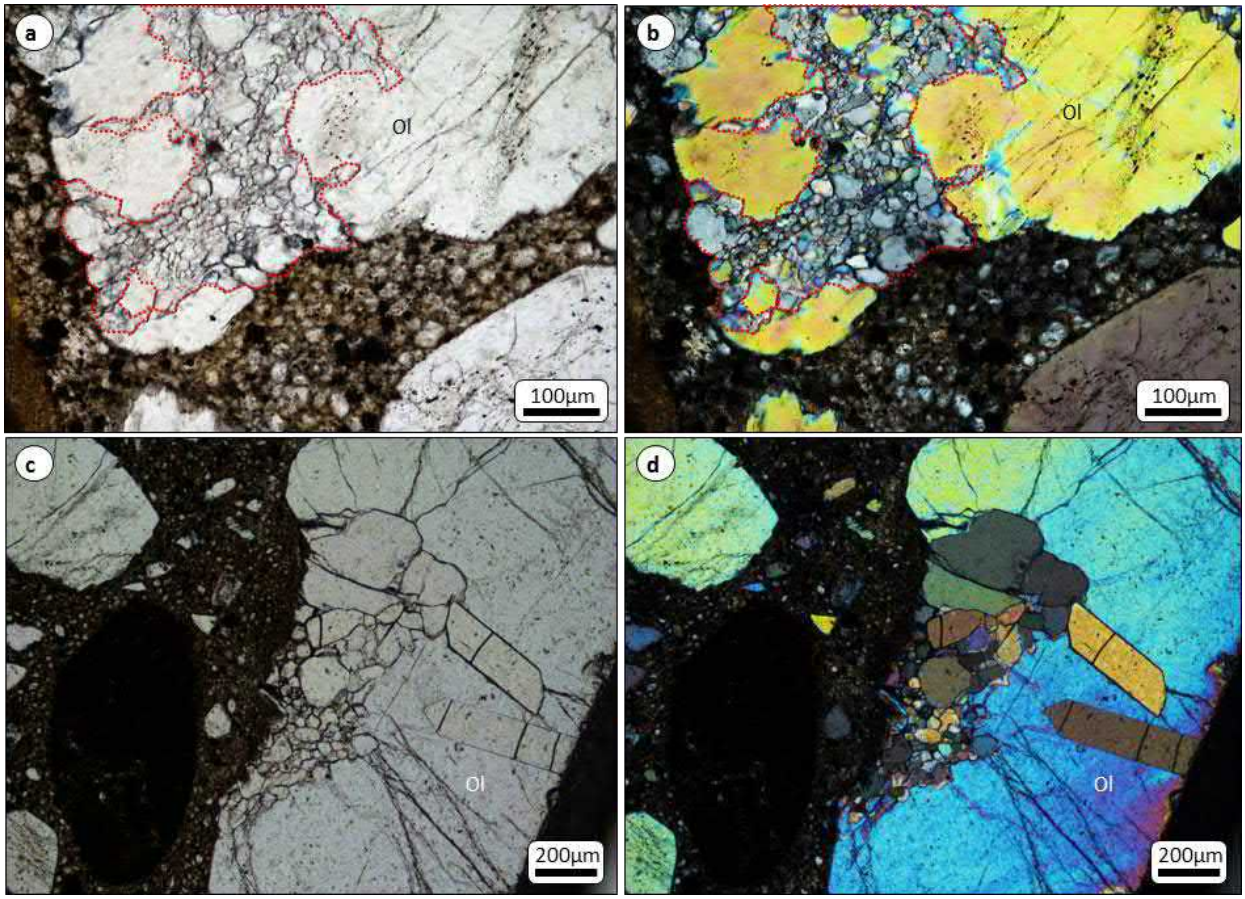

Supplementary Figure 2. Optical photomicrographs in (a, c) plane-polarised light and (b, d) cross-polarised light of olivine with embayments/fractures infilled by euhedral-shaped polycrystalline recrystallised olivine grains.

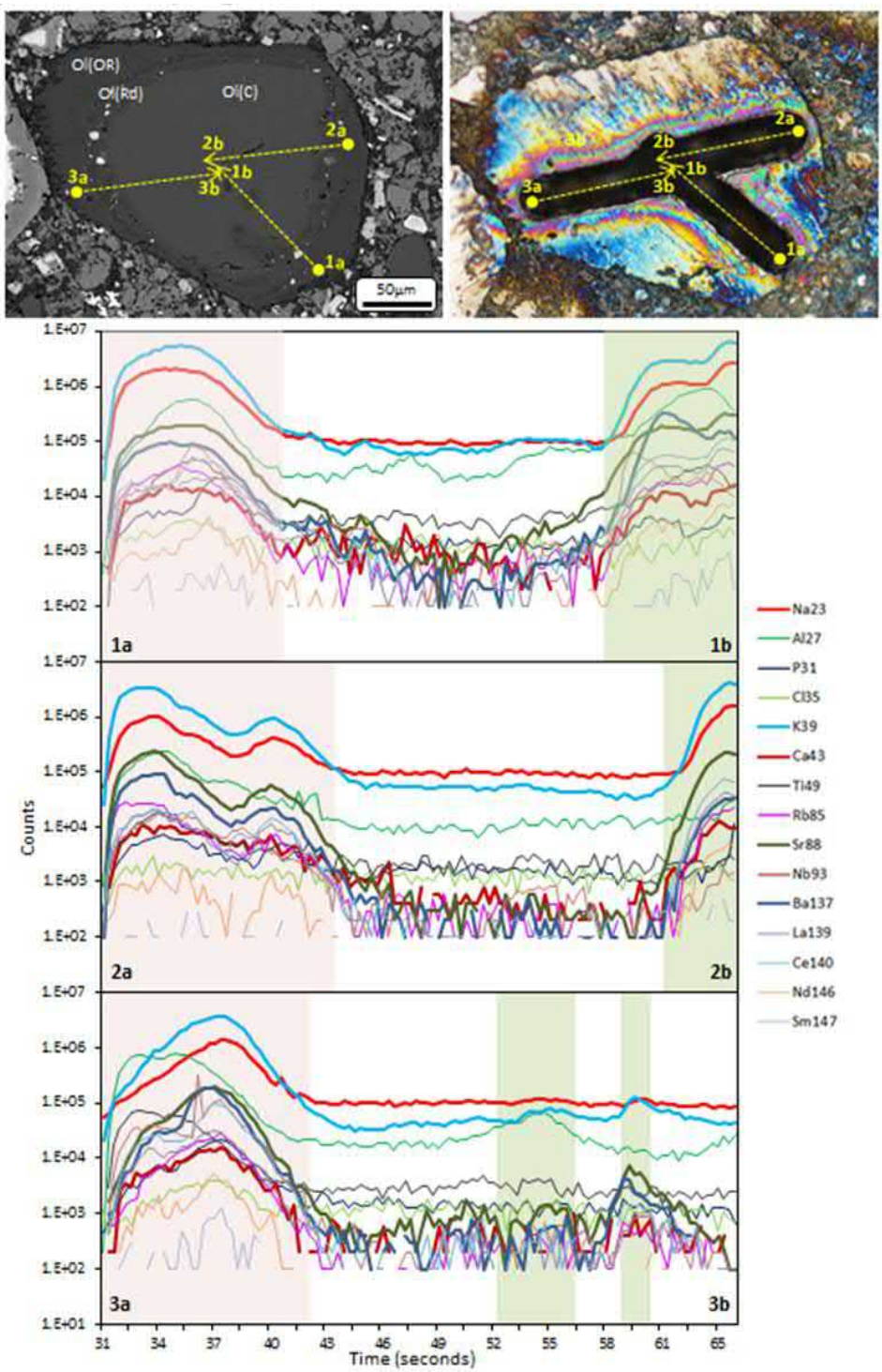

Supplementary Figure 3. Back-scattered electron (BSE) SEM and reflected light images, and representative LA-ICPMS traverses of a zoned olivine (Ol) grain from the Mark kimberlite (Grain 1), showing ablated inclusions in rinds (Rd) as well as in the olivine core (C). Inclusions in the core are interpreted to be pseudosecondary in origin. Inclusions are heterogeneous in composition and reflected by positive anomalies in elements such as alkalis/alkali-earths (Ca, Na, K, Ba, Rb, Cs), light rare earth elements (LREEs), Al, P and Nb. These positive anomalies usually occur in synchronisation with two or more of these elements. The appearance of inclusions in the outmost rind (OR) may be due to the spot size of the laser during analyses overlapping with the rind zone. The yellow arrows show the direction of the laser analyses. The red shaded zone represents primary inclusions hosted in the olivine rind and the green shaded zone represents pseudosecondary inclusion trails.

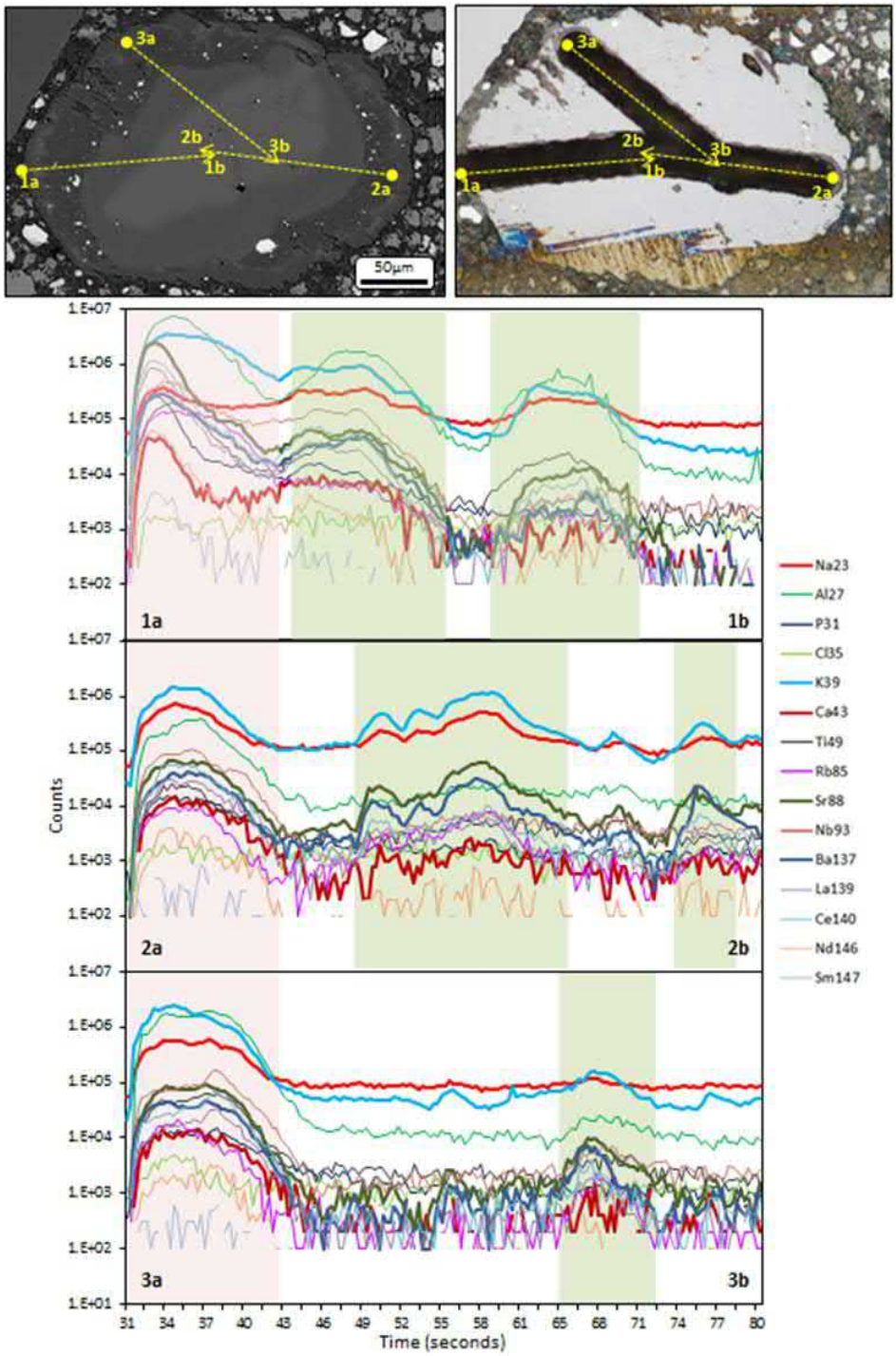

Supplementary Figure 4. Back-scattered electron (BSE) SEM and reflected light images, and representative LA-ICPMS traverses of a zoned olivine (Ol) grain from the Mark kimberlite (Grain 2), showing ablated inclusions in rinds (Rd) as well as in the olivine core (C). Inclusions in the core are interpreted to be pseudosecondary in origin. Inclusions are heterogeneous in composition and reflected by positive anomalies in elements such as alkalis/alkali-earths (Ca, Na, K, Ba, Rb, Cs), light rare earth elements (LREEs), Al, P and Nb. These positive anomalies usually occur in synchronisation with two or more of these elements. The appearance of inclusions in the outmost rind (OR) may be due to the spot size of the laser during analyses overlapping with the rind zone. The red shaded zone in the laser ablation traverse represents primary inclusions hosted in the olivine rind and the green shaded zone represents pseudosecondary inclusion trails.

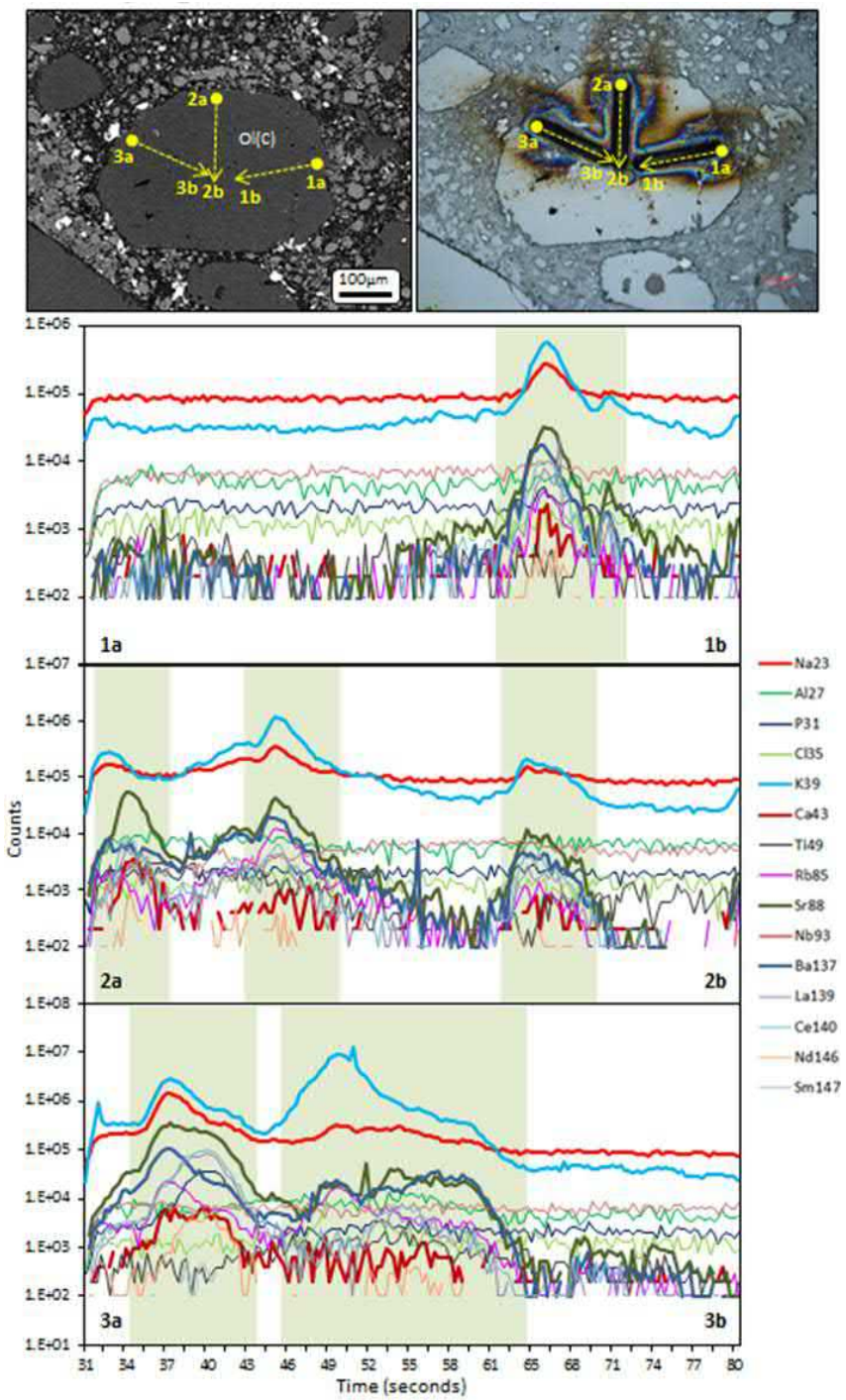

Supplementary Figure 5. Back-scattered electron (BSE) SEM and reflected light images, and representative LA-ICPMS traverses of an unzoned olivine (Ol) grain from the Mark kimberlite (Grain 3), showing ablated inclusions in rinds (Rd) as well as in the olivine core (C). Inclusions in the core are interpreted to be pseudosecondary in origin. Inclusions are heterogeneous in composition and reflected by positive anomalies in elements such as alkalis/alkali-earths (Ca, Na, K, Ba, Rb, Cs), light rare earth elements (LREEs), Al, P and Nb. These positive anomalies usually occur in synchronisation with two or more of these elements. The appearance of inclusions in the outmost rind (OR) may be due to the spot size of the laser during analyses overlapping with the rind zone. The green shaded zones represent pseudosecondary inclusion trails.

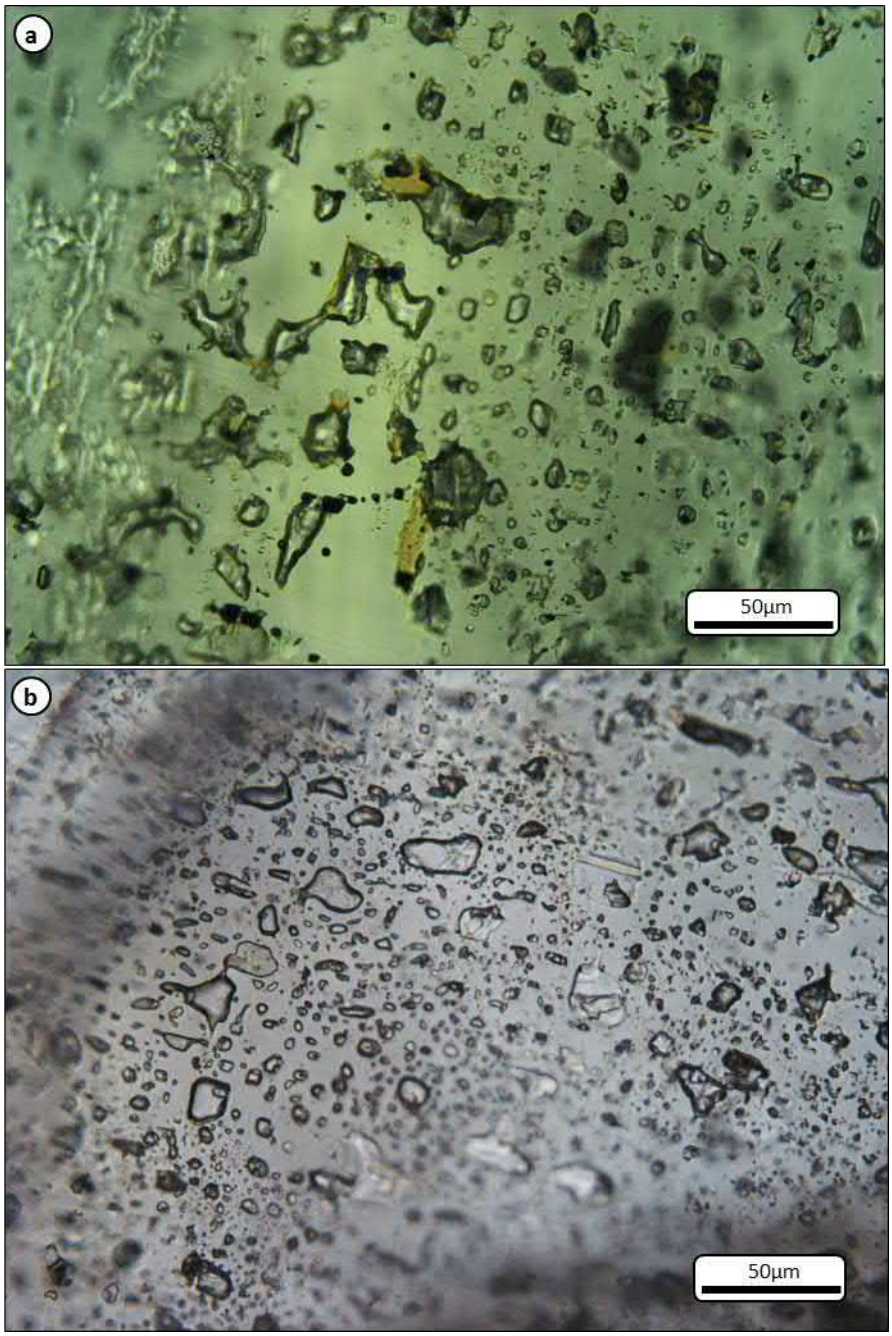

Supplementary Figure 6. Optical photomicrographs in plane-polarised light of pseudosecondary melt/fluid inclusion trails in olivine.

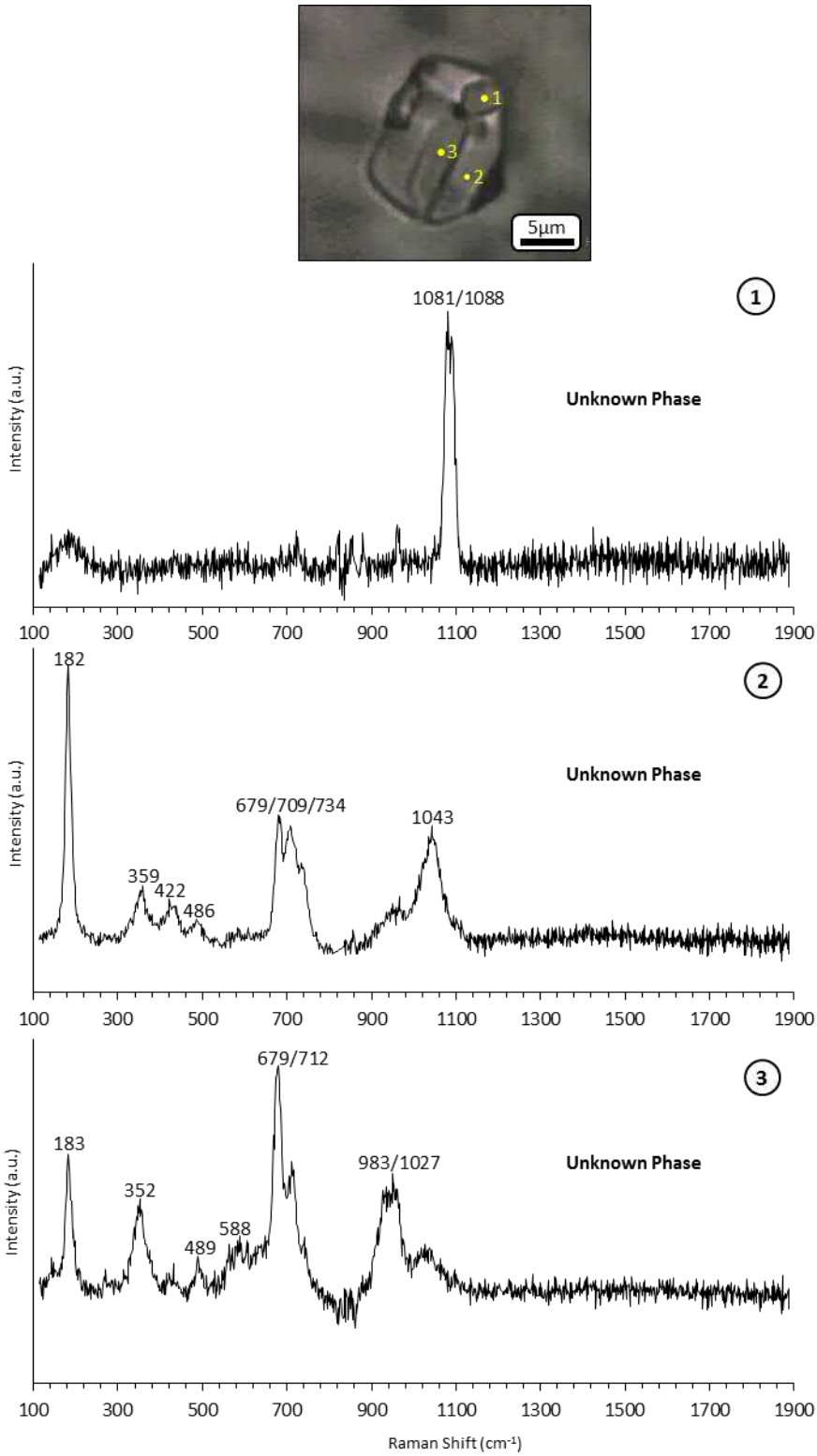

Supplementary Figure 7. Representative Raman spectra of an olivine-hosted pseudosecondary melt inclusion and the corresponding optical (transmitted light) image. Points 1 – 3 (yellow dots) are the locations where Raman spectra were collected (see 'Inclusion 4' in Supplementary Table S2). a.u.: arbitrary units.

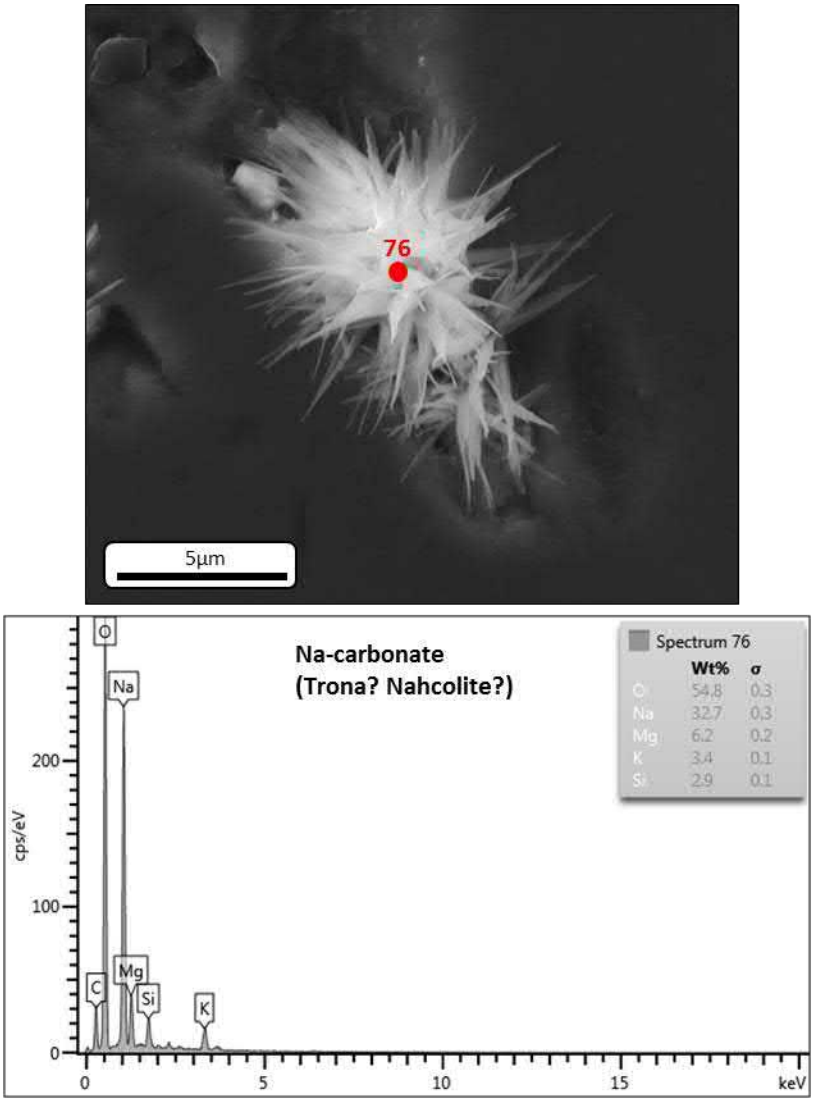

Supplementary Figure 8. Back-scattered electron (BSE) SEM image and corresponding EDS-spectra of a decrepitated olivine-hosted pseudosecondary melt inclusion. The hosted inclusion phases have re-crystallised on the olivine surface and around the inclusion cavity. The re-crystallised minerals (Na-carbonate – trona or nahcolite) are secondary in origin and formed due to atmospheric interaction after exposure of the inclusion. The red dots represent the corresponding analytical points.

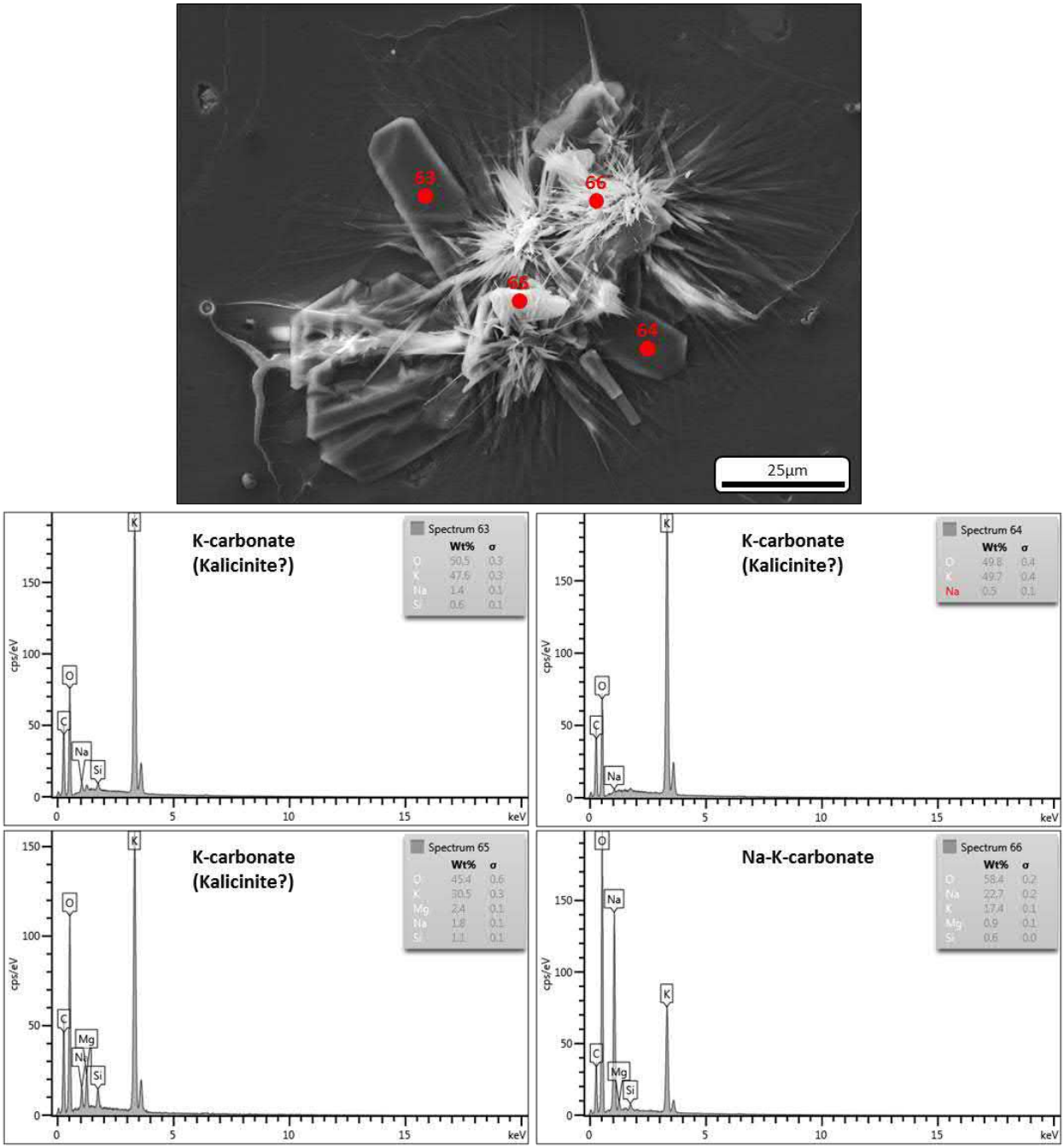

Supplementary Figure 9. Back-scattered electron (BSE) SEM image and corresponding EDS-spectra of a decrepitated olivine-hosted pseudosecondary melt inclusion. The hosted inclusion phases have re-crystallised on the olivine surface and around the inclusion cavity. The re-crystallised minerals (K-carbonates – kalicinite(?) and an unidentified Na-K carbonate) were formed due to atmospheric interaction after exposure of the inclusion. The red dots represent the corresponding analytical points.

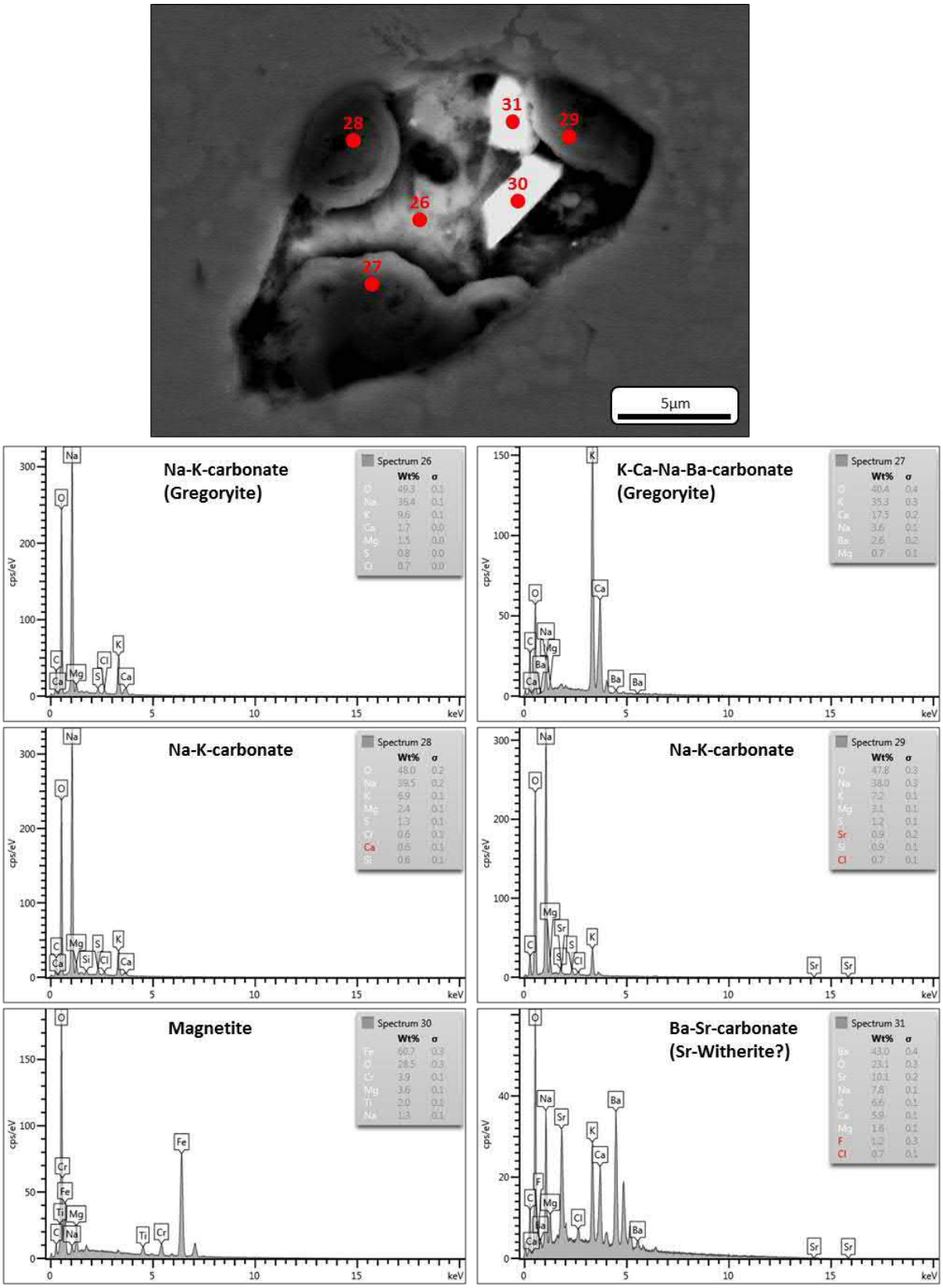

Supplementary Figure 10. Back-scattered electron (BSE) SEM image and corresponding EDS-spectra of a olivine-hosted pseudosecondary melt inclusion. The inclusion contains magnetite, gregoryite, unidentified Na-K carbonates and Sr-bearing witherite. Cavities within the inclusion likely formed due to polishing and exposure of the inclusion. The red dots represent the corresponding analytical points.

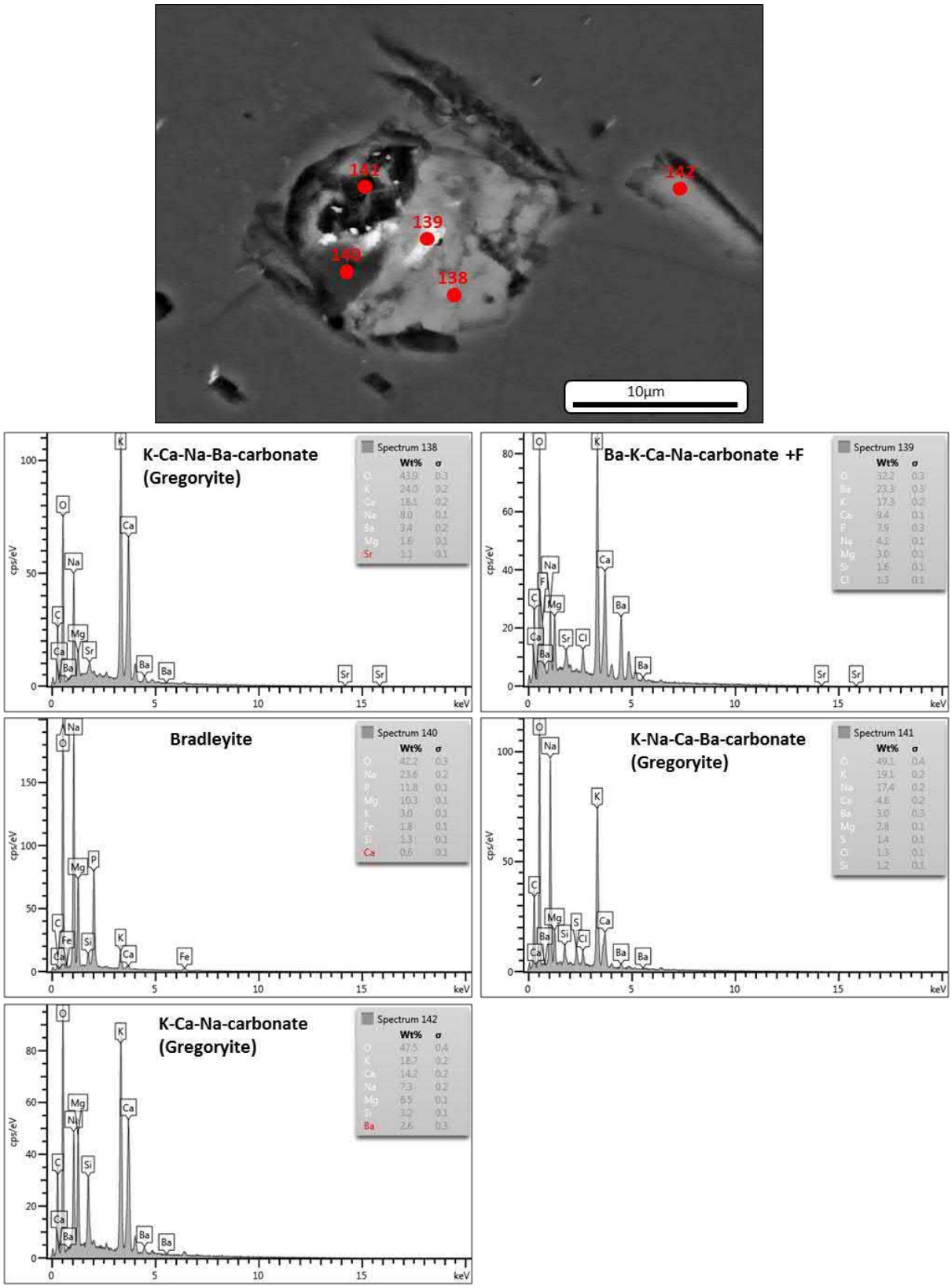

Supplementary Figure 11. Back-scattered electron (BSE) SEM image and corresponding EDS-spectra of a olivine-hosted pseudosecondary melt inclusion. The inclusion contains gregoryite, unidentified F-bearing Ba-K-Ca-Na carbonates and bradleyite. Cavities within the inclusion likely formed due to polishing and exposure of the inclusion. The red dots represent the corresponding analytical points.

Electronic Appendix C: Supplementary Tables

Table S1 [Electronic Appendix]

Electronic Appendix C: Supplementary Tables

Supplementary Table S2

Supplementary Table S2. Raman compositions of olivine-hosted pseudosecondary inclusions

Sample	Phase	Wave Number cm^{-1}					
Inclusion 1*	**(1) Dolomite**	183m	304m		727	1100s	
	(4) Magnetite		310	545	676s		
	(3) Carbonate?	214m	268m			1107s	
	(4) Magnetite		319	545	672s		
	(5) Unknown	183m		431	707m	931m/1041m	
	(6) Sulphate?		337	458m	625	996s	1098
	(7) Carbonate?				975	1083m	
	(8) Magnesite	218	333m		740	1099s	
	Unknown	167	222		971s/975s	1083s	
	Unknown					975	1083m/1104
Inclusion 2	**CO_2**					1288	1392
	Magnesite		329m		737	1093s	
	Magnetite		325	542	672s		
	Allanite?	225m	288s	401m	595m/652m	860	1283
Inclusion 3	**Sulphate?**		456	617	984s	1104	1145
Inclusion 4*	**(1) Unknown**					1081s/1088s	
	(2) Unknown	182s	359/422/486		679m/709m/734m	1043m	
	(3) Unknown	183m	352m	489	588	679s/712m	950m/1027

Raman shifts for analyses points. s: strong intensity; m: medium intensity and weak intensities are unlabelled.

*Inclusion 1 sites are shown in Figure 9.

*Inclusion 4 sites are shown in Figure 10.

Evolution of kimberlite magmas in the crust: A case study of groundmass and mineral-hosted inclusions in the Mark kimberlite (Lac de Gras, Canada)

Submitted to Lithos

Adam Abersteiner[1,2*], Vadim S. Kamenetsky[1,2,3], Karsten Goemann[4], Bruce A. Kjarsgaard[5], Kathy Ehrig[6], Maya Kamenetsky[1]

[1] *School of Natural Sciences and Centre of Excellence in Ore Deposits (CODES), University of Tasmania, Hobart, Tasmania 7001, Australia*
[2] *Institute of Volcanology and Seismology, Far East Branch, Russian Academy of Sciences, 683006 Petropavlovsk-Kamchatsky, Russia*
[3] *Institute of Experimental Mineralogy RAS, Chernogolovka 142432, Russia*
[4] *Central Science Laboratory, University of Tasmania, Hobart, Tasmania 7001, Australia*
[5] *Geological Survey of Canada, 601 Booth Street, Ottawa, ON K1A 0E8, Canada*
[6] *BHP Olympic Dam, Adelaide, SA 5000, Australia*

Abstract

Kimberlite are the surface manifestation of deeply-derived (>150 – 200 km) and rapidly ascended magmas. Fresh kimberlite rocks are exceptionally rare, as most of them are invariably modified by pervasive deuteric and/or post-magmatic fluids that overprint the original mineralogy. In this study we examined the fresh archetypal Mark kimberlite (Lac de Gras, Canada), which is characterised by well-preserved olivine and groundmass minerals. The sequence of crystallisation of the parental melt and its major compositional features were reconstructed using textural relationships between magmatic minerals, their zoning patterns and crystal/melt/fluid inclusions. Crystal and multiphase primary, pseudosecondary and secondary melt/fluid inclusions in olivine, Cr-diopside, spinel, perovskite, phlogopite/kinoshitalite, apatite and calcite preserve a record of different stages of kimberlite melt evolution. Melt/fluid inclusions are generally more depleted in silica and more enriched

in alkalis (K, Na), alkali-earth (Ba, Sr) and halogens (Cl, F) relative to the whole-rock composition of the Mark kimberlite. These melt/fluid inclusion compositions, in combination with presence of elevated CaO (up to 1.73 wt.%), in Mg-rich olivine rinds, crystallisation of groundmass kinoshitalite, carbonates (calcite, Sr-Ba-bearing) and alkali-enriched rims around apatite suggests that there was progressive enrichment in CO_2, alkalis and halogens in the evolving parental melt.

The Mark kimberlite groundmass is characterised by the following stages of *in-situ* crystallisation: (1) olivine rims around xenocrystic cores + Cr-spinel/TIMAC. (2) Mg-rich olivine rinds around olivine rims/cores + MUM-spinel (followed by pleonaste and Mg-magnetite) + monticellite (+ partial resorption of olivine, along with the formation of ferropericlase and CO_2 as a result of decarbonation reactions) + perovskite + apatite. (3) Olivine outmost rinds, which are coeval with phlogopite/kinoshitalite → apatite + sulphides + carbonate (calcite, Ba-Sr-Na-bearing varieties). (4) Deuteric (i.e. late-stage magmatic) and/or post-magmatic (i.e. external fluids) alteration of magmatic minerals (e.g., olivine, monticellite, ferropericlase) and crystallisation of mesostasis serpentine, K-bearing chlorite and brucite (i.e. replacement of ferropericlase). The absence of any groundmass minerals that can accommodate significant amounts of alkalis (Na, K) and halogens (F, Cl) resulted in these elements becoming concentrated in the late-stage melt where they potentially formed unstable, water-soluble carbonates (such as those observed in melt inclusions). Consequently, these minerals were most likely removed from the groundmass by deuteric and/or post-magmatic alteration.

1. Introduction

Kimberlites are rare and volumetrically minor igneous rocks that are volatile-rich (CO_2, H_2O) and composed of variable mixtures of xenocrystic, magmatic and hydrothermal minerals (Mitchell et al., 2019). The magmas that give rise to kimberlites are the most deeply derived (>150km; Clement et al., 1984; Mitchell, 1986; Pearson et al., 2014) and can therefore provide important insights into the composition and nature of the sub-continental lithospheric and asthenospheric mantle. However, there are many uncertainties regarding the evolution and crystallisation of kimberlite magmas due to the ubiquitous effects of contamination by mantle and crustal material, volatile exsolution and degassing, and crystallisation. Following their emplacement in the crust, kimberlites are almost always pervasively altered by deuteric (i.e. late-stage magmatic; Mitchell, 2008, 2013; Wilson et al.,

2007) and/or infiltrating hydrothermal and meteoric fluids (Giuliani et al., 2014, 2017; Sparks et al., 2006, 2009; Stripp et al., 2006). These processes result in the overprinting of primary minerals (e.g., olivine, monticellite, carbonate) by assemblages of serpentine, brucite, chlorite and calcite (Clement, 1982; Mitchell, 1986; Skinner, 1989; Stripp et al., 2006). Furthermore, water soluble minerals (e.g., alkali-carbonates and chlorides) are the least stable in kimberlites and are invariably leached out by hydrous fluids (e.g., Abersteiner et al., 2018; Kamenetsky et al., 2004; Kamenetsky et al., 2012).

Reconstructing kimberlite petrogenesis is further obscured by the fact that there are very few examples of kimberlites worldwide that exhibit well-preserved olivine phenocrysts, groundmass minerals and original magmatic textural relationships (e.g., Leslie and Aaron (Canada; Fedortchouk and Canil, 2004), Diavik (Canada; Brett et al., 2009), Koala (Canada; Kamenetsky et al., 2013), Grizzly (Canada; Lim et al., 2018), Udachnaya-East (Russia; Kamenetsky et al., 2007), Bultfontein (South Africa; Giuliani et al., 2017), Benfontein (South Africa; Howarth et al., 2016), De Beers (South Africa; Soltys et al., 2018), Majuagaa (Greenland; Nielsen and Sand, 2008)). Recently, the Mark kimberlite (Lac de Gras, Canada) was shown to contain very fresh (i.e. unserpentinised) olivine, which is characterised by compositional zoning and different generations of olivine-hosted melt/fluid inclusions (i.e. primary and pseudosecondary), reflecting multistage growth (Abersteiner et al., 2020). Similar to olivine, the groundmass in general is reasonably well-preserved and consists of spinel, perovskite, monticellite, apatite and phlogopite-kinoshitalite set in a mesostasis assemblage of serpentine, calcite, brucite, chlorite, apatite and rare Cu-Fe sulphides and witherite.

We present a detailed investigation of the petrography, geochemistry and hosted crystal/melt/fluid inclusions of a hypabyssal (coherent) sample of the Mark kimberlite. Here, we link the textural relationships between different crystallising minerals and their zoning patterns, along with their hosted inclusions, in order to reconstruct the relative sequence of magmatic crystallisation and fluid precipitation to constrain the major compositional features of the parental melt.

2. Geology

The Mark kimberlite (Fig. 1) is part of the diamondiferous Lac de Gras kimberlite field, which is located in Archean Slave Province (Canada). The kimberlite outcrops as a small (~100 × 150m in diameter, based on geophysical interpretation) hypabyssal (coherent)

body, which intruded cordierite porphyroblastic metagreywackes of the Yellowknife Supergroup (Davis and Kjarsgaard, 1997). Due to limited exposed outcrop, geological data and reverse circulation drill chips, the internal structure and dimensions of the Mark kimberlite body is poorly constrained. The level of erosion of Cretaceous±Eocene sediments, which were present during Eocene kimberlite emplacement in the Lac de Gras region, are estimated to be between 100 – <300m (Field and Scott Smith, 1999). Rb-Sr isochron age determination using macrocrystic phlogopite grains produced an age of ~47.5 ± 0.5Ma (Davis and Kjarsgaard, 1997).

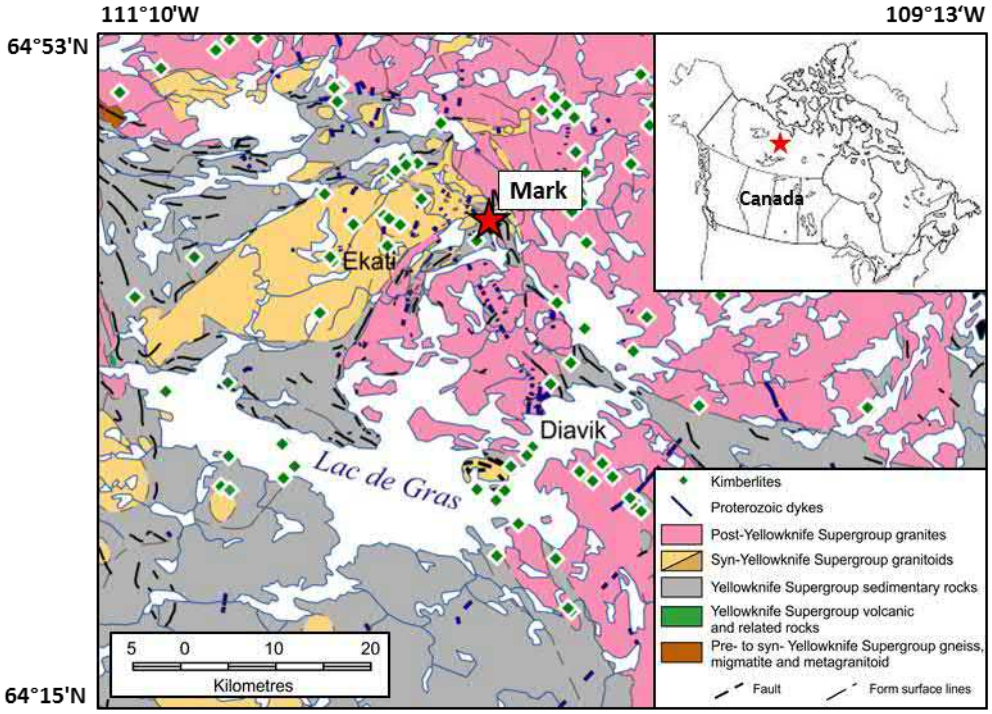

Figure 1. Geological map of the central Slave Province showing the location of the Mark kimberlite in the Lac de Gras area (adopted from Abersteiner et al., 2020 and modified after Kjarsgaard et al., 2002).

3. Petrography and Geochemistry of the Mark Kimberlite

Sample (KIA93-K136) was selected for this study as it represents the freshest available piece of the Mark kimberlite. The sample was derived from surface outcrop and was previously studied by Davis and Kjarsgaard (1997) and Abersteiner et al. (2020). The sample is macrocrystic in texture and dominated by abundant macrocrystic olivine (~55 vol.%), along with lesser amounts of (<5 vol.%) macrocrysts of phlogopite, Cr-pyrope, Cr-diopside and rare Mg-ilmenite (Fig. 2). The groundmass is fine-grained and consists principally of monticellite (~20 vol.%) along with (in order of decreasing abundance)

euhedral olivine microphenocrysts, spinel (i.e. chromite, titanian magnesian aluminous chromite (TIMAC; Mitchell, 1986), pleonaste, magnesian ulvöspinel – magnetite (MUM) and Mg-magnetite), perovskite, apatite and phlogopite-kinoshitalite. The mesostasis assemblage is composed of interstitial serpentine, calcite, brucite, chlorite, apatite and rare Cu-Fe sulphides and disseminated witherite. This mineral assemblage is typical of archetypal kimberlites worldwide (Mitchell, 1995).

3.1 Petrography and Mineral Compositions

The petrography and mineral compositions of sample KIA93-K136 was examined by optical microscope and field emission SEM (scanning electron microscopy) and energy-dispersive X-ray spectroscopy (EDS). Quantitative analyses of olivine, monticellite and spinel were acquired by EMP (see Table 1). In addition, EMP X-ray element maps were used to characterise the compositional zoning patterns in perovskite and apatite (see Supplementary Material). The composition of apatite cores and zoned rims was extracted from these EMP X-ray element maps (see Table 1).

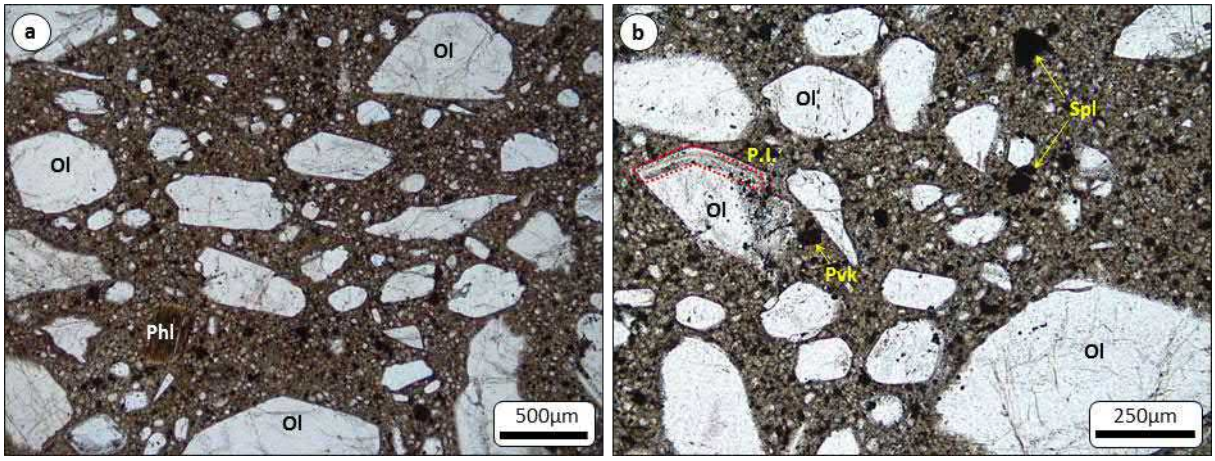

Figure 2. Optical transmitted light image photomicrographs of the studied Mark kimberlite, which exhibits a macrocrystic texture defined by olivine (Ol) and kinoshitalite (Kin) macrocrysts. Spl: spinel, Pvk: perovskite, P.I: primary inclusions, which occur as parallel aligned trails that are located along the periphery of a zoned olivine grain.

3.1.1 Olivine

The petrography and compositions of olivine from Mark kimberlite sample (KIA93-K136) was previously examined in detail by Abersteiner et al. (2020), therefore only a summary is presented here. Olivine grains occur as both large (0.3 – 1.5 cm) rounded-to-anhedral macrocrysts and angular fragments, and as smaller (50µm – 2 mm) subhedral-to-

euhedral phenocrysts (Figs. 2, 3). The majority of olivine grains are fresh and exhibit either negligible or minor serpentinisation (<5vol.% replacement by serpentine) along rims and internal fractures. Olivine is typically zoned, where it consists of a core, which in turn may be overgrown by between one and four compositionally distinct overgrowths (i.e. transitional zone, rim, rind and outmost rind). A summary of olivine major and trace element compositions is presented in Table 1 and in Abersteiner et al. (2020).

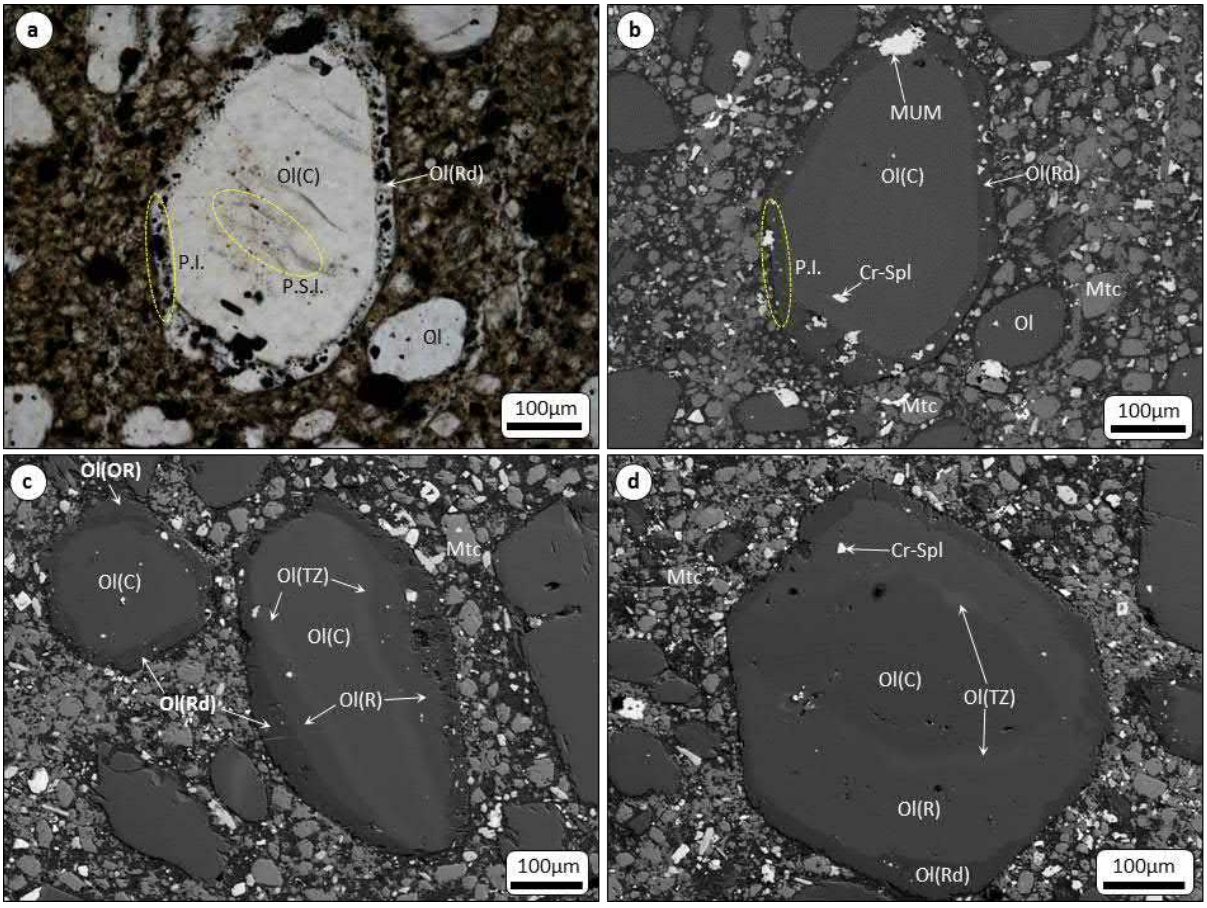

Figure 3. (a) optical transmitted light microphotograph and (b – d) back-scattered electron (BSE) SEM images of zoned olivine (Ol) grains. C: core, TZ: transitional zone, R: rim, Rd: rind, OR: outmost rind. Images panels (a) and (b) show corresponding optical and BSE image of the same olivine grain. Olivine rinds are distinguished by their darker response in BSE-imaging due to their high Mg-content and abundance of hosted crystal and melt inclusions. (a) This image shows the distribution of primary melt/crystal inclusions (P.I) in the rind, whereas pseudosecondary inclusions (P.S.I) are restricted to the core. (c) and (d) show variations in thicknesses and dimensions of zoning patterns between different olivine grains. Cr-spinel: Cr-Spl, magnesian ulvöspinel – magnetite (MUM). Mtc: monticellite.

Olivine cores are variable in shape (e.g., ovoid, anhedral, angular and subhedral) and are relatively homogeneous in composition, but show wide intergranular variation in terms of

Fo-content (Mg/(Mg+Fe2+)×100; Fo88.1-93.6; Table 1). Olivine cores are sometimes characterised by a thin (<30 – 40 µm) transitional zone, which occurs along the boundary between the core and surrounding rim or rind (Fig. 3c, d). These transitional zones are compositionally intermediate between the olivine core and surrounded rim/rind zone (i.e. increasing Mg-content relative to the core). Olivine rims (Fig. 3c, d) vary in width from 10 – 150 µm and form sharp boundaries with the core and are characterised by a narrow Fo-range (Fo91.4–92.1; Table 1). Approximately ≤10% of olivine grains, regardless of their size, morphology or interior zoning patterns are surrounded by a variably thick rind (10 – 100 µm; Fig. 3), which contains abundant crystal/melt/fluid inclusions (see section 4). Rinds are characterised by significantly higher MgO (Fo95.3–98.1) and CaO (0.26 – 1.73 wt.%) rich compositions compared to cores and rims (Table 1). Olivine rinds are sometimes overgrown by an 'outmost rind' that is variable in thickness (10 – 70 µm), characterised by elevated Fe-content (Fo92.7-95.4) relative to the Mg-rich rinds, and are free of inclusions (Fig. 3c). Outmost rinds were only identified surrounding Mg-rich rinds, but not cores or rims.

3.1.2 Macrocryst Assemblage

Olivine is described above. Macrocrystic phlogopite (Fig. 2a) occurs as elongated and rounded grains that are up to 1 cm in size and zoned along the periphery towards the kinoshitalite endmember. In addition, these grains are corroded along the margins and partially altered to chlorite. Macrocrystic Cr-pyrope occurs as large (up to 1 cm) rounded crystals and is typically surrounded by variably thick rims of fine-grained intergrowths of kelyphite. Cr-diopside macrocrysts are up to 0.5cm in size and typically rounded. The margins of these grains are typically corroded with numerous embayments, which are composed of admixtures of serpentine and carbonate.

3.1.3 Monticellite

Monticellite is the most abundant groundmass constituent that occurs as subhedral-to-euhedral grains between 10 – 80 µm in size (Figs. 3, 4). The majority of monticellite grains are partially corroded along their margins. In addition, monticellite rarely form rims surrounding olivine (Abersteiner et al., 2020). Similar features were previously described in the neighbouring monticellite-rich Leslie kimberlite (Abersteiner et al., 2018; Bussweiler et al., 2015). Discrete groundmass monticellite grains are relatively homogeneous and do not exhibit any zonation. However, monticellite grains show a wide variation in composition, where they form solid solutions between monticellite (74.7 – 97.3 mol.%), kirschsteinite (2.7

– 5.1 wt.%) and forsterite (0 – 20.3 mol.%; Table 1). These compositions show compositional overlap with monticellite from other Lac de Gras and Canadian kimberlites (Abersteiner et al., 2018; Armstrong et al., 2004; Zurevinski et al., 2008). Monticellite grains also contains very minor amounts of alkalis (Na_2O + K_2O: up to 0.29 wt.%) as well as appreciable P_2O_5 (0.16 – 0.85 wt.%), which shows coupling with Na_2O. Analysis of a single monticellite rim surrounding olivine found it to be compositionally similar to groundmass monticellite grains.

3.1.4 Spinel

Spinel is a minor constituent mineral of the groundmass (~1 – 2 vol.%) and occurs as euhedral crystals, which range in size considerably from <20 – 500 µm (Fig. 4a, b). Larger spinel grains (i.e. >100 µm) are usually zoned, where the core is typically chromian-rich (Cr-spinel, chromite) in composition and characterised by very high Cr_2O_3 (41.1 – 62.0 wt.%) along with moderate FeO_{total} (17.0 – 22.4 wt.%), low Al_2O_3 (4.8 – 13.3 wt.%) and very low TiO_2 (0.08 – 5.1 wt.%). Spinel are usually zoned towards TIMAC/MUM-spinel compositions from core to rim, which is reflected by progressive enrichment in TiO_2, Fe^{3+} (and to a lesser extent Fe^{2+}; Table 1), MgO, Al_2O_3 and MnO, and significant decreases in Cr_2O_3 concentrations (Supplementary Figure 1). This is consistent with magmatic spinel Trend 1 (Mitchell, 1986). Zoned chromian-rich spinel (i.e. chromite to TIMAC/MUM compositions) cores are herein collectively referred to as 'Cr-spinel' and usually characterized by an abrupt change in composition to pleonaste, where it forms a variably thick rim up to 50 µm wide (Fig. 4a, b). Pleonaste is characterised by very high Al_2O_3 (40.5 – 50.4 wt.%), along with moderate FeO_{total} (22.7 – 30.3 wt.%) and MgO (21.3 – 22.4 wt.%), and low TiO_2 (2.6 – 5.4 wt.%) and very low Cr_2O_3 (0.4 – 2.3 wt.%; Supplementary Figure S1; Table 1). Pleonaste is in turn sometimes surrounded by a very thin (<2 µm) and discontinuous rim of Mg-magnetite, which was too thin be accurately determined by EMPA. Smaller spinel grains (<80 µm) also can occur in the groundmass as individual euhedral grains of MUM and/or pleonaste that are usually surrounded by thin rims (<3 µm) of Mg-magnetite.

3.1.5 Perovskite

Perovskite is a minor (~1 vol.%) groundmass mineral that occur as exceptionally large (up to 400 µm) euhedral crystals, which are observed intergrown around olivine, or as interpenetrant twinned clusters of multiple perovskite grains (Figs. 4c, d, 5). Perovskite is characterised by concentric oscillatory zoning with individual zones typically between 1 – 10 µm in thickness. Some perovskite grains can contain between 30 - >40 individual zones,

which are characterised by changes in brightness in BSE-SEM imaging. It is noteworthy that zoning is not always perfectly straight, but occasionally exhibits kinks, which surround fractures, or individual zones may be convoluted and irregular-shaped (Figs. 4c, d, 5, 7). Brighter zones are characterised by elevated LREE (e.g., La, Ce, Nd), Na, Nb and Th.

Figure 4. Back-scattered electron (BSE) SEM images of groundmass: (a, b) euhedral zoned spinel, which is composed of a Cr-rich (Cr-spinel to titanian magnesian aluminous chromite – TIMAC) core (Cr-Spl) that is zoned towards magnesian ulvöspinel-magnetite (MUM) compositions. This in turn is mantled by a variably thick rim of pleonaste (Ple), which is surrounded by a thin discontinuous rim of Mg-magnetite (Mg-Mag). (b) The Cr-Spinel/MUM core occasionally shows uneven and embayed contacts with the pleonaste rim. (c, d) Intergrown clusters of euhedral perovskite (Pvk) grains. Perovskite is oscillatory zoned, which is distinguished by lighter and darker zones in BSE-imaging. In addition, perovskite also contains abundant crystal inclusions of olivine (Ol) and spinel (e.g., pleonaste, MUM) and primary melt inclusions (P.I.). (e) Acicular apatite, and (f) poikilitic apatite segregation. Acicular apatite shows subtle zoning (Z) along the rims to brighter (under BSE-imaging) towards more REE- and Sr-rich compositions. Both types of apatite contain rounded inclusions of ferropericlase (Per). (g) Poikilitic kinoshitalite (Kin) with oikocrysts of monticellite (Mtc). (h) Interstitial groundmass calcite (Cal) with disseminated inclusions of Ba- and Ba-Sr-carbonates (Cb). P.I: primary melt inclusions, Ol; olivine (C: core, Rd: rind), Srp: serpentine, Brc: brucite.

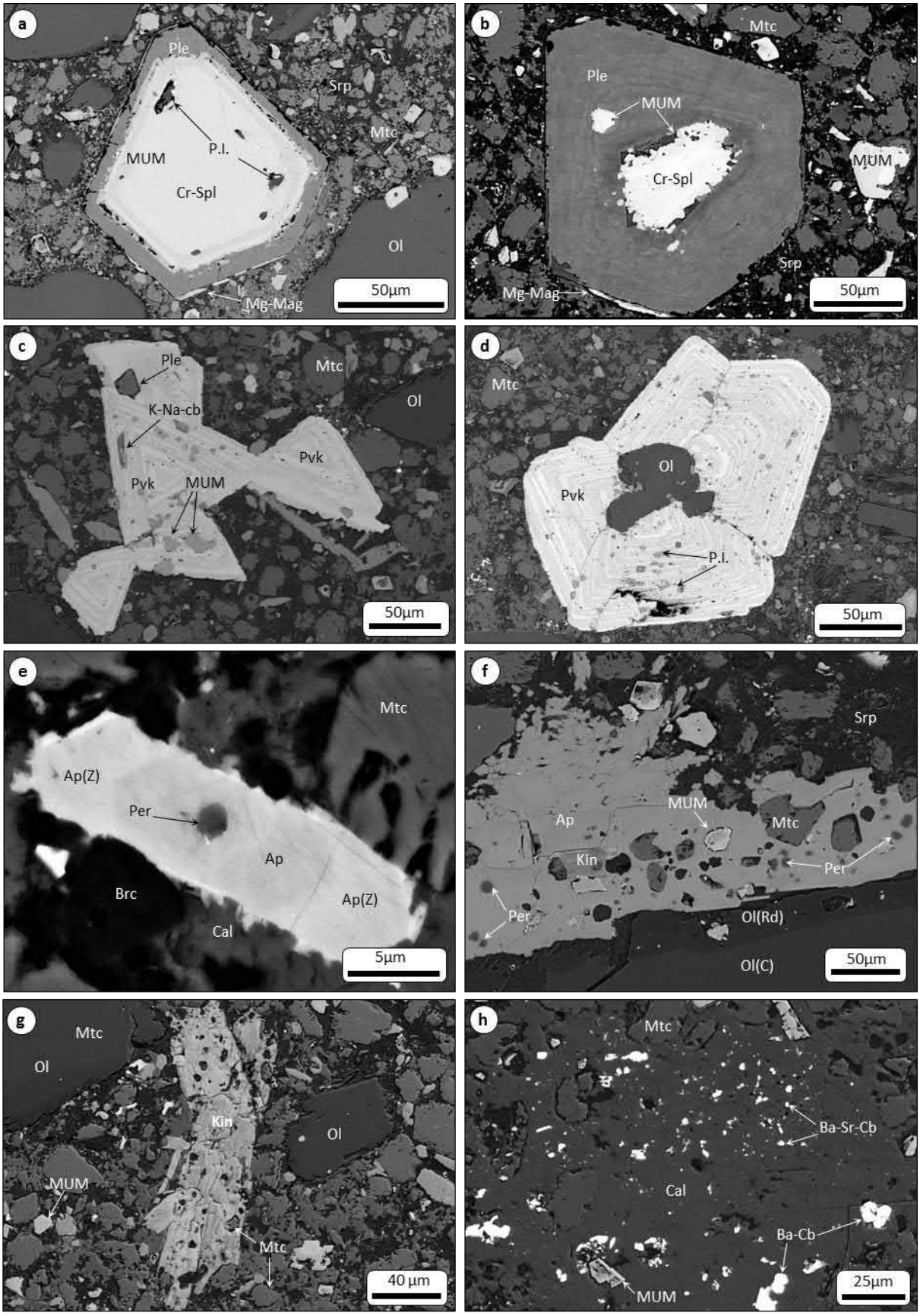
a
Ple
Srp
Mtc
MUM
P.I.
Cr-Spl
Ol
Mg-Mag
50µm
b
Mtc
Ple
MUM
MUM
Cr-Spl
Srp
Mg-Mag
50µm
c
Ple
Mtc
Ol
K-Na-cb
Pyk
Pyk
MUM
50µm
d
Mtc
Ol
Pyk
P.I.
50µm
e
Mtc
Ap(Z)
Per
Ap
Brc
Ap(Z)
Cal
5µm
f
Srp
MUM
Ap
Mtc
Kin
Per
Per
Ol(Rd)
Ol(C)
50µm
g
Mtc
Ol
Kin
Ol
MUM
Mtc
40 µm
h
Mtc
Ba-Sr-Cb
Cal
Ba-Cb
MUM
25µm

238

3.1.6 Apatite

Apatite is as a minor (~1 vol.%) groundmass mineral that has three distinct habits: i) abundant ultrafine (1 – 5 μm) euhedral crystals that are dispersed throughout the mesostasis assemblage (see below), ii) larger (20 – 200μm) elongated acicular crystals and/or crystal clusters (Figs. 4e, 6), and iii) rare poikilitic grains in segregations up to 250 μm in size that are interstitial to other groundmass minerals (Fig. 4f). The cores of apatite grains contain moderate SrO (up to 2 – 4 wt.%) and CeO_2 (up to 1.28 wt.%; Table 1). Larger poikilitic apatite grains are homogeneous but surrounded by a thin rim (<5 μm), that is more enriched in Sr, Na, Ba, K up to a combined total of 6 – 8 wt.% (see also Fig. 6), but poorer in F and Ce (Table 1). Acicular apatite grains can also be zoned, but usually show subtle enrichment in Sr (up to ~3 wt.%) and LREEs (~2 – 3 wt.%; Fig. 4e).

3.1.7 Phlogopite-kinoshitalite

Kinoshitalite is a rare phase (<1 vol.%) that occurs in the groundmass as pristine grains (10 – 50μm) or even rarer as poikilitic grains (up to 200μm in size), which contain chadocrysts of other groundmass minerals such as spinel, monticellite and perovskite (Fig. 4g). Only a single poikilitic phlogopite (200μm in size) grain was observed.

3.1.8 Carbonate

Calcite occurs as interstitial segregations, which commonly contain disseminated Sr-Ba-Na carbonates (e.g., witherite; Fig. 4h). It is noteworthy that the Mark kimberlite is carbonate (~2 – 3 vol.%) poor as compared to other studied hypabyssal kimberlites from the Ekati cluster (Abersteiner et al., 2018; Armstrong et al., 2004; Wilson et al., 2007).

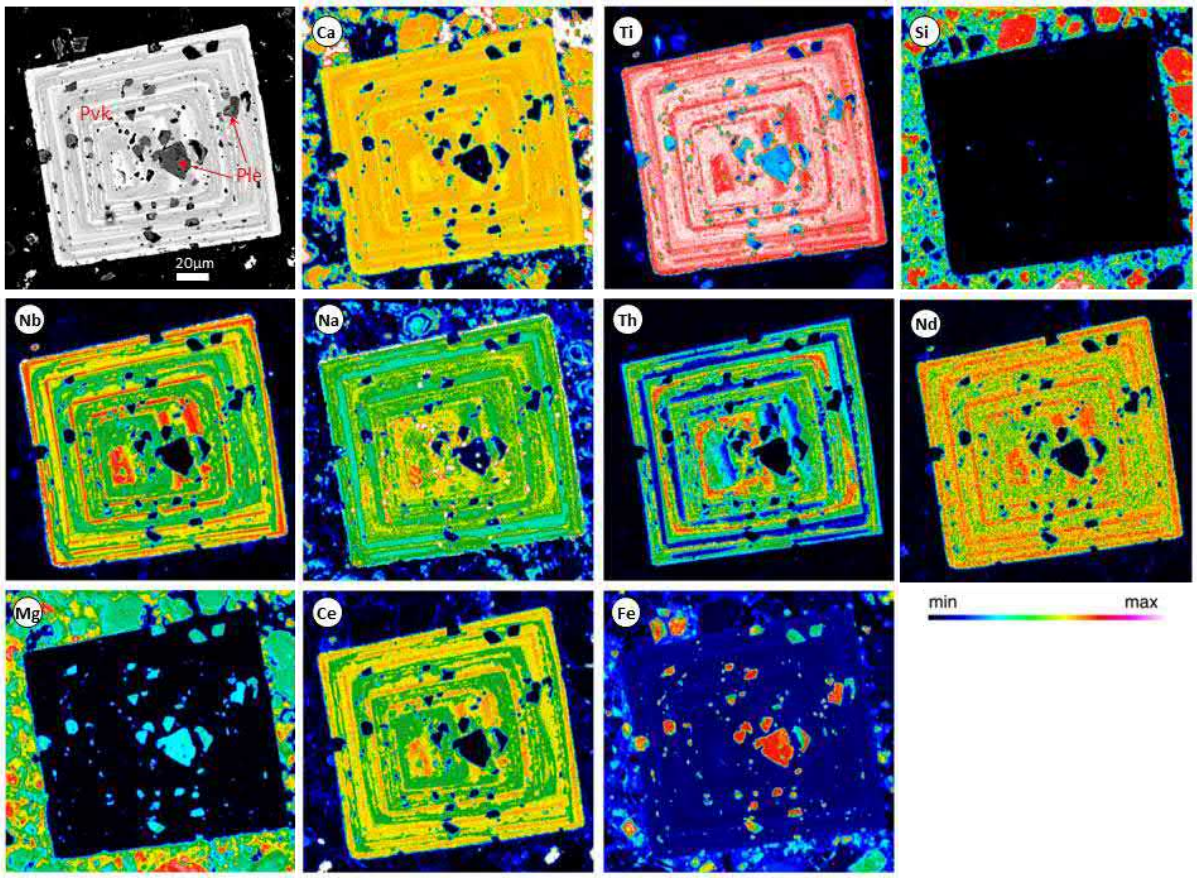

Figure 5. Back-scattered electron (BSE) image of a oscillatory zoned perovskite (Pvk) grain. Electron microprobe (EMP) x-ray element maps show brighter layers to be more enriched in Nb, Na, Th and light rare earth elements (LREEs – Ce, Nd) compared to darker zones, which are more Ca and Ti rich. The compositional (wt.%) range for each element is: Ca: 0 – 38, Ti: 0 – 30, Si: 0 – 22, Nb: 0 – 6, Na: 0 – 0.7, Th: 0 – 2.4, Nd: 0 – 2, Mg: 0 – 40, Ce: 0 – 7, Fe: 0 – 50. Perovskite also includes abundant melt and crystal inclusions. Crystal inclusions (up to 40 µm in size) largely consist of pleonaste (Ple), which is indicated by enrichments in Mg and Fe, and depletion in all other elements displayed.

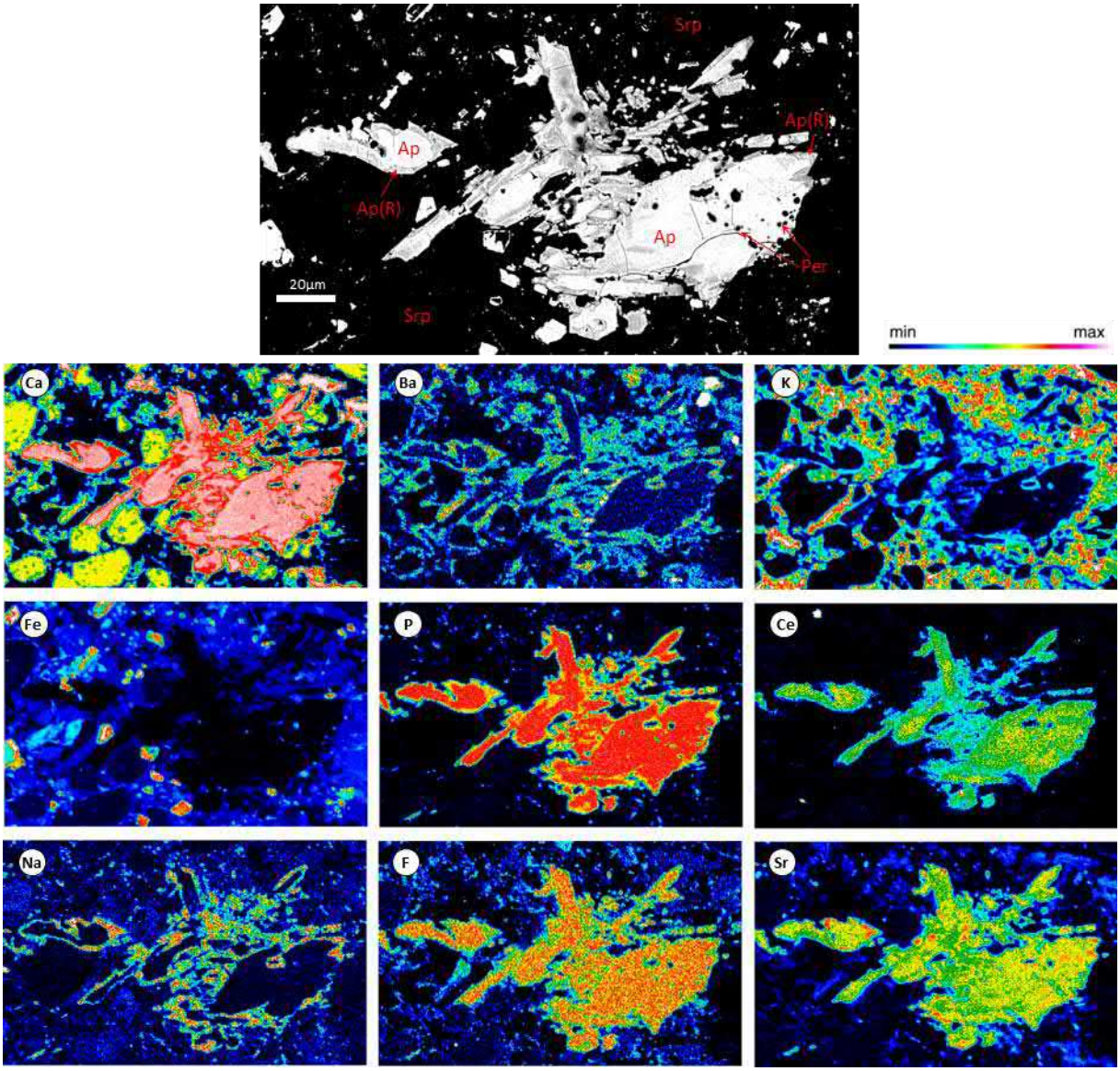

Figure 6. Back-scattered electron (BSE) image of clusters of acicular apatite (Ap) grains, which are sometimes surrounded by darker rims (R). Electron microprobe (EMP) X-ray element maps show the rims to be more enriched in Sr, Na, Ba and K relative to the core, which is more F and light rare earth element (LREE) enriched. The compositional (wt.%) range for each element is: Ca: 0 – 40, Ba: 0 – 3, K: 0 – 2, Fe: 0 – 45, P: 0 – 22, Ce: 0 – 2, Na: 0 – 3, F: 0 – 3.5, Sr: 0 – 5. Apatite also contains micro rounded inclusions of periclase (Per). The surrounding groundmass is mostly composed of interstitial K-bearing serpentine (Srp).

Table 1. Average major element (EMP) compositions for olivine, monticellite and spinel from the Mark kimberlite.

Mineral	Olivine								Monticellite		Spinel						Apatite			
Zone	Core		Rim		Rind		Outmost Rind				Core		Core (zoned)		Pleonaste Rim		Core		Rim	
	n=31		n=14		n=27		n=10		n=18		n=17		n=5		n=14		n=5		n=5	
	Mean	1sd	Mean	1sd	Mean	1sd	Mean	1sd	Mean	1sd	Mean	1sd	Mean	1sd	Mean	1sd	Mean	1sd	Mean	1sd
SiO_2	41.24	0.44	41.39	0.27	42.17	0.54	41.37	0.45	37.61	0.52	0.08	0.03	0.04	0.01	0.06	0.02				
TiO_2											1.92	1.26	16.97	5.09	3.62	0.67				
ZnO											0.08	0.04	0.04	0.01	0.06	0.02				
Al_2O_3					0.04	0.04			0.06	0.06	7.33	2.40	6.18	0.64	46.44	2.22				
V_2O_3											0.26	0.04	0.10	0.03	0.03	0.01				
Cr_2O_3	0.03	0.01	0.05	0.01	0.01	0.01	0.01	0.01	0.02	0.01	57.17	4.91	9.55	14.40	1.00	0.55				
Fe_2O_3											4.76	1.34	27.94	6.20	17.91	1.79				
FeO	8.24	1.39	8.13	0.16	2.96	0.94	5.32	0.94	1.84	0.35	15.11	0.97	19.61	3.77	8.60	0.38				
NiO	0.34	0.03	0.18	0.06	0.09	0.03	0.09	0.02	0.03	0.01	0.12	0.05	0.18	0.03	0.11	0.01				
MnO	0.12	0.02	0.15	0.02	0.25	0.04	0.27	0.01	0.24	0.02	0.28	0.10	0.86	0.17	0.32	0.06				
MgO	50.88	1.32	51.13	0.33	54.99	0.98	52.71	1.07	25.31	0.83	12.63	1.07	17.62	2.50	21.79	0.36				
CaO	0.02	0.01	0.06	0.02	0.88	0.40	0.28	0.04	35.02	0.57							51.56	0.08	50.62	0.52
Na_2O									0.15	0.05							0.07	0.02	3.36	0.22
K_2O									0.03	0.02							0.03	0.01	0.70	0.24
P_2O_5									0.51	0.17							41.10	0.26	37.10	0.38
F																	2.48	0.06	2.09	0.08
SrO																	3.33	0.16	3.81	0.69
BaO																	0.16	0.07	1.54	0.14
CeO_2																	1.28	0.10	0.78	0.25
									mol.%											
Fo	91.66	1.50	91.81	0.17	97.07	0.94	94.63	1.00	3.91	0.64										
Mo									92.65	2.92										
Ki									3.50	2.47										
Cr/(Cr+Al)											0.84	0.06	0.35	0.27	0.01	0.01				
$Fe^{2+}/(Fe^{2+}+Mg)$											0.40	0.03	0.38	0.06	0.18	0.01				

295 *3.2 Geochemistry*

296 The whole-rock composition of the Mark kimberlite sample was determined by two
297 different methods (see Supplementary Material).

298 The Mark kimberlite is characterised by very high MgO (38.2 – 41.0 wt.%), moderate
299 SiO_2 (33.0 – 35.4 wt.%) and CaO (7.6 – 8.8 wt.%), low Al_2O_3 (1.2 – 1.4 wt.%) and extremely
300 low K_2O (0.1 – 0.3 wt.%) and Na_2O(<0.1 wt.%; Table 2). These major element compositions
301 are consistent with previous analyses of the Mark kimberlite and are typical for Lac de Gras
302 kimberlites (Kjarsgaard et al., 2009; Tappe et al., 2013). It is noteworthy that the Mark
303 kimberlite is one of the most depleted in K_2O relative to other Lac de Gras kimberlites. The
304 high modal abundances of olivine and monticellite, along with macrocrystic Cr-pyrope, Cr-
305 diopside and phlogopite, as well as serpentine and brucite are responsible for the high MgO-
306 content of the Mark kimberlite. Primitive mantle normalised (after Sun and McDonough
307 (1989)) lithophile trace element patterns exhibit typical kimberlitic enrichment in most
308 incompatible trace elements (Supplementary Figure S3). Heavy rare earth elements (HREEs)
309 are strongly depleted in comparison to light rare earth elements (LREEs), where La/Yb_N =
310 646 (N = normalised). Elements such as Ba, Th, U, Nb, Ta, La and Ce exceed primitive
311 mantle abundances by up to 100 times and moderate-to-strong negative anomalies (i.e.
312 depletions) relative to elements of similar compatibility are reflected in Rb, K, Pb, P, Zr, Hf,
313 Ti.

314

315

316

Table 2. Major and trace element abundances for the Mark kimberlite.

	1	2	3		1	2	3
SiO_2	33.03	33.26	35.40	Cs	0.8	0.9	0.2
TiO_2	0.39	0.39	0.37	Rb	62	62	9
Al_2O_3	1.21	1.25	1.37	Ba	2812	2720	1501
$FeO_{(total)}$	7.74	7.85	8.84	Th	20	21	20
MnO	0.19	0.21	0.16	U	3	3	3
MgO	40.94	40.96	38.20	Nb	206	199	208
CaO	7.57	7.56	8.81	Ta	11.2	11.1	10.3
Na_2O	0.08	0.08	bdl	La	159	156	127
K_2O	0.29	0.30	0.12	Ce	244	243	204
P_2O_5	0.78	0.80	0.47	Pb	bdl	bdl	8.5
LOI	6.65	6.63	6.80	Pr	22.9	22.9	21.3
Total	98.88	99.28	100.54	Sr	1176	1171	582
F	0.09	n/a	n/a	Nd	70	68	64
CO_2	3.63	3.63	n/a	Sm	6.5	6.6	6.0
H_2O	3.02	3.00	n/a	Zr	30	34	28
				Hf	0.8	1.0	0.7
				Eu	1.4	1.3	1.4
Co	101	102	95	Gd	2.9	3.0	2.9
Cr	2337	2457	2545	Tb	0.3	0.3	0.2
Ni	1654	1628	1795	Dy	1.1	1.0	1.0
Sc	12	11	12	Y	4.0	3.7	3.9
V	64	68	64	Ho	0.1	0.1	0.1
Cu	60	58	39	Er	0.3	0.3	0.3
Zn	21	23	40	Tm	0.1	0.1	0.0
Ga	1.6	1.6	2.7	Yb	0.2	0.2	0.2
				Lu	bdl	bdl	bdl

Major elements are in wt.%, trace elements in ppm. LOI: lost on ignition

*H_2O was determined by Element Analyser (see Supplementary Material)

bdl: below detection limit, n/a: not analysed

4. Inclusions

Crystal inclusions, along with multiphase melt/fluid inclusions were analysed in olivine, perovskite, spinel, apatite, monticellite, calcite and Cr-diopside by field emission scanning electron microscope (FE SEM-EDS; see Supplementary Material for methodology). High-resolution backscattered electron (BSE) images and EDS analyses of daughter minerals in melt/fluid inclusions were also undertaken. A summary of crystal inclusion data is presented in Table 3and of melt/fluid inclusion data in Table 4.

4.1 Olivine

Detailed examinations of the different generations of crystal and melt/fluid inclusions in Mark kimberlite olivine are presented in Abersteiner et al. (2020), therefore only a brief summary of inclusion results are presented. Olivine contains two texturally distinct generations of melt/fluid inclusions: i) Primary melt inclusions (i.e. not associated with any fracture system; Fig. 3a, b), which are restricted to Mg-rich olivine rinds and occur as trails aligned parallel with the shape of the olivine crystal shape or are randomly distributed throughout this zone. ii) Pseudosecondary melt/fluid inclusions are typically restricted to interior olivine zones (cores and rims) and occur as trails/clusters that are aligned along planar fractures (Fig. 3a). These inclusions trails typically terminate at the boundary with Mg-rich rinds.

Primary and pseudosecondary melt/fluid inclusions were shown to contain similar, but not identical daughter minerals assemblages, that are composed of abundant Ca-Mg (e.g., calcite, dolomite) and alkali/alkali-earth (K-Na-Ba-Sr) carbonates (e.g., fairchildite, gregoryite, zemkorite, witherite), K-Na chlorides and subordinate silicates (e.g., phlogopite, monticellite) and lesser spinel, perovskite, phosphates and Fe-Cu-sulphides. In addition, pseudosecondary melt/fluid inclusions were commonly shown to contain a CO_2 fluid phase, as well as more diverse daughter minerals, such as magnesite, tetraferriphlogopite, Ba- or K-sulphates (e.g., barite, arcanite), kalsilite, Na-phosphates (bradleyite), Cu-Fe-sulphides and a rare earth element (REE)-Nb-Zr phase (Tables 3, 4; Abersteiner et al., 2020).

4.2 Cr-Diopside

Macrocrystic Cr-diopside contains abundant micro-inclusions that are typically 1 – 10 µm in size and subrounded-to-irregular in shape (Supplementary Figure S4). These micro-inclusions are clustered around grain boundary and surrounding internal fractures, forming a

371 'sponge-like' texture, and are therefore considered to be secondary in origin. These features
372 are identical to micro-inclusions that occur in kimberlite-hosted Cr-diopside megacrysts
373 (Abersteiner et al., 2019b; Bussweiler et al., 2016). Isolated inclusions (i.e. not connected to
374 any fractures) may be monomineralic or multiphase and composed of (in order of decreasing
375 abundance) phlogopite, carbonates (dolomite, calcite and K-Ba-Na-Sr varieties), Cr-spinel
376 and apatite (Supplementary Figure S7) as previously observed by Bussweiler et al. (2016 and
377 references therein) and were interpreted as melt inclusions. Inclusions transected by micro-
378 fractures are usually empty, or are composed of serpentine/chlorite.

379 *4.3 Cr-Spinel*

380 Cr-spinel contains subhedral-to-rounded crystal inclusions of olivine (Mg# ~91 – 93)
381 and rare orthopyroxene (up to 10 – 20 µm in size). In addition, Cr-spinel also hosts angular-
382 to-irregular shaped inclusions (up to 10 µm in size) of dolomite and phlogopite, however, it is
383 difficult to discern whether these inclusions represent monomineralic crystal inclusions, or
384 are a single exposed mineral of a multimineralic melt inclusion (see below) due to their two
385 dimensional representation on the polished surface. Cr-spinel is host to sporadic angular,
386 round or amoeboid shaped multiphase melt inclusions (1 – 20 µm in size) that are randomly
387 distributed throughout the grain (Figs. 4a, 7a-d), and therefore interpreted to be primary in
388 origin. These inclusions contain heterogeneous daughter mineral assemblages composed of
389 (in order of relative abundance) phlogopite, dolomite, alkali (K, Na, Ba) carbonates, sylvite
390 (+lesser Na-K chlorides), monticellite, perovskite and rare kalsilite and an unidentified K-F
391 phase (carobbiite?). Cr-spinel also contains trails of very small (1 – 3 µm) inclusions that
392 could not be confidently determined to be pseudosecondary or secondary in origin due to the
393 opacity of spinel. In these inclusions, although individual daughter minerals could not be
394 properly identified, they are composed of abundant Ca-K-Na-Cl-bearing phases, indicating
395 the presence of carbonates and/or chlorides. No inclusions were identified in the pleonaste or
396 Mg-magnetite rims surrounding Cr-spinel cores.

397 *4.4 Perovskite*

398 Perovskite is host to abundant primary inclusions that are subdivided into two types:
399 i) large (30 – 70 µm) irregularly shaped crystal inclusions of olivine and smaller (10 – 50
400 µm) subhedral-to-angular inclusions of spinel (MUM, pleonaste) that are randomly
401 distributed throughout the perovskite grain (Figs. 4c, d; 5, 7e, f). Sometimes olivine
402 inclusions occur within the perovskite core and the surrounding perovskite appears to have

nucleated around the olivine. ii) Small (<1 – 5 μm in size) round-to-irregular shaped multiphase melt inclusions, which are either randomly distributed throughout the host perovskite or are aligned parallel with zonation. These inclusions are dominated by daughter minerals of alkali (K, Na, Ba) carbonates, calcite and to a lesser extent sylvite + Na-K-chloride, and lesser phlogopite, olivine and apatite (Fig. 7e, f).

4.5 Monticellite

Although monticellite is a very abundant groundmass mineral, inclusions in monticellite are extremely rare. These inclusions are typically monomineralic and composed of ferropericlase, Mg-magnetite, apatite and K-Ca carbonates.

4.6 Apatite

Large poikilitic apatite grains in segregations usually contain subhedral-to-rounded chadocrysts (<25 μm in size) of other groundmass minerals (e.g., monticellite, olivine, spinel, kinoshitalite; Fig. 4f). In addition, poikilitic apatite and smaller acicular grains also commonly contain very small (<3 μm) individual rounded inclusions or clusters of ferropericlase, calcite, monticellite, sylvite and Ca-K carbonate (Fig. 4e, f).

4.7 Phlogopite-kinoshitalite

Poikilitic kinoshitalite grains occasionally contains euhedral crystal inclusions (<20 μm in size) of other groundmass phases, such as MUM-spinel, perovskite and monticellite. In addition, kinoshitalite sometimes contains inclusions of calcite or witherite that are elongated and parallel with cleavage.

4.8 Calcite

Interstitial calcite segregations contain abundant small (<3 μm) disseminated inclusions of Sr-Ba carbonates and rare K-rich carbonates (Fig. 4h).

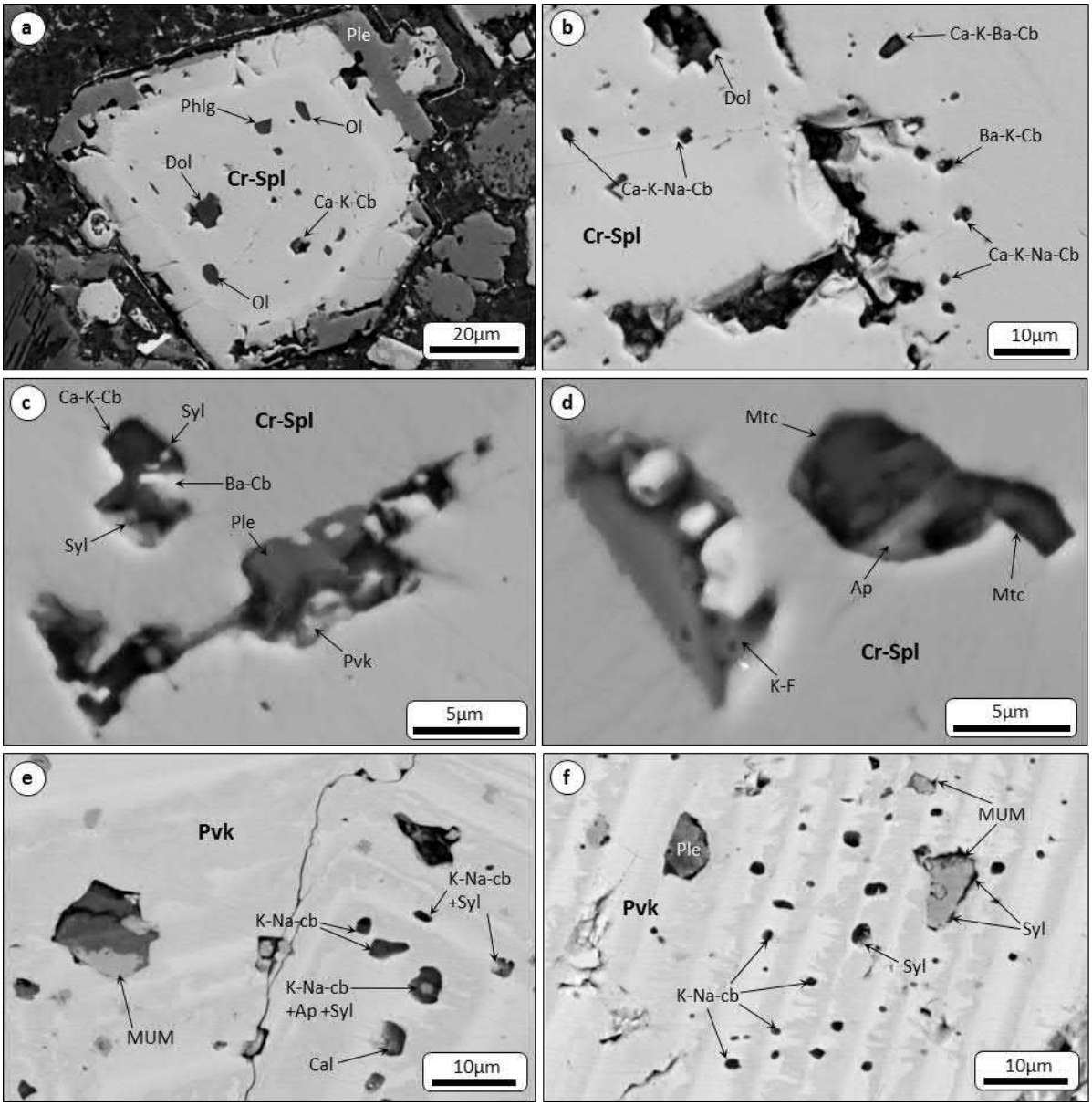

Figure 7. Back-scattered electron (BSE) SEM images of primary melt inclusions in (a – d) Cr-spinel (Cr-Spl), and (e – f) perovskite (Pvk). Perovskite contains abundant angular crystal inclusions of spinel (pleonaste: Ple and magnesian ulvöspinel-magnetite: MUM). Primary inclusions are heterogeneous in daughter mineral assemblage and consist of: dolomite (Dol), phlogopite (Phlg), alkali (Ca, K, Na, Ba) carbonates, olivine (Ol), pleonaste (Ple), sylvite (Syl), K-F phase (carobbiite?), monticellite (Mtc), apaite (Apl), calcite (Cal).

436 *4.9 Potassium and sodium content of melt inclusions*

437 Primary (i.e. entrapped during the growth of the host crystal) and
438 pseudosecondary/secondary melt inclusions in all studied minerals in the Mark kimberlite
439 sample (olivine, Cr-diopside, Cr-spinel, perovskite, monticellite and apatite) appear to be
440 dominated or contain abundant Ca-K-Na-bearing daughter phases, which are typically
441 represented by carbonates (e.g., fairchildite, gregoryite, zemkorite + other unidentified solid-
442 solutions), chlorides (e.g., sylvite, halite) and to a lesser extent aluminosilicates (e.g.,
443 phlogopite/tetraferriphlogopite, kalsilite) and rare Na- or K-bearing sulphates (e.g., arcanite)
444 and phosphates (bradleyite). The ratios of K:Na of exposed primary melt inclusions (acquired
445 by SEM-EDS) were calculated in atomic abundances and normalised to 100. Samples were
446 analysed immediately after sample preparation to mitigate the effect of recrystallization of
447 carbonate/chloride phases due to interaction with atmospheric moisture (see Abersteiner et
448 al., 2020). Calcium was excluded from these calculations due to interference of Ca present in
449 some host minerals (e.g., perovskite, apatite). The calculated K/Na ratios (excluding pure
450 compositional endmembers) for carbonates in primary melt inclusions were: 2.3 (n=29) for
451 Mg-rich olivine rinds, 2.5 (n=60) for perovskite and 2.5 (n=34) for Cr-spinel. The sample
452 size for melt inclusions in monticellite and apatite was too small to be considered here. The
453 K/Na ratios for chlorides in primary melt inclusions show more variability: 3.9 (n=12) for
454 Mg-rich olivine rinds, 2.8 (n=6) for perovskite and 1.4 (n=5) for Cr-spinel.

455

456

457

458

459

460

461

462

463

5.

5.

Table 3. Summary of crystal inclusions hosted in in olivine, perovskite, Cr-spinel, kinoshitalite and apatite from the Mark kimberlite

Mineral	Olivine			Perovskite	Cr-Spinel	Kinoshitalite	Apatite
Zone	**Core**	**Rim**	**Rind**	**Core**	**Core**	**Core**	**Core**
Relative Abundance	Cr-diopside Phlogopite Cr-pyrope Orthopyroxene Fe-Ni-sulphides	Cr-Spinel/MUM	Mg-magnetite/MUM Monticellite Pleonaste Periclase Perovskite Phlogopite	MUM-Pleonaste Olivine	Olivine Orthopyroxene	MUM-spinel Perovskite Monticellite	Monticellite, Olivine Spinel Kinoshitalite

Table 4. Summary of mineral phases hosted in multiphase melt inclusions in olivine, clinopyroxene, perovskite, Cr-spinel, monticellite and apatite from the Mark kimberlite.

	Olivine		Clinopyroxene	Perovskite	Cr-spinel	Monticellite	Apatite
Inclusion	**Psuedosecondary Melt**	**Primary Melt**	**Secondary Melt**	**Primary Melt**	**Primary Melt**	**Primary Melt**	**Primary Melt**
Zone	**Core/Rim**	**Rind**	**Rim/Fractures**	**Core**	**Core**	**Core**	**Core**
Relative Abundance	Ca-Mg-Fe ± K-Na-Ba-Sr ± F Carbonates Sylvite/Halite Calcite Tetraferriphlogopite/Phlogopite Mg-magnetite/MUM Apatite Barite Perovskite Arcanite Monticellite Kalsilite Cu-Fe-Sulphides Bradleyite Periclase Unidentified REE-Nb-Zr phase	Ca-Mg ± K-Na-Ba-Sr Carbonates Sylvite/Halite Mg-magnetite/MUM Phlogopite Monticellite Perovskite Apatite Fe-Cu-Sulphides	Phlogopite Cr-spinel Ca-Mg-carbonates K-Na-Ba-Sr carbonates Apatite	K-Na-Ba-carbonates Calcite Sylvite (+Na-K chloride) Phlogopite Olivine Apatite	Phlogopite Dolomite Ka-Na-Ba carbonate Sylvite (+Na-K chloride) Monticellite Perovskite Kalsilite	Ferropericlase Mg-magnetite, Apatite Ca-K-carbonate	Ferropericlase Calcite Monticellite Sylvite Ca-K-carbonate

Discussion

5.1 Crystallisation of the Mark Kimberlite

In the following sections we examine minerals and inclusions in the Mark kimberlite and reconstruct a sequence of crystallisation along with an interpretation of processes associated changes in melt composition. A diagram depicting the relative sequence of crystallisation and changes in melt composition of the Mark kimberlite is presented in Figure 8.

5.1.1 Olivine

A detailed account on the origin and evolution of olivine in the Mark kimberlite is presented in Abersteiner et al. (2020). Therefore, only a summary is provided order to link olivine formation with different stages of groundmass crystallisation.

The variable, but high Fo (88.1 – 93.6 mol.%) cores of olivine, along with crystal inclusions of enstatite, Cr-pyrope and Cr-diopside indicate a xenocrystic origin, derived from the lithospheric mantle (i.e. peridotites). The cores of a subset of the olivine grains, along with rims surrounding cores that are characterised by a narrow Mg-range ($Fo_{91.4–92.1}$; Table 1), as well as the presence of euhedral crystal inclusions of Cr-spinel/TIMAC, signifying that rims represent the earliest stage of magmatic olivine crystallisation (e.g., Arndt et al., 2010; Brett et al., 2009; Fedortchouk et al., 2004; Kamenetsky et al., 2008). Pseudosecondary melt/fluid inclusion trails traverse olivine cores/rims and terminate at the boundary with olivine rinds, thereby indicating there was a stage of melt/fluid entrapment in olivine prior to rind formation. The Mg-rich ($Fo_{95.3–98.1}$; Table 1) rinds surrounding cores/rims coincided with the crystallisation of the majority of groundmass minerals, as evidenced by crystal inclusions of spinel (MUM, pleonaste, Mg-magnetite), monticellite, perovskite, ferropericlase, phlogopite and apatite. This suggests that olivine rind formation occurred after Cr-spinel, but ceased around the same time that apatite and phlogopite/kinoshitalite formed. The presence of inclusion-free outmost rinds indicates that there was an additional very late-stage episode of olivine crystallisation marked by decreasing MgO-content (Abersteiner et al., 2020).

The variably sharp and diffuse boundaries and embayments that occur between different olivine zones indicate that there was a complex interplay of mechanical abrasion (e.g., Brett et al., 2015; Jones et al., 2014) and chemical resorption processes, which were followed by new stages of olivine crystallisation. Diffusive transitional zones occasionally

occur between olivine cores and rims/rinds and imply that partial diffusive re-equilibration occurred between olivine and the host melt (e.g., Howarth et al., 2016, 2019; Lim et al., 2018; Pilbeam et al., 2013). Based on the random distribution of olivine grains with different morphologies, zoning patterns, presence of monticellite rims and re-crystallisation features, it is inferred that olivine in the studied Mark kimberlite represents a hybrid population. This can be attributed to magma mixing/differentiation and/or the accumulation previously crystallised olivine that formed at different depths within the magma column (Abersteiner et al.,2020; Mitchell, 2008).

5.1.2 Spinel

Zoning in groundmass Cr-spinel cores shows that there was a progressive change in composition towards more Fe-Ti-Mg-enriched and Cr-poor compositions from core to rim (i.e. Cr-spinel to TIMAC to MUM). This evolutionary trend is common in archetypal kimberlites (Abersteiner et al., 2019a; Dalton et al., 2020; Kamenetsky et al., 2013; Mitchell, 1986; Roeder and Schulze, 2008) and is attributed to magma differentiation. The crystallisation of MUM-spinel, pleonaste and Mg-magnetite coincided with the development of Mg-rich olivine rinds, as indicated by inclusions of these evolved spinel varieties in olivine rinds (Fig. 3). Crystallisation of more oxidized Fe^{3+}-bearing varieties of spinel (e.g., MUM, Mg-magnetite) along with Mg-rich olivine rinds is inferred have coincided with increasing oxygen activity (Bussweiler et al., 2015; Fedortchouk and Canil, 2004; Howarth and Taylor, 2016).

The irregularly shaped and embayed boundaries between MUM (rimming Cr-spinel) and pleonaste overgrowths (Fig. 4a, b) indicate that MUM spinel became unstable with the evolving melt and was subsequently partially resorbed and replaced/overgrown by pleonaste. This sharp transition from MUM compositions to pleonaste is attributed to melt differentiation, which occurred in response to Al supersaturation (Abersteiner et al., 2019a; Pasteris, 1983). This could occur if one of the prerequisite components for phlogopite crystallisation (e.g., K_2O, H_2O, F) were insufficient in the melt or volatile exsolution (decreasing H_2O activity) occurred, thereby impeding phlogopite crystallisation, thus Mg and Al could concentrate within the melt to a point where pleonaste would become the dominant Al-rich mineral to crystallise (Pasteris, 1983).

The relative high abundance of pleonaste compared to phlogopite may be explained by three potential evolutionary trends in the crystallising melt: 1) K_2O content was extremely

low in the melt. This is seemingly supported by the extremely low-K_2O (<0.3 wt.%; Table 2; Kjarsgaard et al., 2009; Tappe et al., 2013) in the Mark kimberlite whole-rock. Consequently, spinel (i.e. pleonaste) was the only magmatic phase that could accommodate significant Al_2O_3. However, melt and crystal inclusions hosted in olivine, Cr-diopside and groundmass minerals are enriched in K-rich daughter minerals (e.g., phlogopite, K-bearing carbonates, chlorides, sulphates; Abersteiner et al., 2020; Fig. 7). Based on melt inclusion results, there may have been sufficient potassium in the kimberlite melt to precipitate phlogopite. 2) Silica was preferentially partitioned into constituent olivine and monticellite phases and as a result there was insufficient silica during the later stages of crystallisation to form phlogopite. Consequently, potassium was retained in the melt (see paragraph below). 3) Spinel (i.e. pleonaste) was the preferential host for Al_2O_3. Textural relationships show that pleonaste crystallised before mica (i.e. spinel chadacrysts in phlogopite/kinoshitalite oikocrysts) and may have consequently depleted the late-stage melt in Al_2O_3, thereby limiting the crystallisation of phlogopite-kinoshitalite. Pleonaste is interpreted to be rare in kimberlites due to its susceptibility to alteration and/or resorption back into the late-stage melt (Abersteiner et al., 2019a; Mitchell, 1986; Pasteris, 1983). Given that pleonaste is preserved and was not resorbed suggests that it was in equilibrium, thus the lack of resorption of pleonaste into the melt meant that Al_2O_3 was not 'replenished' in the late-stage kimberlite melt. A similar example is shown in the Benfontein sills (South Africa), where K_2O contents are very low (<0.15 wt.%; Dawson and Hawthorne, 1973), but pleonaste rims are extremely widespread and well-preserved (Abersteiner et al., 2019).

The absence of other K-bearing minerals crystallising in the Mark kimberlite sample may have led to K being concentrated into the late-stage (or residual) kimberlite melt, where it may have formed various K-rich carbonate or chloride minerals (e.g., similar to those hosted in melt inclusions in olivine/Cr-diopside/groundmass minerals).

5.1.3 Monticellite

Monticellite is interpreted to crystallise after olivine (Abersteiner et al., 2018; Mitchell, 2008; Soltys et al., 2018), however, the presence of abundant inclusions of monticellite in Mg-rich olivine rinds (Abersteiner et al., 2020) indicates co-crystallisation of these minerals. In addition, some euhedral olivine grains are partially replaced (i.e. pseudomorphed) by a rim of monticellite (Abersteiner et al., 2020). The replacement of olivine by monticellite in kimberlites was previously attributed to decarbonation reactions,

582 which involved olivine reacting with the CO_3 in the melt resulting in the formation of
583 monticellite, periclase and CO_2 (Abersteiner et al., 2018. This is evident in the Mark samples,
584 where ferropericlase occurs as inclusions in Mg-rich olivine rinds (and in groundmass
585 monticellite and apatite; Fig. 4e, f; Abersteiner et al., 2020). It is speculated that
586 ferropericlase also crystallised in the groundmass, but was subsequently altered by late-stage
587 deuteric and/or post-magmatic fluids to form brucite (i.e. brucite and brucite-serpentine
588 globules; Supplementary Figure S2).

589 The number of olivine grains exhibiting monticellite rims in the studied Mark
590 kimberlite is extremely rare compared to other localities (e.g., Leslie – Canada, Pipe 1 –
591 Finland; Abersteiner et al., 2018; Bussweiler et al., 2015) where this phenomenon is
592 ubiquitous. This further supports the notion that olivine in the Mark kimberlite represents a
593 hybrid population (see section 5.1.1).

594 *5.1.4 Perovskite*

595 The presence of abundant randomly sized and distributed inclusions of MUM-spinel
596 and pleonaste in perovskite (Figs. 4c, d, 5, 7e, f) indicates crystallisation was
597 contemporaneous and/or occurred after spinel crystallisation ceased (Chakhmouradian and
598 Mitchell, 2000; Mitchell, 1986). Groundmass perovskite with large inclusions of olivine
599 likely represent overgrowths, where perovskite grains nucleated around earlier formed olivine
600 and encompassed them, termed ‘necklaces’ (Abersteiner et al., 2017; Castillo-Oliver et al.,
601 2016; Mitchell, 1986).

602 Oscillatory zoning (up to >40 individual zones within a single grain; Figs. 4c, d, 5) is
603 a prominent feature of Mark kimberlite perovskite and suggests *in-situ* growth in a
604 continuously changing melt and environment. In general, oscillatory zoning in perovskite is
605 extremely rare in kimberlites (e.g., Abersteiner et al., 2019; Castillo-Oliver et al., 2016;
606 Chakhmouradian and Mitchell, 2000; Chakhmouradian et al., 2013; Sarkar et al., 2014). One
607 example where perovskite exhibits similar oscillatory zoning (up to 25 individual zones in a
608 single grain) to perovskite grains in our samples are the Benfontein sills (South Africa;
609 Abersteiner et al., 2019; Chakhmouradian and Mitchell, 2000). Groundmass crystallisation in
610 the Benfontein sills is inferred to have occurred under relatively quiescent conditions;
611 rhythmic crystal settling suggests replenishment by multiple magma injections (Abersteiner
612 et al., 2019; Dawson and Hawthorne, 1973). Similar *in-situ* and unperturbed conditions may
613 have permitted the formation of oscillatory zoning in perovskite in our studied samples and

would correspond well with a true hypabyssal (intrusive) origin, as opposed to a coherent kimberlite formed by re-welding of fragmental kimberlite melt. It is further suggested that a combination of *in-situ* and rapid crystallisation was responsible for the formation of interpenetrant twinned perovskite clusters, the entrapment of abundant crystal and melt inclusions, and oscillatory zoning (Castillo-Oliver et al., 2016; Chakhmouradian and Mitchell, 2000).

5.1.5 Phlogopite/Kinoshitalite

Chadacrysts of spinel (MUM, pleonaste), monticellite and perovskite in phlogopite-kinoshitalite oikocrysts indicate that mica crystallised as a relatively late-stage groundmass mineral. The presence of Ba-rich mica is considered to be a feature of crystallisation from a highly differentiated melt (Dalton et al., 2020; Mitchell, 1995).

5.1.6 Apatite

Late-stage crystallisation of apatite (i.e. all three types) is supported by: i) the absence/scarcity of crystal inclusions of apatite in olivine rinds, spinel or perovskite, and ii) presence of poikilitic apatite grains which overgrow earlier formed euhedral groundmass minerals (e.g., monticellite, phlogopite-kinoshitalite, spinel – MUM, pleonaste) and are interstitial to olivine (Figs. 3h, 5; see also Malarkey et al., 2010; Mitchell, 2008). The Sr-Ba-Na-K and LREE-enriched rims around apatite are interpreted to represent crystallisation from the residual kimberlite melt, which was highly enriched in alkalis/alkali-earths.

To our knowledge, we report the first documented occurrence of ferropericlase inclusions in kimberlitic apatite. Inclusions of ferropericlase were previously reported in minerals such as olivine and monticellite (Abersteiner et al., 2018), however, the preservation of ferropericlase inclusions in late-stage apatite supports the notion of low-pressure (i.e. crustal emplacement) formation of ferropericlase in the kimberlite magma system.

5.1.7 Carbonate

The late-stage crystallisation of calcite is indicated by its interstitial growth around other earlier formed groundmass minerals in our samples. This is consistent with previous studies which show carbonates to be the final stage of groundmass crystallisation, such as in other Lac de Gras kimberlites (e.g., Armstrong et al., 2004; Mitchell, 2008).The presence of disseminated Sr-Ba-Na carbonate inclusions in groundmass calcite (Fig. 4h) is consistent

644 with alkali- and alkali-earth- enrichment in the residual melt. It is noteworthy that carbonates
645 are relatively uncommon in the studied Mark kimberlite sample and is reflected in the low
646 measured CO_2 content (3.63 wt.%). On the contrary, the majority of other Ekati kimberlites
647 usually exhibit much higher abundance of carbonates (Armstrong et al., 2004; Kjarsgaard et
648 al., 2009; Wilson et al., 2007). The scarcity carbonate in the groundmass of the studied Mark
649 kimberlite could be attributed to combination of: i) decarbonation reactions (see section
650 5.1.3), which to a certain extent consumed olivine and carbonate melt to produce groundmass
651 monticellite and monticellite rims around olivine, ii) the mechanical separation of denser
652 crystallised minerals (olivine, early groundmass minerals) from the more buoyant carbonate-
653 rich residual melt component during magmatic ascent, and/or iii) the replacement by
654 serpentine (Giuliani et al., 2014; Mitchell, 1986; Podvysotskiy, 1985; White et al., 2012),
655 which is a common mesostasis mineral.
656
657
658
659
660
661
662
663
664
665
666
667
668
669

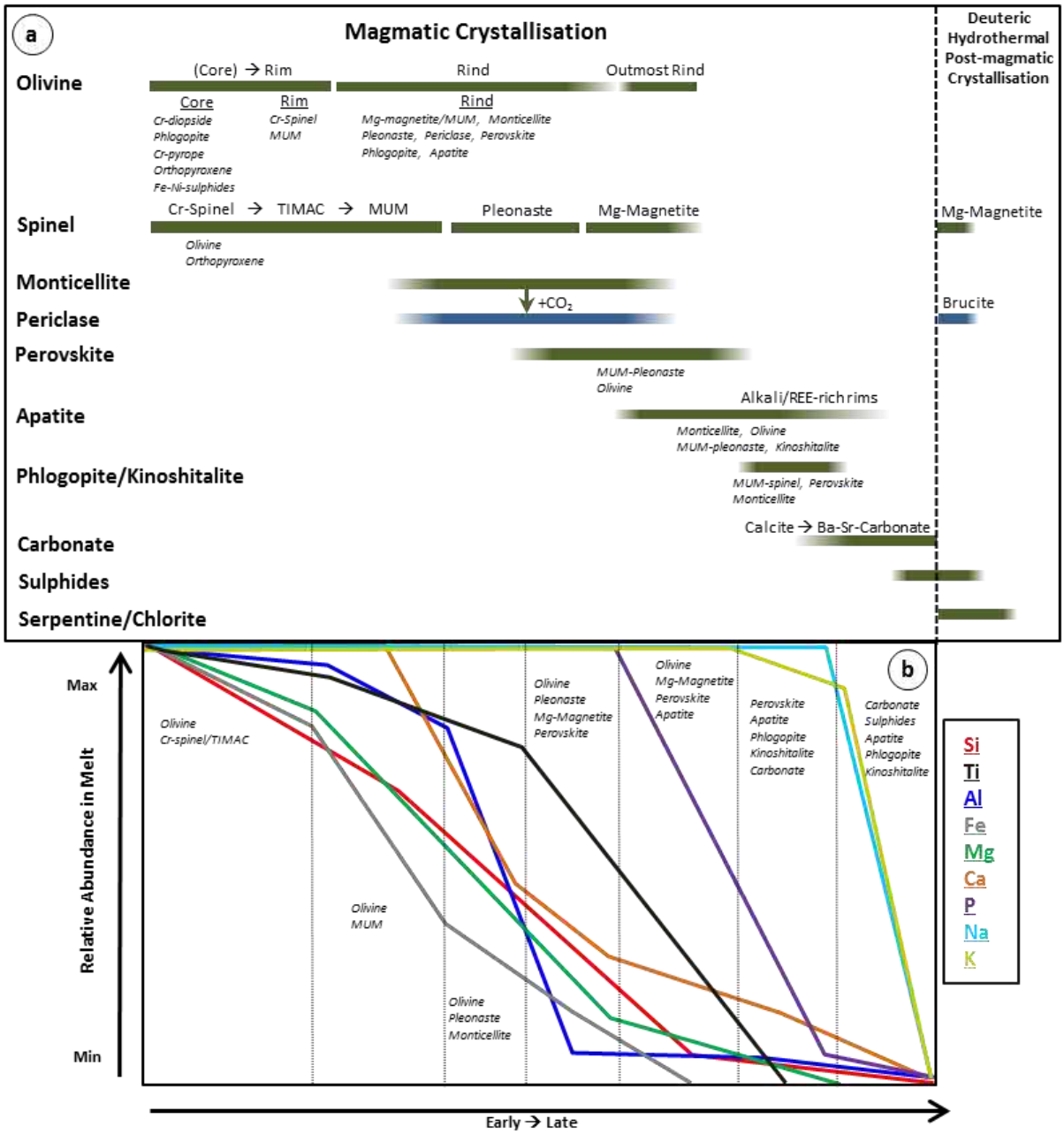

Figure 8. (a) Relative crystallisation history of magmatic minerals from early-stage to late-stage in the studied Mark kimberlite, along with the crystallisation of deuteric/hydrothermal/post-magmatic minerals. (b) Schematic graph showing the relative abundances of key elements (Si, Ti, Al, Fe, Mg, Ca, P, Na, K) in the parental Mark kimberlite melt and the influence of crystallising magmatic minerals on their abundances in the evolving melt (changes in relative abundances in melt correspond with the crystallisation history of magmatic minerals in (a)).

5.2 Fate of alkalis and halogens

Progressive alkali-earth (Mg, Ca, Sr, Ba), alkali (Na, K) and halogen (F, Cl) enrichment during kimberlite melt evolution is supported by several lines of evidence: i) Alkalis and to a lesser extent halogens are significant components within an array of primary, pseudosecondary and secondary melt inclusions hosted in olivine, Cr-diopside, Cr-spinel and groundmass minerals (Table 4). Compositions of daughter carbonates and chlorides in melt inclusions demonstrate that the K and Na were amongst the dominant cations and K/Na ratios remained relatively constant (2.3 – 2.5 for carbonate and 1.4 – 3.5 for chlorides) throughout the crystallisation sequence. ii) Mg-rich olivine rinds contain CaO (up to 1.73 wt.%), which are higher than in the interior (i.e. core, rim) olivine zones (Table 1). The presence of abundant crystal and melt inclusions within olivine rinds, in particular MUM and Mg-magnetite, indicates that olivine rinds crystallised from a late-stage carbonate-rich and oxidised melt. iii) The rims surrounding groundmass apatite are enriched in alkalis, alkali-earths and REEs (up to 8 wt.% total). iv) Interstitial groundmass calcite contains abundant disseminated inclusions of Ba-Sr carbonates. v) Ba-kinoshitalite crystallised as late-stage groundmass crystals and formed magmatic overgrowths around macrocrystic phlogopite.

As previously noted, there is clear discrepancy between K-content in melt inclusions hosted in various Mark kimberlite minerals and the absence of K-bearing minerals (e.g., phlogopite) in the groundmass. If potassium (as well as any other alkalis/alkali-earths/halogens) was concentrated in the late-stage melt and ultimately crystallised to form alkali-carbonates and/or chlorides, such as those observed in melt inclusions, then subsequent alteration by deuteric and/or external fluids could readily leach them from the groundmass due to their high solubility in aqueous solution. The presence of interstitial K-bearing (up to 3 wt.%) chlorite may be evidence of remobilisation of potassium during these stages of alteration, where it became fixed in the chlorite structure. Ultimately, any alkali-halogen bearing phases that crystallised in the groundmass were likely to have interacted with exsolved deuteric fluids, where they could have been released into the surrounding country rocks or were readily removed during post-emplacement alteration by external fluids.

6. Conclusions

The Mark kimberlite (Canada) is considered to be petrographically fresh based on the presence of well-preserved olivine, along with groundmass mineralogy and textures. However, the presence of mesostasis serpentine, chlorite and brucite indicates that the Mark

kimberlite still underwent some deuteric and/or post-magmatic alteration, and therefore cannot be considered 'truly' pristine.

Our study of mineral textures, zoning patterns and hosted inclusions (crystal/melt) reconstructed a complete sequence of groundmass crystallisation. This involved the following broad stages, which involved the crystallisation (see Fig. 8) of: (1) olivine rims around xenocrystic cores + Cr-spinel/TIMAC. (2) Mg-rich olivine rinds around olivine rims/cores + MUM-spinel (followed by pleonaste and Mg-magnetite) + monticellite (+ partial resorption of olivine, along with the formation of ferropericlase and CO_2 as a result of decarbonation reactions) + perovskite + some overlap with apatite. (3) Olivine outmost rinds, which were probably coeval with stage phlogopite/kinoshitalite → apatite → sulphides + carbonate (calcite, Ba-Sr-Na-bearing varieties). (4) Deuteric (i.e. late-stage magmatic) and/or post-magmatic (i.e. external fluids) alteration and crystallisation of mesostasis serpentine, K-rich chlorite and brucite (i.e. replacement of ferropericlase).

Melt inclusions entrapped in zoned olivine and groundmass minerals, along with Cr-diopside macrocrysts, shows that alkalis and halogens are an intrinsic part of the melt parental to the studied Mark kimberlite. These elements were progressively enriched in response to crystallisation of groundmass minerals and were likely a more significant part of the parental melt than in the kimberlite rock. This alkali, alkali-earth and halogen enrichment is most evident in late-stage groundmass minerals, such as in zoned alkali/alkali-earth/REE enriched apatite rims, Ba-rich kinoshitalite, calcite and Ba-Sr carbonates. Since there were no crystallising silicate groundmass minerals that could host significant alkalis and halogens, they became concentrated in the late-stage melt and may have formed water-soluble carbonates or chlorides (such as those observed in melt inclusions) in the groundmass, but were subsequently removed from during deuteric and/or post-magmatic stages of groundmass alteration.

Acknowledgements

This study forms part of A.A's Ph.D and was supported by an Australian Postgraduate Award (APA) and the Max Banks Research Scholarship in Earth Sciences. This work was supported by funding from the Institute of Volcanology and Seismology, Far East Branch, Russian Academy of Sciences. This study benefitted from the helpful comments by Tamsin Mather and two anonymous reviewers.

References

Abersteiner, A., Giuliani, A., Kamenetsky, V.S., Phillips, D., 2017. Petrographic and melt-inclusion constraints on the petrogenesis of a magmaclast from the Venetia kimberlite cluster, South Africa. Chem. Geol. 455, 331-341.

Abersteiner, A., Kamenetsky, V.S., D. Graham, P., Kamenetsky, M., Goemann, K., Ehrig, K., Rodemann, T., 2018a. Monticellite in group-I kimberlites: Implications for evolution of parental melts and post-emplacement CO 2 degassing. Chem. Geol. 478, 76-88.

Abersteiner, A., Kamenetsky, V.S., Golovin, A.V., Kamenetsky, M., Goemann, K., 2018b. Was crustal contamination involved in the formation of the serpentine-free Udachnaya-East kimberlite? New insights into parental melts, liquidus assemblage and effects of alteration. J. Petrol. 59, 1467–1492.

Abersteiner, A., Kamenetsky, V.S., Goemann, K., Giuliani, A., Howarth, G.H., Castillo-Oliver, M., Thompson, J., Kamenetsky, M., Cherry, A., 2019a. Composition and emplacement of the Benfontein kimberlite sill complex (Kimberley, South Africa): Textural, petrographic and melt inclusion constraints. Lithos 324-325, 297-314.

Abersteiner, A., Kamenetsky, V.S., Goemann, K., Golovin, A.V., Sharygin, I.S., Pearson, D.G., Kamenetsky, M., Gornova, M.A., 2019b. Polymineralic inclusions in kimberlite-hosted megacrysts: Implications for kimberlite melt evolution. Lithos 336-337, 310-325.

Abersteiner, A., Kamenetsky, V.S., Goemann, K., Kjarsgaard, B.A., Rodemann, T., Kamenetsky, M., Ehrig, K., 2020. A genetic story of olivine crystallisation in the Mark kimberlite (Canada) revealed by zoning and melt inclusions. Lithos, 105405.

Armstrong, J.P., Wilson, M., Barnett, R.L., Nowicki, T., Kjarsgaard, B.A., 2004. Mineralogy of primary carbonate-bearing hypabyssal kimberlite, Lac de Gras, Slave Province, Northwest Territories, Canada. Lithos 76, 415-433.

Arndt, N.T., Guitreau, M., Boullier, A.M., le Roex, A., Tommasi, A., Cordier, P., Sobolev, A., 2010. Olivine, and the Origin of Kimberlite. J. Petrol. 51, 573-602.

Boyd, F.R., Clement, C.R., 1977. Compositional zoning of olivines in kimberlite from the De Beers mine, Kimberley, South Africa. Carnegie Institute Washington Yearbook vol. 76, pp. 485 –493.

Brett, R.C., Russell, J.K., Moss, S., 2009. Origin of olivine in kimberlite: Phenocryst or impostor? Lithos 112S, 201-212.

Brett, R.C., Russell, J.K., Andrews, G.D.M., Jones, T.J., 2015. The ascent of kimberlite: Insights from olivine. Earth. Planet. Sci. Lett. 424, 119-131.

Brooker, R., Sparks, R., Kavanagh, J., Field, M. (2011). The volatile content of hypabyssal kimberlite magmas: some constraints from experiments on natural rock compositions. Bull. Volcanol. 73, 959-981.

Bussweiler, Y., Foley, S.F., Prelević, D., Jacob, D.E., 2015. The olivine macrocryst problem: New insights from minor and trace element compositions of olivine from Lac de Gras kimberlites, Canada. Lithos 220-223, 238-252.

Bussweiler, Y., Stone, R.S., Pearson, D.G., Luth, R.W., Stachel, T., Kjarsgaard, B.A., Menzies, A., 2016. The evolution of calcite-bearing kimberlites by melt-rock reaction: evidence from polymineralic inclusions within clinopyroxene and garnet megacrysts from Lac de Gras kimberlites, Canada. Contrib. Mineral. Petrol. 171, 65.

Bussweiler, 2019. Polymineralic Inclusions in Megacrysts as Proxies for Kimberlite Melt Evolution—A Review. Minerals 9, 530.

Castillo-Oliver, M., Galí, S., Melgarejo, J.C., Griffin, W.L., Belousova, E., Pearson, N.J., Watangua, M., O'Reilly, S.Y., 2016. Trace-element geochemistry and U–Pb dating of perovskite in kimberlites of the Lunda Norte province (NE Angola): Petrogenetic and tectonic implications. Chem. Geol. 426, 118-134.

Chakhmouradian, A.R., Mitchell, R.H., 2000. Occurrence, alteration patterns and compositional variation of perovskite in kimberlites. Canad. Mineral. 38, 975-994.

Chakhmouradian, A.R., Mitchell, R.H., 2001. Three compositional varieties of perovskite from kimberlites of the Lac de Gras field. Mineral. Mag. 65, 133-148.

Chakhmouradian, A.R., Reguir, E.P., Kamenetsky, V.S., Sharygin, V.V., Golovin, A.V., 2013. Trace-element partitioning in perovskite: Implications for the geochemistry of kimberlites and other mantle-derived undersaturated rocks. Chem. Geol. 353, 112-131.

Clement, C.R., 1982. A comparative geological study of some major kimberlite pipes in the Northern Cape and Orange Free State. Ph.D thesis, University of Cape Town.

Clement, C.R., Skinner, E.M.W., Smith, B.H.S., 1984. Kimberlite Redefined. J. Geol. 92, 223-228.

Cordier, C., Sauzeat, L., Arndt, N.T., Boullier, A.-M., Batanova, V., Barou, F., 2015. Metasomatism of the Lithospheric Mantle Immediately Precedes Kimberlite Eruption: New Evidence from Olivine Composition and Microstructures. J. Petrol. 56, 1775-1796.

844 Dalton, H., Giuliani, A., O'Brien, H., Phillips, D., Hergt, J., 2020. The role of lithospheric
845 heterogeneity on the composition of kimberlite magmas from a single field: The case of
846 Kaavi-Kuopio, Finland. Lithos 354-355, 105333.
847 Davis, W.D., Kjarsgaard, B.A., 1997. A Rb - Sr isochron age for a kimberlite from the
848 recently discovered Lac de Gras field, Slave Province, Northwest Canada. J. Geol. 105,
849 503-509.
850 Dawson, J.B., Hawthorne, J.B., 1973. Magmatic sedimentation and carbonatitic
851 differentiation in kimberlite sills at Benfontein, South Africa. Journal of the Geological
852 Society 129, 61-85.
853 Fedortchouk, Y., Canil, D., 2004. Intensive Variables in Kimberlite Magmas, Lac de Gras,
854 Canada and Implications for Diamond Survival. J. Petrol. 45, 1725-1745.
855 Field, M., Scott Smith, B.H., 1999. Contrasting geology and near-surface emplacement of
856 kimberlite pipes in southern Africa and Canada. In: Gurney, J., et al. (Eds.),
857 Proceedings of the 7th International Kimberlite Conference (Eds. Gurney, J. et al.) vol.
858 1, Red Roof Design, Cape Town, pp. 214 – 237.
859 Giuliani, A., 2018. Insights into kimberlite petrogenesis and mantle metasomatism from a
860 review of the compositional zoning of olivine in kimberlites worldwide. Lithos 312-
861 313, 322-342.
862 Giuliani, A., Phillips, D., Kamenetsky, V.S., Fiorentini, M.L., Farquhar, J., Kendrick, M.A.,
863 2014. Stable isotope (C, O, S) compositions of volatile-rich minerals in kimberlites: A
864 review. Chem. Geol. 374-375, 61-83.
865 Giuliani, A., Phillips, D., Kamenetsky, V.S., Goemann, K., 2016. Constraints on kimberlite
866 ascent mechanisms revealed by phlogopite compositions in kimberlites and mantle
867 xenoliths. Lithos 240-243, 189-201.
868 Giuliani, A., Soltys, A., Phillips, D., Kamenetsky, V.S., Maas, R., Goemann, K., Woodhead,
869 J.D., Drysdale, R., Griffin, W.L., 2017. The final stages of kimberlite petrogenesis:
870 Petrography, mineral chemistry, melt inclusions and Sr-C-O isotope geochemistry of
871 the Bultfontein kimberlite (Kimberley, South Africa). Chem. Geol. 455, 342-356.
872 Golovin, A.V., Sharygin, V.V., Pokhilenko, N.P., 2007. Melt inclusions in olivine
873 phenocrysts in unaltered kimberlites from the Udachnaya-East pipe, Yakutia: Some
874 aspects of kimberlite magma evolution during late crystallisation stages. Petrology 15,
875 168-183.
876 Howarth, G.H., Taylor, L.A., 2016. Multi-stage kimberlite evolution tracked in zoned olivine
877 from the Benfontein sill, South Africa. Lithos 262, 384-397.

878 Howarth, G.H., Gross, J., 2019. Diffusion-controlled and concentric growth zoning revealed
879 by phosphorous in olivine from rapidly ascending kimberlite magma, Benfontein,
880 South Africa. Geochim. Cosmochim. Acta 266, 292-306.
881 Jones, T.J., Russell, J.K., Porritt, L.A., Brown, R.J., 2014. Morphology and surface features
882 of olivine in kimberlite: implications for ascent processes. Solid Earth 5, 313-326.
883 Kamenetsky, M.B., Sobolev, A.V., Kamenetsky, V.S., Maas, R., Danyushevsky, L.V.,
884 Thomas, R., Pokhilenko, N.P., Sobolev, N.V., 2004. Kimberlite melts rich in alkali
885 chlorides and carbonates: A potent metasomatic agent in the mantle. Geology 32, 845-
886 848.
887 Kamenetsky, V.S., Kamenetsky, M.B., Sharygin, V.V., Golovin, A.V., 2007. Carbonate-
888 chloride enrichment in fresh kimberlites of the Udachnaya-East pipe, Siberia: A clue to
889 physical properties of kimberlite magmas? Geophys. Res. Lett. 34, L09316.
890 Kamenetsky, V.S., Kamenetsky, M.B., Sobolev, A.V., Golovin, A.V., Demouchy, S., Faure,
891 K., Sharygin, V.V., Kuzmin, D.V., 2008. Olivine in the Udachnaya-East Kimberlite
892 (Yakutia, Russia): Types, Compositions and Origins. J. Petrol. 49, 823-839.
893 Kamenetsky, V.S., Kamenetsky, M.B., Weiss, Y., Navon, O., Nielsen, T.F.D., Mernagh, T.P.,
894 2009. How unique is the Udachnaya-East kimberlite? Comparison with kimberlites
895 from the Slave Craton (Canada) and SW Greenland. Lithos 112S, 334-346.
896 Kamenetsky, V.S., Kamenetsky, M.B., Golovin, A.V., Sharygin, V.V., Maas, R., 2012.
897 Ultrafresh salty kimberlite of the Udachnaya-East pipe (Yakutia, Russia): A
898 petrological oddity or fortuitous discovery? Lithos 152, 173-186.
899 Kamenetsky, V.S., Grutter, H., Kamenetsky, M.B., Goemann, K., 2013. Parental carbonatitic
900 melt of the Koala kimberlite (Canada): Constraints from melt inclusions in olivine and
901 Cr-spinel, and groundmass carbonate. Chem. Geol. 353, 96-111.
902 Kjarsgaard, B.A., Pearson, D.G., Tappe, S., Nowell, G.M., Dowall, D.P., 2009. Geochemistry
903 of hypabyssal kimberlites from Lac de Gras, Canada: Comparisons to a global database
904 and applications to the parent magma problem. Lithos 112S, 236-248.
905 le Roex, A.P., Bell, D.R., Davis, P., 2003. Petrogenesis of Group I Kimberlites from
906 Kimberley, South Africa: Evidence from Bulk-rock Geochemistry. J. Petrol. 44, 2261-
907 2286.

908 Lim, E., Giuliani, A., Phillips, D., Goemann, K., 2018. Origin of complex zoning in olivine
909 from diverse, diamondiferous kimberlites and tectonic settings: Ekati (Canada), Alto
910 Paranaiba (Brazil) and Kaalvallei (South Africa). Mineral. Petrol. 112, 539–554.

911 Malarkey, J., Pearson, D.G., Kjarsgaard, B.A., Davidson, J.P., Nowell, G.M., Ottley, C.J.,
912 Stammer, J., 2010. From source to crust: Tracing magmatic evolution in a kimberlite
913 and a melilitite using microsample geochemistry. Earth. Planet. Sci. Lett. 299, 80-90.
914 Mitchell, R.H., 1986. Kimberlites: Mineralogy, Geochemistry and Petrology. Plenum
915 Publishing Company, New York.
916 Mitchell, R.H., 2008. Petrology of hypabyssal kimberlites: Relevance to primary magma
917 compositions. J. Volcanol. Geotherm. Res.174, 1-8.
918 Mitchell, R.H., 2013. Oxygen isotope studies of serpentine in kimberlite. In Proceedings of
919 the 10th International Kimberlite Conference (Eds. Pearson, G.D., Grütter, S.H., Harris,
920 W.J., Kjarsgaard, A.B., O'Brien, H., Rao, C.N.V., Sparks, S.) Springer, India, New
921 Dehli, pp. 1-12.
922 Mitchell, R.H., Giuliani, A., O'Brien, H., 2019. What is a Kimberlite? Petrology and
923 Mineralogy of Hypabyssal Kimberlites. Elements 15, 381-386.
924 Nielsen, T.F.D., Sand, K.K., 2008. The Majuagaa kimberlite dike, Maniitsoq Region, West
925 Greenland: constraints on an Mg-rich silicocarbonatitic melt composition from
926 groundmass mineralogy and bulk compositions. Canad. Mineral. 46, 1043-1061.
927 Pasteris, J.D., 1983. Spinel zonation in the De Beers Kimberlite, South Africa: possible role
928 of phlogopite. Canad. Mineral. 21, 41 - 58.
929 Pearson, D.G., Brenker, F.E., Nestola, F., McNeill, J., Nasdala, L., Hutchison, M.T.,
930 Matveev, S., Mather, K., Silversmit, G., Schmitz, S., Vekemans, B., Vincze, L., 2014.
931 Hydrous mantle transition zone indicated by ringwoodite included within diamond.
932 Nature 507, 221-224.
933 Pilbeam, L.H., Nielsen, T.F.D., Waight, T.E., 2013. Digestion Fractional Crystallisation
934 (DFC): an Important Process in the Genesis of Kimberlites. Evidence from Olivine in
935 the Majuagaa Kimberlite, Southern West Greenland. J. Petrol. 54, 1399-1425.
936 Podvysotskiy, V.T., 1985. Serpentine-carbonate mineralization in kimberlites. Int. Geol. Rev.
937 27, 810-823.
938 Price, S.E., Russell, J.K., Kopylova, M.G., 2000. Primitive Magma From the Jericho Pipe,
939 N.W.T., Canada: Constraints on Primary Kimberlite Melt Chemistry. J. Petrol. 41, 789-
940 808.
941 Roeder, P.L., Schulze, D.J., 2008. Crystallisation of Groundmass Spinel in Kimberlite. J.
942 Petrol. 49, 1473-1495.

Sarkar, C., Storey, C.D., Hawkesworth, C.J., 2014. Using perovskite to determine the pre-shallow level contamination magma characteristics of kimberlite. Chem. Geol. 363, 76-90.

Skinner, E.M.W., 1989. Contrasting Group I and Group II kimberlite petrology: towards a genetic model for kimberlites, In: Kimberlites and Related Rocks. 4th International Kimberlite Conference (Eds. Glover, J.E., Harris, P.G.) Geological Society of Australia, Perth, pp. 528-544.

Soltys, A., Giuliani, A., Phillips, D., 2018. Crystallisation sequence and magma evolution of the De Beers dyke (Kimberley, South Africa). Mineral. Petrol. 112, 503–518.

Sparks, R.S.J., Baker, L., Brown, R.J., Field, M., Schumacher, J., Stripp, G., Walters, A., 2006. Dynamical constraints on kimberlite volcanism. J. Volcanol. Geotherm. Res. 155, 18-48.

Sparks, R.S.J., Brooker, R.A., Field, M., Kavanagh, J., Schumacher, J.C., Walter, M.J., White, J., 2009. The nature of erupting kimberlite melts. Lithos 112S, 429-438.

Stripp, G.R., Field, M., Schumacher, J.C., Sparks, R.S.J., Cressey, G., 2006. Post-emplacement serpentinization and related hydrothermal metamorphism in a kimberlite from Venetia, South Africa. J. Metamorph. Geol. 24, 515-534.

Sun, S.-S., McDonough, W.F., 1989. Chemical and isotopic systematics of oceanic basalts: implications for mantle composition and processes. In: Magmatism in the Ocean Basins. Geological Society Special Publication (Eds. Saunders, A.D., Norry, M.J.), London, pp. 313-345.

Tappe, S., Pearson, D.G., Kjarsgaard, B.A., Nowell, G., Dowall, D., 2013. Mantle transition zone input to kimberlite magmatism near a subduction zone: Origin of anomalous Nd–Hf isotope systematics at Lac de Gras, Canada. Earth. Planet. Sci. Lett. 371–372, 235-251.

White, J.L., Sparks, R.S.J., Bailey, K., Barnett, W.P., Field, M., Windsor, L., 2012. Kimberlite sills and dykes associated with the Wesselton kimberlite pipe, Kimberley, South Africa. S. Afr. J. Geol. 115, 1-32.

Wilson, M.R., Kjarsgaard, B.A., Taylor, B., 2007. Stable isotope composition of magmatic and deuteric carbonate phases in hypabyssal kimberlite, Lac de Gras field, Northwest Territories, Canada. Chem. Geol. 242, 435-454.

Zurevinski, S.E., Heaman, L.M., Creaser, R.A., Strand, P., 2008. The Churchill kimberlite field, Nunavut, Canada: petrography, mineral chemistry, and geochronology. Can. J. Earth Sci. 45, 1039-1059.

Chapter 10 Appendices:

Appendix A: Analytical Techniques

Petrographic Analyses

Specimens of the Mark kimberlite were prepared as thin sections and epoxy resin rock chip mounts, which were polished using kerosene as lubricant to avoid dissolution of any water-soluble minerals. Optical examination of the samples was performed on a Nikon Eclipse 50i POL microscope at the University of Tasmania.

Detailed studies of groundmass phases and inclusions in minerals were performed using a Hitachi SU-70 field emission (FE) scanning electron microscope (SEM) equipped with an Oxford AZtec Energy XMax 80 detector at the Central Science Laboratory, University of Tasmania. A beam accelerating voltage of 15 kV was used to produce high-resolution backscattered electron (BSE) images of minerals and energy-dispersive X-ray spectrometry (EDS) semi-quantitative analyses and elemental maps of minerals.

Electron Microprobe Point Analyses

The compositions of olivine and spinel were measured at the Central Science Laboratory, University of Tasmania using a JEOL JXA-8530F Plus field emission electron microprobe.

For spinel, a beam with an accelerating voltage of 15 kV, a beam current of 50 nA and beam size of 2 μm was employed. The on peak and off peak counting time was 20 seconds for Mg, Al, Si, Cr, Mn, Fe, Ni, Zn and V, and 80 seconds for Ca and Ti. The calibration standards were Rutile for Ti, Rhodonite for Mn, Nickel Oxide for Ni, Chromite Tiebaghi NMNH 117075 for Cr, Al, Fe, Mg, Gahnite Brazil NMNH 145883 for Zn, Wollastonite UNE for Si, Ca and Calcium Vanadate $Ca_3(VO_4)_2$ JEOL for V. Detection limits (99% confidence) were <0.01 wt.% for Si, Ti, Al, Mg and Ca, 0.01 wt.% for V and Mn, 0.02 wt.% for Fe and Ni, and 0.03 wt.% for Zn.

For olivine, a beam with an accelerating voltage of 15 kV, a beam current of 300 nA and beam size of 2 μm was employed for combined EDS and wavelength dispersive x-ray spectrometry (WDS) analysis. The EDS counting time was 90 seconds for Mg, Fe and Si, and WDS on peak and off peak counting times were 60 seconds for Al, Cr, Ca, Mn and Ni. The calibration standards were Olivine San Carlos NMNH 111312-44 for Mg, Fe and Si, Corundum Harvard for Al, Wollastonite UNE for Ca, Eskolaite for Cr, Rhodonite for Mn, and Nickel Oxide for Ni. Detection limits (99% confidence) were <0.004 wt.% for Al, Cr, Ca, Mn and Ni.

In addition, a second set of olivine and monticellite analyses was performed to also examine for Na, K and P. Again, a beam with an accelerating voltage of 15 kV, a beam current of 300 nA and beam size of 2 µm was employed. The EDS counting time was 90 seconds for Si, Mg, WDS on peak and off peak counting times were 80 seconds for Mn, 40 seconds for Ni, 30 seconds for Al, P, K, Ca, Cr, Na, and 20 seconds for Fe. The calibration standards were Olivine San Carlos NMNH 111312-44 for Mg, Fe and Si, Corundum Harvard for Al, Wollastonite UNE for Ca, Eskolaite for Cr, Rhodonite for Mn, Nickel oxide for Ni, Anorthoclase Kakanui for Na, Fluor-apatite for P and Orthoclase for K. Detection limits (99% confidence) were <0.006 wt.% for Cr, Fe, Ni, and <0.003 wt% for Al, Ca, Mn, Na, K and P. In the case of monticellite, Ca was analysed by EDS and not WDS.

Electron Microprobe X-Ray Element Mapping

X-ray element maps were acquired by WDS on the same instrument as the point measurements using an accelerating voltage of 15 kV, a dwell time of 200 ms, a beam diameter of 0.2 µm for perovskite and 1 µm for apatite. The following spectrometer configuration and beam current for perovskite:

Spectrometer	1	2	3	4	5
Pass 1, 50 nA	TI Kα, PETJ	Si Kα, PETL	Ca Kα, PETL	Na Kα, TAPL	Fe Kα, LIFL
Pass 2, 300 nA	Ce Lα, PETJ	Nb Lα, LiFL	Th Mα, PETL	Mg Kα, TAPL	Nd Lα LIFL

The step size was 0.5 µm. The calibration standards were synthetic rutile for Ti, natural jadeite for Na (both P&H Developments, UK), Hematite Minas Gerais Harvard 92649 for Fe, Olivine San Carlos NMNH 111312-44 for Mg, natural wollastonite for Si, Ca, synthetic CePO4 and NdPO4 (Cherniak et al., 2004) for Ce, Nd, synthetic potassium niobate $KNbO_3$ (JEOL) for Nb, and synthetic huttonite (J. Hanchar, Memorial University) for Th.

For apatite the configuration was as follows:

Spectrometer	1	2	3	4	5
Pass 1, 20 nA	Na Kα, TAP	Fe Kα, LiFL	F Kα, LDE1L	P Kα, PETL	Ca Kα, PETL
Pass 2, 60 nA	Sr Lα, TAP	Ba Lα, LiFL	-	K Kα, PETL	Ce Lα PETL

The step size was 0.8 µm. The calibration standards were synthetic $SrTiO_3$ for Sr, natural barite for Ba , natural orthoclase for K, natural fluor-apatite for P, Ca (all P&H Developments, UK), Hematite Minas Gerais Harvard 92649 for Fe, Anorthoclase Kakanui NMNH 13386 for Na, synthetic CePO4 for Ce (Cherniak et al., 2004), and natural topaz (Topaz Valley, Utah, Eugene Foord) for F.

The Mean Atomic Number background correction (Donovan & Tingle 1996) was utilised to correct for continuum background for both maps.

Whole-Rock Analyses for Trace Element and Rare Earth Element Concentrations

KIA93-K136 sample numbers 1 and 2 (Table 1) were analysed for their major and trace element concentrations at Intertek Minerals Laboratory (Adelaide, South Australia). Samples were prepared by pulverising ~20g of each sample down to a particle size of 80% passing -75 µm. Subsamples were extracted from each pulverised sample for dissolution and chemical analysis. 0.2g of pulverised sample was fused with lithium borate and then dissolved by a weak acidic solution. The dissolved sample was then analysed for major (Ca, Fe, K, Mg, Mn, Na, P, Si, Ti), trace (Ba, Cr, Cs, Ga, Rb, Sc, Sn, Sr, U, V, W), high field strength elements (HFSE; Ba, Cr, Cs, Ga, Rb, Sc, Sn, Sr, U, V, W), rare earth elements (REE; La, Ce, Pr, Nd, Sm, Eu, Gd, Tb, Dy, Ho, Er, Tm, Yb, Lu) were analysed by a combination of inductively coupled plasma optical emission spectroscopy (ICP-OES) and inductively coupled plasma mass spectrometry (ICP-MS). Samples analysing for trace elements (Ag, As, Be, Bi, Cd, Co, Cu, Ge, In, Li, Mo, Ni, Pb, Re, Sb, Se, Te, Tl, Zn) were prepared by dissolving 0.2g of sample in a 4 acid digest (HF+ HCl + HNO_3 + $HClO_4$) and then analysed by ICP-OES/ICP-MS. CO_2 and S were analysed by a carbon sulphur analyser (CSA) by igniting 0.3g of pulverised sample at high temperature in a stream of O_2. SO_2 and CO_2 produced were then measured via infra-red cells. Samples were analysed for Cl by digesting 0.2g of pulverised sample in a calcium-carbonate leach. Cl was then measured by colorimetry. Samples were analysed for F by fusing 0.2g of pulverised sample with K/Na-carbonate/Zn-oxide, then digested in deionised H_2O. F in solution was then measured via selective ion electrode. Ferrous iron was determined by digesting 0.25g of pulverised sample in sulphuric acid (H_2SO_4) and titrated to determine FeO.

KIA93-K136 sample number 3(Table 1) was analysed for major and trace element concentrations at Acme Analytical Laboratories (Canada). Si, Al, Fe, Mg, Ca, Na, K, Ti, P, Mn, Ni and Ba were analysed by wavelength dispersive X-ray fluorescence (XRF) on a lithium metaborate fused disk. Loss on ignition is determined by gravimetry at 1000 ºC. Trace element determinations for V, Cr also by XRF on fused disc. All other trace elements were determined at Durham University on a Perkin Elmer Sciex Elan 6000 ICPMS instrument (Dowall, 2004) using techniques outlined in detail by Ottley et al. (2003), including comparison to other analytical methods. Seven repeat dissolutions of in-house kimberlite standard K2WI yielded Sm/Nd and Lu/Hf reproducibilities of 1.1% and 2.4%,

respectively, with the reproducibility of REE abundances being generally better than 5% and usually better than 3% RSD.

Raman Spectroscopy

The Raman spectra of CO_2 were recorded on a Renishaw inVia spectrometer with StreamLineHR, using a Helium–neon laser at 532nm with a power setting of 800 mW at the sampling spot, a 100x objective and a 1800 l/mm grating resulting in a spectral range of 115-1887 cm^{-1}. For 2D Raman maps, the following settings were employed: 10 accumulations at 1 s exposure time.

References:

Cherniak D.J., Pyle J. and Rakovan J. (2004) Synthesis of REE and Y phosphates by Pb-free flux methods and their utilization as standards for electron microprobe analysis and in design of monazite chemical U-Th-Pb dating protocol. *Amer. Miner.* **89**, 1533-1539.

Donovan J.J., and Tingle T.N., (1996) An improved mean atomic number background correction for quantitative microanalysis. *Journal of the Microscopy Society of America* **2**, 1-7.

Dowall D.P. (2004) Elemental and isotopic geochemistry of kimberlites from the Lac de Gras field, Northwest Territories, Canada. PhD thesis, Durham University.

Ottley, C.J., Pearson, D.G., Irvine, G.J., (2003) A routine method for the dissolution of geological samples for the analysis of REE and trace elements via ICP-MS. In: Holland, J.G., Tanner, S.D. (Eds.), Plasma source mass spectrometry: applications and emerging technologies. Royal Society of Chemistry, Cambridge, pp. 221-230.

Appendix B: Supplementary Figures

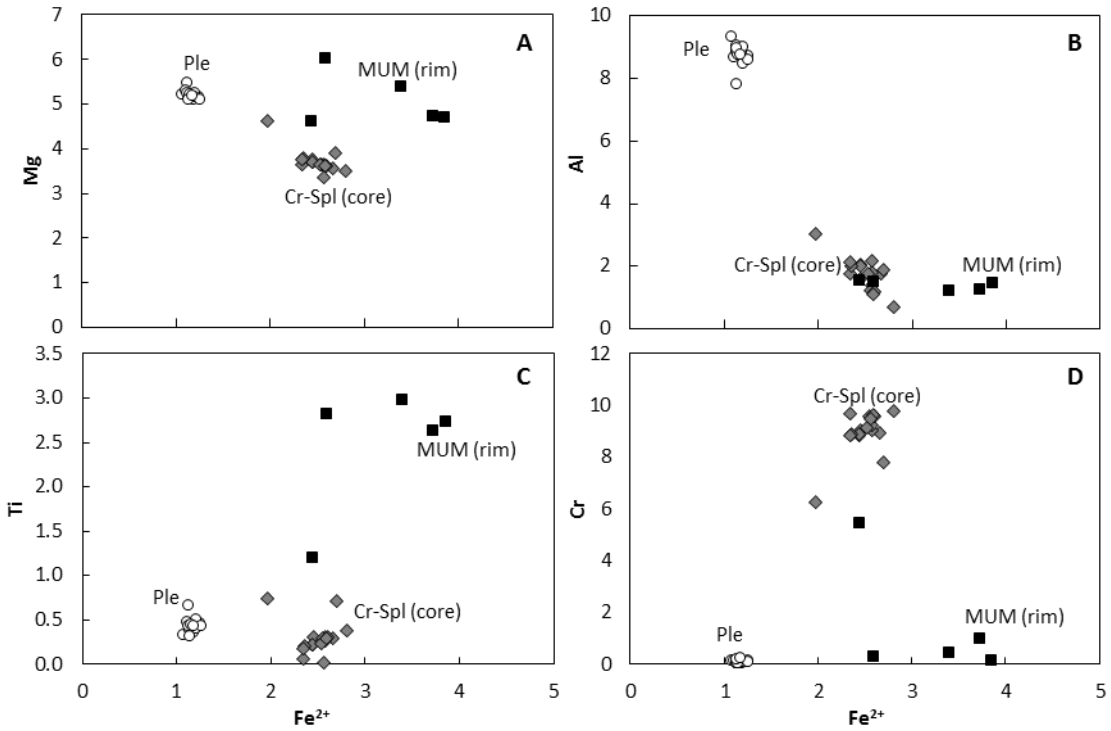

Supplementary Figure 1. Bivariate plots of Fe^{2+} vs: (a) Mg, (b) Al, (c) Ti, and (d) Cr (atoms per formula unit – based on 24 oxygens) for zoned spinel grains (Cr-spinel/TIMAC (Cr-Spl; grey diamond) cores zoned towards MUM-spinel (black squares) rims that in turn surrounded by pleonaste (Ple: white circle) rims.

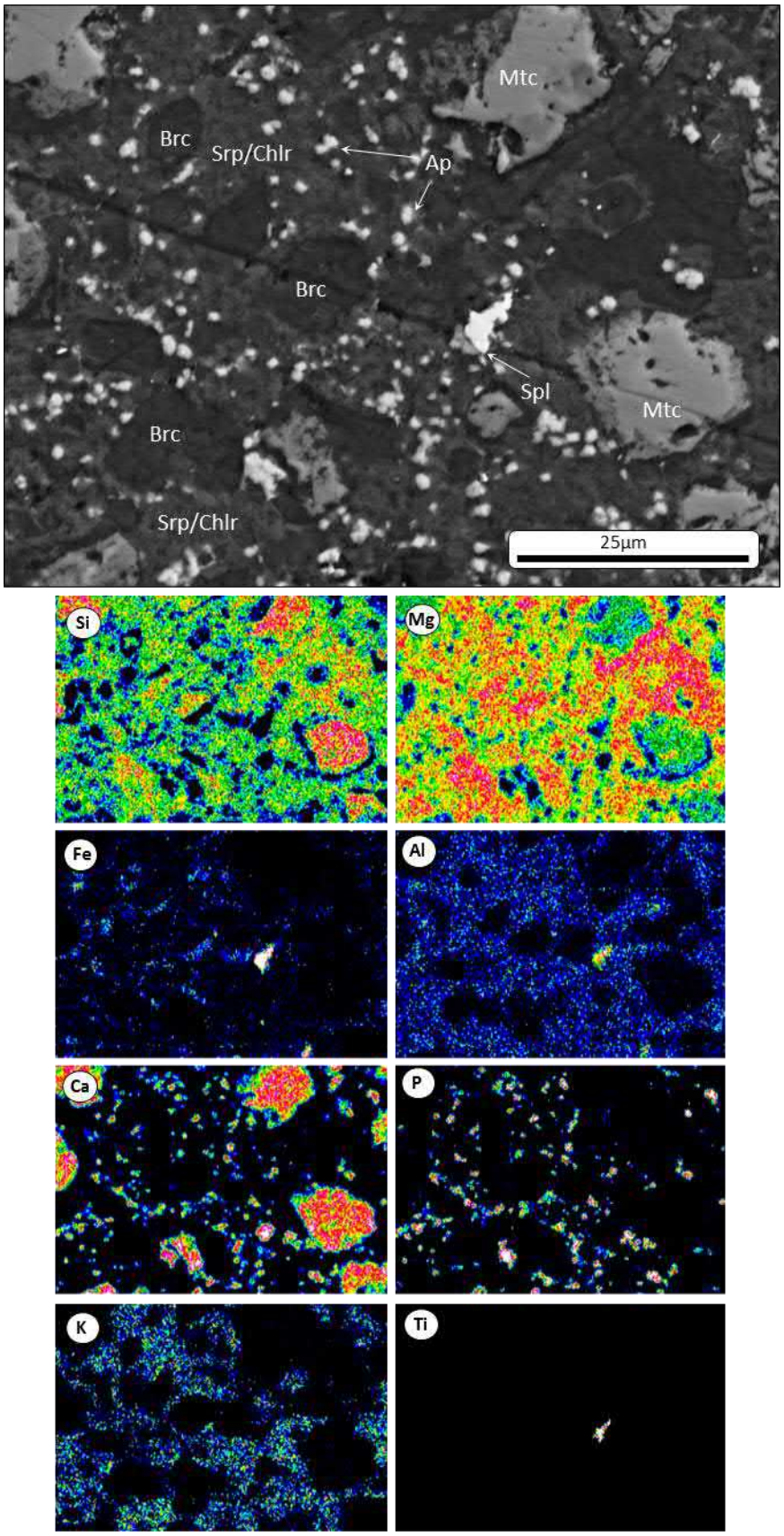

Supplementary Figure 2. Back-scattered electron (BSE) SEM image and X-ray element of mesostasis serpentine (Srp), chlorite (Chlr), apatite (Ap) and brucite (Brc). Note the globular shape of brucite and the absence of potassium. Mtc: monticellite, Spl: spinel.

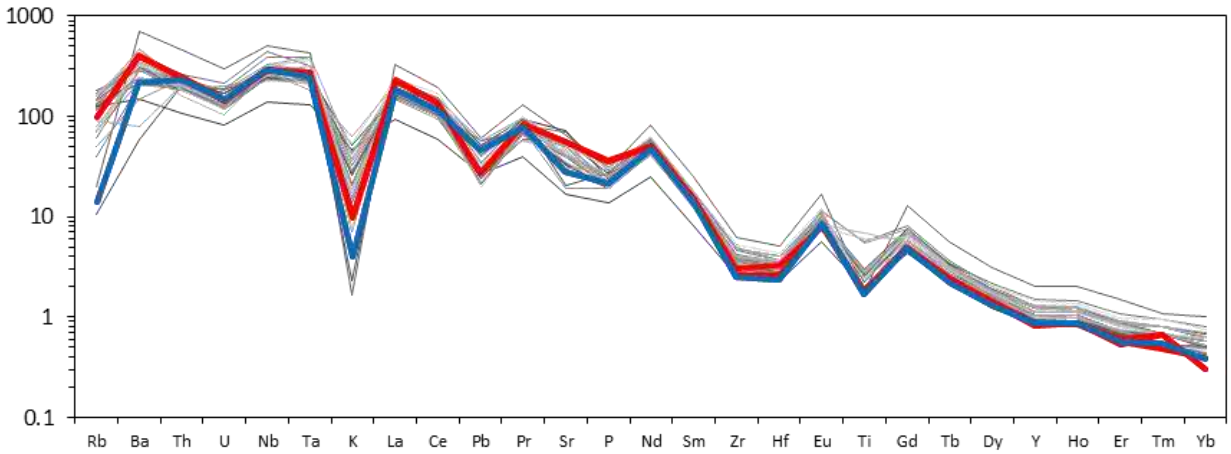

Supplementary Figure 3. Primitive mantle normalised (after Sun & McDonough, 1989) incompatible trace element patterns of Mark kimberlite sample KIA93-K136 (Red lines – this study; Blue line – Tappe et al. 2013). The grey lines represent other Ekati province kimberlites (Canada; Tappe et al., 2013).

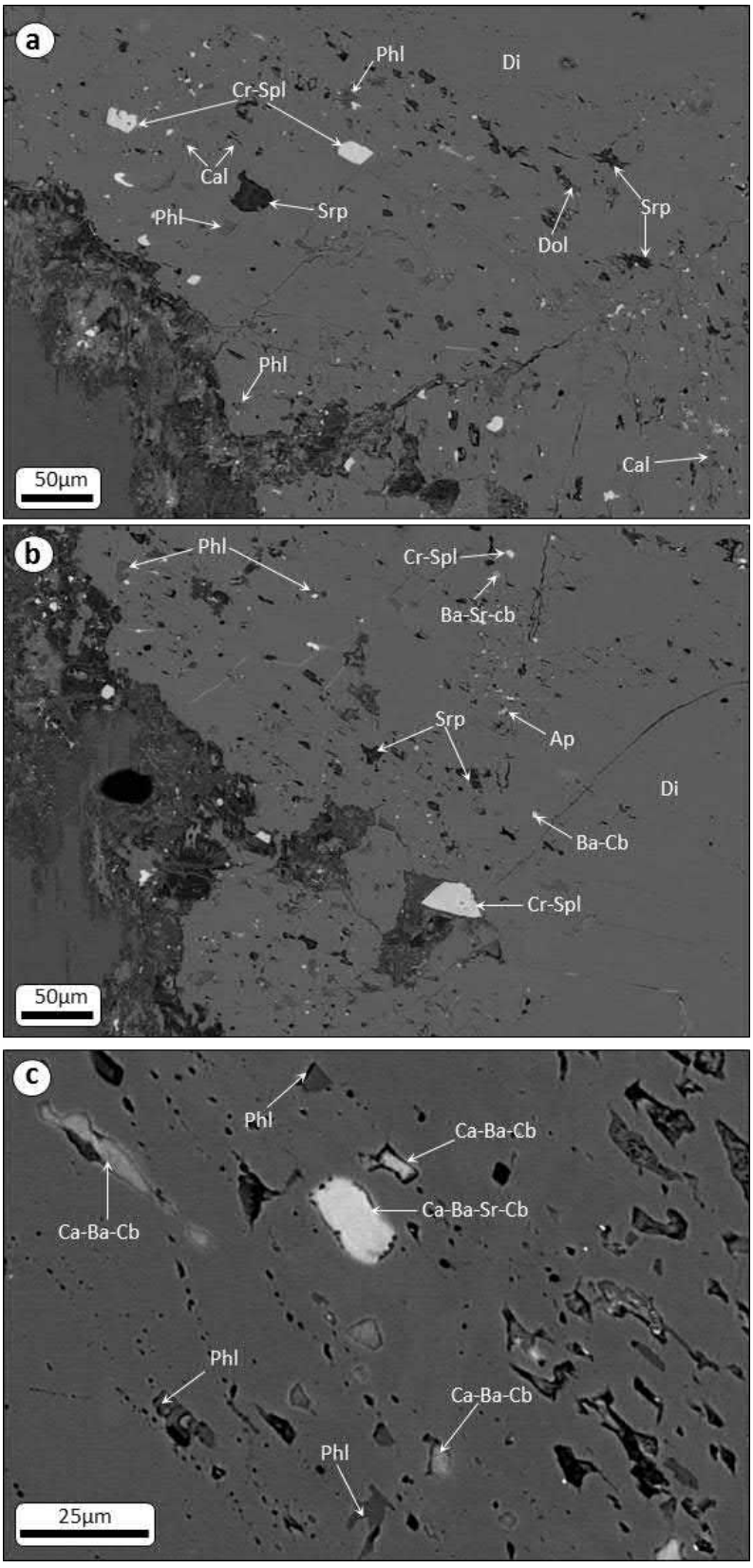

Supplementary Figure 4. (a – c) Back-scattered electron (BSE) SEM images of inclusions in macrocrystic diopside (Di). Diopside is populated by abundant clusters of inclusions forming a 'sponge-like' texture around grain boundaries and around internal fractures. Detected phases include TIMAC-spinel (Cr-Spl), phlogopite (Phl), apatite (Ap), carbonates (cb), serpentine (Srp), calcite (Cal), dolomite (Dol).

Electronic Appendix C: Supplementary Tables - EMPA

[Electronic Appendix]

JOURNAL OF PETROLOGY

Journal of Petrology, 2020, 1–7
doi: 10.1093/petrology/egz054
Advance Access Publication Date: 13 November 2019
Comment and Reply

OXFORD

A Reply to the Comment by Kostrovitsky, S. and Yakovlev, D. on 'Was Crustal Contamination Involved in the Formation of the Serpentine-free Udachnaya-East Kimberlite? New Insights into Parental Melts, Liquidus Assemblage and Effects of Alteration' by Abersteiner *et al.* (J. Petrology, 59, 1467-1492, 2018)

Adam Abersteiner[1,2]*, Vadim S. Kamenetsky [1,3] and Alexander V. Golovin[4]

[1]School of Natural Sciences, University of Tasmania, Hobart, Tasmania 7001, Australia; [2]Institute of Volcanology and Seismology, Far East Branch, Russian Academy of Sciences, Petropavlovsk-Kamchatsky 683006, Russia; [3]Institute of Experimental Mineralogy RAS, Chernogolovka 142432, Russia; [4]Sobolev Institute of Geology and Mineralogy, Siberian Branch of Russian Academy of Sciences, Koptyuga Pr. 3, Novosibirsk 630090, Russian Federation

*Corresponding author. Telephone: +61406717535. E-mail:adam.abersteiner@utas.edu.au

Received May 23, 2019; Accepted November 9, 2019

The Comment by Kostrovitsky & Yakovlev aims to demonstrate that Abersteiner *et al.* (2018) 'presented erroneous statements regarding the genesis' of the mineralogically and geochemically unique Serpentine-Free Udachnaya-East (SFUE) kimberlite (Russia) as it contradicts the views presented by Kostrovitsky *et al.* (2013). Furthermore, these authors reassert that 'the supposition that surfaces salts and sulphates represent the main source for Na–Cl–S mineralization of kimberlites with unaltered olivine (Kostrovitsky *et al.*, 2013) is still valid' and 'the mantle origin of salts is doubtful'. Numerous hypotheses are presented in both Kostrovitsky & Yakovlev (Comment) and Kostrovitsky *et al.* (2013) advocating a crustal brine origin for salts in the SFUE kimberlite. However, we find these interpretations to be poorly substantiated by empirical evidence and often contradictory. It is, therefore, important to revisit the earlier publication by Kostrovitsky *et al.* (2013) that is used to support the Comment by Kostrovitsky & Yakovlev. Here we address some of the erroneous and contradictory points presented by Kostrovitsky *et al.* (2013), which render their interpretations tenuous and misleading:

1. Presence of evaporites in country rocks: Kostrovitsky *et al.* (2013) contradict themselves by suggesting that evaporites in the country rocks are both present and absent at the Udachnaya-East kimberlite. These authors stated that the Udachnaya-East kimberlite 'does not intersect massive evaporites' (p. 77), but later claimed that '…the highest (8 vol %) abundance of halite is restricted to depth levels of southern diatremes (Mir, Udachnaya, and International'naya) where they cut through halite-rich evaporite', (p. 84) and 'The absence of all textural types of serpentine in SFUE kimberlite is easily explained by the model of the evaporite country rock contamination' (p. 88). The published and unpublished reports for parametric and geotechnical drill holes [figures 1 and 2 of Kamenetsky *et al.* (2014)] showed no evidence of sedimentary evaporite beds in or around the Udachnaya-East kimberlite.

2. The composition of the putative kimberlite melt: The composition of the melt that is supposedly parental to Udachnaya-East was suggested by Kostrovitsky *et al.* (2013) to have resulted from 'assimilation of evaporite xenoliths at relatively high, magmatic temperatures producing hybrid melt with elevated contents of Na, K, Cl, and S ', (p.88) and that 'the hybrid residual kimberlite that digested evaporite xenoliths had lower H_2O activity due to increased halogen and alkali abundances' (p. 88). However, these authors also stated that 'the contents of H_2O, Na_2O, and, by inference, the mode of halite are thus controlled only by the spatial position of the kimberlite specimen, rather than by the composition of the kimberlite melt'. Again, Kostrovitsky *et al.* (2013) did not present a consistent view as to whether salt was controlled by assimilation of alleged 'evaporites' or by the spatial position of the kimberlite rock.
3. Primary versus secondary enrichment in Na and Cl: (Kostrovitsky *et al.*, 2013) again presented conflicting views on the origin of Na and Cl mineralisation. On the one hand, these authors considered Na and Cl to be primary magmatic: 'Na-rich kimberlite compositions are not solely restricted to unserpentinized kimberlites and that groundmass serpentine does not replace primary alkali- and chlorine-bearing minerals'. (p. 84), and '... alkali-, sulfur-, and chlorine-rich minerals may have crystallized from this late hybrid melt and may be "comagmatic" with kimberlite' (p.88), but on the other hand they pushed for their secondary origin: 'the strongest evidence for the secondary origin of Na-, Cl-, and S-rich minerals in the Udachnaya-East kimberlite ... is the regional correlation between the geology and hydrogeology of the local country rocks and the mineralogy of Yakutian kimberlites' (p.86).

With this preface, we discuss below the Comment by Kostrovitsky & Yakovlev, and emphasise that previous data and interpretations by Abersteiner *et al.* (2018b) and other works are still valid and concordant with a magmatic origin of alkalis and halogens in the SFUE kimberlite.

SAMPLE COLLECTION

Samples analysed by Abersteiner *et al.* (2018b) were carefully selected from mine stockpiles [see tables 1 and 2 in Abersteiner *et al.* (2018b)] and catalogued by the co-author Alexander Golovin during 2004–2005. Our unserpentinized samples were collected from the exact same depth interval (i.e. 410–500m) as those by Kostrovitsky *et al.* (2013) and they are also considered to belong to the SFUE, which is defined by: i) fresh olivine and the absence of mesostasis serpentine. In SFUE kimberlite samples studied by Abersteiner *et al.* (2018b), olivine is set within a groundmass that consists of both typical [e.g. olivine, monticellite, phlogopite, spinel (chromite, magnesian ulvöspinel, magnetite, pleonaste, Mg–Ti-magnetite], apatite, Fe–Ni sulphides, calcite) and atypical kimberlitic minerals [e.g. halite, sylvite, alkali (Na, K) carbonates ($+SO_4^{2-}$ bearing varieties] and sodalite). The preservation of Al-rich pleonaste in the groundmass is considered to be a feature of fresh kimberlites [see Abersteiner *et al.* (2019a)]. ii) Preservation of water-soluble salts and alkali-carbonates in the groundmass [Figs 1, 2; see also figures 4a, b and 6 of Abersteiner *et al.* (2018b), figure 1 of Kamenetsky *et al.* (2004), figure 2 of Kamenetsky *et al.* (2012), figure 5 of Kamenetsky *et al.* (2014)], and iii) Na–Cl-rich and H_2O-poor whole-rock geochemistry, which is reflected by elevated Na_2O (up to 6·23 wt %), Cl (up to 5·68 wt %) and very low H_2O (0·17–0·56 wt %, 0·3 wt % on average). Based on the above criteria, it is unlikely that the unserpentinized kimberlite sample suite studied by Abersteiner *et al.* (2018b) experienced mineralogical or geochemical degradation during surface exposure. It is noteworthy that in kimberlite samples which were derived from outside the SFUE (i.e. serpentinization of olivine and groundmass minerals has occurred), salts and alkali-carbonates are absent from the groundmass. A question that remains is whether the 'SFUE kimberlite samples' analysed by Kostrovitsky *et al.* (2013) which contain H_2O contents up to six times greater than ours are truly 'unserpentinized' or contaminated by external water.

HYDROGEOLOGY

Since emplacement of the Udachnaya-East kimberlite (~365–367 Ma; Kinny *et al.*, 1997; Kamenetsky *et al.*, 2009b), there has been an estimated 200m–1km of erosion of surface rocks (Brahfogel, 1984). It remains unknown what the hydrogeology of the surrounding country rocks was like during emplacement of the Udachnaya pipes, nor how the hydrogeology has changed over time (~365 Ma). Furthermore, there are numerous considerations such as how, when and where reactions between groundwater aquifers in the sedimentary country rocks and kimberlite rocks occurred, as there may have been numerous tectonic and thermal events that are unaccounted for since kimberlite emplacement. In any case, a crustal brine model would stipulate that there was immediate infiltration into the Udachnaya-East kimberlite rocks at the time of emplacement in order to preserve them. Moreover, Kostrovitsky & Yakovlev (their Comment) do not address what happened to the volumes of water that supposedly transported and precipitated salts in the SFUE kimberlite.

Kostrovitsky & Yakovlev (Comment) argued that within the 400–500 m SFUE kimberlite depth interval there are Na–Cl brine horizons in the surrounding country rocks. They also inform us about Na–Cl brine horizons below 350 meters in the country rocks of the Udachnaya-East pipe (Alexeev, 2009, p. 114). However, we found no record of these 'Na–Cl brine horizons' in the country rocks in any published hydrogeological

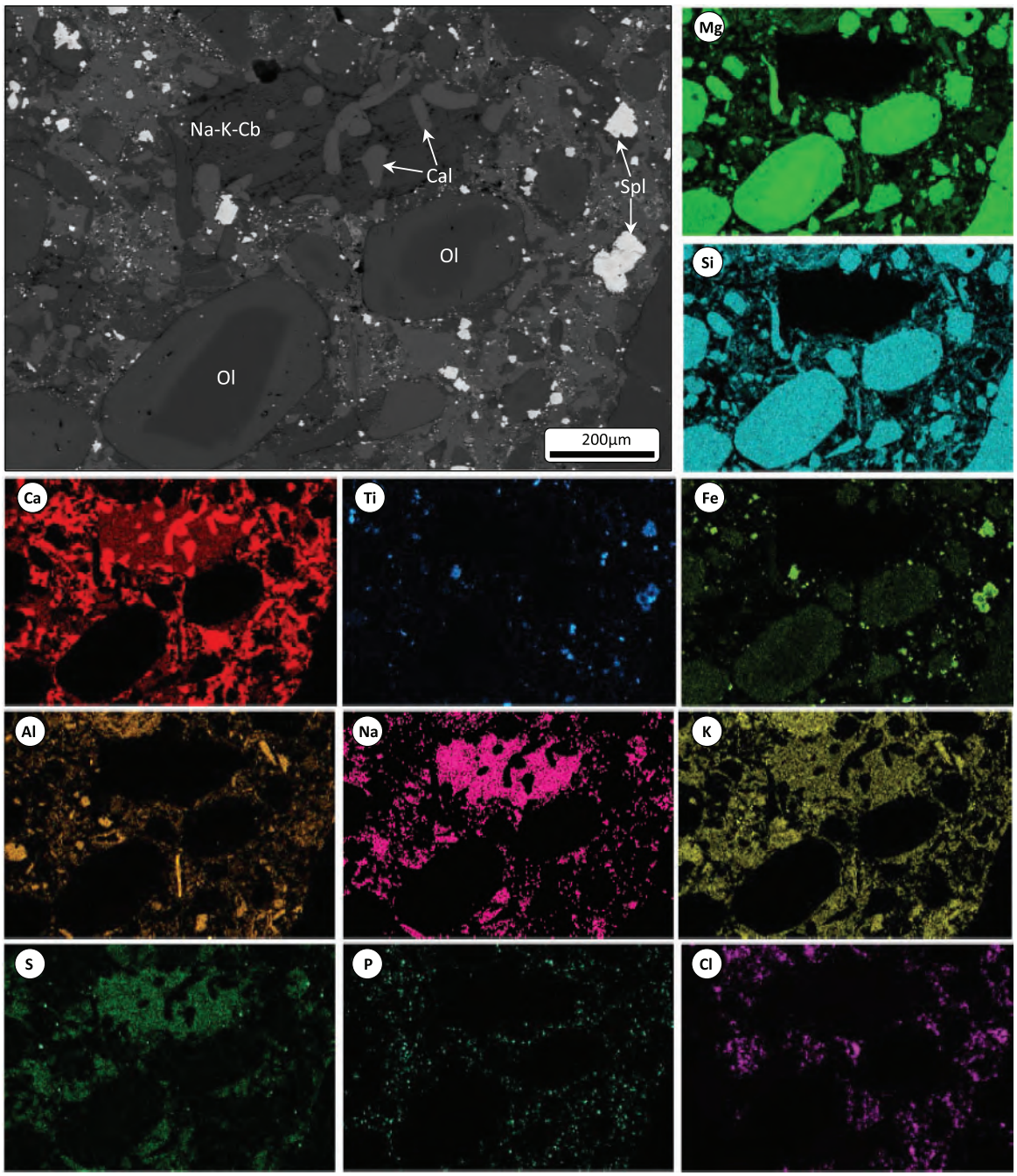

Fig. 1. Back-scattered electron SEM image and X-ray element maps of coherent unserpentinized kimberlite sample K24/04a (see Abersteiner *et al.*, 2018 for methodology). Phases are represented by intensities in: Si–Mg–Fe for olivine (Ol), Fe–Ti–Al for spinel (Spl), Ca for calcite (Cal), Na–K–Ca + S for S-bearing alkali-carbonates (Cb), Ca–P for apatite, Na–K–Cl, K–Al–Si–Mg for phlogopite and Al–Cl–Na for sodalite.

works, including those cited by Kostrovitsky & Yakovlev [see Drozdov *et al.* (1989, 2008) and Alexeev (2009)]. On the contrary, Drozdov *et al.* (2008) and Alexeev (2009) noted that within some porous–cavernous kimberlite rocks from unspecified depths below 350 m, brines with sodium chloride compositions are present. Drozdov *et al.* (2008) observed that: 'Kimberlites with a high content of sodium carbonates (shortite - $Na_2Ca_2(CO_3)_3$ and nyerereite - $Na_2Ca(CO_3)_2$) compose the central part of the eastern ore body, the boundaries of which coincide with the zone of propagation of sodium brines' (p. 271). Furthermore, Drozdov *et al.* (2008) noted that sodium carbonates in the kimberlite are easily decomposed and dissolved in water, whereby the 'hydrochemical (sodium) anomaly of brines in the eastern body was formed due to the process of active interaction of groundwater with kimberlites' [p.271 of Drozdov *et al.* (2008), see also Drozdov *et al.* (1989)]. A similar view

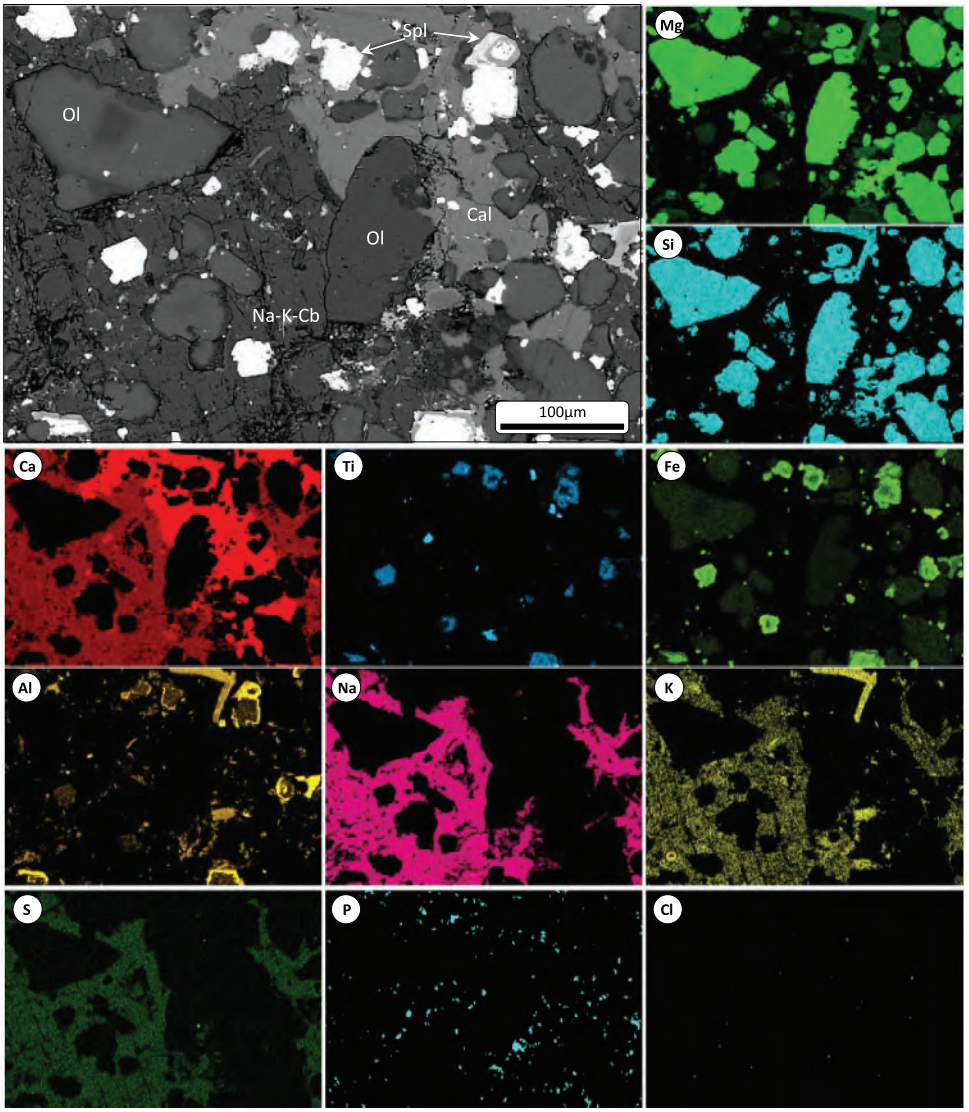

Fig. 2. Back-scattered electron SEM image and X-ray element maps of coherent unserpentinized kimberlite sample K24/04a (see Abersteiner *et al.*, 2018 for methodology). Phases are represented by intensities in: Si–Mg–Fe for olivine (Ol), Fe–Ti–Al for spinel (Spl), Ca for calcite (Cal), Na–K–Ca + S for S-bearing alkali-carbonates (Cb), Ca–P for apatite, Na–K–Cl, K–Al–Si–Mg for phlogopite and Al-Cl-Na for sodalite. Spinel is typically zoned and surrounded by rims of Al-rich pleonaste.

was expressed by Alexeev (2009). In summary, the hydrogeological data suggest that the brines at Udachnaya-East likely acquired their Na salinity from dissolution of water-soluble groundmass minerals in the kimberlite.

PRESERVATION OF OLIVINE

Kostrovitsky & Yakovlev attributed the preservation of olivine to the 'inhibitory (overwhelming) effects of NaCl on the serpentinization processes' due to the incorporation of subsurface salts. In our view, the preservation of olivine is simply attributed to the absence of infiltrating groundwater. The crystallization of magmatic salts could form a ductile and impermeable seal, which prevented the ingress of groundwater through fractures and pores (Kamenetsky *et al.*, 2012; Abersteiner *et al.*, 2018b).

VARIATION IN Na AND Cl

Kostrovitsky & Yakovlev questioned why Na and Cl contents vary widely throughout different positions and units within the Udachnaya-East kimberlite. This may easily be explained by the fact that different units (i.e., volcaniclastic, coherent) have different permeability (volcaniclastic is more permeable than coherent varieties) and are derived from different batches of magma with variable melt/crystal/fluid ratios [see distribution of Na and Cl in Figs 1 and 2; see also figures 4a, b and 6 of Abersteiner *et al.* (2018b), figure 1 of Kamenetsky *et al.* (2004), figure 2 of Kamenetsky *et al.* (2012), figure 5 of

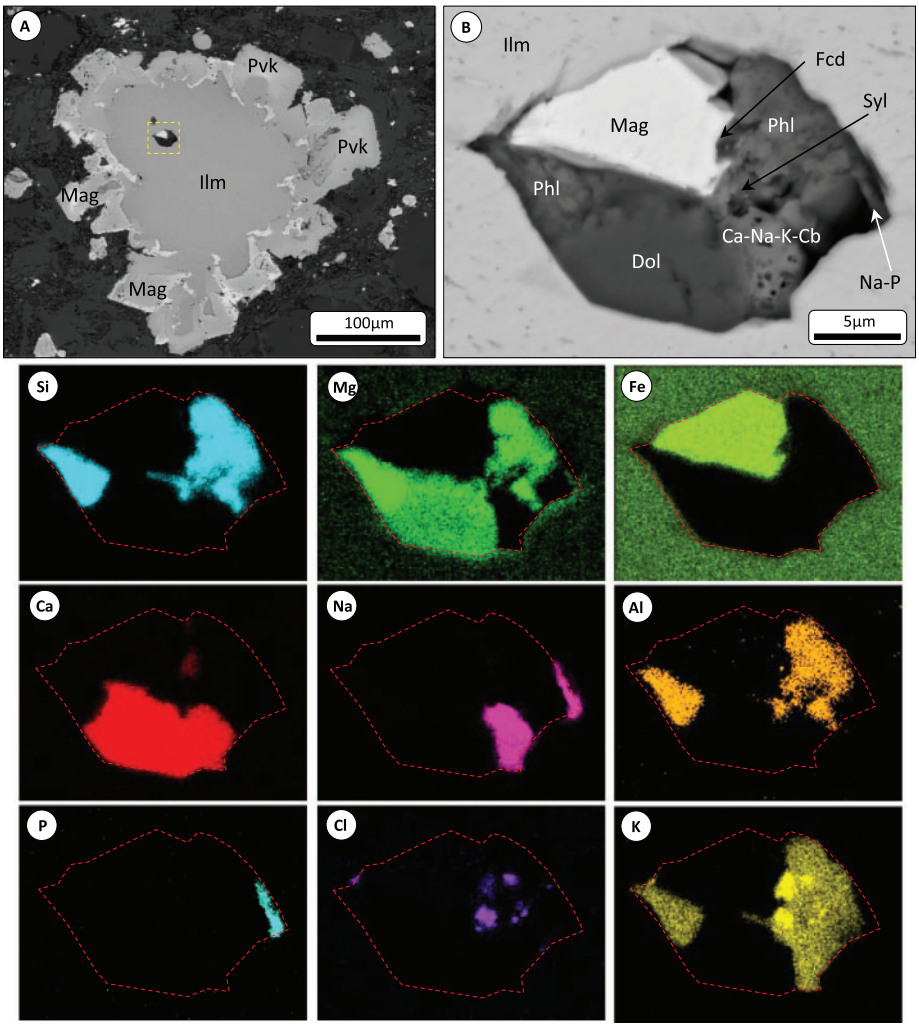

Fig. 3. (a, b) Back-scattered electron SEM images of: (a) a picroilmenite (Ilm) grain, which is partially replaced by a rim of perovskite (Pvk) and magnetite (Mag). (b) shows a zoomed in image of a multiphase melt inclusion (located in the yellow dotted square in (a)) in picroilmentie and accompanying X-ray element maps. Daughter minerals in this inclusion consist of magnetite, phlogopite (Phl), sylvite (Syl), fairchildite (Fcd; $K_2Ca(CO_3)_2$), bradleyite (Bdy; $Na_3Mg(PO_4)(CO_3)$), Ca–K–Na-carbonate (Cb) and dolomite (Dol). The red dotted line indicates the boundary of the inclusion.

Kamenetsky *et al.* (2014)]. Furthermore, the different degrees of alteration that each sample experienced (even within an individual hand specimen) is signified by changes in groundmass mineralogy (i.e. removal of water-soluble alkali-carbonates and salts, and onset of serpentinization), which is reflected by large variations in Na, Cl and H_2O contents. Comparisons between unserpentinized and serpentinized Udachnaya-East kimberlite rocks show that besides these aforementioned variations in Na, Cl and H_2O concentrations, there appears to be no discernible differences in terms of other major and trace elements [see table 2 and figure 9 of Abersteiner *et al.* (2018b)].

ISOTOPES

Maas *et al.* (2005) showed that groundmass minerals in the SFUE kimberlite exhibit $^{87}Sr/^{86}Sr$ ratios that are significantly lower than those of modern brines in the Udachnaya-East mine pit. Furthermore, the Pb isotope composition of chlorides, along with the Nd–Pb isotope composition of alkali-carbonates and Sr–Nd–Hf isotope composition of perovskite are mantle-like, and similar to each other and those of the silicate groundmass component (Maas *et al.*, 2005; Kamenetsky *et al.*, 2009b). A mantle origin for salts and alkali-carbonates is further supported by the S-isotope composition of sulphides and sulphates (Kitayama *et al.*, 2017), which shows the co-magmatic nature of S-bearing minerals, and that the salty units of Udachnaya-East were not contaminated by crustal material (i.e infiltrating brines, hydrothermal alteration or sedimentary country rocks) at magmatic or post-magmatic stages

MELT INCLUSIONS

Perhaps one of the most significant cornerstones supporting a magmatic origin of chlorides and

alkali-carbonates in the Udachnaya-East kimberlite is that melt inclusions hosted in olivine, Mg-ilmenite and other magmatic minerals (e.g. monticellite, perovskite, spinel, phlogopite, apatite) are compositionally and mineralogically similar to the groundmass (Kamenetsky *et al.*, 2004, 2007, 2009b; Golovin *et al.*, 2007; Abersteiner *et al.*, 2018b). Although Kostrovitsky & Yakovlev admit that they could not fully explain the origin of these inclusions, they suggested that the inclusions are 'probably related with secondary formation from surface salts'. Indeed melt inclusions in olivine are secondary in origin (i.e. aligned along annealed fracture planes), but their entrapment coincided with magmatic stages, as the fractures were healed by crystallised olivine. In addition, melt inclusions are compositionally diverse [Fig. 3; see table 3 of Abersteiner *et al.* (2018)] and composed of daughter assemblages that are dominated by chlorides and alkali-carbonates, along with subordinate oxides, silicates and sulphides, which cannot be explained by precipitation from subsurface infiltrating brines. Furthermore, heating experiments show that many of these olivine-hosted melt inclusions homogenise at 660–800 °C (Kamenetsky *et al.*, 2004; Golovin *et al.*, 2017). Thus, this is interpreted to be the minimum temperature for the formation of these inclusions. It is unreasonable that a fluid at such high temperatures can be assigned to any deuteric and/or post-magmatic process.

The most powerful evidence for the involvement of alkali- and chlorine-rich and water-poor carbonatitic melts prior to emplacement of the Udachnaya-East pipe can be found in primary melt inclusions in picroilmenite (Fig. 3), as well as in high pressure secondary melt inclusions in minerals from the deepest-derived peridotite xenoliths (Golovin *et al.*, 2018) and in micro-inclusions in eclogite-hosted diamonds (Zedgenizov *et al.*, 2018). In all these cases, the origin of such inclusions is attributed the mantle processes that occurred shortly before the formation of the Udachnaya pipes.

One of the most compelling points dispelling a crustal brine or assimilated evaporite origin of the Udachnaya-East melt inclusions is their similarity to melt inclusions from kimberlitic minerals from localities worldwide (e.g. Canada, Finland, southern Africa, Greenland; Kamenetsky *et al.*, 2009a, 2013; Mernagh *et al.*, 2011; Abersteiner *et al.*, 2017, 2018a, 2019b, Giuliani *et al.*, 2017). These other studied kimberlites were emplaced in different lithological settings (i.e. sedimentary rocks and brines are absent), therefore the enrichment of chlorides and alkali-carbonates in kimberlitic mineral-hosted melt inclusions cannot be explained by secondary processes, but is inherited from the parental kimberlite melt.

In summary, the observations and arguments by Kostrovitsky & Yakovlev do not provide sufficient evidence to substantiate a crustal brine origin for salts and alkali-carbonates, and absence of serpentine in the SFUE kimberlite. We concur with the conclusions made by hydrogeologists (Drozdov *et al.*, 1989, 2008; Alexeev, 2009) that brines within the Udachnaya acquired their salinity from dissolution of kimberlite groundmass minerals, rather than chlorides and alkali-carbonates precipitating from supposed infiltrating crustal brines. We maintain the position that the SFUE kimberlite horizon represents a unique example of pristine kimberlite with preserved abundant magmatic chlorides and alkali-carbonates in the groundmass.

ACKNOWLEDGEMENTS

This study forms part of A.A's Ph.D and was supported by an Australian Postgraduate Award (APA) and the Max Banks Research Scholarship in Earth Sciences. A.V.G was supported by Russian Federation state assignment of IGM SB RAS. We acknowledge our co-authors Maya Kamenetsky and Karsten Goemann for their assistance, and Executive Editor Marjorie Wilson for the opportunity to 'set the record straight'.

REFERENCES

Abersteiner, A., Giuliani, A., Kamenetsky, V. S. & Phillips, D. (2017). Petrographic and melt-inclusion constraints on the petrogenesis of a magmaclast from the Venetia kimberlite cluster, South Africa. *Chemical Geology* **455**, 331–341.

Abersteiner, A., Kamenetsky, V. S., Goemann, K., Giuliani, A., Howarth, G. H., Castillo-Oliver, M., Thompson, J., Kamenetsky, M. & Cherry, A. (2019). Composition and emplacement of the Benfontein kimberlite sill complex (Kimberley, South Africa): Textural, petrographic and melt inclusion constraints. *Lithos* **324-325**, 297–314.

Abersteiner, A., Kamenetsky, V. S., Goemann, K., Golovin, A. V., Sharygin, I. S., Pearson, D. G., Kamenetsky, M. & Gornova, M. A. (2019). Polymineralic inclusions in kimberlite-hosted megacrysts: Implications for kimberlite melt evolution. *Lithos* **336-337**, 310–325.

Abersteiner, A., Kamenetsky, V. S., Golovin, A. V., Kamenetsky, M. & Goemann, K. (2018). Was crustal contamination involved in the formation of the serpentine-free Udachnaya-East kimberlite? New insights into parental melts, liquidus assemblage and effects of alteration. *Journal of Petrology* **59**, 1467–1492.

Abersteiner, A., Kamenetsky, V. S., Pearson, D. G., Kamenetsky, M., Goemann, K., Ehrig, K. & Rodemann, T. (2018). Monticellite in group-I kimberlites: Implications for evolution of parental melts and post-emplacement CO 2 degassing. *Chemical Geology* **478**, 76–88.

Alexeev, S. V. (2009). *Cryogeological Systems of the Yakutian Diamondiferous Province*. Novosibirsk: Academic Publis hing House "GEO".

Brahfogel, F. F. (1984). *Geological Aspects of Kimberlite Magmatism of the Northeast Siberian Platform*. Yakutsk: Yakutsk Branch of the USSR Academy of Sciences, p. 128.

Drozdov, A. V., Egorov, K. N., Gotovtsev, S. P. & Klimovsky, I. V. (1989). Hydrogeological structure and hydrochemical zonation of the udachnaya kimberlite pipe. In: Anisimova, N.P. (ed) *Combined Permafrost and Hydrogeological Studies*. Yakutsk: Institute of Permafrost Siberian Branch of Academy of Sciences, pp. 146–155.

Drozdov, A. V., Iost, N. A. & Lobanov, V. V. (2008). *Cryohydrogeology of the Diamond Deposits in Western Yakutia*. Irkutsk: Irkutsk State Technical University.

Giuliani, A., Soltys, A., Phillips, D., Kamenetsky, V. S., Maas, R., Goemann, K., Woodhead, J. D., Drysdale, R. & Griffin, W. L. (2017). The final stages of kimberlite petrogenesis: Petrography, mineral chemistry, melt inclusions and Sr-C-O isotope geochemistry of the Bultfontein kimberlite (Kimberley, South Africa). *Chemical Geology* **455**, 342–356.

Golovin, A. V., Sharygin, I. S., Kamenetsky, V. S., Korsakov, A. V. & Yaxley, G. M. (2018). Alkali-carbonate melts from the base of cratonic lithospheric mantle: Links to kimberlites. *Chemical Geology* **483**, 261–274.

Golovin, A. V., Sharygin, I. S. & Korsakov, A. V. (2017). Origin of alkaline carbonates in kimberlites of the Siberian craton: Evidence from melt inclusions in mantle olivine of the Udachnaya-East kimberlite. *Chemical Geology* **455**, 357–375.

Golovin, A. V., Sharygin, V. V. & Pokhilenko, N. P. (2007). Melt inclusions in olivine phenocrysts in unaltered kimberlites from the Udachnaya-East pipe, Yakutia: Some aspects of kimberlite magma evolution during late crystallization stages. *Petrology* **15**, 168–183.

Kamenetsky, V. S., Golovin, A. V., Maas, R., Giuliani, A., Kamenetsky, M. B. & Weiss, Y. (2014). Towards a new model for kimberlite petrogenesis: Evidence from unaltered kimberlites and mantle minerals. *Earth-Science Reviews* **139**, 145–167.

Kamenetsky, V. S., Grütter, H., Kamenetsky, M. B. & Gömann, K. (2013). Parental carbonatitic melt of the Koala kimberlite (Canada): Constraints from melt inclusions in olivine and Cr-spinel, and groundmass carbonate. *Chemical Geology* **353**, 96–111.

Kamenetsky, V. S., Kamenetsky, M. B., Golovin, A. V., Sharygin, V. V. & Maas, R. (2012). Ultrafresh salty kimberlite of the Udachnaya-East pipe (Yakutia, Russia): A petrological oddity or fortuitous discovery? *Lithos* **152**, 173–186.

Kamenetsky, V. S., Kamenetsky, M. B., Sharygin, V. V., Faure, K. & Golovin, A. V. (2007). Chloride and carbonate immiscible liquids at the closure of the kimberlite magma evolution (Udachnaya-East kimberlite, Siberia). *Chemical Geology* **237**, 384–400.

Kamenetsky, V. S., Kamenetsky, M. B., Weiss, Y., Navon, O., Nielsen, T. F. D. & Mernagh, T. P. (2009a). How unique is the Udachnaya-East kimberlite? Comparison with kimberlites from the Slave Craton (Canada) and SW Greenland. *Lithos* **112S**, 334–346.

Kamenetsky, V. S., Maas, R., Kamenetsky, M. B., Paton, C., Phillips, D., Golovin, A. V. & Gornova, M. A. (2009). Chlorine from the mantle: Magmatic halides in the Udachnaya-East kimberlite, Siberia. *Earth and Planetary Science Letters* **285**, 96–104.

Kamenetsky, M. B., Sobolev, A. V., Kamenetsky, V. S., Maas, R., Danyushevsky, L. V., Thomas, R., Pokhilenko, N. P. & Sobolev, N. V. (2004). Kimberlite melts rich in alkali chlorides and carbonates: A potent metasomatic agent in the mantle. *Geology* **32**, 845–848.

Kinny, P. D., Griffin, B. J., Heaman, L. M., Brakhfogel, F. F. & Spetsius, Z. V. (1997). SHRIMP U-Pb ages of perovskite from Yakutian kimberlites. *Geologiya i Geofizika* **38**, 91–99.

Kitayama, Y., Thomassot, E., Galy, A., Golovin, A., Korsakov, A., d'Eyrames, E., Assayag, N., Bouden, N. & Ionov, D. (2017). Co-magmatic sulfides and sulfates in the Udachnaya-East pipe (Siberia): A record of the redox state and isotopic composition of sulfur in kimberlites and their mantle sources. *Chemical Geology* **455**, 315–330.

Kostrovitsky, S. I., Kopylova, M. G., Egorov, K. N. & Yakovlev, D. A. (2013). The Exceptionally Fresh Udachnaya-East Kimberlite: Evidence for Brine and Evaporite Contamination. In: Pearson, D.G., et al. (eds.) *Proceedings of the 10th International Kimberlite Conference*, pp. 75–91.

Maas, R., Kamenetsky, M. B., Sobolev, A. V., Kamenetsky, V. S. & Sobolev, N. V. (2005). Sr, Nd, and Pb isotope evidence for a mantle origin of alkali chlorides and carbonates in the Udachnaya kimberlite, Siberia. *Geology* **33**, 549–552.

Mernagh, T. P., Kamenetsky, V. S. & Kamenetsky, M. B. (2011). A Raman microprobe study of melt inclusions in kimberlites from Siberia, Canada, SW Greenland and South Africa. *Spectrochimica Acta Part A: Molecular and Biomolecular Spectroscopy* **80**, 82–87.

Zedgenizov, D. A., Ragozin, A. L., Shatsky, V. S. & Griffin, W. L. (2018). Diamond formation during metasomatism of mantle eclogite by chloride-carbonate melt. *Contributions to Mineralogy and Petrology* **173**, 84.

Chapter 12 – Synthesis

12.1 Introduction

This thesis aims to improve our understanding of primary/parental kimberlite melt compositions ranging from their generation in the subcontinental lithospheric mantle through to their ascent and emplacement in the upper crust. The studies presented here employed a range of petrographic, geochemical, and melt/fluid inclusion techniques in order to reconstruct the compositional evolution of kimberlite melts/magmas and constrain the various processes that modify them. In this chapter, a summary of the findings and significance of each of the previous chapters is discussed, as well as the overall implications of this research for kimberlite petrogenesis and its links to the origin of diamonds. Finally, a discussion on pathways for future kimberlite research is presented.

12.2 Summary and significance of findings

12.2.1 Chapter 2: Petrographic and melt-inclusion constraints on the petrogenesis of a magmaclast from the Venetia kimberlite cluster, South Africa

This chapter explored the compositional evolution of the melt parental to the Venetia kimberlite (South Africa) as well some of the physical processes that led to the formation of the studied magmaclast.

Examination of primary melt/fluid inclusions in groundmass chromite, perovskite and apatite were shown to contain diversity of daughter phases, which are dominated by carbonates enriched in K-Na-Ba-Sr, phosphates, Na-K chlorides, sulphides as well as rare silicates and spinel. A systematic trend was identified in melt/fluid inclusion daughter mineral assemblages, which was correlated to the relative timing of crystallisation of the host mineral. Melt/fluid inclusions in early forming chromite and perovskite were shown to be broadly silicate-carbonate in composition, whereas late-forming apatite is more enriched in carbonates, chlorides, phosphates and sulphates, whereas silicates are rare. Late-stage groundmass calcite was also shown to be dominated by inclusions of Na-carbonates and chlorides. However, the propensity of groundmass calcite to dissolve and re-precipitate means that inclusions hosted in calcite may be secondary in origin. The variation in melt/fluid inclusion daughter mineral assemblages in different host minerals represents the heterogeneous trapping of a variably differentiated kimberlite melt at different timings. This

kimberlite melt was shown to evolve towards more alkali-halogen-phosphorus enriched carbonate-dominated compositions.

The ovoid shape and concentric mineral alignment in the studied magmaclast is attributed to the rapid rotation of partially crystallised and low viscosity kimberlite melt, or progressive accretion of kimberlite material around an olivine macrocryst kernel. This kimberlite magmaclast was likely entrained by a successive pulse of ascending kimberlite material such as those which produced volcaniclastic units in the Venetia pipe. Although this magmaclast exhibits typical mineralogical characteristics of hypabyssal kimberlites, it is dissimilar from Venetia hypabyssal kimberlite rocks, thus indicating that the magmaclast was likely derived from an earlier batch of compositionally distinct kimberlite magma, or had crystallised under higher P-T conditions.

12.2.2 Chapter 3: Monticellite in group-I kimberlites: Implications for evolution of parental melts and post-emplacement CO_2 degassing

This chapter examined the formation of monticellite-rich varieties of kimberlite (Leslie, Canada; Pipe 1, Finland) and the processes that lead to olivine replacement by pseudomorphic monticellite.

Monticellite was classified into two morphological types: i) discrete and/or intergrown groundmass grains (Mtc-I) and replacement of olivine (Mtc-II). Textural, petrographic and melt inclusion evidence shows that pseudomorphic Mtc-II likely formed due to a decarbonation reaction between olivine and the carbonate component of the kimberlite melt.

$$Forsterite + Carbonate\ (melt) \rightleftharpoons Monticellite + Periclase + CO_2$$

This reaction is supported by the preservation of primary periclase inclusions in groundmass monticellite (both Mtc-I and Mtc-II), perovskite and Mg-magnetite. Periclase is also considered to have crystallised in the groundmass, but was subsequently altered to brucite during groundmass alteration. Degassing of CO_2 from the kimberlite magma was the driving mechanism for this decarbonation reaction, where additional CO_2 removal facilitated further decarbonation reactions and thus produced more monticellite, periclase, Fe-Mg-oxides and CO_2 whilst simultaneously consuming olivine and carbonate melt (Le Chatelier's Principle). Assuming that all monticellite in the studied kimberlites was produced by the proposed decarbonation reactions, calculations predict that approximately 119 kg and 208 kg

of CO_2 in samples LDC7 and FLP1 respectively could be produced in a cubic metre of kimberlite magma. Although these are tentative estimates, this provides important insights into previously overlooked reactions that may be a significant contributor to CO_2 exsolution from kimberlite magmas.

12.2.3 Chapter 4: Significance of halogens (F, Cl) in kimberlite melts: Insights from mineralogy and melt inclusions in the Roger pipe (Ekati, Canada)

This chapter focused on the role and abundances of F and Cl in kimberlite magmas through the study of the anomalously F-enriched Roger kimberlite (Canada).

The Roger kimberlite is mineralogically unique as it contains F-rich minerals (fluorite and bultfonteinite) in the groundmass and as a replacement mineral after olivine. Examination of melt inclusions in olivine, Cr-spinel, monticellite and apatite were shown to be multiphase and contain daughter assemblages dominated by (in order or relative abundance) Ca-Mg and Na-K-Ba-Sr carbonates ± F, Na-K chlorides and sulphates, phosphates, spinel, silicates and sulphides. The abundance of alkalis/alkali-earths and halogens (in particular, F) in these melt inclusions suggests that these elements were an intrinsic (i.e. magmatic) part of the crystallising kimberlite melt. Based on trace elements of similar compatibility (i.e. F/Nd and Cl/U) in the Roger kimberlite and their respective estimated primitive mantle ratios, it is estimated that F and Cl should exist in high concentrations in the Roger kimberlite (and kimberlites in general) than in whole-rock compositions. The general paucity of these alkali/alkali-earth and halogens in the kimberlite groundmass is most likely due to the effects of syn- and/or post-magmatic alteration (i.e. serpentinisation). Fluorine in the Roger kimberlite is considered to be magmatic in origin, but was likely remobilized during hydrothermal alteration and combined with Ca-bearing serpentinising fluids to form fluorite and bultfonteinite, which crystallised interstitially in the groundmass and partially replaced olivine. This study demonstrates that parental/primary kimberlite melts could potentially contain higher abundances of halogens.

12.2.4 Chapter 5: Was crustal contamination involved in the formation of the serpentine-free Udachnaya-East kimberlite? New insights into parental melts, liquidus assemblage and effects of alteration

This chapter employed extensive petrographic, geochemical and melt inclusion data to demonstrate that the unserpentinised and alkali-carbonate and –chloride rich units of the

Udachnaya-East kimberlite (Russia) are pristine magmatic, and were not contaminated by crustal rocks and/or brines.

Serpentinised and unserpentinised coherent and volcaniclastic varieties of the Udachnaya-East kimberlite were shown to be similar in terms of major, compatible and incompatible trace element concentrations, primitive mantle normalised trace element patterns, groundmass textures, and silicate and oxide mineralogy and compositions. However, these kimberlite varieties differ in terms of the presence of: i) fresh olivine, Na-K-Cl-S rich minerals (alkali-carbonates, chlorides, sodalite) and absence of hydrous alteration minerals (e.g., serpentine, iowaite) in the groundmass of unserpentinised samples, and ii) absence of alkali-carbonates/chlorides/sodalite in the groundmass and typical alteration of olivine (i.e. replaced by serpentine ± iowaite) and interstitial groundmass in serpentinised samples. Examination of melt inclusions hosted in olivine, monticellite, apatite, spinel and perovskite from both serpentinised and unserpentinised varieties of kimberlite were shown to be virtually identical and composed of daughter assemblages dominated by alkali-carbonates, chlorides and sulphates/sulphides (i.e. similar in composition and mineralogy to the unserpentinised kimberlite groundmass). It was suggested that the unserpentinised unit of the Udachnaya-East kimberlite represents pristine magmatic (i.e. unaltered) kimberlite, which crystallised from a H_2O-poor and Si-Na-K-Cl-bearing carbonate-rich melt. In addition, this same petrographic, geochemical and melt inclusion evidence indicates that this enrichment of alkalis and halogens in the unserpentinised Udachnaya-East kimberlite units was unlikely to have been caused by external brines or evaporites.

12.2.5 Chapter 6: Djerfisherite in kimberlites and their xenoliths: implications for kimberlite melt evolution

This chapter reviewed and examined the composition and provenance of djerfisherite ($K_6(Fe,Ni,Cu)_{25}S_{26}Cl$), which occurs as an accessory sulphide in kimberlites, kimberlite-hosted mantle xenoliths and as inclusions in diamonds and kimberlitic minerals.

Djerfisherite is shown to be very heterogeneous in composition (i.e. Fe:Ni:Cu ratios), which is likely linked to localised variations in the metasomatic and/or kimberlitic melt/fluid rather than a particular setting (i.e. kimberlite, diamond, xenolith). Some analyses revealed some djerfisherite grains to contain lower than average K and Cl contents, which results in below average atoms per formula unit totals. Raman spectroscopy and electron backscatter

dispersive analyses were employed and showed that these djerfisherite grains still maintain the same structure as regular *bona fide* djerfisherite.

Two potential mechanisms for djerfisherite genesis were identified: i) replacement of pre-existing Fe-Ni-Cu sulphides due to interactions with K-Cl-bearing metasomatic melts/fluids in the mantle or kimberlite melt, and ii) direct crystallisation of djerfisherite from the kimberlite melt. Djerfisherite is inferred to be relatively resistant to secondary alteration and thus an important indicator of K and Cl in kimberlite magmas and the mantle.

12.2.6 Chapter 7: Composition and emplacement of the Benfontein kimberlite sill complex (Kimberley, South Africa): Textural, petrographic and melt inclusion constraints

This chapter reconstructed the style of emplacement and compositional evolution kimberlite magmas within intrusive settings by examining the Benfontein sill complex (South Africa).

The Benfontein sills are a rare example where primary magmatic baddeleyite is crystallised in kimberlites. Perovskite and baddeleyite were dated using the U/Pb method and produced ages of 85.7 ± 4.4 Ma and 86.5 ± 2.6 Ma respectively. This is consistent with previous age determinations and consistent with emplacement ages of neighbouring Kimberley kimberlites.

The Benfontein sills were shown to contain relatively low abundances of mantle material (i.e. xenocrysts and xenoliths), which suggests there was significant fractionation of the magma during lateral spreading into the country rock. This resulted in a magma that was more carbonate enriched and thus more buoyant and lower in viscosity. Carbonate diapirs underlie and intrude upwards into dense oxide-rich layers within the Lower Benfontein Sill and contain abundant exotic and incompatible element enriched minerals. These diapirs are considered to represent extreme melt differentiation, which was followed by physical separation and isolation from the parental carbonate-rich magma.

Petrographic data of spinel shows that it exhibits atoll-textures. These atoll spinels are composed of a magnesian ulvöspinel – magnetite or chromite core, which is sometimes surrounded by an intermediate zone containing typical alteration minerals (e.g., serpentine), which is in turn surrounded by an outer rim of Mg-Al-magnetite which mirrors the shape of the spinel core exactly. Pleonaste infills this intermediate zone only observed in the freshest

kimberlite samples. Therefore, it is suggested that pleonaste was a magmatic phase, but was resorbed back into the host melt and/or removed by alteration, thereby resulting in the typical 'atoll-spinel' texture.

Analyses of melt inclusions in olivine, monticellite, oxides and apatite were shown to be dominated by daughter assemblages of Ca-Mg and Na-K-Ba-Sr carbonates, phosphates, oxides, silicates, sulphides, Na-K sulphates and halides. The compositions of these inclusions suggests that the melt parental to the Benfontein sills was probably more enriched in alkalis, halogens and sulphur, but these components were likely leached during groundmass alteration.

12.2.7 Chapter 8: Polymineralic inclusions in kimberlite-hosted megacrysts: Implications for kimberlite melt evolution

This chapter examined the compositions and origin of inclusions hosted in clinopyroxene and olivine megacrysts from the Udachnaya-East (Russia), Diavik, Leslie and Jericho kimberlites (Canada).

Two types of inclusions were identified in megacrysts: i) large (<0.5 – 5 mm) polymineralic inclusions, which are composed of mineral assemblages similar to their respective host kimberlite groundmass, and typically consist of olivine, calcite, spinel, perovskite, phlogopite and apatite (± serpentine, alkali-carbonates, alkali-chlorides, barite), and ii) swarms/trails of micro (<1 – 5 μm) melt inclusions, which surround polymineralic inclusions, veins and fractures. These inclusions are multiphase and contain assemblages similar to polymineralic inclusions, as well as additional phases, such as alkali-carbonates or alkali-chlorides, which are usually absent in polymineralic inclusions and the surrounding kimberlite groundmass.

Textural evidence suggests that polymineralic inclusions and micro melt inclusions formed due to kimberlite melt infiltrating the host megacryst along crystal defects. It is likely that there was significant disequilibria between the infiltrating kimberlite melt and host megacryst, which resulted in partial dissolution of the megacryst, thereby resulting in the formation of polymineralic inclusions and micro melt inclusions. The connectivity between polymineralic inclusions and kimberlite groundmass due to networks of fractures/veins suggests that polymineralic inclusions are susceptible to infiltrating secondary fluids, and thereby cannot be considered pristine magmatic. In contrast, micro melt inclusions remained

isolated and entrapped remnants of the infiltrating kimberlite melt, which was likely more enriched in alkalis-Cl-S-CO_2 relative to polymineralic inclusions and the host kimberlite rocks.

12.2.8 Chapter 9: A genetic story of olivine crystallisation in the Mark kimberlite (Canada) revealed by zoning and melt inclusions

This chapter documented pseudosecondary melt/fluid inclusions, as well as for the first time primary melt inclusions in kimberlitic olivine from the Mark kimberlite (Canada). This study presents new implications for the timing of multi-stage olivine growth in kimberlites and the evolution of the magma from which it was crystallised and transported in.

Olivine in the Mark kimberlite is remarkably fresh and contains multiple zones (i.e. core, rim, rind and outmost rind), which record evidence of different stages of olivine dissolution and crystallisation. Textural relationships and crystal inclusions in different zones of olivine were used to determine the relative timing of each stage of olivine crystallisation. Olivine cores are interpreted to be xenocrystic, whereas rims represent the earliest stage of magmatic olivine growth. Rinds represent late-stage olivine crystallisation from more oxidised and evolved melt compositions, whereas the outmost rinds represent an additional and previously undocumented episode of olivine growth in kimberlites.

Primary melt inclusions were shown to be restricted to Mg-rich olivine rinds. In addition, melt inclusion trails located along healed fractures traversing olivine cores/rims were shown to terminate at the contacts with rinds were interpreted to be pseudosecondary in origin. Both primary and pseudosecondary melt inclusions are compositionally similar and indicate that a silica-poor, halogen-bearing and alkali-dolomitic melt crystallised and transported olivine.

12.2.9 Chapter 10: Evolution of kimberlite magmas in the crust: A case study of groundmass and mineral-hosted inclusions in the Mark kimberlite (Lac de Gras, Canada)

This chapter is an extended study of Chapter 9 on the Mark kimberlite (Canada), where it focuses on the petrography and geochemistry of groundmass minerals in order to establish a sequence of crystallisation and reconstruct the major compositional features of the parental melt.

Textural relationships, zoning patterns and crystal/melt/fluid inclusions in olivine and groundmass minerals were combined to produce a relative sequence of groundmass mineral crystallisation. Furthermore, mineral zoning patterns and melt inclusions in olivine, groundmass minerals and Cr-diopside macrocrysts were used to constrain the evolution of the parental kimberlite melt, which was shown to become progressively enriched in alkalis/alkali-earths and halogens during melt crystallisation. The absence of any crystallising minerals in the groundmass that host significant alkalis or halogens likely resulted in these elements crystallising in the groundmass as unstable and waters-soluble phases, which were subsequently removed by alteration.

12.2.10 Chapter 11: A Reply to the Comment by Kostrovitsky, S. and Yakovlev, D. on 'Was crustal contamination involved in the formation of the serpentine-free Udachnaya-East kimberlite? New insights into parental melts, liquidus assemblage and effects of alteration' by Abersteiner et al. [J. Petrol. 59 (2018) 1467-1492]

This chapter addresses a Comment published in Journal of Petrology critiquing Chapter 5. Arguments challenging the magmatic model for the unserpentinised Udachnaya-East kimberlite (Russia) are rebutted and supported by reinforced additional data and interpretations.

Inconsistencies by Kostrovitskiy et al. (2013) regarding the presence of country rock evaporites, composition of the putative kimberlite melt and primary versus secondary enrichment of Na and Cl at the Udachnaya-East kimberlite are emphasised. Furthermore, additional data and interpretations are presented regarding the: i) quality of sample collection in Chapter 5, ii) hydrogeology in and around the Udachnaya-East kimberlite, iii) preservation of olivine in unserpentinised kimberlite units, iv) variations in Na and Cl in different samples, v) radiogenic (Pb, Sr, Nd, Hf) and S isotopic signature of brines, chlorides, alkali-carbonates and groundmass components, and vi) melt inclusion compositions. This combined evidence demonstrates that crustal brines acquired their salinity from the salty kimberlite units, and not vice versa. Furthermore, the position that groundmass chlorides and alkali-carbonates in the serpentine-free Udachnaya-East kimberlite units are magmatic in origin is reasserted.

12.3 Reconstructing kimberlite melt compositions from melt inclusions

Kimberlite rocks represent the final products of deeply-derived magmas that originated in the mantle and underwent widely varying degrees of differentiation, contamination and alteration processes that modified their composition. Furthermore, the complex compositional and mineralogical diversity of different kimberlite localities, including within individual pipes, renders producing a universal model for kimberlite petrogenesis challenging. Elucidating the initial composition of kimberlite melts is essential to understanding the nature of the SCLM, pressures and temperatures of melt generation, as well as kimberlite magma rheology, viscosity, emplacement mechanisms, and volatile inventory, and even their relationship to diamonds.

The traditional approach of reconstructing primary kimberlite melt compositions using whole-rock analyses proved to be highly problematic as any model must take into full account the numerous processes of xenogenic material entrainment and assimilation, volatile exsolution, magma differentiation and alteration. Furthermore, experimental studies were unable to successfully reproduce pure melts at pressure and temperature conditions of kimberlite emplacement (Brooker et al., 2011; Moussallam et al., 2016; Sparks et al., 2009). One of the most significant limitations to the whole-rock method is the vastly variable effects of syn- and post-magmatic alteration of kimberlites by deuteric (i.e. late-stage magmatic; Mitchell, 2008l, 2013) and/or external fluids (Brooker et al., 2011; Giuliani et al., 2014, 2017; Sparks et al., 2006; Stripp et al., 2006). To circumvent this problem, this thesis has focussed on melt/fluid inclusions, which can provide unique insights into a particular stage of kimberlite melt evolution, ranging from its ascent *en route* to the surface and/or emplacement. Once entrapped within the host mineral, melt inclusions are often isolated from the effects of secondary processes, which are pervasive throughout the groundmasses of most kimberlites. Previous studies of melt inclusions in kimberlites were largely restricted to secondary inclusions in olivine (Golovin et al., 2003, 2007, 2017; Kamenetsky et al., 2004, 2009a, 2012, 2014; Mernagh et al., 2011) with the addition of a few *ad hoc* studies on primary melt inclusions in magmatic minerals (e.g., spinel, phlogopite, apatite; Giuliani et al., 2017; Kamenetsky et al., 2009b, 2013).

Advancements in micro-analytical techniques have allowed the study of inclusions to be rapidly expanded. This thesis presents new advances in this research field by conducting systematic studies of melt/fluid inclusions in olivine, megacrysts (Cr-diopside, olivine) and

magmatic minerals from kimberlite localities worldwide (e.g., Russia, Canada, Finland, South Africa). These studies are combined with detailed petrography along with mineral and rock geochemistry in order to produce new perspectives on the compositions of parental kimberlite melts and their evolution. Significant findings of this thesis demonstrate that:

1. All types of melt/fluid inclusions (i.e. primary, secondary or pseudosecondary) in all kimberlite-hosted minerals, regardless of locality or position of the studied sample in the kimberlite body, are consistently shown to be silica-poor and enriched in CO_2, alkalis/alkali-earths (Na, K, Ba, Sr), halogens (F, Cl), phosphorus and sulphur relative to the kimberlite groundmass mineralogy and whole-rock composition. Although daughter mineral assemblages in melt inclusions are extremely diverse, they are typically represented by carbonates, chlorides/halides, phosphates, sulphates/sulphides and oxides (e.g., spinel, perovskite). Silicate minerals are rare, but usually occur in the form of phlogopite/tetraferriphlogopite and/or olivine. Hydrous minerals such as serpentine are completely absent and were only identified in polymineralic inclusions in megacrysts, which were interpreted to have interacted with external fluids.
2. There are systematic changes in the composition and mineral assemblages in melt inclusions, which are dependent on their relative timing of entrapment by the host mineral. Olivine and Cr-spinel are interpreted to be the earliest phases to crystallise (Fedortchouk and Canil, 2004; Mitchell, 2008) and thus entrap the earliest (i.e. least evolved) snapshots of the kimberlite melt (i.e. carbonate-silicate bearing), whereas late-stage minerals (e.g., apatite, carbonate) entrap the most evolved samples of kimberlite melt (i.e. more alkali, halogen and incompatible element enriched).
3. Alkali and halogen enrichment in melt inclusions in kimberlite-hosted minerals presents strong evidence against the crustal contamination (i.e. brines, evaporites) model proposed for the origin of groundmass alkali-chlorides and alkali-carbonates in the Udachnaya-East kimberlite, as suggested by (Kopylova et al., 2013, 2016; Kostrovitskiy et al., 2013). Melt inclusions in olivine and groundmass minerals from both the unserpentinised and serpentinised units of the Udachnaya-East kimberlite show that alkalis and halogens were intrinsic components in the parental melt, which originated in the mantle. Furthermore, identical alkali and halogen enrichment trends were observed in melt inclusions in kimberlite minerals from localities worldwide, which emplaced in different cratons and intruded different country rock lithologies.

Although the unserpentinised units of Udachnaya-East may be considered as examples of pristine kimberlite, this is a mineralogically and geochemically unique locality and therefore using it as the basis for reconstructing a universal kimberlite melt model is tenuous.

4. The Benfontein Kimberlite Sill complex provided a unique opportunity to examine how kimberlite magmas may evolve intrusively during emplacement in the upper crust. The Benfontein sills show that the substantial fractionation of mantle material can occur during lateral spreading of magma into the country rock, resulting in a magma that became more carbonate-rich. This buoyant and viscous magma is likely responsible for the non-explosive emplacement of the sills and rhythmic mineral layering is attributed to multiple injections of magma.
5. The absence and/or paucity of alkali/alkali-earth- and halogen-rich minerals (e.g., carbonates, chlorides, sulphates, phosphates), such as those commonly documented in melt inclusions hosted in kimberlitic minerals, in the groundmass of most kimberlites is attributed to their instability and dissolution during syn- and/or post-magmatic alteration. The rapid degradation of phases such as alkali-carbonates and chlorides may be comparable to the natrocarbonatite lavas erupted from Oldoinyo Lengai (Tanzania), where significant mineralogical and compositional changes can occur within days to months upon exposure to the atmosphere (Dawson, 1993; Dawson et al., 1987; Zaitsev and Keller, 2006). The only evidence of former alkali-rich minerals in the groundmass of such carbonatitic rocks is preserved in melt inclusions (e.g., magnetite, apatite (Chen et al., 2013; Guzmics et al., 2011; Zaitsev et al., 2010, 2013). A similar process of alkali and halogen leaching during secondary alteration may be inferred for kimberlite rocks. This removal of alkali-carbonate and chloride minerals is evident in co-existing serpentinised and unserpentinised units of the Udachnaya-East kimberlite. Therefore, it is suggested that alkalis and halogens may exist in potentially higher (yet unconstrained) concentrations in the parental kimberlite melt.
6. Melt inclusions can preserve a record of decarbonation reactions in kimberlites, such as between the carbonate melt component and olivine. Although reaction products, such as CO_2, are inevitably lost to degassing, other minerals such as periclase may be preserved as inclusions in groundmass minerals.
7. Throughout this study, there have been numerous, yet only slightly varying compositional models for the parental kimberlite melt. This probably reflects the varying degrees of differentiation that kimberlite melts experienced prior to the

entrapment of inclusions in their respective host mineral or compositional heterogeneities between different kimberlite pipes. In general, it is proposed that kimberlite melts likely originated from aluminosilicate- and H_2O-poor, halogen (F, Cl), alkali (Na, K) bearing dolomitic melts, which contain varying amounts of alkali-earths (Ba, Sr), phosphorus and sulphur.

In summary, this study supports the notion of that kimberlites originated from essentially transitional silica-carbonate or even carbonatite melts. This is a paradigm shift away from the previously proposed H_2O-bearing 'ultramafic' compositions of kimberlite melts. A silica-carbonate or carbonatitic, as opposed to ultramafic kimberlite melt, can help to explain numerous characteristics of kimberlite petrogenesis, such as rapid magmatic ascent (i.e. due to wetting properties and low viscosity of carbonate melts) and massive exsolution of CO_2, which can be facilitated by a more buoyant carbonate-rich melt.

12.4 Kimberlites and diamonds

It is widely accepted that diamonds are xenocrysts in kimberlites and that their genesis is not directly related to the generation of kimberlite magmas (Kramers, 1979; Gurney et al., 2010). However, cubic fibrous diamonds and occasionally gem quality diamonds commonly contain inclusions of high density fluids (HDF), which are interpreted to represent the diamond growth medium (Izraeli et al., 2001; Klein-BenDavid et al., 2007, 2009; Tomlinson et al., 2006; Weiss et al., 2011; Zedgenizov et al., 2018). Four main endmembers of HDFs are identified: high-Mg and low-Mg carbonatitic, siliceous and saline, all of which are enriched in alkalis. The origin of saline (i.e. Na-K-bearing) fluids in the lithospheric mantle is thought to originate from subducting seawater hosted in oceanic crust (Weiss et al., 2015; Kendrick et al., 2017). Recent experimental studies have shown that alkali-chlorides are stable within the lithospheric mantle and were likely derived from subducted marine sediments reacting with mantle peridotite (Förster et al., 2019), which in turn may explain the origin of Mg-carbonates and saline fluids commonly found in diamond-hosted inclusions as well as in Cl-enriched kimberlite magmas, such as Udachnaya-East. The striking similarity between HDF inclusions in diamonds and melt inclusions hosted in kimberlitic minerals kindles the idea that there may be common Na-K and Cl enriched source in the mantle.

12.5 Future Research

The fashion in which we think changes like the fashion of our clothes and it is difficult if not impossible for most people to think otherwise than in the fashion of their own period.

George Bernard Shaw

Throughout the course of this study, several avenues for future research were identified:

1. Development of improved methodologies to accurately reconstruct bulk compositions of inclusions in kimberlitic minerals.

Although melt/fluid inclusions provide snapshots of the composition of the kimberlite melt at a particular stage of its evolution, accurate quantitative analyses of their composition is hampered due to: i) the extremely small sizes of inclusions, ii) exposed inclusions are a only a two dimensional representation and may have lost and fluid/gas phases during polishing, iii) instrument limitations (e.g., beam damage to phases, secondary fluorescence of neighbouring phases, anisotropic beam scatter) during analyses, iv) inclusions are unable to be successfully quenched into glasses, v) inclusions are extremely heterogeneous and thus any method of study would require a statistically high number of analyses. Taking into consideration all these obstacles, accurate quantification of melt inclusions is fundamental to understanding the compositions of kimberlite melts prior to emplacement and/or alteration.

2. Resolving the origin and evolution of olivine through zoning patterns and inclusion studies.

The most recent studies of olivine zoning patterns and inclusions (e.g., Giuliani, 2018; Howarth and Taylor, 2016; Lim et al., 2018; Chapters 9 and 10) have revealed remarkable insights into how olivine may preserve a remarkable record of kimberlite magma evolution. Further detailed studies of zoning, trace element distributions and the compositions and types of inclusions in olivine may hold fundamental insights into the stages of olivine growth, and thus enable more clear insights into the early evolution of kimberlite magma systems, especially at mantle depths.

3. Pursuit of pristine kimberlite rocks.

A significant problem encountered throughout this study and all previous works is that almost all kimberlites are serpentinised to some extent. Even in the Mark kimberlite, which contains extremely well-preserved olivine and groundmass minerals, the presence of mesostasis serpentine and brucite still suggests that some low temperature hydrous alteration occurred. The Udachnaya-East kimberlite, despite the absence of serpentinisation in some units, is still considered largely by the geological community to be a petrological 'anomaly' due to its atypical mineralogy and uniqueness. Discovery of a 'truly' unaltered, or another Udachnaya-East-like kimberlite, or even witnessing an active kimberlite eruption may only be a fantasy, but could provide the necessary answers to the kimberlite petrogenesis conundrum.

4. Constraining the abundances and role of volatiles in kimberlite melts.

One of the key findings from melt inclusion studies of kimberlitic minerals is that alkalis and halogens appear to be enriched relative to the kimberlite whole-rock. The majority of alkalis and halogens are inferred to have been removed from the kimberlite groundmass due to their partitioning into water-soluble minerals (e.g., carbonates, chlorides; Kamenetsky et al., 2009a; 2014) and/or exsolution during ascent and/or emplacement (Giuliani et al., 2017; Soltys et al., 2018). Therefore, it is likely that alkalis and halogens existed in appreciably higher abundances in the parental kimberlite melt, but their potential concentrations remain unconstrained. Elucidating the concentrations of alkalis and halogens, as well as CO_2 and more importantly H_2O-content, of parental melts is be important in understanding aspects of kimberlite petrogenesis, such as how they influence temperatures and pressures of melting in the mantle (e.g., Brey et al., 2009; Dasgupta and Hirschmann, 2006).

12.6 References

Brey, G.P., Bulatov, V.K., Girnis, A.V., 2009. Influence of water and fluorine on melting of carbonated peridotite at 6 and 10 GPa. Lithos 112, 249-259.

Brooker, R., Sparks, R., Kavanagh, J., Field, M., 2011. The volatile content of hypabyssal kimberlite magmas: some constraints from experiments on natural rock compositions. Bulletin of Volcanology 73, 959-981.

Chen, W., Kamenetsky, V.S., Simonetti, A., 2013. Evidence for the alkaline nature of parental carbonatite melts at Oka complex in Canada. Nat Commun 4, 2687.

Dasgupta, R., Hirschmann, M.M., 2006. Melting in the Earth's deep upper mantle caused by carbon dioxide. Nature 440, 659-62.

Dawson, J.B., 1993. A Supposed Sövite from Oldoinyo Lengai, Tanzania: Result of Extreme Alteration of Alkali Carbonatite Lava. Mineralogical Magazine 57, 93-101.

Dawson, J.B., Garson, M.S., Roberts, B., 1987. Altered former alkalic carbonatite lava from Oldoinyo Lengai, Tanzania: inferences for calcite carbonatite lavas. Geology 15, 765-768.

Fedortchouk, Y., Canil, D., 2004. Intensive Variables in Kimberlite Magmas, Lac de Gras, Canada and Implications for Diamond Survival. Journal of Petrology 45, 1725-1745.

Förster, M.W., Foley, S.F., Marschall, H.R., Alard, O., Buhre, S., 2019. Melting of sediments in the deep mantle produces saline fluid inclusions in diamonds. Science Advances 5, eaau2620.

Giuliani, A., 2018. Insights into kimberlite petrogenesis and mantle metasomatism from a review of the compositional zoning of olivine in kimberlites worldwide. Lithos 312-313, 322-342.

Giuliani, A., Phillips, D., Kamenetsky, V.S., Fiorentini, M.L., Farquhar, J., Kendrick, M.A., 2014. Stable isotope (C, O, S) compositions of volatile-rich minerals in kimberlites: A review. Chemical Geology 374-375, 61-83.

Giuliani, A., Soltys, A., Phillips, D., Kamenetsky, V.S., Maas, R., Goemann, K., Woodhead, J.D., Drysdale, R., Griffin, W.L., 2017. The final stages of kimberlite petrogenesis: Petrography, mineral chemistry, melt inclusions and Sr-C-O isotope geochemistry of the Bultfontein kimberlite (Kimberley, South Africa). Chemical Geology 455, 342-356.

Golovin, A.V., Sharygin, I.S., Korsakov, A.V., 2017. Origin of alkaline carbonates in kimberlites of the Siberian craton: Evidence from melt inclusions in mantle olivine of the Udachnaya-East kimberlite. Chemical Geology 455, 357-375.

Golovin, A.V., Sharygin, V.V., Pokhilenko, N.P., 2007. Melt inclusions in olivine phenocrysts in unaltered kimberlites from the Udachnaya-East pipe, Yakutia: Some aspects of kimberlite magma evolution during late crystallization stages. Petrology 15, 168-183.

Golovin, A.V., Sharygin, V.V., Pokhilenko, N.P., Mal kovets, V.G., Kolesov, B.A., Sobolev, N.V., 2003. Secondary Melt Inclusions in Olivine from Unaltered Kimberlites of the Udachnaya-East Pipe, Yakutia. Doklady Earth Sciences 388, 93-96.

Gurney, J.J., Helmstaedt, H.H., Richardson, S.H., Shirey, S.B., 2010. Diamonds through time. Economic Geology 105, 689-712.

Guzmics, T., Mitchell, R.H., Szabó, C., Berkesi, M., Milke, R., Abart, R., 2011. Carbonatite melt inclusions in coexisting magnetite, apatite and monticellite in Kerimasi calciocarbonatite, Tanzania: melt evolution and petrogenesis. Contributions to Mineralogy and Petrology 161, 177-196.

Howarth, G.H., Taylor, L.A., 2016. Multi-stage kimberlite evolution tracked in zoned olivine from the Benfontein sill, South Africa. Lithos 262, 384-397.

Izraeli, E.S., Harris, J.W., Navon, O., 2001. Brine inclusions in diamonds: a new upper mantle fluid. Earth and Planetary Science Letters 187, 323-332.

Kamenetsky, M.B., Sobolev, A.V., Kamenetsky, V.S., Maas, R., Danyushevsky, L.V., Thomas, R., Pokhilenko, N.P., Sobolev, N.V., 2004. Kimberlite melts rich in alkali chlorides and carbonates: A potent metasomatic agent in the mantle. Geology 32, 845-848.

Kamenetsky, V.S., Golovin, A.V., Maas, R., Giuliani, A., Kamenetsky, M.B., Weiss, Y., 2014. Towards a new model for kimberlite petrogenesis: Evidence from unaltered kimberlites and mantle minerals. Earth-Science Reviews 139, 145-167.

Kamenetsky, V.S., Grutter, H., Kamenetsky, M.B., Goemann, K., 2013. Parental carbonatitic melt of the Koala kimberlite (Canada): Constraints from melt inclusions in olivine and Cr-spinel, and groundmass carbonate. Chemical Geology 353, 96-111.

Kamenetsky, V.S., Kamenetsky, M.B., Golovin, A.V., Sharygin, V.V., Maas, R., 2012. Ultrafresh salty kimberlite of the Udachnaya-East pipe (Yakutia, Russia): A petrological oddity or fortuitous discovery? Lithos 152, 173-186.

Kamenetsky, V.S., Kamenetsky, M.B., Weiss, Y., Navon, O., Nielsen, T.F.D., Mernagh, T.P., 2009a. How unique is the Udachnaya-East kimberlite? Comparison with kimberlites from the Slave Craton (Canada) and SW Greenland. Lithos 112S, 334-346.

Kamenetsky, V.S., Maas, R., Kamenetsky, M.B., Paton, C., Phillips, D., Golovin, A.V., Gornova, M.A., 2009b. Chlorine from the mantle: Magmatic halides in the Udachnaya-East kimberlite, Siberia. Earth and Planetary Science Letters 285, 96-104.

Kendrick, M.A., Hémond, C., Kamenetsky, V.S., Danyushevsky, L., Devey, C.W., Rodemann, T., Jackson, M.G., Perfit, M.R., 2017. Seawater cycled throughout Earth's mantle in partially serpentinized lithosphere. Nature Geoscience 10, 222-228.

Klein-BenDavid, O., Izraeli, E.S., Hauri, E., Navon, O., 2007. Fluid inclusions in diamonds from the Diavik mine, Canada and the evolution of diamond-forming fluids. Geochimica et Cosmochimica Acta 71, 723-744.

Klein-BenDavid, O., Logvinova, A.M., Schrauder, M., Spetius, Z.V., Weiss, Y., Hauri, E.H., Kaminsky, F.V., Sobolev, N.V., Navon, O., 2009. High-Mg carbonatitic microinclusions in some Yakutian diamonds—a new type of diamond-forming fluid. Lithos 112, 648-659.

Kopylova, M.G., Gaudet, M., Kostrovitsky, S.I., Polozov, A.G., Yakovlev, D.A., 2016. Origin of salts and alkali carbonates in the Udachnaya East kimberlite: Insights from petrography of kimberlite phases and their carbonate and evaporite xenoliths. Journal of Volcanology and Geothermal Research 327, 116-134.

Kopylova, M.G., Kostrovitsky, S.I., Egorov, K.N., 2013. Salts in southern Yakutian kimberlites and the problem of primary alkali kimberlite melts. Earth-Science Reviews 119, 1-16.

Kostrovitskiy, S.I., Kopylova, M.G., Egorov, K.N., Yakovlev, D.A., 2013. The Exceptionally Fresh Udachnaya-East Kimberlite: Evidence for Brine and Evaporite Contamination. In: Pearson, D.G., et al. (Eds.), Proceedings of the 10th International Kimberlite Conference, 75-91.

Kramers, J.D., 1979. Lead, uranium, strontium, potassium and rubidium in inclusion-bearing diamonds and mantle-derived xenoliths from Southern Africa. Earth and Planetary Science Letters 42, 58-70.

Lim, E., Giuliani, A., Phillips, D., Goemann, K., 2018. Origin of complex zoning in olivine from diverse, diamondiferous kimberlites and tectonic settings: Ekati (Canada), Alto Paranaiba (Brazil) and Kaalvallei (South Africa). Mineralogy & Petrology 112, 539–554.

Mernagh, T.P., Kamenetsky, V.S., Kamenetsky, M.B., 2011. A Raman microprobe study of melt inclusions in kimberlites from Siberia, Canada, SW Greenland and South Africa. Spectrochimica Acta Part A: Molecular and Biomolecular Spectroscopy 80, 82-87.

Mitchell, R.H., 2008. Petrology of hypabyssal kimberlites: Relevance to primary magma compositions. Journal of Volcanology and Geothermal Research 174, 1-8.

Mitchell, R.H., 2013. Oxygen isotope studies of serpentine in kimberlite, Proceedings of the 10th International Kimberlite Conference. Geological Society of India, Bangalore, pp. 1-12.

Moussallam, Y., Morizet, Y., Gaillard, F., 2016. H2O–CO2 solubility in low SiO2-melts and the unique mode of kimberlite degassing and emplacement. Earth and Planetary Science Letters 447, 151-160.

Soltys, A., Giuliani, A., Phillips, D., 2018. A new approach to reconstructing the composition and evolution of kimberlite melts: A case study of the archetypal Bultfontein kimberlite (Kimberley, South Africa). Lithos 304-307, 1-15.

Sparks, R.S.J., Baker, L., Brown, R.J., Field, M., Schumacher, J., Stripp, G., Walters, A., 2006. Dynamical constraints on kimberlite volcanism. Journal of Volcanology and Geothermal Research 155, 18-48.

Sparks, R.S.J., Brooker, R.A., Field, M., Kavanagh, J., Schumacher, J.C., Walter, M.J., White, J., 2009. The nature of erupting kimberlite melts. Lithos 112S, 429-438.

Stripp, G.R., Field, M., Schumacher, J.C., Sparks, R.S.J., Cressey, G., 2006. Post-emplacement serpentinization and related hydrothermal metamorphism in a kimberlite from Venetia, South Africa. Journal of Metamorphic Geology 24, 515-534.

Tomlinson, E.L., Jones, A.P., Harris, J.W., 2006. Co-existing fluid and silicate inclusions in mantle diamond. Earth and Planetary Science Letters 250, 581-595.

Weiss, Y., Griffin, W.L., Bell, D.R., Navon, O., 2011. High-Mg carbonatitic melts in diamonds, kimberlites and the sub-continental lithosphere. Earth and Planetary Science Letters 309, 337-347.

Weiss, Y., McNeill, J., Pearson, D.G., Nowell, G.M., Ottley, C.J., 2015. Highly saline fluids from a subducting slab as the source for fluid-rich diamonds. Nature 524, 339-42.

Zaitsev, A., Keller, J., 2006. Mineralogical and chemical transformation of Oldoinyo Lengai natrocarbonatites, Tanzania. Lithos 91, 191-207.

Zaitsev, A.N., Wenzel, T., Vennemann, T., Markl, G., 2013. Tinderet volcano, Kenya: an altered natrocarbonatite locality? Mineralogical Magazine 77, 213-226.

Zaitsev, A.N., Williams, C.T., Britvin, S.N., Kuznetsova, I.V., Spratt, J., Petrov, S.V., Keller, J., 2010. Kerimasite, Ca3Zr2(Fe3+2Si)O12, a new garnet from carbonatites of Kerimasi volcano and surrounding explosion craters, northern Tanzania. Mineralogical Magazine 74, 803-820.

Zedgenizov, D.A., Ragozin, A.L., Shatsky, V.S., Griffin, W.L., 2018. Diamond formation during metasomatism of mantle eclogite by chloride-carbonate melt. Contributions to Mineralogy and Petrology 173.